*Author:*
**Hughes, Ery**

*Title:*
**Microanalytical techniques and experimental studies of the volatile and fO2 history of magmas using melt inclusions**

# MICROANALYTICAL TECHNIQUES AND EXPERIMENTAL STUDIES OF THE VOLATILE AND $fO_2$ HISTORY OF MAGMAS USING MELT INCLUSIONS


Ery C. Hughes

Supervisors: Jon D. Blundy, Heidy M. Mader, and Geoff Kilgour

A dissertation submitted to the University of Bristol in accordance with the requirements for award of the degree of Doctor of Philosophy in the Faculty of Science

School of Earth Sciences

March 1, 2019

Word Count:

46,227

# ABSTRACT

Melt inclusions are tiny pockets of melt trapped inside crystals, which allow us to sample the magma prior to eruption. Melt inclusion chemistry is used to infer magmatic processes that can help us to understand eruption dynamics and the role of volcanoes in the global volatile cycle. This thesis addresses three gaps in our current use of melt inclusions, which will help us to measure the oxygen fugacity and volatile content of magmas.

Firstly, many melt inclusions are too small to analyse for $H_2O$ concentration using most microanalytical techniques. The electron probe is able to estimate the $H_2O$ concentration of such melt inclusions using the volatiles by difference (VBD) technique, but a review of the literature data ($n$ = 524) reveals that VBD consistently overestimates $H_2O$ concentrations by $\sim$1 wt% for hydrous silicate glass ($>$2 wt% $H_2O$). Monte Carlo modelling using Win X-ray shows that the effects of sub-surface charging, whereby electrons are trapped within the glass structure during EPMA and impose an electric field in the sample, can account for this discrepancy. An accuracy of $\pm$0.1 wt% on VBD can be achieved by calibrating VBD using hydrous glass standards.

Secondly, the only technique currently available to measure the Fe oxidation state of melt inclusions (which is a proxy for oxygen fugacity) requires access to a synchrotron. Here, a technique using the electron probe is presented, which is much more widely accessible. The technique can be applied to basaltic and peralkaline hydrous glass compositions, which contain $FeO_T > 5$ wt%. The precision on $Fe^{2+}/Fe_T$ is $\pm$0.03 (10 wt% $FeO_T$ and 0.5 $Fe^{2+}/Fe_T$) and the accuracy is $\pm$0.1, at a spatial resolution of $\sim$20–60 $\mu$m. The controls on electron beam induced redox changes in silicate glass during analysis are also investigated.

Finally, carbon concentration measurements of melt inclusions alone are not able to constrain the initial carbon concentration of magmas. Groundwork towards using measurements of carbon isotope ratios of hydrous basaltic glasses are carried out, both technically using SIMS and experimentally to constrain key parameters required for interpreting natural data. Three new hydrous, carbon-rich, basaltic glass $\delta^{13}C$ standards have been characterised as no basaltic glass standards of this type were previously available.

A correlative microanalysis study of melt inclusions (and minerals) from the 23 November 2013 paroxysmal eruption of Etna was undertaken using these new techniques and others such as Raman and SIMS. This is the first geochemical data available on this eruption, and the only melt inclusion data for the 2011–2013 eruptive sequence. An injection of deeper, more primitive magma mixed with a shallower, more evolved magma, which likely triggered the event. The melt composition is intermediate between the highly explosive, flank eruptions of 2001 and 2002–2003 and the effusive eruptions in 2004–2007. The volatile isotope data are consistent with other data available for Etna.

# Author's declaration

I declare that the work in this dissertation was carried out in accordance with the requirements of the University's Regulations and Code of Practice for Research Degree Programmes and that it has not been submitted for any other academic award. Except where indicated by specific reference in the text, the work is the candidate's own work. Work done in collaboration with, or with the assistance of, others, is indicated as such. Any views expressed in the dissertation are those of the author.

Ery C. Hughes

March 1, 2019

# Acknowledgments

This Ph.D. was funded by a NERC GW4+ DTP and GNS Science CASE-funded scholorship (NE/L002434/1). The SIMS analysis was funded by a NERC Ion Micro-probe grant (IMF560/0515). I would like to also thank the European Microbeam Analysis Society, Microbeam Analysis Society, Deep Carbon Observatory, and Geoscience Society of New Zealand for additional funding that allowed me to attend many fantastic conferences and workshops to present my work and meet so many amazing people.

My supervisors have been fantasic and I am truely grateful for their help during my PhD. Thank you to Jon for all the ideas and eternal optimism in the data; to Heidy for all the advice and making my writing understandabl; and to Geoff for all the fun in the field and keeping things realistic.

This project would not have been possible without the help and expertise from all the different institutions I was lucky enough to work with. Firstly, those at the University of Bristol: I'd like to say a massive thank you to Stu Kearns and Ben Buse for teaching me how to use the electron probe, putting up with a lot of questions, and introducting me to the microanalysis community. Richard Brooker for working out how we were going to do the necessary experiments, always having the right extra samples and, if not, going out and collecting them. Danilo di Genova for all your help interpretting Raman spectra and lending me so many samples, as well as Jenny Riker. Charles Clapham for making the many mini-mounts required for individual melt inclusion prep and the probe mount so I could analyse them. Serginio Remmelzwaal for helping to prepare the Seaford Head Chalk carbonate. At the Edinburgh Ion Micro-probe facility, I'd like to thank Richard Hinton and John Craven (Smudge Cat) for putting up with me for many weeks, not giving up on my analysis, and providing me with whiskey. At IPGP, Pierre Cartigny for teaching me how to run SHMS and letting me come back after the kit broke within a week of me arriving. At Leibniz Universitat Hannover, Roman Botcharnikov and Robert Balzer for running my IHPV experiments (mostly) successfully and David Neave for swooping in at the last moment to run the last set for me; Renat Almeev for lending me the most amazing set of standards; and Stephen Schuth for teaching me how to use the CSA. At the University of Oregon, Ilya Bindemann for collecting all the TCEA data for me. The late David Hilton for giving me the first carbon isotope standard we had. At Cardiff University, Alexander Nederbragt for analysing the $\delta^{13}C$ of the starting carbonates. At INGV, Catania, Daniele Andronico for collecting the Etna samples for me. Although none of the data ended up in thesis, a big thank you goes to those at GNS Science (+ interns) who helped me collect samples and data during my fieldwork and internship: Agnes Mazot, Cam Asher, Yves Feisel, and Marco Michelini; and to Ken Raureti (and the Ruwahia 2B tribe) for welcoming me onto Tarawera. And all the awesome people who kept me company when I was away attempting to collect data. And of course, thank you to the volcanology and petrology group at Bristol for being awesome.

A massive thank you goes to Becky, Ryan, Keri, Nicky, Neil, Emily, and Serginio. I couldn't have done it without you guys, you have been the best over the last four years and have made my time at Bristol amazing. Also, a thanks to my housemates Jack and Jeroen for keeping me grounded and reminding me there is a life outside of the PhD. Finally, a thank you to my parents for getting me into science.

# Contents

# List of Figures

# List of Tables

# Chapter 1

# Introduction

## 1.1. Aims and motivation

The aim of this thesis is to provide new techniques to quantify the oxygen fugacity ($fO_2$) and volatile composition (carbon and hydrogen) of magmas prior to eruption. These are key parameters required to understand the global volatile cycle and the dynamics of volcanic eruptions. This study focuses on microanalytical techniques that are used to analyse melt inclusions, tiny pockets of melt trapped inside crystals, which sample the magma during its ascent to the surface prior to eruption. Specifically, techniques are developed to analyse Fe oxidation state (which is a proxy for $fO_2$), hydrogen concentration, and initial carbon composition (using carbon isotope ratios) in basaltic magmas.

Melt inclusion analysis is often used to reconstruct the volatile content and $fO_2$ of magmas. However, there are two problems with this approach: (a) many eruptions contain crystals which only have small melt inclusions (e.g., $<$20 μm in diameter), which are too small to analyse using microanalytical techniques required for volatile analysis (e.g., SIMS and FTIR); and (b) the long-standing problem that the $CO_2$ concentration measured in these melt inclusions would not represent the initial $CO_2$ due to the low solubility of $CO_2$ in silicate melts and hence the possibility of degassing prior to melt inclusion trapping (e.g., Blundy et al., 2010; Wallace, 2005; Anderson and Brown, 1993). Therefore, in order to combat these problems, new analytical techniques are required to use melt inclusions to understand compositional changes prior to eruption.

Electron probe micro-analysis (EPMA) was chosen to analyse small melt inclusions. EPMA has excellent spatial resolution ($<$1 μm in diameter using a field-emission gun electron source) and can analyse almost all the elements required in melt inclusions, including many of the volatiles of interest (e.g., S, Cl, and F). However, H cannot be detected directly by EPMA as it only contains a single electron in its electronic configuration, and thus the H concentration is inferred using the 'volatiles by difference' (VBD) technique (e.g., Devine et al., 1995; Nash, 1992; King et al., 2002). In the VBD technique, all possible elements in the glass are analysed and the difference between the measured total and 100 wt% is assumed to be $H_2O$. However, Chapter 2 finds that EPMA literature data consistently overestimates $H_2O$ using VBD by $\sim$1 wt%. The effect of sub-surface charging during EPMA is modelled using the program Win X-ray (Demers and Gauvin, 2004; Gauvin et al., 2006). This shows that sub-surface charging can account for the overestimation of $H_2O$ concentration observed in the literature data. An empirical calibration curve produced during each analytical session can correct for this problem as described in Chapter 2.

Correct use of the VBD technique requires knowledge of the Fe oxidation state because oxygen is not typically measured during EPMA and is instead calculated using stoichiometry (e.g., Devine et al., 1995; Nash, 1992; King et al., 2002). Hence, an unknown Fe oxidation in the glass leads to large errors on VBD estimates. Fe oxidation state is also a proxy for $fO_2$, which is an important parameter to constrain in magmatic systems as it controls volatile element speciation, phase relations, and the physical properties of magma (e.g., Hamilton et al., 1964; Dingwell and Virgo, 1987; Kress and Carmichael, 1991; Vicenzi et al., 1994; Bouhifd et al., 2004; Wilke et al., 2005). Currently, the preferred technique for measuring the Fe oxidation state in melt inclusions is micro X-ray absorption near-edge structure (μXANES) spectroscopy (e.g., Cottrell et al., 2009), but this requires access to a synchrotron and cannot be used reliably on hydrous glass as it causes oxidation of the Fe during analysis (Cottrell et al., 2018). Chapter 3 develops a new technique for measuring Fe oxidation state using EPMA, which can be used on hydrous glass. The technique

is calibrated on a wide range of glass compositions and is applicable to both basaltic and peralkaline glasses. The discussion extends to considering the causes and mechanisms of electron beam damage during EPMA.

Stable isotope fractionation during degassing was investigated as a tool to estimate the initial carbon (and hydrogen) composition (concentration and isotope ratio) of magmas, and the style (equilibrium or disequilibrium, closed- or open-system) of magmatic degassing (e.g., Taylor, 1986; Pineau and Javoy, 1994, 1983; Macpherson and Mattey, 1994; Newman et al., 1988). Secondary ion mass spectrometry (SIMS) was chosen as the analytical technique because it can measure the concentration and isotope ratio of trace elements with high spatial resolution ($\sim$20 μm region in diameter) (e.g., Hauri et al., 2002; Hinton, 1995). Additionally, as SIMS sputters material from the surface during analysis, it can analyse elements such as carbon and hydrogen, which commonly suffer from surface contamination (e.g., Blundy and Cashman, 2008). A protocol for analysing carbon stable isotopes in basaltic glass using SIMS was developed, including producing $\delta^{13}C$ standards, and is discussed in Chapter 4. Chapter 5 presents attempts to determine, for the first time, the fractionation factor of carbon and hydrogen between exsolved fluid and melt in the system basalt-$H_2O$-$CO_2$, which is a fundamental parameter in stable isotope fractionation. Glasses were experimentally synthesised to simulate equilibrium, closed-system degassing and characterised for their carbon and hydrogen concentration and isotope ratios. The bulk volatile composition was modified by contamination (carbon) and infiltration during synthesis (hydrogen), hence the bulk volatile composition was calculated, rather than assumed using initial values. This chapter explores many of the technical issues involved in determining isotopic fractionation factors experimentally.

Etna is a well-studied volcano which provides a wealth of literature data for comparison, and crystals from Etna contain many, large melt inclusion. This makes it an ideal case study to apply the techniques developed during this thesis, which is discussed in Chapter 6. The 23 November 2013 eruption was one of the most explosive events of the 2011–2013 eruptive sequence and is thought to have been triggered by an injection of more primitive, volatile-rich magma (Bonaccorso et al., 2014). Magma mixing prior to eruption likely triggered the eruption, and the volatile concentration of the magma was intermediate between the highly explosive flank eruptions of 2001 and 2002–2003 (Métrich et al., 2004; Spilliaert et al., 2006) and the effusive eruptions in 2004–2006 (Collins et al., 2009).

To conclude, Chapter 7 discusses future avenues to improve the techniques developed in this thesis for melt inclusion analysis. The remainder of this introductory chapter is devoted to background information on magmatic systems and how melt inclusions can be used to unravel their histories. The importance of $fO_2$ and volatile composition as key parameters to the understanding of magmatic systems is covered. Additionally, the theory of stable isotope fractionation is discussed in relation to the magmatic degassing of volatiles. Specific details pertaining to individual chapters are covered in their respective introductions.

## 1.2. Magmatic systems

Magma is a multiphase material, which can contain melt, crystals and bubbles. The number of individual components, and their proportions and compositions, depends upon the intensive thermodynamic parameters imposed on the system, such as bulk composition, pressure, temperature, and $fO_2$. Understanding the history of the magma prior to eruption involves constraining these parameters, and how they change with time. This thesis looks in detail at constraining the $fO_2$ and volatile content of magmas.

### 1.2.1. Oxygen fugacity

Oxygen fugacity ($fO_2$) is equivalent to the equilibrium partial pressure that oxygen gas would have in the system. $fO_2$ varies by orders of magnitude within the Earth, from the core where metallic Fe is stable, to the surface where $Fe_2O_3$ is stable (e.g., Frost and McCammon, 2008). $fO_2$ is therefore a key variable in magmatic systems. It controls the valence state of multi-valent elements in silicate melts, the most important being Fe, which is present as both $Fe^{2+}$ and $Fe^{3+}$, although many trace elements (e.g., Mn, Cr, V, Ce, and Eu) are also multi-valent (e.g., Kennedy, 1948; Kress and Carmichael, 1991; Wilke et al., 2005; Vicenzi et al., 1994). Additionally, volatiles can have many valence states and as a result their speciation is controlled by $fO_2$ (e.g., Holloway and Blank, 1994). For instance, sulphur can be present as $H_2S$ to $SO_2$, carbon as $CH_4$ to $CO_2$, and hydrogen as $H_2$ to $H_2O$ in melts and the solubility of volatiles is a strong function of $fO_2$, hence $fO_2$ influences the degassing process (e.g., Sato, 1978; Mathez, 1984; Wallace and Carmichael, 1992; Moussallam et al., 2014).

$fO_2$ also impacts the chemical and physical properties of the magma. For instance, as $fO_2$ changes the Fe oxidation state of silicate melts, it changes the melt viscosity (e.g., Cukierman and Uhlmann, 1974; Dingwell and Virgo, 1987). This is because $Fe^{2+}$ and $Fe^{3+}$ occupy different structural roles in the melt as network modifier and former, respectively (e.g., Virgo and Mysen, 1985; Wilke et al., 2005), therefore changes in their relative proportions affects the viscosity. As minerals have charge-balanced compositions, the amount of $Fe^{2+}$ and $Fe^{3+}$ they can accommodate is dictated by their chemical formula. Therefore, $fO_2$ changes the mineral assemblage stable at specific pressures and temperatures (e.g., Hamilton et al., 1964; Carmichael and Ghiorso, 1990). This will additionally affect the magma rheology because crystallisation (timing and phase sequence) has a large impact on magma viscosity (e.g., Bouhifd et al., 2004).

$fO_2$ is thought to be inhomogeneous within the mantle, hence different magmatic systems may have different initial $fO_2$. For instance, arc magmas are more oxidised than MORB magmas due to the influence of the subducting plate (e.g., Osborn, 1959; Wood et al., 1990; Cottrell and Kelley, 2011; Grocke et al., 2016; Kelley and Cottrell, 2009). Inhomogeneity can also be inherited from previous subduction, and can therefore be present within MORB (e.g., Arculus, 1985; Cottrell and Kelley, 2013; Shorttle et al., 2015). The $fO_2$ of magma can also be changed by magmatic processes. For instance, degassing changes the oxidation state of magmas in the shallow crust (e.g., Mathez, 1984; Moussallam et al., 2016, 2014).

As $fO_2$ is such an important parameter in magmatic systems, it is important to quantify its variation and there are many proxies for $fO_2$ based on measuring the effect $fO_2$ has on the system. These include, but are not limited to: the oxidation state of multivalent elements in minerals (e.g., $Fe^{2+}/Fe_T$ in spinel, Wood, 1990) or silicate glass (e.g., $Fe^{2+}/Fe_T$, Kress and Carmichael, 1991); changes in trace element partitioning resulting in changes in trace element ratios (e.g., V/Sc in basalts, Li and Lee, 2004) or partition coefficients (e.g., Ti between ilmenite-magnetite, Buddington and Lindsley 1964; and V between olivine-liquid, Canil 1997); changes in oxidation state cause stable isotope fractionation, hence stable isotope ratios of multi-valent elements can also be used (e.g., $\delta^{57/54}$Fe, Williams et al., 2004).

### 1.2.2. Volatiles

Magmatic systems are an integral part of the global volatile cycle (e.g., C, H, S, Cl, and F), transferring volatiles from the mantle to the atmosphere (e.g., Jambon, 1994; Fischer, 2008; Burton et al., 2013, for

reviews). Volatiles are incompatible in most minerals and thus partition strongly into the melt during mantle melting. These melts are buoyant, and therefore migrate through the crust, sometimes erupting at the surface. The solubility of volatiles varies strongly as a function of pressure, therefore during ascent through the crust, volatiles exsolve from the melt to form an additional fluid phase (e.g., Burnham, 1979; Holloway, 1981). Carbon has the lowest solubility of the major volatile species and so exsolves first, which provides bubbles into which other volatiles may partition (e.g., Mysen et al., 1975; Blank and Brooker, 1994; Ni and Keppler, 2013). Volatiles reach the surface through cracks in the crust resulting in wide areas of diffusive degassing, often surrounding volcanoes (e.g., Allard et al., 1991; Baubron et al., 1990). Alternatively, volatiles can reach the surface through the volcanic conduit, either coupled to the melt during eruptions or decoupled from the melt during passive degassing (e.g., Burton et al., 2013, for a review). These volatiles can have significant impacts once in the atmosphere. For instance, carbon degassed from volcanoes is an important component of the global carbon cycle, which regulates the Earth's temperature (e.g., Walker et al., 1981). Magmatic degassing of carbon also influences the carbon redox balance in the Earth and the amount of organic carbon buried (e.g., Mason et al., 2017). Additionally, the sulphur output during volcanic eruptions can cause global temperature to decrease due to the properties of sulphur aerosols in the atmosphere (e.g., Pyle et al., 1996).

Volatiles also play a critical role in the eruption dynamics of volcanoes (e.g., Wilson et al., 1980; Huppert and Woods, 2002; Papale et al., 1998; Papale, 1999). During ascent to the surface, volatiles saturate and nucleate as bubbles which expand and grow as the pressure decreases, driving eruptions (e.g., Sparks, 1978). These volatiles then escape from the magma, either explosively during fragmentation or as they decouple from the magma. High concentrations of volatiles, such as $H_2O$ and $CO_2$, are associated with explosive eruptions. For instance, at Axial seamount on the Juan de Fuca Ridge, high $CO_2$ concentrations in the magma have been measured in explosive submarine eruptions (Helo et al., 2011). At Cerro Negro, magma that stalled at higher pressures pre-eruption, (and therefore retained higher volatile contents of both $H_2O$ and $CO_2$ pre-eruption), erupted more explosively than magma that reached shallower depths pre-eruption and lost these volatiles (Roggensack, 1997). Externally added volatiles can also enhance explosivity. For instance, $H_2O$ added to the system from surface water, the sea, and glaciers, can produce highly explosive phreatomagmatic eruptions, whilst external $CO_2$ from decarbonation of country rocks can add volatiles prior to magma reaching the surface (e.g., Lorenz, 1987; Freda et al., 2011). High volatile concentrations do not necessarily dictate the eruption style, as style of degassing (closed- vs open-system) is also important (see Cassidy et al., 2018, for a review).

Additionally, volatiles have a profound effect on the viscosity of magmas. Viscosity is a key parameter controlling the explosivity of eruption as it affects the degassing style, ascent rate and fragmentation mechanism (e.g., Wilson et al., 1980; Dingwell, 1996; Zhang, 1999; Namiki and Manga, 2008). Dissolved volatiles have a major impact on the viscosity of melts, for instance $H_2O$ which changes melt viscosity by orders of magnitude as it depolymerises the melt structure (e.g., Shaw, 1963; Friedman et al., 1963; Di Genova et al., 2013). Degassing produces bubbles, which either decrease or increase the magma viscosity with increasing bubble proportion, depending on the flow regime; and induces crystallisation, which generates crystals that increase the viscosity of the magma (see Mader et al., 2013, for a review).

As volatiles can decouple from the melt, they can reach the surface without magma erupting. This can be used to probe the magma prior to eruption and gas emissions are often used to monitor volcanoes (e.g.,

Galle et al., 2010). For instance, changes in the absolute concentration, isotope ratio, redox state, and relative proportion of volatile species has been used to infer changes in the magmatic system (e.g., Martini, 1996). Increases in $CO_2$, or $CO_2$/S ratios, are linked to deep injections of new, primitive, volatile-rich magma in the system because carbon exsolves at high pressures (e.g., Roberge et al., 2009). This loss of volatiles to the atmosphere precludes the use of bulk rock samples in studies of the volatile history of magmas. While gas emissions can be analysed from currently active volcanoes, understanding past eruptions requires melt inclusion analysis.

## 1.3. Mineral-hosted melt inclusions

Melt inclusions are small pockets of melt (1–100 μm in diameter), trapped inside crystals as they grow from the magma (e.g., Sorby, 1858; Roedder, 1979) (Figure 1.1). They provide a unique opportunity to sample the magma from various depths throughout the magmatic plumbing system, prior to eruption. Melt inclusions form in a variety of ways (Figure 1.1, after Roedder, 1979) and can be primary or secondary in origin, depending on whether the crystal surrounding the melt inclusion grew from the same melt or not. Primary processes include trapping melt during rapid growth of the crystal caused by supersaturation. Supersaturation can cause a rim of skeletal growth, (e.g., due to volatile loss, Figure 1.1a), or a skeletal/dendritic crystal to grow, (e.g., inhibited nucleation followed by rapid growth due to cooling, Figures 1.1b and c), which can trap melt inclusions when the crystal continues to grow subsequently (Roedder, 1979). Dissolution of the crystal, followed by overgrowth of the crystal, can trap melt inclusions as well (Figure 1.1d) (Roedder, 1979). Melt inclusions can be trapped where a different crystal is attached to the host-crystal surface, which disrupts subsequent crystal growth (Figure 1.1e) (Roedder, 1979). A crack in the crystal, which subsequently heals, is a secondary process that can trap melt inclusions (Figure 1.1f) (Roedder, 1979). If a melt inclusion does not completely isolate itself from the surrounding magma, it forms an embayment. As melt inclusions form at the host-mineral surface, they may not represent the bulk magma and instead represent a boundary layer composition. Fortunately, boundary layer diffusion is typically fast enough to prevent this (e.g., Lu et al., 1995).

### 1.3.1. Post-entrapment modification processes

At the time of melt inclusion entrapment, the composition and structure of the melt inclusion records the melt at that instance in time. However, there are a variety of processes that can modify the composition and structure of this melt post-entrapment (e.g., Roedder, 1979; Sorby, 1858; Danyushevsky et al., 2002, 2000; Di Genova et al., 2018; Gaetani et al., 2012; Nielsen et al., 1998; Steele-Macinnis et al., 2011). Post-entrapment modification can occur prior to, or after, eruption, when the melt inclusion is still liquid. This occurs as a consequence of changes in the composition of the surrounding magma; such as slow cooling at depth and in lava flows, or in response to degassing and crystallisation during ascent (e.g., Gaetani and Watson, 2000; Hartley et al., 2017, 2015; Moussallam et al., 2016, 2014). Modification post-entrapment can also occur on the quench as the melt inclusion passes through the glass transition (e.g., Di Genova et al., 2018).

There are different types of post-entrapment processes, which effect different aspects of the melt inclusion composition and structure (Figure 1.2). Continued crystallisation of the host mineral on the walls of the melt inclusion post-entrapment can change the melt composition, whereby compatible elements are depleted and

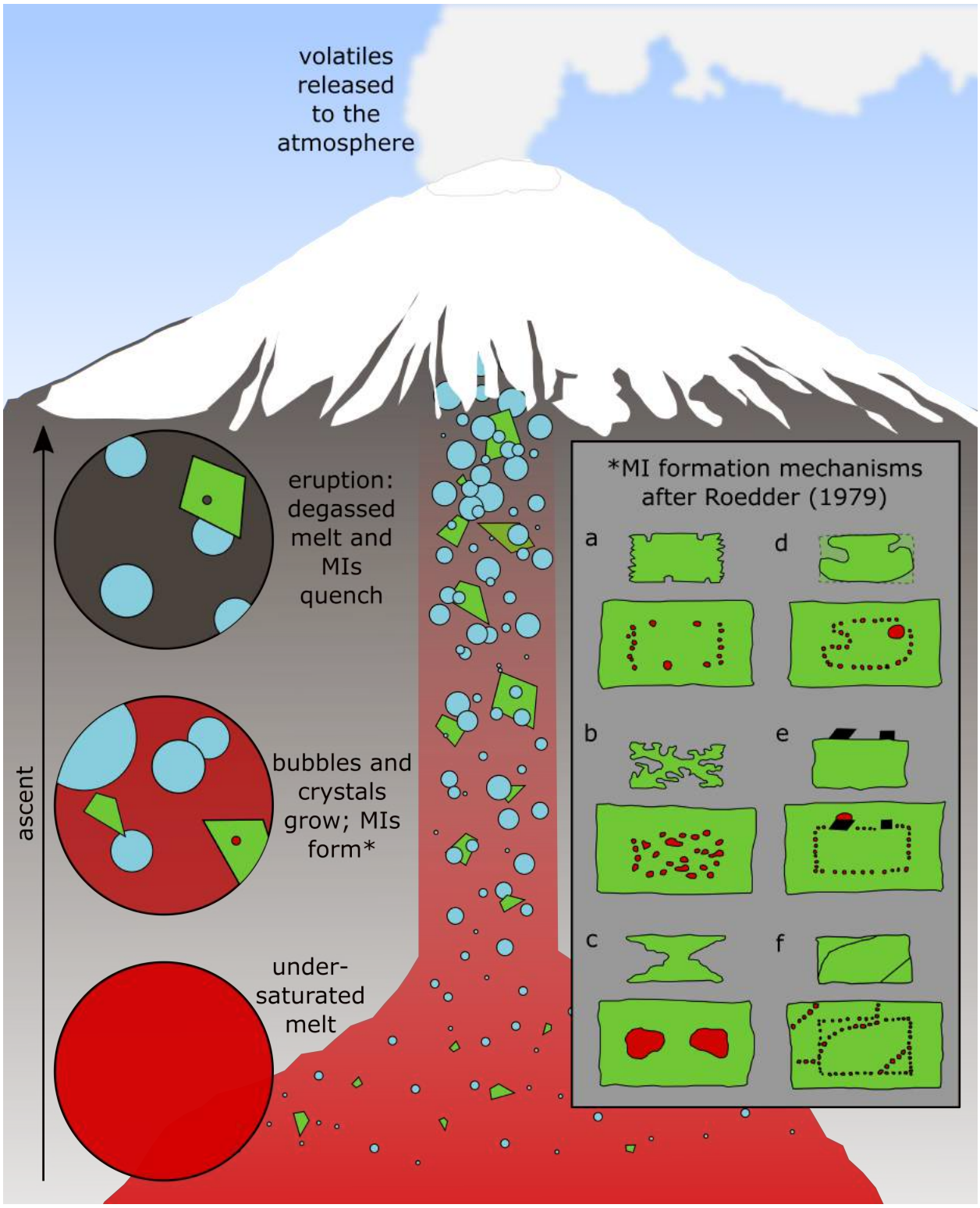


**Figure 1.1:** Schematic illustration of melt inclusion formation, and quenching, as the magma ascends and erupts. Trapping mechanisms included are after Roedder (1979): primary melt inclusions form due to crystal overgrowth of **(a)** a skeletal rim, **(b)** a dendritic crystal, **(c)** a hollow crystal, **(d)** previous dissolution of the crystal, **(e)** crystals attached to the host-crystal surface; and secondary melt inclusions form by **(f)** infilling of cracks that subsequently heal.

incompatible elements are enriched (e.g., Danyushevsky et al., 1988; Dungan and Rhodes, 1978; Gaetani and Watson, 2002; Nielsen et al., 1998; Sobolev and Shimizu, 1993; Witham et al., 2012). The melt inclusion can

diffusively re-equilibrate with its host-mineral, and even the surrounding magma through the host-mineral, which also changes the melt composition (e.g., Danyushevsky et al., 2000; Gaetani et al., 2012; Gaetani and Watson, 2002, 2000; Hartley et al., 2017, 2015). Pressure changes during ascent and cooling can cause the melt in the melt inclusion to shrink more than the host-crystal, which can lead to the formation of a bubble (e.g., Bucholz et al., 2013; Lowenstern, 2003, 1995; Maclennan, 2017; Métrich et al., 2009; Roedder, 1979; Sorby, 1858; Schiano, 2003). This bubble can sequester volatiles, resulting in the bubble becoming enriched, and the melt depleted, in those volatiles; this is especially important for volatiles with low solubility such as $CO_2$. Therefore, the glass volatile content of a melt inclusion may not represent the total volatile content of the melt at the time of entrapment. Furthermore, if the melt inclusion cools slowly, the melt inclusion can begin to, or even completely, crystallise (e.g., Tuttle, 1952; Hartley et al., 2017; Nielsen et al., 1998) and nanolites can precipitate during the quench (e.g., Di Genova et al., 2018, 2017a; Mujin et al., 2017; Mujin and Nakamura, 2014).

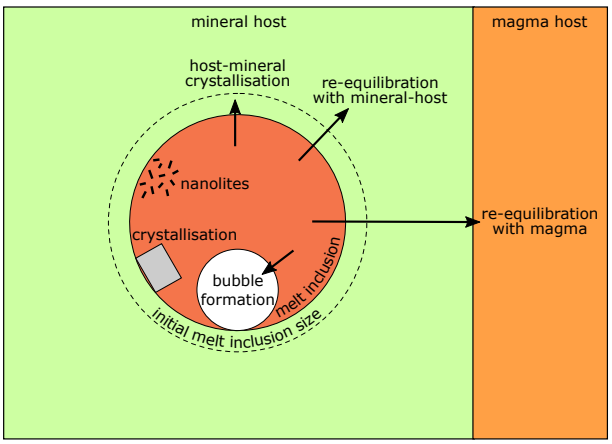


**Figure 1.2:** Schematic illustration of post-entrapment processes that can modify melt inclusion composition. The melt inclusion is shown in red, the host-mineral in green, and the host magma in orange. The initial size of the melt inclusion is shown by the black, dashed line, which becomes the size of the red melt inclusion due to continued crystallisation of the host-mineral on the inclusion walls. The composition of the melt inclusion can re-equilibrate with the host-mineral and the host-magma. Bubbles (white circle), crystals (grey rectangle), and nanolites (black lines) can exsolve from the melt within the melt inclusion as well. Black arrows show where species in the melt inclusion diffuse to during these processes.

### 1.3.2. Unravelling magmatic histories

Notwithstanding post-entrapment modification processes, melt inclusion chemistry can be used to unravel the history of the magma prior to eruption (see Blundy and Cashman, 2008; Métrich et al., 2009, for reviews). Major, minor and trace element concentrations are used to estimate the initial composition of the magma, fingerprint its source and identify the chronology and conditions (such as pressure and temperature) of mineral crystallisation (e.g., Watson, 1976; Kent, 2008; Michael and Cornell, 1998; Blundy and Cashman, 2008; Roedder, 1979). As the relationship between Fe oxidation state and $fO_2$ has been parameterised for temperature, pressure and melt composition, the Fe oxidation state of the melt can be used to calculate $fO_2$ (Kress and Carmichael, 1991). At constant $fO_2$, melt composition and pressure have a minor effect on the Fe oxidation state, but temperature has a dramatic effect (Figure 1.3).

The volatile (H, C, S, Cl, and F) concentrations of melt inclusions are used to estimate pressures of entrapment, volatile budgets of eruptions and degassing styles (e.g., Blundy and Cashman, 2008; Métrich et al., 2009; Sommer, 1977; Métrich and Clocchiatti, 1989; Clocchiatti, 1971). If the melt is fluid-saturated, the entrapment pressure can be calculated using melt $H_2O$ and $CO_2$ concentrations and a solubility model (e.g., Figure 1.4; VolatileCalc, Newman and Lowenstern 2002; SolEx, Witham et al. 2012; or MagmaSat, Ghiorso and Gualda 2015).

If melt inclusions trap undersaturated melt, the concentration of volatiles can be used to estimate the bulk

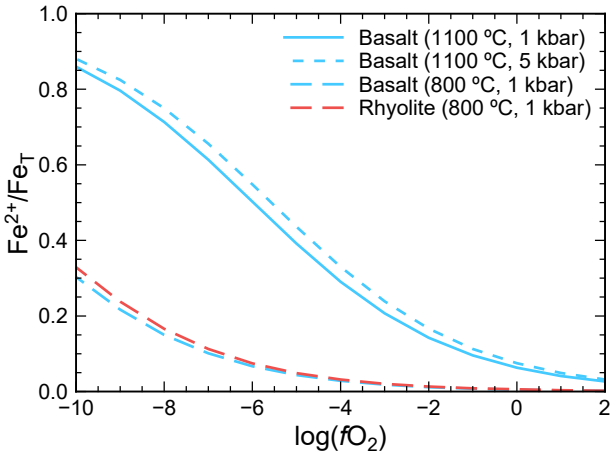


**Figure 1.3:** Effect of melt composition, temperature and pressure on Fe oxidation state ($Fe^{2+}/Fe_T$) at different $fO_2$. Fe oxidation state calculated using Kress and Carmichael (1991). The basaltic composition (blue) is Etna from Shishkina et al. (2014) and the rhyolitic composition (red) is Mount St Helens (DS-63) from Riker et al. (2015).

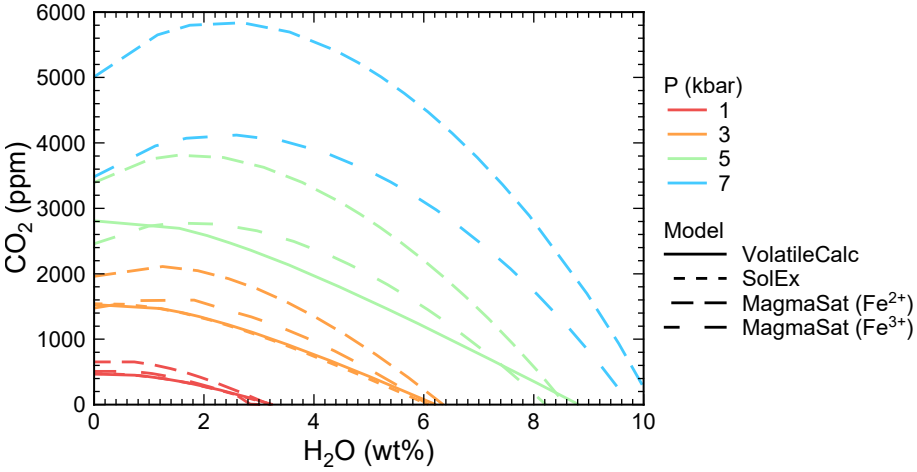


**Figure 1.4:** Isobars of $CO_2$ and $H_2O$ at 1250 °C using VolatileCalc, SolEx and MagmaSat for a basaltic melt. VolatileCalc is calcualted using 49 wt% $SiO_2$, whilst SolEx and MagmaSat are calcualted using the ETNA-A composition in Table 3.1. MagmaSat is calculated at the extremes of $Fe^{2+}/Fe_T$ (i.e., all $Fe^{2+}$ or all $Fe^{3+}$).

volatile content of the magma (e.g., Blundy and Cashman, 2008; Métrich et al., 2009). Often the highest measured concentration of the volatile in a suite of melt inclusions is used to represent the bulk concentration prior to degassing. This assumes that degassing, and the subsequent volatile loss, is the only process controlling the volatile concentration in the melt. However, if the melt was significantly undersaturated in volatiles before it began to crystallise, the concentration of volatiles would increase until volatile saturation was reached. This would lead to an overestimate of the bulk volatile concentration. Assuming the maximum measured concentration is equal to the bulk magma concentration is only appropriate for volatiles that have naturally low concentrations compared to their solubilities (e.g., S, Cl, F, and sometimes $H_2O$; Figure 1.5). Conversely, $CO_2$ has low solubility and potentially high concentrations in magmas, therefore it begins to exsolve at higher pressures than the onset of crystallisation (Figure 1.5). As a result, crystals are unlikely to trap melt inclusions with $CO_2$ concentrations representative of the original magma (e.g., Blundy et al., 2010; Wallace, 2005; Anderson and Brown, 1993). Additionally, large melt inclusions trapped at high pressures (which are easier to analyse and more likely to record high $CO_2$ concentrations) are most prone to decrepitation, which biases our sampling of $CO_2$ concentrations (Maclennan, 2017). This explains why the highest $CO_2$ concentrations measured in melt inclusions are insufficient to explain the $CO_2$ emissions from arc volcanoes (Wallace, 2005). Additionally, volatile concentration data alone makes it difficult to fingerprint the volatile source. For instance, carbon may come from the mantle or be added to the magma during interaction with basement limestone (e.g., Mason et al., 2017; Freda et al., 2011), which cannot be discriminated based on only $CO_2$ concentration.

The relationship between $H_2O$ and $CO_2$ concentrations in the melt depends upon the degassing style (Figure

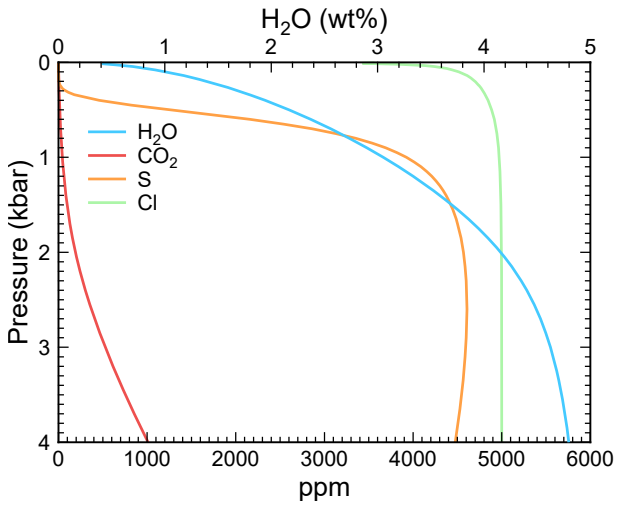


**Figure 1.5:** Changes to melt volatile concentrations ($H_2O$, $CO_2$, S, and Cl) with pressure using SolEx for a basaltic melt (composition of ETNA in Table 3.1) decompressing under closed-system conditions with initial volatile concentrations of 5 wt% $H_2O$, 5000 ppm $CO_2$, 5000 ppm S, and 5000 ppm Cl at 1250 °C and NNO+1.8. $H_2O$ concentration uses the top axis, whilst $CO_2$, S, and Cl concentrations used the bottom axis.

1.6). Equilibrium degassing requires the exsolved fluid and coexisting melt to maintain chemical equilibrium during changes to the intensive conditions of the system (e.g., pressure and temperature). Disequilibrium degassing occurs when chemical equilibrium is not maintained, likely due to slow diffusivities of the volatile species through the melt into the bubble (e.g., Javoy and Pineau, 1991; Aubaud et al., 2004; Pichavant et al., 2018). Even during disequilibrium degassing, local equilibrium may be achieved between the bubble and the directly surrounding melt. Even so, the bulk melt volatile concentration may not equal the equilibrium values (i.e., they will not lie on an isobar) and will be spatially heterogenous (e.g., Pichavant et al., 2018).

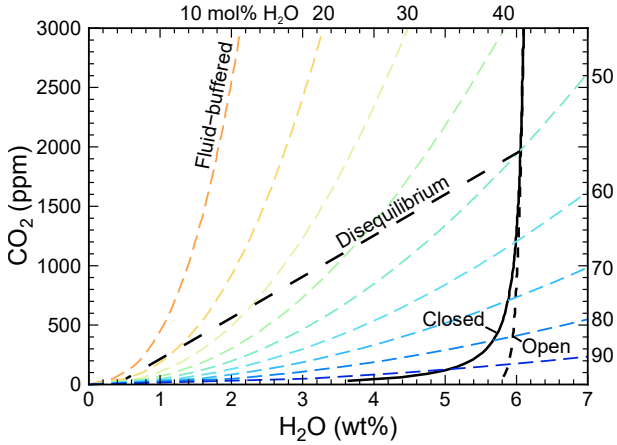


**Figure 1.6:** Equilibrium closed- (solid, black line) and open- (small-dashed, black line) system degassing trends, and isopleths (small-dashed, coloured lines) calculated using VolatileCalc (49 wt% $SiO_2$ and 1250 °C). The numbers on the isopleths (e.g., 20) refer to the composition of the coexisting fluid (i.e., 20 mol% $H_2O$ and 80 mol% $CO_2$). Disequilibrium closed-system degassing path (long-dashed, black line) shown schematically from Pichavant et al. (2018).

During closed-system degassing, the exsolved fluid and coexisting melt maintain equilibrium throughout the degassing process. During open-system degassing, the melt and fluid are physically separated during degassing, but exsolution can occur under equilibrium or disequilibrium conditions. Alternatively, the melt composition can be buffered by a fluid (e.g., Métrich et al., 2004; Barsanti et al., 2009; Caricchi et al., 2018). These different processes have profound implications for eruption styles and using volcanic gas emissions to infer changes in the magmatic system. The difference between the path of an equilibrium degassing magma and a fluid-buffered magma are sufficiently different in $H_2O$-$CO_2$ space to be discriminated (Figure 1.6). On the other hand, closed- and open-system equilibrium degassing are very similar until shallow pressures, and are therefore difficult to distinguish (Figure 1.6). Little data is available on disequilibrium degassing, however, Pichavant et al. (2018) suggest that at natural decompression rates, $H_2O$ maintains an equilibrium composition whilst $CO_2$ is retained in the melt. Therefore, disequilibrium degassing paths have elevated $CO_2$ concentrations for the same $H_2O$ concentration, and hence are difficult to distinguish from

fluid-buffered systems (Figure 1.6).

### 1.3.3. Analytical techniques

As melt inclusions are small (1–100 μm in diameter), microanalytical techniques are required for their analysis (Table 1.1) (e.g., Ihinger et al., 1994; Blundy and Cashman, 2008, for reviews). The major and minor element chemistry of melt inclusions is typically analysed using EPMA. Trace element chemistry can be measured using laser ablation inductively coupled plasma mass spectrometry (LA-ICP-MS) (e.g., Halter et al., 2002) or SIMS (e.g., Hinton, 1995). LA-ICP-MS is a more destructive technique than SIMS, but both can also give isotopic information. Alternatively, if the element of interest is not present in the host-mineral, the crystal containing the melt inclusion can be dissolved, and the concentration and isotope ratio of the trace element in solution analysed (Koornneef et al., 2015).

**Table 1.1:** Techniques for analysing melt inclusions.

| Technique | Description | Accessibility | Spatial resolution | Variable |
|---|---|---|---|---|
| Raman | Section 6.3.2 | High | ∼1 μm | H concentration, Fe oxidation state, bubble composition, nanolites |
| FTIR | Section 4.2.2 | High | ∼100 μm | H and C concentration and speciation |
| μXANES | | Low | ∼2 μm | Fe oxidation state |
| SIMS | Section 4.1 | Low | ∼20 μm | Trace, H, and C concentration and isotope ratio |
| EPMA | Section 2.2 | High | ∼1 μm | Major, minor, and volatile element concentration |
| LA-ICP-MS | | High | ∼25 μm | Trace element concentration and isotope ratio |

Volatiles are commonly analysed in melt inclusions. The hydrogen concentration can be measured using Fourier transform infra-red (FTIR) spectroscopy (e.g., Stolper, 1982), Raman spectroscopy (e.g., Thomas, 2000), and SIMS (e.g., Hauri et al., 2002). FTIR can identify volatile speciation but requires large melt inclusions (>100 μm in diameter) and exposure of the melt inclusion on both sides (i.e., double-polished sections). Raman has high spatial resolution, but spectra can be compromised by the glass structure and composition (Di Genova et al., 2018). Carbon concentration can be measured using FTIR (e.g., Fine and Stolper, 1986) and SIMS (e.g., Hauri et al., 2002) with similar advantages and drawbacks. Other volatiles (e.g., S, Cl, and F) can be measured using EPMA and SIMS.

The Fe oxidation state can be measured using μXANES (e.g., Cottrell et al., 2009) and Raman (e.g., Di Genova et al., 2016). μXANES requires access to a synchrotron and can cause beam damage in hydrous samples (Cottrell et al., 2018). Additionally, Raman can be used to detect nanolites in the glass (e.g., Di Genova et al., 2018). The composition of minerals and bubbles hosted in the melt inclusion can be measured using EPMA and Raman, respectively, (e.g., Moore et al., 2015).

## 1.4. Stable isotope fractionation

Stable isotope fractionation of volatiles during degassing has been used to infer the bulk volatile composition (concentration and isotope ratio) of magmas, and the style of degassing, prior to eruption (e.g., Taylor, 1986). The use of stable isotope fractionation requires measurement of both the concentration and isotope ratio of volatiles in variably degassed volcanic products, such as groundmass glass (e.g., Barry et al., 2014; Macpherson and Mattey, 1994; Newman et al., 1988), melt inclusions (e.g., Hauri et al., 2002), vesicles (e.g., Aubaud et al., 2004), fluid inclusions (Gennaro et al., 2017) and volcanic gases (e.g., Gerlach and

Taylor, 1990). Crucially, it does not require finding a melt inclusion that has trapped undegassed melt to estimate the bulk volatile composition. This makes it particularly useful for carbon as some degassing is likely to precede crystallisation and melt inclusion formation.

Stable isotope fractionation causes the relative abundances of isotopes to change during physio-chemical processes due to chemical fractionation, as opposed to nuclear processes such as radioactive decay (Urey, 1947). The chemical behaviour of atoms and molecules depends primarily on their electronic configuration, which is not affected by their isotopic composition. However, rotational, translational, and vibrational energies have a secondary effect on chemical behaviour. These are affected by the nuclear mass of the atoms and hence the isotopic composition. The vibrational energy depends on temperature, hence isotopic fractionation is temperature-dependent. The vibrational energy in a molecule is quantised and, for a specific vibrational energy level, the bond energy will be lower in a bond containing the heavier isotope. During equilibrium processes, where the energy of the system is at a minimum, the heavier isotope will be enriched in phases with the stronger, lower energy bond. In kinetic processes, the products of the reaction will be enriched in the lighter isotope because the lighter isotope diffuses more quickly and forms weaker bonds, which will be more easily broken. These equilibrium and kinetic fractionation effects are largest at low temperatures and when there is a large relative mass difference between isotopes.

Degassing is the exsolution of a fluid phase from a melt. This involves a phase change and, if the speciation of the volatile is different in the exsolved fluid and melt, a chemical change: hence, degassing isotopically fractionates volatiles (e.g., Taylor, 1986). Volatiles commonly consist of light elements (e.g., hydrogen and carbon) where the relative change in mass between isotopes is large, therefore the effects of stable isotope fractionation are often measurable. The isotope ratio of the melt and exsolved fluid depend on the extent of degassing; whether degassing occurs under closed- or open-system conditions; and the fractionation factor, which describes the magnitude and direction of isotopic enrichment.

Closed- and open-system degassing give different graphical relationships between the volatile concentration and isotope ratio in variably degassed samples (Section A.3). During closed-system degassing, the melt and fluid maintain equilibrium throughout, hence by mass balance:

$$\delta_m = \left(\frac{\Delta_{f\text{–}m}}{C_b}\right) \cdot C_m + (\delta_b - \Delta_{f\text{–}m}) \tag{1.1}$$

where $\delta_m$ and $\delta_b$ are the volatile isotope ratios of the melt and bulk system, respectively; $C_m$ and $C_b$ are the volatile concentrations of the melt and bulk system, respectively; and $\Delta_{f\text{–}m}$ is the volatile isotopic fractionation factor between the melt and exsolved fluid (Section A.3.1). Therefore, in $\delta_m$-$C_m$ space, closed-system degassing is a straight line where the slope ($m$) is inversely proportional to the bulk concentration:

$$m = \frac{\Delta_{f\text{–}m}}{C_b} \tag{1.2}$$

and the intercept ($c$) is related to the bulk isotope ratio:

$$c = \delta_b - \Delta_{f\text{–}m} \tag{1.3}$$

If $\Delta_{f-m}$ is known, both the bulk concentration and isotope ratio can be calculated independently from a graph of $\delta_m = f(C_m)$. Therefore, the bulk (initial) composition of the melt prior to volatile saturation and degassing can be calculated.

For open-system degassing, the exsolved fluid is separated from the melt instantaneously when it is formed, which can be calculated by integrating the closed-system degassing equation (Section A.3.2):

$$\delta_m = \Delta_{f-m} \cdot \ln C_m + (\delta_b - \Delta_{f-m} \cdot \ln C_b) \tag{1.4}$$

In $\delta_m$-ln$C_m$ space, open-system degassing is a straight line where the slope ($m$) equals $\Delta_{f-m}$ and the intercept ($c$) is a function of the bulk concentration and isotope ratio:

$$c = \delta_b - \Delta_{f-m} \cdot \ln C_b \tag{1.5}$$

In this case, although no knowledge of $\Delta_{f-m}$ is needed *a priori*, knowledge of either the bulk concentration or isotope ratio is required to calculate the other.

Figure 1.7 shows a schematic illustration of the changes in the carbon isotope ratio of the melt during closed- followed by open-system equilibrium degassing, for two different initial $CO_2$ concentrations (2000 ppm and 1 wt%). Disequilibrium degassing would result in the melt become isotopically heavier (i.e., more positive $\delta^{13}C$ with decreasing $CO_2$ concentration). The grey boxes show the $CO_2$ concentrations of submarine groundmass glass and melt inclusions (darker and lighter grey, respectively), and hence the range of isotope ratios each sample type would capture. In all cases, accurate knowledge of $\Delta_{f-m}$ is critical, and currently there are no data available for mixed ($H_2O$-$CO_2$) volatile systems. Additionally, there has been little work on analysing melt inclusions for their carbon isotope ratios. These two factors need to be addressed to use this tool effectively on melt inclusions to reconstruct initial carbon compositions.

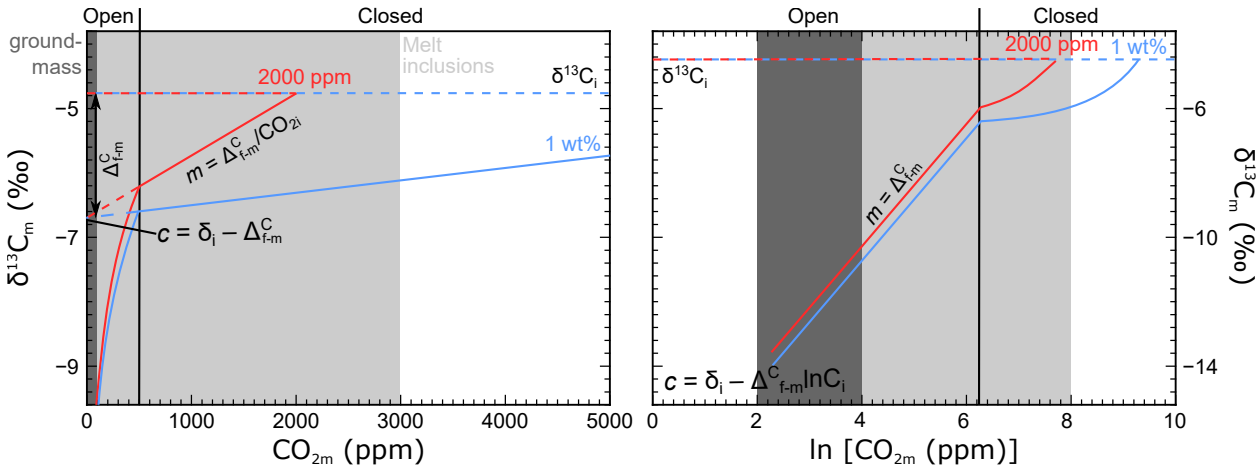


**Figure 1.7:** Closed- followed by open-system (change in degassing style occurs at 500 ppm $CO_2$) equilibrium degassing for $CO_2$ using $\Delta^C_{f-m}$ = +2 ‰ (Mattey, 1991; Mattey et al., 1990). The red curve has 2000 ppm initial $CO_2$ and the blue curve has 1 wt% initial $CO_2$. The light grey box shows $CO_2$ concentrations trapped by melt inclusions, and the dark grey box $CO_2$ in submarine groundmass glass.

# Chapter 2

# Low analytical totals in EPMA of hydrous silicate glass due to sub-surface charging: Obtaining accurate volatiles by difference

**Hughes, E. C.**, Buse, B., Kearns, S. L., Blundy, J. D., Kilgour, G., and Mader, H. M. (2019). Low analytical totals in EPMA of hydrous silicate glass due to sub-surface charging: Obtaining accurate volatiles by difference, *Chemical Geology*, 505, 48–56.

**Author contributions and declaration:** E.C. Hughes collected, processed, and interpretted the data, and wrote the manuscript with the help of B. Buse, S.L. Kearns, J.D. Blundy, G. Kilgour, and H.M. Mader. The manuscript was improved from helpful comments from M. Stock, an anonymous reviewer, and the editor B. Kamber. The R code to calcualte glass density was provided by D. Neave. All content is included as displayed in the submitted paper, except Section 2.5.3 has been added to explain the protocol used throughout the thesis for EPMA of silicate glass for major and minor element chemistry.

## ABSTRACT

The major and minor element chemistry of silicate glass is commonly measured using electron probe microanalysis (EPMA). The volatile content ($H_2O\pm$ $CO_2$) can, additionally, be quantified using volatiles by difference (VBD), but a review of literature data shows that this method consistently overestimates the volatile content. We propose that sub-surface charging during EPMA reduces analytical totals, consequently elevating VBD. Sub-surface charging produces an internal electric field due to trapped implanted electrons, resulting in fewer X-rays being generated and their depth of generation being shallower. The maximum electric field strength required to produce the observed overestimation of VBD is calculated to be ~$10^{-1}$ V·nm$^{-1}$. Crystals are often used as standards for glass analysis but, as amorphous materials have more defects in the band gap, glasses can trap more electrons resulting in greater amounts of sub-surface charging. As this is not included in matrix corrections, it causes errors for glass analyses, but not for crystal analyses. By calibrating VBD using hydrous glass standards, the effect of charging can be incorporated, and volatile contents can be determined to an accuracy of $\pm$0.1 wt%, compared to an overestimation of ~1 wt.% using conventional VBD methods.

## 2.1. Introduction

Electron probe micro-analysis (EPMA) is a critical technique for analysing the composition of silicate glass in volcanology and petrology, such as in melt inclusions and interstitial glass (e.g., Faure and Schiano, 2005). Major and minor element concentration changes, which can be quantified directly using EPMA, provide information on the diversity of magmas (e.g., primary magma compositions and mixing events prior to eruption) and their pre-eruptive crystallisation history (e.g., Kent, 2008; Michael and Cornell, 1998). Glass composition can be used in combination with mineral chemistry to test for equilibrium conditions (e.g., Fe-Mg exchange between melt and olivine, Roeder and Emslie, 1970) and estimate magma pressures and temperatures (e.g., olivine- feldspar-, and pyroxene-melt thermobarometry, see Putirka, 2008, for a review) However, the concentration of the key volatile components ($H_2O$ and $CO_2$) that have a profound effect on the physical properties of melts (density and viscosity, e.g., Giordano and Dingwell, 2003; Ochs and Lange, 1999), phase relations (e.g. Feig et al., 2006), degassing and eruptive style (e.g., Métrich et al., 2009), cannot be easily and directly determined by EPMA. This shortcoming limits significantly the utility of EPMA in understanding volcanic processes.

One approach to this issue is to estimate the $H_2O$+$CO_2$ content of silicate glass by EPMA using the indirect 'volatiles by difference' (VBD) method, whereby the discrepancy between the analytical total for measurable (major and minor) elements and 100 wt% provides an estimate for the total volatile content (Blundy and Cashman, 2008; Devine et al., 1995; Humphreys et al., 2006; King et al., 2002; Nash, 1992). Many trace elements are not analysed by EPMA and if they occur in high abundences this will lead to an underestimation of the total. Typically, individual major elements are measured to ~1 % relative error, which results in a $\pm$0.5–0.7 wt% error on VBD, corresponding to a combination of the errors on the individual elements (Devine et al., 1995; Humphreys et al., 2006). The volatile component by VBD cannot be separated into $H_2O$ and $CO_2$ but, as $H_2O$ is an order of magnitude more soluble in silicate melts than $CO_2$, most of the VBD is $H_2O$. The VBD method has been used widely to quantify the volatile content of experimental samples (e.g., Botcharnikov et al., 2008; Di Carlo et al., 2006; Erdmann and Koepke, 2016) and natural samples such as melt inclusions (e.g., Holtz et al., 2004; Métrich et al., 2004; Rutherford and Devine, 1996; Sommer, 1977).

There are a variety of techniques that can directly and precisely analyse $H_2O$ and $CO_2$ in silicate glass, such as SIMS, FTIR, and Raman (e.g., Hauri et al., 2002; Newman et al., 1986; Thomas, 2000). For comparison, EPMA has higher spatial resolution than SIMS and FTIR (~5 μm diameter using EPMA compared to ~15 μm for SIMS and ~100 μm for FTIR) and is more widely accessible (and less expensive) than SIMS. Also, EPMA does not suffer from problems due to fluoresence or the prescence of nanolites, which can effect quantification using Raman (e.g., Di Genova et al., 2017b). Therefore, EPMA is often used to estimate $H_2O$ when other techniques are unavailable and, uniquely, provides the complete major and minor element glass chemistry in a single analysis.

A review of literature data ($n$ = 524, Table B.1) of VBD compared to measured volatile content ($H_2O$, and $CO_2$ where available) is summarised in Table 2.1 and Figure 2.1. In these studies, $H_2O$ concentration is measured using FTIR, SIMS, Karl-Fischer titration, or assumed in accordance with experimental conditions (e.g., solubility), whilst $CO_2$ concentration is measured using SIMS or FTIR (Table 2.1). Errors are not shown but are typically $<$10 % relative for measured volatile content and $<$0.7 wt% for VBD. Most ($n$

= 287) of the data is for measured volatile contents <2 wt%, with slightly fewer ($n$ = 226) analyses for volatile-rich glasses with 2–6 wt% measured volatiles. There are few data ($n$ = 11) for glasses with >7 wt% measured volatile content. If VBD and measured volatile content agreed, the data would be evenly distributed around the 1-to-1 trend (Figure 2.1a), with equal number of analyses under- and overestimating the measured volatile content (Figure 2.1c). Instead, most of the data lie above the 1-to-1 trend (Figure 2.1a), with more analyses (>50 %) overestimating the measured volatile content (Figure 2.1c). This indicates a systematic error, which is not necessarily obvious in small datasets. Including all data ($n$ = 524), the volatile content is overestimated in 63.5 % of analyses (mean overestimation 0.41 wt% with one standard deviation, 1$\sigma$, 1.16 wt%). For data with measured volatile contents <2 wt% ($n$ = 287), VBD overestimates the volatile content in 54.7 % of analyses (mean overestimation 0.08 wt%, 1$\sigma$ 0.72 wt%) (Figure 2.1b). For measured volatiles >2 wt% ($n$ = 237), overestimation occurs in 74.3 % of analyses (mean overestimation 0.81 wt%, 1$\sigma$ 1.43 wt%). Either EPMA VBD overestimates the true volatile content, or techniques such as SIMS, FTIR, or Karl-Fischer titration underestimate the true volatile content. As a variety of different techniques are used to quantify the measured volatile content in these literature data, it seems unlikely that all these techniques would underestimate the true volatile content to the same degree. Hence, it is considered more likely that VBD consistently overestimates the true volatile content.

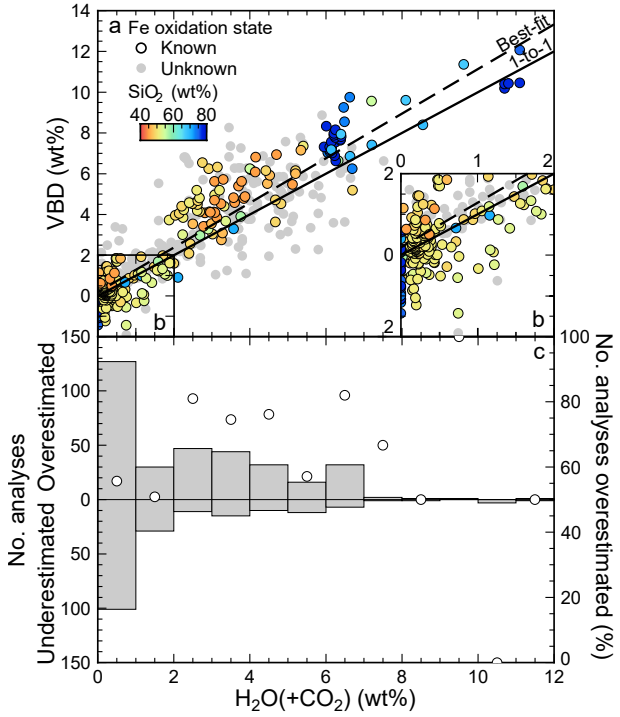


**Figure 2.1:** **(a)** Volatiles by difference (VBD) calculated using EPMA against measured volatile content ($H_2O$, and $CO_2$ where available). Analyses are coloured by $SiO_2$ concentration where Fe oxidation state is known. The solid line indicates the 1-to-1 trend and the dashed line the best-fit to all data. **(b)** An expansion of the data from **(a)** at low volatile contents. **(c)** Histogram, binned by measured volatile content, showing the number of VBD analyses that over- and under-estimate the measured volatile content on the left-hand axis, and the proportion of VBD analyses that overestimate the measured volatile content in white circles on the right-hand side axis. Dataset includes 524 analyses.

Evidently, VBD is accurate at low volatile contents (<2 wt%), but consistently overestimates the volatile content in volatile-rich glasses (>2 wt%) by nearly 1 wt%. Such large discrepancies would have significant impact on the calculated physical and chemical properties of the melt and, in turn, its behaviour before and during volcanic eruptions. For instance, a 1 wt% overestimation in $H_2O$ concentration could change the calculated entrapment pressure of water-saturated melt inclusions by up to ~0.5 kbar, equivalent to ~2 km depth change (Newman and Lowenstern, 2002). Similarly, Di Genova et al. (2013) calculate that the viscosity difference between 2.5 and 4.0 wt% dissolved $H_2O$ is approximately an order of magnitude ($10^{2.4}$ to $10^{3.3}$ Pa·s at 1023 K). Therefore, it is important to understand the cause of the overestimation of VBD and to develop a method to improve the accuracy of VBD measurements.

**Table 2.1:** Literature data to compare VBD and measured volatiles.

| Study | Composition | *n* | Method $H_2O$ | Method $Fe^{2+}/Fe_T$ | Method $CO_2$ | Measured volatiles (wt%) Range | Measured volatiles (wt%) Average | Measured volatiles (wt%) *s.d.* | Overestimation (wt%) Average | Overestimation (wt%) *s.d.* |
|---|---|---|---|---|---|---|---|---|---|---|
| *Natural* | | | | | | | | | | |
| Cottrell and Kelley (2011) | Basalt | 59 | FTIR | µXANES | n.d. | 0.02–0.76 | 0.28 | *0.15* | -0.05 | *0.54* |
| Nichols et al. (2002); Shorttle et al. (2015) | Basalt | 62 | FTIR | µXANES | n.d. | 0.12–0.40 | 0.22 | *0.07* | 0.04 | *0.37* |
| Kelley and Cottrell (2009) | Basalt[a] | 37 | FTIR, SIMS | µXANES | FTIR, SIMS | 0.14–5.40 | 1.52 | *1.30* | -0.03 | *1.05* |
| Naumov et al. (2008) | Rhyodacite | 16 | SIMS | n.d. | n.d. | 0.90–6.68 | 4.56 | *1.60* | 0.16 | *0.82* |
| Blundy et al. (2010) | Dacite to rhyolite | 38 | SIMS | n.d. | SIMS | 0.09–6.11 | 1.68 | *1.55* | 0.42 | *0.77* |
| Chabiron et al. (2001) | Rhyolite | 9 | SIMS | n.d. | n.d. | 0.57–3.73 | 1.92 | *0.90* | 0.05 | *0.32* |
| Delaney and Karsten (1981) | Rhyolite | 11 | SIMS | n.d. | n.d. | 0.20–3.70 | 1.92 | *1.75* | 0.17 | *0.91* |
| Drew et al. (2016) | Rhyolite | 11 | FTIR | n.d. | FTIR | 2.27–5.33 | 4.20 | *0.89* | 2.15 | *1.65* |
| Gurenko et al. (2005) | Rhyolite | 12 | SIMS, Raman | n.d. | n.d. | 1.70–6.50 | 4.78 | *1.29* | -2.22 | *0.74* |
| Naumov (2011) | Rhyolite | 15 | SIMS | n.d. | n.d. | 0.07–6.40 | 1.86 | *2.16* | 1.31 | *1.47* |
| Smith et al. (2010) | Rhyolite | 25 | SIMS | n.d. | SIMS | 0.74–7.52 | 4.32 | *1.62* | 1.17 | *1.61* |
| Webster and Duffield (1991) | Rhyolite | 19 | SIMS | n.d. | n.d. | 0.40–2.70 | 1.07 | *0.63* | -0.09 | *0.77* |
| Webster et al. (1995) | Rhyolite | 27 | SIMS | n.d. | n.d. | 1.60–6.50 | 3.77 | *1.16* | 0.99 | *1.69* |
| Webster et al. (1996) | Rhyolite | 24 | SIMS | n.d. | n.d. | 0.20–3.60 | 1.34 | *1.11* | 0.41 | *0.34* |
| *Experimental* | | | | | | | | | | |
| Botcharnikov et al. (2005) | Ferrobasalt | 16 | FTIR | µMössbauer | n.d. | 0.72–4.82 | 2.23 | *1.42* | -0.03 | *0.41* |
| Lesne et al. (2011) | Basalt | 20 | SIMS, FTIR | Titration | SIMS, FTIR | 1.88–3.32 | 2.59 | *0.40* | 2.14 | *0.65* |
| Melekhova et al. (2015) | Basalt | 11 | SIMS | µXANES | n.d. | 0.60–7.20 | 4.27 | *1.91* | 1.13 | *0.97* |
| Stamper et al. (2014) | Basalt | 25 | SIMS | µXANES | SIMS | 0.03–5.20 | 2.98 | *1.53* | 1.24 | *1.53* |
| Di Genova et al. (2014, 2013) | Various[b] | 13 | KFT | Titration | n.d. | 0.02–6.32 | 1.99 | *1.81* | -0.13 | *0.40* |
| Riker et al. (2015) | Dacite | 8 | SIMS | µXANES | SIMS | 6.14–9.63 | 7.42 | *1.22* | 0.71 | *0.85* |
| Wilke et al. (2002) | Dacite | 5 | KFT | µMössbauer | n.d. | 10.7–11.1 | 10.88 | *0.20* | -0.17 | *0.65* |
| Devine et al. (1995) | Rhyolite | 10 | SIMS, FTIR | n.d. | n.d. | 0.16–6.38 | 3.11 | *2.31* | 0.14 | *0.36* |
| Di Genova et al. (2017a) | Rhyolite | 11 | * | Titration | n.d. | | 0.00 | | -0.50 | *0.66* |
| Zhang et al. (1997) | Rhyolite | 8 | FTIR | n.d. | n.d. | 0.75–5.40 | 2.18 | *1.69* | 0.14 | *0.21* |
| Gaillard et al. (2001) | Rhyolite[c] | 23 | FTIR | Titration | n.d. | 5.95–6.63 | 6.23 | *0.16* | 1.47 | *0.64* |
| Di Genova et al. (2016) | Pantellerite | 9 | * | Titration | n.d. | | 0.00 | | -0.55 | *0.45* |

*Notes: n* is the number of analyses in each study; n.d. means not determined; * assumed due to experimental conditions; for measured volatiles, the range of the study is given followed by the average; the overestimation is the average of (VBD – measured volatiles) for each study; [a] are basaltic to basaltic andesite; [b] are latite, basalt and pantellerite; and [c] are metaluminous to peralkaline rhyolites. Errors of one standard deviation (*s.d.*) are given in *italics*. The complete dataset is available in Table B.1.

## 2.2. Volatiles by difference using electron probe micro-analysis

EPMA uses the intensity of characteristic X-rays, generated by bombarding a sample with an electron beam, to measure its composition. Typically, $K\alpha$ X-ray lines are used for quantification of elements with an atomic number <30, as they have the highest intensity of X-rays emitted from a specific atom. $K\alpha$ X-rays are generated by an incident electron ejecting an electron from the innermost shell ($K$ shell) of a target atom, which is replaced by an electron from the shell above ($L$ shell), emitting the $K\alpha$ X-ray. Element concentrations are calculated by comparing the intensity of X-rays emitted by standards of known composition to those emitted by the unknown. Emitted X-ray intensity depends on the number of X-rays generated and how much absorption and fluorescence occurs as they travel through the sample, which in turn depends on the sample composition. Matrix corrections are used to correct for differences in composition between the standards and unknowns that would affect mean atomic number, absorption, and fluorescence. As oxygen, a very important component of silicate glass, is not typically measured during EPMA, element concentrations are treated as oxide components, with the amount of oxide calculated stoichiometrically from the element at the assumed valence state. Glass is an insulator and therefore builds-up sub-surface charging during analysis as electrons become trapped within the sample (Bastin and Heijligers, 1991). This causes element migration, as ions are displaced in response to the build-up of charge at depth, and changes the generation and emission of X-rays (Cazaux, 1996). These potential causes for discrepent VBD analyses are addressed individually below.

### 2.2.1. Converting to oxides: Oxidation state of multi-valent elements

The valence state of cation species in the glass must be known in order to calculate oxygen using stoichiometry. If oxygen itself is measured, the excess oxygen not required stoichiometrically by other elements can be used to calculate the unmeasured volatile component. For most elements in natural silicate glass there is a single valence state, but Fe and S can have multiple oxidation states, e.g., Fe can be present as FeO, $Fe_2O_3$, or a mixture of both. Per Fe atom, $Fe_2O_3$ is ~10 % heavier than FeO which results in a $\pm$5 % relative error in oxide concentration when converting from elemental Fe if the oxidation state is unknown. This is important for basalts which contain 5–14 wt% $FeO_T$ ($FeO_T$ = all Fe reported as FeO), as the uncertainty in the amount of oxygen assigned to Fe leads to a $\pm$0.3–0.7 wt.% error in VBD. Consequently, to obtain reliable VBD, an independent constraint on Fe oxidation state is required (Donovan and Vicenzi, 2008; Nash, 1992). Rhyolites typically contain only 1–4 wt.% $FeO_T$, therefore the uncertainty from the amount of stoichiometric oxygen assigned to Fe is small ($\pm$0.1–0.2 wt.%), and has a correspondingly smaller effect on the VBD error. For rhyolites, therefore, an independent constraint on Fe oxidation state is less critical.

As the Fe oxidation state is important in estimating VBD for silicate glass containing significant Fe, only data with measured Fe oxidation state are included in our compilation of literature data for silicate glass with $FeO_T > 2$ wt% (e.g., basalts and pantellerites). In these cases, the measured Fe oxidation state is used to assign $FeO_T$ into FeO and $Fe_2O_3$ to calculate VBD. Where $FeO_T < 2$ wt% (e.g., rhyolites) the data are included even when no independent measurements of Fe oxidation state are available. At high concentrations sulphur oxidation state will also impact the analytical total, and therefore VBD. At S < 2500 ppm, the error due to the uncertainty in sulphur speciation ($S^{2-}$ to $S^{6+}$) is $<\pm$0.2 wt.%. If no Fe oxidation state is available and when S is reported, VBD is calculated assuming all Fe is $Fe_2O_3$ and all S is $SO_3$. Such

VBDs represent a minimum estimate.

### 2.2.2. Matrix corrections

The matrix correction accounts for the differences in mean atomic number, absorption, and fluorescence of X-rays for samples with different compositions. If the unmeasured volatile is not included in the matrix correction for analyses without measured oxygen, the mean atomic number used for the matrix correction is incorrect and absorption by oxygen underestimated. This can lead to analytical totals being underestimated by ~1 wt% (Devine et al., 1995; Donovan and Vicenzi, 2008; Roman et al., 2006). This is corrected for by calculating the unmeasured volatiles (typically specified as $H_2O$) by difference within the matrix correction routine (Donovan and Tingle, 1996).

### 2.2.3. Element migration

Silicate glass can become unstable during EPMA due to the diffusive migration of mobile elements (e.g., Na), sometimes referred to as 'beam damage'. Glass composition controls the severity of beam damage and hydrous glass is more susceptible than anhydrous glass (e.g., Section 3.5; Humphreys et al., 2006; Zhang et al., 2018). Element migration can also occur in hydrous minerals, such as amphibole and apatite, causing errors in VBD estimates of these minerals (e.g., Stock et al., 2015). Beam damage is accompanied by a corresponding increase in the concentration of immobile elements (e.g., Si and Al) referred to as 'grow-in' (e.g., Morgan and London, 2005; Nielsen and Sigurdsson, 1981). These problems can be corrected for by monitoring the X-ray intensity over time and extrapolating back to the initial value (Nielsen and Sigurdsson, 1981), often referred to as 'time-dependent intensity' (TDI) corrections . As the change in X-ray intensity with time is not necessarily linear, only elements measured at the onset of the analysis can be corrected for (one per spectrometer, or typically five out of the twelve commonly analysed elements). Therefore, it is important to measure those elements that are likely to diffuse away or grow-in first. Measuring mobile elements first and for short times, even where the TDI correction is not required, is now routinely employed to address this problem (e.g., Blundy and Cashman, 2008).

### 2.2.4. Sub-surface charging

Electrical insulators (e.g., silicate crystals and glass) have a large band gap, which is the energy difference between the valence and conduction bands where no electroncs can reside. Hence, for insulators a large amount of energy is required to promote an electron from the valence band into the conduction band. For electron imaging and EPMA, insulating materials are routinely coated with a thin layer of conductive layer, typically carbon, to prevent surface charging. This conductive coat does not, however, prevent *sub-surface* charging, whereby incident electrons are trapped within the sample (Cazaux, 1996). Charge is trapped as electronss occupying energy levels in the band gap produced by defects, such as vacanies, interstial atoms, or substitutions within the lattice structure.

Trapped electrons generate an electric field within the sample, which enhances the deceleration of electrons as they pass through the sample. Hence, X-ray ionisations are reduced, generated closer to the surface, and undergo less absorption. This is reflected in the change in calculated $\varphi(\rho Z)$ curves, which depict intensity variations in X-ray generation and emission with depth relative to a thin film (e.g., Figure 2.2), by an internal electric field (Cazaux, 1996). The resulting measured X-ray intensity is a trade-off between these two

effects. For low energy X-rays, e.g., O$K\alpha$, where X-ray absorption by the matrix is reduced, the intensity may increase; but for most higher energy X-rays, intensity will fall as a consequence of charge trapping.

Charge-trapping sites (i.e., defects in the band gap) are more common in amorphous materials than in single crystals (Bonnelle, 2004). Therefore, the magnitude of sub-surface charging effects is greater in glasses than in crystals, all else being equal. Furthermore, charge-trapping is dynamic and can increase as a result of electron beam irradiation (Bonnelle, 2004). Typically, crystalline materials that are stable under the electron beam are used as standards. When these crystalline standards are used for crystal analysis they should experience a similarly small magnitude of charging and no quantification error will be observed. Hence, the issue of sub-surface charging has little impact on the analysis of anhydrous minerals (individual crystals), which typically yield totals of $100 \pm 0.5$ wt% when oxygen is calculated by stoichiometry, notwithstanding Fe redox issues described above. Conversely, when crystals are used as standards for glass analysis, the magnitude of charging will likely be different, providing a potential explanation for the discrepancy in analytical totals. Sub-surface charging is not included in current matrix corrections, as the amount of charging is difficult to determine. If standards and unknowns experience different amounts of charging during analysis, errors in quantification may result.

Direct measurements of sub-surface charging are difficult, but are possible post-irradiation within ground-coated insulators using the pressure wave propagation method (Maeno et al., 1989), thermal pulse method (Cherifi et al., 1992), or electrical methods (Sessler and Yang, 1998). To measure the dynamic build-up of charge, the electrostatic influence method can be used on coated (Jbara et al., 2002) and uncoated (Fakhfakh et al., 2003) samples. Using this technique, maximum electric field strengths ($F_{\max}$) of ~1 V·nm$^{-1}$ have been measured in silicate glass (Jbara et al., 2004, 2002), that would cause significant distortion to the $\varphi(\rho Z)$ curve (Cazaux, 1996; Jbara et al., 1997). Sub-surface charging has been observed indirectly by measuring the migration of alkali elements in silicate glass over time (e.g., Gedeon et al., 1999; Gedeon and Jurek, 2002; Jbara et al., 1995; Lineweaver, 1963), and by comparing the X-ray intensity of charged and uncharged polycrystalline $Al_2O_3$ (e.g., Benhayoune and Jbara, 1996; Ghorbel et al., 2005). Using the decay of Na$K\alpha$ X-ray intensities over time and measured diffusivities of Na through silicate glass, Jbara et al. (1995) calculated $F_{\max}$ of $10^{-4}$–$10^{-1}$ V·nm$^{-1}$. As these magnitudes of sub-surface charging may measurably impact quantitative EPMA, we investigate the effects of sub-surface charging on the analysis of hydrous glass to see whether this additional effect could cause an underestimation of analytical totals and concurrent elevation of VBD.

## 2.3. Methods

We modelled the effect of sub-surface charging on glass analysis using the Monte Carlo simulation program Win X-ray (Demers and Gauvin, 2004; Gauvin et al., 2006), which incorporates the charge density model proposed by Cazaux (1996). We then use the results from Win X-ray to calculate VBD.

### 2.3.1. Sub-surface charging model

Sub-surface charging can be modelled using the steady-state sub-surface charging model of Cazaux (1996). This uses a one-dimensional charge distribution, which is valid if the irradiated area is large compared to the maximum penetration depth of electrons and charge builds up instantaneously. The sample thickness must greatly exceed the maximum penetration depth of electrons, and the top and bottom surfaces of the

sample must be grounded (Cazaux, 1996; Demers and Gauvin, 2004). In this case, the electric field within the sample is described by:

$$F = \frac{\rho_t (z_{max} - z)}{\varepsilon} \tag{2.1}$$

Where $F$ is the electric field strength ($V \cdot m^{-1}$), $\rho_t$ is the trapped charge density ($C \cdot m^{-3}$), $z_{max}$ is the maximum penetration depth of electrons (m), $z$ is the depth in the sample (m), and $\varepsilon$ is the permittivity of the sample ($F \cdot m^{-1}$) (Cazaux, 1996). The maximum electric field ($F_{max}$) occurs at the interface between the sample and the conductive coat ($z = 0$). The magnitude of the electric field is thus dependent on both the material properties of the sample and the analytical conditions.

### 2.3.2. Win X-ray: Monte Carlo simulation program

The inputs for Win X-ray are the sample composition and density ($\rho_m$), analytical conditions (accelerating voltage, beam current, and beam diameter), and maximum electric field strength ($F_{max}$). The maximum penetration depth of electrons within the sample ($z_{max}$), $\varphi(\rho Z)$ curves (generated and emitted), and measured X-ray intensity ($I$) for the principal characteristic X-rays (e.g., $K\alpha$, $K\beta$, $L\alpha$) of each target element are calculated.

We choose glass St8.1.B from Lesne et al. (2011) as the sample composition as it is a typical basalt. To simplify the composition, all Fe is FeO and volatiles other than $H_2O$ (S, Cl, and $CO_2$) are excluded. We modelled typical analytical conditions used to analyse silicate glass (15 kV accelerating voltage, 10 nA beam current, and 10 μm beam diameter), with dissolved $H_2O$ concentrations of 0–10 wt%. $\rho_m$ for each $H_2O$ concentration was calculated using density models of melts at room temperature and pressure, which were 2.793, 2.652, and 2.524 $g \cdot cm^{-3}$ for 0, 5, and 10 wt% $H_2O$, respectively, (Bottinga and Weill, 1970; Lange, 1997; Lange and Carmichael, 1990; Ochs and Lange, 1999; Toplis et al., 1994). We varied $F_{max}$ between 0.00 and 0.20 $V \cdot nm^{-1}$ for each $H_2O$ concentration, and the maximum penetration depth ($z_{max}$) was calculated using the Kanaya-Okayama Range (Kanaya et al., 1972). The large beam diameter satisfies the requirement of one-dimensional charge distribution (i.e., charge distribution only varies in $z$ as the irradiated area is large compared to the electron penetration depth). Each simulation was run for one million electrons.

### 2.3.3. Calculating volatiles by difference from Win X-ray results

X-ray intensities without sub-surface charging ($I$) were used as standards to derive k-ratios ($k$) using:

$$k = \frac{I'}{I} \tag{2.2}$$

where $I'$ is the X-ray intensity with sub-surface charging at each $H_2O$ concentration. Concentrations when sub-surface charging was imposed ($C'$) were calculated using:

$$C' = k \cdot C \tag{2.3}$$

where $C$ is the specified concentration. The measured analytical total and VBD were calculated. An example

calculation is shown in Table 2.2.

**Table 2.2:** Example calculation of modelled oxide concentration ($C'$) by comparing uncharged X-ray intensities ($I$) to charged X-ray intensities ($I'$) for $F_{max}$ = 0.20 V·nm$^{-1}$.

| Oxide | $I$ | $I'$ | $k$ | $C$ (wt%) | $C'$ (wt%) |
|---|---|---|---|---|---|
| $SiO_2$ | $5.96 \times 10^4$ | $5.85 \times 10^4$ | 0.980 | 51.86 | 50.08 |
| $TiO_2$ | $7.97 \times 10^2$ | $7.65 \times 10^2$ | 0.960 | 0.84 | 0.81 |
| $Al_2O_3$ | $1.99 \times 10^4$ | $1.96 \times 10^4$ | 0.983 | 18.63 | 18.31 |
| $Fe_2O_3$ | $4.52 \times 10^3$ | $4.36 \times 10^3$ | 0.964 | 8.12 | 7.83 |
| MgO | $4.67 \times 10^3$ | $4.62 \times 10^3$ | 0.990 | 6.02 | 5.96 |
| CaO | $1.79 \times 10^4$ | $1.72 \times 10^4$ | 0.961 | 11.11 | 10.68 |
| $Na_2O$ | $7.42 \times 10^2$ | $7.40 \times 10^2$ | 0.997 | 1.98 | 1.97 |
| $K_2O$ | $2.86 \times 10^3$ | $2.76 \times 10^3$ | 0.963 | 1.44 | 1.39 |
| $H_2O$ | | | | 0.00 | – |
| Total | | | | 100.00 | 97.78 |
| VBD | | | | | 2.22 |

## 2.4. Results

Figure 2.2 gives the $\varphi(\rho Z)$ curves of the $K\alpha$ lines of interest, in order of increasing X-ray energy from upper left to lower right. Values of the $\varphi(\rho Z)$ function of the emitted curve $[\varphi(\rho Z)_e]$ are always less than the generated curve $[\varphi(\rho Z)_g]$, as some X-rays are always absorbed. At shallow depths in the sample, $\varphi(\rho Z)_g$ for $F_{max}$ = 0.00 and 0.20 V·nm$^{-1}$ are comparable, but at greater depths, the intensity of generated X-rays falls off more quickly for $F_{max}$ = 0.20 V·nm$^{-1}$. For Si, Al, Mg, and Na calculated values of $\varphi(\rho Z)_e$ for $F_{max}$ = 0.00 and 0.20 V·nm$^{-1}$ are similar, whereas for Ti, Fe, Ca, and K $\varphi(\rho Z)_e$ for $F_{max}$ = 0.20 V·nm$^{-1}$ is noticeably less than for $F_{max}$ = 0.00 V·nm$^{-1}$.

Figure 2.3 shows that for X-rays with energies $<$ 1 keV, $k > 1.00$, whereas for X-rays with energies $>$ 1 keV, $k < 1.00$. Measured X-ray intensities are reduced by the presence of an electric field for most elements routinely measured by EPMA (Figure 2.3). On the other hand, the intensity of heavily absorbed X-rays, such as O$K\alpha$, increases in the presence of an electric field. Broadly, $k$ decreases with increasing X-ray energy, $F_{max}$, and $H_2O$ concentration of the glass but does not do so smoothly. The effect of $F_{max}$ and $H_2O$ concentration increases with increasing X-ray energy. For $H_2O$ concentrations of 0 and 5 wt%, $k$ increases again for X-ray energies $>$ 5 keV, whereas for 10 wt% $H_2O$ it does not change. The effect of $H_2O$ concentration on $k$ increases with increasing $F_{max}$.

Reduction in X-ray intensities means the VBD, calculated using $C'$, is always greater than the specified $H_2O$ (Figure 2.4). The value of VBD increases with increasing $F_{max}$, and lines of equal $F_{max}$ appear parallel (Figure 2.4).

## 2.5. Discussion

### 2.5.1. Effect of $F_{max}$

Modelling results confirm that more low energy X-rays ($<$1 keV) and fewer high energy X-rays ($>$1 keV) are emitted when an electric field is present. This is because, although fewer X-rays are generated overall, they are generated at shallower depths reducing X-ray absorption which most affects strongly absorbed,

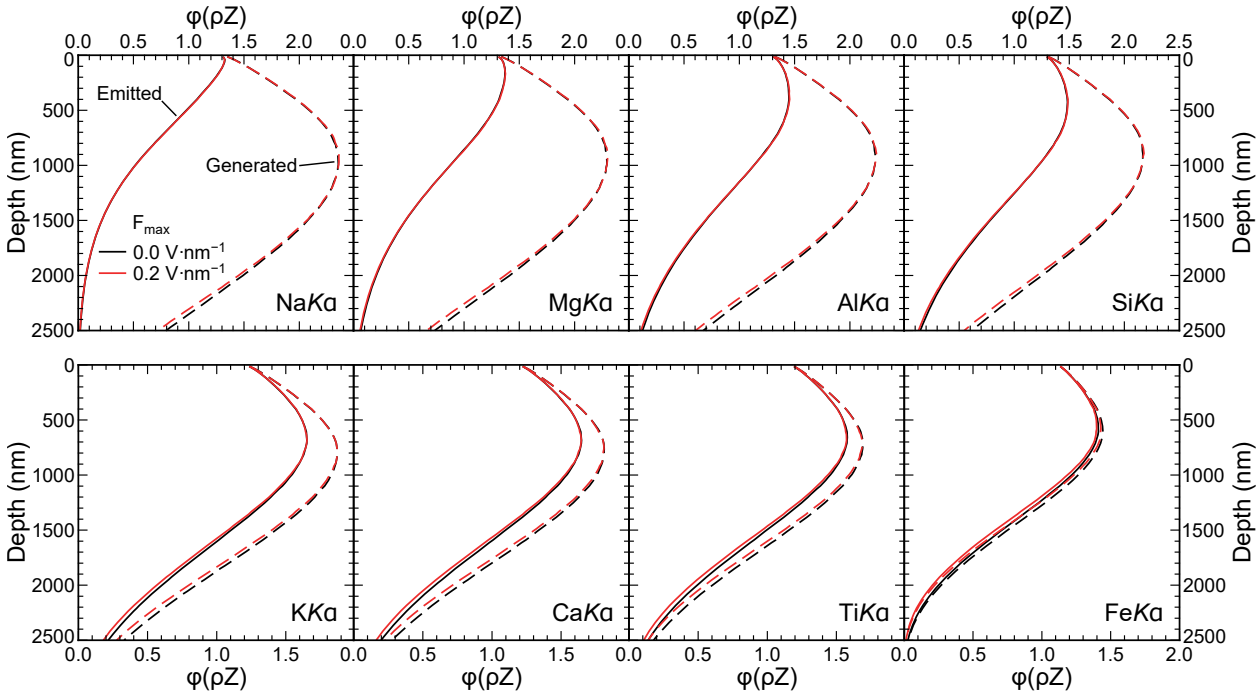


**Figure 2.2:** Generated and emitted $\varphi(\rho Z)$ curves against depth for the $K\alpha$ lines of different elements (in ascending order of X-ray energy, indicated in the top right corner of each panel) for St8.1.B with 5 wt% $H_2O$, for $F_{max}$ = 0.00 (black) and 0.20 V·nm$^{-1}$ (red).

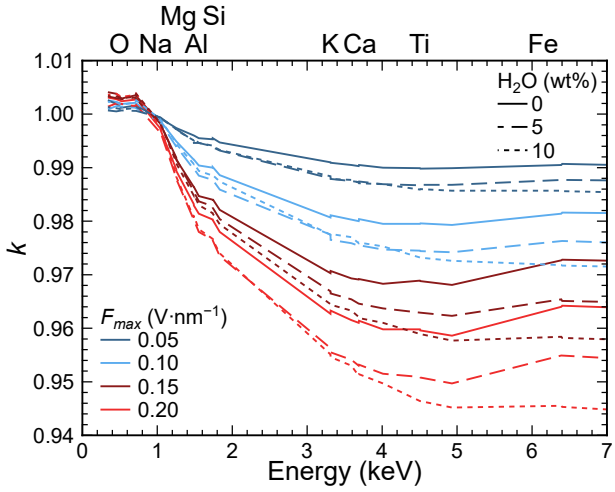


**Figure 2.3:** $k$ against X-ray energy with energy of $K\alpha$ X-rays indicated along the top. Different values of $F_{max}$ are shown using different line colours, whilst different glass $H_2O$ concentrations are shown by different line styles. For instance, results using an $F_{max}$ of 0.10 V·nm$^{-1}$ for 5 wt% $H_2O$ are shown in the long dashed, light blue line. Data are available in Table C.1.

rather than weakly absorbed, X-rays. Moreover, the deceleration of electrons will affect high energy X-rays more than the low energy X-rays as the overvoltage (ratio of the accelerating voltage to the critical excitation energy of the X-ray) is smaller; the magnitude of intensity reduction will therefore vary with primary accelerating voltage (Ghorbel et al., 2005). As the $K\alpha$ X-rays used for quantification are >1 keV, the presence of an electric field in the glass reduces the emitted X-ray intensity (Figures 2.2 and 2.3), resulting in low analytical totals and overestimated VBD (Figure 2.4). Oxygen can be measured to calculate the volatile content, but this would also lead to an overestimation of volatiles because the intensity of O$K\alpha$ increases with an electric field present. At a constant $F_{max}$, $k$ decreases with increasing $H_2O$ concentration, which is likely due to the decrease in $\rho_m$ that results from increasing amounts of dissolved $H_2O$ in the glass. For most $K\alpha$ lines this effect is small, as reflected in almost parallel lines of modelled VBD at different values of $F_{max}$.

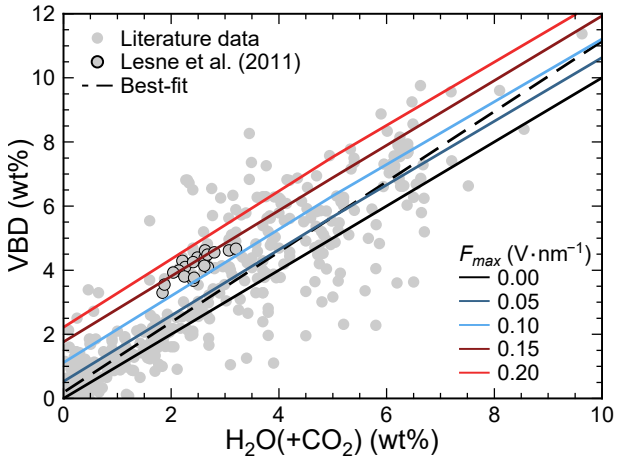


**Figure 2.4:** Volatiles by difference (VBD) calculated using Win X-ray against volatile content, for different $F_{max}$ (line colour). Literature data included for comparison in grey. Data for basaltic glasses of Lesne et al. (2011) are outlined in black.

We can compare our results to the studies of Jbara et al. (2004, 2002, 1995) that irradiated silicate glass at 13.0–18.5 kV accelerating voltage, 2–3 nA beam current, and $10^1$–$10^7$ μm$^2$ irradiated area, giving doses of $10^{-4}$–$10^2$ C·m$^{-2}$·s$^{-1}$, similar to those modelled here (~$10^1$ C·m$^{-2}$·s$^{-1}$). The $F_{max}$ we inferred using Win X-ray (~$10^{-1}$ V·nm$^{-1}$) is in the range measured by Jbara et al. ($10^{-4}$–$10^0$ V·nm$^{-1}$).

### 2.5.2. Controls on $F_{max}$

Win X-ray adopts a user-selected $F_{max}$ during simulations, but it is important to understand what might control this value. $F_{max}$ is inversely proportional to $\varepsilon$, and glass has a value of $\varepsilon_r$ (relative permittivity, or dielectric constant) of 3–10, which depends on composition, temperature, and frequency. For anhydrous basalt $\varepsilon_r \approx 4.8$ (Carmisciano et al., 2011). Unfortunately, there are no data available for the effect of $H_2O$ concentration on $\varepsilon_r$.

$F_{max}$ is proportional to $z_{max}$, which increases with decreasing $\rho_m$ and increasing accelerating voltage. $\rho_m$ is a function of glass composition, including $H_2O$ concentration, hence $z_{max}$ and $F_{max}$ will increase with increasing $H_2O$ concentration. This is consistent with the increased discrepancy between measured volatile content and VBD at elevated $H_2O$ concentration (Table 2.1 and Figure 2.1). For glasses with measured volatile content <2 wt%, the mean overestimation is 0.08 wt% (with one standard deviation, 1$\sigma$, 0.72 wt%); whereas for glasses with measured volatile contents >2 wt%, the mean overestimation is 0.81 (1.43 1$\sigma$) wt% (Figure 2.1).

$F_{max}$ is also proportional to $\rho_t$. Intrinsic charge trapping sites are a material property, caused by defects in the band gap (Bonnelle, 2004), which is partly a function of glass composition (Fakhfakh et al., 2010). Bombarding the sample with electrons will create additional charge trapping sites (Bonnelle, 2004), hence $\rho_t$ is also dependent on analytical conditions. Jbara et al. (1995) found that a constant proportion of charge (relative to the number of incident electrons per unit area, dose) was trapped in the glass during analysis. This requires the number of charge-trapping sites to increase linearly with electron dose. Using results from Win X-ray gives a $\rho_t$ of ~$10^2$ C·m$^{-3}$ for our data. The dose rate is ~$10^1$ C·m$^{-2}$·s$^{-1}$ which means that ~$10^{-3}$ % of incident electrons are trapped, an order of magnitude larger than $2.6 \times 10^{-4}$ % from Jbara et al. (1995) at similar analytical conditions. The main differences between our study and that of Jbara et al. (1995) are the concentrations of $SiO_2$ (73 wt% in Jbara et al. vs. 52 wt% in this study) and $H_2O$ (0 wt% in Jbara et al. vs. 1–3 wt% in this study). In the literature data (Figure 2.1a), there is no significant difference in the magnitude of charging between glasses with different $SiO_2$ concentrations. Conversely, glasses with measured volatiles

$<$ 2 wt% appear to suffer little charging whereas those with $>$2 wt% are more affected (Figure 2.1). We conclude that the order of magnitude difference in charge-trapping proportion between our study and Jbara et al. (1995) is most likely caused by $H_2O$ concentration. Hydrous glass is more unstable during electron beam irradiation (Section 3.5; Humphreys et al., 2006; Zhang et al., 2018), which could create more charge-trapping sites during analysis compared to anhydrous glass or crystals, and hence increase $F_{\max}$.

### 2.5.3. Analysing hydrous silicate glass

The analytical set-up for glass analysis was chosen considering the potential problems described in Section 2.2. An accelerating voltage of 15 kV was used, which gives an analytical volume 2–3 μm in depth, which is likely to be smaller than the depth of the melt inclusion. This avoids interactions with the host-mineral whilst allowing accurate quantification of Fe. A beam current of 10 nA was used which generates sufficient X-rays to get good counting statistics in a reasonable analysis time, whilst not causing significant beam damage. A defocused beam of 5–10 μm diameter was used to allow a range melt inclusions sizes to be analysed and ensure the spectrometers remained in focus.

All elements (majors, minors, and volatiles) were measured using their $K\alpha$ X-ray line. Oxygen was not measured and hence was calculated by stoichiometry. The Amstrong-Love Scott $\varphi(\rho Z)$ matrix correction was used, and hydrogen was included as an element by difference (Donovan and Vicenzi, 2008). Broadly two TAP-type crystals were used to measure Si, Al, Na, Mg, and F; two PET-type crystals were used for Ca, Ti, K, P, and S; and one LIF-type crystal was used to measure Fe and Mn. Mobile elements (e.g., Si, Na, and K) were measured first to allow TDI-corrections to be applied (Nielsen and Sigurdsson, 1981). Measuring the intensity over time lengthens the analysis time, hence a small number of bins was chosen (e.g., 6) to get sufficient data to fit a TDI correction but not result in too long an analysis time. To achieve a reasonable error on VBD, count times were chosen to achieve a ~1 % relative error ($\sigma$) on each element based on the typical number of counts ($n$) achieved in a basaltic glass using:

$$\sigma = \frac{\sqrt{n}}{n} \tag{2.4}$$

as a guide. If TDI corrections were not used, short count times and averaging many analyses were used instead, although this could only be done on experimental glasses where there was sufficient room for many analyses.

Typically, a background correction is made by measuring the X-ray intensity at wavelength positions either side of the peak of interest (high and low), avoiding any positions with known interferences from other elements. Count times for high and low background measurements are normally half those of measuring on peak, hence using off-peak background doubles the analysis time. This increases the likelihood of beam damage and hence the potential for errors in quantification. Another option is to use mean atomic number (MAN) backgrounds, which uses the measured relationship between background X-ray intensity and the MAN of the sample (Donovan and Tingle, 1996). This involves measuring the on-peak X-ray intensity on a variety of samples with different MAN *without* the element of interest to calculate the background intensity at the MAN of interest. Calculating the MAN backgrounds for each unknown is an iterative process, as the backgrounds inform the matrix correction which calculates the MAN of the sample. MAN curves were manually reviewed before being applied to check the quality of the fit.

Minerals were typically used for peaking and calibration standards, although anhydrous basaltic glass standards, such as Columbia River Basalt (BCR-2), were sometimes used for major element calibration (Tables 2.3 and 2.4). Six to ten 10 s analyses were collected for calibration, and a defocused beam was used on basaltic glass and albite as they can be unstable under electron beams. As the peak position of S$K\alpha$ depends on the oxidation state of S, barite was used to initially find the peak position and for calibration, but before analysis on glass S$K\alpha$ was repeaked on the Juan de Fuca basaltic glass (VG-2, Table 2.4). Basaltic glasses not used as primary standards were used as secondary standards to check the quality of analysis during data collection (Table 2.4). A typical analytical routine is given in Table 2.5.

**Table 2.3:** Compositions of primary mineral standards for EPMA.

| Oxide (wt%) | Albite | Wollastonite | SJIO | Sanidine | Fayalite Ward | Durango apatite | Andradite |
|---|---|---|---|---|---|---|---|
| $SiO_2$ | 68.52 | 51.36 | 40.83 | 64.76 | 28.80 | | 35.94 |
| $TiO_2$ | | | | | | | 0.08 |
| $Al_2O_3$ | 19.54 | 0.06 | | 18.52 | | | 1.78 |
| $Fe_2O_3$ | | 0.49 | 9.54 | | 66.98 | | 26.21 |
| MnO | | 0.06 | 0.12 | | 4.09 | | 0.43 |
| MgO | | 0.28 | 49.19 | | 0.49 | | |
| CaO | 0.11 | 48.01 | | | 0.10 | 54.02 | 31.50 |
| $Na_2O$ | 11.61 | | | 2.12 | | 0.23 | |
| $K_2O$ | 0.24 | | | 14.21 | | | |
| $P_2O_5$ | | | | | | 40.78 | |
| NiO | | | 0.36 | | | | |

*Notes:* SJIO is St Johns Island Olivine and $FeO_T$ is all Fe reported as FeO.

**Table 2.4:** Compositions of anhydrous basaltic glass primary and secondary standards.

| Oxide | BCR-2 | VG-2 | VG-A99 | 3570 |
|---|---|---|---|---|
| $SiO_2$ | 54.1 | 50.81 | 51.06 | 50.64 |
| $TiO_2$ | 2.26 | 1.89 | 3.95 | 1.43 |
| $Al_2O_3$ | 13.5 | 14.00 | 12.44 | 15.87 |
| $FeO_T$ | 12.42 | 11.84 | 13.15 | 10.52 |
| MnO | 0.20 | 0.21 | 0.19 | 0.21 |
| MgO | 3.59 | 6.66 | 5.04 | 6.39 |
| CaO | 7.12 | 11.06 | 9.04 | 9.33 |
| $Na_2O$ | 3.16 | 2.62 | 2.72 | 3.82 |
| $K_2O$ | 1.79 | 0.19 | 0.82 | 0.95 |
| $P_2O_5$ | 0.35 | 0.20 | 0.43 | |
| $H_2O$ | | 0.02 | | |
| S | | 1305 | 96 | |
| Cl | | 300 | | |
| F | 440 | [a]225 | | |
| $Fe^{2+}/Fe_T$ | | 0.83 | 0.87 | |

*Notes:* BCR-2 is the USGS basaltic glass standard Columbia River Basalt, VG-2 and VG-A99 are the Smithsonian microbeam Juan de Fuca and Kilauea basaltic glass standards, respectively, (Jarosewich et al., 1980), and 3570 is an internal secondary standard. Oxides are in wt% and elements are in ppm. [a] Value from Métrich et al. (2004).

**Table 2.5:** Example set-up for EPMA of hydrous basaltic glass: 15 kV accelerating voltage, 10 nA beam current, and 5–10 μm beam diameter.

| Spectrometer – Crystal | | | | |
|---|---|---|---|---|
| 1 – PETJ | 2 – TAP | 3 – TAPH | 4 – PETH | 5 – LIFL |
| Ca$K\alpha^a$ (30) | Si$K\alpha^a$ (30) | Na$K\alpha^a$ (30) | K$K\alpha^a$ (120) | Fe$K\alpha^a$ (60) |
| *Wollastonite* | *Albite* | *Albite* | *Sanidine* | *Andradite* |
| Ti$K\alpha$ (60) | Al$K\alpha$ (30) | Mg$K\alpha$ (60) | P$K\alpha$ (60) | Mn$K\alpha$ (180) |
| *$TiO_2$* | *Sanidine* | *SJIO* | *Durango apatite* | *Mn metal* |
| Cl$K\alpha$ (150) | | F$K\alpha$ (120) | S$K\alpha$ (60) | |
| *NaCl* | | *$MgF_2$* | *VG-2* | |
| | | | Barite | |

*Notes:* Elements listed in order of analysis from top to bottom; peak counting times (s) in brackets and background countings times are half these times unless MAN backgrounds were used; elements were peaked on the 1st standard in italics and calibrated on the 2nd standard if different; and VG-2 is the Smithsonian microbeam basaltic glass standard and SJIO is St Johns Island Olivine. [a] indicates TDI data collected to extrapolate to time 0 if element migration occurred. Compositions of standards are in Tables 2.3 and 2.4.

### 2.5.4. Obtaining accurate volatiles by difference

There are a few options available for correcting for charging during EPMA. Firstly, matrix corrections could include the effects of sub-surface charging on X-ray generation, therefore allowing primary standards that are affected by different amounts of charging (e.g. crystals and anhydrous glass) to be used for calibration (Cazaux, 1996). Unfortunately, this requires accurate calculation of $F_{\max}$ in both primary standards and unknowns at the analytical conditions used. As $\rho_t$ depends on the composition, structure, and analytical conditions, it must be measured rather than calculated on the primary standards and unknowns during analysis. Such measurements are not routine and there are few data for the effect of composition (especially $H_2O$ concentration) on $\varepsilon_r$, a requisite for calculating $F_{\max}$ (Equation 2.1).

Alternatively, matrix-matched primary standards (i.e., hydrous glasses of appropriate composition) can be used for major element calibration, such that primary standards and unknowns would experience similar amounts of charging. This would require different major element primary standards for each glass $H_2O$ concentration. Currently few, if any, hydrous glass primary standards with independent measurements of composition exist. However, the error on any single element is small and typically within analytical error. Hence in practice only VBD needs to be corrected for the effect of sub-surface charging and this can be done by internally calibrating VBD using a set of well characterised matrix-matched secondary standards with known volatile content (e.g., Botcharnikov et al., 2008; Holtz et al., 2004; Di Carlo et al., 2006) and Fe ($\pm$ S) oxidation states. The VBD secondary standards should be analysed using the same analytical conditions and calibration as the unknowns to generate an empirical calibration curve for each session. This will result in similar amounts of charging in the secondary standards as in the unknowns. To produce a reliable calibration curve, a range of $H_2O$ concentrations covering those expected in the unknowns should be used to avoid extrapolation. Additionally, there must also be an independent constraint on the Fe oxidation state (and S if the concentration is high) of the unknowns if they are Fe-rich basalts or pantellerites.

From Figure 2.4 it can be seen that the Lesne et al. (2011) data have measured VBD data comparable to modelled VBD for an $F_{\max} \approx 0.15$ V·nm$^{-1}$. An example of the empirical correction using these data is

shown in Figure 2.5. Lesne et al. (2011) measured the glass composition and S oxidation state by EPMA, Fe oxidation state by wet chemistry, and $H_2O$ and $CO_2$ by SIMS and/or FTIR. Samples from St8.1.B are used as VBD secondary standards as they cover the widest range in $H_2O$ concentrations (1.87–3.11 wt%), and samples from MAS.1.A and MAS.1.B are treated as unknowns (Table 2.6 and Figure 2.5). The average accuracy improves from +1.69 (0.23 1$\sigma$) to a slight underestimate of -0.06 (0.32 1$\sigma$) wt%. This demonstrates the viability of using an empirical correction to achieve high accuracy VBD, accounting for both variations in sub-surface charging and calibration errors.

**Table 2.6:** Example VBD correction using data from Lesne et al. (2011).

| | Measured volatiles | | VBD | | VBD corrected | |
|---|---|---|---|---|---|---|
| Sample | wt% | *s.d.* | wt% | *s.d.* | wt% | *s.d.* |
| MAS.1.B2[a] | 2.21 | *0.13* | 4.30 | *0.40* | 2.60 | *0.48* |
| MAS.1.B3[a,b] | 2.49 | *0.13* | 4.39 | *0.84* | 2.72 | *1.01* |
| MAS.1.B4[a,b] | 2.62 | *0.13* | 4.39 | *0.36* | 2.70 | *0.43* |
| MAS.1.B5[a,b] | 2.26 | *0.13* | 4.10 | *0.52* | 2.36 | *0.63* |
| MAS.1.B6 | 2.41 | *0.13* | 3.68 | *0.73* | 1.85 | *0.87* |
| MAS.1.B7[b] | 1.84 | *0.12* | 3.30 | *0.75* | 1.41 | *0.90* |
| MAS.1.A1[a] | 2.63 | *0.13* | 4.62 | *0.50* | 2.98 | *0.60* |
| MAS.1.A2[a] | 2.14 | *0.13* | 3.99 | *0.44* | 2.24 | *0.53* |
| MAS.1.A3[a] | 2.68 | *0.13* | 4.09 | *0.57* | 2.36 | *0.68* |
| MAS.1.A4[a] | 2.62 | *0.13* | 4.15 | *0.48* | 2.42 | *0.57* |
| MAS.1.A5[a] | 2.24 | *0.13* | 3.81 | *0.46* | 2.01 | *0.55* |
| MAS.1.A6 | 2.42 | *0.13* | 3.77 | *0.88* | 1.97 | *1.05* |
| MAS.1.A7[a] | 2.04 | *0.10* | 3.93 | *0.90* | 2.15 | *1.08* |
| St8.1.B2[a] | 2.41 | *0.13* | 4.26 | *0.73* | 2.55 | *0.88* |
| St8.1.B3[a] | 3.07 | *0.13* | 4.63 | *0.51* | 2.99 | *0.61* |
| St8.1.B4[a,b] | 3.20 | *0.13* | 4.67 | *0.40* | 3.05 | *0.48* |
| St8.1.B5[a] | 2.67 | *0.13* | 4.48 | *0.57* | 2.82 | *0.68* |
| St8.1.B6 | 2.80 | *0.13* | 4.56 | *0.65* | 2.91 | *0.78* |
| St8.1.B7[a] | 1.88 | *0.14* | 3.55 | *0.47* | 1.70 | *0.57* |

*Notes:* Measured volatiles is $H_2O$ (+$CO_2$) using SIMS and/or FTIR, VBD includes [a]$Fe^{2+}/Fe_T$ and [b]$S^{6+}/S^T$, and VBD corrected uses an empirical correction based on St8.1.B data such that VBD corrected = (VBD – 2.13)/0.83. Errors of one standard deviation (*s.d.*) are in *italics*.

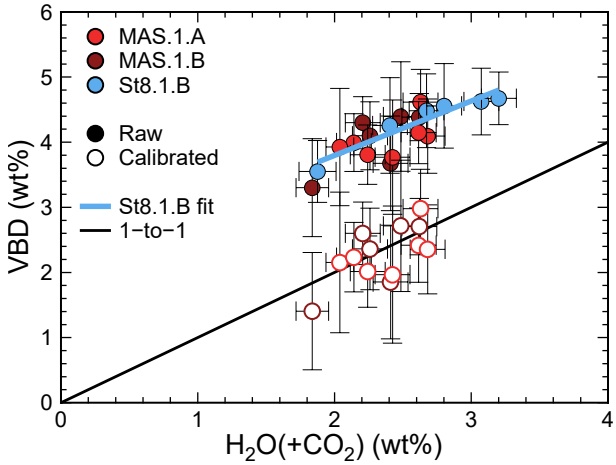


**Figure 2.5:** VBD against measured volatiles ($H_2O$+$CO_2$) from Lesne et al. (2011), where VBD includes $Fe^{2+}/Fe_T$ and $S^{6+}/S_T$ if measured. Closed symbols are the raw data and open symbols have been calibrated using a fit to the St8.1.B glasses (blue line). The VBD errors are calculated using the standard deviations on each measured oxide and the analytical error on Fe (0.03) and S (0.05) oxidation states, rather than the precision on VBD. If there was no measurement of Fe and/or S oxidation state, a value of 0.5 ± 0.5 (i.e., unknown) was used. The black line indicates the 1-to-1 trend.

## 2.6. Conclusions

Sub-surface charging is an important process to consider during EPMA of insulating materials, especially hydrous silicate glass, due to its effect on quantitative analysis (Cazaux, 1996). Sub-surface charging causes element migration and redox changes during analysis (e.g., Section 3.5; Humphreys et al., 2006; Zhang et al., 2018). Our Win X-ray modelling shows that sub-surface charging can also have a measurable effect on X-ray generation and emission, resulting in low analytical totals and high VBD contents. The ~1 wt% overestimation of volatiles, predominantly $H_2O$, observed in the literature data when hydrous glass contains $>$2 wt% volatiles, could cause a ~0.5 kbar overestimation of the entrapment pressures of melt inclusions (Newman and Lowenstern, 2002), often used to decipher the architecture of volcano plumbing systems (e.g., Blundy and Cashman, 2008), resulting in ~2 km depth change which is on the order of the resolution of geophysical observations for shallow magma chambers (e.g., Field et al., 2012). The same issue would also cause an order of magnitude underestimation in the viscosity (e.g., Di Genova et al., 2013), which could change the inferred flow regime (e.g., Turner and Campbell, 1986), fragmentation mechanism (e.g., Namiki and Manga, 2008; Zhang, 1999), and whether the melt remained coupled to entrained bubbles and crystals (e.g., Jaupart and Vergniolle, 1988). Using an empirical correction to correct VBD removes the systematic overestimation of volatiles, and provides accurate volatile contents using EPMA. This makes EPMA a useful, low-cost alternative to other techniques such as FTIR, SIMS, and Raman, for analysis of volatiles at high spatial resolution, using a more readily available analytical instrument that does not suffer problems due to fluorescence and nanolites.

# Chapter 3

# High spatial resolution analysis of the iron oxidation state in silicate glass using the electron probe

**Hughes, E. C.**, Buse, B, Kearns, S. L., Blundy, J. D., Kilgour, G., Mader, H. M., Brooker, R. A., Balzer, R., Botcharnikov, R. E., Di Genova, D., Almeev, R. R., and Riker, J. M. (2018). High spatial resolution analysis of the iron oxidation state in silicate glasses using the electron probe. *American Mineralogist*, 103(9), 1473–1486.

**Author contributions and declaration:** E.C. Hughes collected, processed, and interpretted the data, and wrote the manuscript with the help of B. Buse, S.L. Kearns, J.D. Blundy, H.M. Mader, G. Kilgour, D. Di Genova, and R.A. Brooker, with comments from R.E. Botcharnikov, R.R. Almeev, and J.M. Riker. R. Brooker, R. Balzer, and R.E. Botcharinkov helped with the experimental synthesis of the glasses, which are described in Chapter 5, but were initially published in this manuscript. R.A. Brooker, R.E. Botcharnikov, D. Di Genova, R.R. Almeev, and J.M. Riker provided samples. The manuscript was improved by comments from J. Donovan and two anonymous reviewers. The manuscript appears as published, except where edited for consistency in the thesis.

## ABSTRACT

The iron oxidation state in silicate melts is important for understanding their physical properties, although it is most often used to estimate the oxygen fugacity of magmatic systems. Often high spatial resolution analyses are required, yet the available techniques, such as μXANES and μMössbauer, require synchrotron access. The flank method is an electron probe technique with the potential to measure Fe oxidation state at high spatial resolution, but requires careful method development to reduce errors related to sample damage, especially for hydrous glass. The intensity ratios derived from measurements on the flanks of Fe$L\alpha$ and Fe$L\beta$ X-rays (Fe$L\beta_f$/Fe$L\alpha_f$) over a time interval (time-dependent ratio flank method) can be extrapolated to their initial values at the onset of analysis. We have developed and calibrated this new method using silicate glass with a wide range of compositions (43–78 wt% $SiO_2$, 0–10 wt% $H_2O$, and 2–17 wt% $FeO_T$, which is all Fe reported as $FeO_T$), including 68 glasses with known Fe oxidation state. The Fe oxidation state ($Fe^{2+}/Fe_T$) of hydrous (0–4 wt% $H_2O$) basaltic (43–56 wt% $SiO_2$) and peralkaline (70–76 wt% $SiO_2$) glasses with $FeO_T >$ 5 wt% can be quantified with a precision of $\pm$0.03 (10 wt% $FeO_T$ and 0.5 $Fe^{2+}/Fe_T$) and accuracy of $\pm$0.1. We find basaltic and peralkaline glasses each require a different calibration curve, and analysis at different spatial resolutions ($\sim$20 and $\sim$60 μm diameter regions, respectively). A further 49 synthetic glasses were used to investigate the compositional controls on redox changes during electron beam irradiation, where we found that the direction of redox change is sensitive to glass composition. Anhydrous alkali-poor glass becomes reduced during analysis, whilst hydrous and/or alkali-rich glass becomes oxidised by the formation of magnetite nanolites identified using Raman spectroscopy. The rate of reduction is controlled by the initial oxidation state, whereas the rate of oxidation is controlled by $SiO_2$, Fe, and $H_2O$ concentration.

## 3.1. Introduction

Oxygen fugacity is an important control on the chemical and physical properties of silicate melts, the stability of magmatic phases, and the multiphase rheology of magmas (Hamilton et al., 1964; Dingwell and Virgo, 1987; Kress and Carmichael, 1991; Vicenzi et al., 1994; Bouhifd et al., 2004; Wilke, 2005). It also determines the valence state of multivalent elements, such as Fe, Mn, Cr, V, Ce, Eu, and S, hence the ratio of oxidised to reduced species in the glasses quenched from melts provides a proxy for oxygen fugacity during natural processes and laboratory experiments (e.g., Carmichael, 1991; Kress and Carmichael, 1991; Herd, 2008). Many petrological and volcanological applications, such as analysis of glassy melt inclusions in minerals from volcanic rocks or interstitial glass in natural and experimental vesiculated and/or partially crystalline samples, require measurements at high spatial resolutions.

There are various techniques for quantifying the Fe oxidation state of silicate glass, with trade-offs between resolution, error, sample preparation requirements, necessity for standards, and instrument accessibility (see McCammon, 1999). Wet chemistry is a destructive bulk technique, requiring a minimum of 5 mg of material (e.g., Schuessler et al., 2008), which does not require standards but some expertise. Synchrotron-based absorption techniques, such as μXANES (>2×2 μm, e.g., Cottrell et al., 2009) and μMössbauer (>10×5 μm, e.g., Potapkin et al., 2012) allow high spatial resolution analysis, but the need for access to synchrotron facilities limits their utility. Also, μXANES can oxidise Fe in hydrous glass during analysis, producing erroneous Fe oxidation state values (Cottrell et al., 2018). Raman spectroscopy also has high spatial resolution (1 μm diameter), but has lower sensitivity for basaltic compositions and problems related to background fluorescence (e.g., Di Muro et al., 2009; Di Genova et al., 2016). Electron energy loss spectroscopy (EELS) would offer superior spatial resolution (nm) but standards are inhomogeneous at this scale and beam damage is significant (Burgess et al., 2016).

Conversely, the electron probe is widely available and has the potential for routine analysis of Fe oxidation state in geological materials (mainly garnet and amphibole) at high spatial resolution (Höfer et al., 1994; Enders et al., 2000; Höfer and Brey, 2007; Creighton et al., 2009, 2010; Malaspina et al., 2010; Lamb et al., 2012; Matjuschkin et al., 2014) but also silicate glass (Fialin et al., 2001, 2004, 2011). Typically, the electron probe uses the intensity of emitted characteristic X-rays to quantify chemical composition (e.g., Section 2.2), such as Fe$K\alpha$ to quantify Fe concentration (Figure 3.1a), however a variety of other factors can affect the intensity of characteristic X-rays. The Fe$L\alpha$ and Fe$L\beta$ lines are sensitive to the Fe oxidation state as their X-ray generation involves outer shell electrons (3d) affected by chemical bonding (Figure 3.1a) (Gopon et al., 2013). The energy of X-ray emission and absorption associated with the Fe$L$ lines are very similar, which leads to self-absorption. The Fe$L\alpha$ and Fe$L\beta$ peaks coincide with the $L_3$ and $L_2$ absorption edges, respectively, and hence are distorted by them, resulting in asymmetric peak shapes and peak shifts due to the differing amounts of absorption on each side of the absorption edges (Smith and O'Nions, 1971). The wavelength of the energy of the absorption edges shift due to changes in the coordination and oxidation state of Fe (De Groot, 2001; Höfer and Brey, 2007). The $L_3$ absorption edge shifts more than the $L_2$ absorption edge, resulting in greater changes to the Fe$L\alpha$ peak than the Fe$L\beta$ (Höfer and Brey, 2007). Thus, for a given chemical system (e.g., garnet, olivine, silicate glass), the Fe$L\alpha$ and Fe$L\beta$ peak positions and intensities vary depending on Fe concentration, oxidation state, and coordination (Figure 3.1b; Höfer and Brey, 2007).

There are two EPMA methods that exploit variations in Fe$L\alpha$ and Fe$L\beta$ to quantify Fe oxidation state (Figure

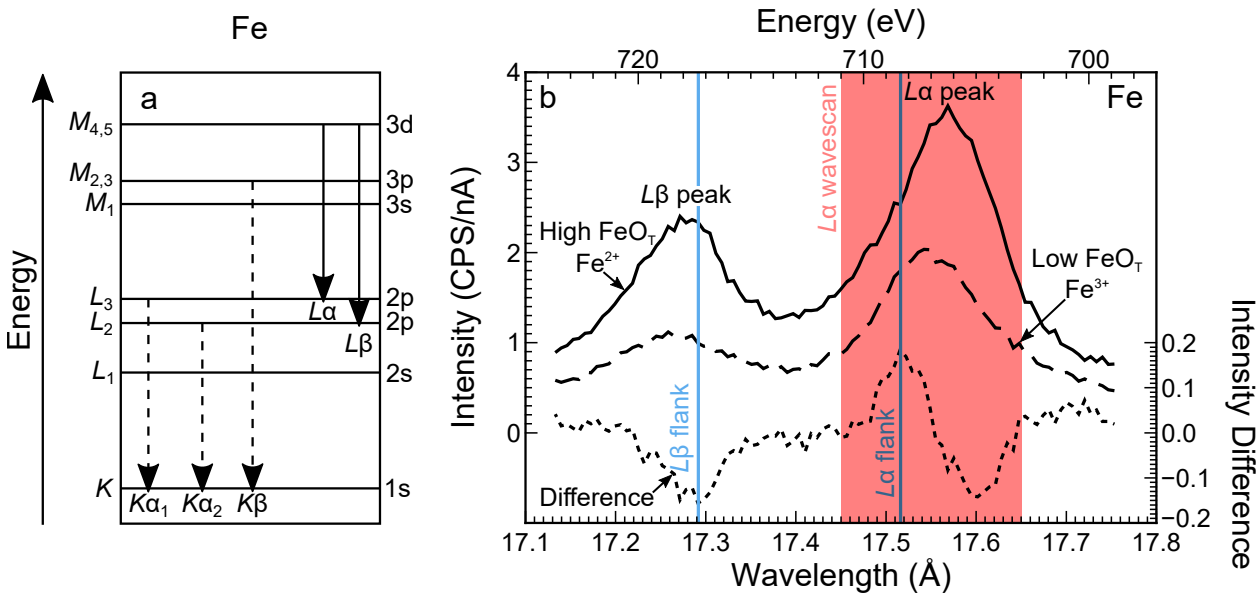


**Figure 3.1: (a)** Energy level diagram of the electron transitions that generate characteristic Fe X-rays, and **(b)** wavelength spectra of the Fe$L\alpha$ and Fe$L\beta$ peaks for a reduced, high $FeO_T$ (solid, AR19) and oxidised, low $FeO_T$ (dashed, AR14) silicate glass (Tables 3.1 and 3.2) plotted using the left-hand axes, and the difference spectrum (dotted, calculated once the wavescans are normalised to their maximum Fe$L\alpha$ peak intensity) plotted using the right-hand axes. The red box indicates the wavelengths measured for the peak shift method (Fe$L\alpha$ wavescan). The blue vertical lines indicate optimum wavelength positions measured for the flank method, which correspond to the maximum and minimum of the difference spectrum.

3.1b). The peak shift method uses the linear relationship between the wavelength of the Fe$L\alpha$ peak with Fe oxidation state at a given $FeO_T$ (Höfer et al., 1994; Fialin et al., 2004) (Figure 3.1b). To measure the Fe$L\alpha$ peak position, wavescans across the Fe$L\alpha$ peak are collected and a peak-fitting algorithm is applied to locate its wavelength. This method has been applied to silicate glass with a statistical error on $Fe^{2+}/Fe_T$ of $\pm 0.05$, although the error on individual analyses was greater (Fialin et al., 2004). Alternatively, the flank method uses changes in the wavelength and intensity of both the Fe$L\alpha$ and Fe$L\beta$ peaks by measuring the intensity ratio of positions on the low wavelength flank of Fe$L\alpha$ (Fe$L\alpha_f$) and high wavelength flank of Fe$L\beta$ (Fe$L\alpha_f$), termed Fe$L\beta_f$/Fe$L\alpha_f$ (Höfer et al., 1994; Höfer, 2002; Höfer and Brey, 2007) (Figure 3.1b). These flank positions coincide with the $L_2$ and $L_3$ absorption edges and, as the $Fe^{2+}$ content changes, the $L_3$ absorption edge shifts. The sensitivity of the flank method results from the opposite sense of intensity change at each of the flank positions, as Fe$L\alpha_f$ is on the high absorption side of the $L_3$ absorption edge, whereas Fe$L\beta_f$ is on the low absorption side of the $L_2$ absorption edge, which utilises changes in both peak position and intensities (Höfer et al., 1994). Optimum flank positions can be found by collecting absorption spectra or using the maximum and minimum in the difference spectrum between samples with different Fe concentration and oxidation states (Figure 3.1b; Höfer and Brey, 2007). The Fe$L\beta_f$/Fe$L\alpha_f$ intensity ratio is dependent primarily on total ferrous iron ($Fe^{2+}$), with a secondary dependence on total Fe ($Fe_T$), hence

$$Fe^{2+} = A + B \cdot (\text{Fe}L\beta_f/\text{Fe}L\alpha_f) + C \cdot Fe_T + D \cdot Fe_T \cdot (\text{Fe}L\beta_f/\text{Fe}L\alpha_f) \quad (3.1)$$

where $A$, $B$, $C$, and $D$ are fitting coefficients (Höfer and Brey, 2007). The flank method has greater sensitivity than the peak shift method and does not require wavescans as measurements are made at two specific, pre-

defined wavelengths (Höfer et al., 1994; Zhang et al., 2018). This method has been applied to some mineral groups (e.g., garnet, spinel) with an error on $Fe^{2+}/Fe_T$ of $\pm 0.02$ (Höfer and Brey, 2007) and silicate glass to within $\pm 0.1$ (Zhang et al., 2018).

The Fe*L* lines have low intensity and therefore high beam currents and/or long count times are required to record them. Silicate glass is typically unstable under these conditions, leading to changes in Fe oxidation state during analysis (Fialin et al., 2004, 2011; Fialin and Wagner, 2012; Zhang et al., 2018). Similar problems have also been observed for Fe in amphiboles (Wagner et al., 2008; Lamb et al., 2012) and S in silicate glass and anhydrite (Wallace and Carmichael, 1994; Rowe et al., 2007; Klimm et al., 2012). Fialin and Wagner (2012) observed two competing mechanisms of redox change during electron beam irradiation of alkali-bearing silicate glass leading to either oxidation or reduction. As glass is an insulator, electrons are trapped within the subsurface during electron beam irradiation, causing a region of negative charge to build-up at depth in the sample, even with a conductive coat (e.g., Section 2.2.4; Cazaux, 1996). Alkali ions (predominantly $Na^+$, but also $K^+$) migrate towards the region of negative charge (e.g., Humphreys et al., 2006) leaving behind interstitial $O^{2-}$ that migrates and either outgasses or combines with two FeO precipitating $Fe_2O_3$, thus causing oxidation (e.g., Lineweaver, 1963). This is different to oxidation processes driven by changes in oxygen fugacity. For basaltic glass, $Fe^{3+}$ is stabilised by the migration of $Na^+$ and $K^+$ towards them preventing $Fe_2O_3$ precipitation (Cooper et al., 1996). Concurrently, during electron beam irradiation electrons move away from the negatively charged region from O to $Fe^{3+}$ sites resulting in net reduction (Nishida, 1995).

To minimise beam damage and prevent redox changes a sample can be moved during analysis, which reduces the electron dose per unit area (Métrich and Clocchiatti, 1996; Rowe et al., 2007; Fialin et al., 2011; Zhang et al., 2018). Unfortunately, this requires large regions of glass for analysis making it unfeasible for analysing small areas, such as melt inclusions and interstitial glasses. Therefore, we adapt the flank method for high spatial resolution analysis of silicate glass due to its greater sensitivity and the ability to measure at single spectrometer positions (Höfer et al., 1994). This is important because it is easier to measure time-dependent changes at specific wavelengths rather than using wavescans, as required for the peak shift method. We measured Fe$L\beta_f$/Fe$L\alpha_f$ over time, based on the time-dependent intensity (TDI) technique first developed for alkali migration during EPMA of glasses by Nielsen and Sigurdsson (1981). Fe$L\beta_f$/Fe$L\alpha_f$ is extrapolated to time zero to correct for changes over time, which we refer to as the time-dependent ratio (TDR) correction, comparable to TDI corrections for alkalis (Section 2.2.3). Due to the small sample size of silicate glasses analysed by Fialin and Wagner (2012) and Zhang et al. (2018), the controls on Fe redox processes during electron beam irradiation have not been explored and, crucially, few hydrous glasses have been analysed. Therefore, we also investigate the compositional and analytical controls on Fe redox changes (Section 3.5).

## 3.2. Samples

Silicate glass of known (68 samples) and unknown (47 samples) Fe oxidation state from a variety of studies were mounted in epoxy and carbon coated (~15 nm thickness). The sample set covers a wide compositional range (anhydrous normalised $SiO_2$ 43–78 wt%, total alkalis ($Na_2O$+$K_2O$) 1–12 wt%, and $H_2O$ 0–10 wt%; Figure 3.2a and Table 3.1), which are used to investigate the effect of composition on Fe oxidation state changes during analysis. Silicate glass of known Fe oxidation state (independently measured using wet

chemistry, μMössbauer or μXANES), spanning 0.1–1.0 $Fe^{2+}/Fe_T$ and 2–18 wt% $FeO_T$ (Figure 3.2b), are used to calibrate the technique.

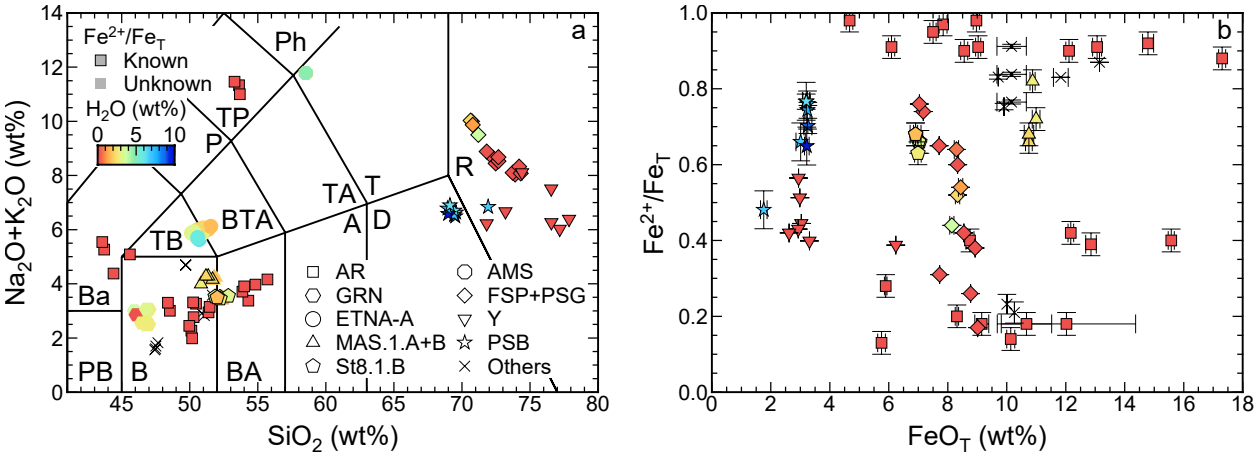


**Figure 3.2:** **(a)** Total alkalis ($Na_2O+K_2O$) against silica (where $SiO_2$, $Na_2O$, and $K_2O$ are normalised to the volatile-free total), and **(b)** $Fe^{2+}/Fe_T$ against $FeO_T$ for samples with known Fe oxidation state. Symbol shape indicates glass composition (Table 3.1), colour indicates $H_2O$ concentration, and a black outline indicates known Fe oxidation state; those without an outline have unknown Fe oxidation state. TAS classification abbreviations: PB = picrobasalt, B = basalt, BA = basaltic andesite, A = andesite, D = dacite, TB = trachybasalt, BTA = basaltic trachyandesite, TA = trachyandesite, T = trachyte, R = rhyolite, Ba = basanite, P = phonotephrite, TP = tephriphonolite, and Ph = phonolite.

There are 16 suites of experimental silicate glasses that have different average glass compositions with variable Fe oxidation state and/or $H_2O$. The normalised (volatile-free) average glass compositions, which are either taken from the literature or measured using EPMA, are given in Table 3.1. AR samples are anhydrous, low-silica glasses with a range of glass compositions: KLA-1-6-22 (Fuchs et al., 2014), SC1 (Botcharnikov et al., 2008), 140ox (Almeev et al., 2007), LS (previously unpublished studies conducted at the Institut für Mineralogie, Leibniz Universität Hannover, Germany), PF22 (Wengorsch et al., 2012), and BezBA (Almeev et al., 2013). These glass compositions were re-synthesised at various oxygen fugacities and analysed using wet chemistry by Zhang et al. (2018), where they have been analysed by the flank method using a moving stage approach. Hydrous, low-silica glasses are GRN (Stamper et al., 2014), ETNA-A (ETNA24 from Chapter 4 and ETNA01–ETNA17 and ETNA25–ETNA30 from Chapter 5), MAS.1.A, MAS.1.B and St8.1.B (Lesne et al., 2011), and AMS (Di Genova et al., 2014). GRN samples may have suffered oxidation during μXANES (Cottrell et al., 2018), therefore their reported Fe oxidation state values are not considered further and the samples are only used to explore the effects of composition on redox changes during EPMA. The high-silica glasses range from peralkaline (FSP in Di Genova et al. 2016; and PSG in Di Genova et al. 2013) to calcalkaline (Y in Di Genova et al. 2017b; and PSB in Riker et al. 2015), with both anhydrous (FSP and Y) and hydrous (PSG and PSB) compositions.

Additional anhydrous, low-silica glasses analysed are AII and LW (Table B.1, Cottrell et al., 2009), Smithsonian microbeam basaltic glass standards VG-2 and VG-A99 (Table 2.4, Jarosewich et al., 1980) and PU (Table B.1, Ulmer, 1989; Blundy et al., 2018).

**Table 3.1:** Normalised (volatile-free), average glass composition for the suites of experimental silicate glasses.

| | AR KLA-1-6-22 | AR SC1 | AR 140ox | AR LS | AR PF22 | AR BezBA | GRN | ETNA-A |
|---|---|---|---|---|---|---|---|---|
| *n* | 4 | 4 | 3 | 4 | 3 | 4 | 10 | 24 |
| $SiO_2$ | 44.32 | 49.42 | 50.08 | 51.85 | 53.53 | 54.6 | 46.66 | 50.75 |
| $TiO_2$ | 3.91 | 2.91 | 0.99 | 3.51 | 1.60 | 0.99 | 1.00 | 1.72 |
| $Al_2O_3$ | 13.24 | 15.37 | 15.83 | 12.02 | 19.66 | 17.53 | 13.55 | 17.63 |
| $FeO_T$ | 10.96 | 11.09 | 8.68 | 15.04 | 5.45 | 7.92 | 9.60 | 10.03 |
| MnO | 0.20 | 0.00 | 0.17 | 0.33 | 0.17 | 0.18 | 0.20 | 0.33 |
| MgO | 9.20 | 6.71 | 9.81 | 4.22 | 2.88 | 5.92 | 12.96 | 6.12 |
| CaO | 8.76 | 11.39 | 12.11 | 9.30 | 4.97 | 8.56 | 13.05 | 7.02 |
| $Na_2O$ | 2.99 | 2.78 | 2.16 | 2.93 | 7.49 | 2.99 | 2.16 | 4.05 |
| $K_2O$ | 0.95 | 0.31 | 0.07 | 0.26 | 3.78 | 0.95 | 0.58 | 1.85 |
| $P_2O_5$ | 0.16 | 0.03 | 0.08 | 0.54 | 0.48 | 0.16 | 0.24 | 0.5 |
| $H_2O$ | 0 | 0 | 0 | 0 | 0 | 0 | [a]0.28–3.50 | [a]1.58–6.07 |
| $Fe^{2+}/Fe_T$ | [c]0.14–0.98 | [c]0.19–0.95 | [c]0.18–0.97 | [c]0.18–0.92 | [c]0.13–0.98 | [c]0.20–0.91 | [e] | n.d. |
| | MAS.1.A | MAS.1.B | St8.1.B | AMS | FSP | PSG | Y | PSB |
| *n* | 6 | 6 | 8 | 3 | 9 | 4 | 7 | 8 |
| $SiO_2$ | 50.86 | 50.84 | 51.86 | 57.72 | 73.16 | 70.84 | 75.37 | 69.61 |
| $TiO_2$ | 1.17 | 1.18 | 0.86 | 0.39 | 0.43 | 0.50 | 0.17 | 0.35 |
| $Al_2O_3$ | 18.91 | 18.76 | 19.13 | 18.4 | 8.95 | 9.24 | 12.25 | 16.06 |
| $FeO_T$ | 11.18 | 11.19 | 7.53 | 4.51 | 8.14 | 8.49 | 3.43 | 3.30 |
| MnO | n.d. | n.d. | n.d. | 0.10 | 0.35 | 0.38 | 0.04 | 0.06 |
| MgO | 3.41 | 3.17 | 6.24 | 1.46 | 0.17 | 0.07 | 0.53 | 0.78 |
| CaO | 9.23 | 9.41 | 10.85 | 4.23 | 0.44 | 0.60 | 1.45 | 3.05 |
| $Na_2O$ | 2.77 | 2.9 | 2.67 | 3.72 | 4.34 | 5.78 | 2.69 | 4.81 |
| $K_2O$ | 1.23 | 1.29 | 1.80 | 7.90 | 4.08 | 4.07 | 4.06 | 1.87 |
| $P_2O_5$ | n.d. | n.d. | n.d. | 0.19 | 0 | 0.03 | 0.03 | 0.10 |
| $H_2O$ | [a]1.58–2.86 | [a]1.64–2.55 | [a]1.03-3.38 | [b]1.29–4.78 | 0 | [b]0.72–3.57 | 0 | [a]6.00–9.62 |
| $Fe^{2+}/Fe_T$ | [c]0.66–0.72 | [c]0.68–0.82 | [c]0.63–0.68 | n.d. | [c]0.17–0.76 | [c]0.44–0.64 | [c]0.39–0.56 | [d]0.48–0.77 |

*Notes: n* is the number of samples in the experimental suite. Oxides (in wt%) are measured using EPMA (all Fe reported as FeO, $FeO_T$), except $H_2O$ which is measured by [a]SIMS, [b]KFT, or 0 indicates assumed due to experimental conditions. $Fe^{2+}/Fe_T$ is measured by [c]wet chemistry, [d]μXANES or not determined (n.d.). [e]Fe oxidation state measurements may have suffered from oxidation during μXANES and are therefore not used in this study (Cottrell et al., 2018). Individual glass compositions are available in Table B.1, except ETNA-A which are in Tables 4.10 (ETNA24) and 5.6 (ETNA01–ETNA17 and ETNA25–ETNA30).

## 3.3. Methods

### 3.3.1. Fe*L* wavescans

Wavescans of the Fe*L* peaks on glasses with varying $FeO_T$ and Fe oxidation state (Table 3.2) were analysed to examine the controls on peak position and intensity. Data were collected on the JEOL JXA 8530F Hyperprobe at the School of Earth Sciences, University of Bristol, UK, using a 50 nA beam current, 10 μm beam diameter, and 15 or 30 kV accelerating voltage. Three spectrometers, with two TAP and one TAPH crystals, were moved 0.071 mm per step for 100 steps with 0.5 s dwell time over the Fe*L* peaks whilst the stage moved at 1 $\mu m \cdot s^{-1}$ to minimise beam damage. To improve signal to noise ratio, multiple wavescans (40–80, depending on the accelerating voltage and glass $FeO_T$) were collected, and the spectra from the three spectrometers were combined to produce a single wavescan per sample.

**Table 3.2:** Fe content and oxidation state of glasses analysed using wavescans.

| Sample | AR10 | AR14 | AR16 | AR19 | AR20 |
|---|---|---|---|---|---|
| Glass composition | 140ox | PF22 | 140ox | LS | PF22 |
| $FeO_T$ (wt%) | $9.16 \pm 0.24$ | $5.75 \pm 0.13$ | $7.85 \pm 0.13$ | $14.79 \pm 0.19$ | $4.67 \pm 0.12$ |
| $Fe^{2+}/Fe_T$ | $0.18 \pm 0.03$ | $0.13 \pm 0.03$ | $0.97 \pm 0.03$ | $0.97 \pm 0.03$ | $0.98 \pm 0.03$ |

*Notes:* Glass composition refers to Table 3.1. $FeO_T$ (all Fe reported as FeO) measured using EPMA and $Fe^{2+}/Fe_T$ using wet chemistry. Errors are of one standard deviation ($1\sigma$).

### 3.3.2. Time-dependent ratio Fe$L\beta_f$/Fe$L\alpha_f$ measurements

#### Selecting flank positions

To identify the optimum flank positions for Fe$L\beta_f$/Fe$L\alpha_f$, the method of Höfer and Brey (2007) (Section 3.1 and Figure 3.1b) was used. Two spectra, representing the range of $FeO_T$ and Fe oxidation state (AR14 and AR19, Figure 3.3a), were normalised to the maximum intensity of their Fe$L\alpha$ peak from which the difference spectrum was calculated (AR14 – AR19, Figures 3.3c and d). Optimum flank positions correspond to the maximum (low wavelength flank of Fe$L\alpha$, Fe$L\alpha_f$) and minimum (high wavelength flank of Fe$L\beta$, Fe$L\beta_f$) of the difference spectrum. To avoid collecting wavescans on these glasses every session, the flank positions were measured relative to the F$K\alpha$ peak measured on $MgF_2$ for each TAP/TAPH crystal. This reduced the time required to find the flank positions during future analytical sessions and minimised the area damaged by electron beam irradiation.

#### Electron probe set-up

Each spectrometer measured a single wavelength and the spectrometer set-up (referred to by crystal) was two TAP crystals to measure Fe$L\alpha_f$, TAPH for Fe$L\beta_f$, LLIF for Fe$K\alpha$, and PETH for K$K\alpha$. At the wavelengths of interest, the TAPH crystal offers twice the peak intensity of the TAP crystals, and the Fe$L\beta$ has roughly half the intensity of the Fe$L\alpha$ peak, therefore we chose the above combination of spectrometers to maximise count rates. The full-width half-maximum wavelength resolution for F$K\alpha$ in $MgF_2$ here is 0.0813, 0.0835, and 0.1034 Å (0.8792, 1.1235, and 0.9079 mm spectrometer units, L) for the two TAP and TAPH crystals, respectively (Buse and Kearns, 2018). Differential pulse height analysis (PHA) mode was used to remove interferences such as the $9^{th}$ order Fe$K\alpha$, and PHA scans were collected every session on each spectrometer

on F$K\alpha$ in $MgF_2$. Na is typically the most mobile element measured during electron beam irradiation and therefore commonly used to monitor beam damage. However, in the absence of an additional TAP crystal, we measured K (also highly mobile) instead on a PETH crystal. For each analytical session, Fe$K\alpha$ was peaked-up on BCR-2 (USGS basaltic glass standard, Table 2.4), K$K\alpha$ on sanidine (Table 2.3), and the peak position of F$K\alpha$ was measured on $MgF_2$ to calculate the wavelengths of the flank positions on each TAP/TAPH crystal. Spectrometers were static during analysis as backgrounds are not required for flank analyses (Höfer and Brey, 2007). As no other elements (or backgrounds) were measured, no matrix correction could be performed to quantify Fe or K, thus only their relative intensity over time is used. Analytical conditions were a 15 kV accelerating voltage, 50 nA beam current, and 4–15 μm beam diameter, which allows the analysis of small volumes of glass (Table 3.3). Intensity measurements were collected over 5 s for a total duration of ~150 s on the same spot of glass. Ten repeat analyses on fresh glass per sample were collected, resulting in a total analysis area of ~20–60 μm diameter. Data were collected over five sessions. A summary of the analytical protocol is provided in Section D.1.

**Table 3.3:** EPMA conditions for time-dependent ratio Fe$L\beta_f$/Fe$L\alpha_f$ measurements.

| Conditions | Accelerating voltage (kV) | Beam current (nA) | Beam diameter (μm) | No. of analyses | Total duration (s) |
|---|---|---|---|---|---|
| 1 | 15 | 50 | 4 | 10 | 150 |
| 2 | 15 | 50 | 10 | 10 | 150 |
| 3 | 15 | 50 | 15 | 10 | 150 |
| 4 | 15 | 50 | 20 | 10 | 150 |
| 5 | 15 | 500 | 10 | 1 | 150 |
| 6 | 30 | 50 | 10 | 10 | 150 |

*Notes:* Conditions 1–3 were used to quantify Fe oxidation state, and additional measurements were made at conditions 4–6 on AR10, AR16, MAS.1.B4, and PSB63 to investigate redox stability.

### Redox stability

To investigate the effect of analytical conditions on redox changes, additional measurements were made at different analytical conditions (Table 3.3) on four glasses chosen to represent the range of glass compositions studied (Table 3.4). AR10 and AR16 are anhydrous low-silica glasses, that are oxidised and reduced, respectively. MAS.1.B4 and PSB63 are hydrous glasses that are low- and high-silica, respectively.

### Data processing

To check for sample homogeneity, Fe$K\alpha$ was compared between repeat analyses. If the Fe$K\alpha$ intensity was significantly outside the counting error for other repeats, the erroneous repeat analysis was removed from further processing and, if the sample was too inhomogeneous, the sample was not processed further. The analyses were then averaged at each time interval for Fe$L\alpha_f$ (separately for each spectrometer), Fe$L\beta_f$, Fe$K\alpha$, and K$K\alpha$. Using these averages at each time interval, Fe$L\beta_f$ was divided by the sum of Fe$L\alpha_f$ from the two spectrometers to calculate Fe$L\beta_f$/Fe$L\alpha_f$. Errors on Fe$K\alpha$, K$K\alpha$, Fe$L\beta_f$/Fe$L\alpha_f$, and time are the standard deviation of the repeat measurements. An exponential equation of the following form was fitted to each sample:

$$I = (I_0 - I_\infty)\exp\left(\frac{I_0' t}{I_0 - I_\infty}\right) + I_\infty \tag{3.2}$$

Where $I$ is the Fe$L\beta_f$/Fe$L\alpha_f$ intensity ratio and $t$ is time, subscripts refer to the values at time = 0 and $\infty$, and $I_0'$ is the rate of change of $I$ with time at time = 0. When the minimisation failed to converge, $I_\infty$ was fixed to the last measured value for the sample. The error in both these cases is the standard error on the fit coefficients. In those cases where Fe$L\beta_f$/Fe$L\alpha_f$ was constant with time, convergence is not possible, therefore the average of Fe$L\beta_f$/Fe$L\alpha_f$ with time was used, where the error was the standard deviation of these data. Analyses with large errors ($>\pm0.1$ for $I_0$ and $>\pm0.01$ for $I_0'$), likely due to inhomogeneity, extremely rapid redox changes or analytical problems, are discarded.

**Table 3.4:** Glass compositions of AR10, AR16, MAS.1.B4, and PSB63.

| | AR10 | *s.d.* | AR16 | *s.d.* | MAS.1.B4 | *s.d.* | PSB63 | *s.d* |
|---|---|---|---|---|---|---|---|---|
| $SiO_2$ | 49.91 | *0.30* | 50.46 | *0.27* | 49.72 | *0.22* | 64.21 | *0.32* |
| $TiO_2$ | 0.97 | *0.02* | 1.00 | *0.02* | 1.16 | *0.03* | 0.33 | *0.02* |
| $Al_2O_3$ | 15.67 | *0.01* | 16.08 | *0.03* | 16.60 | *0.05* | 14.81 | *0.18* |
| $FeO_T$ | 9.16 | *0.24* | 7.85 | *0.13* | 10.88 | *0.09* | 3.26 | *0.08* |
| MnO | 0.17 | *0.01* | 0.18 | *0.01* | 0.03 | *0.01* | 0.07 | *0.06* |
| MgO | 9.49 | *0.02* | 10.38 | *0.05* | 3.28 | *0.03* | 0.75 | *0.06* |
| CaO | 11.89 | *0.10* | 12.53 | *0.05* | 8.89 | *0.07* | 2.91 | *0.06* |
| $Na_2O$ | 2.20 | *0.20* | 1.93 | *0.03* | 2.89 | *0.04* | 4.35 | *0.28* |
| $K_2O$ | 0.06 | *0.01* | 0.06 | *0.01* | 1.35 | *0.01* | 1.70 | *0.12* |
| $P_2O_5$ | 0.08 | *0.01* | 0.09 | *0.01* | 0.03 | *0.01* | 0.10 | *0.05* |
| $H_2O$ | 0 | | 0 | | 2.55 | *0.13* | 7.11 | *0.16* |
| $Fe^{2+}/Fe_T$ | [a]0.18 | *0.03* | [a]0.97 | *0.03* | [a]0.82 | *0.03* | [b]0.76 | *0.02* |

*Notes:* Oxides (in wt%) are measured using EPMA (all Fe reported as FeO, $FeO_T$), except $H_2O$ which is measured by SIMS or 0 indicates assumed due to experimental conditions. $Fe^{2+}/Fe_T$ is measured by [a]wet chemistry or [b]μXANES. Errors of one standard deviation (*s.d.*) are shown in *italics*.

### 3.3.3. Raman spectroscopy

Raman spectroscopy was used to detect the presence of nanolites before and after electron beam irradiation as nanolites alter the Raman spectra of silicate glass. Magnetite nanolites produce a peak due at ~670 $cm^{-1}$, which also decreases the intensity of the surrounding silicate peaks (Di Genova et al., 2017a,b). Carbon coats were removed prior to analysis. Raman spectra were collected using the Thermo Scientific DXRxi Raman Imaging Microscope at the School of Earth Sciences, University of Bristol, UK, with a green (520 nm) laser, 50× (long distance) or 100× objective, and 3–5 mW power to avoid sample oxidation. An extended grating was used to also collect data on $H_2O$ concentration. All samples, except AMS, FSP, PSG, and Y which have been previously analysed by Di Genova et al. (2017a,b), were analysed on non-irradiated areas of glass. Selected glasses that cover a range of compositions (ETNA08, MAS.1.A5, FSP1, FSP9, PSG6, and PSB63) were additionally analysed following electron beam irradiation.

## 3.4. Results

### 3.4.1. Electron probe micro-analysis

#### Wavelength and intensity changes of Fe*L* lines in silicate glass

For the same Fe oxidation state, peak intensity increases and peak positions shift to higher wavelengths with increasing $FeO_T$ (Figure 3.3a). For the same $FeO_T$, oxidised samples have greater peak intensities and lower wavelength peak positions than reduced samples (Figure 3.3a). At higher accelerating voltages (30 vs.15 kV) the intensity of Fe$L\alpha$ and Fe$L\beta$ decrease, but there is no appreciable shift in peak positions (Figures 3.3b and c). Therefore, there is no appreciable change in optimum flank positions, although the difference between the flank intensities decreases (Figure 3.3d).

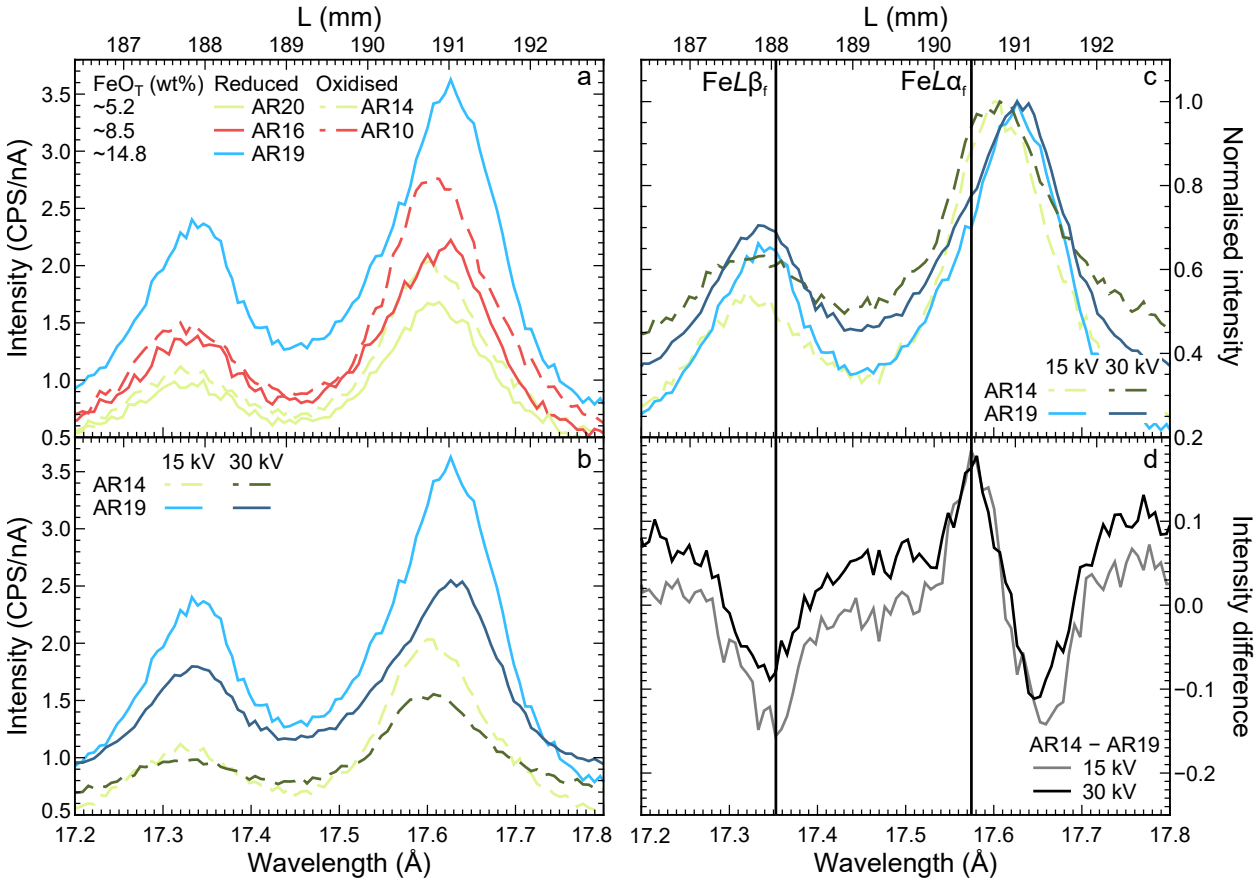


**Figure 3.3:** Wavescans of Fe*L* for silicate glass (see Table 3.2 for compositions). Analytical conditions were: 50 nA beam current and 10 μm beam diameter, whilst the stage moved at 1 $\mu m \cdot s^{-1}$. Spectrometer position (L) is shown along the top and equivalent wavelength along the bottom. **(a)** Different $FeO_T$ and Fe oxidation states at 15 kV accelerating voltage, **(b)** different accelerating voltages, **(c)** different accelerating voltages with the intensity normalised to the maximum Fe$L\alpha$ intensity, and **(d)** difference spectra (AR14 – AR19) at different accelerating voltages, calculated from the normalised spectra, with optimum flank positions shown (vertical lines). The Fe$L\beta_f$/Fe$L\alpha_f$ ratio is 0.55 for AR14 and 0.92 for AR19 at 15 kV. Data are available in Table D.1.

### Time-dependent intensity changes during electron beam irradiation

During electron beam irradiation, the intensity of K$K\alpha$ remains stable (anhydrous glass) or decreases (hydrous glass) over time (Figure 3.4), whereas for Fe$K\alpha$ the intensity remains stable (anhydrous glass) or increases (hydrous glass) (Figure 3.5). The ratio of Fe$L\beta_f$/Fe$L\alpha_f$ increases (anhydrous low-silica), remains stable (anhydrous low-silica and hydrous high-silica) or decreases (hydrous low-silica) over time (Figure 3.6). In those cases where intensity changes are observed, the rate typically increases with decreasing beam diameter, decreasing accelerating voltage, and increasing beam current. Data were collected during different sessions, therefore differences in the absolute intensity at different conditions are not meaningful.

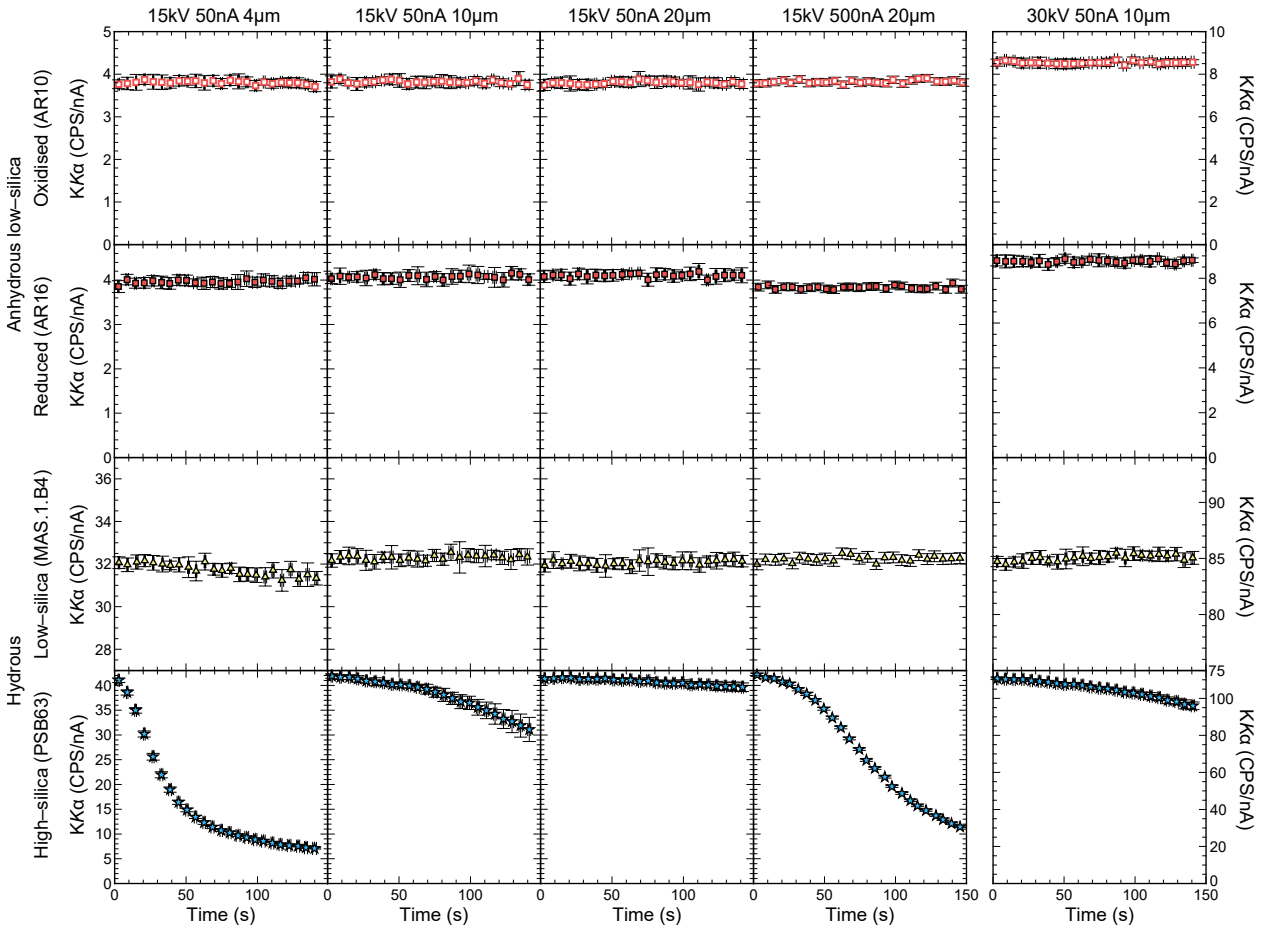


**Figure 3.4:** Intensity of K$K\alpha$ with time. Analytical conditions (accelerating voltage, beam current, beam diameter) shown along the top and sample description on the left-hand side. Symbols and colours as Figure 3.2a except that open/closed symbol indicates initial Fe oxidation state: open symbols are oxidised ($Fe^{2+}/Fe_T < 0.2$); closed symbols are reduced ($Fe^{2+}/Fe_T > 0.7$).

## 3.4.2. Raman spectroscopy

### Before electron beam irradiation

The majority of glasses analysed are nanolite-free prior to electron beam irradiation (Figures 3.7a and b). Exceptions are AR37 (composition LS) and ETNA(2) (samples ETNA03, ETNA06, ETNA07, ETNA08, ETNA14, ETNA16, and ETNA30; Appendix E), with a peak at ~670 $cm^{-1}$ indicating magnetite nanolites. Magnetite nanolites were detected in AMS4 and Y-L using Raman spectroscopy by Di Genova et al.

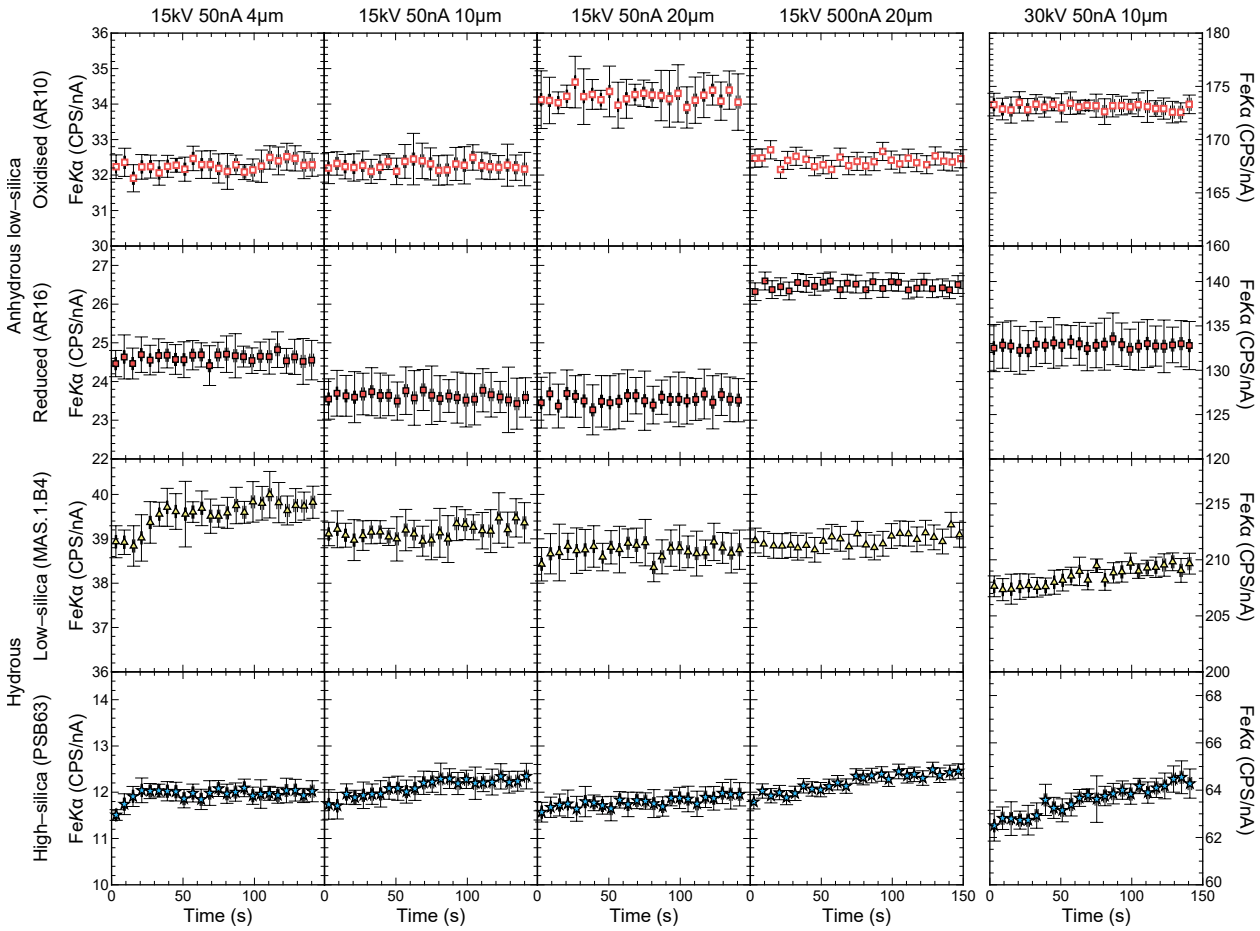


**Figure 3.5:** Intensity of Fe$K\alpha$ with time. Analytical conditions (accelerating voltage, beam current, beam diameter) shown along the top and sample description on the left-hand side. Symbols and colours as Figure 3.4.

(2017a,b).

**After electron beam irradiation**

Most glasses analysed following electron beam irradiation (MAS.1.A4, FSP1, FSP9, and PSG6) exhibit new magnetite nanolites (peak at ~670 $cm^{-1}$) when irradiated using a 4 µm beam diameter implying oxidation (Figure 3.7c). Additionally, ETNA08, MAS.1.A4, and PSG6 have a new peak at ~1350 $cm^{-1}$, which corresponds to haematite (RUFF Raman spectra database, http://rruff.info/, Lafuente et al. 2015), implying the formation of haematite nanolites following electron beam irradiation (Figure 3.7c). PSB63 shows no evidence for the presence of Fe-bearing nanolites following electron beam irradiation. The $H_2O$ peak (~3600 $cm^{-1}$) shows a decrease in height after electron beam irradiation for hydrous samples (ETNA08, MAS.1.A4, PSG6, and PSB63), implying loss of water.

## 3.5. Controls on Fe redox changes in silicate glass during electron beam irradiation

The ratio of Fe$L\beta_f$/Fe$L\alpha_f$ over time increased, remained stable, or decreased (Figure 3.6), which could be due to a variety of causes as Fe$L\beta_f$/Fe$L\alpha_f$ depends on Fe concentration, oxidation state, and coordination.

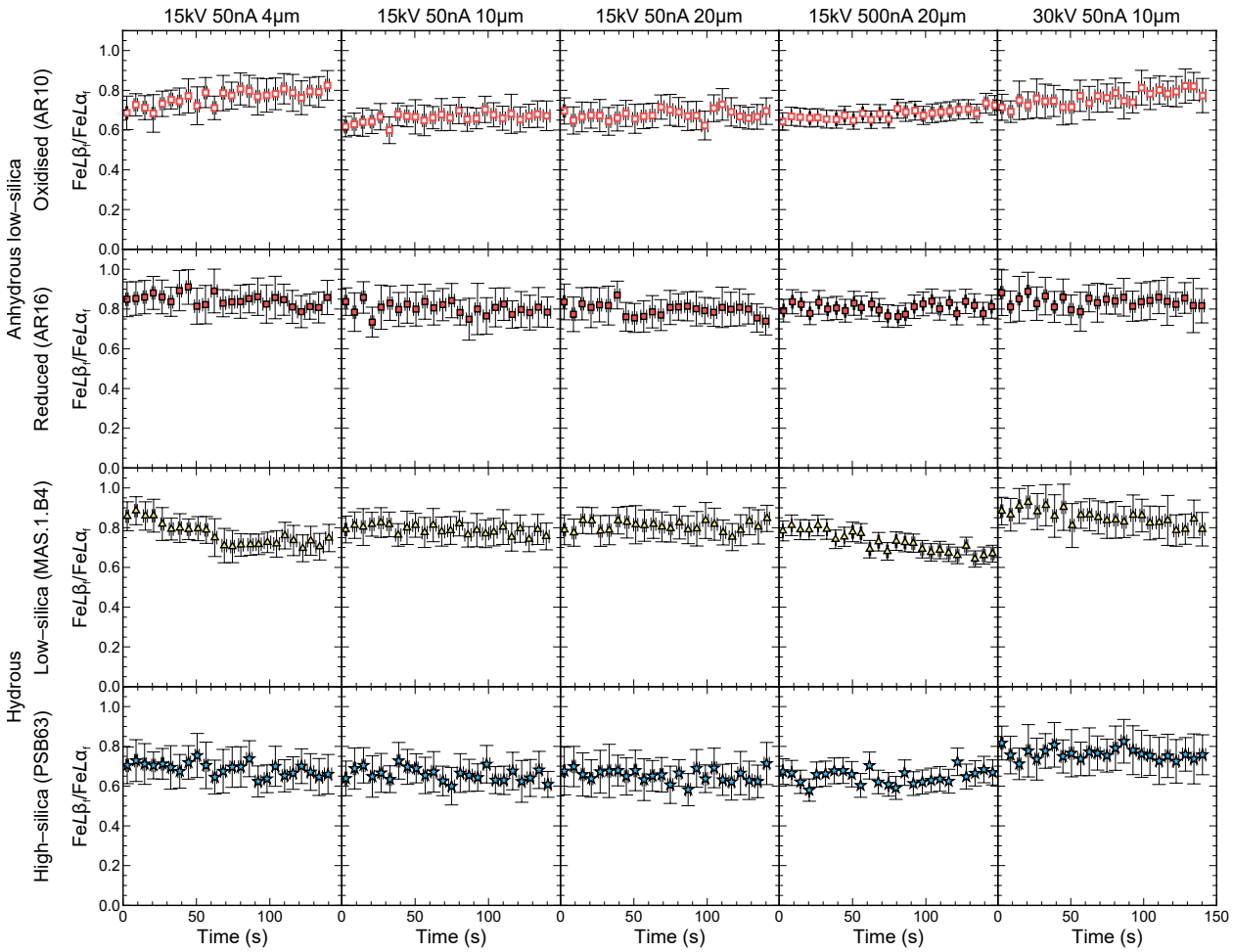


**Figure 3.6:** Intensity ratio of Fe$L\beta_f$/Fe$L\alpha_f$ with time. Analytical conditions (accelerating voltage, beam current, beam diameter) shown along the top and sample description on the left-hand side. Symbols and colours as Figure 3.4.

Fe$K\alpha$ increases over time (Figure 3.5), implying an increase in $Fe_T$. This is due to the process of 'grow-in' (Morgan and London, 2005), where the concentration of immobile elements (e.g., Si, Al, and Fe) increases due to the migration of alkalis (e.g., $Na^+$ and $K^+$, Figure 3.4) and $H^+$ (Figure 3.7c) towards the build-up of negative charge at depth (e.g., Humphreys et al., 2006) and possible density changes. The increase in $Fe_T$ implied by the increase in Fe$K\alpha$ for hydrous silicate glass (MAS.1.B4 and PSB63, Figure 3.5) is small (~0.13 wt% $FeO_T$). This is calculated to cause a negligible change on Fe$L\beta_f$/Fe$L\alpha_f$ (~0.004, within measurement error), and therefore changes due to Fe concentration are not considered further.

Additional carbon contamination can be deposited on the sample during electron beam irradiation (Bastin and Heijligers, 1988). This can change X-ray intensities over time due to reduction of the electron landing energy caused by energy loss within, and X-ray absorption by, the contaminant (Reed, 1975). The former is negligible at the high voltages used here, whereas the latter should not affect Fe$L\beta_f$/Fe$L\alpha_f$ as the mass absorption coefficients of Fe$L\alpha$ and Fe$L\beta$ by carbon are very similar (5762.34 and 5485.53 $cm^2 \cdot g^{-1}$, respectively, from the FFAST database). To change Fe$L\beta_f$/Fe$L\alpha_f$ by 1 % relative (within measurement error) would require >100 nm of carbon contamination (calculated using CalcZAF) during the 150 s analysis. This is far more than has been measured in previous studies (e.g., 8 ± 2 nm over 180 s; Buse et al., 2016), therefore the effect of contamination can be considered negligible.

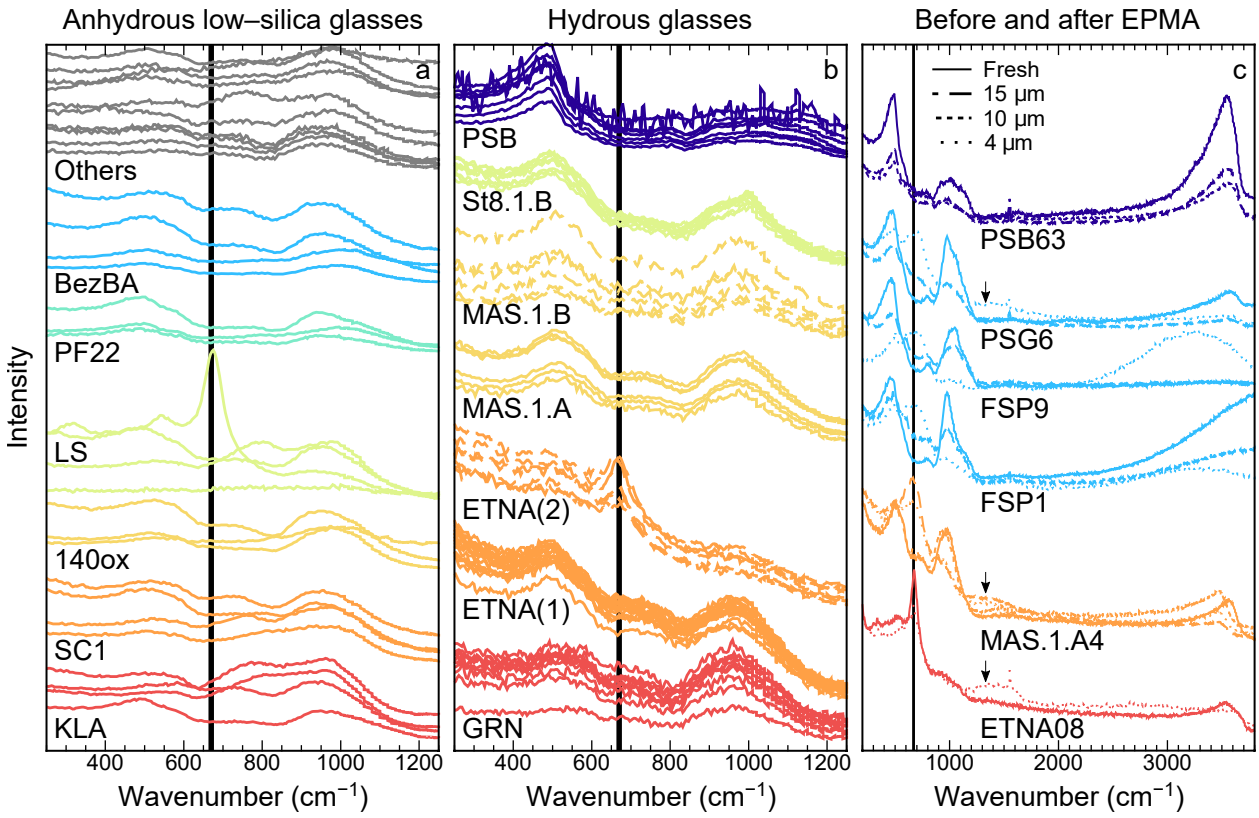


**Figure 3.7:** Raman spectra (one spectrum shown for each sample) for **(a)** anhydrous low-silica and **(b)** hydrous glasses, where spectra are grouped, coloured, and offset vertically by average glass composition (labelled under the group of spectra), and intensity is in arbitrary units, and **(c)** selected glasses before ('fresh') and after (referred to by beam diameter) electron beam irradiation at a 15 kV accelerating voltage, 50 nA beam current, and beam diameter indicated by line style. Black vertical lines indicate the wavenumber of magnetite, and arrows indicate the wavenumber of haematite.

These considerations imply that any changes observed in $FeL\beta_f/FeL\alpha_f$ are due primarily to changes in Fe oxidation state over time. Increasing $FeL\beta_f/FeL\alpha_f$ is caused by increasing $Fe^{2+}/Fe_T$ and hence Fe reduction ($Fe^{3+} \rightarrow Fe^{2+}$). Conversely, decreasing $FeL\beta_f/FeL\alpha_f$ is caused by decreasing $Fe^{2+}/Fe_T$ and hence Fe oxidation ($Fe^{2+} \rightarrow Fe^{3+}$). Finally, no change in $FeL\beta_f/FeL\alpha_f$ with time implies stable $Fe^{2+}/Fe_T$ during analysis. The presence of predominantly magnetite nanolites after electron beam irradiation (Figure 3.7c) implies that oxidation proceeds via precipitation of $FeO{\cdot}Fe_2O_3$, not just $Fe_2O_3$, as has been previously suggested (Fialin and Wagner, 2012).

### 3.5.1. Direction of redox change: Total mobile cations

To investigate the compositional controls on the rate and mechanism of redox changes during electron beam irradiation, we define the parameter total mobile cations (TMC):

$$\mathrm{TMC} = H_2O + Na_2O + K_2O \tag{3.3}$$

where $H_2O$, $Na_2O$, and $K_2O$ are in moles per gram of glass (units: $mol{\cdot}g^{-1}$). This provides a maximum estimate of the moles of available oxygen if all the $H^+$, $Na^+$, and $K^+$ migrated due to the build-up of negative charge (Humphreys et al., 2006). TMC is typically dominated by $H_2O$ due to the low atomic mass

of H compared to Na and K. Figure 3.8 shows the rate of change of Fe$L\beta_f$/Fe$L\alpha_f$ with time at time zero ($I'_0$) against TMC. Silicate glass with TMC $< 0.1$ mol·g$^{-1}$ remain stable or reduce over time ($I'_0 \geq 0$ s$^{-1}$), corresponding to anhydrous ($H_2O < 0.38$ wt%), alkali-poor ($Na_2O+K_2O < 5.5$ wt%) glasses. Conversely, glasses with TMC $> 0.1$ mol·g$^{-1}$ remain stable or oxidise over time ($I'_0 \leq 0$ s$^{-1}$) corresponding to either hydrous ($H_2O > 1.03$ wt%) or alkali-rich ($11.3 \pm 0.2$ wt% $Na_2O+K_2O$) glasses. The mechanisms causing reduction are likely always to occur in the glass during electron beam irradiation, therefore it appears that at TMC $\geq 0.1$ mol·g$^{-1}$ the rate of oxidation is greater than the rate of reduction, hence oxidation prevails.

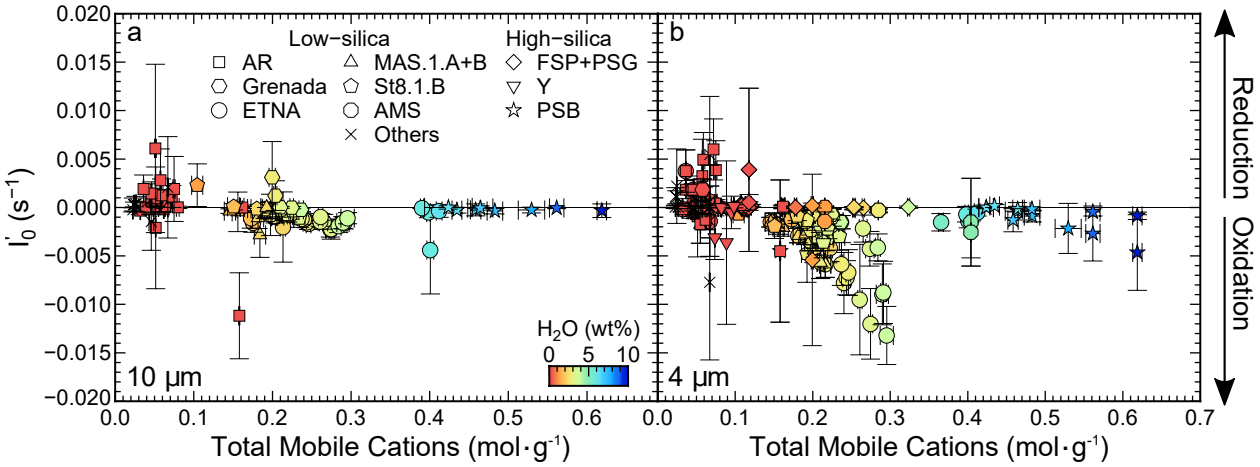


**Figure 3.8:** Rate of change of Fe$L\beta_f$/Fe$L\alpha_f$ with time at time zero ($I'_0$) against total mobile cations (TMC, Equation 3.3), where symbol shape indicates average glass composition (Table 3.1) and colour indicates $H_2O$ concentration. Analytical conditions were: 15 kV accelerating voltage, 50 nA beam current, and **(a)** 10 and **(b)** 4 µm beam diameter. Data are available in Table D.3.

### 3.5.2. Rate of reduction: Initial Fe oxidation state

Figure 3.9 shows $I'_0$ against initial $Fe^{2+}/Fe_T$ for anhydrous, low-silica (43–56 wt% $SiO_2$) glasses. Using a beam diameter of 4 µm, for a specific glass composition, $Fe^{2+}/Fe_T$ correlates negatively with rate of reduction (3.9b), whilst at 10 µm there is no correlation (3.9a). Glasses that are mostly reduced ($Fe^{2+}/Fe_T > 0.9$) cannot reduce any further and remain stable, therefore reduction is confined to initially oxidised glasses. Between the suites of glasses with different compositions, there is no obvious compositional control on $I'_0$.

### 3.5.3. Rate of oxidation

#### $H_2O$ concentration

Figure 3.10 shows the rate of change of Fe$L\beta_f$/Fe$L\alpha_f$ over time at time zero ($I'_0$) against TMC for suites of low-silica glasses (43–56 wt% $SiO_2$) that have variable $H_2O$ concentrations, but constant glass composition. Broadly, $I'_0$ becomes more negative with increasing TMC using a 4 µm beam diameter (Figure 3.10b), whilst the effect is reduced when using a 10 µm beam diameter (Figure 3.10a). For a fixed glass composition the increase in TMC is due to increasing $H_2O$ concentration, therefore the rate of oxidation increases with increasing $H_2O$. The diffusivity of $H_2O$ in basaltic glass is dependent on the total $H_2O$ concentration (Okumura and Nakashima, 2006), thus the rate of oxidation increases with increasing $H_2O$ diffusivity. These results show that the migration of $H^+$, in addition to $Na^+$ and $K^+$ as previously suggested by Fialin and Wagner (2012), leads to oxidation of Fe during electron beam irradiation. In fact, when considering the

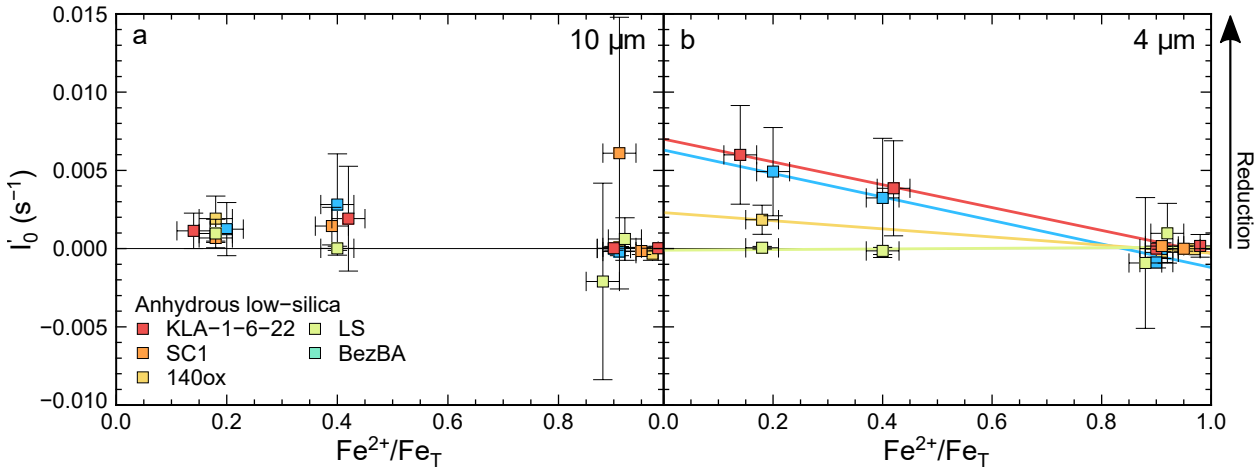


**Figure 3.9:** Rate of change of Fe$L\beta_f$/Fe$L\alpha_f$ with time at time zero ($I_0'$) against $Fe^{2+}/Fe_T$ for anhydrous low-silica glasses, where symbol colour indicates average glass composition (Table 3.1) and linear regressions are shown in **(b)** (solid lines). Analytical conditions were: 15 kV accelerating voltage, 50 nA beam current, and **(a)** 10 and **(b)** 4 µm beam diameter. Data are available in Table D.3.

mobile cation responsible for Fe oxidation, $H^+$ plays a more important role than might be expected from its oxide wt% concentration alone due to the low atomic mass of H.

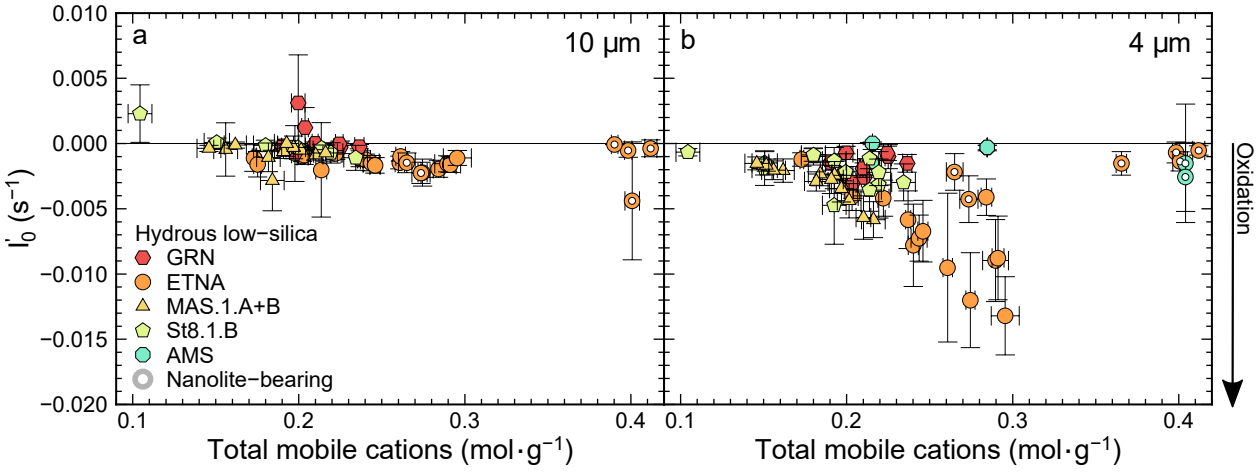


**Figure 3.10:** Rate of change of Fe$L\beta_f$/Fe$L\alpha_f$ with time at time zero ($I_0'$) against total mobile cations (TMC) for hydrous low-silica glasses, where symbol shape and colour indicates average glass composition (Table 3.1), and open symbols indicate the presence of nanolites. Analytical conditions were: 15 kV accelerating voltage, 50 nA beam current, and **(a)** 10 and **(b)** 4 µm beam diameter. Data are available in Table D.3.

### $SiO_2$ concentration

High-silica (61–78 wt% $SiO_2$) glasses remain broadly stable during electron beam irradiation (Figure 3.8), despite the Raman spectra of electron beam irradiated areas using a 4 µm beam diameter indicating the formation of magnetite nanolites (Figure 3.7c). This implies extremely rapid oxidation at 4 µm, which is consistent with the rate of alkali migration, and probably H, being faster during electron beam irradiation of high- compared to low-silica glasses (e.g., Figure 3.4; Hayward, 2011). This may be due to the more polymerised structure of high-silica glasses (Mysen et al., 1982).

**Fe content**

PSB glasses do not oxidise ($I'_0 \approx 0$ s$^{-1}$, Figure 3.8), and there are no Fe-bearing nanolites observable in the Raman spectra prior to or following electron beam irradiation (Figure 3.7c), despite TMC $> 0.4$ mol·g$^{-1}$ due to their high alkali and water contents. These glasses contain little Fe ($FeO_T \leq 3.2$ wt%), which could hinder oxidation as FeO groups may need to lie close together in order to produce $Fe_2O_3$.

**Presence of nanolites**

Surprisingly, low-silica (47–58 wt% $SiO_2$) glasses with TMC $> 0.35$ mol·g$^{-1}$, which corresponds to $H_2O >$ 4 wt% (Figure 3.10), appear stable ($I'_0 \approx 0$ s$^{-1}$). It is possible that they oxidised very quickly and the change is not observable. Analyses using a 10 μm beam size are also stable (Figure 3.8a), but there is evidence for the formation of haematite nanolites during electron beam irradiation (Figure 3.7c). This either means the oxidation is extremely rapid, due to the very high $H_2O$ concentration, or not occurring due to the presence of magnetite nanolites before irradiation where the Fe may be stable, but further study is required to understand this process fully.

### 3.5.4. Effect of analytical conditions

For all X-rays measured (K$K\alpha$, Fe$K\alpha$, and Fe$L\beta_f$/Fe$L\alpha_f$), the rate of change of intensity increases with decreasing beam diameter and accelerating voltage, and increasing beam current (Figures 3.4–3.6 and 3.8, as is commonly observed during electron beam irradiation (e.g., Morgan and London, 2005). The analytical conditions control the electron density implanted into the sample and therefore the magnitude of sub-surface charging. Increasing the beam current increases the electron dosage to the sample. The interaction volume is reduced by decreasing both the accelerating voltage and beam diameter, limiting the depth these electrons penetrate and the irradiated area respectively. Overall, the rate of intensity change increases with increasing implanted electron density (i.e., decreased interaction volume and/or increased electron dosage).

## 3.6. Quantifying Fe oxidation state: Time-dependent ratio flank method

### 3.6.1. Calibration and errors

Höfer and Brey (2007) found that the ratio of Fe$L\beta_f$/Fe$L\alpha_f$ correlated linearly with $Fe^{2+}$ for garnets, with a small secondary dependence on $Fe_T$ (Equation 3.1). Consequently, their coefficients ($m$ and $c$) of $Fe^{2+}$ = $m$·(Fe$L\beta_f$/Fe$L\alpha_f$) + $c$ were dependent on $Fe_T$. Our data showed no improvement to the correlation between Fe$L\beta_f$/Fe$L\alpha_f$ and $Fe^{2+}$ by allowing the coefficients to depend on $Fe_T$, therefore $m$ and $c$ are fitted without $Fe_T$ dependence using a weighted least squares regression (weighted using error on independently-constrained $Fe^{2+}$). The lack of dependence on $Fe_T$ is likely because the composition of natural silicate glasses investigated here covers a much narrower range of $Fe_T$ compared to garnets (<18 vs. 64 wt% $FeO_T$, respectively). The calibration curve is not constant between sessions (Figure 3.11 and Table 3.5), therefore a new calibration curve should be produced for each session.

It appears that low-silica and peralkaline glasses require different calibration curves (Figure 3.11e), therefore these two sample groups were fitted separately. Using these different calibration curves, $Fe^{2+}/Fe_T$ is replicated well for both compositions (Figures 3.12a and b). Fe coordination also effects the Fe$L$ lines but

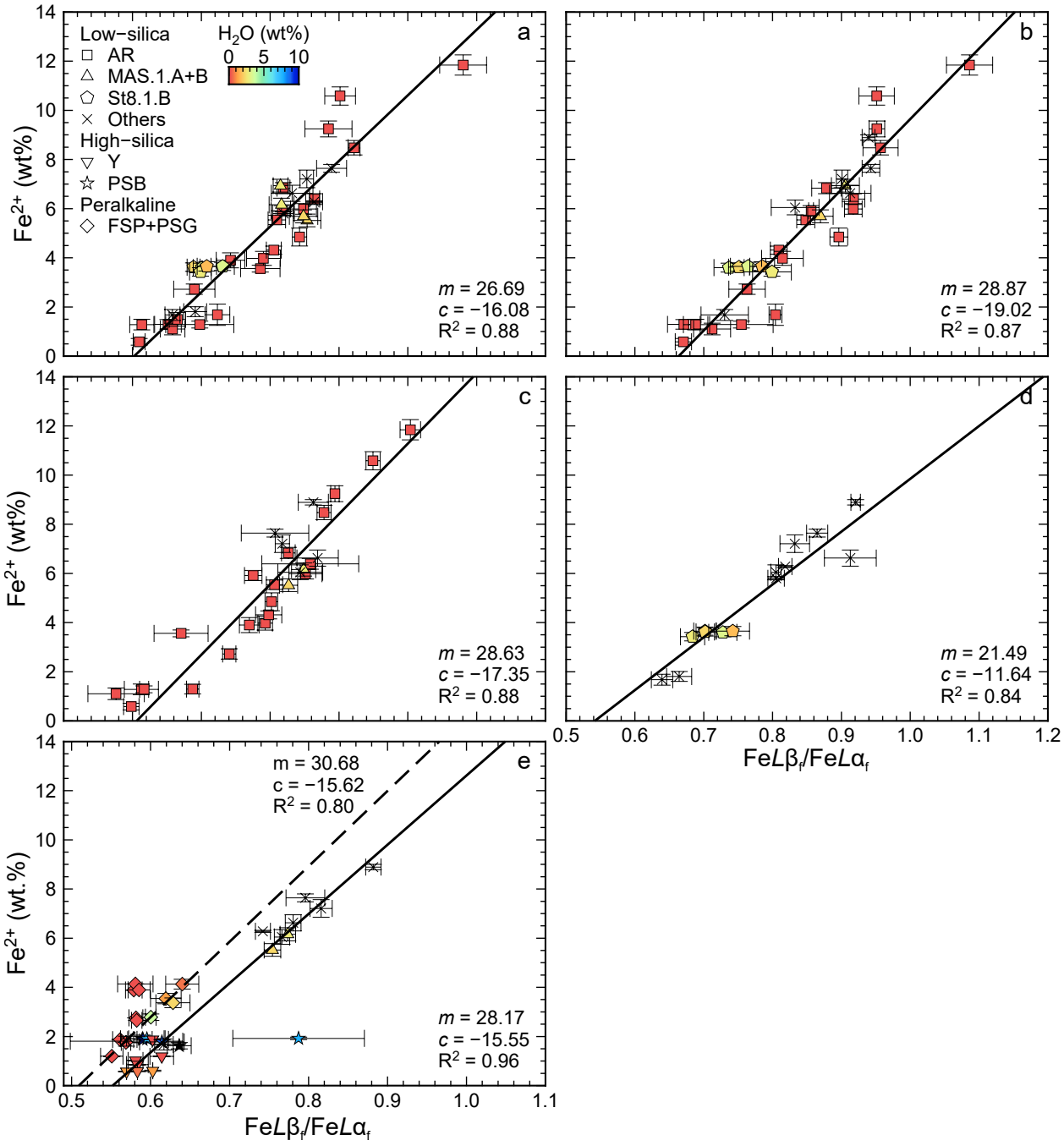


**Figure 3.11:** Calibration curves derived for each session, where $Fe^{2+}$ is constrained using $Fe^{2+}/Fe_T$ from independent techniques and $Fe_T$ from EPMA. Symbol shape indicates average glass composition (Table 3.1) and colour indicates $H_2O$ concentration. Analytical conditions were: 15 kV accelerating voltage and 50 nA beam current. **(a)** Low-silica glasses using 10 μm beam diameter, **(b)–(d)** low-silica glasses using 4 μm beam diameter, and **(e)** all glasses with separate calibration curves for low-silica (solid) and peralkaline (dashed) glasses (high-silica glasses are shown but not included in the fit), using a 15 μm beam diameter. Data are available in Table D.3.

the coordination of silicate glasses is very similar (Cottrell et al., 2009). Instead, it may be that absorption within the glass of the Fe*L* lines is different between these two broad compositional groups due to their different compositions, although this was not observed for garnets (Höfer and Brey, 2007). Compositional differences within the low-silica glasses may also explain the scatter observed in the calibration curves, but it is not possible to explore this fully using the current dataset. It may be that errors on $Fe^{2+}/Fe_T$ can be

**Table 3.5:** Results for weighted linear regression for $Fe^{2+}$ calibration for each session.

| No. | Beam diameter (μm) | *n* | *m* | *c* | Adj. $R^2$ | R.S.E. (wt%) |
|---|---|---|---|---|---|---|
| 1 | 10 | 38 | 26.87 ± 1.70 | -16.08 ± 1.37 | 0.88 | 0.51 |
| 2 | 4 | 32 | 28.67 ± 2.05 | -19.02 ± 1.77 | 0.87 | 0.55 |
| 3 | 4 | 27 | 28.63 ± 2.12 | -17.35 ± 1.75 | 0.88 | 0.50 |
| 4 | 4 | 14 | 21.49 ± 2.72 | -11.64 ± 2.16 | 0.84 | 0.36 |
| 5 | 15 | 10 | 28.17 ± 1.91 | -15.55 ± 1.47 | 0.96 | 0.17 |
| 5[a] | 15 | 12 | 30.68 ± 8.50 | -15.92 ± 5.29 | 0.80 | 0.11 |

*Notes:* Data were collected using analytical conditions of a 15 kV accelerating voltage and 50 nA beam current. *n* is the number of measurements included in the fit. *m* and *c* are the slope and intercept respectively for $Fe^{2+} = m{\cdot}(FeL\beta_f/FeL\alpha_f) + c$. Adj. $R^2$ is the adjusted $R^2$. R.S.E. is the residual standard error on estimated $Fe^{2+}$. Fits are for low-silica and [a]peralkaline glasses.

reduced by using compositionally-matched glass standards. In practice such standards are unlikely to be available, therefore we recommend using standards with broadly similar compositions (i.e., low-silica or peralkaline) when using this technique.

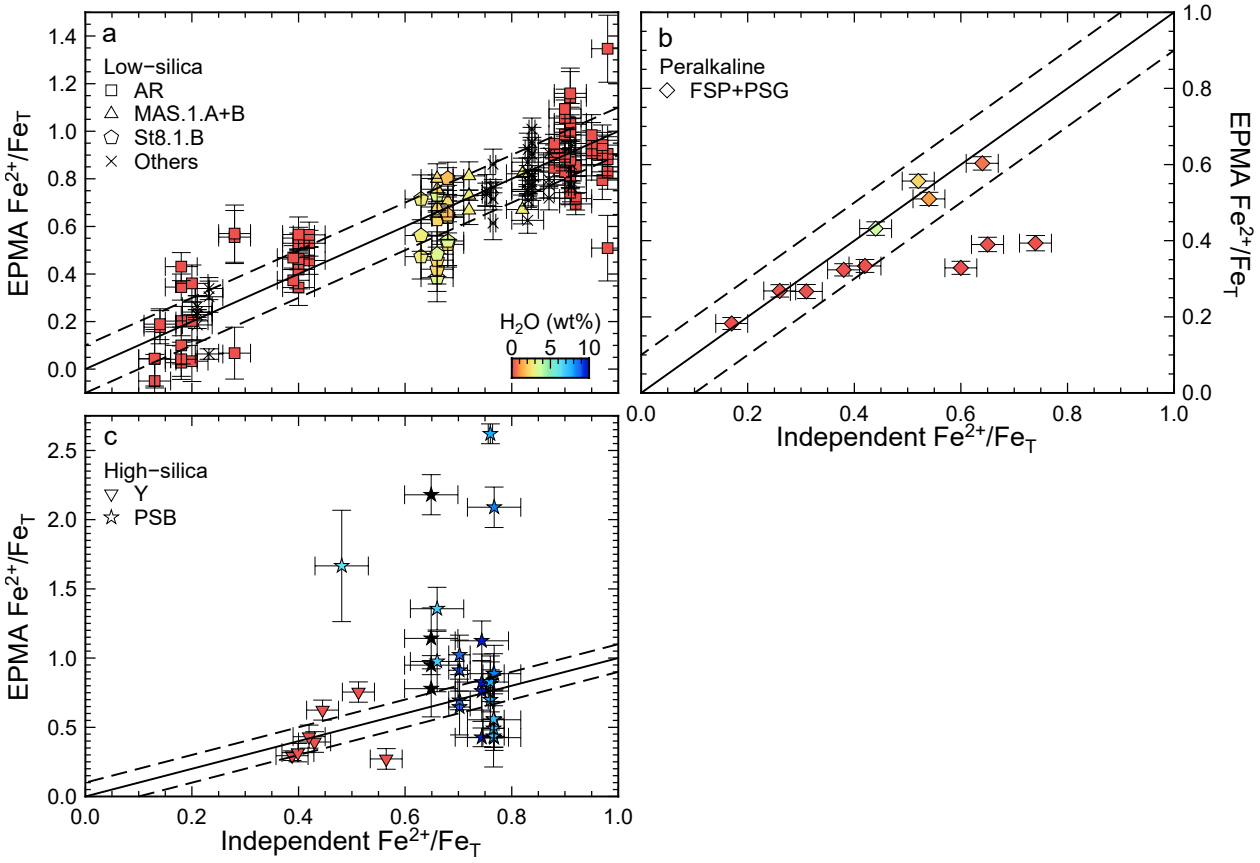


**Figure 3.12:** EPMA against independently constrained $Fe^{2+}/Fe_T$ collected during all sessions for **(a)** low-silica (43–56 wt% $SiO_2$), **(b)** peralkaline (FSP+PSG), and **(c)** high-silica (69–78 wt% $SiO_2$, using low-silica glass derived calibration curves) glasses, where symbol shape indicates average glass composition (Table 3.1) and colour indicates $H_2O$ concentration. Analytical conditions were: 15 kV accelerating voltage, 50 nA beam current, and 4–15 μm beam diameter. The solid line indicates the 1-to-1 relationship, whilst the dashed lines indicate ±0.1 limits.

A calibration curve could not be created for high-silica glasses PSB and Y as they cover a narrow range of $Fe^{2+}$ (<2 wt% $Fe^{2+}$). Their $Fe^{2+}/Fe_T$ are poorly replicated by the low-silica calibration curve (Figure

3.12c), to which they lie more closely than the peralkaline calibration curve (Figure 3.11e). This is likely due to their low Fe content ($FeO_T < 3.3$ wt%, except Y-L with 6.2 wt% $FeO_T$), therefore this technique is unsuitable for low Fe glasses (i.e., $FeO_T < 5$ wt%).

The $Fe^{2+}/Fe_T$ precision, using a residual standard error of 0.5 wt% on $Fe^{2+}$ and 1 % relative error on $FeO_T$, depends on the Fe concentration and oxidation state:

$$Fe^{2+}/Fe_T \text{ error} = (Fe^{2+}/Fe_T)_{EPMA} \cdot \sqrt{\left(\frac{0.5}{Fe^{2+}}\right)^2 + (0.01)^2} \tag{3.4}$$

e.g., $\pm 0.03$ for 10 wt% $FeO_T$ and 0.5 $Fe^{2+}/Fe_T$. The average accuracy for low-silica (43–56 wt% $SiO_2$) and peralkaline (70–76 wt% $SiO_2$) glasses with 5–18 wt% $FeO_T$, and 0–4 wt% $H_2O$, when the appropriate analytical conditions and calibration curves are used, is $\pm 0.1$ (Figures 3.12a and b).

### 3.6.2. Recommended analytical conditions

Analytical conditions can be optimised according to the nature of any given sample as different conditions (beam diameter and current, total count time of a single analysis, and number of analyses averaged) can be used on the standards and unknowns, so long as the accelerating voltage and flank positions remain the same. Höfer and Brey (2007) showed that for garnets the optimum accelerating voltage is 15 kV; at lower and higher accelerating voltages the sensitivity of the flank method is reduced. For glasses, the sensitivity of the flank method also decreased at higher accelerating voltages (Figures 3.3b and d). An accelerating voltage of 15 kV allows the composition of the sample to be analysed, via conventional EPMA, without further calibration or beam focussing.

The error on the corrected Fe$L\beta_f$/Fe$L\alpha_f$ is a function of counting statistics, the fit of an exponential function to the change in Fe$L\beta_f$/Fe$L\alpha_f$ with time (Equation 3.2), and the number of analyses averaged. Counting statistics can be improved by using a higher beam current, but this can cause the rate of change to occur too quickly to be observed. Decreasing the beam diameter will also increase the rate of change, as seen here for high-silica glasses, but improves spatial resolution. Therefore, it is important to know the approximate composition of the target glass (e.g., by EDS analysis) to understand how quickly the change in Fe oxidation is likely to occur. If redox changes occur too quickly, the time-corrected Fe$L\beta_f$/Fe$L\alpha_f$ will be wrong leading to erroneous $Fe^{2+}/Fe_T$ values. Our data at a 15 kV accelerating voltage, 50 nA beam current, 4 μm beam diameter, and averaging 10 analyses produced a relative error on the corrected Fe$L\beta_f$/Fe$L\alpha_f$ of ~3 %, and gave the flexibility to analyse a variety of glass morphologies for hydrous low-silica glasses. A larger beam size (10–15 μm diameter) is needed to analyse high-silica samples containing sufficient iron (i.e., peralkaline) due to the rapid rate of oxidation, which unfortunately sacrifices spatial resolution. This technique may not be appropriate if samples contain fine-scale heterogeneities (e.g., nanolites), as the Fe coordination in these phases may differ to that in the glass.

### 3.6.3. Further applications

The TDR flank method presented here could be applied to other beam-sensitive samples. Electron probe induced dehydrogenation has been observed for kaersutitic amphibole, resulting in the underestimation of $Fe^{2+}/Fe_T$ due to oxidation (Wagner et al., 2008). Wagner et al. (2008) showed the severity of damage

correlated with analytical conditions and $H_2O$ concentration of the amphibole, in much the same way as shown here for silicate glass. Therefore, applying the TDR flank method to amphibole may provide robust Fe oxidation state estimates without sacrificing spatial resolution.

Oxidation and reduction of S has been observed during analysis of silicate glass and anhydrite when using the S$K\alpha$ peak shift to measure S oxidation state (Wallace and Carmichael, 1994; Rowe et al., 2007; Wilke et al., 2011). Sulphur oxidation in silicate glass appeared to follow an exponential trend and, as observed here, the estimate of redox state at time zero was found to agree with μXANES measurements of the same sample (Wilke et al., 2011). Sulphur redox changes are controlled by similar factors to Fe such as initial S oxidation state (Rowe et al., 2007) and $H_2O$ concentration (Wilke et al., 2008). If a flank-type method was developed for S (Wilke et al., 2011), time-dependent measurements could also be applied, negating the need to move samples during analysis (Métrich and Clocchiatti, 1996; Rowe et al., 2007), thereby improving spatial resolution.

## 3.7. Implications

Measuring the Fe oxidation state of silicate melts allows estimation of oxygen fugacity prevailing during natural processes and in experiments. The time-dependent ratio flank method presented here combines the ability to measure the Fe oxidation state at high resolution with the utility of the electron probe. This will allow routine measurement of Fe oxidation state of melt inclusions and interstitial glass, previously hampered by the need for synchrotron access. Melt inclusions provide a unique insight into the pre-eruptive magma but studies have shown that the Fe oxidation state can be altered by degassing (e.g., Moussallam et al., 2014) and cooling (e.g., Hartley et al., 2017) post-entrapment, complicating their use as a proxy for oxygen fugacity. Hence, larger datasets generated due to easier access, will allow the importance of these processes to be further investigated, although for some applications smaller errors will be required. For instance, the difference between MORB (0.83–0.87 $Fe^{2+}/Fe_T$), back arcs (0.81–0.85) and arcs (0.68–0.82) would be difficult to distinguish with the current errors of this technique (Kelley and Cottrell, 2009), although degassing induced changes maybe resolvable (e.g., 0.60–0.85 $Fe^{2+}/Fe_T$, Moussallam et al., 2014). Also, a better understanding of the analytical and compositional controls on redox changes during electron beam irradiation of silicate glass (summarised in Figure 3.13) can aid our understanding of glass structure and improve analytical routines.

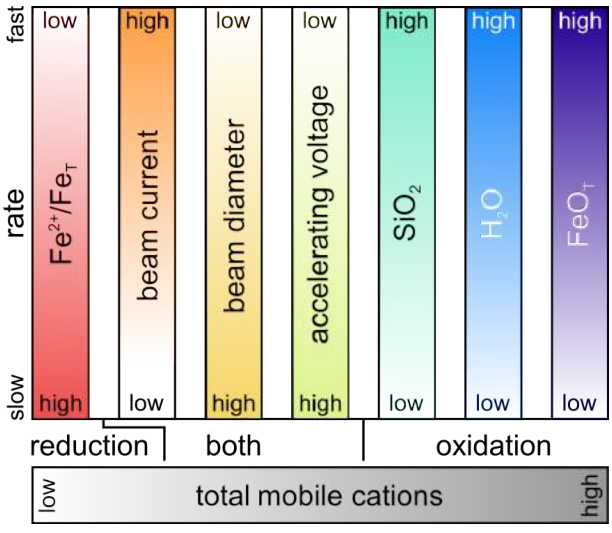


**Figure 3.13:** Schematic diagram showing the controls on the direction and rate of Fe redox changes in silicate glass during electron beam irradiation.

# Chapter 4

# High spatial resolution SIMS analysis of carbon stable isotopes in basaltic glass

**Author contributions and declaration:** E.C. Hughes made the experimental capsules with the help of R.A. Brooker. Glasses were exerimentally synthesised by R. Balzer and D.A. Neave. R.A. Brooker collected SHC and S. Remmelzwall helped to clean the sample. G. Kilgour collected the Rangitoto olivine and J. Craven provided the San Carlos olivine. D. Hilton provided ALV981-R23 and C. Aubaud the CH9 samples. All data were collected by E.C. Hughes except: $\delta^{13}C$ of the starting $CaCO_3$ (A. Nederbragt); $\delta^{13}C$ of the released gas from SHMS (P. Cartigny); TCEA data (I. Bindemann); and some of the SIMS data (J. Craven). E.C. Hughes processed and interpretted the data, and wrote the chapter, with the help of J.D. Blundy and H.M. Mader.

## ABSTRACT

Analysing carbon isotope ratios in melt inclusions would greatly enhance our understanding of the pre-eruptive degassing process and the initial carbon budget of magmas. The standard method to measure the carbon isotope ratio of silicate glass uses the bulk technique of stepped-heating gas extraction in a vacuum line followed by mass spectrometry of the released gas due to the low concentration of carbon in silicate glasses, but a micro-analytical technique is required for melt inclusions. Here, secondary ion mass spectrometry (SIMS) with negative ions is used to measure carbon stable isotopes at high spatial resolution. Care must be taken to ensure low levels of carbon background during SIMS analysis, which consists of surficial contamination and background carbon in the vacuum. Carbon concentration can be measured at the same time as carbon isotope ratios by measuring $^{18}O^-$ in combination with $^{12}C^-$ and $^{13}C^-$. A precision of 5 ‰ on $CO_2$ concentrations $> 400$ ppm, or 2 ‰ for $CO_2 > 2000$ ppm, could be achieved using high beam currents (~50 nA), although this requires further investigation.

## 4.1. Introduction

The carbon isotope ratio of silicate melts provides a unique insight into the degassing histories of magmas because it is typically the first volatile to exsolve (e.g., Macpherson and Mattey, 1994; Pineau and Javoy, 1994, 1983). Particularly, analysing melt inclusions provides a potential avenue for reconstructing the initial carbon concentration of magmas, fingerprinting its source, and deciphering the style of degassing prior to eruption (Section 1.4). Analysing experimental glasses for carbon isotope ratios at high spatial resolution would reduce the amount of material needed to investigate the process of stable isotope fractionation. Also, measuring the isotopic effect of carbon diffusion through silicate melts (e.g., to understand kinetic fractionation during bubble growth, Watson, 2017) requires spatially resolved analysis. Unfortunately, carbon is difficult to analyse because of its low concentration in silicate glass ($<$5000 ppm $CO_2$). Additionally, its detection is adversely affected by carbon contamination such as adsorption onto the glass surface, carbon on the sample surface, and carbon inherently present in the vacuum of analytical equipment (termed the 'blank').

Currently, carbon isotope ratios in silicate glass are analysed in bulk samples, using stepped-heating mass spectrometry (SHMS) (e.g., Macpherson et al., 1999). This technique separates out different types of carbon present in silicate glass by sequentially heating the sample to higher temperatures in a vacuum line (e.g., Swart et al., 1983; Mattey et al., 1989, 1984). Silicate glass readily absorbs $CO_2$ onto its surface, which is released from the glass at low temperature ($<$600 °C) (Des Marais, 1986; Mattey et al., 1984; Exley et al., 1986). On the other hand, the structurally bound oxidised carbon is released at high temperature ($>$1000 °C). Additionally, natural samples release $CO_2$ trapped in vesicles at intermediate temperatures (600–1000 °C) (e.g., Mattey et al., 1984). If carbon is present as a reduced species (i.e., graphite) it will be released at even higher temperatures ($>$1200 °C) (Mattey et al., 1989). There is also carbon present in the vacuum line and sufficient material must be measured to ensure the blank is a small proportion of the carbon analysed. This technique is not appropriate for melt inclusions because $\sim 10^2$–$10^3$ mg of material are required (depending on the instrumental blank and the concentration of $CO_2$ in the glass), which is far greater than the mass of material in melt inclusions ($\sim 10^{-8}$ mg). Spectroscopic techniques (e.g., Raman and FTIR) could also be used to analyse carbon isotopes as the molecular frequencies shift depending on the isotopic ratio of the sample (e.g., Urey, 1947). Raman spectroscopy has been used in this way (Mysen, 2017, 2016), but typically the carbon concentration is too low in silicate glass to observe the carbonate ion peak (Morizet et al., 2013).

Secondary ion mass spectrometry (SIMS) is often used to measure the carbon concentration of silicate glass at high spatial resolution, such as in melt inclusions (e.g., Blundy and Cashman, 2008). A primary ion beam sputters material from the surface of the sample, which generates secondary ions (e.g., Hinton, 1995). The concentration of these secondary ions is measured based on their mass-charge ratio, therefore isotope ratios can be analysed. The high vacuum analytical chamber leads to low backgrounds for elements such as carbon. Additionally, SIMS pre-sputters material prior to analysis, which removes the surface layer of the sample, hence SIMS can analyse elements which otherwise suffer from high levels of surface contamination, such as carbon (Blundy and Cashman, 2008; Hauri et al., 2002; Hauri, 2002). Although samples are often mounted in epoxy for grinding and polishing, epoxy outgasses carbon into the analysis chamber which elevates the blank, hence samples are mounted in indium. The sample composition effects the sputtering processes, which is not well understood and therefore cannot be corrected for (unlike with EPMA, Section 2.2) when quantifying SIMS data. Additionally, there are instrumental mass fractionation

effects which change the measured isotope ratio from the true isotope ratio (e.g., Hauri et al., 2002). Hence, matrix-matched standards are required for accurate quantification.

Hauri (2002) and Hauri et al. (2002) reported the first carbon isotope ratio measurements of silicate glass, including melt inclusions, using SIMS. There have been no published results since, except a conference abstract by Le Voyer et al. (2014). Hauri et al. (2002) used two basaltic (Hauri et al., 2002; Macpherson et al., 1999) and four andesitic (King, unpublished) glass standards. The basaltic glass ALV981-R23 was used, which is a natural submarine glass with 406 $\pm$ 8 ppm $CO_2$ and -5.70 $\pm$ 0.41 ‰ $\delta^{13}C$ (see Section A.1 for notation). Additionally, SAV-C-1 was synthesised at 10 kbar and 1400 °C to produce an undersaturated glass with 7000 ppm $CO_2$ (measured using SIMS) and -8.0 ‰ $\delta^{13}C$ based on the isotope ratio of the Iceland spar calcite used in the starting powder. The andesite glasses were synthetic and contained 270–1300 ppm $CO_2$, 1.09–3.70 wt% $H_2O$ and -27.0 to -29.0 ‰ $\delta^{13}C$. For quantification, a matrix effect was found between the basalts and andesites, but no effect of $H_2O$ concentration on the measured carbon isotope ratio in the andesites was observed. Contamination arose from the intersection of the sputter crater with surface contamination, which continuously created carbon ions. Hauri (2002) reported extremely light carbon isotope ratios (-30 to -10 ‰ $\delta^{13}C$) for melt inclusions from Koolau, Hawaii. Le Voyer et al. (2014) analysed a range of glass standards (100–7000 ppm $CO_2$, -21.9 to -5.7 ‰ $\delta^{13}C$) and achieved 1.0–1.5 ‰ analytical error and 2–3 ‰ reproducibility on low carbon glasses (100–400 ppm $CO_2$). Again, surface contamination caused some instability in their analyses.

The aim of this Chapter is to develop a technique for analysing the carbon isotope ratio of melt inclusions from arc volcanoes, using Etna as case study (Chapter 6). The technique will also be applied to experimental glasses created to quantify the carbon isotope fractionation factor (Chapter 5), which is required to interpret the melt inclusion data. The key difference between these samples and those analysed in previous studies using SIMS (Hauri, 2002; Hauri et al., 2002; Le Voyer et al., 2014) is the basaltic glass is hydrous. Previous studies did not have hydrous basaltic glass standards, hence the matrix effect of $H_2O$ concentration on SIMS analysis in basaltic glass was not tested. Also, carbon concentrations were not quantified at the same time as the carbon isotope ratio. This would greatly help when analysing melt inclusions, where space is limited, as a single SIMS analysis could deliver both the carbon concentration and isotope ratio.

This chapter is split into two sections. Section 4.2 describes experimentally synthesising and characterising the composition of new hydrous basaltic glass standards, particularly measuring their carbon isotope ratio independently using stepped-heating mass spectrometry. Section 4.3 develops an analytical protocol using SIMS to measure the carbon concentration and isotope ratio contemporaneously of hydrous basaltic glass at high spatial resolution. Different analytical routines for measuring the carbon concentration and isotope ratio of basaltic glass are investigated. The spatial resolution is measured using scanning electron microscopy (SEM) and scanning ion microscopy (SIM). The effect of contamination and composition on calibrating carbon concentrations and isotope ratios, using the standards described in Section 4.2, are also considered.

## 4.2. Synthesising and characterising carbon isotope basaltic glass standards

SIMS is a standards-based technique, where the measured secondary ion yield on unknown samples is compared to standards for quantification. The composition of the sample has a major effect on the secondary ion yield, hence matrix-matched standards are required for accurate quantification. Currently, there are no hydrous basaltic glasses with independently constrained carbon isotope ratios available, hence

we synthesised (Section 4.2.1) and characterised (Sections 4.2.2 and 4.2.3) our own (results in Section 4.2.4).

### 4.2.1. Experimental synthesis

Seven experimental glasses were synthesised to produce basaltic glass standards for carbon isotope analysis using two different starting compositions (A: ETNA24, and B: ETNA31–ETNA36, Table 4.1). Albite, anorthite, sanidine, fayalite, wollastonite, $SiO_2$, MnO, MgO, $TiO_2$, $Fe_2O_3$, and $Ca_3(PO_4)_2$ powders were mechanically mixed by grinding under water in an agate mortar. Mixes were initially dried under a heat lamp for 30 mins. B glasses were additionally glassed at 1 atm in air in a Pt-crucible at 1300 °C for one hour in the GERO$^{TM}$ vertical furnace at the School of Earth Sciences, University of Bristol, UK. To avoid oxidation during glassing, fayalite and $Fe_2O_3$ were added after this step for B glasses. Starting compositions are detailed in Table 4.1.

**Table 4.1:** Starting compositions, capsule sizes, and experimental details.

| | ETNA24 | ETNA31 | ETNA32 | ETNA33 | ETNA34 | ETNA35 | ETNA36 |
|---|---|---|---|---|---|---|---|
| Composition | A | B | B | B | B | B | B |
| Pressure (kbar) | 5 | 7 | 7 | 3 | 5 | 5 | 3 |
| Temperature (°C) | 1250 | 1250 | 1250 | 1250 | 1250 | 1250 | 1250 |
| Capsule length (mm) | ∼30 | ∼15 | ∼15 | ∼15 | ∼15 | ∼15 | ∼15 |
| Synthesis time (h) | ∼18 | ∼36 | ∼36 | ∼18 | ∼18 | ∼18 | ∼18 |
| IHPV | Blue | Blue | Blue | Blue | Yellow | Yellow | Blue |
| $SiO_2$ | 46.96 | 46.16 | 46.13 | 46.15 | 46.15 | 45.23 | 45.00 |
| $TiO_2$ | 1.71 | 1.75 | 1.75 | 1.75 | 1.75 | 1.72 | 1.71 |
| $Al_2O_3$ | 15.93 | 14.80 | 14.79 | 14.80 | 14.80 | 14.50 | 14.43 |
| $Fe_2O_3$ | 5.65 | 5.76 | 5.76 | 5.76 | 5.76 | 5.64 | 5.62 |
| FeO | 5.10 | 5.19 | 5.19 | 5.19 | 5.19 | 5.08 | 5.06 |
| MnO | 0.19 | 0.20 | 0.20 | 0.20 | 0.20 | 0.20 | 0.20 |
| MgO | 5.80 | 5.91 | 5.91 | 5.91 | 5.91 | 5.79 | 5.76 |
| CaO | 10.52 | 13.80 | 13.83 | 13.81 | 13.81 | 13.53 | 13.47 |
| $Na_2O$ | 3.36 | 3.42 | 3.42 | 3.42 | 3.42 | 3.36 | 3.34 |
| $K_2O$ | 1.90 | 1.94 | 1.94 | 1.94 | 1.94 | 1.90 | 1.89 |
| $P_2O_5$ | 0.57 | 0.58 | 0.58 | 0.58 | 0.58 | 0.57 | 0.57 |
| $H_2O$ | 2.00 | 0 | 0 | 0 | 0 | 2.00 | 2.49 |
| $CO_2$ (ppm) | 2972 | 4836 | 5129 | 4946 | 4946 | 4847 | 4823 |
| $\delta^{13}C^a$ (‰) | -1.81 | +1.99 | -5.43 | -1.81 | -1.81 | -1.81 | -1.81 |
| $Fe^{2+}/Fe_T$ | 0.50 | 0.50 | 0.50 | 0.50 | 0.50 | 0.50 | 0.50 |

*Notes:* Oxides are in wt%, except where otherwise stated, and are calculated from the weighed-in components. [a] measured on the starting $CaCO_3$ (Table 4.2). Errors of one standard deviation on oxide concentrations are <0.02 wt%, except for $H_2O$ in ETNA35 and ETNA36 (0.03 and 0.04 wt%, respectively) and $CO_2$ (43 ppm for ETNA24, 147 ppm for ETNA31–ETNA32, and 37 ppm for ETNA33–ETNA36).

The mixture was dried overnight (∼100 °C) before $CaCO_3$ was added. To give variable carbon compositions, different quantities of $CaCO_3$ were added as either powdered Seaford Head Chalk (SHC), Oka carbonatite calcite (OKA) or a 50:50 mechanical mixture of the two (MIX). SHC was collected from Hope Gap on the Sussex coast by R. Brooker, where the Turonian to Campanian Chalk is known for its high $\delta^{13}C$ (+1.5 to +2.5 ‰, Jenkyns et al., 1994). Organic matter was removed from SHC using the method of Barker et al. (2003). Calcite grains were picked from the Oka carbonatite, which has more negative $\delta^{13}C$ (-5 ‰; Deines, 1970). The $\delta^{13}C$ and $\delta^{18}O$ of the different types of $CaCO_3$ were measured using the Thermo MAT253 at the School of Earth and Ocean Sciences, Cardiff University, UK, by A. Nederbragt (Table 4.2). The mixture was dried overnight (∼100 °C) before water was added as $H_2O$ dispersed throughout the

capsule.

**Table 4.2:** Carbon and oxygen isotope ratios for $CaCO_3$.

| $CaCO_3$ | Seaford Head Chalk (SHC) | Oka carbonatite calcite (OKA) | 50:50 SHC:OKA (MIX) |
|---|---|---|---|
| *n* | 2 | 2 | 4 |
| $\delta^{13}C$ (‰) | +1.99 ± 0.03 | -5.43 ± 0.02 | -1.81 ± 0.02 |
| $\delta^{18}O$ (‰) | -2.71 ± 0.07 | -23.58 ± 0.01 | -13.21 ± 0.09 |

*Notes: n* is the number of analyses and errors are one standard deviation.

Large capsules, 5 mm in diameter and 15–30 mm in length (Table 4.1) made of $Au_{75}Pd_{25}$, were loaded with starting powders to produce sufficient material for bulk analysis. ETNA24 was ∼30 mm in length with ∼500 mg of starting powder and was triple welded shut at each end. ETNA31–ETNA36 were ∼15 mm in length with ∼300 mg of starting powder and were 'trash can' welded shut at each end, allowing two to be experimentally synthesised at the same time. Capsules were immersed in water at ∼50 °C, then put in a ∼100 °C oven for ∼10 mins, to check for leaks.

Experiments were run in an internally heated pressure vessel (IHPV) at 1250 °C and 3, 5 or 7 kbar (Table 4.1) using Ar gas as the pressurising medium at the Institut für Mineralogie, Leibniz Universität Hannover, Germany, by R. Balzer and D. Neave. All glasses were run for ∼18 hours, except ETNA31–ETNA32 which were run for ∼36 hours in total. ETNA31–ETNA32 failed to quench the first time and were therefore re-run under the same conditions. ETNA24, ETNA31, ETNA33, and ETNA36 were run in the 'Blue' IHPV, whilst ETNA34 and ETNA35 were run in the 'Yellow' IHPV (Blue and Yellow refer to two different IHPVs available at Hannover). The sample holder is equipped with four S-type thermocouples: two are used to control the furnace temperature and two are used to record the sample temperature. Temperature varied by <5 °C during experiments and pressure variations were limited to ±0.02 kbar. Samples were quenched using a rapid-quench device at ∼150 °C· $s^{-1}$ (Berndt et al., 2002).

After each experiment, the capsules were weighed and visually inspected to check for any leaks during the run (Figure 4.1). ETNA24, ETNA32, ETNA33, and ETNA36 did not gain or lose weight outside weighing error during the run and had convex shapes. ETNA31 had a concave shape and gained significant weight. ETNA34 and ETNA35 leaked a small amount of glass, which was presumed to have occurred on the quench as it was still attached to the capsule after the experiment. Capsules were opened under a binocular microscope and glass chips were selected for further analysis. All run products were dark brown and glassy, except for the glass found on the outside of capsules for ETNA34 and ETNA35 which had variation in the glass colour (Figure 4.2). There was no evidence for crystals or microlites in the glass, and no magnetite nanolites were detected using Raman spectroscopy (method is described in Section 6.3.2; results and discussion in Appendix F).

### 4.2.2. Characterising the composition

Independently quantifying the carbon isotope ratio using stepped-heating mass spectrometry (SHMS) is key to producing the hydrous basaltic glass standards. To determine the quantity of glass required for SHMS requires knowledge of the carbon concentration dissolved in the glass. Hence, the carbon (and hydrogen) concentration was initially measured using Fourier transform infra-red (FTIR) spectroscopy,


**Figure 4.1:** Photographs of the capsules post-synthesis. Sample is labelled in the top left corner of each image. For ETNA34 and ETNA35 the top of the capsule is also shown, where glass can be seen on the outside of the capsule.


**Figure 4.2:** Photograph of the piece of glass found on the outside of the capsule for ETNA35. The glass varies in colour from dark brown, which was the area still connected to the inside of the capsule, to light brown, implying a significant compositional gradient.

which additionally gave information about the volatile speciation. FTIR requires accurate knowledge of the glass density, which is dependent upon the $H_2O$ concentration, hence hydrogen concentrations were measured using the bulk technique of thermal conversion element analyser (TCEA, as described in Section 5.2.6 which includes a discussion of the effects of contamination). TCEA was also used to measure $\delta D$, which are not discussed here, but are used for SIMS hydrogen isotope calibration in Section 6.3.3. SIMS was subsequently used to check the homogeneity of the carbon and hydrogen concentrations. The major and minor element chemistry can also have a matrix effect on SIMS analysis, hence these were analysed using EPMA to check the glass composition was appropriate for the samples of interest (i.e., experimental

glasses in Chapter 5 and arc melt inclusions). This is described in Section 2.5.3, using the set-up in Table 5.5 for ETNA24 and Table 4.3 for ETNA31–ETNA36. Additionally, the Fe oxidation state was analysed using EPMA, as described in Section 3.3.2, and fluid compositions were analysed using weight loss due to freezing/boiling, as described in Section 5.2.5. An overview of the techniques is given in Table 4.4.

**Table 4.3:** EPMA set-up for glass composition of ETNA31–ETNA36.

| Spectrometer – Crystal | | | | |
|---|---|---|---|---|
| 1 – PETJ | 2 – TAP | 3 – TAPH | 4 – PETH | 5 – LIFL |
| Ca$K\alpha^a$ (60) | Si$K\alpha^a$ (60) | Na$K\alpha^a$ (60) | K$K\alpha^a$ (120) | Fe$K\alpha^a$ (60) |
| *Wollastonite* | *BCR-2* | *Albite* | *Sanidine* | *Andradite* |
| BCR-2 | | BCR-2 | | BCR-2 |
| Ti$K\alpha$ (60) | Al$K\alpha$ (60) | Mg$K\alpha$ (60) | P$K\alpha$ (60) | Mn$K\alpha$ (60) |
| *$TiO_2$* | *BCR-2* | *SJIO* | *Durango apatite* | *Mn metal* |
| | | BCR-2 | | |
| Cl$K\alpha$ (60) | | | S$K\alpha$(60) | |
| *NaCl* | | | *VG-2* | |
| | | | Barite | |

*Notes:* Elements in order of analysis from top to bottom; peak count times (s) in brackets; and primary standards for peaking are under each element followed by the standard for calibration in *italics* if different, where BCR-2 is the USGS basaltic glass standard Columbia River Basalt, SJIO is St Johns Island Olivine, and VG-2 the Smithsonian Microbeam Juan de Fuca basaltic glass standard. Mean atomic number (MAN) backgrounds were used and [a] indicates TDI data collected to extrapolate to time zero in case of element migration. For each experimental glass, three analyses on fresh areas of glass were averaged. Composition of standards are in Tables 2.3 and 2.4.

**Table 4.4:** Overview of techniques applied to experimental glasses and fluids.

| Technique | Phase | Variable |
|---|---|---|
| FTIR | Glass | $CO_2$ and $H_2O$ (Section 4.2.2) |
| TCEA | Glass | $H_2O$ (and $\delta$D) (Section 5.2.6) |
| SIMS | Glass | $CO_2$ and $H_2O$ (Section 4.2.2) |
| SHMS | Glass | $CO_2$ and $\delta^{13}$C (Section 4.2.2) |
| EPMA | Glass | Majors and minors (Section 2.5.3) |
| | | $Fe^{2+}/Fe_T$ (Section 3.3.2) |
| Weighing | Fluid | $CO_2$ and $H_2O$ (Section 5.2.5) |

### Fourier transform infra-red spectroscopy

FTIR spectroscopy was used to measure the concentration of carbon and hydrogen dissolved in the glass (e.g., Fine and Stolper, 1986; Stolper, 1982), to inform the amount of material required for SHMS. Additionally, FTIR gives information about the speciation of carbon and hydrogen in the glass. Different chemical bonds absorb light of different wavelengths, which can be used to identify different chemical species present in a material. FTIR spectroscopy measures the absorption of infra-red light by the sample. As an absorption technique, the material must be transparent to light and thin enough that some of the light passes through the sample unabsorbed. The amount of absorption for a specific absorption band is dependent on the concentration of the species, the absorption coefficient, and thickness and density of the sample. The Beer-Lambert approximation can be used to quantify the concentration of each species:

$$C_i = \frac{100 \cdot M_i \cdot A_j}{d \cdot \rho \cdot \varepsilon_j} \tag{4.1}$$

where $C_i$ is the concentration of species $i$ (wt%) with molecular mass $M_i$ (g); $A_j$ is the peak height of absorbance band $j$ with absorption coefficient $\varepsilon_j$ (L·mol$^{-1}$·cm$^{-1}$); and $d$ is the thickness (cm) and $\rho$ is the density (g·L$^{-1}$) of the sample. The absorption coefficient must be determined for each absorption band and is composition dependent, for instance varying with the bulk composition (e.g., Ohlhorst et al., 2001) and $H_2O$ speciation (McIntosh et al., 2017). The approximation only holds if $A_j < 2$, hence samples must be thin enough to prevent excessive absorption.

FTIR spectra were collected using the Thermo Nicolet iN10 MX infrared microscope equipped with a MCT/A detector and a coated KBr beam splitter at the School of Earth Sciences, University of Bristol, UK. Glass chips were double-polished and their thickness ($d$) measured using Mitutyo digital micrometer. Four to eight spectra per glass were collected between 675–6000 cm$^{-1}$ at a resolution of 8 cm$^{-1}$, with an aperture of 100×100 μm$^2$, and 64 scans.

To measure the peak height, a background correction was performed. A thickness-adjusted spectrum (by linearly scaling the spectrum to match the unknown spectrum) collected on a volatile-free basaltic glass was subtracted from each spectrum as the background is often non-linear (Figure 4.3). The peak height ($A_j$) was the maximum height of the background corrected spectrum in the wavelength region of each species.

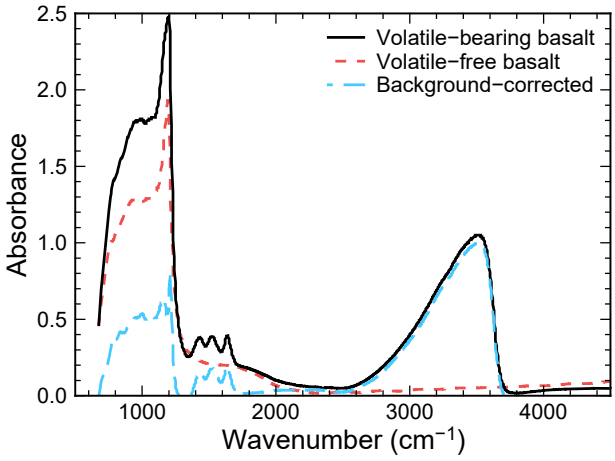


**Figure 4.3:** Example background correction for FTIR spectra. The black, solid curve is a basaltic glass spectrum containing dissolved carbon and hydrogen species. The red, short-dashed curve is a thickness-adjusted (i.e., scaled to fit the black solid curve) spectrum of a basaltic glass that is volatile-free. The blue, long-dashed curve is the background-corrected spectrum (i.e., black – red).

Glass density ($\rho$) was calculated using the equation of Yamashita et al. (1997) for basaltic glass:

$$\rho = 2819 - 20.8 \cdot C_{H_2O} \tag{4.2}$$

where $C_{H_2O}$ is the concentration in wt% using TCEA measurements (Table 4.10).

Carbon concentration was quantified using the $CO_3^{2-}$ peak at ~1430 cm$^{-1}$ ($\varepsilon_{1430}$ = 360 L·cm$^{-1}$·mol$^{-1}$, Shishkina et al., 2014) as the ~1515 cm$^{-1}$ can be affected by the $H_2O^{mol}$ peak at ~1630 cm$^{-1}$. Hydrogen concentration was determined using the $H_2O^T$ peak at ~3550 cm$^{-1}$ ($\varepsilon_{3550}$ = 59.2 L·cm$^{-1}$·mol$^{-1}$, Shishkina et al., 2014), except for ETNA36 where $A_{3550} > 2$. For ETNA36, the hydrogen concentration was calculated as the sum of hydroxyl using the $OH^-$ peak at ~4500 cm$^{-1}$ and molecular water using the $H_2O^{mol}$ peak at ~5200 cm$^{-1}$ ($\varepsilon_{4500}$ = 0.67 L·cm$^{-1}$·mol$^{-1}$ and $\varepsilon_{5200}$ = 0.62 L·cm$^{-1}$·mol$^{-1}$, Dixon et al., 1995). These absorption coefficients were chosen as they were determined for similar glass compositions, especially MgO

concentration which has been shown to have a significant effect on calibration (Fiege et al., 2015). The error on the concentration was determined from the standard deviation on repeat measurements.

### Stepped-heating mass spectrometry

SHMS was used to independently measure the carbon isotope ratios of the hydrous basaltic glass standards. Glass adsorbs $CO_2$ onto its surface, which changes the bulk carbon composition, and does not represent the carbon dissolved in the glass (e.g., Des Marais, 1986). This carbon is not analysed using micro-analytical techniques such as Raman, FTIR, or SIMS, because it is not structurally-bound in the glass. Separation of the adsorbed and dissolved carbon is achieved using stepped-heating gas extraction, whereby a sample is sequentially heated to higher temperature in a vacuum line. This releases the carbon, amongst other volatiles, which can be collected and analysed for concentration and isotope ratio. The exact temperature that these types of carbon is released depends on the glass composition, especially the $H_2O$ concentration. As previous studies have analysed mostly anhydrous, submarine basalts, the temperature the adsorbed and dissolved carbon is released at may be different in these hydrous basaltic glasses.

Stepped-heating extraction of carbon was performed using a vacuum line at the Laboratoire de Géochimie des Isotopes Stables, Institut de Physique du Globe de Paris, France (Figure 4.4). FTIR $CO_2$ concentrations were used to inform the amount of sample to prepare (Table 4.10). Glasses were crushed and sieved, and chips between 240–460 μm were used for subsequent analysis. Prior to analysis, glass chips were washed in a 50:50 mixture of dichloro-methane and -methanol in an ultrasonic bath before being dried in an oven at $\sim$100 °C overnight.

Glass chips were weighed and then transferred into a ball-and-cup holder suspended within the vacuum line (Figure 4.4). Carbon is present in the vacuum line (the 'blank') and its concentration and isotope ratio must be quantified to correct the measurements. The protocol for running blanks (i.e., no sample in the Pt-crucible) and samples (i.e., glass in the Pt-crucible) is the same. The Pt-crucible is heated via induction, where the power of the generator has been calibrated for a given temperature (Figure 4.5). The Pt-crucible is heated for 30 mins, whilst the CuO furnace is heated to 850 °C in a sealed section of the vacuum line containing the Pt-crucible. This releases oxygen into this section of the vacuum line to oxidise any volatiles released. During this time, condensable gases such as $CO_2$ and $H_2O$ are collected in liquid $N_2$ trap (1) at -190 °C, although any gases present that are a liquid at -190 °C will also be collected. The induction coil heating the Pt-crucible coil is switched off, cooling the Pt-crucible, and the CuO furnace is cooled to 250 °C to absorb any remaining free oxygen present for 30 mins. After this, any incondensable gases present in the sealed section of vacuum line are removed by opening the valve to the rest of the vacuum line, drawing any remaining $CO_2$ into liquid $N_2$ trap (1). The area of the vacuum line containing the condensed gases and the barometer is isolated, and liquid $N_2$ trap (1) is heated to -140 °C. This releases $CO_2$, which is transferred to liquid $N_2$ trap (2) for measuring. Liquid $N_2$ trap (2) is isolated and liquid $N_2$ trap (1) is heated to 40 °C to release $H_2O$, which is removed by the vacuum. The pressure of the $CO_2$ is measured using a calibrated barometer as a voltage in a known volume by heating the $CO_2$ in liquid $N_2$ trap (2) to room temperature. The calibration (P. Cartigny, pers. comm. 2017) to covert the voltage ($V$) to moles of carbon ($n$) is:

$$n = 1.076 \cdot V \tag{4.3}$$

The $CO_2$ is then transferred to a sample vial in liquid $N_2$ trap (3) for isotope measurement.

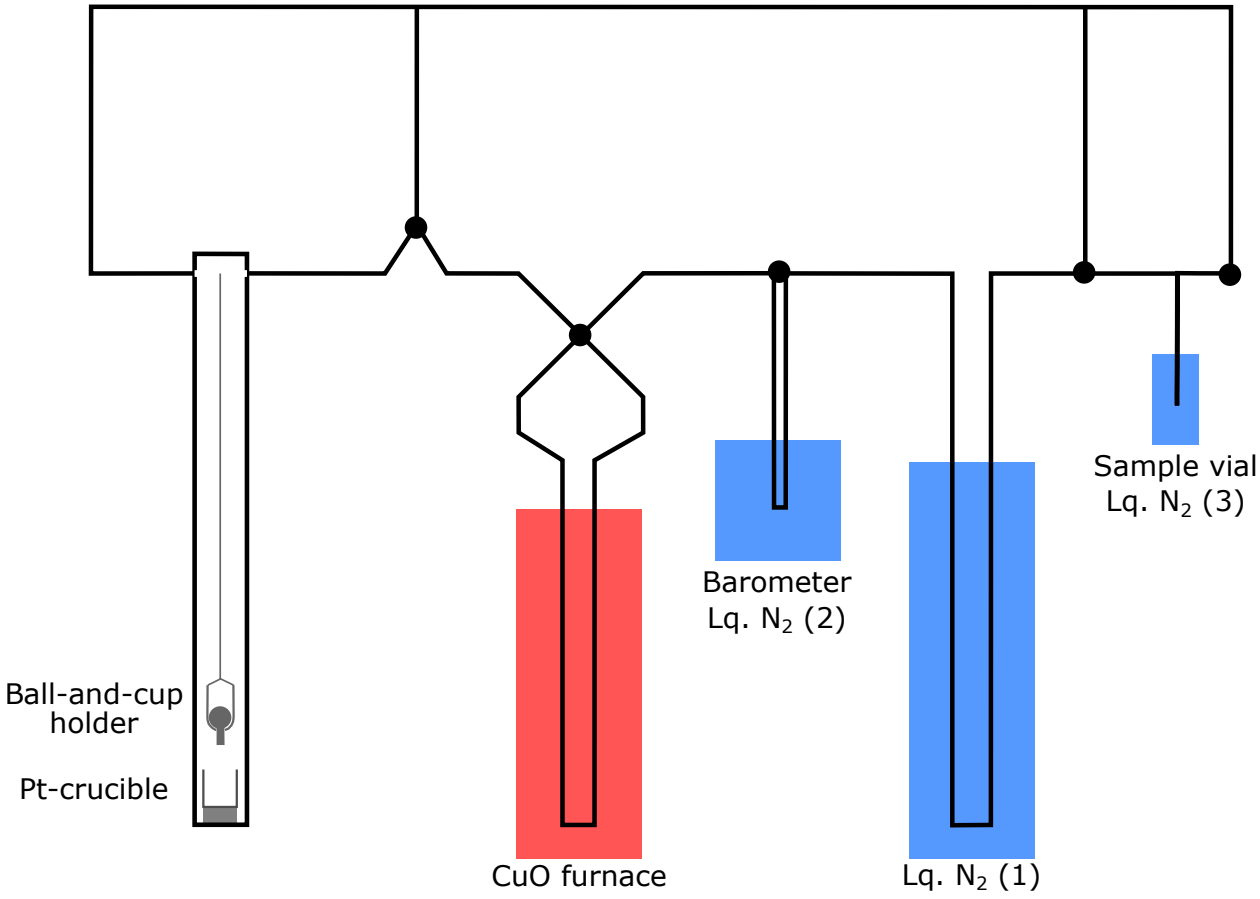


**Figure 4.4:** Schematic of the stepped-heating gas extraction vacuum line at Laboratoire de Géochimie des Isotopes Stables, Institut de Physique du Globe de Paris, France, showing the location of the ball-and-cup holder for loading the sample into the Pt-crucible, CuO furnace (red), and liquid nitrogen traps (blue) associated with **(1)** collecting all condensable gasses (e.g., $H_2O$ and $CO_2$), **(2)** barometer for measuring $CO_2$ pressure and hence concentration, and **(3)** sample vial for isotope ratio analysis.

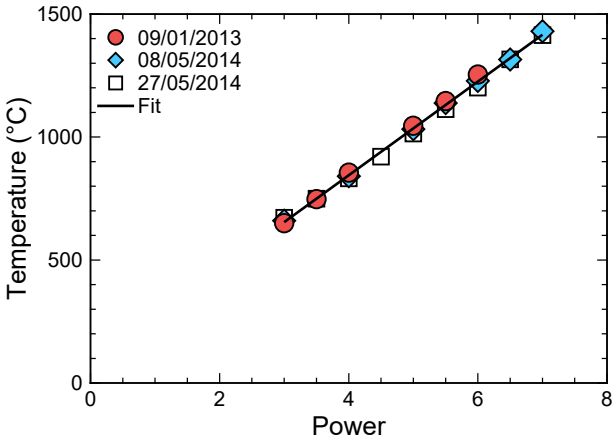


**Figure 4.5:** Calibration curve used to convert generator power to heating temperature in the Pt-crucible. Best fit is to all the data. Data from P. Cartigny (pers. comm., 2018).

After a new sample was introduced into the vacuum line, blank analyses were at ~1400 °C until the carbon concentration was typically ≤0.1 μmol carbon. The carbon released during the last blank, before the actual glass was analysed, was collected for carbon isotope analysis. The sample was introduced into the Pt-crucible by lowering the ball-and-cup holder, which meant the vacuum was not broken between blank and glass analysis. The glass was heated incrementally to higher temperatures to release the volatiles in stages.

The exact temperature steps chosen to release carbon varied between glasses. Typically, the glass was heated in steps of 50–100 °C from ∼500 °C until a near blank value was reached, which indicated all the low temperature, adsorbed $CO_2$ had been released. After this, the sample was heated in one step to ∼1200 °C to release all dissolved carbon. A single heating step was used to release a greater amount of carbon which reduces the proportion of carbon from the blank. The sample was then heated in 100 °C steps to ∼1400 °C to ensure all carbon had been released. In some cases, a temperature step was repeated multiple times to ensure all carbon was released.

The carbon isotope ratio of the gas extracted at each temperature step, and the blanks, was measured using the Thermo DELTA plus XP at the Laboratoire de Géochimie des Isotopes Stables, Institut de Physique du Globe de Paris, France, by P. Cartigny. $^{12}$C and $^{13}$C are measured and the ratio is continuously measured relative to a gas of known isotope ratio to account for instrumental mass fractionation. A minimum flow rate of $CO_2$ through the instrument is required for accurate carbon isotope measurements, hence the $CO_2$ pressure in the sample vial must be high enough for this. Samples containing little $CO_2$ (i.e., few moles of $CO_2$) were cooled in liquid $N_2$ to occupy a smaller volume, which increases their pressure and therefore their flow rate.

**Secondary ion mass spectrometry**

To measure the concentration of carbon and hydrogen, and check the volatile homogeneity, glass chips were mounted in epoxy, then ground and polished to a ∼1–3 μm finish. Glass chips were then extracted from the resin and remounted in indium before gold coating (∼40–80 nm thickness). Measurements were made on the Cameca IMS-4f at the Edinburgh Ion Microprobe Facility, School of GeoSciences, University of Edinburgh, UK. The analytical target was pre-sputtered over a 20×20 μm$^2$ area for 3–4 mins to reduce surface contamination. An $O^-$ beam at 15 kV and 5 nA was used to produce positive ions over a 60 μm$^2$ imaging field which was reduced to ∼20 μm$^2$ using apertures. First, carbon was measured as $^{12}C^+$, where secondary ions were extracted at 4.5 kV with a 50 kV offset and 40 eV window. Mass resolution was sufficient to remove the overlap of $^{24}Mg^{2+}$ on $^{12}C^+$. For each measurement 15 cycles were collected. The first few cycles can be contaminated with surficial carbon, which causes the $^{12}C^+$ counts to drop sharply after the first 1–2 cycles and then remain constant. Hence, typically only the final eight cycles were used. Subsequently, hydrogen as $^1H^+$ was measured in the same pit as carbon and a rastering 25 μm$^2$ image field was used during peak searching. Secondary ions were extracted at 4.5 kV with a 75 kV offset and 40 eV window. Eight to ten cycles were collected for each measurement but, due to potential surficial hydrogen contamination as for carbon, typically only the last six were used. For both carbon and hydrogen, $^{30}Si^+$ was also measured to normalise for any instrumental changes during the analysis (e.g., beam current), due to its high abundance and homogeneous distribution. Species, count times, and wait times are detailed in Tables 4.5 and 4.6 for carbon and hydrogen, respectively. Less cycles and shorter count times are required for hydrogen analysis because it has a higher abundance than carbon. Glasses were analysed 3–7 times (except ETNA24 that was analysed 22 times on three different chips) during different analytical sessions (Aug-16 for ETNA24, and Jun-18 (1) and (2) for ETNA31–ETNA36, Figure 4.6).

Basaltic glass standards with known carbon and hydrogen concentration (Table 4.7) were measured throughout the session to check for drift and for calibration. St glasses are from Shishkina et al. (2010), where $H_2O$ is measured using Karl-Fischer titration and $CO_2$ is measured using a bulk technique based

**Table 4.5:** Species analysed for carbon concentration analysis, including count and wait times.

| Species | $^{24}Mg^{2+}$ | $^{12}C^{+}$ | $^{40}Ca^{+}$ | $^{30}Si^{+}$ |
|---|---|---|---|---|
| Count time (s) | 5 | 10 | 2 | 2 |
| Wait time (s) | 1 | 0.2 | 1 | 1 |

**Table 4.6:** Species analysed for hydrogen concentration analysis, including count and wait times.

| Species | | $^{1}H^{+}$ | $^{7}Li^{+}$ | $^{19}F^{+}$ | $^{7}Na^{+}$ | $^{26}Mg^{+}$ | $^{30}Si^{+}$ | $^{35}Cl^{+}$ | $^{39}K^{+}$ | $^{42}Ca^{+}$ | $^{47}Ti^{+}$ |
|---|---|---|---|---|---|---|---|---|---|---|---|
| Count time (s) | 1 | 4 | *4* | *4* | 4 | 4 | 2 | *5* | 2 | 2 | 2 |
| Wait time (s) | 1.5 | 1 | *0.5* | *1* | 0.1 | 0.2 | 0.2 | *0.2* | 0.2 | 0.2 | 0.2 |
| *Notes:* Species in *italics* were only measured during the Jun-18 (2) session. | | | | | | | | | | | |

on single step pyrolysis (see Section 5.2.3). Such bulk carbon methods normally suffer from carbon contamination (e.g., Section 4.1) but analysis of a carbon-free glass (the air-melted starting glass) measured 8.2 ± 1.4 μm C, where the blank was 5.1 ± 0.4 μm C (Shishkina et al., 2010). The $H_2O$ and $CO_2$ concentration of s glasses and 17-2 was measured using FTIR by Pichavant et al. (2009, 2013). Carbon and hydrogen measured using SIMS were quantified as $CO_2$ and $H_2O$, respectively. After applying a background correction (based on analyses of BIR-1, Table 4.7), counts were divided by $^{30}Si^{+}$ and working curves for each analytical session were constructed (Blundy and Cashman, 2008):

$$CO_2 \propto \frac{^{12}C^{+} - {}^{12}C^{+}_{bkg}}{^{30}Si^{+}} \tag{4.4}$$

$$H_2O \propto \frac{^{1}H^{+} - {}^{12}H^{+}_{bkg}}{^{30}Si^{+}} \tag{4.5}$$

$CO_2$ concentrations were multiplied by ($SiO_2$, wt%)/50, using EPMA $SiO_2$ concentrations (Table 4.10), to account for differences in the silica content between standards and unknowns. The $SiO_2$ correction is not necessary for quantifying $H_2O$ as $^{1}H^{+}$ ion yield correlates with $SiO_2$ (Blundy and Cashman, 2008).

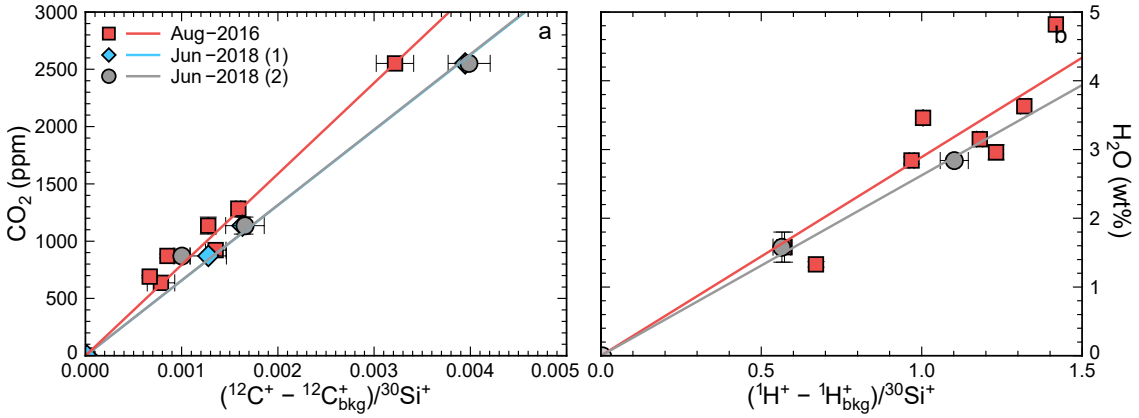


**Figure 4.6:** SIMS-4f calibration curves using standards in Table 4.7, where symbol shape and colour indicate the session of data collection: **(a)** $CO_2$ concentration against $(^{12}C^{+} - {}^{12}C^{+}_{bkg})/^{30}Si^{+}$; and **(b)** $H_2O$ concentration against $(^{1}H^{+} - {}^{1}H^{+}_{bkg})/^{30}Si^{+}$. Error bars are the standard deviation based on repeat SIMS analysis during the session for ratios or those stated in Table 4.7 for concentrations.

**Table 4.7:** Volatile-free glass compositions and volatile concentrations of external basaltic glass standards.

| Oxide (wt%) | BIR-1[a] | St[b] | s[c] | 17-2[c] | Sample | $H_2O$ (wt%) | *s.d.* | $CO_2$ (ppm) | *s.d.* |
|---|---|---|---|---|---|---|---|---|---|
| $SiO_2$ | 47.96 | 50.17 | 50.2 | 51.2 | St-1[b] | 2.96 | *0.09* | 691 | *11* |
| $TiO_2$ | 0.96 | 0.92 | 0.84 | 0.82 | St-2[b] | 2.84 | *0.05* | 1136 | *74* |
| $Al_2O_3$ | 15.5 | 18.28 | 15.20 | 15.9 | St-3[b] | 1.33 | *0.04* | 1394 | *125* |
| $FeO_T$ | 10.17 | 9.37 | 7.81 | 6.29 | St-6[b] | 1.58 | *0.09* | 871 | *16* |
| MnO | 0.175 | 0.17 | 0.16 | 0.14 | s2-3[d] | 3.15 | *0.18* | 636 | *119* |
| MgO | 9.70 | 7.00 | 7.87 | 8.31 | s4-13[d] | 3.63 | *0.32* | 922 | *164* |
| CaO | 13.3 | 11.37 | 12.40 | 12.3 | s5-14[d] | 3.46 | *0.11* | 1284 | *26* |
| $Na_2O$ | 1.82 | 2.33 | 2.29 | 2.44 | 17-2[c] | 4.82 | *0.10* | 2552 | *192* |
| $K_2O$ | 0.030 | 0.23 | 1.86 | 1.85 | | | | | |
| $P_2O_5$ | 0.021 | 0.15 | 0.64 | 0.68 | | | | | |

*Notes:* Data are from: [a]Gladney and Roelandts (1988); [b]Shishkina et al. (2010): major/minor elements measured using EPMA on remelted glass used in the experiments (individual glass compositions not reported), $H_2O$ using Karl-Fischer titration, and $CO_2$ using CSA; [c]Pichavant et al. (2009): major/minor elements measured using EPMA on the PST-9 starting glass (Pichavant et al., 2013) where individual glass compositions are not reported (s glasses) or the actual glass (17-2), and $H_2O$ and $CO_2$ using FTIR; and [d]Pichavant et al. (2013): $H_2O$ and $CO_2$ measured using FTIR. Errors of one standard deviation (*s.d.*) are shown in *italics*.

### 4.2.3. Quantifying the bulk carbon isotope ratio

The measured carbon concentration and isotope ratio of each SHMS temperature step is a mixture of the carbon released from the glass and the instrumental blank, therefore using mass balance:

$$X_{\mathrm{m}} = X_{\mathrm{g}} + X_{\mathrm{b}} \tag{4.6}$$

$$X_{\mathrm{m}} R_{\mathrm{m}} = X_{\mathrm{g}} R_{\mathrm{g}} + X_{\mathrm{b}} R_{\mathrm{b}} \tag{4.7}$$

where $X_{\mathrm{m}}$, $X_{\mathrm{g}}$, and $X_{\mathrm{b}}$ are the moles of carbon measured in each temperature step (m) and in the glass (g) and blank (b), respectively; and $R_{\mathrm{m}}$, $R_{\mathrm{g}}$, and $R_{\mathrm{b}}$ are the isotope ratios expressed as $^{13}C/^{12}C$ actually measured (m) and in the glass (g) and blank (b), respectively. Equation 4.6 can be used to calculate the blank-corrected carbon concentration of the glass ($X_g$) for each temperature step. Substituting Equation 4.6 for $X_{\mathrm{g}}$ into Equation 4.7 and rearranging gives:

$$R_{\mathrm{g}} = \frac{X_{\mathrm{m}} R_{\mathrm{m}} - X_{\mathrm{b}} R_{\mathrm{b}}}{X_{\mathrm{m}} - X_{\mathrm{b}}} \tag{4.8}$$

which is the blank-corrected carbon isotope ratio of the glass ($R_g$) at each temperature step. The blank-corrected values are calculated using the concentration ($X_b$) and isotope ratio ($R_b$) of the blank collected at the start of each sample. If the isotopic ratio of the blank was not measured at the start of the sample, the average of all blanks measured is used.

To calculate the total dissolved carbon composition in the glass, blank-corrected moles of carbon of temperature steps consisting of dissolved, not adsorbed, carbon are summed and divided by the weight of sample analysed. The bulk isotope ratio is calculated by summing the blank-corrected isotope ratios of

dissolved carbon weighted by the blank-corrected moles of carbon in that temperature step. As ensuring dissolved and adsorbed carbon are separated is critical, each sample is discussed to evaluate the reliability of the measurement and estimate its error. The temperature the glass was heated to using an induction coil are quoted to the nearest 100 °C, but Table 4.8 shows the exact temperature values calculated using the temperature calibration in Figure 4.5 for reference. Results from stepped-heated gas extraction, isotope ratio measurements, and blank-corrections are in Table 4.9 and Figure 4.7.

**Table 4.8:** Quoted (to the nearest 100 °C) and exact temperature values using Figure 4.5.

| Quoted T (°C) | 500 | 550 | 600 | 650 | 700 | 800 | 900 | 1000 | 1100 | 1200 | 1300 | 1400 |
|---|---|---|---|---|---|---|---|---|---|---|---|---|
| Exact T (°C) | 499 | 548 | 599 | 650 | 701 | 802 | 904 | 1005 | 1107 | 1209 | 1309 | 1412 |

All glasses show two stages of carbon release, the first at ∼500–600 °C (low) and the second at ∼600–1200 °C (high) temperatures, with light and heavy $\delta^{13}C$ signatures respectively (Table 4.9 and Figure 4.7). The low temperature carbon release is attributed to contamination adsorbed to the surface of the glass and does not represent dissolved carbon within the glass (e.g., Macpherson et al., 1999). Hence, the low-temperature carbon has a very light isotope ratio (<-20 ‰ $\delta^{13}C$) (Macpherson et al., 1999). The high temperature carbon release corresponds to the dissolved carbon in the glass (e.g., Macpherson et al., 1999) and is isotopically heavier than the low temperature contaminant as the $\delta^{13}C$ of the $CaCO_3$ added to the starting materials was heavy (-2 to +2 ‰ $\delta^{13}C$, Table 4.2). Our experimental glasses contain no internal vesicles, hence there should be no intermediate release of $CO_2$ from vesicles. The experimental glasses are hydrous, hence the $CO_2$ is released at lower temperatures compared to previous results on anhydrous glass.

ETNA24 has a very large release of carbon at 600 °C, indicating significant adsorption. The exact mass is unknown as it saturated the pressure gauge in the known volume, therefore it was expanded into a larger, but uncalibrated, volume. The carbon concentration does not return to the blank at 700 °C, and the $\delta^{13}C$ value is higher than expected for the blank, indicating this step likely contains both adsorbed and dissolved carbon. The blank before analysis is twice as large as that after. This implies the initial blank is an overestimate of the true blank, hence the final blanks (0.25 μmol carbon) are used for the blank-correction. The $\delta^{13}C$ gets heavier with increasing temperature. This implies carbon release from the glass is kinetically controlled, hence light carbon is released first and then the carbon becomes progressively isotopically heavier. After 1100 °C, the carbon gets isotopically lighter as the blank becomes a greater proportion of the carbon signature. The carbon concentration returns to the blank value at 1200 °C indicating complete extraction of carbon from the glass. Including the uncertainty in the proportion of dissolved carbon in the 700 °C step, and the value of the blank, the glass $CO_2$ concentration is 2568 ± 321 ppm with a $\delta^{13}C$ of -14.9 ± 1.1 ‰.

ETNA31 has good separation of adsorbed and dissolved carbon, with near-blank values at the 550 °C step. Near-blank values are achieved again at 1300 °C, implying all carbon in the glass has been released, although further carbon is released at 1400 °C. Unfortunately, due to instrumental problems, $\delta^{13}C$ values are not available for this sample therefore it is not possible to calculate the glass $\delta^{13}C$ or identify the source of the $CO_2$ released at very high temperature. The blank-corrected $CO_2$ concentration is 1628 ± 44 ppm.

ETNA32 has good separation between adsorbed and dissolved carbon. This is despite the 550 °C step having a high carbon concentration because its isotope ratio value is isotopically light, which is consistent with the adsorbed carbon. At very high temperature, significant carbon is released. The isotope ratio is very consistent between 600 and 1400 °C therefore, even though it is difficult to determine the source of the very

**Table 4.9:** Raw and blank-corrected carbon compositions using stepped-heating mass spectrometry.

| Temperature (°C) | Baratron (V) | Raw C (μmol) | Raw $\delta^{13}C$ (‰) | *s.d.* | Blank-corrected C (μmol) | Blank-corrected $\delta^{13}C$ (‰) |
|---|---|---|---|---|---|---|
| ETNA24 (0.19933 g) | | | | | | |
| Blank | 0.45 | 0.48 | -23.949 | *0.079* | 0.24 | |
| 600 | [a] | [a] | -19.902 | *0.055* | [a] | [a] |
| 700 | 1.48 | 1.59 | -18.073 | *0.031* | 1.35 | -16.992 |
| 800 | 5.58 | 6.00 | -15.900 | *0.051* | 5.76 | -15.554 |
| 900 | 2.95 | 3.17 | -16.085 | *0.038* | 2.93 | -15.420 |
| 1000 | 1.50 | 1.61 | -14.033 | *0.250* | 1.37 | -12.237 |
| 1100 | 0.40 | 0.43 | -15.201 | *0.150* | 0.18 | -3.366 |
| 1200 | 0.25 | 0.27 | -17.994 | *0.250* | 0.02 | 50.489 |
| 1300 | 0.23 | 0.25 | -25.077 | *0.399* | 0.00 | |
| 1400 | 0.23 | 0.25 | n.d. | | 0.00 | |
| ETNA31 (0.14616 g) | | | | | | |
| Blank | 0.105 | 0.113 | -23.792 | *0.128* | 0 | |
| 500 | 0.879 | 0.945 | -23.337 | *0.027* | 0.833 | -23.275 |
| 550 | 0.237 | 0.256 | -20.414 | *0.244* | 0.142 | -17.727 |
| 600 | 1.141 | 1.228 | n.d. | | 1.115 | |
| 1200 | 3.394 | 3.652 | n.d. | | 3.539 | |
| 1300 | 0.286 | 0.308 | -20.605 | *0.046* | 0.195 | -18.756 |
| 1400 (1) | 0.490 | 0.527 | -20.534 | *0.032* | 0.414 | -19.646 |
| 1400 (2) | 0.253 | 0.272 | -18.034 | *0.026* | 0.159 | -13.949 |
| 1400 (3) | 0.093 | 0.100 | -21.793 | *0.069* | -0.013 | -39.284 |
| ETNA32 (0.14169 g) | | | | | | |
| Blank | 0.089 | 0.096 | *-20* | | 0 | |
| 500 | 1.590 | 1.711 | -25.514 | *0.017* | 1.615 | -25.841 |
| 550 | 0.880 | 0.947 | -21.314 | *0.106* | 0.851 | -21.462 |
| 600 | 0.929 | 1.000 | -12.435 | *0.047* | 0.904 | -11.634 |
| 650 | 4.062 | 4.371 | -11.985 | *0.054* | 4.275 | -11.806 |
| 1200 | 3.780 | 4.067 | -12.782 | *0.033* | 3.972 | -12.608 |
| 1300 | 1.480 | 1.592 | -12.358 | *0.019* | 1.497 | -11.869 |
| 1400 (1) | 1.420 | 1.528 | -13.087 | *0.031* | 1.432 | -12.625 |
| 1400 (2) | 0.330 | 0.355 | n.d. | *0.069* | 0.259 | |
| 1400 (3) | 0.203 | 0.218 | -15.690 | | 0.123 | -12.325 |
| ETNA33 (0.10799 g) | | | | | | |
| Blank | 0.108 | 0.116 | -24.100 | *0.051* | 0 | |
| 500 | 0.346 | 0.372 | -24.850 | *0.083* | 0.256 | -25.198 |
| 550 | 0.159 | 0.171 | -22.875 | *0.200* | 0.055 | -20.306 |
| 600 | 0.604 | 0.650 | -11.277 | *0.057* | 0.534 | -8.495 |
| 650 | 1.586 | 1.707 | -11.884 | *0.094* | 1.591 | -10.994 |
| 1200 | 2.680 | 2.884 | -14.464 | *0.030* | 2.768 | -14.061 |
| 1300 | 0.887 | 0.954 | -18.699 | *0.018* | 0.839 | -17.953 |
| 1400 (1) | 1.240 | 1.334 | *-21* | | 1.218 | -18 |
| 1400 (2) | 0.116 | 0.125 | -13.665 | *0.025* | 0.009 | |
| ETNA34 (0.13684 g) | | | | | | |
| Blank | 0.125 | 0.135 | -20.000 | *0.059* | 0 | |
| 500 | 1.216 | 1.308 | -24.313 | *0.032* | 1.174 | -24.807 |
| 550 | 0.266 | 0.286 | -22.097 | *0.013* | 0.152 | -23.956 |
| 600 | 0.474 | 0.510 | -12.548 | *1.446* | 0.376 | -9.879 |
| 650 | 1.420 | 1.528 | *-10* | | 1.393 | -9.065 |
| 1200 | 2.507 | 2.698 | -10.449 | *0.045* | 2.563 | -9.948 |
| 1300 | 0.275 | 0.296 | -20.783 | *0.020* | 0.161 | -21.436 |
| 1400 (1) | 0.701 | 0.754 | -18.688 | *0.018* | 0.620 | -18.403 |
| 1400 (2) | 0.264 | 0.284 | -21.595 | *0.027* | 0.150 | -23.029 |

**Table 4.9:** Raw and blank-corrected carbon compositions using stepped-heating mass spectrometry *cont.*

| Temperature (°C) | Baratron (V) | Raw C (μmol) | Raw $\delta^{13}C$ (‰) | *s.d.* | Blank-corrected C (μmol) | Blank-corrected $\delta^{13}C$ (‰) |
|---|---|---|---|---|---|---|
| ETNA35 (0.12795 g) | | | | | | |
| Blank | 0.096 | 0.103 | -19.961 | *0.103* | 0 | |
| 500 | 0.850 | 0.915 | -22.651 | *0.027* | 0.811 | -22.994 |
| 550 (1) | 1.187 | 1.277 | -12.016 | | 1.174 | -11.317 |
| 550 (2) | 0.317 | 0.341 | n.d. | | 0.238 | |
| 550 (3) | 0.162 | 0.174 | n.d. | | 0.071 | |
| 600 | 0.262 | 0.282 | n.d. | | 0.179 | |
| 650 | 0.674 | 0.725 | n.d. | | 0.622 | |
| 1200 | 1.788 | 1.924 | n.d. | | 1.821 | |
| 1300 | 0.344 | 0.370 | -16.009 | *0.045* | 0.267 | -14.479 |
| 1400 (1) | 0.386 | 0.415 | -19.895 | *0.027* | 0.312 | -19.873 |
| 1400 (2) | 0.280 | 0.301 | -15.303 | *0.040* | 0.198 | -12.873 |
| 1400 (3) | 0.042 | 0.045 | | | -0.058 | |
| ETNA36 (0.14169 g) | | | | | | |
| Blank | 0.089 | 0.096 | *-20* | | 0 | |
| 500 | 1.590 | 1.711 | -25.514 | *0.017* | 1.615 | -25.841 |
| 550 | 0.880 | 0.947 | -21.314 | *0.106* | 0.851 | -21.462 |
| 600 | 0.929 | 1.000 | -12.435 | *0.047* | 0.904 | -11.634 |
| 650 | 4.062 | 4.371 | -11.985 | *0.054* | 4.275 | -11.806 |
| 1200 | 3.780 | 4.067 | -12.782 | *0.033* | 3.972 | -12.608 |
| 1300 | 1.480 | 1.592 | -12.358 | *0.019* | 1.497 | -11.869 |
| 1400 (1) | 1.420 | 1.528 | -13.087 | *0.031* | 1.432 | -12.625 |
| 1400 (2) | 0.330 | 0.355 | n.d. | | 0.259 | |
| 1400 (3) | 0.203 | 0.218 | -15.690 | *0.069* | 0.123 | -12.325 |

*Notes:* Temperatures are quoted to the nearest 100 °C and exact temperatures are given in Table 4.8; blank-corrections performed using Equations 4.6 and 4.8; weight of the sample is given in brackets after the sample name; errors, where available, of one standard deviation (*s.d.*) are shown in *italics*; [a] indicates pressure saturated the baratron and hence was not quantified; raw $\delta^{13}C$ values in *italics* are not measured but assumed to calculate the carbon composition of the sample; and n.d. means not determined due to analytical problems.

high temperature carbon, it does not affect the calculated isotope ratio. Hence, the $\delta^{13}C$ is -11.75 ± 0.4 ‰. The $CO_2$ concentration is more uncertain, although a maximum estimate, including all high temperature carbon, is 3870 ppm.

ETNA33 has good separation between adsorbed and dissolved carbon, indicated by a low carbon concentration at 550 °C with an isotopically light isotope ratio. The high temperature carbon release pattern is strange as the isotope ratio gets isotopically lighter with increasing temperature. This is the opposite of what would be expected for kinetically-driven carbon release. Also, significant carbon is released at 1300–1400 °C, by which temperature all dissolved carbon should have been released. The trend in isotope ratios looks like a mixture between dissolved carbon with a heavy isotope value and a contaminant with a light isotope ratio. This release pattern makes quantifying the concentration and isotope ratio of the dissolved carbon uncertain. The best estimate is 2584 ± 249 ppm $CO_2$ and -14.3 ± 0.3 ‰ $\delta^{13}C$, assuming it does not contain significant contamination.

ETNA34 has good separation between adsorbed and dissolved carbon. The carbon concentration does not return to the blank at 550 °C but its isotopic value is very light consistent with adsorbed carbon. At very high temperatures the carbon concentration does not return to the blank, but the isotope ratios are very light

consistent with the blank. Including the uncertainty in the origin of the very high temperature carbon gives a $CO_2$ concentration of 1543 $\pm$ 150 ppm and $\delta^{13}C$ of -10.8 $\pm$ 0.5 ‰.

ETNA35 has good separation between adsorbed and dissolved carbon, but an odd release pattern at very high temperatures. Unfortunately, due to instrumental problems, no isotope ratios are available for this sample, therefore it is not possible to calculate the $\delta^{13}C$ of this glass. Including the uncertainty in the source of the high temperature carbon, the $CO_2$ concentration is 1050 $\pm$ 124 ppm.

ETNA36 has good separation of adsorbed and dissolved carbon, with a concentration and isotope ratio consistent with the blank at 550 °C. At very high temperatures (>1300 °C), the carbon concentration does not return to the blank and has a heavy isotope ratio. The blank-corrected $CO_2$ concentration is 1963 $\pm$ 94 ppm, based on the uncertainty of the origin of the very high temperature carbon. Unfortunately, there is no isotopic value for the 650 °C temperature step. Assuming a value of -10 ‰ $\delta^{13}C$, based on the 700 and 1200 °C temperature steps, gives a $\delta^{13}C$ = -10.3 $\pm$ 0.4 ‰ assuming the blank had a $\delta^{13}C$ of -20 to -25 ‰ as no value was measured.

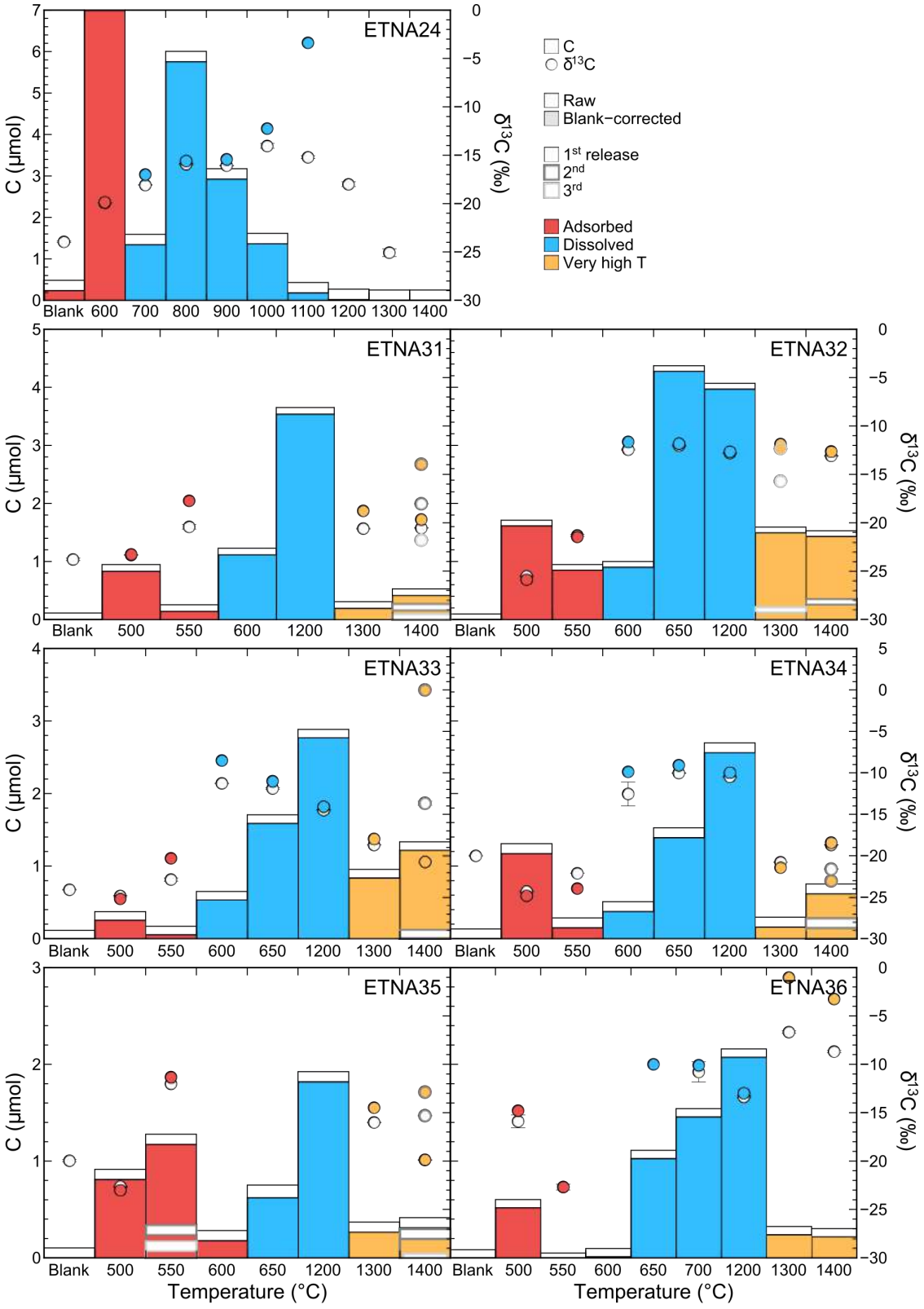


**Figure 4.7:** Stepped-heating mass spectrometry results for each temperature step, where bars indicate mass of carbon released and circles are the corresponding $\delta^{13}C$. Raw values are shown in white and blank-corrected values are coloured by the inferred type of carbon released. If multiple releases were done at the same temperature, they are shown using different outline colours. Sample number is shown in the top right corner. Temperatures are quoted to the nearest 100 °C and exact values are shown in Table 4.8.

### 4.2.4. Hydrous basaltic glass standards

Table 4.10 details the composition of the glass standards produced. All glasses are basaltic, and hence appropriate for use on basaltic arc melt inclusions and the experiments in Chapter 5. They cover a range of carbon isotope ratios (-14.9 to -10.3 ‰ $\delta^{13}$C) and concentrations (644–4629 ppm $CO_2$) present as $CO_3^{2-}$(Figure 4.8). They also cover a range in hydrogen concentration (0.67–2.86 wt% $H_2O$). Glasses are homogeneous and show <10 % variation in $CO_2$ concentration based on spatially-separated, repeated SIMS analyses. The exception to this is ETNA35, which has 30 % variability in $CO_2$ ($n$ = 7). The reproducibility of $CO_2$ using different techniques is somewhat variable, with >20 % difference for some samples (Table 4.10 and Figure F.1b), which may affect the reliability of the $\delta^{13}$C measurements. Unfortunately, repeat measurements of the $\delta^{13}$C of the glasses were not possible due to the large amount of material required, but Macpherson et al. (1999) achieved ±0.5 ‰ in their study of ALV981-R23.

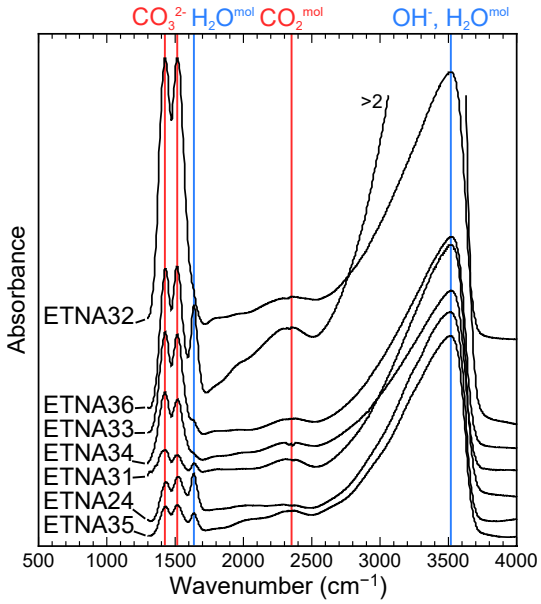


**Figure 4.8:** Background-corrected FTIR spectra of each glass (labelled on the left-hand side), which are offset but use the same relative scale. The ($OH^-$, $H_2O^{mol}$) peak at ~3500 $cm^{-1}$ for ETNA36 is too high (>2 absorbance) so has been cut off. Peaks for carbon- (red) and hydrogen- (blue) bearing species are shown as vertical lines, labelled along the top.

Unfortunately, some of these glasses are not appropriate for use as SIMS standards. Due to problems analytical problems, the carbon isotope ratio for ETNA31 and ETNA35 could not be quantified using SHMS (Section 4.2.3), hence no independent measurements of $\delta^{13}$C are available. Also, ETNA31 gained significant weight during the IHPV run, and ETNA35 leaked some glass on the quench, which are likely to have effected their carbon compositions. The release pattern of ETNA33 implies carbon contamination at high temperature (Figure 4.7). Therefore, the carbon isotope measurement may have been compromised and hence it is not used as a standard for SIMS analysis. ETNA34 leaked a small amount of glass on the quench. This may have caused a brief period of open-system degassing before the glass quenched, consistent with its low volatile content. This is unlikely to be an equilibrium process and, although the carbon concentration is homogeneous (10 % variation based on repeated SIMS analyses, Table 4.10), the carbon isotope ratio may not be. As SHMS is a bulk technique it cannot be used to check sample homogeneity. Hence, ETNA34 is also excluded as a standard for SIMS analysis. ETNA32 was run twice at the same conditions due to a failled quench, but this is unlikely to have affected its carbon composition. Therefore ETNA24, ETNA32, and ETNA36 were chosen as standards for SIMS analysis as these glasses had no problems during synthesis and showed good separation between adsorbed and dissolved carbon (Figure 4.7).

**Table 4.10:** Glass and fluid compositions.

| | ETNA24 | *s.d.* | ETNA31 | *s.d.* | ETNA32 | *s.d.* | ETNA33 | *s.d.* | ETNA34 | *s.d.* | ETNA35 | *s.d.* | ETNA36 | *s.d.* |
|---|---|---|---|---|---|---|---|---|---|---|---|---|---|---|
| $SiO_2$ | 48.65 | *0.11* | 48.50 | *0.11* | 48.72 | *0.12* | 49.06 | *0.13* | 48.65 | *0.11* | 47.88 | *0.16* | 47.60 | *0.09* |
| $TiO_2$ | 1.71 | *0.03* | 1.79 | *0.02* | 1.76 | *0.03* | 1.79 | *0.03* | 1.80 | *0.03* | 1.76 | *0.03* | 1.75 | *0.03* |
| $Al_2O_3$ | 16.92 | *0.07* | 16.01 | *0.05* | 15.86 | *0.05* | 15.95 | *0.04* | 15.94 | *0.05* | 15.75 | *0.03* | 15.62 | *0.08* |
| $FeO_T$ | 10.09 | *0.07* | 8.62 | *0.13* | 8.71 | *0.15* | 8.83 | *0.14* | 9.20 | *0.16* | 9.60 | *0.10* | 9.64 | *0.11* |
| MnO | 0.21 | *0.02* | 0.17 | *0.01* | 0.17 | *0.01* | 0.16 | *0.01* | 0.16 | *0.01* | 0.18 | *0.01* | 0.17 | *0.01* |
| MgO | 5.99 | *0.05* | 6.26 | *0.03* | 6.14 | *0.03* | 6.18 | *0.06* | 6.21 | *0.03* | 6.15 | *0.04* | 6.07 | *0.05* |
| CaO | 6.73 | *0.04* | 10.52 | *0.08* | 10.34 | *0.08* | 10.37 | *0.11* | 10.35 | *0.12* | 10.21 | *0.13* | 10.09 | *0.09* |
| $Na_2O$ | 3.94 | *0.07* | 4.16 | *0.08* | 4.13 | *0.06* | 4.17 | *0.08* | 4.21 | *0.08* | 4.14 | *0.07* | 4.05 | *0.08* |
| $K_2O$ | 1.78 | *0.02* | 1.88 | *0.01* | 1.88 | *0.02* | 1.90 | *0.01* | 1.88 | *0.02* | 1.86 | *0.01* | 1.84 | *0.02* |
| $P_2O_5$ | 0.46 | *0.03* | 0.53 | *0.02* | 0.52 | *0.02* | 0.51 | *0.01* | 0.52 | *0.01* | 0.51 | *0.01* | 0.52 | *0.01* |
| $H_2O^a$ | 2.91 | *0.09* | 0.86 | *0.01* | 0.96 | *0.01* | n.d. | | 0.65 | *0.01* | 1.55 | *0.01* | 2.04 | *0.02* |
| $H_2O^b$ | 3.31 | *0.34* | 1.02 | *0.02* | 1.13 | *0.02* | 1.10 | *0.06* | 0.77 | *0.06* | 2.26 | *0.20* | 1.55 | *0.16* |
| $H_2O^c$ | 2.86 | *0.06* | 0.95 | *0.06* | 1.02 | *0.06* | 1.04 | *0.06* | 0.67 | *0.06* | 1.64 | *0.06* | 2.30 | *0.06* |
| $\delta D^c$ (‰) | -135.7 | *0.9* | -107.1 | *0.9* | -103.9 | *0.9* | -99.0 | *0.9* | -145.1 | *0.9* | -148.2 | *0.9* | -101.6 | *0.9* |
| $CO_2{}^a$ (ppm) | 1764 | *100* | 644 | *68* | 4629 | *256* | 2015 | *31* | 1425 | *160* | 1058 | *295* | 1606 | *46* |
| $CO_2{}^b$ (ppm) | 2564 | *489* | 493 | *117* | 5037 | *216* | 2202 | *154* | 1115 | *157* | 1092 | *110* | 1675 | *151* |
| $CO_2{}^d$ (ppm) | 2568 | *321* | 1628 | *44* | 3870 | | 2584 | *249* | 1543 | *150* | 1050 | *124* | 1963 | *94* |
| $\delta^{13}C^d$ (‰) | -14.9 | *1.1* | n.d. | | -11.75 | *0.4* | -14.3 | *0.3* | -10.8 | *0.5* | n.d. | | -10.3 | *0.4* |
| $Fe^{2+}/Fe_T$ | 0.76 | *0.07* | 0.94 | *0.08* | 0.79 | *0.08* | 0.88 | *0.08* | 0.83 | *0.07* | 0.45 | *0.07* | 0.80 | *0.07* |
| $H_2O^e$ (g) | 0.0026 | *0.0001* | 0.0030 | *0.0001* | 0.0014 | *0.0001* | 0.0007 | *0.0001* | 0.0013 | *0.0001* | 0.0001 | *0.0001* | 0.0009 | *0.0001* |
| $CO_2{}^e$ (g) | 0.0000 | *0.0001* | 0.0465 | *0.0001* | -0.0003 | *0.0001* | 0.0008 | *0.0001* | 0.0000 | *0.0001* | 0.0005 | *0.0001* | 0.0006 | *0.0001* |

*Notes:* All analyses of the glass are in wt% (except where otherwise stated) using EPMA, except for [a]SIMS, [b]FTIR, [c]TCEA, [d]SHMS and [e]weight loss using freezing/boiling to measure the fluid. All Fe is reported as FeO ($FeO_T$). Errors of one standard deviation (*s.d.*) are shown in *italics*. n.d. means not determined.

## 4.3. Carbon isotope analysis using secondary ion mass spectrometry

This section develops an analytical protocol to measure carbon isotope ratios using SIMS, with the aim of analysing single melt inclusions. Different ion probe set-ups using a range of glasses (Section 4.3.1) are investigated to ascertain the best analytical set-up for simultaneous carbon concentration and isotope analysis (Section 4.3.2). The spatial resolution of these analyses is measured by imaging the analytical pits (Section 4.3.3). Sources of contamination, for example from the instrumental vacuum (the 'blank') and on the sample surface, are investigated (Section 4.3.5). Different data processing routines are tested for calibration of carbon concentration and isotope ratios and potential matrix effects are investigated (Section 4.3.6).

### 4.3.1. Samples

Melt inclusions cover a wide range of volatiles compositions, typically containing 0–3000 ppm $CO_2$ and 0–4 wt% $H_2O$ (e.g., Wallace, 2005). Hence, in addition to the hydrous, carbon-rich, basaltic glass standards in Section 4.2.4 (ETNA24, ETNA32, and ETNA36); anhydrous, carbon-poor, basaltic glass standards (i.e., with independently measured carbon isotope ratios using SHMS) are needed.

ALV981-R23 is an anhydrous, submarine basaltic glass from the East Pacific Rise. It is well characterised, having been analysed multiple times at different laboratories using SHMS (Des Marais, 1986; Macpherson et al., 1999; Pineau and Javoy, 1983). We use the values from Macpherson et al. (1999) for the dissolved carbon composition of 405.6 $\pm$ 8 ppm $CO_2$ and -5.70 $\pm$ 0.41 ‰ $\delta^{13}C$ (Table 4.11). This glass was also used as a carbon isotope standard by Hauri (2002) and Hauri et al. (2002). CH9 glasses are submarine basalts from the Mid-Atlantic Ridge, which are mostly glass but do contain some small crystals. Their carbon composition was analysed using SHMS by Aubaud (2002) (Table 4.11). These glasses are used as secondary standards to test analyses on carbon-poor glasses.

**Table 4.11:** Composition of anhydrous, carbon-poor, natural, basaltic glasses with known $\delta^{13}C$.

| Sample | ALV981-R23[a] | CH97DR02[b] | CH98DR07[b] |
|---|---|---|---|
| $SiO_2$ | 49.70 | 50.61 | 49.93 |
| $TiO_2$ | 1.25 | 1.15 | 1.32 |
| $Al_2O_3$ | 16.92 | 15.37 | 15.42 |
| $FeO_T$ | 8.70 | 9.16 | 10.22 |
| MnO | 0.15 | 0.16 | 0.21 |
| MgO | 8.52 | 8.88 | 9.22 |
| CaO | 11.05 | 11.71 | 11.25 |
| $Na_2O$ | 3.05 | 2.04 | 2.48 |
| $K_2O$ | 0.05 | 0.31 | 0.05 |
| $P_2O_5$ | n.d. | 0.17 | 0.14 |
| $H_2O$ | 0.14 | 0.464 | 0.245 |
| $CO_2$ (ppm) | 405.6 $\pm$ 8 | 108 | 95 |
| $\delta^{13}C$ (‰) | -5.70 $\pm$ 0.41 | -10.8 | -7.2 |

*Notes:* [a] major/minor elements and $H_2O$ from Fine and Stolper (1986) and carbon composition from Macpherson et al. (1999), and [b] major/minor elements and $H_2O$ from Jambon and Zimmermann (1990) and carbon composition from Aubaud (2002). Oxides in wt%, except where otherwise stated.

San Carlos olivine and an olivine from Rangitoto, New Zealand, were used to investigate the instrumental

blank, as olivine contains essentially no carbon (e.g., San Carlos olivine <2 ppm $CO_2$; Mathez and Delaney, 1981). Additionally, experimental glasses in Chapter 5 were analysed which, although they have unknown carbon isotope ratio, have known carbon concentrations (Table 5.6) and hence were useful to understand the level of carbon background during analysis.

Glass chips and olivine were mounted in epoxy, ground, and polished to ∼1–3 μm finish. These were plucked out of epoxy and pressed into indium to reduce the carbon background due to outgassing from epoxy. To investigate the potential causes of carbon contamination during sample preparation and analysis, one San Carlos olivine was additionally cleaned prior to gold coating using a Plasma Etcher for three hours at $3 \times 10^{-1}$ mbar oxygen and 100 W power by J. Craven. All mounts were gold coated (∼40–80 nm thickness) to provide a conductive surface.

### 4.3.2. SIMS technique development for carbon isotope analysis

Different ion probe set-ups were tested to measure the carbon isotope ratio in silicate glass. All analyses were carried out on the Cameca IMS-1270 at the Edinburgh Ion Microprobe Facility, School of GeoSciences, University of Edinburgh, UK. Although positive carbon ions ($C^+$) are often used for quantifying carbon concentration (e.g., $^{12}C^+$ in Section 4.2.2), the ion yield is too low to get sufficient counts on $^{13}C^+$ for isotope analysis. Hence, a $Cs^+$ primary beam was used to produce negative carbon ions ($C^-$), which has a higher ion yield (e.g., Hauri et al., 2002). The surface of the sample must be neutralised due to $Cs^+$ implantation and negative secondary ion extraction (e.g., Hauri et al., 2002). Hence, an electron gun floods the analysis area to maintain charge balance. To improve spatial resolution, a field aperture was used so that only secondary ions coming from the central $10 \times 10$ μm$^2$ were analysed (Figure 4.9).

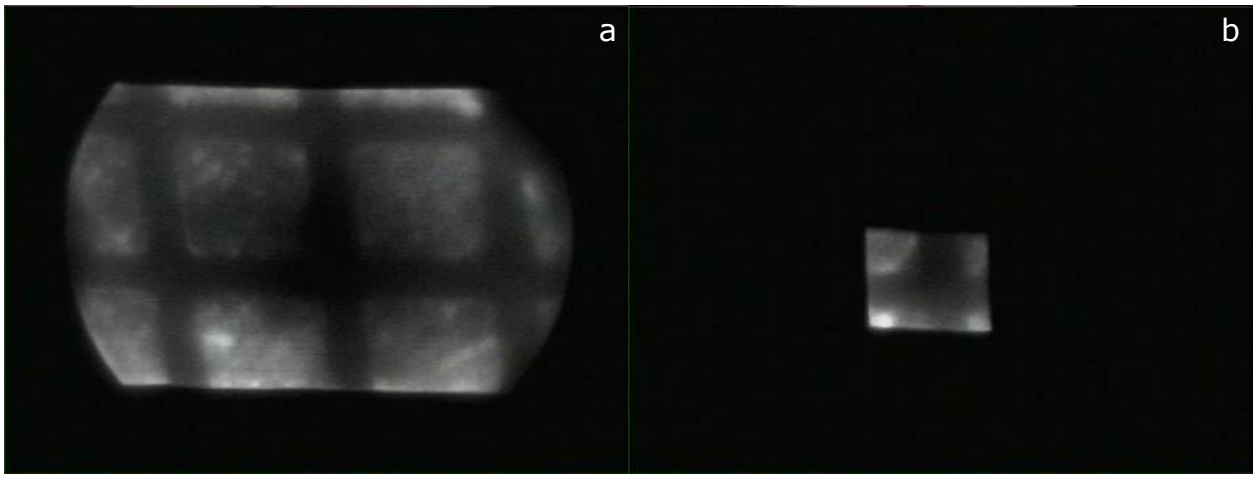


**Figure 4.9:** Scanning ion microscopy (SIM) images at the same scale of a 10 μm spaced grid, where **(b)** uses a field aperture. Images courtesy of J. Craven.

The species analysed were $^{12}C^-$, $^{13}C^-$, and $^{18}O^-$ in mono-collector mode, hence only one species is measured at a time. The count rate of these species changes during the measurement (termed 'internal drift'), hence the species should be cycled through quickly, but wait times are dictated by how long it takes the magnet to switch between masses. The wait time for switching between $^{12}C^-$ and $^{13}C^-$ is short because the mass-charge ratio difference is small. Conversely, between $^{13}C^-$ and $^{18}O^-$ or $^{18}O^-$ and $^{12}C^-$ the wait time is longer due to the greater mass-charge ratio difference. Increasing the number of cycles collects more

counts but drills further into the sample, which limits the spatial resolution in depth. Additionally, this can cause isotopic fractionation and charging if the analysis pit becomes too deep. Therefore, count times and number of cycles are a trade-off to try and achieve the most precise measurement in the shortest amount of time. The analytical precision is dictated by the number of counts on $^{13}C^-$, which is predominantly dictated by the carbon concentration in the sample. The sputtering process is not well understood, hence all standards and samples must be analysed in the same way for quantitative analysis. This means cycle length cannot be changed depending on carbon concentration, and more repeats must be collected on carbon-poor samples to achieve the same precision as carbon-rich samples.

Samples were loaded into the airlock the night before analysis, then transferred to the analysis chamber. Typically, analyses were collected in triplicate, and multiple triplicates were collected on each sample to improve precision depending on the carbon concentration. ETNA24 or ETNA32 were analysed repeatedly throughout the day to correct for external drift. To understand the carbon background, San Carlos olivine that had undergone 'normal' and 'clean' sample preparation was analysed (Section 4.3.1), after being in the sample chamber undisturbed for varying lengths of time by J. Craven. Also, additional analyses on Rangitoto olivine were carried out under different vacuums (count/wait times, s, of 2/6 $^{12}C^-$, 6/2 $^{13}C^-$, and 0.5/4 $^{18}O^-$) and different pre-raster routines (0×0 to 30×30 $\mu m^2$ rastered area, 120–600 s pre-raster time and 20 cycles, using the set-up in Table 4.13).

Two analytical set-ups were used: set-up one ($^{12}C^-|^{13}C^-$) only analysed $^{12}C^-$ and $^{13}C^-$, which would give the highest precision as more time was spent measuring $^{13}C^-$; whilst set-up two ($^{12}C^-|^{13}C^-|^{18}O^-$) additionally measured $^{18}O^-$, which would allow for more accurate quantification of carbon concentration simultaneously.

### Set-up one ($^{12}C^-|^{13}C^-$)

Set-up one ($^{12}C^-|^{13}C^-$) analysed $^{12}C^-$ and $^{13}C^-$ using electron multipliers. The primary beam (∼5 nA beam current) and electron gun were aligned on Monastery Ilmenite each day, which involved moving the sample between the airlock and analysis chamber. The peak positions of $^{12}C^-$ and $^{13}C^-$ were identified using mass-ratio scans, and the $^{13}C^-$ position was chosen to avoid $(^{12}C^1H)^-$. The primary beam was approximately manually aligned if moving large distances in the sample mount. This avoids collecting data under large beam deflections, which can compromise data quality. For each analysis, the primary beam position was aligned, and the magnet calibrated, automatically on $^{12}C^-$ and a linear shift on magnet position was applied to $^{13}C^-$. The analytical target was 'cleaned' by rastering the beam over a 15×15 $\mu m^2$ area for one minute to reduce surface contamination. Count and wait times are detailed in Table 4.12, where 100 cycles were collected resulting in ∼17 mins analysis time.

**Table 4.12:** Species, count, and wait times for set-up one ($^{12}C^-|^{13}C^-$).

| Species | $^{12}C^-$ | $^{13}C^-$ |
|---|---|---|
| Count time (s) | 1 | 6 |
| Wait time (s) | 1.5 | 1.5 |

#### Set-up two ($^{12}C^-|^{13}C^-|^{18}O^-$)

Set-up two ($^{12}C^-|^{13}C^-|^{18}O^-$) analysed $^{12}C^-$ and $^{13}C^-$ on electron multipliers and $^{18}O^-$ on a Faraday cup. Oxygen was chosen as it is abundant in silicate glass. $^{16}O^-$ would overload the detectors at the beam currents needed to analyse carbon, hence the minor isotope of $^{18}O^-$ was used. The addition of $^{18}O^-$ increased the analysis time but meant that $^{12}C^-/^{18}O^-$ could be used for accurate quantification of carbon concentration at the same time as isotope ratio measurements. Also, silicate glass contains ~50 wt% oxygen, therefore the beam position could be aligned, and the magnet calibrated, on $^{18}O^-$ rather than $^{12}C^-$. This improved beam positioning on carbon-poor samples. If standards and unknowns have very different $\delta^{18}O$ values, this may effect quantifying the carbon concentration using this method. Silicon was also considered but the additional analysis time for using $^{30}Si^-$ was too long and the ionisation yield of $^{30}Si^{2-}$ (mass-charge ratio of 15) was too low to be useful.

Primary beam (~7 nA beam current) and electron gun alignment were only conducted on Monastery Ilmenite at the beginning of the analysis week, after which the sample mount remained in the analysis chamber undisturbed. Tweaks to the primary beam and electron gun position were made each day on the glasses, which resulted in slightly worse alignment. On the other hand, the vacuum was significantly improved by not having to open to the airlock each day. A Ti-sublimator was used in addition to rotary pumps to improve the background. Olivine was analysed twice per day to monitor the carbon background. The pre-raster routine was a 10 mins raster over a 30×30 $\mu m^2$ area. Count and wait times are detailed in Table 4.13. Due to the addition of $^{18}O^-$, 40 cycles were collected to avoid drilling too far into the sample resulting, in a ~30 mins analysis time.

**Table 4.13:** Species, count, and wait times for set-up two ($^{12}C^-|^{13}C^-|^{18}O^-$).

| Species | $^{12}C^-$ | $^{13}C^-$ | $^{18}O^-$ |
|---|---|---|---|
| Count time (s) | 1 | 8 | 0.5 |
| Wait time (s) | 6 | 2 | 5 |

### 4.3.3. Imaging SIMS analysis pits

#### Scanning electron microscopy

To measure the spatial resolution of the SIMS analysis, and understand the effect of the analysis on the glass composition, some of the SIMS pits were imaged with scanning electron microscopy (SEM) using the Carl Zeiss SIGMA HD VP Field Emission SEM at the School of Geosciences, University of Edinburgh, UK. Analysis pits imaged were created using set-up one ($^{12}C^-|^{13}C^-$). Samples were taken straight from the SIMS to the SEM, after an additional thin gold coat had been applied. Analytical conditions were an accelerating voltage of 20 kV and a 11.0 mm working distance. Secondary electron (SE) images were used to measure the size of the SIMS analysis pits, whilst energy dispersive spectroscopy (EDS) was used to look at their composition.

#### Scanning ion microscopy

To investigate the location of carbon contamination and measure the spatial resolution of the SIMS analysis, scanning ion microscopy (SIM) images were collected of analysis pits created using set-up two

($^{12}C^-|^{13}C^-|^{18}O^-$). Set-up two ($^{12}C^-|^{13}C^-|^{18}O^-$) (Table 4.13) was used for imaging with a beam current of 0.5 nA, which gives higher spatial resolution and images were collected over $100\times100$ $\mu m^2$, collecting either 13 or 20 cycles. One image is produced per cycle and images were processed using ImageJ (Abramoff et al., 2004). Images from each cycle were summed for $^{12}C^-$ and $^{18}O^-$ separately, and then the summed $^{12}C^-$ image was divided by the summed $^{18}O^-$ image to create a $^{12}C^-/^{18}O^-$ image. Images of $^{13}C^-$ were also collected but not processed due to the low count rate.

### 4.3.4. Sputtering process

During SIMS, material is sputtered from the surface, hence the analysis changes over time as successive cycles of data are collected. This creates a depth profile into the sample, which can reveal compositional changes if the sample is inhomogeneous, such as due to surface contamination. Ions can also be fractionated during this process as the analysis pit gets deeper. Implantation of $Cs^+$ during analysis can change the ionisation yeild over time (e.g., Wittmaack, 1983). These processes cause the count rate of a specific isotopic species to change over time. Therefore, it is important to understand what is causing any changes to the sputtering curve over time to decide whether all cycles should be used or only a subset. For instance, if the first few cycles are affected by surface contamination they should be removed. Sputtering processes are also affected by the instrument set-up, hence sputtering curves can change after the ion probe has been retuned.

Figure 4.10 shows typical sputtering curves for individual species ($^{12}C^-$, $^{13}C^-$, and $^{18}O^-$) and ratios ($^{13}C^-/^{12}C^-$ and $^{12}C^-/^{18}O^-$) for ALV981-R23. $^{12}C^-$ and $^{13}C^-$ either continuously decrease with time, or have an initial increase followed by a decrease with time (Figures 4.10a and b). $^{18}O^-$ initially increases over a longer period of time, then begins to decrease (Figure 4.10c). None of the species reach a steady state within a single analysis. The initial increase in counts is likely due to the implantation of $Cs^+$ at the start of the analysis, which can enhance ionisation (e.g., Wittmaack, 1983).

$^{12}C^-$ and $^{13}C^-$ curves track each other with time, hence $^{13}C^-/^{12}C^-$ is constant throughout the analysis (Figures 4.10a, b, and d). This implies the decline in carbon counts with time is not due to surface contamination, as this would not be expected to have the same isotope ratio as the dissolved carbon in the glass and the decrease in carbon counts would be much more abrupt than the continuous decrease here. This does not rule out continuously added carbon contamination (e.g., from the vacuum or edge of the analysis pit), but olivine analyses show contamination was low during the analyses shown in Figure 4.10, which is discussed in detail in Section 4.3.5. As the $^{12}C^-$ and $^{13}C^-$ ions are not fractionated from each other during analysis, all cycles can be used to calculate $^{13}C^-/^{12}C^-$. The decrease in counts with time means that simply counting for longer (i.e., more cycles) produces diminishing returns in terms of counting statistics and the associated error.

$^{12}C^-$ and $^{18}O^-$ fractionate from each other during the analysis, which causes $^{12}C^-/^{18}O^-$ to initially increase then decrease with time (Figures 4.10a, c, and d). If a second analysis is conducted in the same analysis pit, the initial count rate begins where the previous analysis stopped and then plateaus (Figure 4.10). This implies it is the depth within the analysis pit controlling the fractionation and that a steady state is reached eventually. Different pre-raster durations do not affect the sputtering curves (Figure 4.10), hence the sample surface is defined by the pre-rastered area not the original surface. Although steady-state was not reached within a single analysis of 40 cycles, the change in the last ten cycles is small hence, the last ten cycles were averaged for $^{12}C^-/^{18}O^-$.

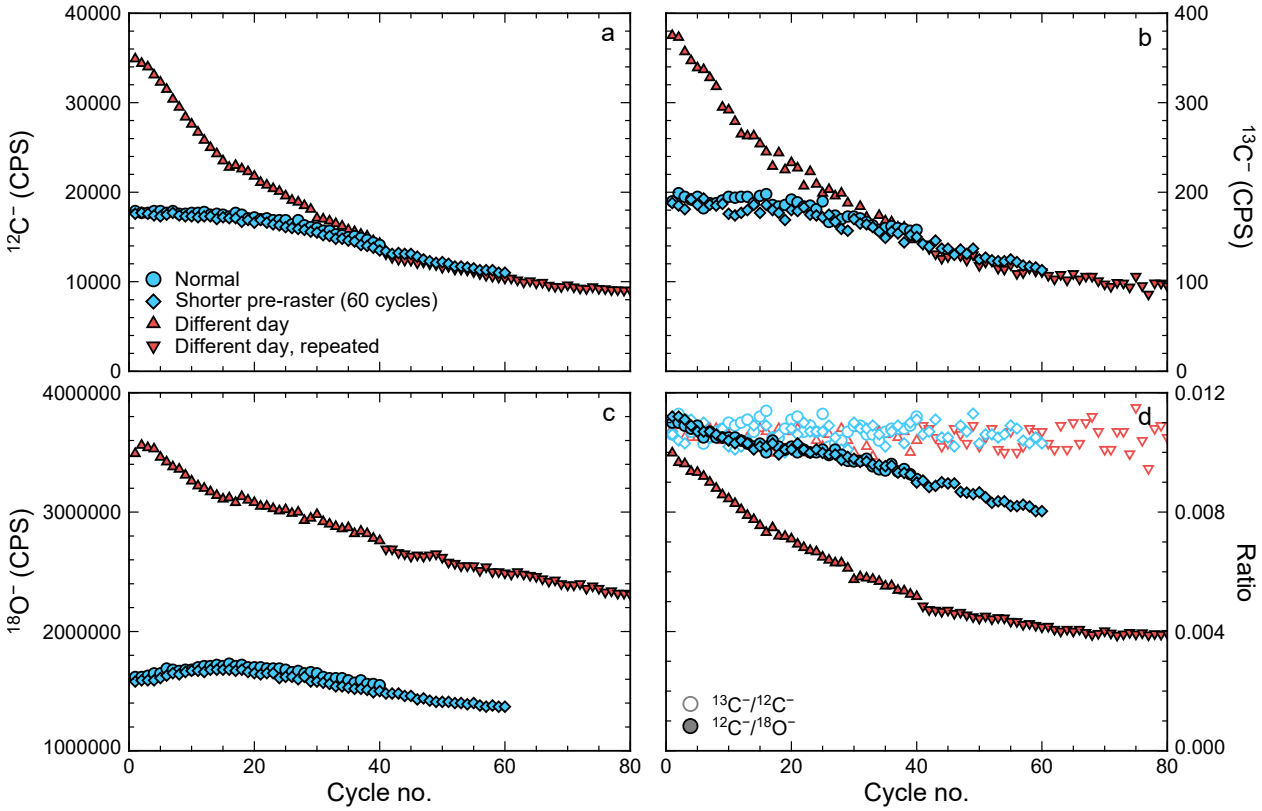


**Figure 4.10:** Example sputter curves for ALV981-R23 collected using set-up two ($^{12}C^-|^{13}C^-|^{18}O^-$): **(a)** $^{12}C^-$, **(b)** $^{13}C^-$, **(c)** $^{18}O^-$, and **(d)** $^{13}C^-/^{12}C^-$ in open symbols and $^{12}C^-/^{18}O^-$ in closed symbols. A 'normal' sputter curve is shown in blue circles (600 s pre-raster, 40 cycles). The sputter curve in blue diamonds has a shorter pre-raster (120 s) but more cycles (60) and hence the same total analysis time. The sputter curve in red triangles was collected under slightly different analytical conditions and was analysed a second time in the same pit as shown in the red inverted triangles.

Figure 4.10 also shows the sputtering curves on the same sample over two days of analysis. Analyses collected on different days were collected under slightly different analytical conditions as the ion probe is retuned each morning to ensure good data collection. If data from different days are to be compared, these changes must be monitored and accounted for.

### 4.3.5. Contamination

Analysis of olivine showed that significant carbon contamination was present during SIMS analysis, leading to a potentially very high carbon background (Figure 4.11). The carbon background can be quantified as the average of the $^{12}C^-$ counts, but this can be affected by differences in ion probe set-up (e.g., beam current), and therefore it is only appropriate for data collected over a short time period (e.g., Figure 4.11c). Using the average $^{12}C^-/^{18}O^-$ ratio removes this problem (e.g., Figure 4.11a). As the $^{12}C^-/^{18}O^-$ changes with time, simply averaging all the cycles may mask variations, hence an exponential function can be fitted to $^{12}C^-/^{18}O^-$ (Equation 3.2 where $I$ is $^{12}C^-/^{18}O^-$). The $^{12}C^-/^{18}O^-$ at $\infty$ time divided by the probe current ($[^{12}C^-/^{18}O^-]_\infty$/PB) is useful for comparing data collected over many sessions (e.g., Figure 4.11b).

The carbon contamination was found to vary with vacuum and pre-raster routine (Figure 4.11). Broadly, carbon contamination decreases with decreasing analysis chamber pressure (Figures 4.11b, c, and d), although there is scatter in these data. After a sample was moved from the airlock into the analysis chamber,

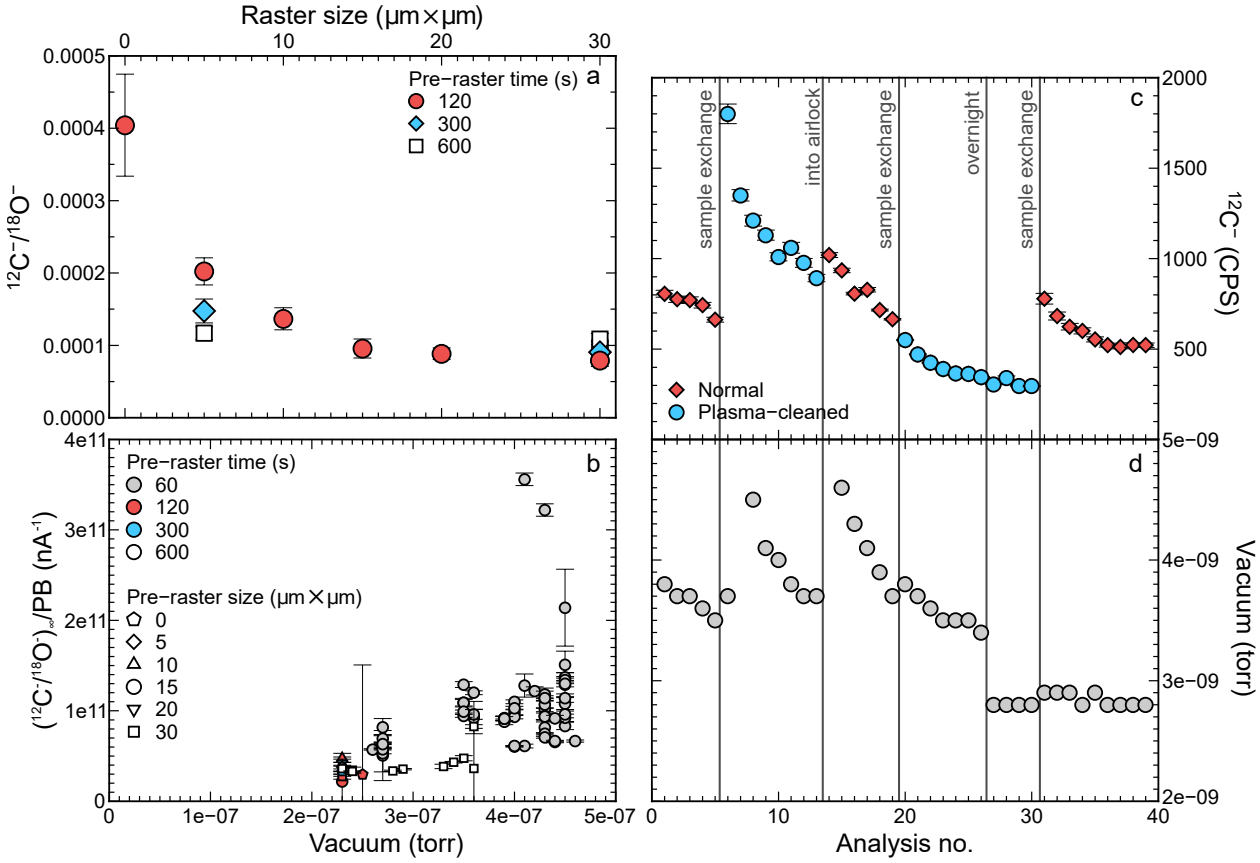


**Figure 4.11:** Olivine analyses to investigate the carbon background: **(a)** $^{12}C^-/^{18}O^-$ against raster size on Rangitoto olivine, where symbol shape and colour indicates pre-raster time; **(b)** $(^{12}C^-/^{18}O^-)_\infty$/PB against vacuum pressure for Rangitoto and San Carlos olivine, where symbol colour indicates pre-raster time and symbol shape indicates pre-raster size; **(c)** $^{12}C^-$ for consecutive analyses on 'normal' (red diamond) and 'cleaned' (blue circle) San Carlos olivine; and **(d)** the vacuum pressure for analyses shown in **(c)**. Vertical lines in **(c)** and **(d)** show when samples were moved between the airlock and analysis chamber (sample exchange), when samples were loaded into the airlock (into airlock), and when samples were left in the analysis chamber overnight (overnight).

the carbon background decreased with time. Eventually the carbon contamination plateaued, although the level at which it reached steady-state was not constant (Figure 4.11c). For the same analysis chamber pressure, enlarging the pre-rastered area or increasing the pre-raster time decreased the carbon contamination (Figure 4.11a). Plasma cleaning the sample appeared to have no effect on the carbon contamination (Figure 4.11c). In fact the contamination increased but this is likely not caused by the cleaning procedure itself. For gold coating the sample, a rotary pump is used, hence any removal of carbon by plasma cleaning maybe reset when the sample is gold coated.

There appear to be two components to the carbon background. As it decreases with vacuum pressure (Figure 4.11b) and time in the analysis chamber (Figures 4.11c and d), some component comes from the analysis chamber itself. Additionally, as it changes with pre-raster routine (Figure 4.11a), some component is likely derived from the sample surface. A small pre-raster area means the analysed area may not have been properly cleaned before analysis. Imaging of the analysis pits after analysis confirmed the presence of elevated regions of carbon at the edges of the raster pits, especially on the vertical edges (Figure 4.12).

Carbon contamination was insignificant when a pre-raster area of 30×30 μm$^2$ and a minimum time of 120

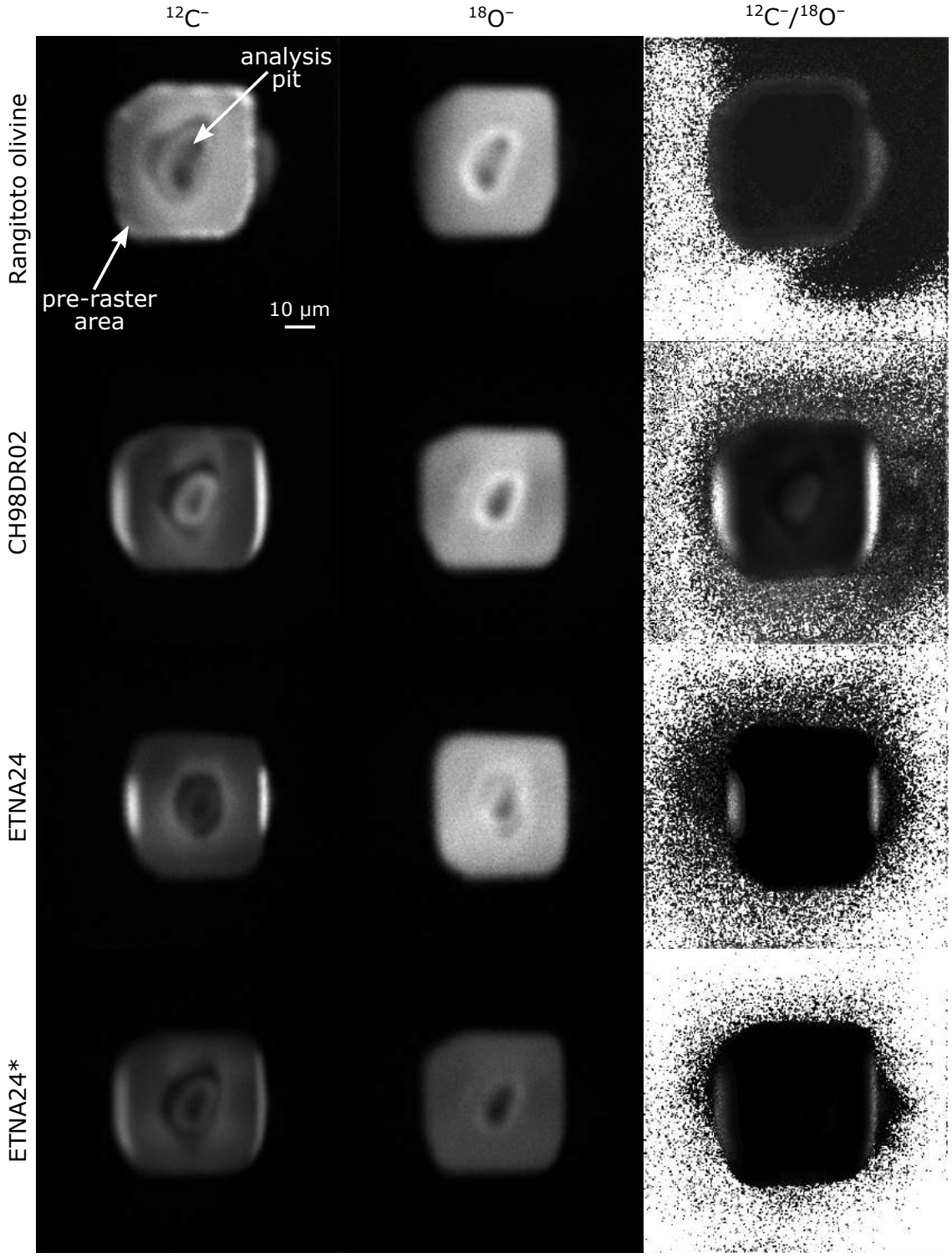


**Figure 4.12:** Scanning ion microscopy (SIM) images of SIMS analysis pits created using set-up two ($^{12}C^-|^{13}C^-|^{18}O^-$): species are shown along the top and sample is shown down the left-hand side. All images are 100×100 μm$^2$ in area. The large square region is the pre-raster area and the smaller, darker area in its centre is the analysis pit. ETNA24 and ETNA24* are two different analysis pits on ETNA24, where ETNA24 was analysed earlier in the week than ETNA24* and they show different beam shapes.

s was used (Figure 4.11a). Additionally, a high vacuum was achieved by leaving the samples in the analysis chamber undisturbed. Conversely, carbon contamination was significant when a pre-raster area of 15×15 μm$^2$ and time of 60 s was used (Figure 4.11b), and samples were switched between the air lock and analysis

chamber each day, which resulted in a poor vacuum. Carbon contamination also causes problems for beam position if $^{12}C^-$ is used. This is because the automatic scan picks up the carbon contamination on the edge of the pre-sputtered area (Figure 4.12), and hence incorrectly calculates the beam position.

### 4.3.6. Calibration

#### Data processing

Carbon isotope ratios were calculated using $^{13}C^-/^{12}C^-$ for both set-ups. For set-up one ($^{12}C^-|^{13}C^-$), carbon concentration was calculated using $^{12}C^-$/PB, where PB is the average of the probe current measured before and after the analysis. For set-up two ($^{12}C^-|^{13}C^-|^{18}O^-$), $^{12}C^-/^{18}O^-$ was used for carbon concentration. Isotope ratios ($^{13}C^-/^{12}C^-$ for both set-ups, and $^{12}C^-/^{18}O^-$ in set-up two) were internally drift corrected by interpolating the $^{13}C^-$or $^{18}O^-$ at the time the $^{12}C^-$ counts were collected. For $^{13}C^-/^{12}C^-$ and $^{12}C^-$/PB the average and standard deviation ($\sigma$) of all cycles were then calculated, after which any datum outside of $3\sigma$ were rejected. The average, standard deviation, and standard error of the remaining data were then recalculated. For $^{12}C^-/^{18}O^-$, only the last ten cycles were averaged, as discussed in Section 4.3.4. To account for daily and day-to-day drift as discussed in Section 4.3.4, external drift was monitored using ETNA24 and ETNA32. These were analysed regularly throughout the day, and linear fits to the drift were fitted in sections (Figure 4.13). External drift was corrected for by dividing the internally drift corrected value ($^{13}C^-/^{12}C^-$, $^{12}C^-/^{18}O^-$, and $^{12}C^-$/PB) by the calculated value of the standard at the time the data was collected, for example:

$$(^{13}C^-/^{12}C^-)^{edc}_{sample} = \frac{(^{13}C^-/^{12}C^-)^{t}_{sample}}{(^{13}C^-/^{12}C^-)^{t}_{standard}} \tag{4.9}$$

where $(^{13}C^-/^{12}C^-)^{edc}_{sample}$ is the externally drift corrected $^{13}C^-/^{12}C^-$ of the sample; $(^{13}C^-/^{12}C^-)^{t}_{sample}$ is the internally drift corrected $^{13}C^-/^{12}C^-$ of the sample collected at time t; $^{13}C^-/^{12}C^-$ is the calculated $^{13}C^-/^{12}C^-$ of the standard at time t; and $^{13}C^-/^{12}C^-$ can be replaced by $^{12}C^-/^{18}O^-$ and $^{12}C^-$/PB. A correction factor was applied when the standard was changed between ETNA32 and ETNA24 to keep all data consistent.

#### Carbon concentration

For calibrating the carbon concentration, the average and standard deviation for each glass collected using set-up one ($^{12}C^-|^{13}C^-$) or two ($^{12}C^-|^{13}C^-|^{18}O^-$) of $(^{12}C^-/PB)^{edc}$ or $(^{12}C^-/^{18}O^-)^{edc}$ were calculated. A weighted (on the standard deviation of $(^{12}C^-/PB)^{edc}$ or $(^{12}C^-/^{18}O^-)^{edc}$) least squares regression was then calculated (Figure 4.14) against independently constrained carbon concentrations. For set-up one ($^{12}C^-|^{13}C^-$), this consisted of ALV981-R23 (Table 4.11), the hydrous carbon-rich ETNA glasses (Table 4.10), and additionally the ETNA glasses described in Chapter 5 (Table 5.6 except ETNA30) (Figure 4.14a). For set-up two ($^{12}C^-|^{13}C^-|^{18}O^-$), this consisted of Rangitoto olivine ($\sim$0 ppm $CO_2$), anhydrous carbon-poor glasses (Table 4.11), some of the hydrous carbon-rich glasses (Table 4.10 except ETNA31, ETNA33, and ETAN35), and some of the ETNA glasses described in Chapter 5 (ETNA12–ETNA14 and ETNA30 in Table 5.6) (Figure 4.14b).

The data using $(^{12}C^-/PB)^{edc}$ are more scattered than $(^{12}C^-/^{18}O^-)^{edc}$ (Figure 4.14). This is because dividing by $^{18}O^-$ is more effective at correcting for instrumental changes during the analysis than dividing by the

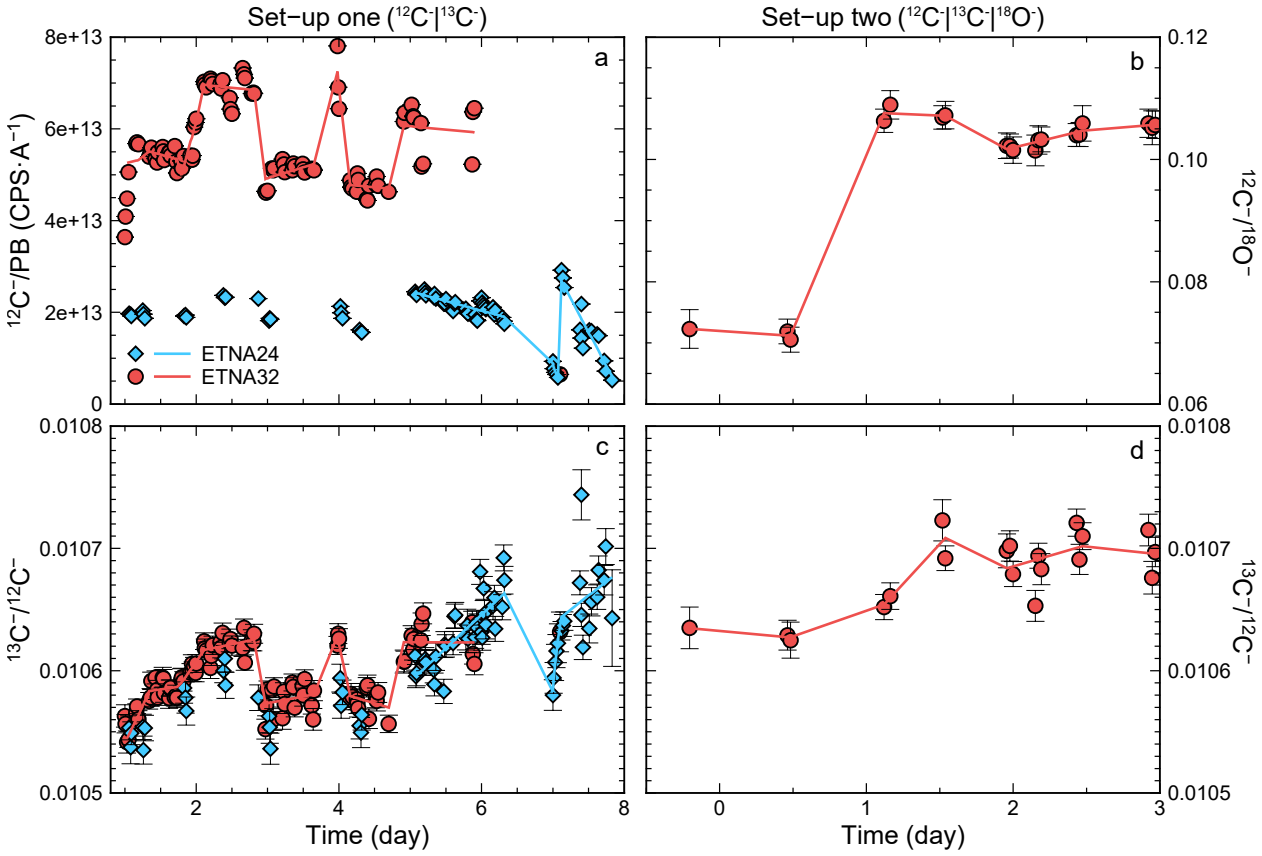


**Figure 4.13:** External drift corrections for **(a)** $^{12}C^-$/PB where PB is the average probe current; **(b)** $^{12}C^-/^{18}O^-$; **(c)** and **(d)** $^{13}C^-/^{12}C^-$, using ETNA24 (blue diamond) and ETNA32 (red circle). Set-up one ($^{12}C^-|^{13}C^-$) is shown in **(a)** and **(c)** and set-up two ($^{12}C^-|^{13}C^-|^{18}O^-$) is shown in **(b)** and **(d)**.

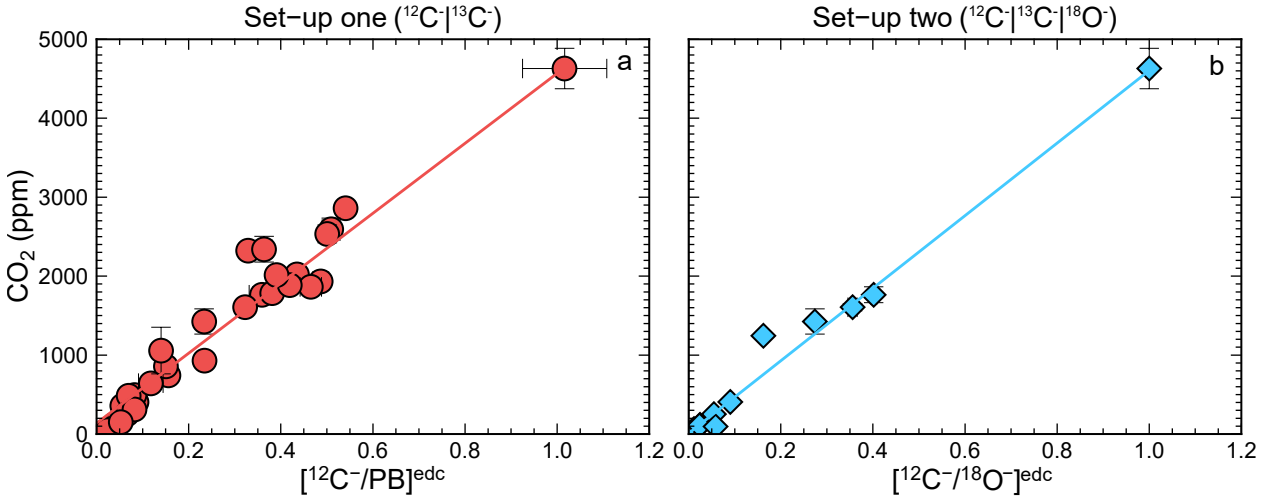


**Figure 4.14:** SIMS-1270 calibration curves for $CO_2$ concentration against external drift-corrected **(a)** $^{12}C^-$/PB for set-up one ($^{12}C^-|^{13}C^-$) and **(b)** $^{12}C^-/^{18}O^-$ for set-up two ($^{12}C^-|^{13}C^-|^{18}O^-$).

average probe current. Also, $(^{12}C^-/PB)^{edc}$ does not pass through the origin (intercept = 137 ± 74 ppm $CO_2$), whereas $(^{12}C^-/^{18}O^-)^{edc}$ does (intercept = 8 ± 77 ppm $CO_2$). Glasses <400 ppm $CO_2$ are consistently offset to higher $(^{12}C^-/PB)^{edc}$ than their $CO_2$ concentration suggests (Figure 4.14a). This implies these low carbon analyses have elevated $^{12}C^-$ counts due to carbon contamination. This carbon contamination does not appear

to affect high carbon analyses as the carbon contamination is a smaller proportion of the measured $^{12}C^-$.

Set-up one ($^{12}C^-|^{13}C^-$) used a small pre-raster size (15×15 $\mu m^2$) and therefore contained high levels of carbon contamination. This explains the offset of low $CO_2$ glasses and possibly the scatter, if contamination was variable during analysis (Figure 4.14a). Unfortunately, no blank material (e.g., olivine) was measured during this session, hence no blank-correction can be performed. Also, the calibration curve is incorrect because $CO_2$ concentrations used do not equal the $CO_2$ concentration at the time of measurement (i.e., $CO_2$ in the glass + $CO_2$ of the contaminant). Using the $(^{12}C^-/PB)^{edc}$ of the lowest carbon glass measured (ETNA15 = 51 ± 19 ppm $CO_2$, Table 5.6) provides a maximum, although overestimate, of the contamination. Comparing this value of $(^{12}C^-/PB)^{edc}$ to ETNA32 (4628 ± 256 ppm $CO_2$, Table 4.10), which due to its high carbon concentration will be least effected by carbon contamination, gives a maximum carbon contamination of 110 ppm $CO_2$. Set-up two ($^{12}C^-|^{13}C^-|^{18}O^-$) used a large pre-raster size (30×30 $\mu m^2$) and therefore had low levels of contamination. This is confirmed by the intercept being close to the origin and the low carbon concentration calculated for Rangitoto olivine (13 ± 1 ppm $CO_2$).

### Carbon isotope ratio

For calibrating the carbon isotope ratio, the average, standard deviation, and standard error of $\delta^{13}C$ for ALV981-R23, ETNA32, ETNA24, and ETNA36 collected using $(^{13}C^-/^{12}C^-)^{edc}_{sample}$ during both set-ups was calculated. A weighted (on the standard error of $(^{13}C^-/^{12}C^-)^{edc}_{sample}$) least squares regression was then calculated against independently constrained $\delta^{13}C$ (Figures 4.15 and 4.16a). For set-up one ($^{12}C^-|^{13}C^-$), there is a good correlation (adjusted $R^2$ = 0.91), whereas for set-up two ($^{12}C^-|^{13}C^-|^{18}O^-$) they are less well correlated (adjusted $R^2$ = 0.72). Unfortunately, as set-up one ($^{12}C^-|^{13}C^-$) contained contamination, this correlation is fortuitous rather than real. Figure 4.16b shows the difference in $(^{13}C^-/^{12}C^-)^{edc}_{sample}$ (set-up one ($^{12}C^-|^{13}C^-$) – two ($^{12}C^-|^{13}C^-$–$^{18}O^-$), i.e., contaminated – uncontaminated analysis) between the two set-ups against carbon concentration. As the external drift calibration was against ETNA32, the point at 4629 ppm $CO_2$ is 0 by default. The standards with lower carbon concentration were lighter for set-up one ($^{12}C^-|^{13}C^-$) (negative on Figure 4.16b), consistent with being contaminated by something isotopically lighter.

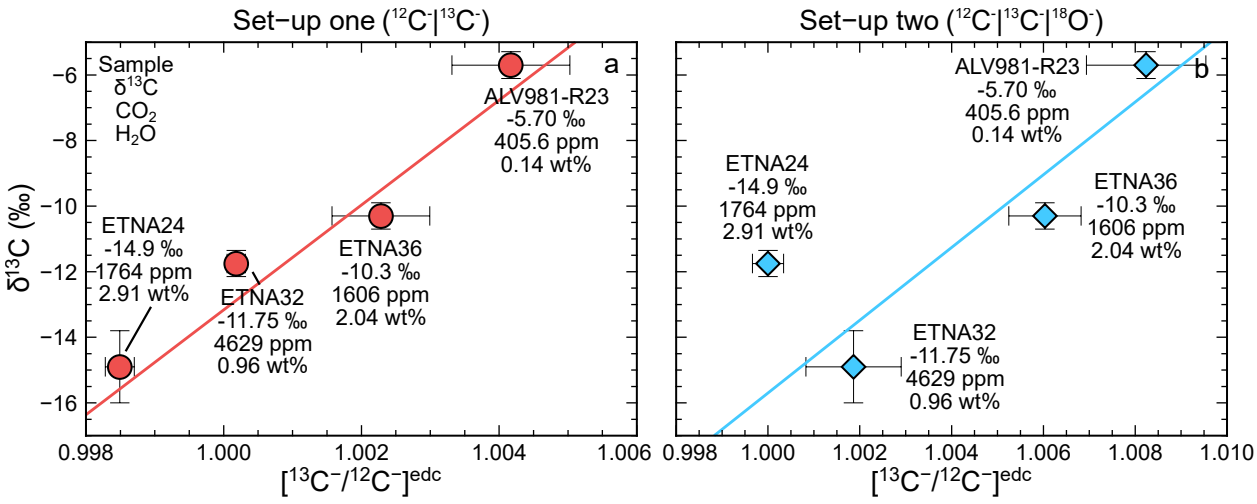


**Figure 4.15:** SIMS-1270 calibration curves for $\delta^{13}C$ against external drift-corrected $(^{13}C^-/^{12}C^-)^{edc}_{sample}$ for set-up **(a)** one ($^{12}C^-|^{13}C^-$) and **(b)** two ($^{12}C^-|^{13}C^-|^{18}O^-$).

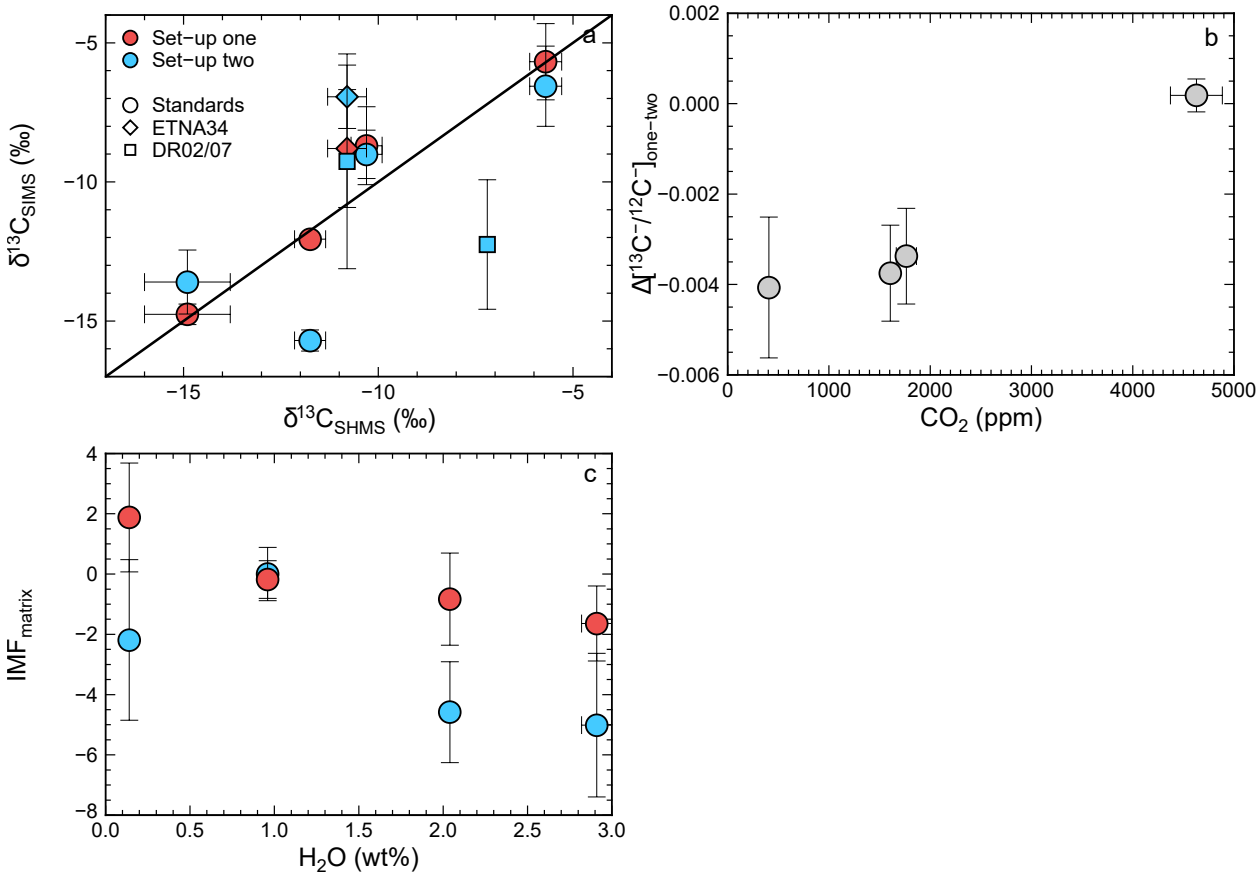


**Figure 4.16:** **(a)** Comparison of $\delta^{13}C$ derived from set-up one ($^{12}C^-|^{13}C^-$, red) and two ($^{12}C^-|^{13}C^-|^{18}O^-$, blue) for standards (circles), including secondary standards ETNA34 (carbon-rich, diamond), and CH97DR02 and CH98DR07 (carbon-poor, squares); **(b)** difference between external drift-corrected $^{13}C^-/^{12}C^-$ for set-up one ($^{12}C^-|^{13}C^-$) and two ($^{12}C^-|^{13}C^-|^{18}O^-$) against $CO_2$ concentration; and **(c)** modified instrumental mass fractionation factor due to the matrix ($IMF_{matrix}$) for set-up one ($^{12}C^-|^{13}C^-$, red) and two ($^{12}C^-|^{13}C^-|^{18}O^-$, blue) against $H_2O$ concentration.

The calibration curve for set-up two ($^{12}C^-|^{13}C^-|^{18}O^-$) implies there is a matrix effect as there is not a simple linear correlation between $(^{13}C^-/^{12}C^-)^{edc}_{sample}$ and $\delta^{13}C$. The main difference in composition between the glasses is $H_2O$ concentration, ranging from 0.14–2.91 wt% $H_2O$ (Tables 4.10 and 4.11). The instrumental mass fractionation (IMF) is a measure of the isotopic fractionation due to the sputtering process and measurement of the ions (e.g., Hauri et al., 2002). It is calculated as the ‰ deviation of the raw isotopic ratio in $\delta$-notation (i.e., raw $^{13}C^-/^{12}C^-$ converted to $\delta$-notation) compared to the known $\delta$ value (Section A.1). As there was external drift, IMF is dependent on the ion probe set-up. To isolate potential matrix effects, a modified IMF is calculated using $(^{13}C^-/^{12}C^-)^{edc}_{sample}$, where the $\delta$-value is calculated relative to ETNA32. This is then shifted to be relative to VPBD:

$$IMF_{matrix} = [((^{13}C^-/^{12}C^-)^{edc}_{sample} - 1) \cdot 1000] - \delta^{13}C_{ETNA32} - \delta^{13}C_{sample} \quad (4.10)$$

where $IMF_{matrix}$ is the IMF excluding the instrument drift; $(^{13}C^-/^{12}C^-)^{edc}_{sample}$ is the externally drift-corrected $^{13}C^-/^{12}C^-$ of the sample, $\delta^{13}C_{ETNA32}$ and $\delta^{13}C_{sample}$ is the known carbon isotope ratio in $\delta$-notation of ETNA32 and the sample from SHMS, respectively. This is plotted against $H_2O$ concentration in Figure 4.16c, where higher $H_2O$ concentrations have a larger ‰ variation than low $H_2O$ concentration, but the

errors are large. Hauri et al. (2002) found no effect of $H_2O$ concentration for andesites for a similar range in $H_2O$ concentration (1.09–3.70 wt% $H_2O$). Additionally, the major element compositions of the glasses are different (Tables 4.10 and 4.11), which may contribute. Hauri et al. (2002) found a 6 ‰ variation between basaltic and andesitic glasses, but the variation in the glass composition here is much smaller. With the glasses available, it is not possible to completely resolve whether a correction for $H_2O$ is necessary during calibration. The residual standard error for set-up two ($^{12}C^-|^{13}C^-|^{18}O^-$) is 0.07 ‰, which is much smaller than the standard error for repeat analyses, hence for now the potential matrix effects of $H_2O$ and major element chemistry are not included.

**Contamination correction**

It may be possible to correct the measured carbon isotope ratios for the background carbon which contaminated analyses collected using set-up one ($^{12}C^-|^{13}C^-$). Excluding the standards, four glasses were analysed during both set-ups (ETNA12–ETNA14 and ETNA34, Tables 4.10 and 5.6). Assuming the contamination was 110 ppm $CO_2$ (maximum value from Section 4.3.5), the carbon isotope ratio of the contaminant can be calculated by mass balance:

$$\delta_c = \frac{\delta_1 \cdot (C_c - C_g) + \delta_2 \cdot C_g}{C_c} \tag{4.11}$$

where $\delta_c$, $\delta_1$, and $\delta_2$ are the carbon isotope ratios in $\delta$-notation for the contaminant and the glass during set-up one ($^{12}C^-|^{13}C^-$, contaminated) and two ($^{12}C^-|^{13}C^-|^{18}O^-$, uncontaminated), respectively; and $C_c$ and $C_g$ are the carbon concentration of contaminant and glass, respectively. Using ETNA12–ETNA14 and ETNA34 gives a value of -34 $\pm$ 10 ‰. The value for Rangitoto olivine is -54 $\pm$ 40 ‰; the very large errors are due to the very low counts on $^{13}C^-$. A contaminant of 110 ppm $CO_2$ and -34 ‰ $\delta^{13}$C changes the $\delta^{13}$C by 1 ‰ if $CO_2 < 2000$ ppm. Hence analyses using set-up one ($^{12}C^-|^{13}C^-$) with $CO_2 > 2000$ ppm will not have been changed substantially. Unfortunately, most of the glasses use for calibration have $CO_2 < 2000$ ppm, and hence will have been affected by contamination, which will affect quantification.

### 4.3.7. Precision, accuracy, and spatial resolution

Count rates at the start of the analysis were $\sim 10^1$ and $\sim 10^{-2}$ $s^{-1}\cdot nA^{-1}\cdot ppm^{-1}$ for $^{12}C^-$ and $^{13}C^-$, respectively, compared to $\sim 10^{-4}$ $s^{-1}\cdot nA^{-1}\cdot ppm^{-1}$ using $^{12}C^+$, although they did decline over time. Hence, carbon as a negative ion is required for carbon isotope analysis. For an analysis, total counts on a species is:

$$^{12}C^-_T = t \cdot \sum_1^n {}^{12}C^- \tag{4.12}$$

where $^{12}C^-_T$ are the total $^{12}C^-$ counts during the analysis; time is the count time on $^{12}C^-$; and $\sum_1^n {}^{12}C^-$ is the sum of the $^{12}C^-$ over $n$ cycles in counts per second. The same can be calculated for $^{13}C^-$. As the count rate declines with time this cannot be used to predict the total counts for longer analyses. This also cannot be extended to different probe currents, as the rate of decline in counts is related to the rate of sputtering. This relates to how far the sample has been drilled into, and therefore probably probe current.

For set-up one ($^{12}C^-|^{13}C^-$) (Table 4.12), $^{12}C^-_T$ per ppm $CO_2 \approx 4400$ and $\approx 440$ for $^{13}C^-_T$; whereas for set-up

two ($^{12}C^-|^{13}C^-|^{18}O^-$) (Table 4.13) $^{12}C^-_T$ per ppm $CO_2 \approx 1600$ and $\approx 140$ for $^{13}C^-_T$. Hence, the precision on $\delta^{13}C$ for a single analysis on a 4000 ppm $CO_2$ glass is $\sim$8 and $\sim$13 ‰ for set-up one ($^{12}C^-|^{13}C^-$) and two ($^{12}C^-|^{13}C^-|^{18}O^-$), respectively. For 100 ppm $CO_2$, the precision on $\delta^{13}C$ is $\sim$50 ‰ for set-up one ($^{12}C^-|^{13}C^-$) compared to $\sim$80 ‰ for set-up two ($^{12}C^-|^{13}C^-|^{18}O^-$). Therefore, many repeat analyses are required to get good precision on $\delta^{13}C$ on carbon-poor glasses. For example, to achieve 5 ‰ precision $\delta^{13}C$ requires $\sim$3 or $\sim$7 analyses for 4000 ppm $CO_2$ for set-up one ($^{12}C^-|^{13}C^-$) and two ($^{12}C^-|^{13}C^-|^{18}O^-$), respectively, but $\sim$90 or $\sim$300 for 100 ppm $CO_2$. For set-up two ($^{12}C^-|^{13}C^-|^{18}O^-$), doubling the number of cycles only increases the counts by a factor 1.5, hence a simply longer analysis time does not help. The difference in set-up one ($^{12}C^-|^{13}C^-$) and two ($^{12}C^-|^{13}C^-|^{18}O^-$) is the addition of oxygen, which results in a significantly longer analysis time (10 and 22.5 s per cycle for set-up one ($^{12}C^-|^{13}C^-$) and two ($^{12}C^-|^{13}C^-|^{18}O^-$), respectively) and proportionally less time spent on $^{13}C^-$ (60 and 37 % of the analysis time for set-up one ($^{12}C^-|^{13}C^-$) and two ($^{12}C^-|^{13}C^-|^{18}O^-$), respectively).

SIM and SEM (Figures 4.12 and 4.17a) images of the analysis pits can be used to estimate the spatial resolution of the analysis. The physical pit size is larger than the actual region from which ions were collected (Figure 4.9), hence this provides a maximum estimate of spatial resolution. For both set-ups, the analysis pit was $\sim 20 \times 15$ μm$^2$. EDS-SEM image of Cs reveals a large area contaminated after analysis (Figure 4.17b), which will affect the ionisation yield. Hence, subsequent analyses in the same region of glass should be conducted $>$30 μm from the centre of previous analysis pits.

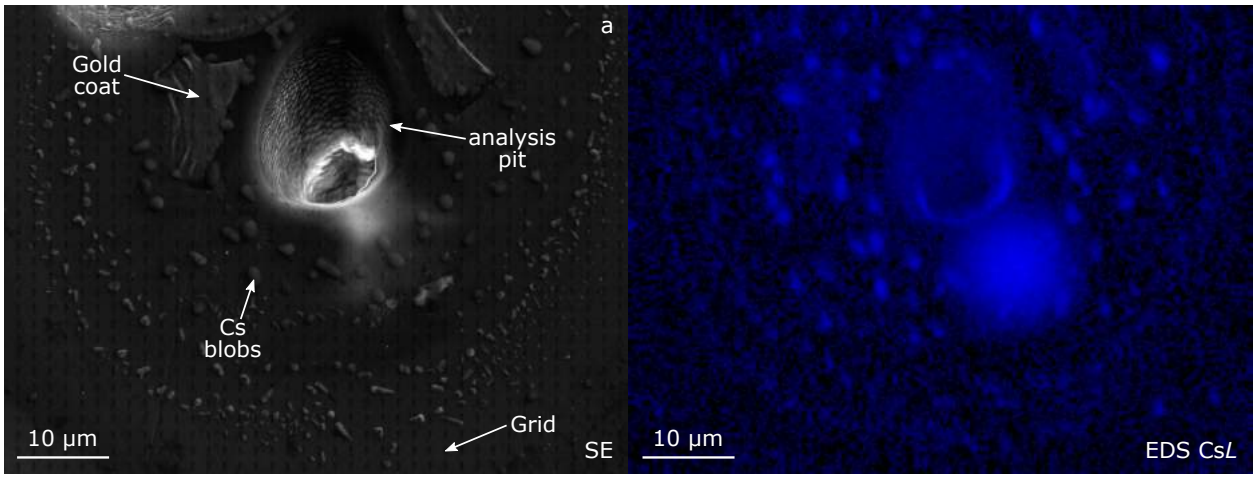


**Figure 4.17:** SEM images of a SIMS analysis pit created using set-up one ($^{12}C^-|^{13}C^-$) (Table 4.12): **(a)** secondary electron (SE) image showing the analysis pit (terraced hole) surrounded by blobs of Cs, where the gold coat has been ripped up at the sides of the pit due to the incoming $Cs^+$ beam (from top of image) and the darker grid pattern observable over the whole image is due to EDS mapping; and **(b)** energy dispersive spectrometry (EDS) map of Cs*L* showing the blobs observable in **(a)** are Cs (high Cs, blue) and the area opposite where the $Cs^+$ hits the sample is elevated in Cs (high Cs, blue circular region).

## 4.4. Implications for analysing single melt inclusions

Analysis of single melt inclusions for carbon isotope ratios requires high: (1) precision ($\sim$1 ‰ $\delta^{13}C$) as the differences in $\delta^{13}C$ in natural samples are small; (2) accuracy so that data can be reliably compared between sessions; and (3) spatial resolution ($\sim$20–30 μm in diameter analytical area) as melt inclusions are small.

A low carbon background is critical, which is related to carbon in the analytical chamber and on the

surface of the sample. To reduce carbon in the analytical chamber, all samples were co-mounted in indium. The mount included all standard material and a material to monitor the carbon background (e.g., olivine). Although not done here, the mount should also include a material to help align the primary and electron beam (e.g., Monastery ilmenite). The mount was pumped down in the airlock overnight before being moved to the analysis chamber, where it remained for the rest of the analytical time as all samples were co-mounted. The carbon background reached acceptable levels after two days of being in the analytical chamber. The vacuum was further improved by using a Ti-sublimator, although a cryo-pump may also improve the background. To minimise the effect of carbon on the sample surface, a large pre-raster area was used (e.g., $30\times30$ $\mu m^2$ for a $\sim15\times20$ $\mu m^2$ analysis area was sufficient in this study). A pre-raster time of 120 s was sufficient as longer pre-raster times did not show improvement on the carbon background. A blank (e.g., olivine) was measured at least twice a day to check the carbon background was low enough and constant.

A $Cs^+$ primary ion beam, plus electron flood gun, were used to generate secondary ions because the carbon yield as a negative ion ($C^-$), rather than positive ion ($C^+$), is far greater. To analyse a single melt inclusion at a reasonable precision will require modifications to the above routines to collect enough counts on $^{13}C^-$. A dual routine, where the magnet is centred on $^{18}O^-$, but $^{18}O^-$ is not actually analysed, would allow accurate peak alignment on low carbon samples. If the carbon concentration is required, the analysis could be split into two sections. Firstly, just $^{12}C^-$ and $^{18}O^-$ are collected for a few cycles. Secondly, $^{12}C^-$ and $^{13}C^-$ are collected in the same pit for many cycles. Analysing $^{12}C^-$ and $^{13}C^-$ in multi-collector mode removes wait times and increases the proportion of time spent collecting $^{13}C^-$ to 100 %. This will be the only way to analyse single melt inclusions.

Figure 4.18 shows the $\delta^{13}C$ ‰ precision based on $^{13}C^-$ counts against concentration for a 60 mins analysis at various beam currents, using an approximate $^{13}C^-$ count rate of 0.08 CPS·nA$^{-1}$·ppm$^{-1}$ of $CO_2$. Beam currents of 5–7 nA were used in this study, but higher beam currents will be required to improve the accuracy, although the effect this has on analysis pit size and depth, and fractionation during analysis will have to be investigated. Longer analyses than 60 mins will also affect analysis pit depth, and hence fractionation during analysis, but will improve precision. Using a 20 nA beam current gives a 5 ‰ error on $CO_2 > 700$ ppm, or 2 ‰ on $CO_2 > 2000$ ppm. Although this is not precise enough to infer initial carbon composition during closed-system degassing, it should be able to estimate the initial carbon concentration or isotope ratio during open-system degassing (Figure 1.7). It should also be able to discern between closed- and open-system, and equilibrium or kinetically-driven, degassing (Figure 1.7). Improvements in detector efficiency will be required to further improve the precision.

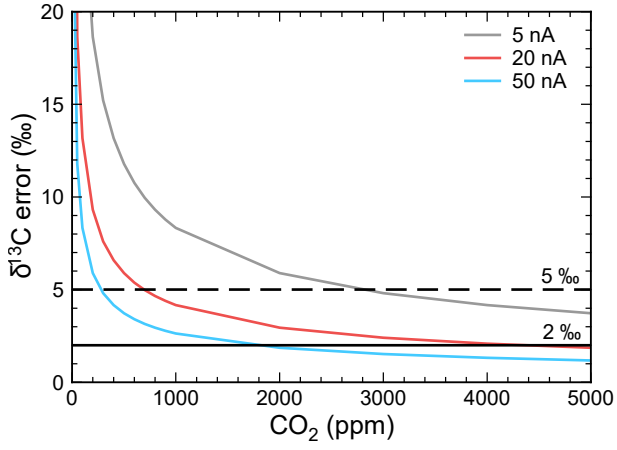


**Figure 4.18:** $\delta^{13}C$ ‰ precision based on an approximate $^{13}C^-$ count rate of 0.08 CPS·nA$^{-1}$·ppm$^{-1}$ of $CO_2$ for different beam currents. A $\delta^{13}C$ precision of 2 and 5 ‰ are shown using horizontal solid and dashed lines, respectively.

# Chapter 5

# Stable isotope fractionation during closed-system degassing in the system basalt-$H_2O$-$CO_2$

**Author contributions and declaration:** E.C. Hughes made the experimental capsules with the help of R.A. Brooker. Glasses were synthesised by R. Balzer. All data were collected by E.C. Hughes (with the help of J. Craven and R. Hinton for SIMS), except TCEA which was collected by I. Bindemann. E.C. Hughes interpretted and processed the data with the help of J.D. Blundy, H.M. Mader, G. Kilgour, and R.A. Brooker.

## ABSTRACT

Stable isotope fractionation of volatiles during degassing provides a tool for constraining the bulk volatile composition of magmas, and their degassing style, prior to eruption. Interpreting stable isotope data from volcanic products requires knowledge of the isotope fractionation factor between exsolved fluid and silicate melt. Currently, experimental data on fractionation factors for carbon and hydrogen are not available for mixed $H_2O$-$CO_2$ fluids, which are critical for interpreting data from arc volcanoes. This study simulates experimentally closed-system degassing in the system basalt-$H_2O$-$CO_2$. The concentration and isotope ratio of carbon and hydrogen in the quenched glass of variably degassed melts is analysed to determine the fractionation factor of carbon and hydrogen. The experimental approach is fraught with difficulty and two issues compromise the veracity of the measured data. First, $H_2$ infiltration during the experiment causes the hydrogen composition to change throughout the run, such that the measured fractionation factor between fluid and melt is unlikely to represent equilibrium. Second, carbon contamination during preparation of the starting powders, and subsequent SIMS analysis of run products, creates uncertainties when determining the fractionation factor. Despite these setbacks, these experimental results provide a valuable benchmark for future studies of stable isotope fractionation between $H_2O$-$CO_2$ fluids and melts and reveal a future methodology to address the problems encountered.

## 5.1. Introduction

Constraining the initial dissolved volatile concentration, especially of carbon, for magmas is still difficult even using melt inclusions, due to the low solubility of carbon in silicate melts (e.g., Fine and Stolper, 1986). Any degassing that precedes crystallisation and entrapment of melt inclusions leads to an underestimate of the original magmatic carbon. Stable isotope fractionation of volatiles during degassing potentially provides a method for reconstructing the initial volatile concentration of magmas (Section 1.4). By analysing a suite of variably degassed glasses (e.g., groundmass glass or melt inclusions) or gases (e.g., vesicles, fluid inclusions, and volcanic gases) for concentration and isotope ratio, the initial volatile composition and the degassing style can be inferred (e.g., Aubaud et al., 2004; Barry et al., 2014; Gennaro et al., 2017; Gerlach and Taylor, 1990; Hauri et al., 2002; Macpherson and Mattey, 1994; Newman et al., 1988; Paonita et al., 2012). To use these data in this way, the isotopic fractionation factor of the volatile species between the exsolved fluid and the melt must be known.

### 5.1.1. The fractionation factor

The fractionation factor describes the direction and magnitude of stable isotope fractionation. There are multiple ways to define the fractionation factor (Section A.2) and here the $\Delta$-notation will be used, defined as:

$$\Delta_{\text{f–m}} = \delta_{\text{f}} - \delta_{\text{m}} \tag{5.1}$$

where $\Delta_{\text{f–m}}$ is the isotopic fractionation factor between exsolved fluid and co-existing melt, and $\delta_{\text{f}}$ and $\delta_{\text{m}}$ are the isotopic ratios in $\delta$-notation (Section A.2) of the exsolved fluid and the melt, respectively. As the behaviour of both carbon and hydrogen during degassing are investigated, the volatile of interest will be indicated using a superscript (e.g., $\Delta^{\text{C}}_{\text{f–m}}$ for carbon and $\Delta^{\text{H}}_{\text{f–m}}$ for hydrogen). The notation $\Delta_{\text{f–m}}$ is used where the speciation of the volatile (e.g., if carbon is present as carbonate ion, $CO_3^{2-}$, or molecular carbon dioxide, $CO_2$) in the melt and exsolved fluid is unknown. The composition of the melt may be substituted for m if it is known (e.g., $\Delta_{\text{f–rhyolite}}$ is the fractionation factor between fluid and rhyolite melt). If the speciation of the volatile in the exsolved fluid and/or melt is known, it will be substituted for 'f' or 'm' in the subscript. For instance, $\Delta^{\text{C}}_{\text{CO}_2\text{–}\text{CO}_3^{2-}}$ is the fractionation factor for carbon between molecular carbon dioxide in the exsolved fluid and carbonate ion in the melt; or $\Delta^{\text{H}}_{\text{H}_2\text{O–rhyolite}}$ is the fractionation factor for hydrogen between molecular water in the exsolved fluid and hydrogen of unknown speciation in the rhyolite melt.

Stable isotope fractionation can occur under equilibrium conditions or be kinetically-driven. These two end-member processes are the extreme cases and give rise to different $\Delta_{\text{f–m}}$, although intermediate scenarios are also possible. During degassing, equilibrium conditions will be favoured for fast diffusing species at high temperatures in low viscosity magmas (e.g., hydrous basalts) if the magma resides at certain conditions (e.g, pressure and temperature) for some time; whilst kinetic conditions will be favoured for slowly diffusing species at lower temperatures in high viscosity magmas (e.g., anhydrous rhyolites) when the magma is quickly ascending (e.g., Pichavant et al., 2018).

During kinetically-driven degassing, the exsolved fluid becomes enriched in the lighter isotope, and hence the melt is enriched in the heavier isotope, therefore $\Delta_{\text{f–m}} < 0$. This is because volatile molecules containing

the lighter isotope will exsolve prior to those containing the heavier isotope, as they will have weaker bonds and higher diffusivities. The magnitude of $\Delta_{\text{f–m}}$ will depend on the process that is controlling the rate of degassing. For instance, Aubaud et al. (2004) assumed a Graham-type law to approximate degassing, which states that the rate of diffusion of a gas through a hole is inversely proportional to the square root of its mass (Graham, 1846). In this case the isotopes will be fractionated according to:

$$\alpha_{\text{f–m}} = \sqrt{\frac{M_1}{M_2}} \tag{5.2}$$

where $\alpha_{\text{f–m}}$ is the $\alpha$ fractionation factor (Section A.2 and Equation A.2), and $M_1$ and $M_2$ are the molecular masses of the lighter and heavier isotopes, respectively. A more rigorous approach was taken by Watson (2017), who investigated kinetically-driven isotopic fractionation during bubble growth. Volatile species should isotopically fractionate during bubble growth as there is an isotopic mass effect on the rate of diffusion in silicate melts (Richter et al., 2009, 2008, 2003, 1999; Watkins et al., 2009), even for relatively heavy volatiles such as Cl (Fortin et al., 2017). The magnitude of fractionation will depend on the bubble growth rate, volatile diffusivity, and relative diffusivities of the isotopes. Using the measured relative diffusivities for $^{6}$Li and $^{7}$Li (Richter et al., 2003) and $^{35}$Cl and $^{37}$Cl (Fortin et al., 2017), gave maximum $\Delta_{\text{f–m}}$ of $\Delta^{\text{Li}}_{\text{f–m}} \approx$ -27 ‰ and $\Delta^{\text{Cl}}_{\text{f–m}} \approx$ -3.5 ‰. Data on the relative diffusivities of carbon and hydrogen isotopes in silicate melts are not currently available, hence such calculations are not possible yet. Hence, the magnitude of $\Delta_{\text{f–m}}$ for carbon and hydrogen is unknown but it is always negative ($\Delta_{\text{f–m}} < 0$).

Conversely, equilibrium fractionation is controlled by the difference in bond energies in the exsolved fluid and melt, therefore $\Delta_{\text{f–m}}$ can be positive or negative. The equilibrium fractionation factor is dependent predominantly on temperature and the volatile speciation in both the exsolved fluid and the coexisting melt, and therefore on oxygen fugacity ($fO_2$).

### 5.1.2. Volatile speciation in the exsolved fluid and melt

For both kinetic and equilibrium isotopic fractionation, the speciation of the volatile dissolved in the melt and exsolved in the fluid is critical. Speciation will affect the diffusivity of the volatile species in the melt, such as for $H_2O^{\text{mol}}$ and $OH^-$ in silicate melts (e.g., Zhang and Behrens, 2000), which is important for isotopic fractionation during bubble growth (Watson, 2017). For equilibrium isotopic fractionation, speciation defines the bond energies in the melt and the exsolved fluid.

In the C-O-H system, the most important species in the fluid are $H_2O$, $CO_2$, CO, $H_2$, and $CH_4$. Magmatic fluids do not contain free $O_2$ as the $fO_2$ is too low, and are rarely rich in $CH_4$ and $H_2$ because the $fO_2$ is too high (Carmichael, 1991; Holloway and Blank, 1994). Pressure, temperature, and fluid composition can also impact speciation, and species such as bicarbonate or carbonic acid in $CO_2$-rich fluids at high pressures and low temperatures have been suggested (Abramson et al., 2017). In most magmatic fluids, the predominant species are $CO_2$ and $H_2O$.

$fO_2$ is again the predominant control on volatile speciation in the silicate melt, although pressure and temperature also effect the speciation of carbon and hydrogen in the melt (Silver and Stolper, 1989; Stolper, 1989). In oxidising conditions relevant to magmatic systems, carbon is predominantly dissolved as carbonate ions ($CO_3^{2-}$) or molecular carbon dioxide ($CO_2^{\text{mol}}$), whilst hydrogen is present as hydroxyl ions

($OH^-$) and molecular water ($H_2O^{mol}$) (Blank and Brooker, 1994; Stolper, 1982). $CH_4$ has been observed in reducing conditions (Mysen, 2016). Melt composition effects volatile speciation, with basalts containing predominantly $CO_3^{2-}$ and rhyolites mostly $CO_2^{mol}$ (Blank and Brooker, 1994). Hydrogen is present as both hydroxyl ions ($OH^-$) and molecular water ($H_2O^{mol}$) in basaltic to rhyolitic melts and the proportion of these species varies significantly with total dissolved $H_2O$ ($H_2O^T$) (Stolper, 1982).

### 5.1.3. Quantifying the fractionation factor

There are a variety of ways to quantify $\Delta_{f-m}$. Equilibrium $\Delta_{f-m}$ can be calculated using the partition function of statistical mechanics, which describes the equilibrium statistical properties of the system (Urey, 1947). This requires knowledge of the molecular frequencies, which can either be measured spectroscopically or calculated (Urey, 1947). The molecular frequencies for simple species can be relatively easily measured, hence $\Delta_{f-m}$ for simple isotopic exchanges (e.g., $CaCO_3$ with $CO_2$) can be calculated over a wide range of temperatures. These can be applied to silicate melts by knowing the volatile speciation in the melt and assuming its behaviour is similar to that in the isolated case (e.g., Chacko et al., 2001). For instance, the equilibrium fractionation factor between $CO_3^{2-}$ (as $CaCO_3$) and $CO_2$ was calculated up to 700 °C by Bottinga (1969) (Figure 5.1). At temperatures $> 200$ °C , $\Delta^C_{CO_2-CaCO_3} > 0$ (i.e., the $CO_2$ becomes enriched in $^{13}C$ and the $CO_3^{2-}$ in $^{12}C$) and has a maximum value of +2.8 ‰ at 500 °C . Extrapolating to magmatic temperatures (700–1400 °C) gives +1 to +2 ‰ (Mattey et al., 1990). Calculated fractionation factors for methane and graphite are much greater at these temperatures (700 °C, $\Delta^C_{CO_2-CH_4}$ = +10.0 and $\Delta^C_{CO_2-C}$ = +7.7 ‰), due to the different speciation of carbon. Richet et al. (1977) also calculated fractionation factors for various carbon-bearing molecules (e.g., $CO_2$, $CH_4$, and CO) up to 1300 °C (Figure 5.1). If the speciation of the volatile does not change between the phases (e.g., $CO_2^{mol}$ in the melt and exsolved fluid), $\Delta^C_{CO_2-CO_2}$ will tend to ~0 ‰. Deines (2004) investigated different carbonates (e.g., Ca, Mg, Mn, Fe, and Na) and showed that the nature of the cation affects the magnitude of isotopic fractionation.

Natural volcanic samples can also be used to measure $\Delta_{f-m}$. From Equation 5.1, the difference between the $\delta$ isotope ratio of the vesicles and the glass, assuming they represent the exsolved fluid and the melt respectively, from the same sample provide an estimate of $\Delta_{f-m}$ (e.g., Pineau and Javoy, 1983). The gas trapped in the vesicles can be released by crushing or lightly heating the sample, whilst the volatiles dissolved in the melt can be extracted using SHMS (Section 4.2.2). Alternatively, closed- or open-system degassing trends (Equations 1.1 and 1.4, respectively) can be fitted to a suite of variably degassed glasses or gases to calculate $\Delta_{f-m}$ (Section 1.4). The gas trapped inside vesicles may not represent the exsolved fluid present at equilibrium as it may have re-equilibrated post-entrapment (Mathez and Delaney, 1981; Watanabe et al., 1983), hence $\Delta_{f-m}$ using vesicle compositions may not be correct. To calculate $\Delta_{f-m}$ from suites of variably degassed glasses or fluids, the initial concentration and isotope ratio, and degassing style must be assumed (e.g., Figure 1.7). In these cases, the $\Delta_{f-m}$ measured could be equilibrium or kinetic. Natural samples provide direct evidence of isotopic fractionation during degassing, although it is difficult to know exactly what conditions the derived $\Delta_{f-m}$ is appropriate for.

Unfortunately, many early studies of carbon heated the glass in a single step, therefore a component of low temperature carbon contamination was included in the dissolved $CO_2$ (e.g., Section 4.1). Additionally, many studies did not crush the sample to remove $CO_2$ trapped in the vesicles (Des Marais, 1986). Even excluding these data, $\Delta^C_{f-m}$ from natural samples using the difference between glass and vesicles have a wide range

of values (-12 to +18 ‰), indicative of the different processes described above (Aubaud et al., 2004; Barry et al., 2014; Des Marais and Moore, 1984; Javoy and Pineau, 1991; Macpherson and Mattey, 1994; Mattey et al., 1989; Pineau and Javoy, 1983). Values from fitting degassing trends are more consistent (e.g., +2.3 to +4.3 ‰, Barry et al., 2014; Macpherson and Mattey, 1994), except for the single study using melt inclusions (∼+20 ‰, Hauri et al., 2002).

There are less data available for hydrogen isotopic fractionation, but the values are more consistent (Figure 5.2). Newman et al. (1988) measured the isotope ratio and concentration of $H_2O$ in bulk glass from Mono Crater, California, and modelled the degassing trend. To fit their data required $\Delta^{H}_{H_2O–OH^-}$ = +51 ‰ and $\Delta^{H}_{H_2O–H_2O}$ = -13 ‰ with closed–followed by open–system degassing. Pineau et al. (1998) report $\Delta^{H}_{f–m}$ of +24–39 ‰ from basaltic glasses containing 0.5–1.5 wt% $H_2O$.

The fractionation factor can also be constrained experimentally, using high-pressure high-temperature equipment to create volatile-saturated melts. Typically, the isotopic composition of the volatile dissolved in the melt and exsolved in the fluid are measured to determine $\Delta_{f–m}$. Unlike theoretically-determined $\Delta_{f–m}$, no assumption about the speciation of the volatile must be made, but the experimental conditions must be chosen to reflect those of interest. Experimental conditions (e.g., run times) can be chosen to ensure equilibrium is reached, unlike when measuring natural samples. Below is a review of the available experimental data on carbon and hydrogen fractionation factors in silicate melts.

### Carbon

There are a variety of studies that have measured the fractionation factor for carbon in basaltic melts ($\Delta^{C}_{f–basalt}$), yielding inconsistent results with $\Delta^{C}_{f–basalt}$ ranging from +1 to +5 ‰ (Figure 5.1 and Table 5.1). There are broadly two sets of values: $\Delta^{C}_{f–basalt} \approx$ +2 ‰ (Mattey, 1991; Mattey et al., 1990), which is similar to the theoretical calculations between $CO_2$ and $CO_3^{2-}$(Bottinga, 1969); and $\Delta^{C}_{f–basalt} \approx$ +4 ‰ (Appora, 1998; Javoy et al., 1978; Trull et al., 1991), which is higher than would be expected if carbon is dissolved as carbonate ions in the melt. This difference is large enough to affect the interpretation of isotopic compositions in natural samples.

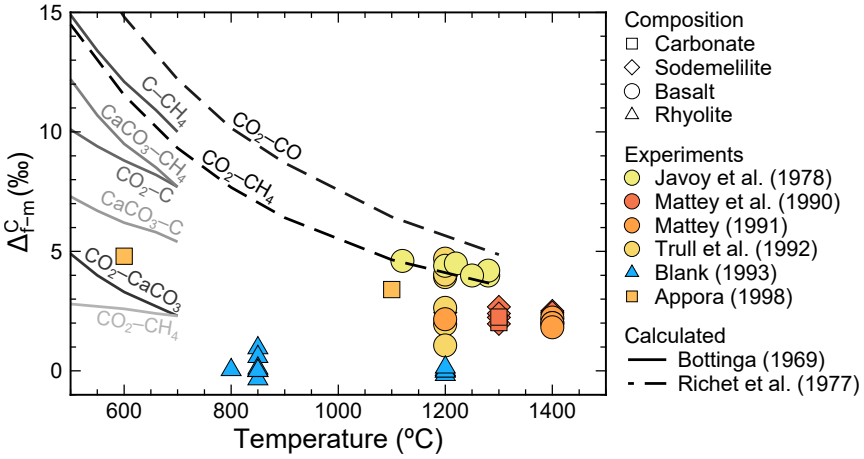


**Figure 5.1:** Calculated and experimental literature data for $\Delta^{C}_{f–m}$. Symbol shape indicates glass composition and colour indicates study. Results from Mysen (2017, 2016) are not included as they are orders of magnitude larger than all other values.

**Table 5.1:** Summary of experimentally derived $\Delta^{C}_{f-m}$ for melts.

| Melt composition | Dissolved species | Fluid | $X_{CO_2}$ | T (°C) | P (kbar) | $\Delta^{C}_{f-m}$ (‰) | Reference |
|---|---|---|---|---|---|---|---|
| Tholeiite | $CO_3^{2-}$ | $CO_2$ ($\pm H_2O$) | 0.5–1 | 1120–1180 | 7.0–8.4 | +4.3 ± 0.3 | Javoy et al. (1978) |
| MORB | $CO_3^{2-}$ | $CO_2$ | | 1200 | 1–2 | +3.1 ± 1.3 | Trull et al. (1991) |
| Sodamelilite | $CO_3^{2-}$ | $CO_2$(+$H_2O$) | ∼1 | 1200–1400 | 5–30 | +2.2 ± 0.2 | Mattey et al. (1990) |
| Carbonate | $CO_3^{2-}$ | $CO_2$ | ∼1 | 1200–1400 | 20–30 | +2.12 ± 0.1 | Mattey et al. (1990) |
| Tholeiite | $CO_3^{2-}$ | $CO_2$(+$H_2O$) | ∼1 | 1200–1400 | 5–20 | +2.0 ± 0.2 | Mattey (1991) |
| Rhyolite | $CO_2$ | $CO_2$(+$H_2O$) | 0.99[c] | 800–1200 | 0.250–1.444 | 0.0 ± 0.2 | Blank (1993) |
| $(Li,Na,K)_2CO_3$ | $CO_3^{2-}$ | $CO_2$ | 1 | 600–1100 | <0.06 | +3.4 to +4.8 | Appora (1998) |
| Haploandesite[a] | $H_2$, $H_2O$, $CH_4$ | $H_2$, $H_2O$, $CH_4$ | <1 | 475–870 | 0.92–11.58 | Large, <0[d] | Mysen (2016) |
| Haploandesite[b] | $H_2O$, $OH^-$, $CO_3^{2-}$, $HCO_3^-$ | $CO_3^{2-}$, $H_2O$, $HCO_3^-$ | <1 | 550–825 | 6.68–13.03 | -100 to +116[c] | Mysen (2017) |

*Notes:* [a] indicates reduced and [b] oxidised conditions; [c] calculated using VolatileCalc (Newman and Lowenstern, 2002) from the $CO_2$ and $H_2O$ concentrations in the glass; [d] $\alpha^{C}_{f-m}$ is not ~1, hence $\Delta^{C}_{f-m} \approx 1000 \cdot \ln\alpha^{C}_{f-m}$ is not appropriate (Section A.2).

**Table 5.2:** Summary of experimentally derived $\Delta^{H}_{f-m}$ for melts.

| Melt composition | Dissolved species | Fluid | T (°C) | P (kbar) | $H_2O$ (wt%) | $\Delta^{H}_{f-m}$ (‰) | Reference |
|---|---|---|---|---|---|---|---|
| Rhyolite | $OH^-$, $H_2O$ | $H_2O$ | | | 2.4–3 | 19–24 | Taylor and Westrich (1985) |
| Alumnosilicate | $OH^-$, $H_2O$ | $H_2O$ | 870–1250 | 2 | ∼7 | 6–23 | Richet et al. (1986) |
| Rhyolite, albite-orthoclase | $OH^-$ | $H_2O$ | 530–850 | 0.002–0.003 | 0.1–0.2 | 31–44 | Dobson et al. (1989) |
| Rhyolite | $OH^-$, $H_2O$ | $H_2O$ | 850 | | | 39 ($OH^-$), 0 ($H_2O$) | Ihinger (1991) |
| Tholeiite | $OH^-$, $H_2O$ | $H_2O$ | 1250 | 3 | | 20.3 | Shilobreeva et al. (1991) |
| Basaltic-andesite | $OH^-$, $H_2O$ | $H_2O$ | 1200–1250 | 0.5–3 | 2–7 | 20–32 | Pineau et al. (1998) |
| Si-Al-Na | $OH^-$, $H_2O$ | $H_2O$ | 300–800 | 2–15 | >4 | [a]100–700 | Dalou et al. (2015); Mysen (2013a,b) |

*Notes:* [a] $\Delta^{H}_{f-m}$ is not strictly appropriate if $\alpha^{H}_{f-m} \gg 1$, as is the case here (Section A.2).

Javoy et al. (1978) conducted experiments using oceanic tholeiitic basalt, in an internally heated autoclave at 1100–1200 °C and 7.0–8.4 kbar. Most of their experiments were anhydrous (i.e., proportion of $CO_2$ in the fluid, $X_{CO_2}$, $\approx$ 1), although one experiment had $X_{CO_2} \approx 0.5$. They used SHMS to measure the $\delta^{13}C$ of the glass, where the $CO_2$ released between 400 and 1000 °C was used to represent the dissolved $CO_2$. Their experiments contained significant excess fluid, hence they calculated $\Delta^C_{f-m}$ by subtracting the $\delta^{13}C$ of the glass from that of the starting material, as for closed-system degassing $\delta_b - \delta_m \rightarrow \Delta_{f-m}$ when $C_m/C_b \rightarrow 0$ (from Equation A.15). They measured $\Delta^C_{f-basalt}$ = +4.0 to +4.6 ‰. As discussed by Mattey et al. (1990), the 400 °C step is likely to correspond to low temperature carbon contamination and $CO_2$ is typically still released above 1000 °C. Therefore, Javoy et al. (1978) are unlikely to have measured the actual dissolved $CO_2$ in their glass.

Trull et al. (1991) conducted experiments on MORB glasses at 1–2 kbar and 1200 °C in an internally heated furnace. As this is a conference abstract there is insufficient detail on the analytical details and method for calculating $\Delta^C_{f-m}$, but they report $\Delta^C_{CO_2-basalt}$ of +1.07 to +4.70 ‰ with an average of +3.1 $\pm$ 1.4 ‰. There were variable $CO_2$ concentrations within the glass, with ~150 ppm at the rim where Fe loss had occurred and ~180 ppm in the core where no Fe loss was observed for some experiments. This may imply equilibrium was not reached throughout the glass.

Mattey et al. (1990) conducted piston-cylinder experiments on sodamelilite (Sm) glass, which is a compositionally simple analogue for basalt, at 5–30 kbar and 1200–1400 °C. At <20 kbar, run products consisted of sodamelilite glass and fluid, and >20 kbar they consisted of sodamelilite glass, fluid, and carbonate (Cb). Minor $H_2O$ was present in both the sodamelilite glass and the fluid but not quantified. Fractionation factors were calculated for $\Delta^C_{CO_2-Sm}$, $\Delta^C_{CO_2-Cb}$, and $\Delta^C_{Cb-Sm}$ by measuring the $\delta^{13}C$ of the coexisting phases. Only the $CO_2$ released at high temperature was considered to be dissolved $CO_2$, resulting in $\Delta^C_{CO_2-Sm}$ of +2.2 $\pm$ 0.2 ‰. Mass balance indicates come carbon may have escaped from the capsules through defects in the capsule walls, but this did not appear to affect the measured $\Delta^C_{f-m}$.

Mattey (1991) conducted piston-cylinder experiments at 5–20 kbar and 1200–1400 °C on a MORB tholeiite, with minor (but unquantified) $H_2O$ present in the glass and fluid. $\delta^{13}C$ of the glass was calculated using only high temperature released carbon and some carbon was lost during unloading. The measured $\Delta^C_{CO_2-basalt}$ is +2.0 $\pm$ 0.2 ‰, which shows no effect of pressure or temperature.

Appora (1998) conducted experiments at <60 bars and 600–1100 °C on $(Li,Na,K)_2CO_3$ and natrocarbonatite melts, where the dissolved species is carbonate ion. Only the abstract of the thesis is available, therefore there are limited experimental details. For 600 and 1100 °C, $\Delta^C_{f-(Li,Na,K)_2CO_3}$ is +4.8 and +3.4 ‰, respectively. For natrocarbonanatite, the exact $\Delta^C_{f-natrocarbonatite}$ value is not reported, but it is intermediate between $(Li,Na,K)_2CO_3$ and calcite.

Experiments have also been conducted on other silicate compositions. Blank (1993) measured the $\Delta^C_{f-m}$ between rhyolite melt and $CO_2$ fluid ($\Delta^C_{f-rhyolite}$) with minor, but quantified, $H_2O$. Experiments were run at 800–1200 °C and 0.250–1.444 kbar using René and TZM bombs with sealed and unsealed capsules. $\Delta^C_{f-rhyolite}$ was calculated by measuring the $\delta^{13}C$ of the coexisting fluid and dissolved $CO_2$ in the glass using SHMS, only including $CO_2$ released at high temperature. From the sealed experiments, which she deems more trustworthy, $\Delta^C_{f-rhyolite}$ = 0.0 $\pm$ 0.2 ‰, consistent with $CO_2^{mol}$ being the predominant dissolved species.

Mysen (2017, 2016) measured the fractionation factor between haploandesite (Ha) melt and a mixed

$CO_2$-$H_2O$ fluid. Experiments were run at 475–850 °C and 0.92–11.58 kbar under reducing conditions, and 500–825 °C and 8–13 kbar under oxidising conditions, using an externally heated hydrothermal diamond cell. The carbon isotope ratios and speciation in the fluid and melt were measured *in situ* using Raman spectroscopy. For reducing conditions, the carbon species was $CH_4$ in the melt and fluid, and the fractionation factor was very large ($\alpha^{C}_{f–m}$ = 0.51–0.88, it is not appropriate to convert these to $\Delta^{C}_{f–m}$ because $\alpha^{C}_{f–m} \ll 1$, Section A.2). For oxidising conditions, the species were $CO_3^{2-}$ and $HCO_3^{-}$ in the melt and fluid and, again, very large fractionation factors ($\alpha^{C}_{f–m}$ = 0.91–1.12, which is -100 to +116 in $\Delta^{C}_{f–m}$, although as $\alpha^{C}_{f–m}$ has values $\ll$ and $\gg$ 1 this conversion is not appropriate, Section A.2). In both cases the fractionation factor became more positive with increasing temperature. These values are one to two orders of magnitude larger than previously measured. Although the cause of this discrepancy is unclear, the experimental set-up in these studies is very different to previous studies. For instance, the Mysen (2017, 2016) experiments were conducted at lower temperatures. Also, these experiments measured the isotopic ratio and concentration *in situ*, whereas previous studies analysed the quenched products after the experiment had been conducted. Additionally, these studies used Raman spectroscopy to measure the isotope ratio, whereas previous studies used SHMS.

Deines (2004) produced a model to predict $\Delta^{C}_{CO_2–m}$ based on melt composition using the experimental data of Blank (1993), Mattey (1991), and Mattey et al. (1990) at 1200 °C. The model assumes dissolved carbon interacts with cations as carbonates. Additionally, carbon interacts with the Si/Al tetrahedra to account for differences between basalts and rhyolites. He produced an empirical relationship by fitting a regression to the experimental data such that:

$$\Delta^{C}_{CO_2–m} = 5.14 \cdot \left( \frac{\Sigma \text{cations}}{\text{Si + Al}} \right) + 0.86 \tag{5.3}$$

where cations (Mg, Fe, Mn, Ca, and Na), Si, and Al are molar quantities.

In summary, $\Delta^{C}_{f–m}$ depends on the composition of the melt (i.e., basalt or rhyolite) but the effect of $H_2O$ has not been investigated. Additionally, the exact value of $\Delta^{C}_{f–basalt}$ is still debated. This excludes the studies of Mysen (2017, 2016) that use a very different experimental and analytical method to previous studies, and yield extremely high values for $\Delta^{C}_{f–m}$.

**Hydrogen**

Under oxidising conditions, isotopic fractionation of hydrogen during degassing is more complicated than carbon as hydrogen is dissolved in silicate melts as both $OH^-$ and $H_2O^{mol}$ as discussed in Section 5.1.2. Hence, $\Delta^{H}_{f–m}$ (bulk, $H_2O^T$, fractionation factor) will be a combination of $\Delta^{H}_{f–OH^-}$ and $\Delta^{H}_{f–H_2O}$, dependent on their proportions in the melt, and it will change during the degassing process.

A big problem with measuring the hydrogen isotope fractionation factor experimentally is that hydrogen can easily diffuse in and out of experimental capsules (e.g., Richet et al., 1986). This will be discussed in detail in Section 5.2.1. There are a variety of studies that have measured $\Delta^{H}_{f–m}$ for silicate melt and, although there is spread in the data ($\Delta^{H}_{f–m}$ = 6–44 ‰, bar controversial Raman-based studies which are discussed later), there is less controversary in the values compared to carbon in basaltic melts. The range in $\Delta^{H}_{f–m}$ can be explained by variable $H_2O^T$ in the glass (Figure 5.2), which implies that as the speciation in the melt changes during degassing $\Delta^{H}_{f–m}$ changes. All of these experimental studies suggest that $\Delta^{H}_{H_2O–OH^-} >$

$\Delta^{H}_{H_2O–H_2O} > 0$ ‰. Hence $\Delta^{H}_{f–m} > 0$ ‰ resulting in the melt becoming isotopically lighter during equilibrium degassing and the exsolved fluid heavier. Table 5.2 contains an overview of the literature data, but a few studies are worth further discussion.

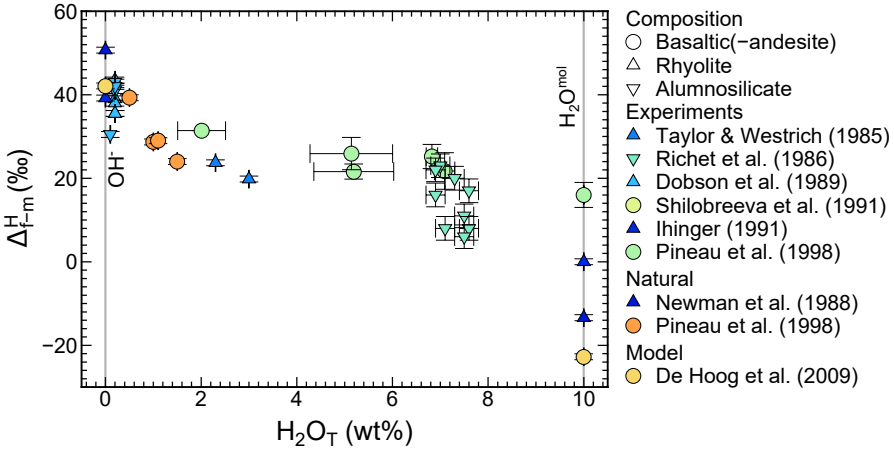


**Figure 5.2:** Experimental, natural, and modelled literature data for $\Delta^{H}_{f–m}$. $\Delta^{H}_{f–m}$ at 0 and 10 wt% $H_2O$ are for pure $OH^-$ and $H_2O^{mol}$, respectively. Symbol shape indicates glass composition and colour indicates study. Results from Dalou et al. (2015) and Mysen (2013a,b) are not included as they are orders of magnitude larger than all other values.

To isolate $\Delta^{H}_{H_2O–OH^-}$, Dobson et al. (1989) conducted experiments at 2 bar using quartz tubes filled with glass and excess $H_2O$ in vertical furnaces at 530–750 °C for rhyolite and albite-orthoclase melt compositions. The glasses contained <0.2 wt% $H_2O^T$ therefore all $H_2O$ was present as $OH^-$, and they calculated $\Delta^{H}_{H_2O–albite}$ = 30–44 ‰.

Two studies have discussed the problems associated with hydrogen infiltration during the experiment. Richet et al. (1986) conducted IHPV experiments on aluminosilicate melt at 2 kbar between 870–1250 °C at high $H_2O$ concentrations (~7 wt%). Hydrogen diffused into their capsules during the experiment, and they conclude that isotopic equilibrium between the fluid and melt was achieved at a slower rate than $H_2$ diffusion into the capsule. They calculated $\Delta^{H}_{H_2O–melt}$ = 6–23 ‰, attributing the spread in values to variable degrees of fluid-melt equilibrium, hence they consider the more positive $\Delta^{H}_{H_2O–melt}$ as more representative. Pineau et al. (1998) used unsealed capsules exposed to excess $H_2O$ in vertical gas-pressure vessels to try and avoid the problem of $H_2$ diffusion into the capsules during experiments. They used basaltic andesite melt, at 0.5–3 kbars and 1200–1250 °C. There were problems of disequilibrium along the capsule length, but they calculated $\Delta^{H}_{f–m}$ = 20–32 ‰ for 2–7 wt% $H_2O$. They inferred that for basalts with very high $H_2O$, $\Delta^{H}_{f–m}$ would tend to 16 ± 3 ‰.

As for carbon, extremely large hydrogen fractionation factors have been measured by Dalou et al. (2015) and Mysen (2013a,b) in the $SiO_2$-$Na_2O$-$Al_2O_3$-$H_2O$ system using an externally heated diamond anvil cell and *in situ* Raman spectroscopy. Experiments were conducted at 300–800 °C and 2–15 kbars and they calculated $\Delta^{H}_{f–m}$ = 100–700 ‰ (although $\Delta^{H}_{f–m}$ is not strictly appropriate if $\alpha^{H}_{f–m} \gg$ or $\ll 1$ as is the case here, Section A.2). This is an order of magnitude larger than previous experiments, similar to the results carbon, and maybe due to the differences in the experimental and analytical set-up compared to previous studies.

De Hoog et al. (2009) use both experimental and natural data to create an empirical model of $\Delta^{H}_{f–m}$ for basaltic andesite (BA) melts. The model includes the effects of total dissolved $H_2O$ (big effect) and temperature (small effect). For 0–7 wt% $H_2O$ at 900–1250 °C, the equation for bulk $\Delta^{H}_{H_2O–BA}$ is:

$$\Delta^{H}_{H_2O\text{–}BA} = 44.53 \cdot \left(\frac{C_{H_2O^T}}{7.03} + 1\right)^{-1.2} \tag{5.4}$$

where $C_{H_2O^T}$ is the $H_2O^T$ concentration (wt%). For instance, at 1250 °C $\Delta^{H}_{H_2O\text{–}OH^-}$ = 42.2 ‰ and $\Delta^{H}_{H_2O\text{–}H_2O}$ = -23 ‰.

In summary, $\Delta^{H}_{f\text{–}m}$ is dependent on the speciation of hydrogen in the melt, which depends on the total $H_2O$ concentration and hence changes during degassing. No studies have carbon also present.

## 5.2. Methods

### 5.2.1. Approach and theory

For both carbon and hydrogen fluid-melt stable isotope fractionation, experiments are lacking for mixed volatile systems at crustal pressures. There are no experiments for carbon at pressures <5 kbar and for hydrogen at >3 kbar. Also, available data are somewhat scattered and often contradictory, yet these data are critical for understanding stable isotope fractionation in arc settings, which are rich in both $H_2O$ and $CO_2$ and often have upper crustal reservoirs. Hence, this study aims to fill in this gap by conducting experiments with $CO_2$- and $H_2O$-bearing basaltic melts at 1–7 kbar to constrain $\Delta^{C}_{f\text{–basalt}}$ and $\Delta^{H}_{f\text{–basalt}}$ under oxidising conditions.

We use a graphical approach to calculate $\Delta_{f\text{–}m}$ using the volatile concentration and isotope ratio of a suite of variably degassed (under equilibrium, closed-system conditions) glasses, whereby:

$$\delta_m = \left(\frac{\Delta_{f\text{–}m}}{C_b}\right) \cdot C_m + (\delta_b - \Delta_{f\text{–}m}) \tag{5.5}$$

where $\delta_m$ and $\delta_b$ are the volatile isotope ratios of the melt and bulk system, respectively; $C_m$ and $C_b$ are the volatile concentrations of the melt and bulk system, respectively; and $\Delta_{f\text{–}m}$ is the volatile isotopic fractionation factor between the melt and exsolved fluid (Section A.3.1). The isotopic composition of the exsolved fluid is not measured in case it is modified after the experiment has been quenched. Mass balance between the bulk system and the melt is not used to estimate the composition of the exsolved fluid as this results in large errors as the error on concentration is far greater than that on the isotope ratio. To use this graphical approach, the experiments must represent equilibrium, closed-system degassing. Additionally, the volatile concentration and isotope ratio in the glass and of the bulk system must be accurately quantified. The concentration and isotope ratios of the initial starting powders are not used to represent the bulk volatile compositions (e.g., $CaCO_3$ for carbon and water for hydrogen) as there are various processes that could modify this after they are added to the starting material. These processes include carbon contamination prior to, and hydrogen infiltration during, experimental synthesis.

Various steps were taken to minimise carbon contamination. Starting powders used minerals (e.g., wollastonite, albite, and sanidine) as sources for Ca, Na, and K instead of carbonates (Section 5.2.2). This avoids a decarbonation step to remove the carbon, which may leave behind small amounts of carbon with an incredibly light isotopic signature due to the open system fractionation that would occur during decarbonation. Solvents such as acetone and ethanol were avoided during grinding, which may also add

organic (isotopically light) carbon. Instead water was used, where evaporation was aided using a heat lamp. Glasses were synthesised in an internally heated pressure vessel (IHPV, Section 5.2.4), which does not contain a graphite furnace thereby avoiding carbon infiltration into the capsule from the furnace, which changes both carbon concentration and isotope ratio (Brooker et al., 1998). The largest source of carbon contamination is $CO_2$ adsorption onto the surface of glasses and powders, which is difficult to prevent unless all materials are stored and loaded in an inert, carbon-free atmosphere. This causes carbon addition and changes to the isotope ratio between the time that the starting powders were created and loaded into the capsules. All glasses used to create the starting powders, except for albite, were large pieces prior to crushing, to reduce the surface area available for adsorption.

$H_2O$ can also adsorb onto the surface of powders, which may cause errors in weighing when preparing the starting powders and add additional $H_2O$. Hence, components to make the starting powders were dried in an oven (except MgO which was heated in a furnace at 1000 °C then kept in a desiccator) prior to weighing. Starting powders were also dried in an oven prior to loading into the capsule. Additionally, hydrogen (as $H_2$) can diffuse through the capsule wall during the experimental run, which will change the concentration and isotope ratio of the bulk hydrogen in the system (e.g., Richet et al., 1986). Ideally, a pure Au capsule would be used, because of the slow diffusivity of hydrogen in Au, but the melting point is too low (1064 °C at 1 atm with a PT slope of ~58 °C·GPa$^{-1}$, Akella and Kennedy, 1971). Instead AuPd capsules are used, which have a higher melting point. Unfortunately, Fe forms an alloy with AuPd which changes the Fe concentration of the glass (e.g., Barr and Grove, 2010; Kawamoto and Hirose, 1994), leading to redox changes that can in turn drive $H_2$ diffusion.

The $H_2O$ concentration in the capsule changes in response to hydrogen fugacity ($fH_2$) gradients between the IHPV and the melt. For instance, if $fH_2$ is greater in the IHPV compared to the starting powders, $H_2$ will infiltrate into the capsule. Inside the capsule, $H_2$ will oxidise to form $H_2O$ by reducing $Fe_2O_3$ in the melt, which increases $Fe^{2+}/Fe_T$:

$$Fe_2O_3 + H_2 \rightleftharpoons H_2O + FeO \tag{5.6}$$

Additionally, Fe forms an alloy with AuPd causing Fe loss. This occurs by FeO in the melt undergoing disproportionation to $Fe_2O_3$ in the melt and Fe alloyed with the AuPd (e.g, Barr and Grove, 2010):

$$3FeO \rightleftharpoons Fe_2O_3 + Fe \tag{5.7}$$

This reaction consumes FeO and produces $Fe_2O_3$, which oxidises the system (decreasing $Fe^{2+}/Fe_T$) and drives the reaction in Equation 5.6. Equilibrium is achieved when the Fe oxidation state of the melt and the Fe concentration in the AuPd are equal to that imposed by the $fO_2$ of the system. This defines the amount of $H_2O$ added via $H_2$ diffusion. If the $fH_2$ gradient is reversed (i.e., the capsule has a higher $fH_2$ than the IHPV), $H_2O$ in the capsule reduces to $H_2$ to migrate through the capsule wall, releasing $O_2$. This oxidises FeO in the melt to $Fe_2O_3$ (decreasing $Fe^{2+}/Fe_T$). If the initial Fe oxidation state of the melt is in equilibrium with the imposed $fH_2$, the reactions in Equations 5.6 and 5.7 have no driving force to occur, hence $H_2O$ addition is minimised. Therefore, the $Fe^{2+}/Fe_T$ of the starting powder was chosen to be similar to the intrinsic oxygen fugacity of the experimental apparatus, which is also appropriate for real melts. We

measure the Fe loss and reduction between the starting powder and the glass and use Equations 5.6 and 5.7 to calculate the amount of $O_2$ produced by the melt. This $O_2$ oxidises the infiltrating $H_2$, and therefore corresponds to the $H_2O$ added to the system.

Additionally, we use graphical tie-line analysis (GTLA), shown schematically in Figure 5.3 (e.g., Papale, 2005). The initial composition of the melt ($H_2O^i$,$CO_2^i$) is defined as the concentration of $H_2O$ and $CO_2$ in the starting powder, whilst the added component ($H_2O^a$,$CO_2^a$) is pure $H_2$ (equal to pure $H_2O$ when oxidised) infiltrating from the IHPV into the capsule. If the melt is $H_2O$ saturated, the melt composition ($H_2O^m$,$CO_2^m$) will lie on an isobar. The exsolved fluid ($H_2O^f$,$CO_2^f$) is assumed to contain only $H_2O$ and $CO_2$ as no other volatiles were added, and hence the exsolved fluid lies on a line connecting 100 wt% $H_2O$ and 100 wt% $CO_2$. The bulk $H_2O$ and $CO_2$ of the system ($H_2O^b$,$CO_2^b$) must lie on a tie-line connecting the initial and added components, but also on the melt-fluid tie-line, hence the bulk volatile content lies at their intersection.

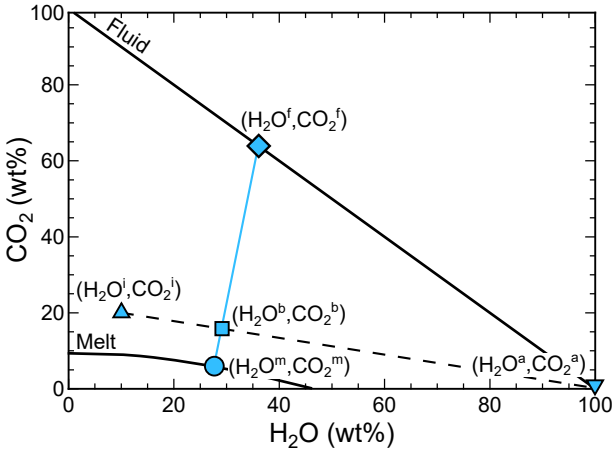


**Figure 5.3:** Schematic of graphical tie-line analysis (GTLA) to calculate the bulk volatile composition, where superscript i is the initial (the composition of the starting powder), a is the added ($H_2$ infiltrating into the capsule from the IHPV), m is the melt, f is the fluid, and b is the bulk volatile component. The straight, solid, black line are all possible fluid compositions when $H_2O$ and $CO_2$ are the only volatiles present. The curved, solid, black line is an isobar (which has been grossly exaggerated in order that the melt and fluid composition can be shown on the same axes), where the composition of $H_2O$-$CO_2$-saturated melt would lie. The straight, dashed, black line is the tie-line connecting the initial and added components. The straight, solid, blue line is the tie-line connecting the melt and fluid components.

The composition of the starting powders and the glass were characterised to calculate the bulk and dissolved volatile composition to allow calculation of the isotopic fractionation factor (Table 5.3). The initial composition of the system is determined by the weighed-in components during preparation of the starting powders (Section 5.2.2), although adsorption may alter this value. Additionally, the carbon concentration of the starting powders was measured using bulk pyrolysis to estimate initial carbon concentration (Section 5.2.3). The concentration of carbon and hydrogen of the exsolved fluid was measured by weighing the capsule after freezing/boiling the gases (Section 5.2.5). The dissolved volatile concentration in run product glasses was measured using SIMS (Section 5.2.7). The isotope ratio of carbon was measured using SIMS (Section 5.2.7) and of hydrogen using bulk pyrolysis (Section 5.2.6). The glass composition, especially Fe concentration and oxidation state, was measured using EPMA (Section 5.2.8). Figure 5.4 is a schematic of the capsule, showing the processes occurring during the experimental runs.

**Table 5.3:** Overview of techniques applied to starting powders, glasses, and fluids.

| Technique | Phase | Variable |
|---|---|---|
| Weighing | Starting powder | Majors, minors, $CO_2$, $H_2O$, and $Fe^{2+}/Fe_T$ (Section 5.2.2) |
| | Fluid | $CO_2$ and $H_2O$ (Section 5.2.5) |
| CSA | Starting powder | $CO_2$ (Section 5.2.3) |
| SIMS | Glass | $CO_2$ and $H_2O$ (Section 4.2.2), $\delta^{13}C$ (Section 4.3.2) |
| TCEA | Glass | $H_2O$ and $\delta D$ (Section 5.2.6) |
| EPMA | Glass | Majors and minors (Section 2.5.3), $Fe^{2+}/Fe_T$ (Section 3.3.2) |

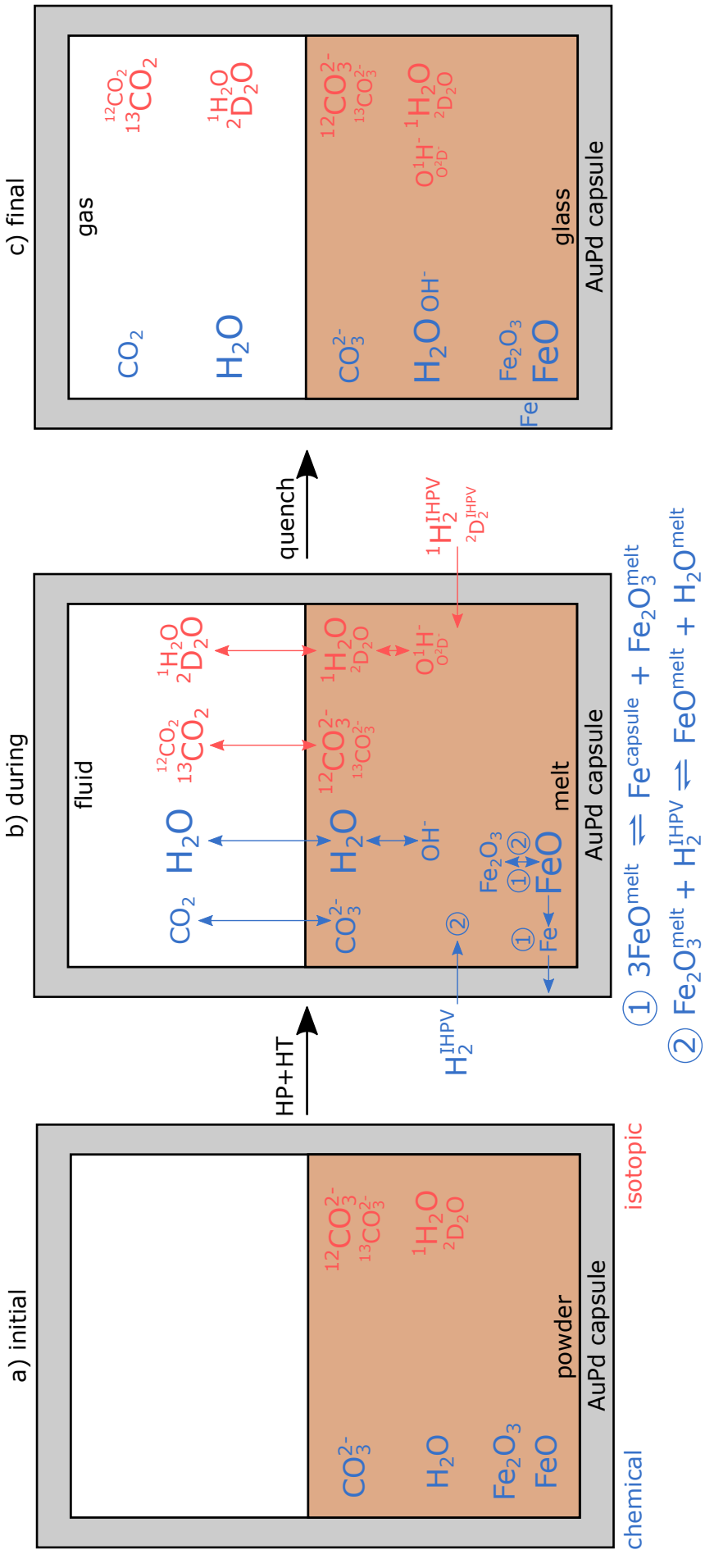


**Figure 5.4:** Schematic illustration of the capsule showing the chemical (blue) and isotopic (red) reactions occurring between the IHPV, AuPd capsule, melt, and fluid during glass synthesis. (**a**) Initial capsule containing the starting powder. (**b**) During glass synthesis, when the capsule is in the IHPV at high-pressure and high-temperature (HP+HT). The starting powder melts and volatiles exsolve into an additional fluid phase. $H_2O$ is dissolved in the melt as both molecular $H_2O$ and $OH^-$. The volatiles isotopically fractionate between the fluid and melt. $H_2$ infiltrates into the capsule from the IHPV, and the rate of diffusion through the capsule is different for $^1H$ and $^2D$. FeO in the melt disproportionates into Fe, which forms an allow with the AuPd capsule, and $Fe_2O_3$ (Reaction 1). Also, the infiltrating $H_2$ combines with $Fe_2O_3$ to produce FeO (Reaction 2). (**c**) The capsule is quenched, and the melt forms a glass, which is analysed.

### 5.2.2. Preparation of the starting powders

Starting powders were made with the compositions in Table 5.6, in multiple batches as outlined. To avoid a decarbonation step, starting powders were made of a mechanical mixture of albite, anorthite, sanidine, fayalite, wollastonite, $SiO_2$, MnO, MgO, $TiO_2$, $Fe_2O_3$, and $Ca_3(PO_4)_2$ powders. Additionally, water was used as a solvent during grinding in an agate mortar for 30 mins under a heat lamp. To try and minimise any flux of $H_2$ into or out of the capsule during the experiments, the ratio of fayalite to $Fe_2O_3$ in all starting powders was chosen to give a $Fe^{2+}/Fe_T$ of 0.5 to match the assumed intrinsic $fO_2$ imposed during the experiment. The mixture was dried overnight (~100 °C) before powdered $CaCO_3$ was added either as Seaford Head Chalk (SHC, +1.99 ± 0.03 ‰), Oka carbonatite calcite (OKA, -5.43 ± 0.02 ‰) or a 50:50 mechanical mixture of the two (-1.81 ± 0.02 ‰) (Section 4.2.1 and Table 4.2).

### 5.2.3. Carbon-sulphur analyser

As a method to check the weighed-in concentrations of $CO_2$ in the starting powders, the carbon concentration (and sulphur, although not reported) of the starting powders, and the albite powder, were measured using a carbon-sulphur analyser (CSA). Samples are melted at temperatures >1800 °C to release all the carbon in the sample. The carbon is then oxidised to allow the concentration of $CO_2$ to be measured using infra-red spectroscopy. Unfortunately, this measures all the carbon in the sample, which for starting powders may include contamination after the batch was prepared. Powders are needed for CSA to ensure complete melting, hence starting powders and the albite powder were measured without further preparation.

Analyses were made using the ELTRA CS800 analyzer at the Institut für Mineralogie, Leibniz Universität Hannover, Germany. Prior to analysis, powders were dried in an ~100 °C and the ceramic crucibles used for analysis were baked at ~1200 °C . Samples were weighed into a ceramic crucible, then chips of iron and tungsten were added to aid melting and oxidation of the sample during combustion. The ceramic crucible was placed in a sealed furnace and heated via an induction coil to melt the sample. Blank runs were performed with ceramic crucibles containing just iron and tungsten chips. Steel standards were used for calibration (Figure 5.5) and run throughout the session to check for instrument drift. As the technique involves complete release of $CO_2$ in the sample through combustion there should be no matrix effect, therefore steel standards can be used for glass analysis. Where possible, multiple analyses of a single starting powder were made to ensure reproducibility of the measurement.

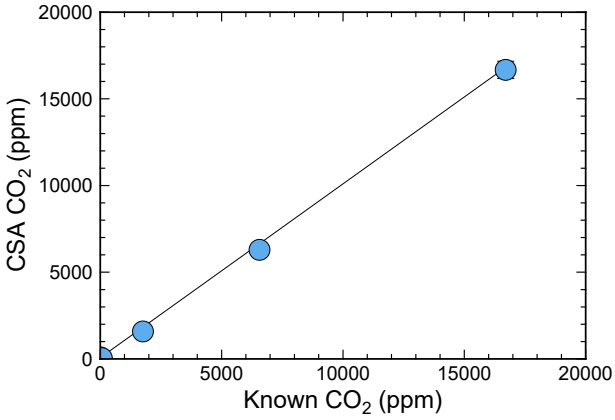


**Figure 5.5:** CSA calibration curve for $CO_2$ concentration using steel standards: 285-2 (66 ± 7 ppm $CO_2$), 281-1 (1759 ± 73 ppm $CO_2$), 92400-4010 (6559 ± 110 ppm $CO_2$), and 030-4 (16708 ± 147 ppm $CO_2$). Errors of one standard deviation are smaller than the symbols

### 5.2.4. Experimental synthesis of the glasses

The starting powders were dried overnight (~100 °C) before being loaded into $Au_{80}Pd_{20}$ capsules, which were 3 mm in diameter by ~15 mm in length and contained ~50 mg of starting powder. Water was added as $H_2O$ dispersed throughout the capsule via microsyringe, but $H_2O$ concentration was measured based on weight rather than volume. The initial composition of the material in the capsules based on the weighed-in powders is given in Table 5.6. Capsules were flat welded shut at each end. Capsules were immersed in water at ~50 °C, then put in a ~100 °C oven for ~10 minutes, to check for leaks.

Experiments were performed in the same IHPV (Blue) at the Institut für Mineralogie, Leibniz Universität Hannover, Germany, by R. Balzer. Experiments were run at 1250 °C (<5 °C variation) and 1, 3, 5, or 7 kbar (<0.02 kbar variation) using Ar gas as the pressurising medium (see Table 5.6 for details). Experiments lasted ~18 hours, except ETNA07 which was run twice: once at 7 kbar then again at 3 kbar, hence its total synthesis time was ~36 hours. Experiments were conducted under intrinsic IHPV $fO_2$ conditions, which range from NNO+2.6 (Schuessler et al., 2008) to NNO+3.5 (Berndt et al., 2002). Samples were quenched using a rapid-quench device at ~150 °C·s$^{-1}$ (Berndt et al., 2002).

After each experiment, the capsules were weighed and visually inspected to check for any leaks during the run. Capsules were opened under a binocular microscope and glass chips were selected for further analysis.

### 5.2.5. Volatile concentrations in the fluid

The concentration of volatiles in the exsolved fluid coexisting with the melt during the experimental run can be measured by analysing the fluid present in the capsule after the experiment. This assumes the composition of the exsolved fluid does not change composition after the quench (e.g., species reacting or precipitating). Visually, there was no evidence of precipitates (e.g., graphite) when the capsules were opened. Volatile concentrations are thought to be maintained, but isotope ratios may change (Mathez and Delaney, 1981; Watanabe et al., 1983), hence only the volatile concentration was measured. $CO_2$ and $H_2O$ have different freezing and boiling temperatures, hence by cooling and heating the capsule to different temperatures, and piercing it to allow the gas to escape, the weight difference can be used to measure the mass of a fluid of certain composition.

The fluids in the capsule were assumed to be $CO_2$ and $H_2O$ as these were the only volatile phases added to the starting powders. $CO_2$ has a much lower boiling point than $H_2O$, therefore capsules were frozen in liquid $N_2$ to freeze $H_2O$. Capsules were then pierced to release any $CO_2$ present as a vapour and reweighed. This cannot discriminate between $CO_2$ and $N_2$ (from the atmosphere when loading capsules), but the contribution of $N_2$ is thought to be small (Shishkina et al., 2010). Capsules were then put in a ~200 °C oven for ~10 mins to evaporate any free water, then reweighed to measure the $H_2O$ in the vapour phase. This could release $H_2O$ dissolved in the glass, but no devitrification of the glass was observed. Weights were measured to ±0.0001 g, which can result in large errors when there is little fluid present.

### 5.2.6. Thermal conversion element analyser

To measure the equilibrium isotope fractionation factor of hydrogen, the dissolved hydrogen concentration and isotope ratio of the glasses were measured. As a bulk technique, TCEA may also measure $H_2O$ absorbed onto the surface or from surface contamination. A comparison of FTIR and TCEA by Dixon et al. (2017)

found good agreement between the two techniques implying this is not a significant issue, although a slight underestimate of TCEA compared to FTIR was observed, which may be due to incomplete extraction of $H_2O$. Hydrogen was extracted from the glass using single-step pyrolysis and its concentration and isotope ratio were measured using isotope ratio mass spectrometry.

Measurements were made by I. Bindeman at Department of Earth Sciences, University of Oregon, USA, using the method of Nolan and Bindeman (2013). Glass chips were crushed to aid melting, weighed to a precision of $10^{-6}$ g and folded into silver foil capsules for analysis. $H_2O$ was extracted using a thermal combustion element analyser (TCEA). The released $H_2O$ is transferred for concentration and isotope measurement to a large radius MAT253 10 kV gas source isotope ratio mass spectrometer. $H_2O$ concentrations were calibrated using mineral standards (Table 5.4). The average accuracy (one standard deviation) of standards run during the analysis were 0.06 wt.% for $H_2O$ and 0.9 ‰ for $\delta D$.

**Table 5.4:** Mineral standards used for TCEA.

| Standard | Material | $H_2O$ (wt%) | *s.d.* | $\delta D$ (‰) | *s.d.* |
|---|---|---|---|---|---|
| NBS30[a] | Biotite | 3.5 | | -65.7 | *0.3* |
| USGS57[b] | Biotite | 3.74 | *0.02* | -91.5 | *2.4* |
| USGS58[b] | Muscovite | 4.03 | *0.02* | -28.4 | *1.6* |

*Notes:* Data from [a]Gonfiantini (1984) and [b]Qi et al. (2017). Errors, where available, of one standard deviation (*s.d.*) are in *italics*.

### 5.2.7. Secondary ion mass spectrometry

SIMS (Chapter 4) was used to measure the volatile concentration and carbon isotope ratio dissolved in the glass, to quantify the carbon isotope fractionation factors. $CO_2$ and $H_2O$ concentrations were measured as described in Section 4.2.2 for ETNA24 and $\delta^{13}C$ was measured as described in Section 4.3.2.

### 5.2.8. Electron probe micro-analysis

All EPMA (Section 2.2) data were collected on the JEOL JXA 8530F Hyperprobe using the Probe for EPMA software at the School of Earth Sciences, University of Bristol, UK. Glass chips were mounted in epoxy then ground and polished to a ~1–3 μm finish. Samples were carbon coated (~15 nm thickness) for analysis. Major and minor element chemistry was analysed as described in Section 2.5.3, with the set-up shown in Table 5.5. Fe oxidation state was measured as described in Section 3.3.2.

**Table 5.5:** Analytical details for EPMA of ETNA glasses.

| Spectrometer – Crystal | | | | |
|---|---|---|---|---|
| 1 – TAP | 2 – TAP | 3 – PETH | 4 – LIFH | 5 – PETL |
| Si$K\alpha$ (10/5) | Na$K\alpha$ (10/5) | Ca$K\alpha$ (10/5) | Fe$K\alpha$ (10/5) | K$K\alpha$ (10/5) |
| *BCR-2* | *BCR-2* | *BCR-2* | *BCR-2* | *Sanidine* |
| Al$K\alpha$ (10/5) | Mg$K\alpha$ (10/5) | Ti$K\alpha$ (10/5) | Mn$K\alpha$ (10/5) | P$K\alpha$ (10/5) |
| *BCR-2* | *BCR-2* | *$TiO_2$* | *Mn metal* | *Durango apatite* |

*Notes:* Elements in order of analysis from top to bottom, peak/background count times (s) in brackets, and primary standards under each element in *italics*, where BCR-2 is the USGS basaltic glass standard Columbia River Basalt. For each sample, 36 analyses on fresh areas of glass were averaged and no TDI correction was used. Compositions of the standards are in Tables 2.3 and 2.4.

## 5.3. Composition of the glass and fluid

Capsules did not gain or lose weight outside weighing error during the run and had convex shapes upon recovery. All capsules had small bubble imprints on the inner surface (Figure 5.6a), but the majority contained no bubbles within the glass itself (Figure 5.6b). Some of the capsules had large bubble imprints on the capsule walls, visible from the outside, and smooth glass interfaces clearly indicating the presence of a fluid (Figure 5.6a).

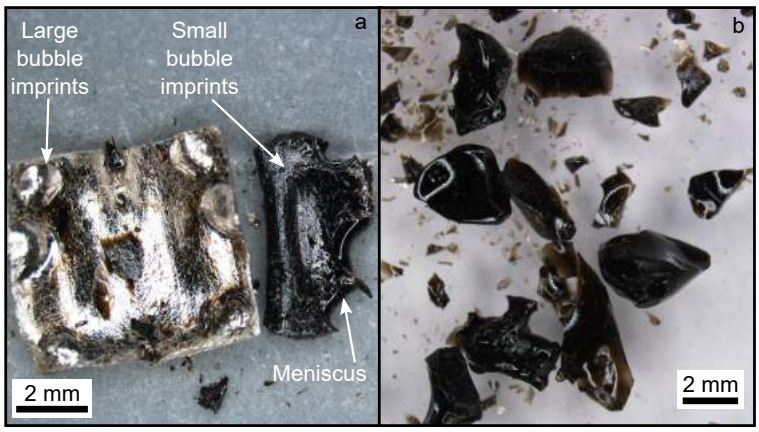


**Figure 5.6:** Example photographs of the capsules post-synthesis: **(a)** example of an opened capsule with small and large bubble imprints and the smooth surface of the meniscus between fluid and melt; and **(b)** example of the dark brown, bubble-free glassy shards typical of the run products.

All run products were dark brown and glassy with no evidence for crystals or microlites (Figure 5.6b). Magnetite nanolites were detected in some glasses using Raman spectroscopy (method is described in Section 6.3.2; results and discussion in Appendix F). Glass compositions are consistent between different starting batches, except ETNA01 which contains ~2 wt% MnO, instead of 0.20 wt%, assumed to be a weighing error. Glass compositions including volatile concentrations, isotope ratios, and Fe oxidation state; and fluid compositions are given in Table 5.6. Figure 5.7 shows the carbon and hydrogen concentrations and isotope ratios for the glass and fluid.

**Table 5.6:** Powder, glass, and fluid compositions for each experimental run.

| | Sample | ETNA01 | *s.d.* | ETNA02 | *s.d.* | ETNA03 | *s.d.* | ETNA04 | *s.d.* | ETNA05 | *s.d.* | ETNA06 | *s.d.* | ETNA07 | *s.d.* |
|---|---|---|---|---|---|---|---|---|---|---|---|---|---|---|---|
| | Batch | 4 | | 2 | | 5a | | 5a | | 5a | | 5a | | 5a | |
| | P (kbar) | 3 | | 3 | | 3 | | 7 | | 7 | | 7 | | 7, 3 | |
| | T (°C) | 1250 | | 1250 | | 1250 | | 1250 | | 1250 | | 1250 | | 1250 | |
| Initial – powders [a] | $SiO_2$ | 46.66 | *0.15* | 45.63 | *0.06* | 47.83 | *0.02* | 47.83 | *0.02* | 46.91 | *0.02* | 45.3 | *0.02* | 45.57 | *0.02* |
| | $TiO_2$ | 1.75 | *0.10* | 1.71 | *0.04* | 1.75 | *0.01* | 1.75 | *0.01* | 1.72 | *0.01* | 1.66 | *0.01* | 1.67 | *0.01* |
| | $Al_2O_3$ | 15.84 | *0.04* | 15.48 | *0.02* | 16.22 | *0.01* | 16.22 | *0.01* | 15.91 | *<0.01* | 15.37 | *<0.01* | 15.46 | *<0.01* |
| | $Fe_2O_3$ | 5.75 | *0.10* | 5.52 | *0.04* | 5.75 | *0.01* | 5.75 | *0.01* | 5.64 | *0.01* | 5.45 | *0.01* | 5.48 | *0.01* |
| | FeO | 5.08 | *0.07* | 4.92 | *0.03* | 5.17 | *0.01* | 5.17 | *0.01* | 5.07 | *0.01* | 4.9 | *0.01* | 4.93 | *0.01* |
| | MnO | 0.29 | *0.10* | 0.19 | *0.04* | 0.2 | *0.01* | 0.2 | *0.01* | 0.2 | *0.01* | 0.19 | *0.01* | 0.19 | *0.01* |
| | MgO | 5.85 | *0.10* | 5.68 | *0.04* | 5.89 | *0.01* | 5.89 | *0.01* | 5.77 | *0.01* | 5.58 | *0.01* | 5.61 | *0.01* |
| | CaO | 10.55 | *0.08* | 10.24 | *0.04* | 10.73 | *0.02* | 10.73 | *0.02* | 10.52 | *0.01* | 10.16 | *0.01* | 10.22 | *0.01* |
| | $Na_2O$ | 3.34 | *0.01* | 3.26 | *<0.01* | 3.42 | *<0.01* | 3.42 | *<0.01* | 3.36 | *<0.01* | 3.24 | *<0.01* | 3.26 | *<0.01* |
| | $K_2O$ | 1.88 | *0.02* | 1.85 | *0.01* | 1.94 | *<0.01* | 1.94 | *<0.01* | 1.9 | *<0.01* | 1.84 | *<0.01* | 1.85 | *<0.01* |
| | $P_2O_5$ | 0.62 | *0.05* | 0.56 | *0.02* | 0.59 | *0.01* | 0.59 | *0.01* | 0.58 | *0.01* | 0.56 | *0.01* | 0.56 | *0.01* |
| | $H_2O$ | 2.39 | *0.27* | 4.75 | *0.16* | 0 | | 0 | | 1.94 | *0.22* | 5.3 | *0.20* | 4.72 | *0.21* |
| | $CO_2$ (ppm) | 0 | | 2010 | *167* | 5011 | *88* | 5011 | *88* | 4914 | *86* | 4746 | *83* | 4774 | *84* |
| | $\delta^{13}C$ (‰) | | | -1.81 | *0.02* | -1.81 | *0.02* | -1.81 | *0.02* | -1.81 | *0.02* | -1.81 | *0.02* | -1.81 | *0.02* |
| | $Fe^{2+}/Fe_T$ | 0.50 | *0.01* | 0.50 | *<0.01* | 0.50 | *<0.01* | 0.50 | *<0.01* | 0.50 | *<0.01* | 0.50 | *<0.01* | 0.50 | *<0.01* |
| Final – glass [b] | $SiO_2$ | 48.88 | *0.11* | 49.47 | *0.14* | 48.25 | *0.10* | 49.10 | *0.12* | 48.26 | *0.11* | 47.47 | *0.13* | 47.68 | *0.10* |
| | $TiO_2$ | 1.84 | *0.02* | 1.64 | *0.03* | 1.53 | *0.02* | 1.65 | *0.02* | 1.63 | *0.03* | 1.59 | *0.03* | 1.62 | *0.02* |
| | $Al_2O_3$ | 17.06 | *0.07* | 17.23 | *0.05* | 16.83 | *0.07* | 17.02 | *0.07* | 16.74 | *0.06* | 16.65 | *0.06* | 16.67 | *0.06* |
| | $FeO_T$ | 8.61 | *0.08* | 9.62 | *0.08* | 9.48 | *0.08* | 9.75 | *0.08* | 9.79 | *0.07* | 9.70 | *0.08* | 9.75 | *0.08* |
| | MnO | 1.92 | *0.04* | 0.27 | *0.02* | 0.30 | *0.03* | 0.28 | *0.03* | 0.28 | *0.02* | 0.27 | *0.02* | 0.27 | *0.02* |
| | MgO | 5.41 | *0.04* | 5.84 | *0.05* | 5.74 | *0.05* | 5.92 | *0.06* | 5.82 | *0.05* | 5.70 | *0.05* | 5.75 | *0.06* |
| | CaO | 7.04 | *0.04* | 6.89 | *0.04* | 6.53 | *0.05* | 6.85 | *0.04* | 6.72 | *0.04* | 6.66 | *0.04* | 6.66 | *0.03* |
| | $Na_2O$ | 3.92 | *0.07* | 4.00 | *0.06* | 3.75 | *0.07* | 3.99 | *0.06* | 3.86 | *0.06* | 3.63 | *0.07* | 3.69 | *0.06* |
| | $K_2O$ | 1.79 | *0.02* | 1.81 | *0.02* | 1.78 | *0.02* | 1.79 | *0.02* | 1.76 | *0.02* | 1.74 | *0.02* | 1.77 | *0.02* |
| | $P_2O_5$ | 0.55 | *0.04* | 0.52 | *0.03* | 0.46 | *0.03* | 0.51 | *0.03* | 0.49 | *0.03* | 0.50 | *0.03* | 0.50 | *0.03* |
| | $H_2O$ [c] | 2.37 | *0.06* | 2.16 | *0.07* | 5.09 | *0.05* | 2.47 | *0.05* | 3.87 | *0.15* | 5.85 | *0.08* | 5.63 | *0.03* |
| | $H_2O$ [d] | 2.53 | *0.06* | 2.20 | *0.06* | 5.01 | *0.06* | 2.32 | *0.06* | 3.80 | *0.06* | 5.60 | *0.06* | 5.21 | *0.06* |
| | $\delta D$ [d] (‰) | -128.4 | *0.9* | -132.3 | *0.9* | -126.6 | *0.9* | -135.2 | *0.9* | -132.1 | *0.9* | -124.8 | *0.9* | -127.9 | *0.9* |
| | $CO_2$ [c] (ppm) | 745 | *40* | 929 | *32* | 494 | *2* | 2862 | *47* | 2596 | *128* | 360 | *19* | 484 | *43* |
| | $\delta^{13}C$ [e] (‰) | -24.7 | *2.8* | | | | | -15.2 | *1.2* | -13.3 | *0.7* | | | | |
| | $Fe^{2+}/Fe_T$ | 0.71 | *0.08* | 0.74 | *0.07* | | | 0.75 | *0.07* | 0.64 | *0.07* | 0.68 | *0.07* | 0.54 | *0.07* |
| [f] | $H_2O$ [d] (g) | -0.0001 | *0.0001* | -0.0001 | *0.0001* | -0.0001 | *0.0001* | 0.0001 | *0.0001* | 0.0000 | *0.0001* | 0.0000 | *0.0001* | -0.0001 | *0.0001* |
| | $CO_2$ [d] (g) | 0.0002 | *0.0001* | 0.0004 | *0.0001* | 0.0005 | *0.0001* | 0.0004 | *0.0001* | 0.0002 | *0.0001* | 0.0012 | *0.0001* | 0.0012 | *0.0001* |

**Table 5.6:** Powder, glass, and fluid compositions for each experimental run *cont.*

| | Sample | ETNA08 | *s.d.* | ETNA09 | *s.d.* | ETNA10 | *s.d.* | ETNA11 | *s.d.* | ETNA12 | *s.d.* | ETNA13 | *s.d.* | ETNA14 | *s.d.* |
|---|---|---|---|---|---|---|---|---|---|---|---|---|---|---|---|
| | Batch | 5a | | 5b | | 5c | | 3 | | 5a | | 5a | | 5a | |
| | P (kbar) | 7 | | 7 | | 7 | | 3 | | 1 | | 1 | | 1 | |
| | T (°C) | 1250 | | 1250 | | 1250 | | 1250 | | 1250 | | 1250 | | 1250 | |
| Initial – powders [a] | $SiO_2$ | 45.32 | *0.02* | 46.79 | *0.02* | 46.76 | *0.02* | 46.52 | *0.10* | 47.83 | *0.02* | 46.91 | *0.02* | 45.62 | *0.02* |
| | $TiO_2$ | 1.66 | *0.01* | 1.71 | *0.01* | 1.71 | *0.01* | 1.68 | *0.06* | 1.75 | *0.01* | 1.72 | *0.01* | 1.67 | *0.01* |
| | $Al_2O_3$ | 15.37 | *<0.01* | 15.87 | *<0.01* | 15.86 | *<0.01* | 15.8 | *0.03* | 16.22 | *0.01* | 15.91 | *<0.01* | 15.47 | *<0.01* |
| | $Fe_2O_3$ | 5.45 | *0.01* | 5.63 | *0.01* | 5.62 | *0.01* | 5.69 | *0.06* | 5.75 | *0.01* | 5.64 | *0.01* | 5.48 | *0.01* |
| | FeO | 4.90 | *0.01* | 5.06 | *0.01* | 5.06 | *0.01* | 5.06 | *0.05* | 5.17 | *0.01* | 5.07 | *0.01* | 4.94 | *0.01* |
| | MnO | 0.19 | *0.01* | 0.20 | *0.01* | 0.20 | *0.01* | 0.19 | *0.06* | 0.20 | *0.01* | 0.20 | *0.01* | 0.19 | *0.01* |
| | MgO | 5.58 | *0.01* | 5.76 | *0.01* | 5.76 | *0.01* | 5.75 | *0.06* | 5.89 | *0.01* | 5.77 | *0.01* | 5.62 | *0.01* |
| | CaO | 10.17 | *0.01* | 10.47 | *0.06* | 10.47 | *0.06* | 10.49 | *0.06* | 10.73 | *0.02* | 10.52 | *0.01* | 10.23 | *0.01* |
| | $Na_2O$ | 3.24 | *<0.01* | 3.35 | *<0.01* | 3.35 | *<0.01* | 3.32 | *0.01* | 3.42 | *<0.01* | 3.36 | *<0.01* | 3.26 | *<0.01* |
| | $K_2O$ | 1.84 | *<0.01* | 1.90 | *<0.01* | 1.89 | *<0.01* | 1.89 | *0.01* | 1.94 | *<0.01* | 1.90 | *<0.01* | 1.85 | *<0.01* |
| | $P_2O_5$ | 0.56 | *0.01* | 0.58 | *0.01* | 0.58 | *0.01* | 0.59 | *0.03* | 0.59 | *0.01* | 0.58 | *0.01* | 0.56 | *0.01* |
| | $H_2O$ | 5.24 | *0.18* | 2.22 | *0.22* | 2.29 | *0.23* | 2.69 | *0.22* | 0 | | 1.94 | *0.24* | 4.63 | *0.22* |
| | $CO_2$ (ppm) | 4748 | *83* | 4733 | *430* | 4730 | *430* | 3127 | *284* | 5011 | *88* | 4914 | *86* | 4779 | *84* |
| | $\delta^{13}C$ (‰) | -1.81 | *0.02* | +1.99 | *0.03* | -5.43 | *0.02* | -1.81 | *0.02* | -1.81 | *0.02* | -1.81 | *0.02* | -1.81 | *0.02* |
| | $Fe^{2+}/Fe_T$ | 0.50 | *<0.01* | 0.50 | *<0.01* | 0.50 | *<0.01* | 0.50 | *0.01* | 0.50 | *<0.01* | 0.50 | *<0.01* | 0.50 | *<0.01* |
| Final – glass [b] | $SiO_2$ | 47.20 | *0.10* | 48.64 | *0.12* | 48.64 | *0.12* | 48.98 | *0.13* | 49.76 | *0.11* | 49.04 | *0.13* | 48.86 | *0.11* |
| | $TiO_2$ | 1.58 | *0.03* | 1.56 | *0.02* | 1.58 | *0.03* | 1.63 | *0.03* | 1.67 | *0.02* | 1.65 | *0.02* | 1.64 | *0.03* |
| | $Al_2O_3$ | 16.46 | *0.06* | 16.75 | *0.07* | 16.78 | *0.05* | 16.86 | *0.06* | 17.17 | *0.07* | 17.01 | *0.09* | 17.00 | *0.08* |
| | $FeO_T$ | 9.63 | *0.08* | 9.57 | *0.07* | 9.68 | *0.08* | 9.94 | *0.09* | 9.70 | *0.07* | 9.84 | *0.08* | 9.79 | *0.09* |
| | MnO | 0.27 | *0.02* | 0.25 | *0.02* | 0.27 | *0.02* | 0.04 | *0.01* | 0.28 | *0.02* | 0.28 | *0.02* | 0.27 | *0.02* |
| | MgO | 5.63 | *0.05* | 5.60 | *0.05* | 5.71 | *0.06* | 6.22 | *0.06* | 5.85 | *0.07* | 5.81 | *0.06* | 5.79 | *0.06* |
| | CaO | 6.58 | *0.04* | 6.91 | *0.04* | 6.77 | *0.04* | 6.60 | *0.03* | 6.90 | *0.04* | 6.84 | *0.03* | 6.76 | *0.04* |
| | $Na_2O$ | 3.53 | *0.07* | 3.85 | *0.07* | 3.87 | *0.06* | 3.91 | *0.05* | 3.94 | *0.07* | 3.87 | *0.06* | 3.88 | *0.06* |
| | $K_2O$ | 1.72 | *0.02* | 1.77 | *0.02* | 1.77 | *0.02* | 1.82 | *0.01* | 1.82 | *0.02* | 1.79 | *0.01* | 1.80 | *0.02* |
| | $P_2O_5$ | 0.50 | *0.03* | 0.48 | *0.03* | 0.49 | *0.03* | 0.29 | *0.03* | 0.52 | *0.03* | 0.52 | *0.03* | 0.51 | *0.03* |
| | $H_2O^c$ | 6.08 | *0.06* | 3.67 | *0.05* | 3.77 | *0.14* | 3.22 | *0.05* | 2.19 | *0.01* | 2.97 | *0.05* | 3.47 | *0.1* |
| | $H_2O^d$ | 6.25 | *0.05* | 3.70 | *0.06* | 4.09 | *0.06* | 3.11 | *0.06* | 1.95 | *0.06* | 2.83 | *0.06* | 3.19 | *0.06* |
| | $\delta D^d$ (‰) | -130.9 | *0.9* | -131.2 | *0.9* | -128.2 | *0.9* | -127.2 | *0.9* | -124.8 | *0.9* | -125.3 | *0.9* | -119.3 | *0.9* |
| | $CO_2^c$ (ppm) | 2321 | *48* | 2535 | *114* | 2341 | *164* | 859 | *14* | 252 | *15* | 116 | *6* | 63 | *16* |
| | $\delta^{13}C^e$ (‰) | -14.2 | *0.8* | -12.6 | *3.3* | -19.4 | *1.2* | | | -10.5 | *3.8* | -17.6 | *2.3* | -15.2 | *2.6* |
| | $Fe^{2+}/Fe_T$ | 0.55 | *0.07* | 0.72 | *0.07* | 0.69 | *0.07* | 0.72 | *0.07* | 0.74 | *0.07* | 0.75 | *0.07* | 0.70 | *0.07* |
| [f] | $H_2O^d$ (g) | 0.0001 | *0.0001* | 0.0000 | *0.0001* | 0.0002 | *0.0001* | 0.0002 | *0.0001* | 0.0000 | *0.0001* | 0.0002 | *0.0001* | 0.0003 | *0.0001* |
| | $CO_2^d$ (g) | 0.0005 | *0.0001* | 0.0001 | *0.0001* | 0.0002 | *0.0001* | 0.0004 | *0.0001* | 0.0003 | *0.0001* | 0.0009 | *0.0001* | 0.0019 | *0.0001* |

**Table 5.6:** Powder, glass, and fluid compositions for each experimental run *cont.*

| | Sample | ETNA15 | *s.d.* | ETNA16 | *s.d.* | ETNA17 | *s.d.* | ETNA25 | *s.d.* | ETNA26 | *s.d.* | ETNA27 | *s.d.* | ETNA28 | *s.d.* |
|---|---|---|---|---|---|---|---|---|---|---|---|---|---|---|---|
| | Batch | 2 | | 2 | | 2 | | 7 | | 7 | | 7 | | 7 | |
| | P (kbar) | 1 | | 1 | | 1 | | 5 | | 5 | | 5 | | 5 | |
| | T (°C) | 1250 | | 1250 | | 1250 | | 1250 | | 1250 | | 1250 | | 1250 | |
| Initial – powders [a] | $SiO_2$ | 47.9 | *0.06* | 45.58 | *0.06* | 46.95 | *0.06* | 47.83 | *0.02* | 47.26 | *0.02* | 46.8 | *0.02* | 45.83 | *0.01* |
| | $TiO_2$ | 1.8 | *0.04* | 1.71 | *0.04* | 1.76 | *0.04* | 1.76 | *0.01* | 1.74 | *0.01* | 1.72 | *0.01* | 1.69 | *0.01* |
| | $Al_2O_3$ | 16.25 | *0.02* | 15.47 | *0.02* | 15.93 | *0.02* | 16.22 | *<0.01* | 16.03 | *<0.01* | 15.87 | *<0.01* | 15.55 | *<0.01* |
| | $Fe_2O_3$ | 5.8 | *0.04* | 5.52 | *0.04* | 5.68 | *0.04* | 5.75 | *0.01* | 5.68 | *0.01* | 5.63 | *0.01* | 5.51 | *0.01* |
| | FeO | 5.16 | *0.03* | 4.91 | *0.03* | 5.06 | *0.03* | 5.18 | *0.01* | 5.12 | *0.01* | 5.07 | *0.01* | 4.97 | *0.01* |
| | MnO | 0.2 | *0.04* | 0.19 | *0.04* | 0.2 | *0.04* | 0.19 | *0.01* | 0.19 | *0.01* | 0.19 | *0.01* | 0.18 | *0.01* |
| | MgO | 5.96 | *0.04* | 5.67 | *0.04* | 5.84 | *0.04* | 5.91 | *0.01* | 5.84 | *0.01* | 5.78 | *0.01* | 5.66 | *0.01* |
| | CaO | 10.76 | *0.04* | 10.24 | *0.04* | 10.54 | *0.04* | 10.71 | *0.01* | 10.59 | *0.01* | 10.48 | *0.01* | 10.27 | *0.01* |
| | $Na_2O$ | 3.43 | *<0.01* | 3.26 | *<0.01* | 3.36 | *<0.01* | 3.42 | *<0.01* | 3.38 | *<0.01* | 3.35 | *<0.01* | 3.28 | *<0.01* |
| | $K_2O$ | 1.94 | *0.01* | 1.85 | *0.01* | 1.9 | *0.01* | 1.94 | *<0.01* | 1.92 | *<0.01* | 1.9 | *<0.01* | 1.86 | *<0.01* |
| | $P_2O_5$ | 0.59 | *0.02* | 0.56 | *0.02* | 0.57 | *0.02* | 0.58 | *<0.01* | 0.57 | *<0.01* | 0.57 | *<0.01* | 0.56 | *<0.01* |
| | $H_2O$ | 0 | | 4.84 | *0.21* | 2 | *0.22* | 0 | | 1.19 | *0.20* | 2.14 | *0.20* | 4.17 | *0.19* |
| | $CO_2$ (ppm) | 2110 | *176* | 2008 | *167* | 20.68 | *172* | 5055 | *44* | 4995 | *43* | 4947 | *43* | 4844 | *42* |
| | $\delta^{13}C$ (‰) | -1.81 | *0.02* | -1.81 | *0.02* | -1.81 | *0.02* | -1.81 | *0.02* | -1.81 | *0.02* | -1.81 | *0.02* | -1.81 | *0.02* |
| | $Fe^{2+}/Fe_T$ | 0.5 | *<0.01* | 0.5 | *<0.01* | 0.5 | *<0.01* | 0.5 | *<0.01* | 0.5 | *<0.01* | 0.5 | *<0.01* | 0.5 | *<0.01* |
| Final – glass [b] | $SiO_2$ | 50.50 | *0.13* | 49.10 | *0.13* | 49.35 | *0.11* | 50.03 | *0.12* | 49.10 | *0.13* | 48.32 | *0.12* | 47.81 | *0.12* |
| | $TiO_2$ | 1.61 | *0.03* | 1.57 | *0.03* | 1.58 | *0.03* | 1.78 | *0.03* | 1.74 | *0.02* | 1.74 | *0.02* | 1.69 | *0.03* |
| | $Al_2O_3$ | 17.46 | *0.08* | 17.00 | *0.08* | 17.12 | *0.07* | 17.29 | *0.06* | 17.02 | *0.07* | 16.88 | *0.08* | 16.70 | *0.08* |
| | $FeO_T$ | 9.23 | *0.08* | 9.66 | *0.08* | 9.76 | *0.09* | 8.71 | *0.07* | 9.63 | *0.07* | 10.00 | *0.08* | 9.93 | *0.09* |
| | MnO | 0.31 | *0.02* | 0.30 | *0.02* | 0.30 | *0.02* | 0.22 | *0.02* | 0.21 | *0.03* | 0.21 | *0.02* | 0.20 | *0.02* |
| | MgO | 6.05 | *0.06* | 5.90 | *0.06* | 6.01 | *0.05* | 6.49 | *0.05* | 6.26 | *0.06* | 6.22 | *0.05* | 6.05 | *0.06* |
| | CaO | 6.81 | *0.04* | 6.64 | *0.03* | 6.73 | *0.04* | 6.86 | *0.03* | 6.83 | *0.03* | 6.84 | *0.04* | 6.71 | *0.04* |
| | $Na_2O$ | 4.08 | *0.05* | 3.90 | *0.07* | 3.94 | *0.06* | 4.16 | *0.07* | 4.04 | *0.07* | 3.93 | *0.05* | 3.85 | *0.07* |
| | $K_2O$ | 1.84 | *0.02* | 1.81 | *0.02* | 1.79 | *0.02* | 1.85 | *0.02* | 1.79 | *0.02* | 1.73 | *0.01* | 1.74 | *0.02* |
| | $P_2O_5$ | 0.48 | *0.03* | 0.46 | *0.03* | 0.46 | *0.03* | 0.51 | *0.03* | 0.50 | *0.03* | 0.50 | *0.03* | 0.49 | *0.03* |
| | $H_2O^c$ | 1.58 | *0.01* | 3.30 | *0.09* | 2.85 | *0.05* | 1.59 | *0.03* | 2.13 | *0.06* | 2.80 | *0.02* | 3.80 | *0.06* |
| | $H_2O^d$ | 1.32 | *0.06* | 3.40 | *0.06* | 2.58 | *0.06* | 1.51 | *0.06* | 1.94 | *0.06* | 2.84 | *0.06* | 3.91 | *0.06* |
| | $\delta D^d$ (‰) | -125.3 | *0.9* | -117.8 | *0.9* | -124.1 | *0.9* | -166.5 | *0.9* | -165.7 | *0.9* | -168 | *0.9* | -167.1 | *0.9* |
| | $CO_2^c$ (ppm) | 312 | *13* | 51 | *19* | 151 | *7* | 2022 | *40* | 1935 | *40* | 1864 | *19* | 1787 | *41* |
| | $\delta^{13}C^e$ (‰) | | | | | | | -7.5 | *1.7* | -6 | *0.7* | -6.8 | *0.9* | -6.9 | *1.2* |
| | $Fe^{2+}/Fe_T$ | 0.81 | *0.07* | 0.69 | *0.07* | 0.75 | *0.07* | 0.90 | *0.08* | 0.80 | *0.07* | 0.78 | *0.07* | 0.75 | *0.07* |
| [f] | $H_2O^d$ (g) | 0.0001 | *0.0001* | 0.0004 | *0.0001* | 0.0000 | *0.0001* | 0.0002 | *0.0001* | 0.0002 | *0.0001* | 0.0005 | *0.0001* | 0.0004 | *0.0001* |
| | $CO_2^d$ (g) | 0.0003 | *0.0001* | 0.0011 | *0.0001* | 0.0008 | *0.0001* | 0.0002 | *0.0001* | 0.0003 | *0.0001* | 0.0001 | *0.0001* | 0.0003 | *0.0001* |

**Table 5.6:** Powder, glass, and fluid compositions for each experimental run *cont.*

| | Sample | ETNA29 | *s.d.* | ETNA30 | *s.d.* |
|---|---|---|---|---|---|
| | Batch | 7 | | 7 | |
| | P (kbar) | 5 | | 5 | |
| | T (°C) | 1250 | | 1250 | |
| Initial – powders[a] | $SiO_2$ | 46.61 | *0.02* | 45.45 | *0.01* |
| | $TiO_2$ | 1.71 | *0.01* | 1.67 | *0.01* |
| | $Al_2O_3$ | 15.81 | *<0.01* | 15.42 | *<0.01* |
| | $Fe_2O_3$ | 5.6 | *0.01* | 5.46 | *0.01* |
| | FeO | 5.05 | *0.01* | 4.92 | *0.01* |
| | MnO | 0.19 | *0.01* | 0.18 | *0.01* |
| | MgO | 5.76 | *0.01* | 5.62 | *0.01* |
| | CaO | 10.44 | *0.01* | 10.18 | *0.01* |
| | $Na_2O$ | 3.34 | *<0.01* | 3.25 | *<0.01* |
| | $K_2O$ | 1.89 | *<0.01* | 1.84 | *<0.01* |
| | $P_2O_5$ | 0.57 | *<0.01* | 0.55 | *<0.01* |
| | $H_2O$ | 2.55 | *0.20* | 4.97 | *0.19* |
| | $CO_2$ (ppm) | 4926 | *43* | 4804 | *42* |
| | $\delta^{13}C$ (‰) | -1.81 | *0.02* | -1.81 | *0.02* |
| | $Fe^{2+}/Fe_T$ | 0.5 | *<0.01* | 0.5 | *<0.01* |
| Final – glass[b] | $SiO_2$ | 48.24 | *0.12* | 47.36 | *0.22* |
| | $TiO_2$ | 1.71 | *0.03* | 1.62 | *0.03* |
| | $Al_2O_3$ | 16.77 | *0.08* | 16.63 | *0.12* |
| | $FeO_T$ | 9.91 | *0.07* | 9.66 | *0.11* |
| | MnO | 0.20 | *0.02* | 0.19 | *0.02* |
| | MgO | 6.17 | *0.04* | 5.75 | *0.06* |
| | CaO | 6.71 | *0.03* | 6.58 | *0.04* |
| | $Na_2O$ | 3.92 | *0.07* | 3.63 | *0.06* |
| | $K_2O$ | 1.76 | *0.01* | 1.72 | *0.02* |
| | $P_2O_5$ | 0.49 | *0.04* | 0.46 | *0.03* |
| | $H_2O$[c] | 3.48 | *0.04* | 5.81 | *0.04* |
| | $H_2O$[d] | 3.32 | *0.06* | 5.69 | *0.06* |
| | $\delta D$[d] (‰) | -166.6 | *0.9* | -166.5 | *0.09* |
| | $CO_2$[c] (ppm) | 1886 | *37* | 1245 | *6* |
| | $\delta^{13}C$[e] (‰) | -10.1 | *0.3* | -11.2 | *0.9* |
| | $Fe^{2+}/Fe_T$ | 0.78 | *0.07* | 0.53 | *0.07* |
| [f] | $H_2O$ (g) | 0.0001 | *0.0001* | -0.0001 | *0.0001* |
| | $CO_2$ (g) | 0.0001 | *0.0001* | 0.0004 | *0.0001* |

*Notes* : ETNA18–ETNA23 do not exist as they were lost in the post prior to glass synthesis. ETNA24 is discussed in Chapter 4. [a]Measurements are calculated from the weighed-in components of the starting powders in wt% unless specified otherwise. [b]Measurements are in wt% measured by EPMA unless specified otherwise: [c]SIMS-4f, [d]TCEA, [e]SIMS-1270. [d] is 'Final – fluid' measured using weight-loss during freezing/boiling. Errors of one standard deviation (*s.d.*) are in *italics*.

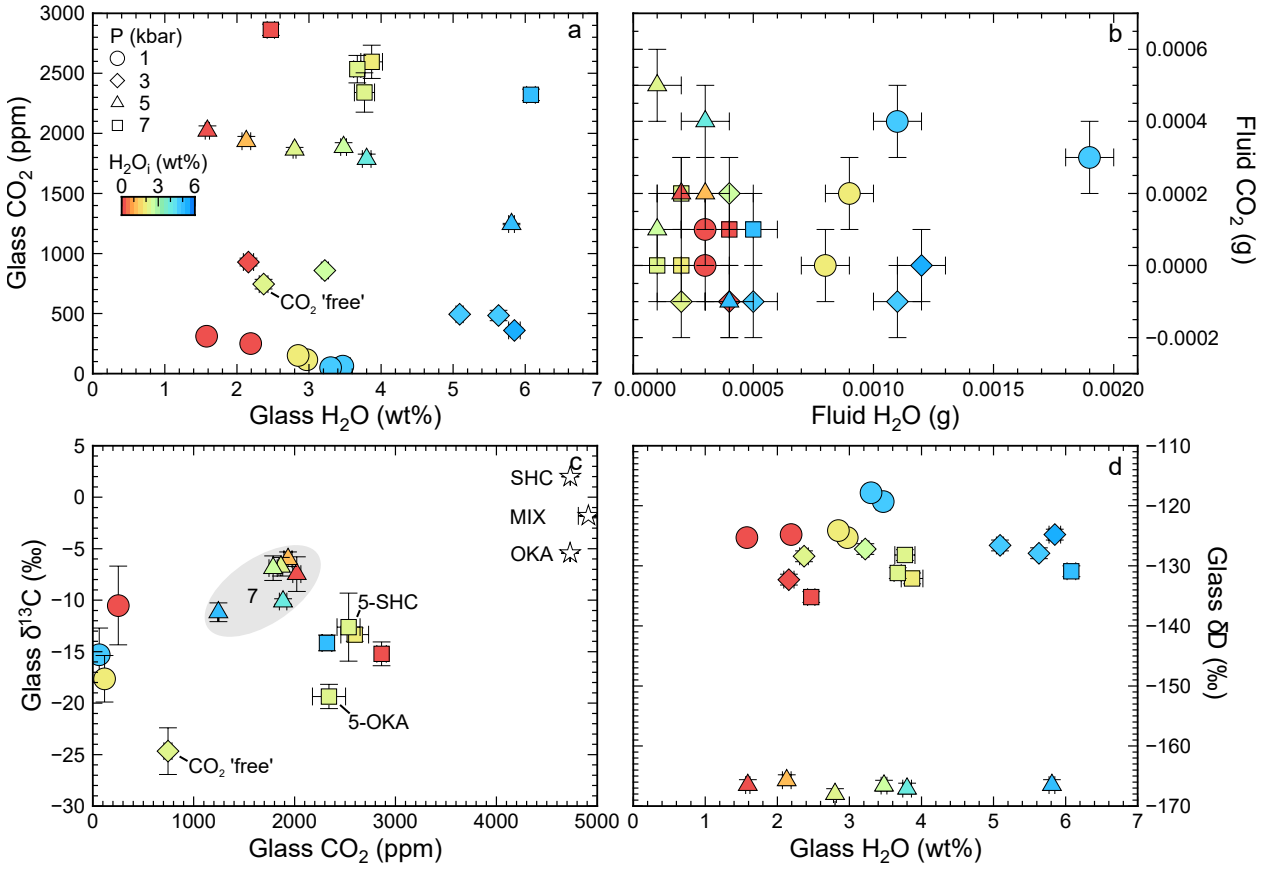


**Figure 5.7:** Volatile composition of the glass and fluid: **(a)** $CO_2$ and $H_2O$ of the glass; **(b)** $CO_2$ and $H_2O$ of the fluid; **(c)** $\delta^{13}C$ and $CO_2$ of the glass; and **(d)** $\delta D$ and $H_2O$ of the glass, where symbol shape indicates pressure and colour indicates initial $H_2O$ concentration. In **(c)** the initially loaded values (except for the $CO_2$ 'free' glass) are shown by white stars and labelled according to the type of $CaCO_3$ (Table 4.2); and different starting batches are labelled, where the six data points not labelled belong to 5a and all started with MIX unless otherwise stated.

Figure 5.8 compares the measured glass and fluid composition against various solubility models: VolatileCalc (Newman and Lowenstern, 2002), SolEx (Witham et al., 2012), and MagmaSat (Ghiorso and Gualda, 2015). All model calculations were performed at 1250 °C. VolatileCalc was modelled for a nominal 49 wt% $SiO_2$ basalt composition, whereas SolEx and MagmaSat used the average glass composition from Table 5.6 (ETNA-A in Table 3.1). MagmaSat was modelled at the extremes of potential iron oxidation states (i.e., all $Fe^{2+}$ and all $Fe^{3+}$), although these glasses contain predominantly $Fe^{2+}$ (0.5–0.9 $Fe^{2+}/Fe_T$). The isobars calculated with different models agree at low pressures, but diverge increasingly at higher pressures, with MagmaSat predicting higher solubilities than both VolatileCalc and SolEx (Figure 5.8a). MagmaSat predicts a distinct decrease in $CO_2$ solubility at low $H_2O$ concentrations (Figure 5.8a).

Figure 5.8b shows the $H_2O$-$CO_2$ data coloured by the measured $X_{H_2O}$ ($H_2O/(H_2O+CO_2)$ in moles) fluid composition, with isopleths calculated using VolatileCalc. Figure 5.8c shows $X_{H_2O}$ measured using the fluid composition compared to that calculated using VolatileCalc. $X_{H_2O}$ measured using the fluid composition has very large error bars because of the small quantities of fluids measured, but the measured fluid composition always overestimated $X_{H_2O}$ calculated using VolatileCalc. The consistent sense of discrepancy suggests that either $H_2O$ is overestimated, $CO_2$ is underestimated, or VolatileCalc is incorrect. The dissolved glass compositions agree well with VolatileCalc, hence it seems more likely there is a bias in the fluid

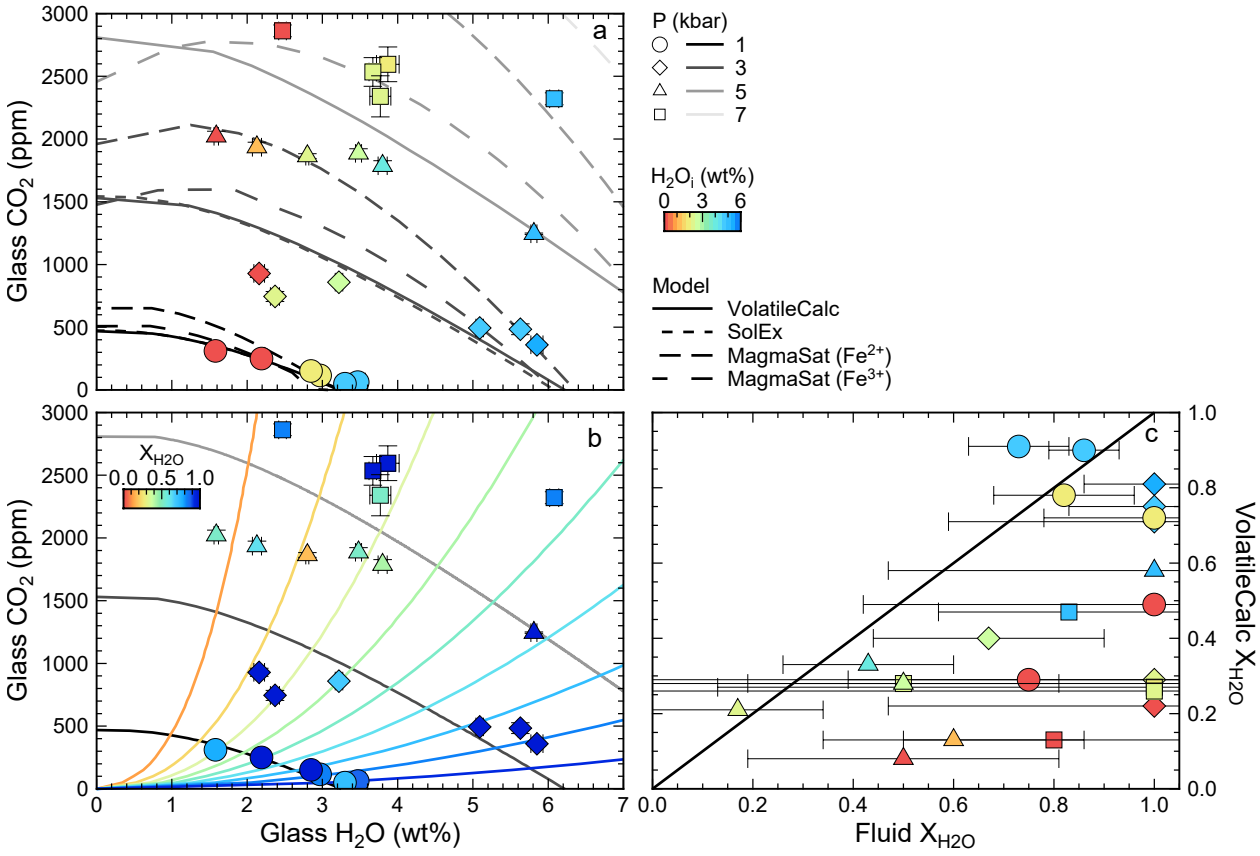


**Figure 5.8:** Comparison of measured and modelled volatile concentrations of the glass and fluids, where symbol shape indicates pressure: **(a)** glass $H_2O$ and $CO_2$ concentration coloured by initial $H_2O$ concentration, with isobars calculated using VolatileCalc, SolEx, and MagmaSat; **(b)** glass $H_2O$ and $CO_2$ concentration coloured by measured $X_{H_2O}$ of the fluid, with isobars and isopleths using VolatileCalc; and **(c)** $X_{H_2O}$ of the exsolved fluid measured using the fluid composition and calculated from the glass composition using VolatileCalc, which are coloured by initial $H_2O$ concentration and the 1-to-1 line is shown.

measurements. Fluids condense on the outside of the capsule when it is frozen in liquid $N_2$, potentially masking any $CO_2$ released, causing $CO_2$ to be underestimated. When the capsule is then put in the oven all these fluids, plus any $H_2O$, are released, which may overestimate the $H_2O$.

## 5.4. Constraining the bulk volatile composition

To calculate $\Delta_{f-m}$ using a graphical approach (Equation 5.5), the bulk concentration and isotope ratio of carbon and hydrogen need to be established.

### 5.4.1. Carbon

The $CO_2$ concentration of the starting powders as measured by CSA is significantly higher than that weighed in (8000–20000 ppm using CSA in Table 5.7 vs. 0–5000 ppm weighed-in in Table 5.6). This is due to sustained adsorption of $CO_2$ onto the powders over time as CSA was conducted almost a year after the powders were created. Hence, these $CO_2$ concentrations do not represent those at the time of the experiments. The relative errors on the fluid $CO_2$ concentrations mean that using these values to quantify the bulk $CO_2$ (i.e., fluid+glass) of the system is not possible.

**Table 5.7:** $CO_2$ concentration of starting powders using CSA.

| Batch | $CO_2$(ppm) | *s.d.* |
|---|---|---|
| 2 | 9010 | |
| 4 | 8997 | |
| 5a | 14425 | *190* |
| 5b | 16129 | *1* |
| 5c | 19490 | *83* |
| 7 | 8152 | *263* |

Experiments run at 5 (except the most hydrous glasses) and 7 kbar have $CO_2$ concentrations significantly below the isobars (Figure 5.8a), implying they are undersaturated, but contain less $CO_2$ than was initially weighed-in (Table 5.6 and Figure 5.7c). This is likely an error in the initial weighing of $CO_2$ concentration into the starting materials. Alternatively, the solubility models are vastly incorrect for this composition. The agreement with published solubility models for saturated runs at lower pressures implies chemical equilibrium between the melt and the fluid was achieved.

Notably, the $CO_2$ 'free' run (ETNA01), which had no $CaCO_3$ added to the starting powder and therefore should contain no $CO_2$, contains 745 $\pm$ 40 ppm $CO_2$ with -24.7 $\pm$ 2.3 ‰ $\delta^{13}C$. Also, all glasses are lighter (more negative) than their initial $\delta^{13}C$ (Figure 5.7c). Glasses initially loaded with OKA carbonate (-5.43 $\pm$ 0.02 ‰ $\delta^{13}C$) are lighter (more negative) than those loaded with either SHC (1.99 $\pm$ 0.03 ‰) or MIX (-1.81 $\pm$ 0.02 ‰), consistent with the lighter (more negative) isotopic source. SHC glasses are not heavier (more positive) than MIX glasses. The high $CO_2$ concentration of the $CO_2$ 'free' glass (ETNA01) requires carbon addition. The isotopic signature of ETNA01 is typical of carbon contamination. Carbon contamination is consistent with all glasses being lighter (more negative) than their initial $\delta^{13}C$, even when no degassing has occurred.

Carbon contamination may vary between starting batches, but is consistent within a starting batch. For instance, undersaturated glasses from the same starting batch run at 5 (except the most hydrous glass) and 7 kbar have similar values of anhydrous $CO_2$ and $\delta^{13}C$. Assuming: the carbon contaminant ($C_c$ $CO_2$ concentration and $R_c$ $\delta^{13}C$, which is the $^{13}C/^{12}C$ ratio rather than $\delta^{13}C$ using $\delta$-notation) is represented by ETNA01 (745 $\pm$ 40 ppm $CO_2$ with -24.7 $\pm$ 2.3 ‰ $\delta^{13}C$); the isotope ratio of the initial carbon ($R_i$) is that of the added $CaCO_3$ (Table 5.6); and the undersaturated runs represent the actual carbon composition of the starting batch after contamination ($C_b$ and $R_b$, normalised to $H_2O$-free), the $CO_2$ originally in the starting powder ($C_i$, prior to $H_2O$ addition) can be estimated using:

$$C_i = \frac{C_b R_b + C_c R_c}{R_i} \tag{5.8}$$

Starting batch 5a originally contained 1940 $\pm$ 228 ppm and starting batch 7 contained 1237 $\pm$ 58 ppm $CO_2$ prior to $H_2O$ being added (Table 5.8). Therefore, we can use undersaturated runs to constrain the bulk $CO_2$ composition for each starting batch. For starting batches 5 and 7, the initial $CO_2$ and $\delta^{13}C$ are calculated by averaging the anhydrous $CO_2$ concentration and $\delta^{13}C$ of undersaturated glasses. For starting batch 2, which does not have an undersaturated run, the anhydrous $CO_2$ composition of the highest pressure run (3 kbar) is used, and hence this bulk value is a minimum. Unfortunately, experiments where only one capsule was run (i.e., ETNA09–ETNA11) cannot be used further as there is no constraint on their initial $CO_2$ compositions.

**Table 5.8:** Calculating the $CO_2$ concentrations of the starting powders prior to contamination.

| | | Glass[a] | | | Anhydrous[c] | Initial[d] |
|---|---|---|---|---|---|---|
| Sample | $CO_2$ (ppm) | $H_2O$ (wt%) | $\delta^{13}C$ (‰) | $R^b$ | $CO_2$ (ppm) | $CO_2$ (ppm) |
| *Contaminant* | | | | | | |
| ETNA01 | 745 | 2.37 | -24.7 | 0.010960 | | |
| *Starting batch 5a* | | | -14.2 ± 0.9 | | 2702 ± 232 | 1940 ± 228 |
| ETNA04 | 2862 | 2.47 | -15.2 | 0.011066 | 2935 | 2168 |
| ETNA05 | 2569 | 3.87 | -13.3 | 0.011087 | 2700 | 1941 |
| ETNA08 | 2321 | 6.08 | -14.2 | 0.011078 | 2470 | 1712 |
| *Starting batch 7* | | | -7.6 ± 1.8 | | 1976 ± 58 | 1237 ± 58 |
| ETNA25 | 2022 | 1.59 | -7.5 | 0.011153 | 2054 | 1315 |
| ETNA26 | 1935 | 2.13 | -6.0 | 0.011169 | 1978 | 1241 |
| ETNA27 | 1864 | 2.80 | -6.8 | 0.011161 | 1917 | 1180 |
| ETNA29 | 1886 | 3.48 | -10.1 | 0.011123 | 1954 | 1210 |

*Notes:* [a]Glass values are measured using SIMS; [b]$R$ is the $^{13}C/^{12}C$ calculated from the glass $\delta^{13}C$ using Equation A.1; [c]anhydrous $CO_2$ calculated using glass $CO_2$ and $H_2O$ concentrations; [d]initial $CO_2$ calculated using Equation 5.8; and the average ± one standard deviation is calculated for each starting batch.

### 5.4.2. Hydrogen

Most glasses, except the most hydrous 1 kbar experiments, contain more $H_2O$ than was initially loaded (Figure 5.7a). Also, the Fe concentration of the glass was less, and the Fe oxidation state more reduced, than the initial values (Figure 5.9). These observations all indicate that the initial $H_2O$ composition of the capsules was modified by $H_2$ infiltration into the capsule due to the $fH_2$ gradient between the IHPV and the capsule as described in Section 5.2.1 via Equations 5.6 and 5.7. Hence, Fe was lost to the capsule wall, $Fe_2O_3$ in the melt was reduced, and the bulk $H_2O$ became higher than that initially loaded. As $H_2O$ was loaded into each capsule individually, and $H_2$ gain can differ for each capsule, undersaturated runs cannot be used to constrain the initial $H_2O$ concentration and $\delta D$ for families of experiments as done for $CO_2$.

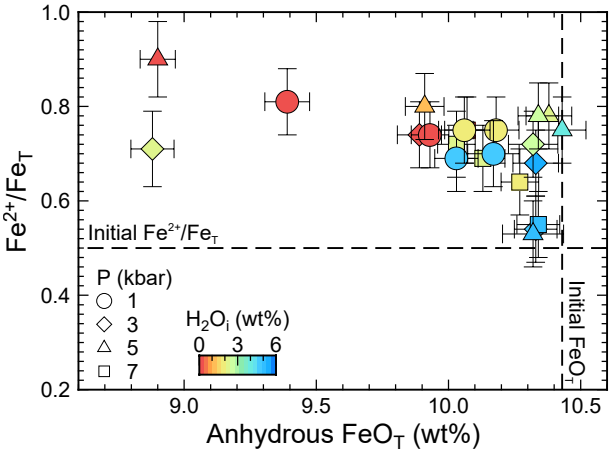


**Figure 5.9:** Fe oxidation state against anhydrous total Fe concentration ($FeO_T$, all Fe expressed as FeO) of the glass, where symbol shape indicates pressure and colour indicates initial $H_2O$ concentration. Initial, weighed-in values are shown as dashed lines.

There are three ways to estimate the total $H_2O$ budget of the capsules (Section 5.2.1). Firstly, the melt and fluid $H_2O$ concentrations can simply be added together (fluid+glass), as more $H_2O$ was present in the fluid phase than for $CO_2$ (Figure 5.7b). Although the relative errors are smaller on the fluid composition than for $CO_2$, there may be a systematic overestimation as discussed in Section 5.3. Secondly, as described by Equations 5.6 and 5.7, we can use the initial weighed-in and final measured $FeO_T$, $Fe^{2+}/Fe_T$, and $H_2O$, to calculate the $H_2O$ added due to Fe loss and reduction.

Thirdly, we can use graphical tie-line analysis (GTLA) described in Section 5.2.1. For this, the melt composition is the measured $H_2O$ and $CO_2$ in the glass; the fluid composition is calculated using VolatileCalc from the glass volatile concentrations; the initial $H_2O$ concentration is the weighed-in $H_2O$; the initial $CO_2$ concentration is that estimated from undersaturated runs as described in Section 5.4.1; and the added component (i.e., $H_2$ diffusing through the capsule) is pure $H_2O$. As initial $CO_2$ concentration is required, only experiments with well-constrained initial $CO_2$ can be used, which are shown in Figure 5.10.

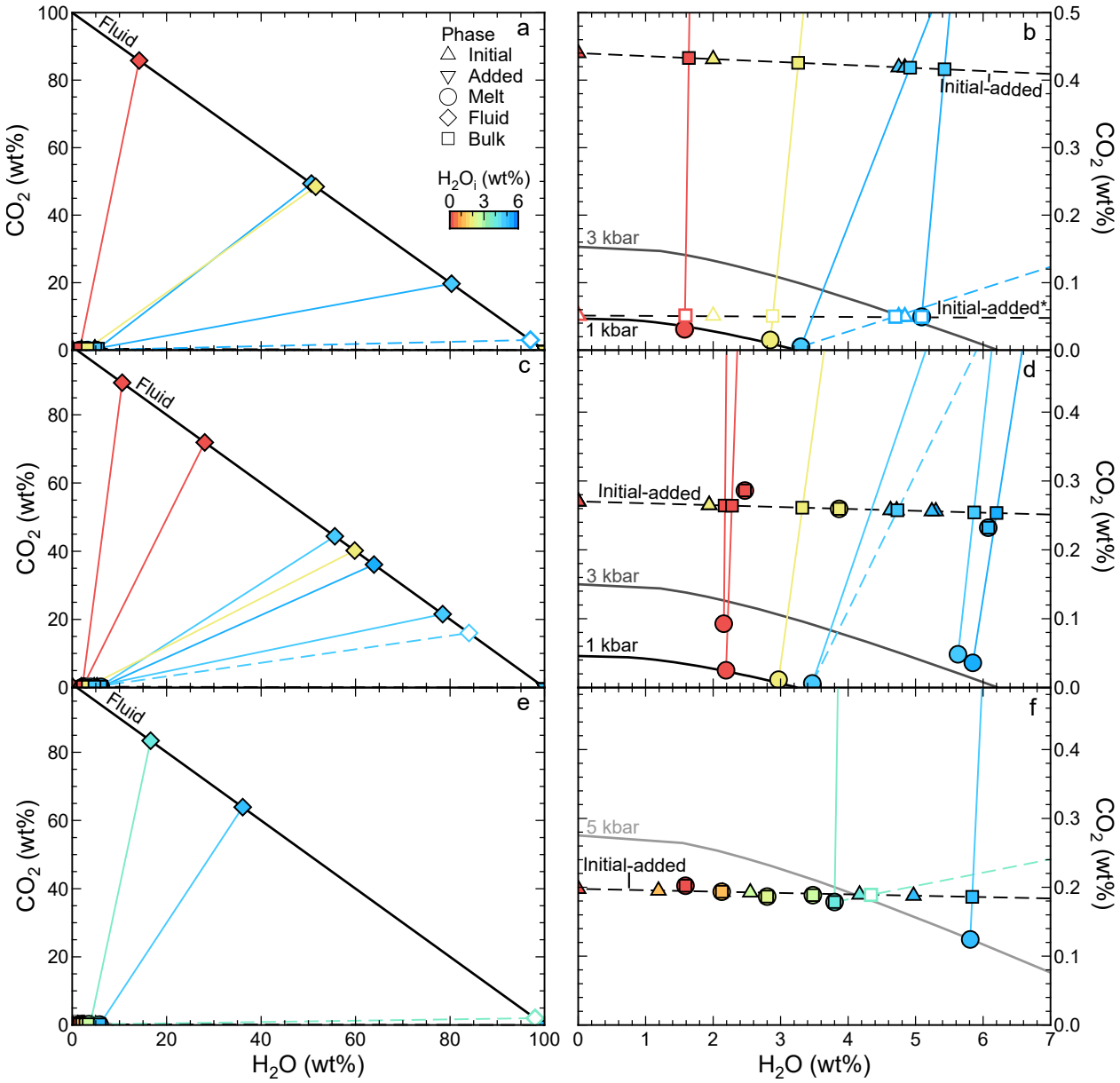


**Figure 5.10:** Graphical tie-line analysis (GTLA) for calculating bulk volatile concentration. Left panels show the fluid composition as calculated using VolatileCalc (filled symbols) or modified as described in the text (open symbols), whilst right panels show the melt and bulk values. The fluid composition must lie on the black line in the left panels. Isobars are shown in the right panels as solid, curved lines. Tie-lines connecting the initial volatile composition and the added component (100 wt% $H_2O$) are dashed lines. Tie-lines connecting the melt and fluid compositions are coloured lines, where solid lines use VolatileCalc calculated fluid compositions, whilst dashed lines use modified fluid compositions as discussed in the text. Results are shown for batch **(a)**–**(b)** 2, **(c)**–**(d)** 5a, and **(e)**–**(f)** 7 (Table 5.6). Symbol shape indicates phase, colour indicates initial $H_2O$ concentration, and open/closed indicates whether VolatilCalc or modified fluid compositions are used.

Only compositions on the tie-lines connecting two components are possible from a mixture of the two components (e.g., fluid-melt or initial-added). Therefore, crossing tie-lines means there is a unique bulk $H_2O$ and $CO_2$ concentration which satisfies the composition of the fluid-melt and initial-added components. Hence, if the tie-lines do not cross, there is no bulk $H_2O$ and $CO_2$ concentration which can explain the composition of all components. For batch 2, only the minimum initial $CO_2$ is known. Using this minimum, one saturated experiment does not have crossing tie-lines and requires modifying the fluid composition from 80 wt% $H_2O$ and 20 wt% $CO_2$ to 97 wt% $H_2O$ and 3 wt% $CO_2$ (Figure 5.10a). On the other hand, if we assume VolatileCalc calculates the correct fluid composition, the minimum initial $CO_2$ required for the tie-lines to cross is an order of magnitude larger (~4000 ppm) (Figure 5.10b). Although this $CO_2$ concentration is possible, it does not change the bulk $H_2O$ greatly. For batch 5a, all but one saturated experiment have crossing tie-lines (Figure 5.10d). By changing the fluid composition slightly, from 78 wt% $H_2O$ and 22 wt% $CO_2$ to 84 wt% $H_2O$ and 16 wt% $CO_2$ (Figure 5.10c), all tie-lines just cross. This gives a minimum estimate of the bulk $H_2O$ concentration, as the fluid composition could be more $CO_2$-rich which would have required even more $H_2O$ addition. For batch 7, one saturated experiment does not have crossing tie-lines. It may in fact not be saturated, but this would mean it gained no $H_2O$ (Figure 5.10f). The change in fluid composition to get the tie-lines to cross is large, from 17 wt% $H_2O$ and 83 wt% $CO_2$ to 98 wt% $H_2O$ and 2 wt% $CO_2$, and again represents a minimum bulk $H_2O$ (Figure 5.10e).

A comparison of the three techniques is shown in Figure 5.11, which agree fairly well. The glass $H_2O$ concentration represents the minimum bulk $H_2O$. All techniques lie close to the 1-to-1 line compared to the glass $H_2O$ concentration. This is reasonable given that most of the glasses have not undergone significant $H_2O$ degassing, hence most of the $H_2O$ is still in the glass. Using the fluid+glass composition, or GTLA, always has bulk $H_2O$ greater than the melt because of how they are calculated. Using Fe loss and reduction often estimates bulk $H_2O$ less than the glass concentration. This might imply there is an additional reduction reaction not considered occurring in the capsule. Another element may be alloying with AuPd, but no other element shows significant decrease in concentration. As the bulk $H_2O$ concentration cannot be less than the glass $H_2O$ concentration, and the $H_2O$ concentration in the fluid phase may have been overestimated, the values from GTLA are used as the most reliable.

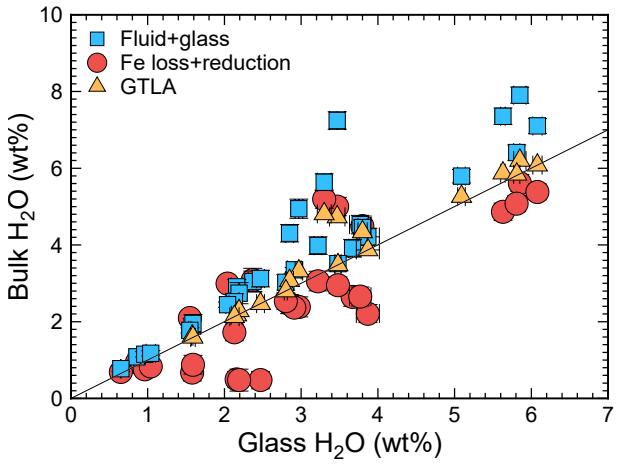


**Figure 5.11:** Comparison of bulk $H_2O$ estimates using fluid+glass, Fe loss+reduction, and graphical tie-lie approach (GTLA) against the glass $H_2O$ concentration, with the 1-to-1 line shown in black.

Constraining the total $\delta D$ of the system is more difficult as the $\delta D$ of the added $H_2O$ was not measured. Also the $\delta D$ of the $H_2$ infiltrating into the capsule is unknown and may not be constant between runs. If the system has reached isotopic equilibrium with the IHPV, the total $H_2O$ and its $\delta D$ will be controlled by the intrinsic IHPV value. If the system has not reached isotopic equilibrium with the IHPV, the $\delta D$ of the

total $H_2O$ in the capsule will be controlled by the initial δD and $H_2O$, extent of equilibrium attained ($fH_2$ gradient, temperature and time dependent), relative diffusivities of $H_2$ and $D_2$ (temperature and pressure dependent), and IHPV δD (experiment date and IHPV).

ETNA07, which was run for ~36 hours, has a similar $H_2O$ and δD to equivalent ~18 hours runs. Therefore, it appears diffusion into the capsule was kinetically-driven and little isotopic equilibration occurred between the IHPV and the capsule. If isotopic equilibrium had been achieved between the IHPV and the capsule, undersaturated runs would have the same δD regardless of the initial $H_2O$ concentration, but δD becomes heavier (more positive) with increasing $H_2O$ (Figure 5.7d). This is likely because the driving force to chemically equilibrate the $H_2O$ concentration between the IHPV and the capsule is much larger than the driving force to equilibrate the isotopic difference. Hence, H equilibrium is achieved, but D equilibrium is not. Because of this, the δD of the bulk $H_2O$ in the system is given by:

$$R_bH_b = R_iH_i + R_a(H_b - H_i) \tag{5.9}$$

where R is the isotope ratio expressed as D/H; H is the $H_2O$ concentration; and the subscripts refer to the bulk (b), initial (i), and added (a) components. The initial $H_2O$ is the weighed-in value and the bulk $H_2O$ is the value from either fluid+glass or GTLA (Figure 5.11). The isotope ratio of the added component is assumed to be the same for capsules run during the same experiment. This is constrained using initially anhydrous experiments, which have experienced little/no degassing. The isotope ratio of the initial $H_2O$ is assumed to be the same for 1, 3, and 7 kbar experiments, but different for the 5 kbar experiments as they have very different δD. This is constrained using undersaturated experiments.

### 5.4.3. Calculated bulk volatile compositions

For subsequent discussion, only experiments with well constrained bulk volatile composition are used (batches 2, 5a and 7). These are summarised in Table 5.9 and Figure 5.12. Excluded experiments are those for which only a single capsule was run from a batch of starting powder (ETNA01 and ETNA09–ETNA11).

**Table 5.9:** Bulk volatile compositions.

| | $CO_2$ | $\delta^{13}C$ | | $H_2O$ | δD | | $CO_2$ | $\delta^{13}C$ | | $H_2O$ | δD |
|---|---|---|---|---|---|---|---|---|---|---|---|
| Sample | (ppm) | (‰) | *s.d.* | (wt%) | (‰) | Sample | (ppm) | (‰) | *s.d.* | (wt%) | (‰) |
| *Starting batch 2* | | | | | | *Starting batch 5a* | | | | | |
| ETNA03 | 496 | -18.9 | *2.0* | 5.26 | -129.8 | ETNA02 | 2702 | -14.2 | *0.9* | 2.17 | -132.2 |
| ETNA15 | 521 | -18.9 | *2.0* | 1.62 | -125.3 | ETNA04 | 2702 | -14.2 | *0.9* | 2.47 | -135.2 |
| ETNA16 | 496 | -18.9 | *2.0* | 4.81 | -129.6 | ETNA05 | 2650 | -14.2 | *0.9* | 3.87 | -132.1 |
| ETNA17 | 506 | -18.9 | *2.0* | 3.07 | -128.1 | ETNA06 | 2559 | -14.2 | *0.9* | 6.20 | -130.0 |
| *Starting batch 7* | | | | | | ETNA07 | 2574 | -14.2 | *0.9* | 5.87 | -130.1 |
| ETNA25 | 1976 | -7.6 | *1.8* | 1.59 | -166.5 | ETNA08 | 2560 | -14.2 | *0.9* | 6.08 | -130.9 |
| ETNA26 | 1952 | -7.6 | *1.8* | 2.13 | -165.7 | ETNA12 | 2702 | -14.2 | *0.9* | 2.27 | -125.3 |
| ETNA27 | 1934 | -7.6 | *1.8* | 2.80 | -168.0 | ETNA13 | 2650 | -14.2 | *0.9* | 3.32 | -127.8 |
| ETNA28 | 1893 | -7.6 | *1.8* | 4.34 | -166.7 | ETNA14 | 2577 | -14.2 | *0.9* | 4.73 | -129.5 |
| ETNA29 | 1925 | -7.6 | *1.8* | 3.48 | -166.6 | | | | | | |
| ETNA30 | 1878 | -7.6 | *1.8* | 5.84 | -166.7 | | | | | | |

*Notes:* Errors, where available, of one standard deviation (*s.d.*) are in *italics*. $H_2O$ and δD using GTLA.

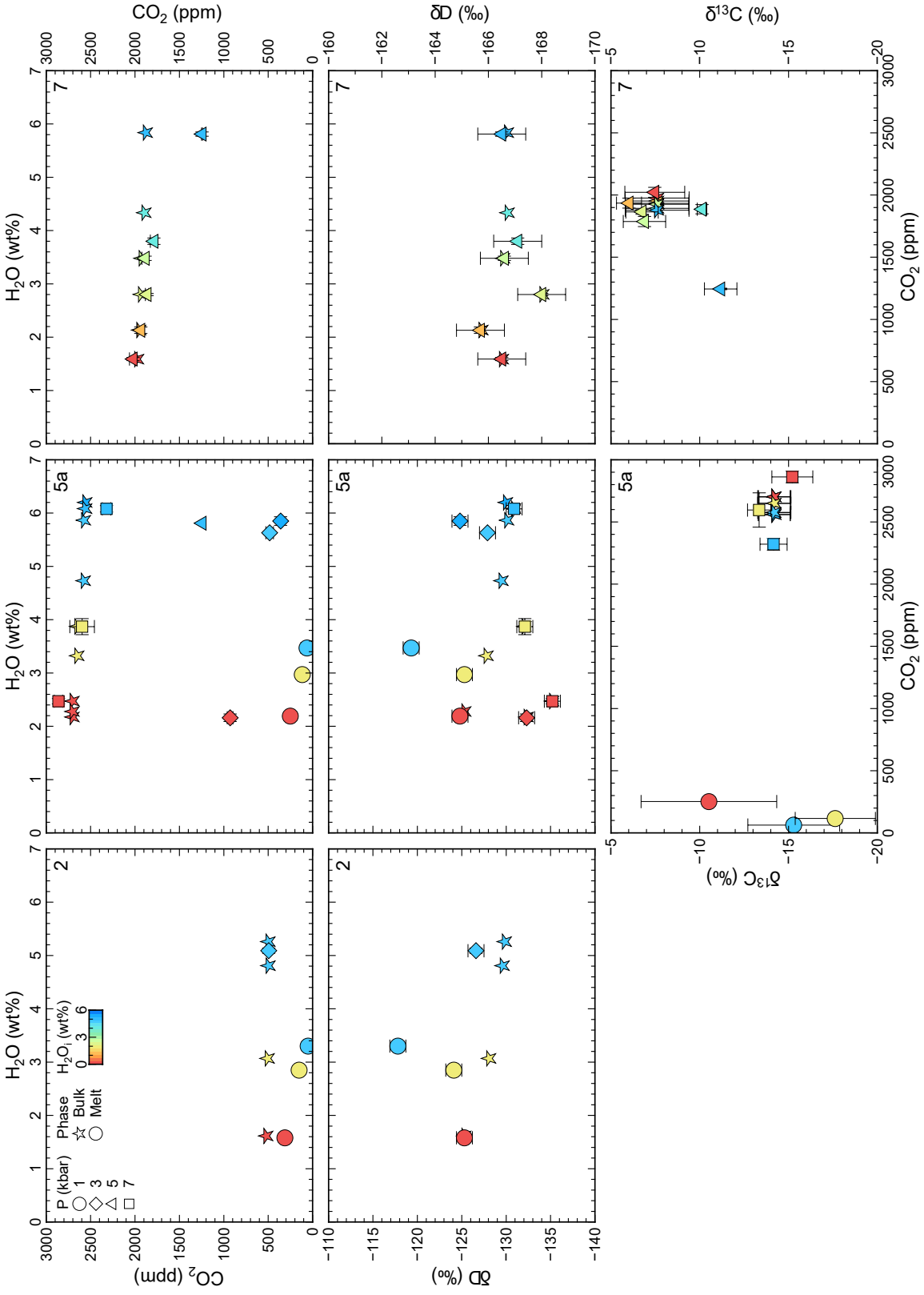


**Figure 5.12:** Bulk (GTLA) and melt volatile composition for starting batches 2, 5a, and 7, where symbol shape indicates bulk value or experimental pressure for glass values; and symbol colour indicates initial $H_2O$ concentration.

## 5.5. Volatile speciation

The stable isotope fractionation factor is dependent on the molecular bonds present in the volatiles, hence volatile speciation has a big effect. The $fO_2$ controls the speciation of volatiles and, as the experiments were unbuffered, it is important to estimate the $fO_2$ during experimental runs to see what natural conditions they are relevant to. The glass $Fe^{2+}/Fe_T$ can be used to infer the $fO_2$ of the system at a given pressure, temperature and melt composition using the algorithm of Kress and Carmichael (1991) (Figure 5.13). Our experiments range from NNO-1 to NNO+4. Magmatic $Fe^{2+}/Fe_T$ range from 0.68–0.87 (Kelley and Cottrell, 2009), similar to the values observed in our experiments (0.54–0.90 $Fe^{2+}/Fe_T$, Table 5.13). The speciation of carbon and hydrogen in the fluid at these oxidising conditions is likely to be exclusively $CO_2$ and $H_2O$, and the melt will likely contain $CO_3^{2-}$, $OH^-$, and $H_2O$.

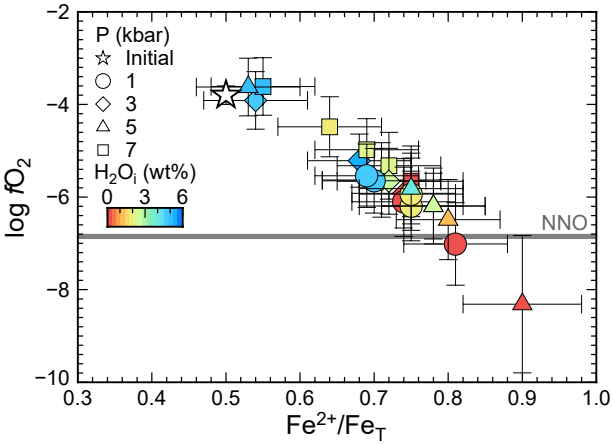


**Figure 5.13:** Log $fO_2$ calculated using Kress and Carmichael (1991) against EPMA $Fe^{2+}/Fe_T$ including the initial value, where symbol shape indicates pressure, symbol colour indicates initial $H_2O$ concentration, and the NNO buffer is shown for reference.

## 5.6. Degassing style

To model the fractionation factor, it is important to verify that the experiments represent closed-system degassing, and hence Equation 5.5 can be used. VolatileCalc was used to model degassing trends as the isobars calculated using VolatileCalc best matched the saturated runs (Figure 5.8a). All VolatileCalc models were run at 49 wt% $SiO_2$ and 1250 °C. Figure 5.14 shows the results for closed- and open-system degassing trends for the experiments highlighted in Figure 5.12, and experiments lie on closed-system degassing trends. This is especially evident for $H_2O$-rich runs at 1 kbar which have far less $H_2O$ than would be expected for open-system degassing (Figure 5.14). Closed system degassing is expected as the capsules did not leak during experimental runs, although they were open to $H_2$ diffusion.

## 5.7. Volatile isotope systematics

### 5.7.1. Carbon

As the changes to the bulk carbon composition occurred before the experiments were run, any changes in carbon composition in the melt are attributed to stable isotope fractionation between fluid and melt. Hence, the bulk and melt carbon composition for starting batches 5a and 7 can be used to calculate $\Delta^C_{f-basalt}$. $\Delta^C_{f-basalt}$ is calculated assuming closed-system degassing (Equation 5.5) using weighted (on the $\delta^{13}C$ error) least squares regression. Starting batch 5a gives $\Delta^C_{f-basalt}$= -0.3 ± 3.4 ‰, whereas starting batch 7 gives $\Delta^C_{f-basalt}$= +10.2 ± 3.8 ‰. These two estimates are very different, despite similar sized uncertainties.

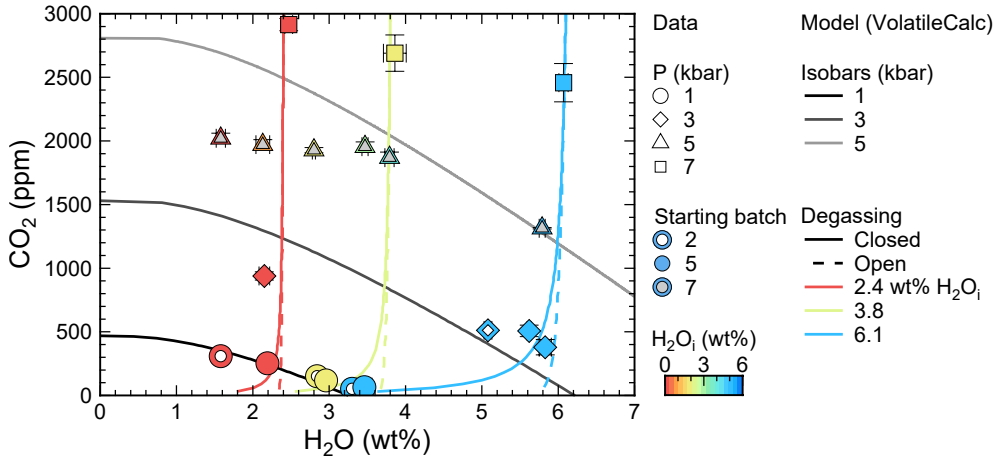


**Figure 5.14:** Glass $CO_2$ and $H_2O$ concentration for starting batches 2, 5a, and 7, including equilibrium isobars and closed- and open-system degassing trends calculated using VolatileCalc (1250 °C and 49 wt% $SiO_2$).

Analytical problems for measuring the carbon isotope ratios in the glasses using SIMS are discussed in Chapter 4. A few of these make calculating the $\Delta^{C}_{f-basalt}$ difficult and potentially explain the odd values obtained. Firstly, carbon isotope ratios for $CO_2$-rich glasses were obtained in a separate session to $CO_2$-poor glasses. Also, $CO_2$-rich glasses used a calibration curve that included contaminated analyses, which may have impacted their quantification. These two factors probably compromise the bulk values, which therefore cannot be linked to the degassed glasses. For instance, if the degassed sample in starting batch 7 has a carbon isotope ratio 1 ‰ lighter, $\Delta^{C}_{f-basalt}$ becomes +7.5 ± 3.5 ‰, which is radically different to the value reported above. Additionally, for starting batch 5a, the large error bars associated with the low $CO_2$ glasses result in a large range of $\Delta^{C}_{f-basalt}$ being possible. Unfortunately, this means these measurements cannot realistically be used to constrain $\Delta^{C}_{f-basalt}$ accurately.

### 5.7.2. Hydrogen

$H_2$ and $D_2$ diffused into the capsule during experimental runs due to the $fH_2$ gradient between the IHPV and the capsule). Most experiments experienced little $H_2O$ degassing, therefore most of the variation in δD is due to this diffusive process.

The δD of the added component ($\delta D_a$) ranged between -125 and -167 ‰, which means $H_2$ rather than $D_2$ is the dominant diffusive species through the capsule. This provides either information about the relative diffusivities of $H_2$ and $D_2$ through AuPd or reflects the intrinsic δD of the IHPV. $\delta D_a$ becomes lighter with decreasing pressure (-125, -132, and -135 ‰ at 1, 3, and 7 kbar, respectively). This could be due to increased $D_2$ diffusivity relative to $H_2$ with decreasing pressure, reflecting the different volumes of the two species. Other studies have found that $H_2$ diffuses faster than $D_2$, and although no pressure effect has been reported, the effect increases with increasing temperature in Pt (Ebisuzaki et al., 1968; Richet et al., 1986). Alternatively, 5 kbar experiments have a very different $\delta D_a$ (-167 ‰). This could reflect a very different intrinsic δD in the IHPV, as these capsules were run at a different time. It could also be that the intrinsic IHPV δD is highly variable (and dynamic) and it is coincidence that $\delta D_a$ correlates with pressure for the other experiments. The 5 kbar experiments also require a very different $\delta D_i$ to model their melt δD, therefore perhaps the very different $\delta D_a$ is due to a relatively constant intrinsic IHPV δD but a different H isotope gradient due to the different $\delta D_i$ of the capsule. In other experiments this has been thought to change the isotope ratio of the capsules (Graham et al., 1980; Richet et al., 1986). Further work is required to fully understand these different potential effects.

Figure 5.15 shows the $\Delta^{H}_{f-basalt}$ calculated assuming closed-system degassing (Equation 5.5) using the bulk $H_2O$ and $\delta D$ values from either GTLA or fluid+glass calculations. All values are negative, suggesting the melt becomes heavier during degassing ($^2$D-enriched) whereas the fluid becomes lighter ($^1$H-enriched). This is at odds with previous experiments (Figure 5.15). As $\Delta^{H}_{f-basalt}$ is negative it suggests that changes in the isotope ratio due to degassing are kinetically-driven. This might be due to the continuously changing bulk $H_2O$ of the system from $H_2$ infiltration, as suggested previously by Richet et al. (1986). The large magnitude of $\Delta^{H}_{f-basalt}$ suggests the isotopic degassing might be more similar to open-system degassing, which results in larger overall isotopic fractionation. Equation 1.4, which describes open-system degassing, requires $\Delta^{H}_{f-basalt}$ to be constant throughout degassing. During degassing the $H_2O$ concentration decreases, which changes the proportion of $OH^-$ and $H_2O^{mol}$ in the melt, hence $\Delta^{H}_{f-basalt}$ changes during degassing. Alternatively, previous experiments did not have mixed fluids present, therefore these data may suggest carbon has a dramatic effect on the isotopic fractionation during degassing. This is unlikely as it would require carbon to radically change the speciation of hydrogen in the melt and/or fluid. Further experiments with mixed fluids, where either $H_2$ infiltration into the capsule is minimised/eliminated or more accurate methods for characterising the bulk $H_2O$ and $\delta D$ of the system, including measuring the initial $\delta D$ of the system and final $\delta D$ of the fluid, are required.

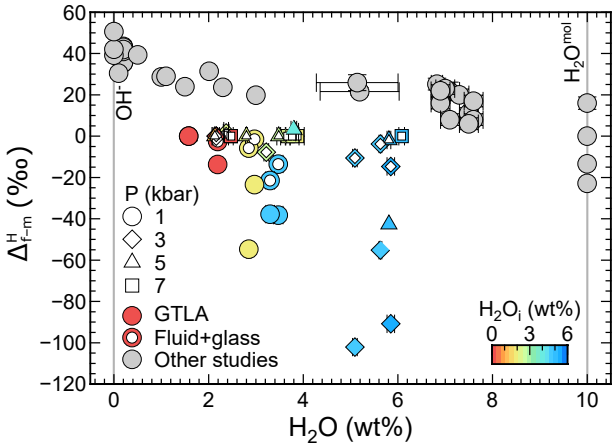


**Figure 5.15:** $\Delta^{H}_{f-m}$ against $H_2O$ derived from this study using bulk $H_2O$ and $\delta D$ from GTLA (closed) and fluid+glass (open), where symbol shape indicates pressure and colour indicates initial $H_2O$ concentration, with other studies shown for comparison from Figure 5.2.

## 5.8. Conclusions

Although these experiments were not able to quantify the equilibrium isotope fractionation factors for carbon and hydrogen, they are useful for providing a perspective for conducting future experiments that obviates the pitfalls encountered. Firstly, carbon contamination during preparation of the starting powders must be eliminated. Starting powders and capsules will need to be prepared in an inert, carbon-free atmosphere, such as a laminar flow cabinet with a slight positive pressure of an inert gas (e.g., $N_2$ or Ar). A large quantity of undersaturated, hydrous basaltic glass with and without $CO_2$ (to verify contamination has been minimised) should be synthesised at high pressure (7–9 kbar) in an IHPV. The carbon and hydrogen concentration and isotope ratio of these glasses should be analysed using SIMS to quantify the bulk volatile composition of the subsequent experiments. The carbon concentration and isotope ratio should match the weighed-in quantity of $CaCO_3$ and its isotope ratio, which is an additional check on the contribution of contamination. These glasses should be stored in Ar-purged dessicators to avoid contamination and hydration after glass synthesis.

To avoid crushing the starting glass, which facilitates carbon contamination, cores should be taken from the starting glass and loaded into capsules, with as little air in them as possible. Alternatively, glasses could be

crushed and loaded in the inert atmosphere as for the initial powders. Capsule loading should be done at the same time to ensure consistency. Experiments should be run at undersaturated conditions (again, to check the levels of contamination), and one or two saturated conditions to simulate degassing. The Fe oxidation state of the starting glass should be measured and, in conjunction with the $H_2O$ concentration, be used to set the $fH_2$ in subsequent experiments using a Shaw-membrane to prevent $H_2$ infiltration into the capsule. Oxidising conditions will help to limit Fe loss to the capsule (and hence $H_2$ infiltration) and will ensure the volatiles speciation is appropriate for arc settings. Ideally, experiments would be run at multiple different water concentrations (including anhydrous) but this would require separate experimental runs for each water content at each pressure as the $fH_2$ would be different.

The capsules should be crushed in a vacuum line to measure the concentration and isotope ratio of the hydrogen and carbon in the fluid. This will allow direct identification of the species present in the fluid, rather than just assuming them based on their freezing/boiling points, which will help to check whether the fluid re-equilibrated on the quench. The concentration and isotope ratio of the glass should be measured using SIMS. Mass balance of the fluid and glass can be compared to the undersaturated run and the initially added volatile components to check for contamination or volatile leaks. The fractionation factor of carbon and hydrogen can be calculated graphically through all the undersaturated and degassed glasses (Equation 5.5), which can be compared to the difference between the fluid and glass (Equation 5.1).

# Chapter 6

# Insights into the 23 November 2013 paroxysm at Etna, Sicily, using melt inclusions

**Author contributions and declaration:** E.C. Hughes collected, processed, and interpretted the data, and wrote the chapter with the help of J.D. Blundy, H.M. Mader, G. Kilgour, and D. Andronico, who also provided the samples.

## ABSTRACT

Etna, Sicily, is one of the most frequenctly active basaltic volcanoes in the world, with periodic changes in eruption intensity. In 2011–2013, the volcano had repeated paroxysmal events of which the 23 November 2013 eruption was one of the most explosive episodes. Olivine, pyroxene, and melt inclusions chemistry, including volatile concentrations and isotope ratios, were measured to investigate the cause of the high explosivity of the 23 November 2013 eruption. Melt inclusions have undergone varying degrees of post-entrapment modification, resulting in Mg-, Fe-, and $H_2O$-loss, and Fe oxidation. The olivine forsterite content suggests two populations, in equilibrium with a more primitive ($Fo_{81}$) and more evolved ($Fo_{72}$) magma, respectively, derived from the same parental magma. The eruption was likely triggered by an injection of the more primitive magma (>2 kbar) into the shallow plumbing system (<1 kbar), where the more evolved magma resided. The more primitive magma contained at least 1600 ppm $CO_2$ and ∼3 wt% $H_2O$ and underwent closed-system degassing during ascent. This magma mixed with the more evolved magma, containing less $H_2O$, which may have experienced $CO_2$-flushing previously. Carbon and hydrogen isotope ratios of the melt inclusions are consistent with previous data at Etna.

## 6.1. Introduction

Mount Etna, Sicily, is one of the worlds most active basaltic volcanoes. Mount Etna occurs in an unusual geodynamic setting and its chemistry is intermediate between ocean island and island arc basalts (e.g., Schiano et al., 2001). The volcano sits between the Aeolian arc to the north, caused by the collision of the African and European plates, and the transform Malta escarpment to the west (e.g., Barberi et al., 1974) (Figure 6.1). Primary magmas at Etna are thought to have been sourced through a variety of processes, such as the Ionian slab migrating south, upper mantle upwelling due to rollback, a slab window opening, and melting of variably metasomatised mantle, amoungst others (e.g., Schiano et al., 2001; Schellart, 2010; Gvirtzman and Nur, 1999; Viccaro and Cristofolini, 2008).

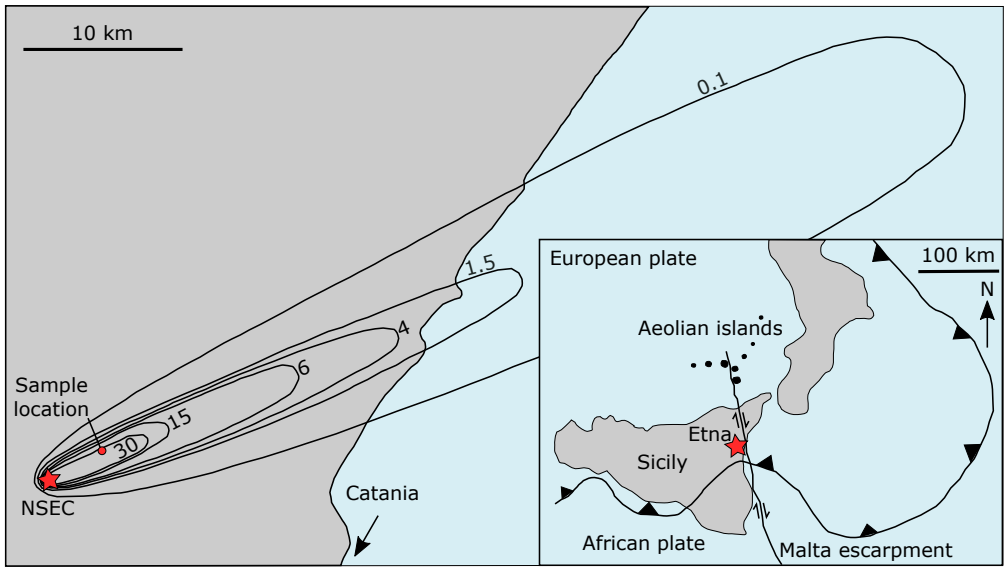


**Figure 6.1:** Map of Etna and the sample locality. Inset maps shows the tectonic setting of Etna after Kahl et al. (2015). Main map shows the location of the New South East Crater (NSEC), isomass lines (in kg·m$^2$) of the 23 November 2013 tephra fallout deposit after Andronico et al. (2015), and the sample locality of the 23 November 2013 eruption used in this study.

The plumbing system of Etna is complicated, with magmatic environments (also called magmatic facies) characterised by different intensive parameters such as pressure, temperature, $fO_2$, $H_2O$, concentration and bulk melt composition (e.g., Giuffrida and Viccaro, 2017; Giacomoni et al., 2018; Kahl et al., 2015). There are also different pathways for the magma to take to reach the surface between these environments, which occur over a variety of timescales (e.g., Kahl et al., 2015). Broadly, there are four magmatic environments, which are summarised in Table 6.1 and Figure 6.2 for three different studies that used the composition of predominantly olivine to infer the intensive parameters. Kahl et al. (2015) analysed olivine from eruptions from 1991–2008, whilst Giuffrida and Viccaro (2017) and Giacomoni et al. (2018) analysed olivine from the 2011–2013 sequence. With decreasing pressure: the melt composition becomes more evolved, the temperature decreases, the Fo of the olivine becomes more Fe-rich, the $H_2O$ concentration decreases, and the system becomes more reduced (Giuffrida and Viccaro, 2017; Giacomoni et al., 2018; Kahl et al., 2015). The system is generally more $CO_2$-rich in the more primitive magma, but $CO_2$-flushing can increase the $CO_2$ concentration of the shallow magma (e.g., Collins et al., 2009).

Etna is persistently active, continuously releasing volatiles into the atmosphere, e.g., as much as 5–10 %

**Table 6.1:** Plumbing system at Etna from the olivine geochemistry.

| | Kahl et al. (2015) | Giuffrida and Viccaro (2017) | Giacomoni et al. (2018) |
|---|---|---|---|
| Environment | | $M_{00}$ | F1 |
| Olivine Fo | | 85 | 88 |
| P (kbar) | | 6 | 16 |
| T (°C) | | 1200 | 1270 |
| log($fO_2$, bars) | | -6.8 | |
| $H_2O$ (wt%) | | 1.4 | |
| $CO_2$ (ppm) | | 6000 | |
| Environment | $M_0$ | $M_0$ | F2 |
| Olivine Fo | 79–83 | 80–82 | 78–84 |
| P (kbar) | 1 | 3.9 | 6–8 |
| T (°C) | 1110 | 1160 | 1165 |
| log($fO_2$, bars) | NNO–QFM | -8.5 | |
| $H_2O$ (wt%) | 3.5–5.2 | 1.6 | |
| $CO_2$ (ppm) | | 3000 | |
| Environment | $M_1$ | $M_{1a}/M_{1b}$ | F3 |
| Olivine Fo | 75–78 | 75–78 | 74–79 |
| P (kbar) | 0.25–2 | 1.4–2.9 | 2–4.5 |
| T (°C) | 1110 | 1110–1130 | 1130 |
| log($fO_2$, bars) | NNO–QFM | -9 to -9.3 | |
| $H_2O$ (wt%) | 0.1–1.4 | 1.4–1.5 | 3 |
| $CO_2$ (ppm) | | 1000–2000 | |
| Environment | $M_2/M_3$ | $M_2$ | F4 |
| Olivine Fo | 65–72 | 70–72 | 70–75 |
| P (kbar) | 0.2–1.1 | 0.3 | 0–2 |
| T (°C) | 1080 | 1090 | 1130 |
| log($fO_2$, bars) | QFM | -9.7 | |
| $H_2O$ (wt%) | 0-1.1 | 1 | $<3$ |
| $CO_2$ (ppm) | | 100 | |

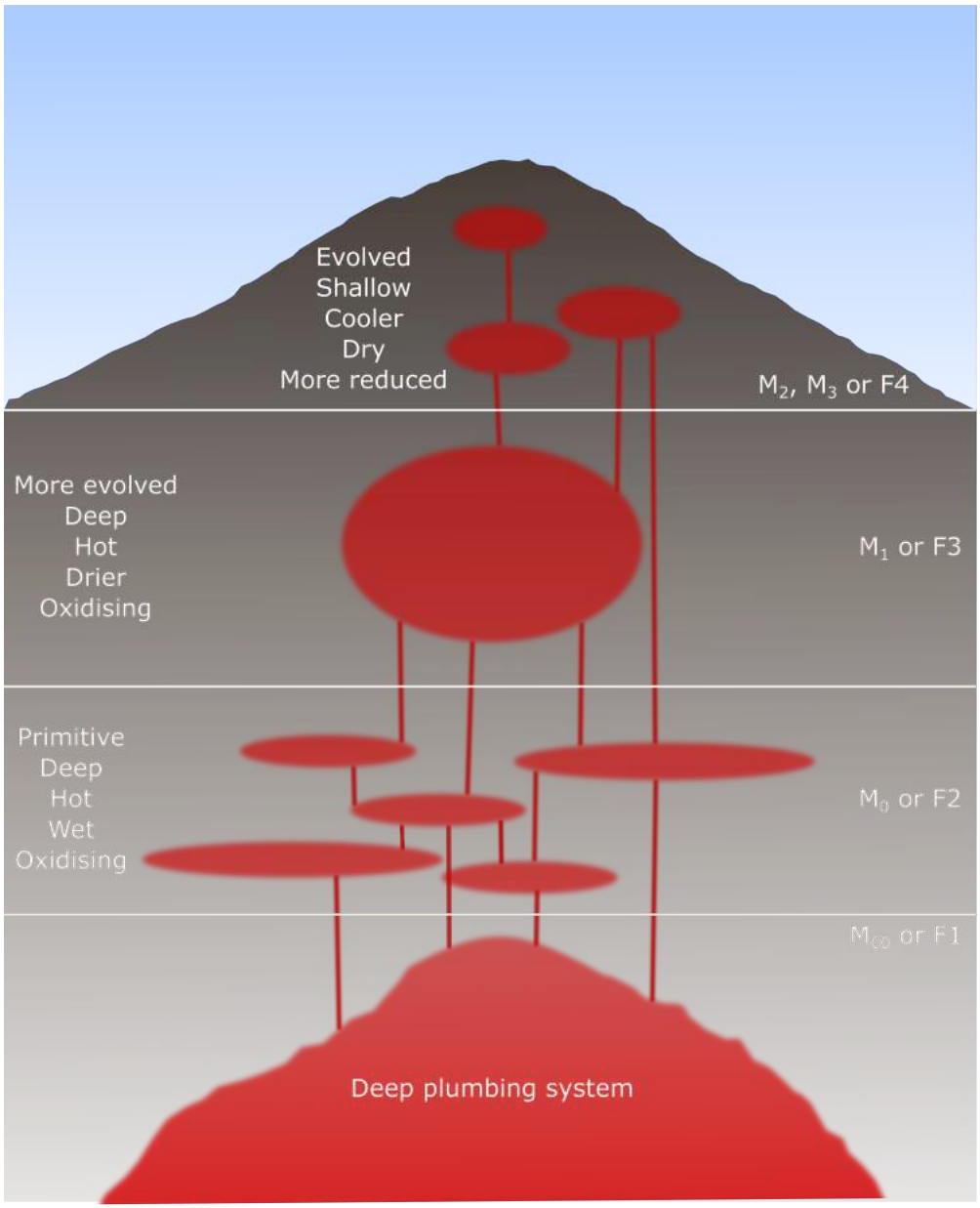


**Figure 6.2:** Schematic illustration of the plumbing system at Etna, based on the work of Giuffrida and Viccaro (2017), Giacomoni et al. (2018) and Kahl et al. (2015). There are four distinct magmatic environments (or facies), which are summarised in Table 6.1.

of $CO_2$ and S global emissions (Aiuppa et al., 2006; Allard et al., 2006a), and often erupting volatile-rich magma (e.g., Métrich et al., 2004). Etna exhibits a wide range of eruptive styles, from effusive lava flows (e.g., 2004–2005; Burton et al., 2005) to Plinian eruptions (e.g., 122 B.C.; Coltelli et al., 1998). Since 1998, the most common eruptive style is paroxysmal activity at the summit craters, characterised by sequences of fire-fountaining episodes (e.g., Andronico et al., 2014). Furthermore, the highly explosive flank eruptions in 2001 and 2002–2003 (Andronico et al., 2005, and references therein) were driven by a new batch of primitive magma entering the system and ponding at 4–6 km depth (Métrich et al., 2004; Spilliaert et al., 2006). The magmas had extremely high volatile contents, up to 4100 ppm $CO_2$ and 3.5 wt% $H_2O$, which rose rapidly to the surface under closed-degassing (Métrich et al., 2004; Spilliaert et al., 2006). In contrast, between 2004–2007 the behaviour was dominated by effusive eruptions driven by gas-

poor magmas which represented the residual magmas from the 2001–2003 eruptions, but with significant evolution of the volatiles (Collins et al., 2009). These magmas had been dehydrated and $CO_2$-enriched by sustained $CO_2$-flushing during storage (Collins et al., 2009). There were seven fire-fountaining events in 2007–2008 (e.g., Aiuppa et al., 2010; Andronico et al., 2008; Bonaccorso et al., 2011b), after which began the effusive flank eruption from 2008–2009 (e.g., Bonaccorso et al., 2011a, 2013).

Almost one million people live on the slopes of Etna and the international airport of Catania (the biggest city around the volcano) is one of busiest in Italy. Therefore, understanding the causes of the differing eruption styles and changes in behaviour at Etna is critical. As such, Etna is well-studied and -instrumented, which makes it an ideal candidate to test new techniques and understand the fundamental processes driving basaltic eruptions.

### 6.1.1. 2011–2013 eruptive sequence

Between 2011–2013 there were 46 paroxysmal episodes consisting of lava fountains accompanied by lava flows, each one lasting from hours to one or two days. Since the first episode on 12 January 2011, the eruptive activity took place on the east slope of the South East Crater (Andronico et al., 2014), which over time formed the New South East Crater (NSEC) (e.g., Behncke et al., 2014; Bonaccorso et al., 2014) (Figure 6.1). The 46 episodes can be subdivided into three main episodic sequences. The first sequence consisted of 25 episodes between January 2011 and April 2012. After a ten-month hiatus, a further eleven episodes occurred between February and April 2013. The last sequence started after a six-month hiatus, occurring between October and December 2013, consisting of ten episodes. All the 2011–2013 episodes displayed similar behaviour, which have been observed in past episodic sequences (e.g., in 2000; Alparone et al., 2003; Andronico and Corsaro, 2011). Typically, episodes began with Strombolian explosions and weak effusive activity for a few hours. This increased quickly to lava fountaining and strong lava flows before rapid cessation of all eruptive phenomena. However, the last two episodes in December 2013 were less violent and were characterised by prolonged, powerful Strombolian activity, which did not evolve into lava fountaining, and a greater volume of lava flows. Magmas in the 2011–2013 sequence are thought to be the result of fractional crystallisation, combined with mixing, of more primitive magmas from different depths in the plumbing system (Giacomoni et al., 2018; Giuffrida and Viccaro, 2017; Viccaro et al., 2015).

### 6.1.2. 23 November 2013 eruption

The 23 November 2013 eruption of Etna provides an excellent case study to apply the techniques and ideas developed during this thesis (Figure 6.1). Strombolian activity began the day before (22/11/13) at 15:40 (UT) and increased in intensity throughout the night into the next morning (Bonaccorso et al., 2014). At 08:00, an eruption cloud formed above the NSEC and at 09:30 discontinuous lava fountaining began, which became more sustained. According to Bonaccorso et al. (2014), at 09:50, the lava fountain reached 2.5 km high, whilst Andronico et al. (2015) evaluated the maximum height as $\sim$800 m. The eruption column was estimated to reach 5–6 km above the cone (Andronico et al., 2015; Bonaccorso et al., 2014). The paroxysmal phase began to decline at 10:05 and was finished by 10:15 (45 mins in total), with a climatic phase of only 25 mins. There were moderate Strombolian explosions and a weak ash plume until 11:13, and column collapse produced two small flows. Despite a similar total erupted volume to previous events, there was no lava flow associated with the eruption. Using the time-averaged discharge rate from deformation data (360 $m^3 \cdot s^{-1}$),

the total erupted mass was $4.8 \times 10^6$ kg ($1.6 \times 10^6$ m$^3$ dense rock equivalent using a density of $\sim$3 kg·m$^3$) (Bonaccorso et al., 2014). Conversely, Andronico et al. (2015) and Poret et al. (2018) estimated $1.3 \times 10^9$ kg and $1.2 \times 10^6$ kg using field data and numerical simulations, respectively.

### 6.1.3. Hypothesis and approach

Two mechanisms are thought to cause intense paroxysms at Etna, which will have different precursory signals. Either these paroxysms are caused by a new injection of gas-rich, primitive magma, or from evolved magma that has been enriched in volatiles that have accumulated at the top of the magma (Jaupart and Vergniolle, 1989). The height of the lava fountain has been used by Bonaccorso et al. (2014) to infer that a more primitive, gas-rich magma entered the system, but the volatile content of that magma is unknown. This theory is tested by analysing melt inclusions for major and minor element chemistry, volatile concentrations and isotope ratios ($H_2O$, $CO_2$, S, Cl, and F; $\delta$D and $\delta^{13}$C), and Fe oxidation state. Additionally, major and minor element chemistry of olivine and pyroxene are measured. The extent of post-entrapment modification to the melt inclusion composition is evaluated. This new geochemical dataset is compared to previous analyses on the 2011–2013 eruptive sequence; gas-rich (2001–2002) and -poor (2004–2007) eruptions; and volcanic gas data.

## 6.2. Theory: Post-entrapment modification of melt inclusions

Various processes after the melt inclusion has been trapped can alter its composition and structure (Figure 6.3). The extent to which these processes have occurred needs to be evaluated to accurately interpret melt inclusion data.

### 6.2.1. Continued host-mineral crystallisation

The host mineral is on the liquidus when the melt inclusion is trapped, hence it will tend to crystallise on the walls of the inclusion after entrapment (e.g., Danyushevsky et al., 1988; Dungan and Rhodes, 1978; Gaetani and Watson, 2002; Nielsen et al., 1998; Sobolev and Shimizu, 1993; Witham et al., 2012). Crystallisation also occurs in olivine-hosted melt inclusions due to re-equilibration of the melt inclusion with a more reduced magma by diffusion of metal vacancies through the olivine (Section 6.2.3). Crystallisation will change the composition of the melt inclusion, reducing the concentration of compatible elements and increasing the concentration of incompatible elements. This also effects the Fe oxidation state of the melt inclusion as $Fe^{2+}$ is compatible in olivine, whilst $Fe^{3+}$ is incompatible, causing apparent oxidation. If the melt inclusion continues to cool slowly, further crystallisation will occur on its walls.

For olivine-hosted melt inclusions, it is possible to reconstruct the initial composition of the melt if the extent of crystallisation can be estimated. This can be done by simulating dissolving olivine back into the melt inclusion composition to calculate the initial melt inclusion composition. At equilibrium, $Fe^{2+}$ and Mg are distributed between the melt and olivine such that:

$$K_{D(Fe-Mg)}^{ol-melt} = \frac{(FeO/MgO)_{ol}}{(FeO/MgO)_{melt}} \tag{6.1}$$

where FeO and MgO are mole fractions in the olivine (ol) and melt, as indicated by the subscript (Roeder and

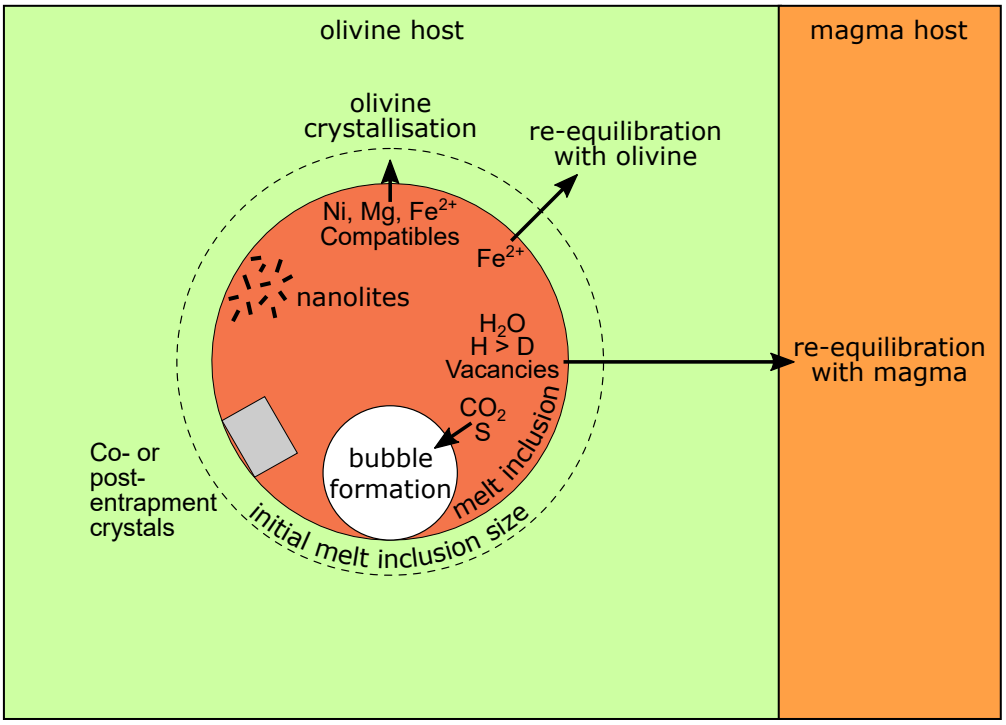


**Figure 6.3:** Schematic illustration of post-entrapment processes that can modify olivine-hosted melt inclusions. The melt inclusion is shown in red, the host-olivine is shown in green, and the host magma is shown in orange. The initial size of the melt inclusion is shown by the black, dashed line, which becomes the size of the red melt inclusion due to continued crystallisation of olivine on the melt inclusion walls, which removes Ni, Mg, $Fe^{2+}$, and other elements that are compatible in olivine from the melt. The composition of the melt inclusion can re-equilibrate with the host-olivine, which removes $Fe^{2+}$ from the melt inclusion. It can also re-equilibrate with the host-magma, which removes $H_2O$ from the melt inclusion if the host-magma is more dehydrated than the melt inclusion, and H will diffuse faster than D changing the $\delta$D of the melt inclusion. Bubbles (white circle) can form post-entrapment, which may sequester volatiles such as $CO_2$ and S. Crystals (grey rectangle) can either be co-entrapped with the melt during melt inclusion formation, or exsolve from the melt within the melt inclusion post-entrapment. Nanolites (black lines) can also precipitate from the melt within the melt inclusion. Black arrows show where species in the melt inclusion diffuse to during post-entrapment processes.

Emslie, 1970). Therefore, olivine can be 'dissolved' into the melt inclusion until the equilibrium $K^{ol-melt}_{D(Fe-Mg)}$ value has been reached. The composition of the olivine host is assumed to be that at equilibrium and remains unaffected by post-entrapment crystallisation as it is a much larger volume than the melt inclusion. Olivine contains Fe as only $Fe^{2+}$ (i.e., FeO) but the melt contains Fe as both $Fe^{2+}$ and $Fe^{3+}$ (i.e., FeO and $Fe_2O_3$, respectively). Typically, only the total Fe of the melt is known (often reported as $FeO_T$, all Fe as FeO) and not the Fe oxidation state. Using $FeO_T$, not actual FeO, to calculate $K^{ol-melt}_{D(Fe-Mg)}$ in Equation 6.1 gives different equilibrium values, which depend on the Fe oxidation state. Blundy et al. (2018) have empirically shown that:

$$K^{ol-melt}_{D(Fe-Mg)} = 0.317 \cdot Fe^{2+}/Fe_T \tag{6.2}$$

Melt $Fe^{2+}/Fe_T$ is often unknown, therefore a $K^{ol-melt}_{D(Fe-Mg)} \approx 0.3$ is typically used (Kress and Carmichael, 1991; Roeder and Emslie, 1970). A measured $K^{ol-melt}_{D(Fe-Mg)} < 0.3$ either means $Fe^{3+}$ is present in the melt (i.e., melt $Fe^{2+}/Fe_T < 1$ at the time of melt inclusion entrapment) or post-entrapment crystallisation of olivine has

occurred (i.e., removed Mg from the melt).

Alternatively, the degree of olivine crystallisation can be estimated using Ni partitioning between the olivine and melt. Ni is very compatible in olivine, hence any post-entrapment crystallisation will reduce the Ni content of the melt inclusion. $K_{D(Ni)}^{ol-melt}$ has been parameterised empirically for MgO concentration (wt%) of the melt by Hart and Davis (1978), such that:

$$K_{D(Ni)}^{ol-melt} = \frac{124}{MgO_{melt}} - 0.9 \tag{6.3}$$

If olivine has crystallised the melt MgO will have decreased, hence this provides a maximum $K_{D(Ni)}^{ol-melt}$.

Using pyroxene as a host mineral is more complicated than olivine because it is not a binary system and it can contain both $Fe^{2+}$ and $Fe^{3+}$ in its structure. Hence, it is currently not possible to estimate the degree of post-entrapment pyroxene crystallisation.

### 6.2.2. Mineral-melt diffusive re-equilibration

Melt inclusions may re-equilibrate diffusively with their host mineral, modifying their composition. For instance, if the magma cools slowly there is time for the rim of olivine that crystallised post-entrapment on the walls of the melt inclusion to equilibrate with the host-olivine (Figure 6.4). The melt in the melt inclusion will then re-equilibrate with this olivine composition, by $Fe^{2+}$ diffusing out of, and Mg into, the melt inclusion (Danyushevsky et al., 2000; Gaetani and Watson, 2002, 2000). This process can be corrected for but requires knowledge of the initial Fe content of the melt inclusions, which is unknown although bulk rock Fe is often used (e.g., Danyushevsky and Plechov, 2011; Gaetani and Watson, 2002).

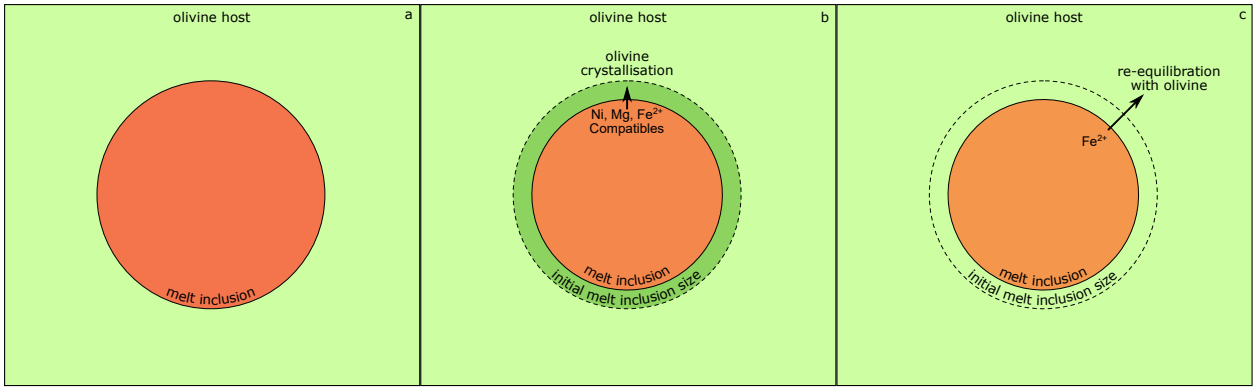


**Figure 6.4:** Schematic illustration showing post-entrapment modification due to olivine crystallisation followed by diffusion: **(a)** melt inclusion as trapped in olivine; **(b)** a rim of olivine has crystallised on the walls of the melt inclusion with a different composition to the host-olivine and the melt composition has also changed; and **(c)** the olivine rim diffusively equilibrates with the host-olivine and so the melt re-equilibrates with this composition by $Fe^{2+}$ diffusion into, and Mg diffusion out of, the host-olivine.

The extent of Fe-loss can be estimated by comparing the FeO of melt inclusions and bulk rock against Fo of the olivine, which can be calculated for bulk rock using equilibrium models (e.g., Danyushevsky and Plechov, 2011). The 'Fe-loss triangle' is defined by two trends in FeO-Fo space: olivine crystallisation from the melt; and complete melt inclusion re-equilibration defining the greatest Fe-loss possible, which results in a negative trend between FeO and Fo (Figure 6.5). The area within this triangle is due to

partial re-equilibration and variable Fe-loss. This process is complicated by re-equilibration of $fO_2$, as Fe-Mg exchange is dependent on $fO_2$ as shown in Equation 6.2 (Chakraborty, 1997; Jurewicz and Watson, 1988). Diffusion profiles surrounding melt inclusions can be also used to correct for Fe-loss, but are time-consuming to collect and process (Danyushevsky et al., 2000).

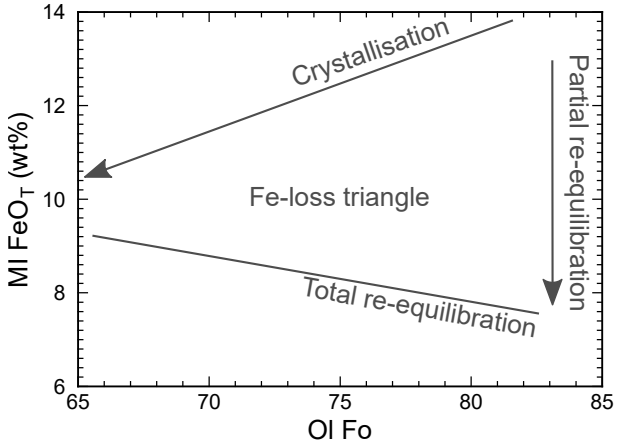


**Figure 6.5:** Fe-loss triangle for melt inclusion (MI) Fe concentration (where all Fe is expressed as FeO, $FeO_T$) against host-olivine forsterite content (Fo), where the sides of the triangle are defined by crystallisation of olivine from the host magma (the original trend in the melt inclusion composition) and partial and total re-equilibration of the melt inclusion composition (Danyushevsky et al., 2000).

This is also a problem for other minerals, but Fe-Mg exchange between olivine and melt is fast and relatively simple to model. For instance, major element diffusion rates are slower in clinopyroxene compared to olivine, therefore it is harder to re-equilibrate (Cherniak and Dimanov, 2010).

### 6.2.3. Magma-melt diffusive re-equilibration

Melt inclusions can also re-equilibrate with the external melt due to gradients in $fH_2O$ and $fO_2$ by diffusing species through the host mineral (e.g., Gaetani et al., 2012; Hartley et al., 2017, 2015). In olivine these occur via two independent reactions, which can be denoted using Kröger-Vink notation for point defects, whereby the subscript indicates the lattice site (e.g., melt, Me = octahedral, or O = oxygen) and the superscript the effective charge ($\times$ = neutral, $\bullet$ = positive, and $'$ = negative).

The first reaction involves proton exchange through the olivine, which results in oxidation (conversely, reduction) of Fe in octahedral lattice sites ($Fe^{\times}_{Me}$ and $Fe^{\bullet}_{Me}$ for $Fe^{2+}$ and $Fe^{3+}$, respectively) and creation (destruction) of two $OH^-$ defects in oxygen sites ($(OH)^{\bullet}_{O}$) which are associated with an octahedral site metal vacancy ($V''_{Me}$) (Kohlstedt and Mackwell, 1998):

$$2H_{melt} + 2Fe^{\bullet}_{Me} + 2O^{\times}_{O} + V''_{Me} = \{(OH)^{\bullet}_{O} - V''_{Me} - (OH)^{\bullet}_{O}\} + 2Fe^{\times}_{Me} \tag{6.4}$$

where additionally $O^{\times}_{O}$ is an $O^{-}_{2}$ in an oxygen site and $\{\}$ indicates associated point defects. This will modify the $\delta D$ of the melt inclusion, as $^1H$ diffuses much faster than $^2D$ through olivine (e.g., Gaetani et al., 2012; Hauri, 2002; Shaw et al., 2008).

The second reaction involves oxygen incorporation into the olivine from the melt (conversely, oxygen loss from the olivine to the melt) via oxidation (reduction) of Fe in an octahedral site in the olivine, which creates (destroys) an octahedral site metal vacancy and causes olivine precipitation (dissolution) (Nakamura and Schmalzried, 1983):

$$O_{melt} + \frac{1}{2}[SiO_2]_{melt} + 3Fe^{\times}_{Me} = V''_{Me} + 2Fe^{\bullet}_{Me} + \frac{1}{2}Fe_2SiO_4 \quad (6.5)$$

These reactions (Equations 6.4 and 6.5) can be combined to allow $H_2O$ concentrations to re-equilibrate between the host-magma and the melt inclusion (Gaetani et al., 2012) via:

$$H_2O_{melt} + \frac{1}{2}[SiO_2]_{melt} + Fe^{\times}_{Me} + 2O^{\times}_{O} = \{(OH)^{\bullet}_{O} - V''_{Me} - OH)^{\bullet}_{O}\}^{\times} + \frac{1}{2}Fe_2SiO_4 \quad (6.6)$$

As there is no $Fe^{\bullet}_{Me}$ in this reaction, it also can be applied to forsterite ($Mg_2SiO_4$). Reactions via Equations 6.4 and 6.5 occur independently, hence $H_2O$ equilibration is not limited by the Fe oxidation state of the melt inclusion (Gaetani et al., 2012). Similar problems are not encountered for $CO_2$ as the solubility and diffusivity of carbon in olivine are extremely low (Keppler et al., 2003; Tingle et al., 1988). Understanding these reactions in pyroxenes is more complicated.

Typically, these reactions cause dehydration of melt inclusions if the surrounding magma is more degassed, such as stalling in a shallow magma chamber or slowly cooling in a lava flow, but can result in hydration, if surrounding magma is more hydrous, such as during magma mixing (e.g., Hartley et al., 2017, 2015). Changes in $fO_2$ can be the result of S degassing or magma mixing events (e.g., Hartley et al., 2017; Moussallam et al., 2014). The extent of melt inclusion re-equilibration depends on the size of the inclusion and the host, the relative position of the melt inclusion within the host, temperature, and $fH_2O$ or $fO_2$ gradient. Small, $H_2O$-rich melt inclusions in a degassed magma will re-equilibrate $H_2O$ faster due to their smaller volume, greater surface area to volume ratio, and large $fH_2O$ gradient (e.g., Bucholz et al., 2013). Re-equilibration of $fO_2$ and $fH_2O$ have knock-on effects to the concentration of other volatile species in melt inclusions, such as $CO_2$ and S (Bucholz et al., 2013; Hartley et al., 2017).

### 6.2.4. Bubble formation

During cooling, ascent, post-entrapment host-crystallisation (due both to continued crystallisation because of cooling, Section 6.2.1, and in response to $fO_2$ re-equilibration, Section 6.2.3), and melt inclusion dehydration (Section 6.2.3), the pressure inside the melt inclusion decreases. This often leads to the formation of a bubble or possibly decrepitation of the melt inclusion (e.g., Bucholz et al., 2013; Lowenstern, 2003, 1995; Maclennan, 2017; Métrich et al., 2009; Roedder, 1979; Schiano, 2003). The bubble can simply be a vacuum, or it can contain fluids if volatiles from the melt are able to diffuse into the bubble (e.g., Anderson and Brown, 1993; Hartley et al., 2014; Roedder, 1979; Steele-Macinnis et al., 2011). The composition of the fluid in the bubble can be measured using Raman spectroscopy (e.g., Moore et al., 2015). Unfortunately, this is associated with large errors as it is difficult accurately to estimate the bubble volume.

Notwithstanding these issues, up to 90 % of the $CO_2$ content of melt inclusions has been measured in their bubbles (e.g., Hartley et al., 2014). Consequently, neglecting the $CO_2$ content in the bubbles can lead to vast underestimations of the $CO_2$ concentration of melt inclusions (e.g., Hartley et al., 2014; Wallace et al., 2015). This assumes the fluid in these bubbles was originally in the melt when the melt inclusion was formed, which is not the case if the bubble was co-entrapped at the time of melt inclusion formation. Similarly, S concentrations have been seen to decrease during melt inclusion dehydration and it is therefore presumed that S has been sequestered into bubbles (e.g., Bucholz et al., 2013). $H_2O$, F, and Cl appear to

be less affected by this problem (e.g., Robidoux et al., 2018). The fluid phases in the bubble have also been found to precipitate out on the bubble walls, forming carbonate phases during cooling (Moore et al., 2015; Mathez and Delaney, 1981). During bubble formation, $CO_2$ (and other volatiles) will isotopically fractionate under either kinetic or equilibrium conditions (Section 5.1.1), which will change the isotope ratio of the melt.

### 6.2.5. Crystallisation

Crystallisation of daughter minerals can occur within the melt inclusion, which will change the melt inclusion composition. Sometimes the melt inclusion can completely recrystallise if the cooling rate is slow enough, requiring homogenisation to measure the original composition (e.g., Nielsen et al., 1998). Also, re-equilibration of $fO_2$ in melt inclusions can cause sulphide precipitation (Hartley et al., 2017).

Nanolites are nano-crystals (30–1000 nm in diameter; Mujin et al., 2017) that can change the viscosity of magmas by two orders of magnitude and provide nucleation sites for bubbles (Di Genova et al., 2018, 2017a; Mujin et al., 2017; Mujin and Nakamura, 2014). Hence, depending on when they form, they can have a major impact on magma rheology and eruption dynamics. Typically, they form on the quench, during ascent and degassing, as the glass passes through the glass transition (Di Genova et al., 2017a; Mujin et al., 2017; Mujin and Nakamura, 2014). Their formation depends on quench rate, melt viscosity, $H_2O$, and Fe oxidation state (e.g., Appendix F, Di Genova et al., 2018, 2017a).

## 6.3. Methods

### 6.3.1. Sample collection and preparation

Scoria clasts 11.2–31.5 mm (-3.5 to -5 $\varphi$) in size were collected in 2015, from an area known to contain only clasts from the 23 November 2013 eruption (37.762915 °N 15.046130 °E) (Figure 6.1). Small clasts were selected, as these were assumed to have cooled rapidly thereby limiting the extent of post-entrapment modification of melt inclusion composition after eruption (Lloyd et al., 2013). Smaller clasts ($<$11.2 mm) were not collected to avoid contaminating the sample with fine lapilli from previous fallout eruptions.

To liberate crystals, scoria clasts were repeatedly lightly crushed and sieved between 250 $\mu$m and 1 mm. Olivine and pyroxene crystals were hand-picked under a binocular microscope. To find melt inclusions, crystals of primarily olivine were placed in a glass dish and ethanol was added to cover all crystals. Ethanol has a higher refractive index than air, hence it is easier to see into the crystals and check for melt inclusions under a binocular microscope. Crystals containing melt inclusions were individually mounted in epoxy, ground, and polished to a $\sim$1–3 $\mu$m finish to expose the melt inclusion at the surface. Additionally, many crystals were mounted together in epoxy mounts, then ground, and polished to a $\sim$1–3 $\mu$m finish for mineral chemistry analysis. Any melt inclusions intersected in these mounts were also analysed.

Melt inclusions were analysed using Raman ($H_2O$ and nanolites), SIMS ($CO_2$, $H_2O$, $\delta^{13}C$, and $\delta D$), and EPMA (majors, minors, volatiles, including $H_2O$ using VBD, and $Fe^{2+}/Fe_T$) (Table 6.2). When multiple analyses were carried out on the same melt inclusion the order was: Raman (single analysis for both $H_2O$ and nanolites), SIMS ($\delta D$), SIMS ($\delta^{13}C$), SIMS ($CO_2$ and $H_2O$), EPMA (majors, minors, and volatiles), then EPMA ($Fe^{2+}/Fe_T$). Raman is non-destructive and therefore was carried out first. EPMA was used

**Table 6.2:** Overview of methods applied to melt inclusions and minerals.

| Technique | Phase | Variable |
|---|---|---|
| Raman | Melt inclusion | $H_2O$ and nanolites (Section 6.3.2) |
| SIMS | Melt inclusion | $CO_2$ and $H_2O$ (Section 4.2.2) |
| | | $\delta^{13}C$ (Section 4.3.2) |
| | | $\delta D$ (Section 6.3.3) |
| EPMA | Melt inclusion | Majors, minors, and volatiles (Section 2.5.3) |
| | | VBD (Section 2.5.4) |
| | | $Fe^{2+}/Fe_T$ (Section 3.3.2) |
| | Olivine, pyroxene and plagioclase inclusions | Majors and minors (Section 6.3.4) |

last as it causes hydrogen migration and nanolite formation, which would effect Raman and SIMS analyses (Humphreys et al., 2006, Section 3.5). $Fe^{2+}/Fe_T$ using EPMA was analysed last as it causes the most severe beam damage due to the analytical conditions required (Section 3.3.2). Olivine and pyroxene crystals, and plagioclase inclusions, were analysed using EPMA (majors and minors).

### 6.3.2. Raman spectroscopy

Raman spectroscopy was used to measure the $H_2O$ concentration and identify the presence of nanolites in melt inclusions (e.g., Di Genova et al., 2018, 2017b). Monochromatic light from a laser is used to excite chemical bonds in the glass, putting them into a virtual energy state by absorbing a photon. These virtual energy states quickly decay and most of the photons emitted are of the same energy as those absorbed (Rayleigh scattering). A small proportion of the photons are emitted with a different energy, reflecting characteristic molecular vibrations. This shift in energy emitted (up or down) is called Raman scattering and gives rise to the Raman spectrum. Different bonds have different wavelengths to which the monochromatic light is shifted, hence Raman spectra can be used to fingerprint which species are present. For instance Fe-bearing nanolites produce a peak due to magnetite at $\sim$670 $cm^{-1}$ (Di Genova et al., 2017a,b) and $H_2O$ produces a peak at $\sim$3600 $cm^{-1}$ (e.g., Di Muro et al., 2006; Di Genova et al., 2017b).

Raman spectra were collected using the Thermo Scientific DXRxi Raman Imaging Microscope at the School of Earth Sciences, University of Bristol, UK. Melt inclusions exposed at the surface, mounted in epoxy and polished to a $\sim$1–3 μm finish were analysed. A green (520 nm) laser, 10× or 50× (long distance) objective, and an extended grating (0–5000 $cm^{-1}$) were used, with a power of 3–5 mW to avoid sample oxidation (Di Genova et al., 2017b). Spectra were corrected for temperature and the frequency-dependent scattering of intensity (Long, 1977), and background-corrected using the R code of Di Genova et al. (2017b) prior to processing. Spectra were visually checked for the presence of olivine contamination, which prevents quantitative analysis of the spectra (Figure 6.6).

To quantify the amount of nanolites present, Di Genova et al. (2018) defined the degree of nanolitisation (N#) as:

$$N\# = \frac{I_{670-690}}{I_{785-795}} \tag{6.7}$$

where $I_{670-690}$ is the average intensity for the magnetite peak (670–690 $cm^{-1}$) and $I_{785-795}$ is the average

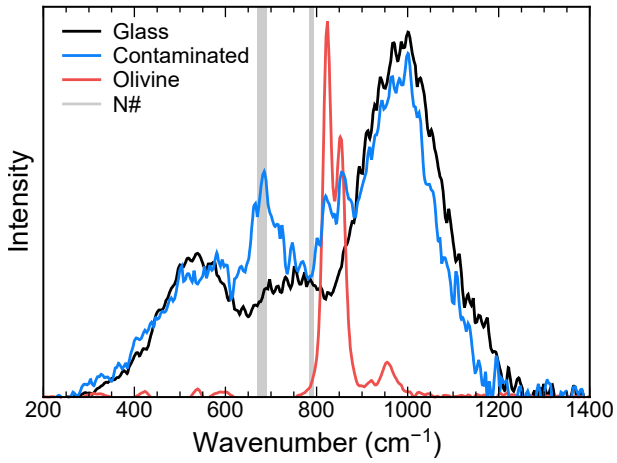


**Figure 6.6:** Example raman spectra in the low-wavelength region (LW) of a basaltic glass (black), olivine (red), and basaltic glass containing nanolites and contaminated with host olivine (blue). The vertical grey lines are the wavenumbers used in Equation 6.7 of magnetite (670–690 cm$^{-1}$, thick) and the peak associated with the melt Fe oxidation state (785–795 cm$^{-1}$, thin).

intensity of the peak associated with the glass Fe oxidation state (785–795 cm$^{-1}$) (Figure 6.6). This was based on the observation by Di Genova et al. (2018) that the magnetite peak increased, whilst the Fe oxidation state of the glass reduced, due to $Fe_2O_3$ transfer from the melt to the nanolites during formation. The error on N# was calculated by combining the standard deviations of the intensities between these wavenumbers in quadrature.

The method of Di Genova et al. (2017b) was used to quantify the $H_2O$ concentration, where the area of the $H_2O$ peak 2700–4000 cm$^{-1}$ (high wavenumber region, HW) is proportional to the $H_2O$ concentration (Figure 6.7). The further below the surface of the glass the spectra are collected, the more absorption occurs for the whole spectra, reducing the area under the $H_2O$ peak. To correct for this, the area of the $H_2O$ peak (HW) is normalised to the silicate peak region (low wavenumber region, LW, $<$1500 cm$^{-1}$). Spectra containing nanolites cannot be processed in this way as the magnetite peak at $\sim$670 cm$^{-1}$ changes the area of the silicate peaks (LW) (Di Genova et al., 2017b). This changes the normalisation procedure; hence $H_2O$ concentrations were not estimated for nanolite-bearing glasses. Di Genova et al. (2017b) found the Fe concentration effected the quantification of $H_2O$. Hence, the area of the $H_2O$ peak (HW) divided by the silica peak region (LW) is multiplied by a coefficient dependent on the Fe concentration (all Fe expressed as FeO, $FeO_T$) measured using EPMA, where:

$$H_2O = [(0.096 \cdot Fe^{2+}/Fe_T) + 0.663] \times \frac{HW}{LW} \tag{6.8}$$

from Di Genova et al. (2017b). Sometimes it was not possible to analyse a melt inclusion using EPMA (e.g., it was polished away during SIMS preparation), hence no $FeO_T$ value was available. In this case, the average $FeO_T$ concentration of all analysed melt inclusions was used.

Data were collected during two analytical sessions. The $H_2O$ concentration calculated using Equation 6.8 did not reproduce the $H_2O$ concentration of basaltic glasses with known $H_2O$ run during each session (Figure 6.8). For session one, ETNA glasses (ETNA05, ETNA24–ETNA26, and ETNA31–ETNA36, Tables 4.10 and 5.6) were used; and for session two MAS.1.A (4, 5, 6, 9, 10, and 10b in Table B.1) from Lesne et al. (2011) were used. This implies the empirical calibration of Di Genova et al. (2017b) is instrument specific and may change with time. Hence, an empirical correction to the $H_2O$ concentration was performed, using the basaltic glasses with known $H_2O$ concentration (Figure 6.8).

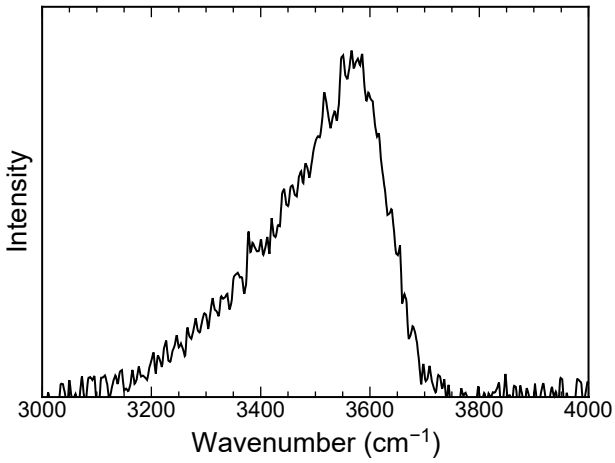


**Figure 6.7:** Example raman spectra in the high-wavelength region (HW) of a basaltic glass. The peak between 2700–4000 cm$^{-1}$ is due to dissolved $H_2O$ in the glass.

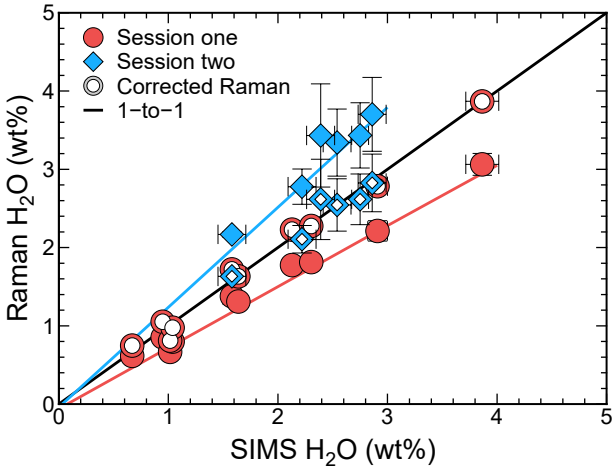


**Figure 6.8:** Empirical corrections for Raman $H_2O$: session one in blue uses ETNA05, ETNA24–ETNA26, and ETNA31–ETNA36; and session two in red uses MAS.1.A 4, 5, 6, 9, 10, and 10b.

### 6.3.3. Secondary ion mass spectrometry

SIMS was used to measure the concentration and isotope ratio of carbon and hydrogen dissolved in melt inclusions. Exposed melt inclusions were extracted from epoxy mounts and pressed into indium, then gold coated (∼40–80 nm thickness) for analysis at the Edinburgh Ion Microprobe Facility, School of GeoSciences, University of Edinburgh, UK.

First, δD and $H_2O$ were measured on the Cameca 1270 using a $O_2^-$ primary beam at 22.5 kV impact energy and 12 nA current. Secondary positive ions were extracted at 10 kV and no energy filtering was used meaning low energy ions were measured with a 100 eV energy window. A mass resolution of 2000 was used. As it takes a long time for the magnet to stabilise when jumping between mass-charge ratios of ∼2 and ∼1, extra time was spent before measuring $^1H^+$ to stabilise the magnet and check the peak was centred. $^1H^+$ was measured using a Faraday cup whilst $^2D^+$ and $^1H_2^+$ were measured using electron multipliers. Count and wait times are detailed in Table 6.3 and 80 cycles were collected for each analysis. External basaltic glasses GLD48, EN6D, and EN41 (Table 6.4); and ETNA glasses (ETNA02, ETNA03, ETNA06, ETNA07, ETNA11–ETNA17, ETNA24–ETNA27, ETNA29, ETNA30, and ETNA36) from Chapters 4 and 5 (compositions in Tables 4.10 and 5.6) were analysed as standards. The spatial resolution of these analyses is 22.5 × 37.0 μm by SE-SEM imaging of the analysis pit using the Carl Zeiss SIGMA HD VP Field Emission SEM at the School of Geosciences, University of Edinburgh, UK, as described in Section 4.3.3 (Figure 6.9).

**Table 6.3:** Species analysed for δD and $H_2O$ analysis, including count and wait times.

| Species | Magnet delay | Peak centring | $^1H^+$ | $^2D^+$ | $^1H_2^+$ |
|---|---|---|---|---|---|
| Count time (s) | 0.5 | 0.5 | 4 | 12 | 4 |
| Wait time (s) | 4 | 0.5 | 0.5 | 3 | 1 |

**Table 6.4:** Composition of external basaltic glass standards for δD and $H_2O$ SIMS analysis.

| Oxide (wt%) | EN6D | EN41 | GLD48 |
|---|---|---|---|
| $SiO_2$ | 50.42 | 49.81 | 48.29 |
| $TiO_2$ | 2.20 | 2.54 | 2.84 |
| $Al_2O_3$ | 15.40 | 16.27 | 15.82 |
| $FeO_T$ | 10.12 | 10.09 | 12.25 |
| MnO | 0.19 | 0.15 | 0.22 |
| MgO | 7.02 | 7.14 | 5.38 |
| CaO | 11.41 | 10.18 | 9.13 |
| $Na_2O$ | 3.06 | 3.02 | 3.57 |
| $K_2O$ | 0.20 | 0.45 | 0.87 |
| $P_2O_5$ | 0.28 | 0.30 | 0.50 |
| $H_2O$ | 0.74 | 0.45 | 1.07 |
| δD (‰) | -51.1 ± 2.7 | -65.7 ± 2.5 | -52.7 ± 2.5 |

*Notes:* Data are from EPMA (Pan and Batiza, 1998; Schilling et al., 1985), except $H_2O$ and δD which are measured using TCEA (Dixon et al., 2017; Kingsley et al., 2002). Errors of one standard deviation are shown for δD.

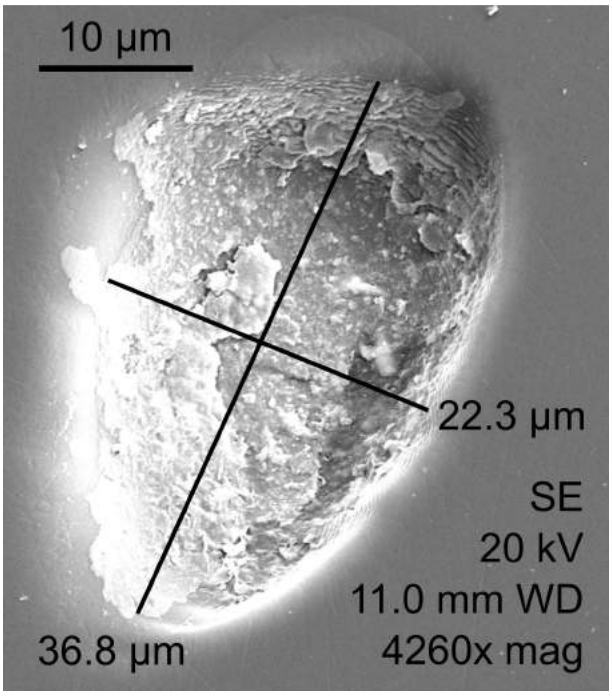


**Figure 6.9:** Secondary electron scanning electron microscopy (SE-SEM) image of the δD SIMS analysis pit.

$^1H^+$, $^2D^+$, and $^1H_2^+$ counts were corrected for Faraday cup background and deadtime. For δD quantification, $^2D^+/^1H^+$ ratios were calculated. As the background $H_2$ was low, $^1H_2^+$ was directly proportional to $^1H^+$, as its production is governed by the probability of two $^1H$ coming together and hence $^1H_2^+/^1H^+$ will be proportional to $H_2O$. At low $H_2O$ concentrations, even the low $^1H_2^+$ backgrounds can lead to artificially high $H_2O$ concentrations, hence $^1H^+$/PB (where PB is the average probe current measured before and

after analysis) was also calculated. External drift was monitored using GLD48 and ETNA24, which were analysed regularly throughout the day, and linear fits to the drift were fitted in sections (Figures 6.10a, c, and e). External drift was corrected for by dividing $^{2}D^{+}/^{1}H^{+}$, $^{1}H_{2}^{+}/^{1}H^{+}$, and $^{1}H^{+}$/PB by the corresponding calculated value of the standard at the time of measurement, with a correction factor applied when switching between GLD48 and ETNA24 to keep the data consistent. Weighted (using the error on the SIMS data) least squares calibration curves using the external basaltic glass standards (GLD48, EN6D, and EN41) and ETNA glasses were constructed for known $\delta$D against $^{2}D^{+}/^{1}H^{+}$ (Figure 6.10b), and $H_2O$ (wt%) against $^{1}H_{2}^{+}/^{1}H^{+}$(Figure 6.10d) and $^{1}H^{+}$/PB (Figure 6.10e). $H_2O$ concentrations calculated from $^{1}H_{2}^{+}/^{1}H^{+}$and $^{1}H^{+}$/PB, where either value was <0.2 wt% $H_2O$, were rejected as the $^{1}H^{+}$ counts would be too low to derive meaningful $\delta$D.

Melt inclusions were subsequently analysed for $\delta^{13}C$ as described in Section 4.3.2 for set-up one ($^{12}C^{-}|^{13}C^{-}$, Table 4.12), except that 140 cycles were collected instead of 100. Raw count data for $^{12}C^{-}$ and $^{13}C^{-}$ were checked to ensure they showed smooth changes with time for all melt inclusions analysed to ensure the analysis had not intersected a microlite or fluid inclusion, which resulted in rapid, noisy changes in counts (Figure 6.11). Noisy data were removed and, if sufficient data remained, the rest of the data were processed for carbon isotope ratios. Melt inclusions were then plucked from the indium mount, mounted in dental resin, re-polished to expose fresh glass, then repressed into indium and gold coated. Concentrations of $CO_2$ and $H_2O$ were then analysed as described for ETNA31–ETNA36 in Section 4.2.2.

The melt inclusions analysed for $\delta^{13}C$ had low $CO_2$ concentrations (50–460 ppm $CO_2$), and hence suffered from carbon contamination during analysis. Therefore, only the highest $CO_2$ melt inclusion was used (460 ppm $CO_2$) and its measured $\delta^{13}C$ (-10.8 ‰) was corrected for carbon contamination using Equation 4.8 (assuming the contamination was 110 ppm $CO_2$ with -34 $\pm$ 10 ‰). This gave a $\delta^{13}C$ -5.3 $\pm$ 2.4 ‰, which may still be affected by contamination in the initial calibration curve.

### 6.3.4. Electron probe micro-analysis

EPMA was used to measure the major, minor, and volatile element chemistry of minerals and glasses (Chapter 2) and Fe oxidation state (Chapter 3) of glasses. All EPMA data was collected on the JEOL JXA 8530F Hyperprobe at the School of Earth Sciences, University of Bristol, UK. Minerals and exposed melt inclusions were mounted in epoxy, polished to a $\sim$1–3 μm finish, and carbon coated ($\sim$15 nm) for analysis.

#### Minerals

The major and minor element mineral chemistry of olivine and pyroxene were analysed using an accelerating voltage of 15 or 20 kV, beam current of 20 nA, and a beam size of 1 μm. A similar spectrometer set-up (2 TAP, 2 PET, and 1 LIF) used for the analysis of the glass composition was used to allow analysis of minerals and melt inclusions in the same session without crystal-switching, which can effect peak positions. Count times were chosen to achieve a $\sim$1 % relative error (Equation 2.4). Mean atomic number (MAN) backgrounds were used (Donovan and Tingle, 1996, Section 2.5.3) . Peak positions were selected using the highest intensity on a smoothed wavescan. Spectrometer set-up, primary standards for peaking and calibration, and count times are detailed in Tables 6.5 and 6.6 for olivine and pyroxene, respectively. Six to ten 10 s analyses were collected for calibration, and a defocused beam of 10 μm was used on albite as it can

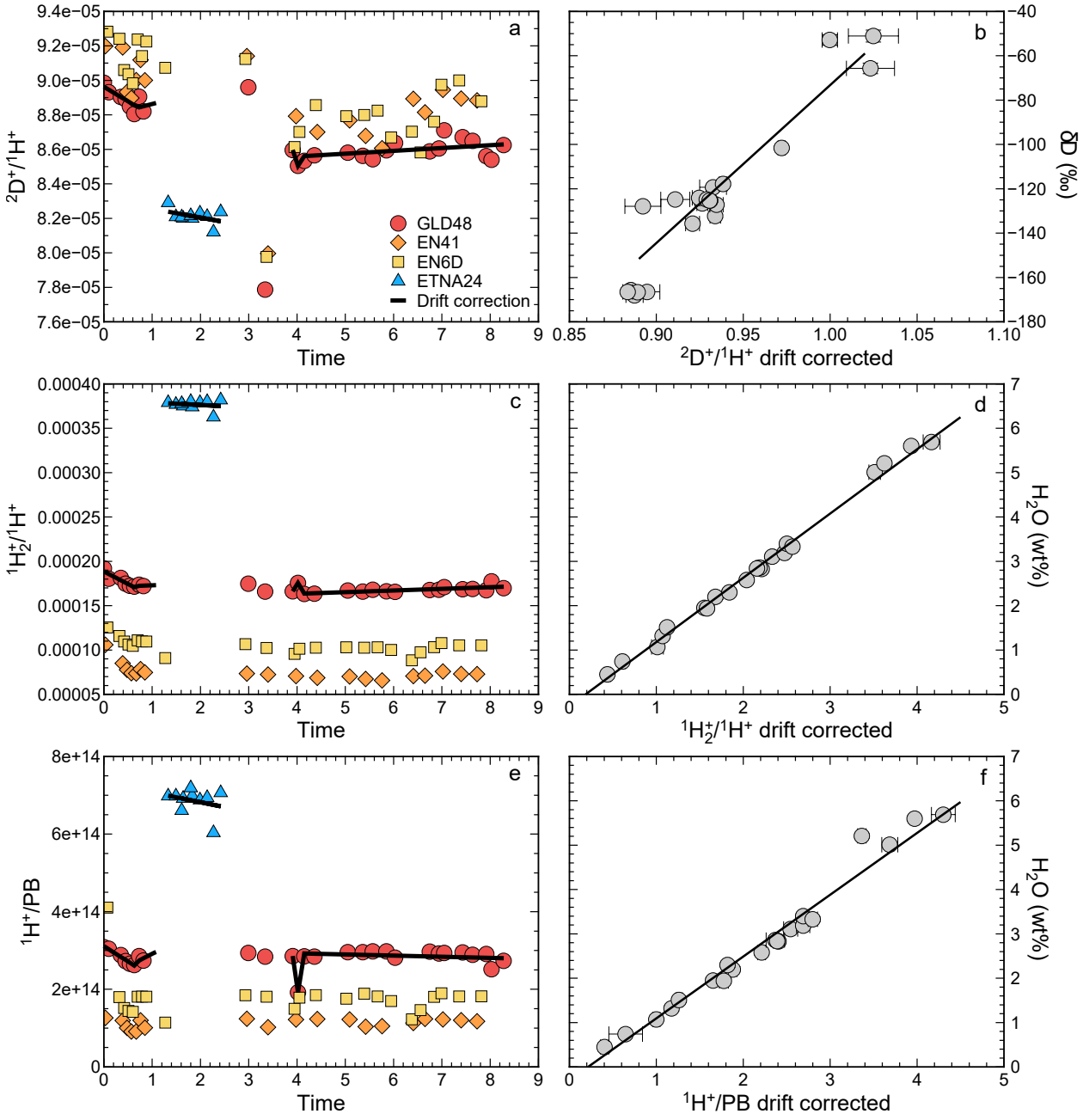


**Figure 6.10:** Drift corrections are shown in **(a)**, **(c)**, and **(e)** and calibrations in **(b)**, **(d)**, and **(f)** for **(a)**–**(b)** $^2D^+/^1H^+$, **(c)**–**(d)** $^1H_2^+/^1H^+$, and **(e)**–**(f)** $^1H^+$/PB. Weighted (using the error on the SIMS data) least squares regression lines are shown in **(b)**, **(d)**, and **(f)**.

be unstable under a focused beam. Secondary standards were SH11 and Navajo for olivine, and diopside and KK1 for pyroxene (Table 6.7). The Amstrong-Love Scott $\varphi(\rho Z)$ matrix correction was used and oxygen was calculated by stoichiometry. Additionally, the set-up in Table 6.8 was used to analyse the occasional plagioclase inclusion using a 3 μm beam diameter, where SPH was used as a secondary standard (Table 6.7).

### Melt inclusions

The major, minor and volatile (S, Cl, F, and $H_2O$ using volatiles by difference) element chemistry of melt inclusions was measured as described in Sections 2.5.3 and 2.5.4. Data were collected over two analytical

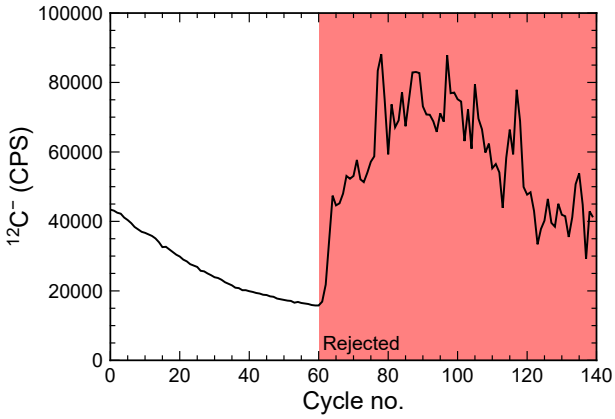


**Figure 6.11:** Example of a $^{12}C^-$ sputter curve for a melt inclusion where the beam may have intersected a fluid inclusion. Data highlighted in red were rejected from further processing.

**Table 6.5:** Analytical details for EPMA of olivine.

| Spectrometer – Crystal | | | | |
|---|---|---|---|---|
| 1 – PETJ | 2 – TAP | 3 – TAPH | 4 – PETH | 5 – LIFL |
| Ca$K\alpha$ (150) | Si$K\alpha$ (30) | Na$K\alpha$ (110) | P$K\alpha$ (150) | Fe$K\alpha$ (30) |
| *Wollastonite* | *Albite* | *Albite* | *Durango apatite* | *Andradite* |
| | Al$K\alpha$ (30) | Mg$K\alpha$ (30) | | Mn$K\alpha$ (60) |
| | *Sanidine* | *SJIO* | | *Mn metal* |
| | | | | Ni$K\alpha$ (60) |
| | | | | *Ni metal* |

*Notes:* Elements in order of analysis from top to bottom, peak count times (s) in brackets, and primary standards under each element in *italics* where SJIO is St Johns Island Olivine. Standard compositions are given in Table 2.3.

**Table 6.6:** Analytical details for EPMA of pyroxene.

| Spectrometer – Crystal | | | | |
|---|---|---|---|---|
| 1 – PETJ | 2 – TAP | 3 – TAPH | 4 – PETH | 5 – LIFL |
| Ca$K\alpha$ (30) | Si$K\alpha$ (30) | Na$K\alpha$ (90) | K$K\alpha$(120) | Fe$K\alpha$ (60) |
| *Wollastonite* | *Albite* | *Albite* | *Sanidine* | *Andradite* |
| Ti$K\alpha$ (60) | Al$K\alpha$ (30) | Mg$K\alpha$ (60) | | Mn$K\alpha$ (60) |
| $TiO_2$ | *Sanidine* | *SJIO* | | *Mn metal* |
| | | | | Cr$K\alpha$ (60) |
| | | | | $Cr_2O_3$ |

*Notes:* Elements in order of analysis from top to bottom, peak count times (s) in brackets, and primary standards under each element in *italics* where SJIO is St Johns Island Olivine. Standard compositions are given in Table 2.3.

sessions with slightly different set-ups, outlined in Table 6.8.

Fe oxidation state was measured using EPMA as described in Chapter 3.3.2, except Ni$K\alpha$ was measured on spectrometer 4 using a LILF instead of K$K\alpha$ on a PETH, to measure the Ni concentration in the glass (Table 6.9). For Ni quantification, Ni-metal was used as a standard for finding the peak positions and calibration, MAN backgrounds were used, no TDI correction was applied, and the glass composition as measured by EPMA (majors and minors) and SIMS ($H_2O$) was specified for the matrix correction. PU glasses (glass composition in Table B.1 and Ni concentration in Table 6.10) were used as secondary standards.

**Table 6.7:** Compositions of secondary mineral standards for EPMA.

| Oxide (wt%) | Diopside | KK1 | Navajo | SH11 | SPH |
|---|---|---|---|---|---|
| $SiO_2$ | 54.981 | 40.33 | 41.27 | 40.74 | 53.26 |
| $TiO_2$ | | 5.75 | 0.00 | 0.01 | |
| $Al_2O_3$ | 0.567 | 14.62 | 0.01 | 0.05 | 29.81 |
| $FeO_T$ | 0.618 | 9.61 | 8.41 | 10.17 | 0.33 |
| MnO | | 0.06 | 0.12 | 0.14 | |
| MgO | 17.993 | 7.97 | 49.98 | 48.79 | 0.10 |
| CaO | 25.829 | 13.22 | 0.09 | 0.09 | 12.16 |
| $Na_2O$ | | 2.57 | | 0.02 | 4.37 |
| $K_2O$ | | 2.12 | | | 0.28 |
| $P_2O_5$ | | | | 0.02 | |

*Notes:* KK1 is an amphibole, Navajo and SH11 are olivines, and SPH is a plagioclase. $FeO_T$ is all Fe reported as FeO.

**Table 6.8:** Set-up for major, minor, and volatile element chemistry using EPMA of melt inclusions.

| Spectrometer – Crystal | | | | |
|---|---|---|---|---|
| 1 – PETJ | 2 – TAP | 3 – TAPH | 4 – PETH | 5 – LIFL |
| Ca$K\alpha$[a] (60/30) | Si$K\alpha$[a] (60/30) | Na$K\alpha$[a] (30) | K$K\alpha$[a] (120) | Fe$K\alpha$[a] (60) |
| *Wollastonite* | *BCR-2* | *Albite* | *Sanidine* | *Andradite* |
| BCR-2 | | BCR-2 | | BCR-2 |
| Ti$K\alpha$ (60) | Al$K\alpha$ (60/30) | Mg$K\alpha$ (60) | P$K\alpha$ (60) | Mn$K\alpha$ (60/180) |
| *$TiO_2$* | *BCR-2* | *SJIO* | *Durango apatite* | *Mn metal* |
| | | BCR-2 | | |
| Cl$K\alpha$ (60/150) | | F$K\alpha$[b] (120) | S$K\alpha$ (60) | |
| *NaCl* | | *$MgF_2$* | *VG-2* | |
| | | | Barite | |

*Notes:* Elements in order of analysis from top to bottom; peak count times (s) in brackets – if two numbers are present these represent the count times used in the two different sessions; and primary standards used to find the peak position are under each element in *italics* followed by the standard for calibration if different. BCR-2 is the USGS basaltic glass standard Columbia River Basalt, SJIO is St Johns Island Olivine and VG-2 the Smithsonian Microbeam Juan de Fuca basaltic glass standard. MAN backgrounds were used. [a] TDI data collected to extrapolate to time zero in case of element migration using 6 intervals. [b] Only analysed during session two. Standard compositions are given in Tables 2.3 and 2.4.

**Table 6.9:** Set-up for Fe oxidation state and Ni concentration using EPMA on melt inclusions.

| Spectrometer – Crystal | | | | |
|---|---|---|---|---|
| 1 – TAP | 2 – TAP | 3 – TAPH | 4 – LILF | 5 – LIFL |
| Fe$L\alpha_f$ (150) | Fe$L\alpha_f$ (150) | Fe$L\beta_f$ (150) | Ni$K\alpha$ (150) | Fe$K\alpha$[a] (150) |
| | | | *Ni-metal* | *BCR-2* |

*Notes:* Flank positions (Fe$L\alpha_f$ and Fe$L\beta_f$) chosen as outlined in Section 3.3.2. Count times (s) are in brackets and primary standards used are under each element in *italics*. TDI was collected on all elements but was not used for quantification of Ni. Only Ni was quantified, using MAN backgrounds and the glass composition was specified for the matrix correction using EPMA (majors and minors) and SIMS ($H_2O$) data. Standard compositions are given in Table 2.4.

**Table 6.10:** Independent and EPMA Ni concentration for PU glasses.

| Glass | Independent Ni (ppm) | EPMA Ni (ppm) | *s.d.* |
|---|---|---|---|
| PU32 | 387 | 358 | *84* |
| PU58 | 360 | 342 | *64* |
| PU359 | 288 | 320 | *88* |
| PU361 | 463 | 424 | *61* |

*Notes:* Independent Ni from Blundy et al. (2018) using EPMA, and errors of one standard deviation (*s.d.*) are shown for EPMA Ni in *italics*.

## 6.4. Mineral and melt inclusion compositions

### 6.4.1. Minerals

Olivine, pyroxene, plagioclase, and oxide were present, but only olivine and pyroxene were analysed (data are available in Appendix H). As crystals were picked from crushed scoria, it was not possible to measure mineral modal abundances. Where the groundmass material, which consists of microlite-bearing glass (Figure 6.12c), is still attached to the crystal, olivine and pyroxene have (sub-)euhedral crystal faces (Figure 6.12). Both olivine and pyroxene contain abundant inclusions of melt and oxide, and pyroxene also contains inclusions of plagioclase (Figure 6.12).

Olivine (number of analyses, $n$, = 282; data are available in Table H.1) is $Fo_{65-83}$ where forsterite (Fo) is:

$$\mathrm{Fo} = \frac{100 \cdot \mathrm{Mg}}{\mathrm{Fe} + \mathrm{Mg}} \tag{6.9}$$

where Fe and Mg are the number of ions in the formula. Olivine composition has a bimodal distribution, with modes at $Fo_{72}$ and $Fo_{81}$ (Figure 6.13). Olivine contains trace amounts of MnO (0.24–0.90 wt%, detection limit (dl) = 92 ppm), CaO (0.12–0.44 wt%, dl = 57 ppm), $Na_2O$ (below detection limit (bdl)–0.04 wt%, dl = 89 ppm) that negatively correlate with Fo; NiO (bdl–0.11 wt%, dl = 105 ppm) that positively correlates with Fo; and $P_2O_5$ (bdl–0.10 wt%, dl = 57 ppm) and $Al_2O_3$ (0.02–0.09 wt%, dl = 86 ppm) that do not correlate with Fo (Figure 6.14).

Pyroxene ($n$ = 68; data are available in Table H.2) is $Wo_{46-56}En_{40-45}Fs_{3-11}$ where:

$$X = \frac{100 \cdot Y}{\mathrm{Mg} + \mathrm{Fe} + \mathrm{Ca}} \tag{6.10}$$

where $X$ is the end-member (wollastonite – Wo, enstatite – En, and ferrosilite – Fs), and $Y$ is the element (Mg, Fe, and Ca for Wo, En, and Fs, respectively) in number of ions in the formula, and Fe has been redistributed as $Fe^{2+}$ and $Fe^{3+}$ to maintain stoichiometry and charge balance (Lindsley, 1983). Pyroxene composition is unimodally distributed with mean and one standard deviation ($\pm 1\sigma$) of 51.1 $\pm$ 1.8 Wo, 7.1 $\pm$ 1.6 Fs and 41.9 $\pm$ 1.3 En (Figure 6.15). Pyroxene contains minor amounts of $TiO_2$ (0.59–2.08 wt%, dl = 329 ppm) that correlates positively with Wo. Pyroxene contains trace amounts of MnO (0.07–0.46 wt%, dl = 168 ppm) that correlates negatively with Wo; and $Na_2O$ (0.24–0.65 wt%, dl = 123 ppm), $K_2O$ (bdl–0.02 wt%, dl = 37 ppm) and $Cr_2O_3$ (bdl–0.35 wt%, dl = 410 ppm) that do not correlate with Wo (Figure 6.16).

Plagioclase inclusions ($n$ = 5; data are available in Table H.3) are $An_{79-92}Or_{0-2}Ab_{8-20}$ where:

$$X = \frac{100 \cdot Y}{\text{Ca} + \text{K} + \text{Na}} \tag{6.11}$$

where $X$ is the end-member (anorthite – An, orthoclase – Or, and albite – Ab) and $Y$ is the element (Ca, K, and Na for An, Or, and Ab, respectively) in number of ions in the formula.

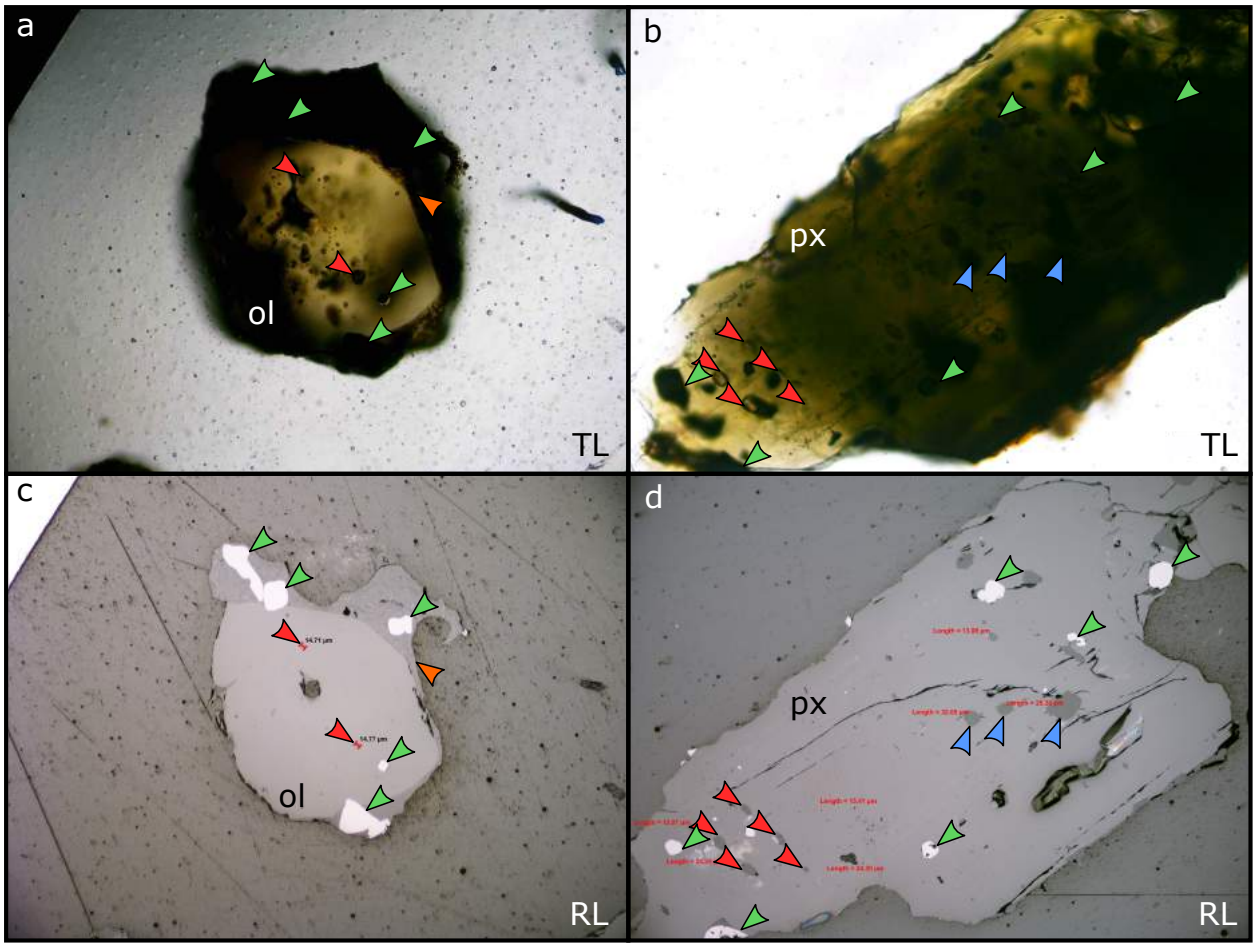


**Figure 6.12:** Example annotated photomicroscope images in transmitted light (TL) in **(a)** and **(b)** and reflected light (RL) in **(c)** and **(d)** (indicated in the bottom right corner) of olivine (ol) in **(a)** and **(c)** and pyroxene (px) in **(b)** and **(d)**. Red annotations in **(c)** and **(d)** are melt inclusion sizes, but are not meant to be legible. The colour and orientation (direction arrow is pointing to) of the arrow indicates the phase highlighted: red bottom-right arrows are melt inclusions, blue top-right arrows are plagioclase inclusions, green bottom-left arrows are oxides, and orange top-right arrows are groundmass glass (not all appearances of each phase are indicated for clarity).

### 6.4.2. Melt inclusions

Data for all melt inclusions, embayments, and groundmass glass can be found in Tables H.4–H.7. Melt inclusions analysed were hosted in olivine ($Fo_{66-82}$) and pyroxene ($Wo_{48-56}En_{40-43}Fs_{3-8}$) (Table H.4). Melt inclusions vary greatly in size (5–100 μm in diameter), but most are 20–30 μm in diameter (Figure 6.17). Olivine-hosted melt inclusions are typically rounded and isolated (Figure 6.17a), although melt inclusion assemblages do occur (Figure 6.17b), and some melt inclusions occur along growth faces (Figure

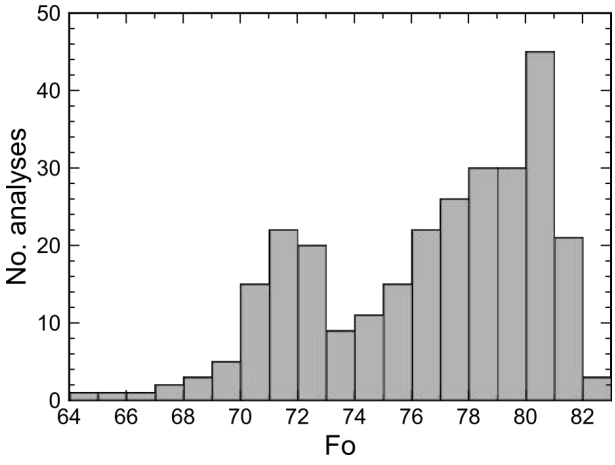


**Figure 6.13:** Histogram of olivine forsterite (Fo) content ($n$ = 282). Data are available in Table H.1.

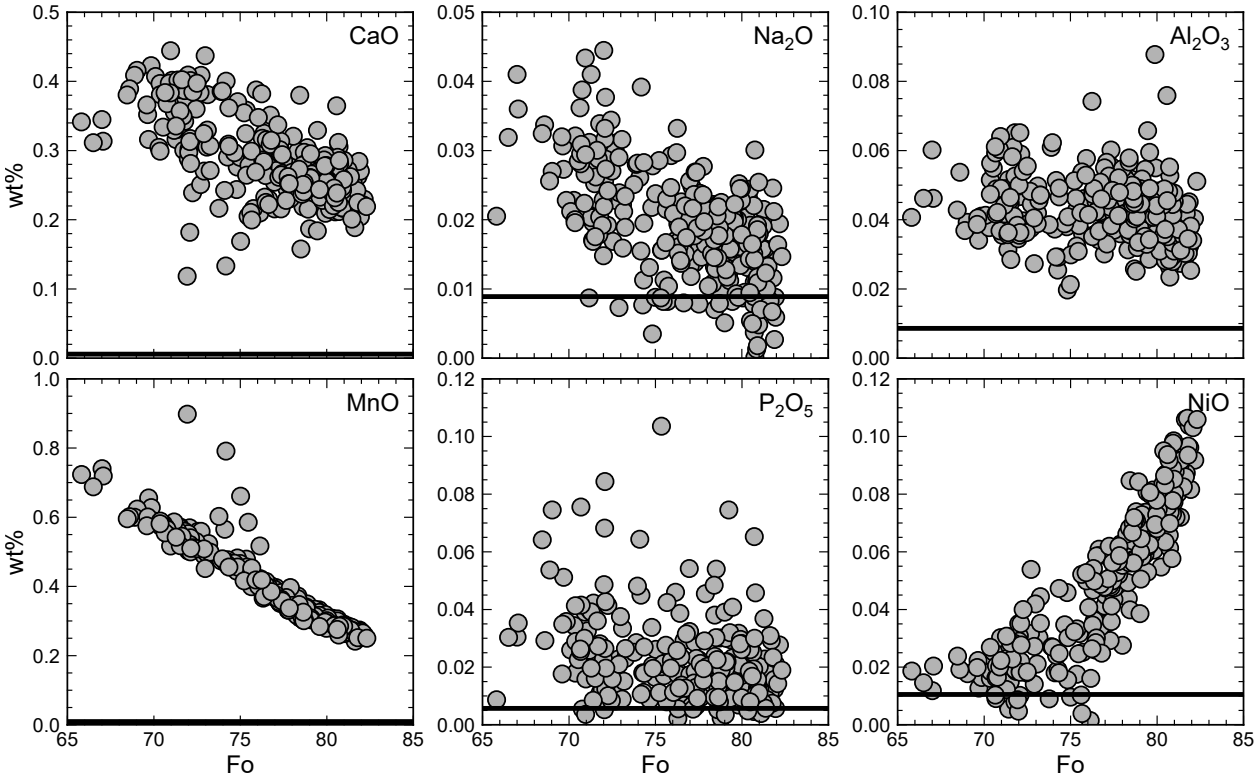


**Figure 6.14:** Olivine trace element composition, where the black horizontal line indicates the detection limit (dl). Data are available in Table H.1.

6.17c). Pyroxene-hosted melt inclusions are less rounded than those in olivine (Figure 6.17d). All inclusions analysed were naturally glassy and brown, and most of the melt inclusions observed were glassy. Some inclusions contain a large oxide crystal on the interface with the host mineral (Figure 6.17b). Bubbles are common in the melt inclusions and are mostly a small proportion of the melt inclusion volume (Figures 6.17a, b, c, d, and f), but rarely the bubble occupies most of the melt inclusion volume (Figure 6.17e). Embayments, melt pockets still connected to the outside of the crystal, were also observed (Figure 6.17f).

Figure 6.18 shows the glass chemistry from melt inclusions, embayments and groundmass glass using EPMA ($n$ = 169; data are available Table H.7). All oxide concentrations shown in Figure 6.18 are above their detection limits. Broadly, $TiO_2$, $Al_2O_3$, CaO, and MgO correlate negatively with $SiO_2$; whilst MnO, $Na_2O$, $K_2O$, and $P_2O_5$ correlate postively with $SiO_2$; and $FeO_T$ does not correlate with $SiO_2$. $Al_2O_3$, $K_2O$,

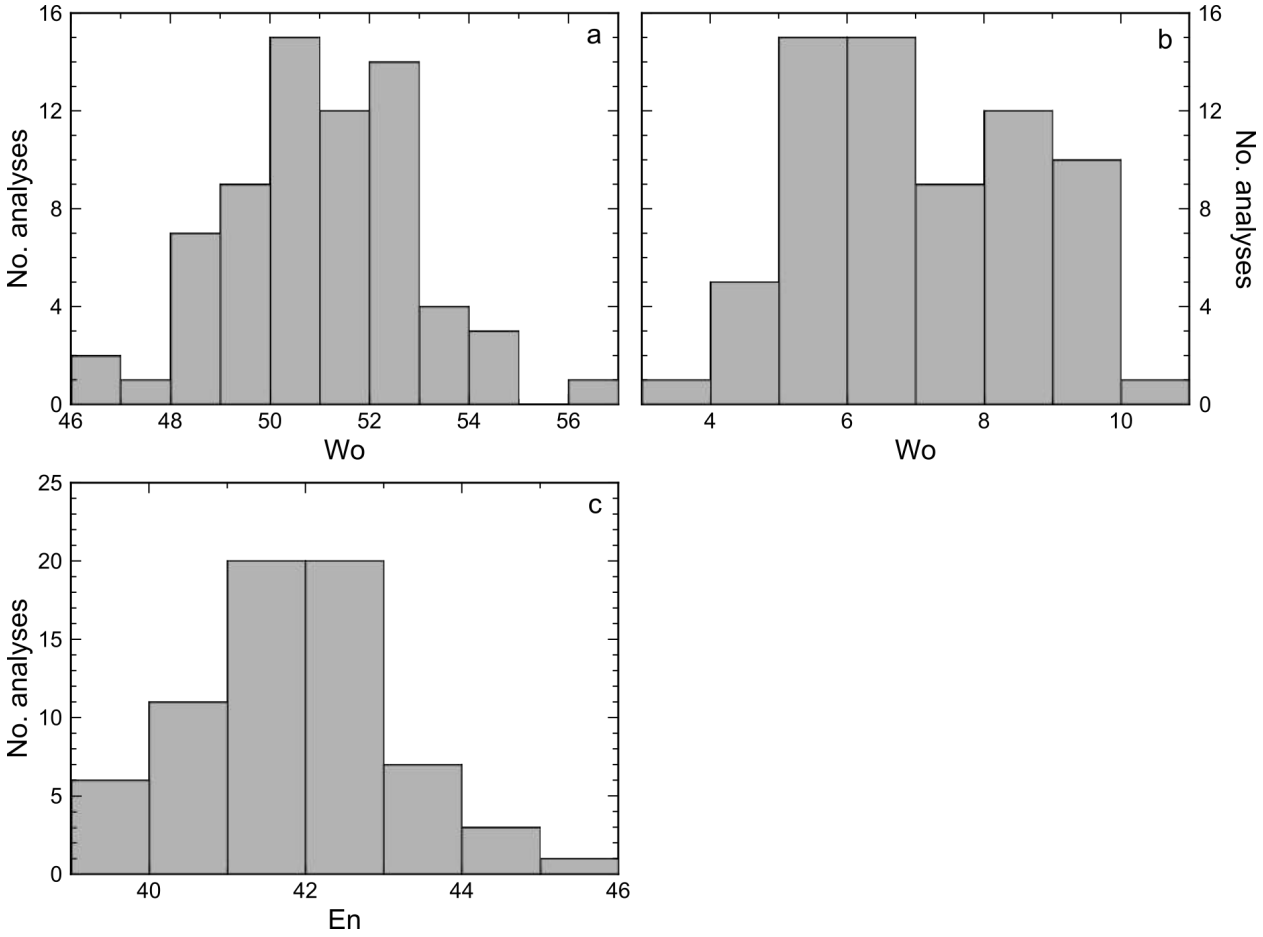


**Figure 6.15:** Histogram of pyroxene wollastonite (Wo), ferrosilite (Fs), and enstatite (En) content ($n$ = 68). Data are available in Table H.2.

and $P_2O_5$ may contain inflection points, where $Al_2O_3$ initially increases then decreases whereas $K_2O$ and $P_2O_5$ are initially constant then increase. Fo decreases with increasing $SiO_2$, although there is a wide range of Fo at ∼47 wt% $SiO_2$. NiO is below detection in all but three inclusions ($n$ = 23, dl = 60 ppm). The three inclusions with measurable NiO have large standard deviations (125 ± 189, 80 ± 84, and 70 ± 80 ppm NiO, mean and 1$\sigma$ of ten analyses), and are therefore likely to be contaminated analyses containing host olivine.

Figure 6.19 shows the volatile element compositions of melt inclusions, embayments and groundmass glass (data are available in Tables H.5–H.7). $H_2O$ measurements are either from SIMS-4f, SIMS-1270, Raman, or EPMA-VBD data. A comparison of these techniques is shown in Figure E.2 where individual melt inclusions have been analysed with multiple techniques, which in general agree well (Appendix E). SIMS and Raman have smaller errors compared to EPMA-VBD (Appendix E), hence SIMS and Raman $H_2O$ values are used in preference in EPMA-VBD (no melt inclusions were analysed using both SIMS and Raman). Some melt inclusions were analysed using both SIMS-4f and SIMS-1270, in which case SIMS-4f $H_2O$ values are used as SIMS-1270 measurements are more effected by high H backgrounds and changes in the probe current than SIMS-4f measurements. $CO_2$ concentrations are all from SIMS-4f data. Cl, S, and F concentrations are from EPMA, with detection limits of 114, 50, and 305 ppm, respectively. S negatively correlates with $SiO_2$; Cl has a wider range with increasing $SiO_2$; and F does not correlate with $SiO_2$. In high Fo olivine, $H_2O$ decrease with increasing $SiO_2$, whilst in low Fo olivine there is no correlation. $CO_2$ initially

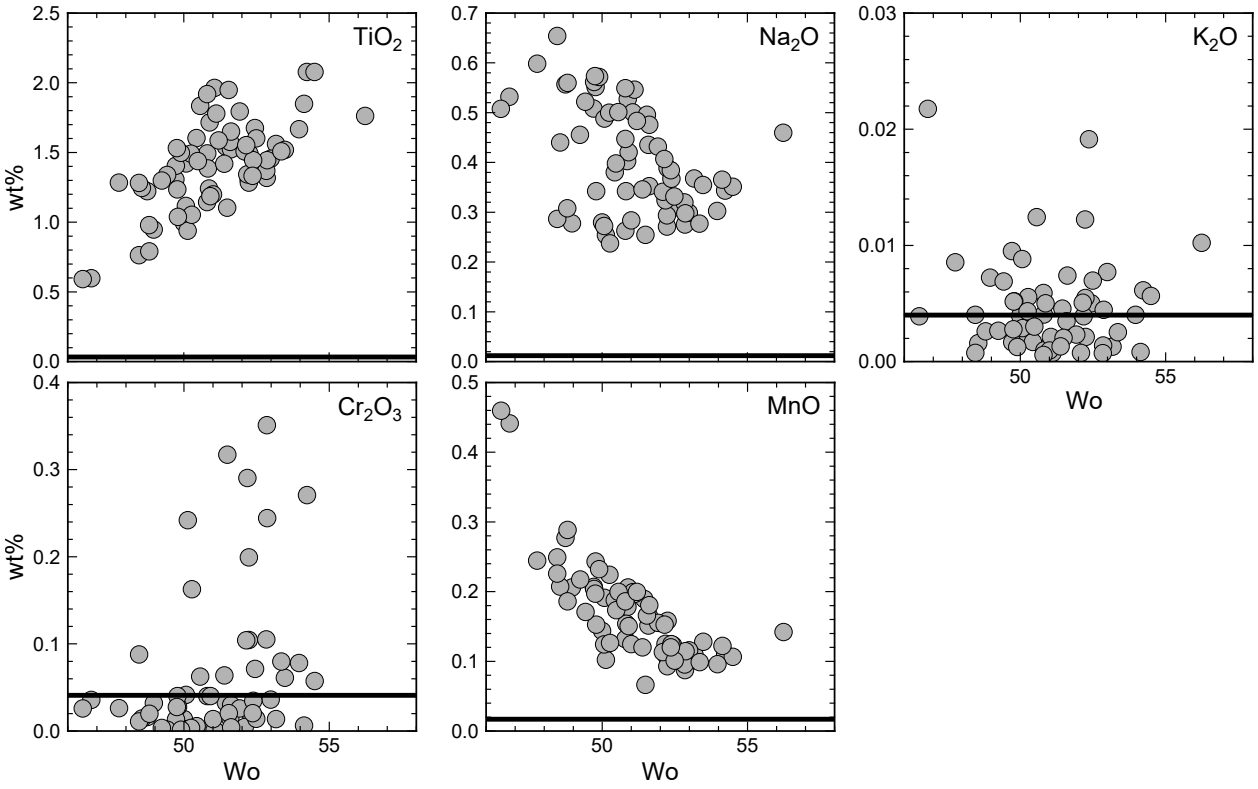


**Figure 6.16:** Pyroxene trace element composition, where the black horizontal line indicates the detection limit (dl). Data are available in Table H.2.

decreases with $SiO_2$ and then remains low at higher $SiO_2$, except one melt inclusion with the highest $CO_2$ measured which is at high $SiO_2$. Figure 6.20 shows the concentration and isotope ratios for $H_2O$ and $CO_2$. There is a large range of $CO_2$ (0–1100 ppm) at high $H_2O$ (2–3 wt%). At low $H_2O$ (<2 wt%) $CO_2$ is low (<300 ppm), although there are two melt inclusions with high $CO_2$. There is no correlation between $\delta$D and $H_2O$ or $CO_2$. One melt inclusion has a measured carbon isotope ratio of -5.27 $\pm$ 2.4 ‰ $\delta^{13}C$ with 460 ppm $CO_2$ and 2.24 wt% $H_2O$.

Figure 6.21 shows the glass Fe oxidation state and degree of nanolitisation (N#, Equation 6.7) of melt inclusions, embayments, and groundmass glass (data are available in Tables H.5 and H.7). Fe oxidation state is measured using EPMA and N# by Raman spectroscopy. Fe oxidation state does not correlate with $SiO_2$ and N# does not correlate with $H_2O$, but Fe oxidation state negatively correlates with N#. Of the glass analysed using Raman ($n$ = 119), 52 % contained nanolites.

## 6.5. Evaluation of melt inclusion modification

All melt inclusions were hosted in crystals found in small scoria that will have cooled quickly post-eruption (Lloyd et al., 2013). This is supported by observed melt inclusions being naturally glassy. Hence, the effect of modification after eruption is assumed to be negligible. Still, melt inclusions may have suffered post-entrapment modification prior to eruption.

As discussed in Section 6.2.1, the degree of post-entrapment crystallisation of olivine on the walls of the melt inclusion can be evaluated using $K^{ol-melt}_{D(Fe-Mg)}$ and $K^{ol-melt}_{D(Ni)}$. Using Equation 6.1 and the $FeO_T$ and MgO

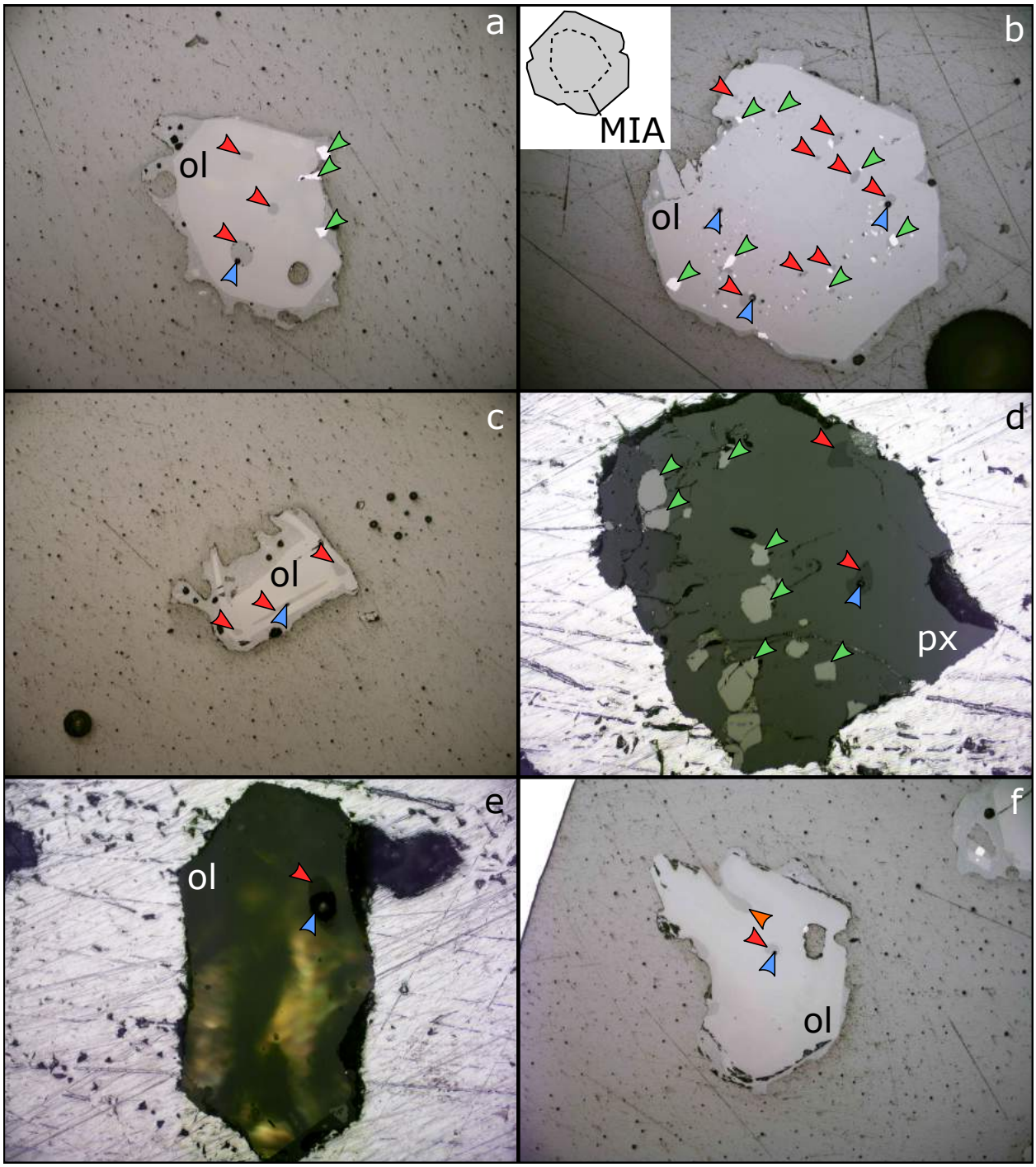


**Figure 6.17:** Annotated reflected light photomicroscope images: **(a)** isolated, glassy olivine-hosted melt inclusion containing small bubble, **(b)** olivine-hosted melt inclusion assemblage (MIA), with oxides trapped in the melt inclusions, **(c)** olivine-hosted melt inclusions along a growth face, **(d)** pyroxene-hosted melt inclusions, **(e)** large bubble in an olivine-hosted melt inclusion, and **(f)** olivine-hosted embayment. The mineral type is labelled, where ol is olivine and px is pyroxene. The colour and orientation (direction arrow is pointing to) of the arrow indicates the phase highlighted: red bottom-right arrows are melt inclusions, blue top-right arrows are bubbles, green bottom-left arrows are oxides, and orange top-right arrows are embayments (not all appearances of each phase are indicated for clarity).

concentrations of melt inclusions and their host-olivine (Tables H.1 and H.7), $K^{ol–melt}_{D(Fe–Mg)}$ is 0.11–0.30. The range in $K^{ol–melt}_{D(Fe–Mg)}$ either requires a range in melt $Fe^{2+}/Fe_T$ at the time of entrapment (0.34–0.95 $Fe^{2+}/Fe_T$

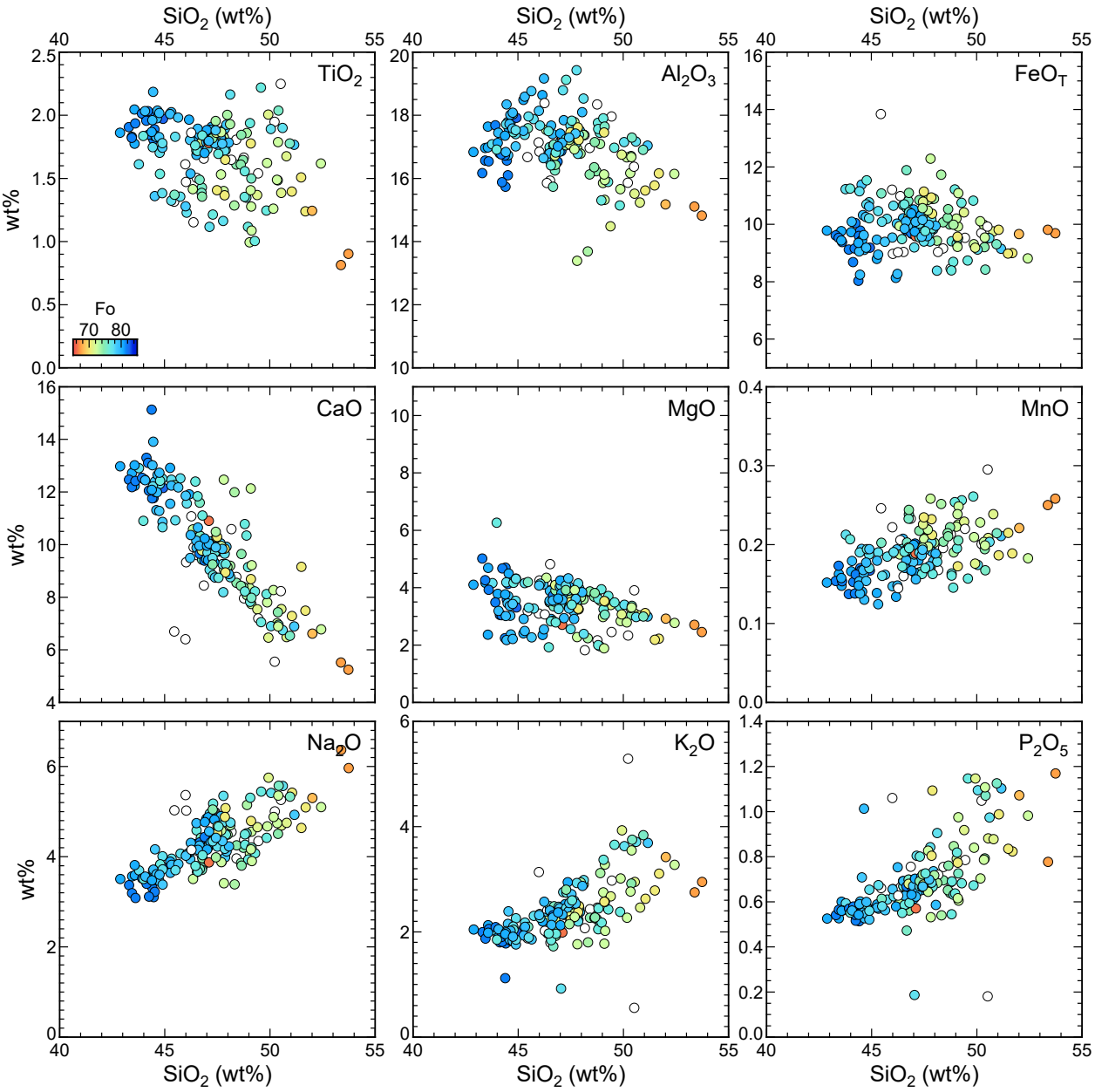


**Figure 6.18:** Glass major and minor element chemistry for melt inclusions, embayments, and groundmass glass, coloured by Fo if olivine-hosted or white if pyroxene-hosted. The oxide is labelled in the top right corner ($FeO_T$ is all Fe reported as FeO) and all concentrations are in wt%. Data are available in Table H.7.

using Equation 6.2), post-entrapment olivine crystallisation from an initially homogeneous $K^{ol-melt}_{D(Fe-Mg)}$ (and hence homogeneous melt $Fe^{2+}/Fe_T$), or a combination of both. Figure 6.22 shows $K^{ol-melt}_{D(Fe-Mg)}$ against measured $Fe^{2+}/Fe_T$ with Equation 6.2 shown. The data point with $Fe^{2+}/Fe_T > 1$ is likely contaminated by the olivine host or an oxide grain within the melt inclusion. Some melt inclusions have low $K^{ol-melt}_{D(Fe-Mg)}$ consistent with their $Fe^{2+}/Fe_T$, whilst others fall below Equation 6.2. This implies some melt inclusions may have suffered host olivine crystallisation, but $Fe^{2+}/Fe_T$ can also be modified post-entrapment, which is discussed in Section 6.2.3. The range of MgO in the melt inclusions (1.89–6.27 wt%, Table H.7) gives $K^{ol-melt}_{D(Ni)}$ 19–64 using Equation 6.3, which results in a maximum equilibrium NiO of 41 ppm using the measured NiO the olivines (Table H.1). Unfortunately, the detection limit for NiO in the glass was 60 ppm, hence it is not possible to evaluate the extent of olivine crystallisation in this way.

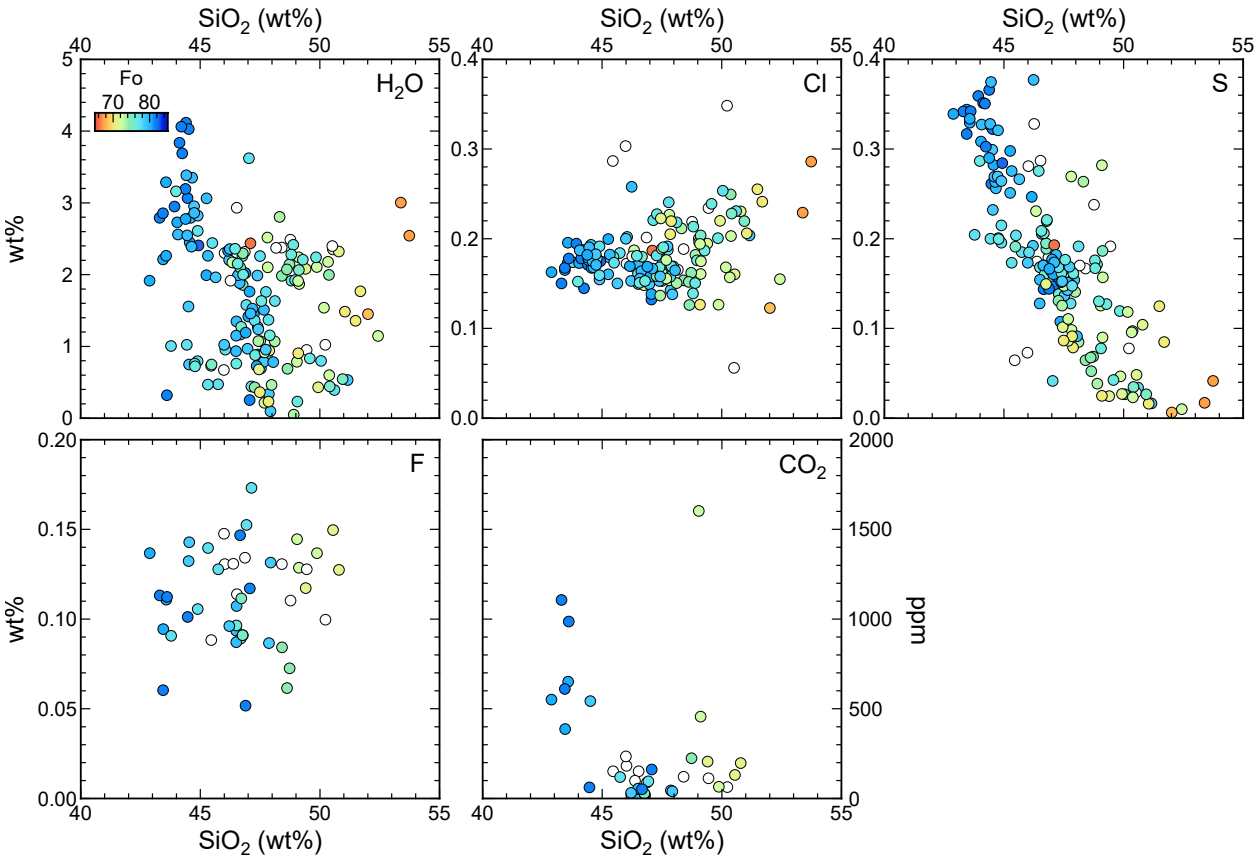


**Figure 6.19:** Glass volatile content from melt inclusions, embayments, and groundmass glass, coloured by Fo if olivine-hosted or white if pyroxene-hosted. The volatile species is labelled in the top right corner. All volatile concentrations are in wt%, except $CO_2$ (ppm). Data are available in Tables H.5–H.7.

To estimate the degree of post-entrapment diffusive re-equilibration with the host olivine (Section 6.2.2), the olivine composition of one transect away from an olivine-hosted melt inclusion was measured using EPMA (Figure 6.23). Away from the melt inclusion, FeO decreases and Fo increases consistent with Fe diffusion from the melt into the olivine. There are no bulk data available for the 23 November 2013 eruption, but Viccaro et al. (2015) measured bulk rock for eruptions from January 2011 to April 2013, which show varying degrees of differentiation and magma mixing from a similar parental magma. Assuming the bulk magma from the 23 November 2013 eruption lies on the FeO-MgO trend defined by the January 2011 to April 2013 bulk rock data, melt inclusions have lower MgO and FeO than would be expected (Figure 6.24a). The Fo of olivine in equilibrium with the bulk rock was calculated using Petrolog 3.1.1.3 (Danyushevsky and Plechov, 2011) at 1 kbar and FMQ (model of Borisov and Shapkin 1990) using the Ford et al. (1983) olivine model (Figure 6.24b). Extending the Fo-FeO trend from the bulk rock implies that significant Fe loss has occurred, consistent with the 'Fe-loss triangle' of Danyushevsky et al. (2000), but complete re-equilibration has not been achieved for most melt inclusions.

$H_2O$ concentration and Fe oxidation state may have been modified prior to eruption. Negative correlations between $\delta D$ and $H_2O$ are indicative of $H_2O$ loss by Equation 6.4 (e.g., Gaetani et al., 2012; Hauri, 2002; Shaw et al., 2008), but for olivine-hosted melt inclusions in Figure 6.20 the relationship has no clear negative trend, therefore dehydration is not the sole process controlling the relationship between $\delta D$ and $H_2O$. Relationships between size of melt inclusion, $H_2O$ concentration, and $\delta D$ have been used to identify

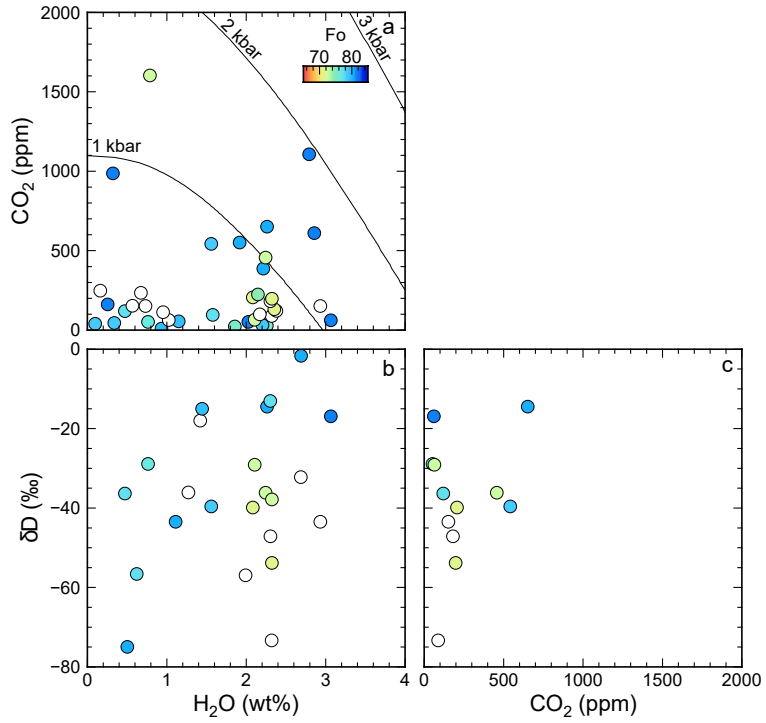


**Figure 6.20:** Glass $CO_2$, $H_2O$, and δD from melt inclusions coloured by Fo if olivine-hosted or white if pyroxene-hosted: **(a)** $CO_2$-$H_2O$ with isobars calculated using VolatileCalc (46 wt% $SiO_2$ and 1140 °C), **(b)** δD-$H_2O$, and **(c)** δD-$CO_2$. Data are available in Tables H.1 and H.6.

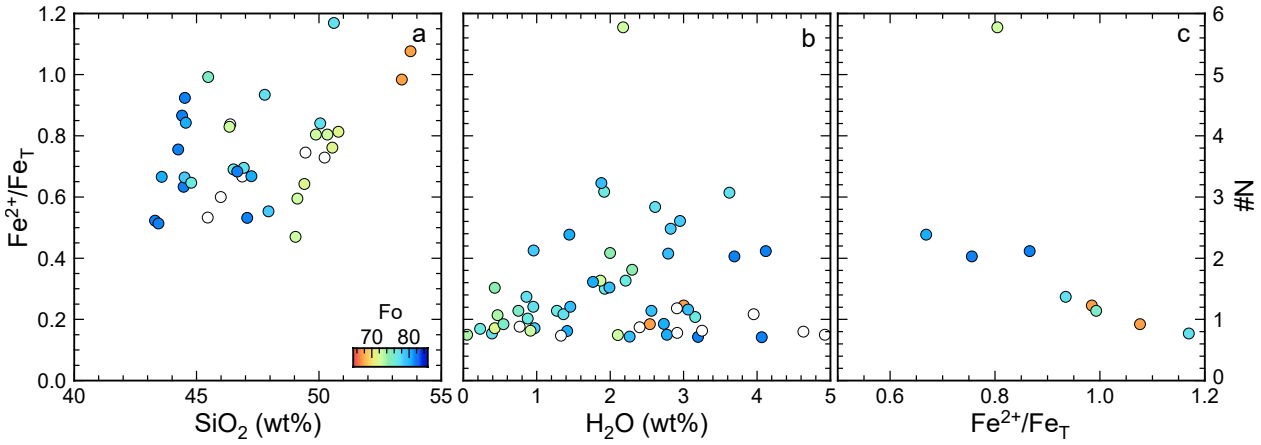


**Figure 6.21:** Glass Fe oxidation state and degree of nanolitisation (N#) from melt inclusions, embayments, and groundmass glass, coloured by Fo if olivine-hosted or white if pyroxene-hosted: **(a)** Fe oxidation state against $SiO_2$, and N# against **(b)** $H_2O$ and **(c)** Fe oxidation state. Data are available in Tables H.5–H.7.

dehydration (e.g., Métrich and Deloule, 2014), but this depends on the position of the melt inclusion within the olivine which is hard to gauge when crystals have been picked from crushed scoria and polished. Some melt inclusions are more reduced than would be expected using $K_{D(Fe-Mg)}^{ol-melt}$ (Figure 6.22), which either indicates host crystallisation or $fO_2$ re-equilibration. Magma reduction can occur due to S degassing during ascent, hence this could drive re-equilibration in these melt inclusions.

Some melt inclusions contain large bubbles (e.g., Figure 6.17e), which are likely co-entrapped fluid bubbles. Therefore, the volatiles in these large bubbles were not in the melt within the melt inclusion at the time of

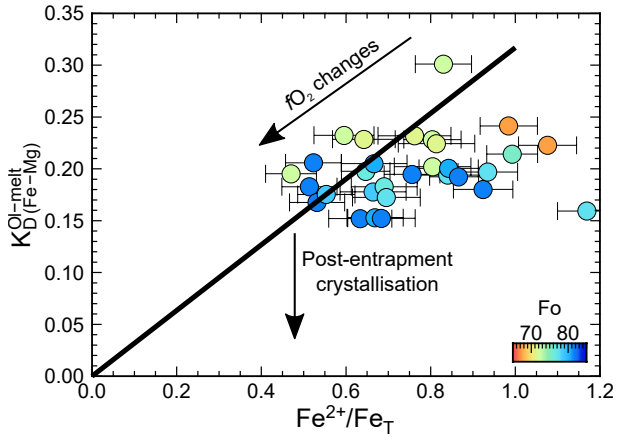


**Figure 6.22:** $K^{ol-melt}_{D(Fe-Mg)}$ (Equation 6.1) against EPMA $Fe^{2+}/Fe_T$, where the solid black line is the relationship expected at equilibrium from Blundy et al. (2018) (Equation 6.2). Data are available in Tables H.1 and H.7

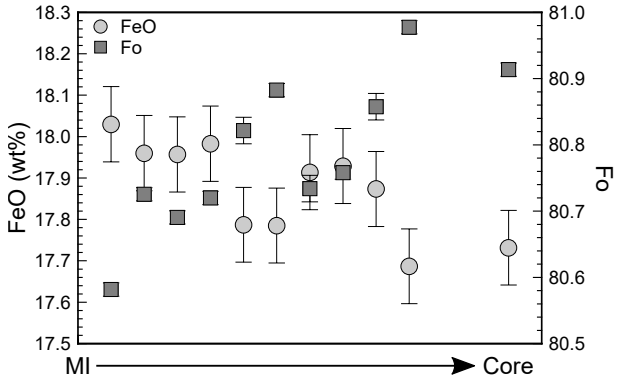


**Figure 6.23:** Transect away from a melt inclusion into the core of the olivine crystal (MI → Core) for FeO (circle) and Fo (square). Data are available in Table H.1.

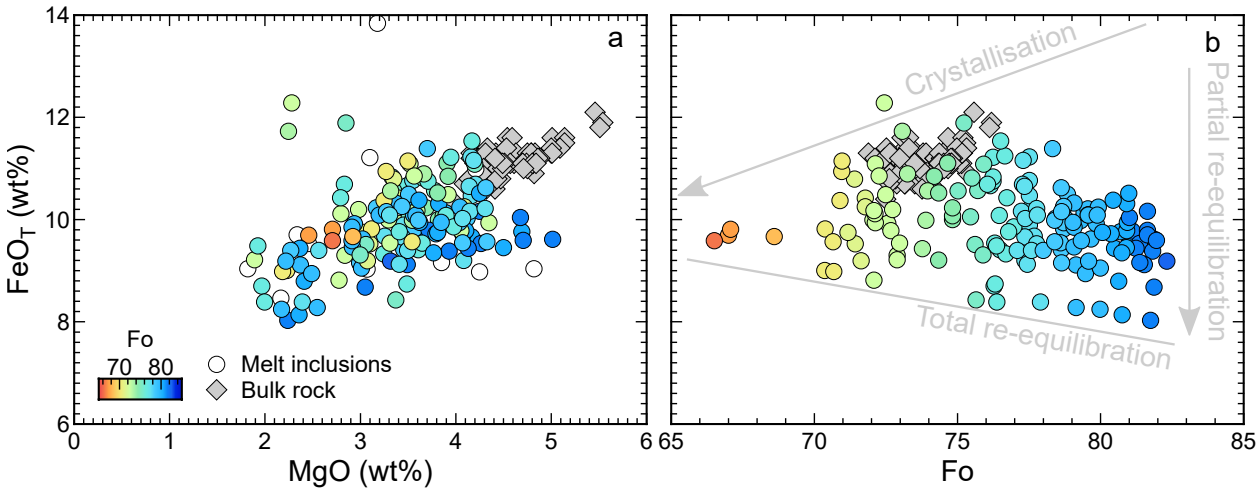


**Figure 6.24:** Evaluating Fe loss by comparing melt inclusion (this study) and bulk rock (Viccaro et al., 2015) data, where melt inclusions are coloured by Fo if olivine-hosted or white if pyroxene-hosted: **(a)** $FeO_T$ (all Fe reported as FeO) against MgO, and **(b)** $FeO_T$ against Fo, which has been calculated for bulk rock using Petrolog 3.1.1.3 (Danyushevsky and Plechov, 2011) at 1 kbar and FMQ (Borisov and Shapkin, 1990) using the olivine model of Ford et al. (1983), with annotations of the 'Fe-loss triangle' from Danyushevsky et al. (2000) shown in grey.

entrapment. Most melt inclusions contain small bubbles (e.g., Figures 6.17a–d and f), which are likely post-entrapment shrinkage bubbles and therefore may contain significant $CO_2$ related to the melt. Rapidly cooled samples (i.e., scoria rather than lava flows) may contain no measurable $CO_2$ in their bubbles, as there is insufficient time for the $CO_2$ to diffuse into the bubble (Hartley et al., 2014). The $CO_2$ content of the bubbles was not measured, therefore reported $CO_2$ concentrations in the melt inclusions are minimum

estimates. If $CO_2$ is present in the bubble, it will also change the $\delta^{13}C$ of the melt. This process can either be kinetically-driven or under equilibrium conditions depending on the time available for $CO_2$ to diffuse into the bubble. Assuming equilibrium, closed-system degassing to form the bubble would cause the melt to become heavier by at maximum +2 to +4 ‰, whilst kinetically-controlled bubble formation would cause the melt to become lighter (e.g., Mattey, 1991; Mattey et al., 1990; Aubaud et al., 2004).

As all melt inclusions analysed were glassy (Figure 6.17), no homogenisation was required. Some inclusions contain oxide crystals (Figure 6.17b) but, due to their large size and location on the melt-host interface, these are interpreted to be co-entrapped oxide crystals as oxide crystals can act as nucleation sites for melt inclusions (Roedder, 1979).

Nanolites were observed in many of the melt inclusions analysed, hence it is important to understand when they formed. Figure 6.25 shows a Raman transect across an embayment. $H_2O$ concentration (qualitatively from the area of the HW region, Figure 6.25b) decreases from the inner to outer part of the embayment, whilst degree of nanolitisation (quantitatively from N#, Figure 6.25) decreases. This was also observed in an embayment from Pantelleria (Di Genova et al., 2018), indicating $H_2O$ degassing during ascent from the $H_2O$ concentration gradient across the embayment, and nanolitisation where diffusion was fast enough (i.e., high $H_2O$). This implies these nanolites formed on the quench in melt inclusions where the conditions were favourable (i.e., low viscosity due to high $H_2O$), and they were not present in the melt at the time of entrapment.

Melt inclusions have been affected by varying degrees of post-entrapment modification (Figure 6.3). Most melt inclusions have lost MgO and FeO, due to continued host crystallisation and re-equilibration (Figure 6.24). Some melt inclusions have undergone a degree of re-equilibration of $H_2O$ and Fe oxidation state, therefore $H_2O$ concentrations are a minimum estimate and $\delta D$ are a maximum (Figure 6.22). Some $CO_2$ may have been sequestered into bubbles, therefore $CO_2$ concentrations are a minimum and $\delta^{13}C$ are a minimum/maximum, depending on whether the process occurred under equilibrium or kinetic conditions (Figures 6.17a–d and f). Oxide crystals were co-entrapped rather than crystallising post-entrapment (Figure 6.17b) and nanolites are a quench feature (Figure 6.25).

## 6.6. Comparison with previous eruptions at Etna

### 6.6.1. 2011–2013 eruptive sequence

Giuffrida and Viccaro (2017) give five different magmatic environments (referred to as $M_{00}$, $M_0$, $M_{1a}$, $M_{1b}$, and $M_2$ in Table 6.1 and Figure 6.2) to account for the variation in olivine composition found in the 2011–2013 eruptions using rhyolite-MELTS to constrain the intensive parameters of the environments. The volatile concentrations are set to be $H_2O$-poor and $CO_2$-rich (Aiuppa et al., 2007; Collins et al., 2009; Nicotra and Viccaro, 2012). Higher volatile concentrations do not match their phase equilibria and mineral compositions. They infer that $M_{00}$, $M_0$, and $M_{1a}$ were active in 2011–2012, whilst $M_{1b}$ and $M_2$ only became active in 2013, and magmas do not have to pass through all environments during ascent. Alternatively, Giacomoni et al. (2018) define four different magmatic facies (referred to as F1, F2, F3, and F4 in Table 6.1 and and Figure 6.2) to the plumbing system of Etna during the 2011–2012 eruptive sequence, based on mineral, bulk rock, and groundmass glass chemistry. In general, for equivalent olivine compositions, 'M' environments are cooler, shallower and drier than 'F' facies. Neither study contains data from the 23

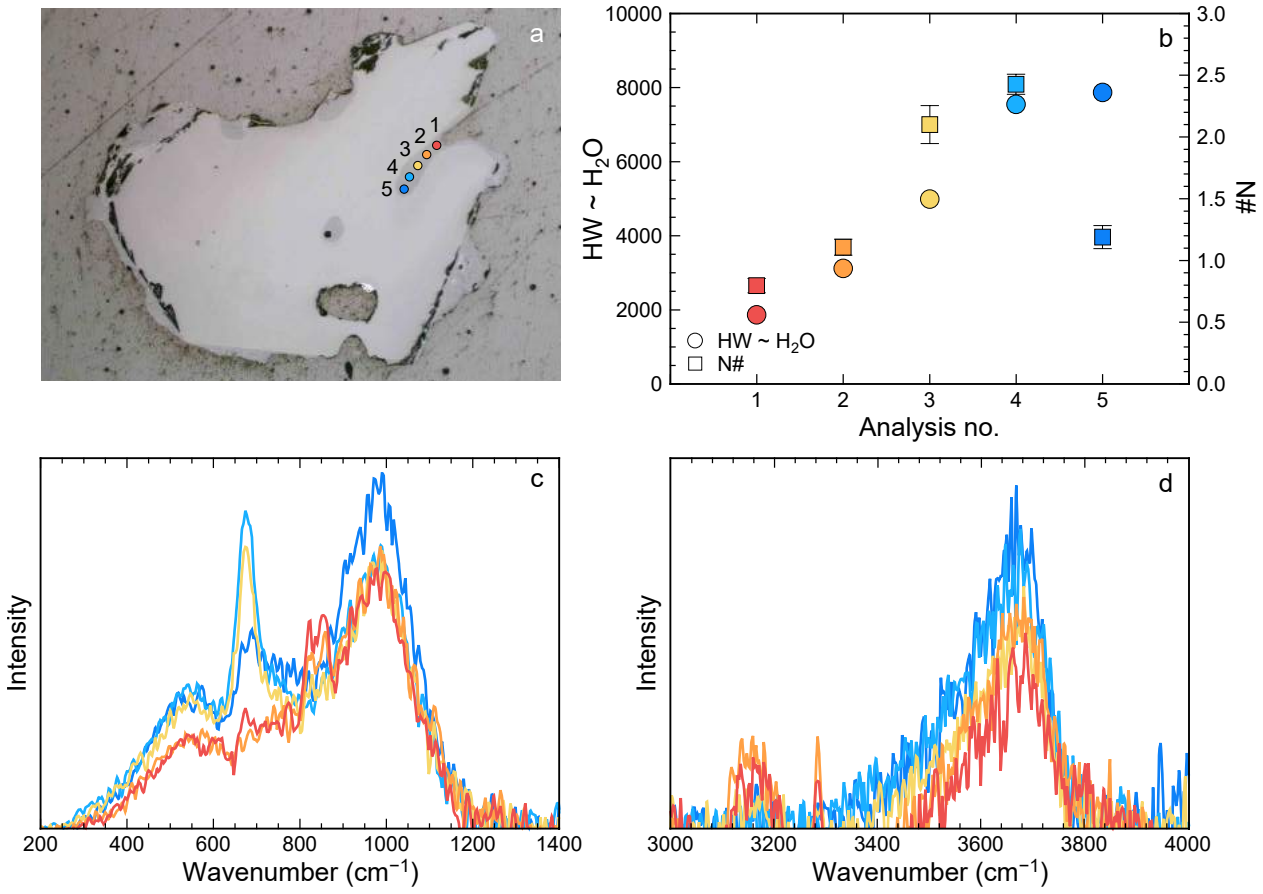


**Figure 6.25:** Raman transect across an embayment in olivine: **(a)** photomicroscope image in reflected light showing the approximate position where the Raman spectra were collected; **(b)** area of HW region as a proxy for $H_2O$ concentration and degree of nanolitisation (N#) along the embayment; and **(c)** low-wavelength and **(d)** high-wavelength region of the Raman spectra, which are corrected for temperature, excitation line effects and backgrounds according to (Di Genova et al., 2017b). Colours from **(a)** used in **(b)**–**(d)**.

November 2013 eruption itself.

Olivine from the 23 November 2013 eruption has modes at $Fo_{72}$ and $Fo_{81}$, which would correspond to $M_2$ and $M_0$ or F4 and F2, respectively. $M_0$ and F2 are hotter and deeper than $M_2$ and F4, hence this implies a mixing event between deep, hotter magma with shallower, cooler magma prior to eruption. This is consistent with Viccaro et al. (2015) who thought injections of fresh magma, and mixing, were triggers for paroxysmal events during 2011–2013 eruptive sequence. Melt inclusions from the 23 November 2013 eruption contain 0–3 wt% $H_2O$, which is inconsistent with the rhyolite-MELTS modelling of Giuffrida and Viccaro (2017). Either the 23 November 2013 eruption was much more hydrous than the other 2011–2013 eruptions, or the intensive parameters need to be re-evaluated at higher $H_2O$ concentrations. Melt inclusions are trapped between 0 and 2 kbars (Figure 6.20), which encompasses the range suggested for $M_2$ and F4, but is far lower than that of $M_0$ and F2. Either these inclusions have lost $CO_2$ to a bubble or are undersaturated, and hence the pressure is underestimated, or high Fo olivine is crystallised at shallower depths than implied by either of these models.

### 6.6.2. 2001–2007 eruptions

Figure 6.26 shows a comparison of major and minor element chemistry of melt inclusions from 23 November 2013 paroxysm with bulk rock from the 2011–2013 eruptive sequence (Viccaro et al., 2015) and melt inclusions from gas-rich eruptions in 2001 and 2002 and gas-poor eruptions in 2004, 2006, and 2007 (Collins et al., 2009; Métrich et al., 2004; Schiavi et al., 2015). All data lie on the same differentiation trend, implying all melts are formed by the same process from the same magma source, as has been previously discussed for the 2001–2007 eruptions (Collins et al., 2009). MgO shows different trends with $SiO_2$, but this is due to post-entrapment crystallisation corrections. The inflection points seen in $Al_2O_3$, $K_2O$, and $P_2O_5$ are also seen in previous eruptions (and perhaps in $FeO_T$). Data from the 23 November 2013 eruption cover a similar range to the 2001–2002 eruptions and extend to more primitive compositions than the 2004–2007 melt inclusion and 2011–2013 bulk rock data. The Fo of the 23 November 2013 also covers the whole range seen in 2001–2007 eruptions. This suggests the 23 November 2013 eruption was fed by a more primitive magma than the 2004–2007 eruptions, similar to the 2001–2002 eruptions.

Figure 6.27 shows the same comparison for the volatile concentration of melt inclusions. For $H_2O$, S, and F, the 23 November 2013 paroxysm covers the whole range shown in the 2001–2007 eruptions. Cl has a similar range, although there are some data with Cl $>$0.3 wt% for the other eruptions which are not present in the 23 November 2013 dataset. $CO_2$ concentrations are mostly lower than either the 2001–2002 or 2004–2007 eruptions, although the trend with $SiO_2$ is more similar to the 2001–2002 eruptions.

The 2001–2002 eruptions are thought to have been fed by primitive, volatile-rich magma, whilst the 2004–2007 eruptions were fed by the degassed, residual of this magma (Collins et al., 2009; Métrich et al., 2004; Spilliaert et al., 2006). The inflections seen in $Al_2O_3$, $K_2O$, and $P_2O_5$ (and perhaps $FeO_T$) may require fractional crystallisation to explain their behaviour. The 2001–2002 $H_2O$-$CO_2$ trend is predominantly closed-system degassing during fast ascent to the surface (Métrich et al., 2004; Spilliaert et al., 2006), whilst the 2004–2007 eruptions have high $CO_2$ at low $H_2O$ concentrations caused by $CO_2$-flushing (Collins et al., 2009) (Figure 6.28). As the 23 November 2013 paroxysm spans the compositional range of both these types of eruptions, a combination of these processes maybe important in driving the eruption (Figure 6.28). The main feature for the 23 November 2013 eruption is a degassing trend, where there is a wide range in $CO_2$ at high $H_2O$ and then low $CO_2$ at low $H_2O$, similar to the 2001–2002 eruptions. Some melt inclusions have less $H_2O$ than might be expected for their $CO_2$ concentration, which could be post-entrapment $H_2O$-loss, $CO_2$-flushing, or disequilibrium $CO_2$ degassing (Caricchi et al., 2018; Collins et al., 2009; Pichavant et al., 2018). The high $CO_2$ melt inclusions are hosted in $Fo_{78-82}$ olivine in the 2001–2002 eruptions, with decreasing $CO_2$ concentration with decreasing Fo implying the melt is crystallising during degassing (Collins et al., 2009) (Figure 6.29). Conversely, in the 2004–2007 eruptions, high $CO_2$ melt inclusions are hosted by $Fo_{70-72}$ olivine (Collins et al., 2009) (Figure 6.29). Most of the high $CO_2$ melt inclusions from the 23 November 2013 eruptions are in high Fo olivine ($Fo_{82}$), although one is in a low Fo olivine ($Fo_{73}$), perhaps showing that there was a combination the 2001–2002 and 2004–2007 eruptive processes occurring (Figure 6.29).

The relationship between $K_2O$-$CO_2$-$H_2O$ can be used to track degassing, $H_2O$-loss, and $CO_2$-flushing (Caricchi et al., 2018). Crystallisation increases $K_2O$ as it is incompatible: $H_2O$-loss does not change $K_2O$ whereas $CO_2$-flusing and degassing increase $K_2O$ as they dehydrate the melt promoting crystallisation. The apparent fluid composition (molar proportion of $H_2O$ in the fluid, $X_{H_2O}$) inferred from glass $CO_2$-$H_2O$ also

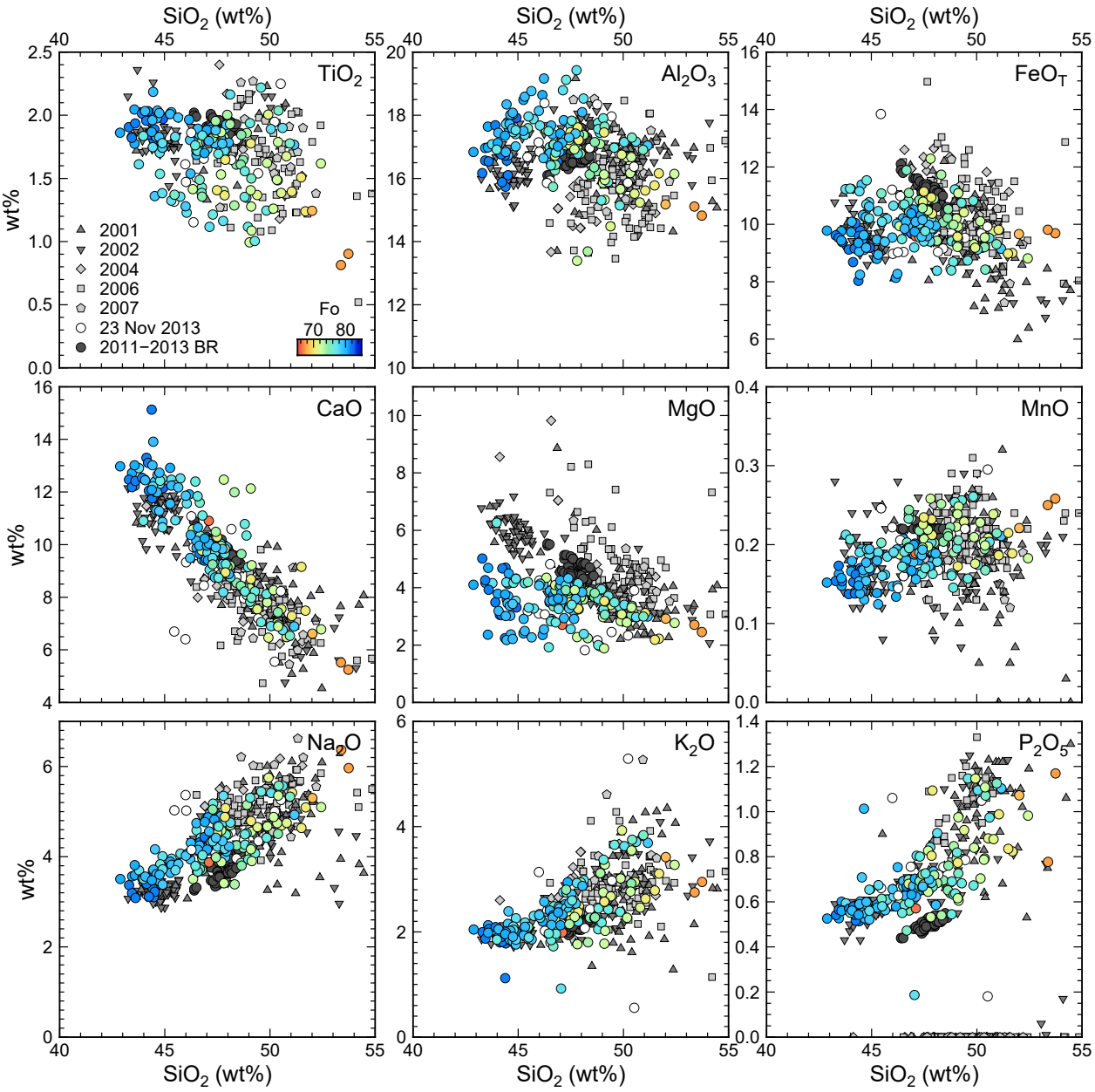


**Figure 6.26:** Major and minor element chemistry for melt inclusions, embayments, groundmass glass, and bulk rock (BR, 2011–2013 only), where symbol shape indicates eruption year and colour eruption type (dark grey is gas-rich and light grey is gas-poor) for literature data from Métrich et al. (2004) [2001], Spilliaert et al. (2006) [2002], Collins et al. (2009) [2001, 2002, 2004, 2006, and 2007], Schiavi et al. (2015) [2001, 2002, 2004, and 2006], and Viccaro et al. (2015) [2011–2013 BR]. Data from this study [23 November 2013] are coloured by Fo or white if pyroxene-hosted.

changes with these processes: $CO_2$-flushing leads to a decrease in $X_{H_2O}$, $H_2O$-loss to an apparent decrease in $X_{H_2O}$, and degassing to an increase in $X_{H_2O}$. Therefore, these processes have different trajectories, as shown in Figure 6.30 (Caricchi et al., 2018). The data, albeit scattered, points to a combination of $CO_2$-flushing and $H_2O$-loss.

Alternatively, experiments to simulate closed-system degassing using decompression rates appropriate to eruptions have shown that disequilibrium degassing may occur during basaltic eruptions (Pichavant et al., 2018). Typically, degassing of basaltic magmas during eruption has been assumed to be an equilibrium

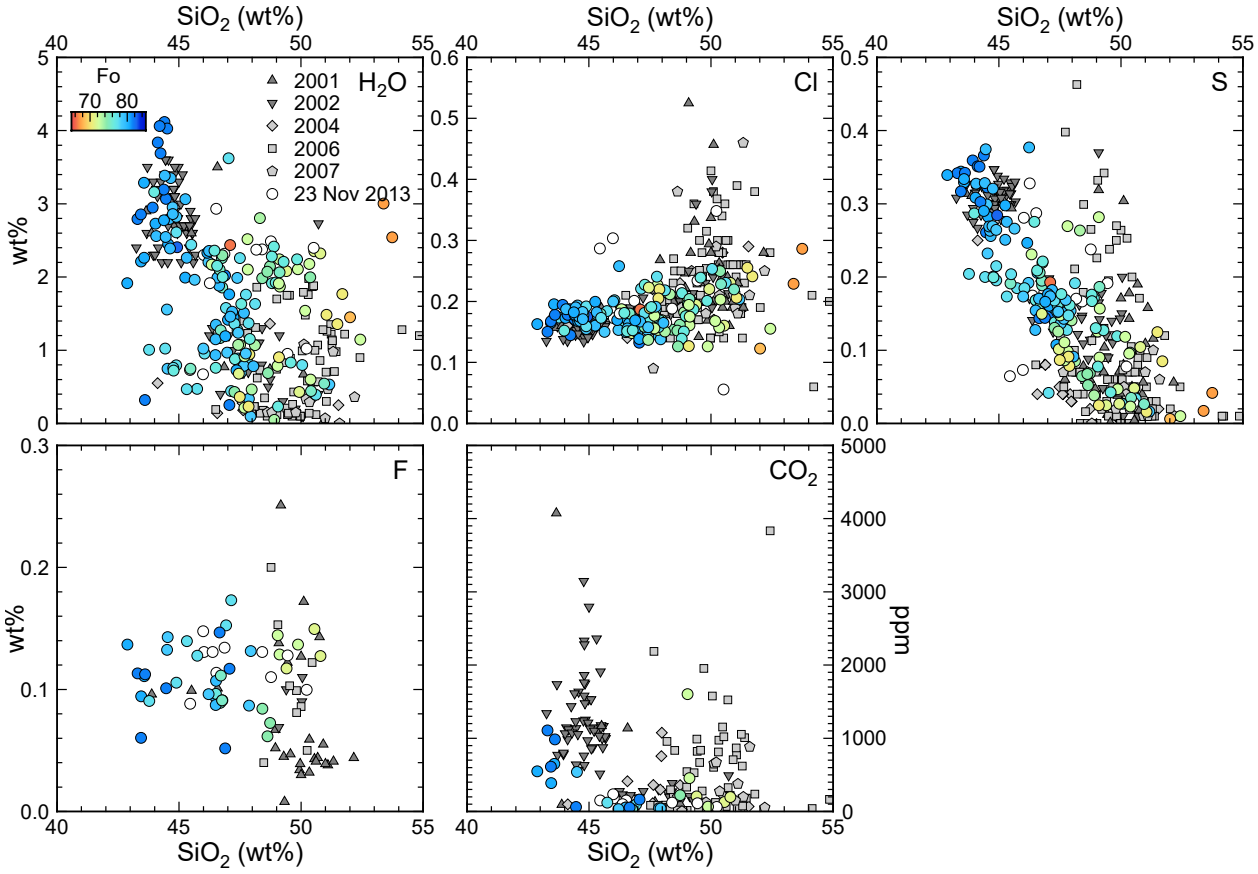


**Figure 6.27:** Volatile concentrations for melt inclusions, embayments, and groundmass glass where symbol shape indicates eruption year and colour eruption type (dark grey is gas-rich and light grey is gas-poor) for literature data from Métrich et al. (2004) [2001], Spilliaert et al. (2006) [2002], Collins et al. (2009) [2001, 2002, 2004, 2006, and 2007], and Schiavi et al. (2015) [2001, 2002, 2004, and 2006]. Data from this study [23 November 2013] are coloured by Fo or white if pyroxene-hosted.

process because of the high temperatures and low viscosities of the magma. Pichavant et al. (2018) found that whilst $H_2O$ and S had equilibrium concentrations in the melt after decompression, $CO_2$ concentrations were elevated. This implied that the $CO_2$ concentration was in disequilibrium, likely due to the slow diffusivity of $CO_2$ in silicate melts, which hindered its diffusion into bubbles (Zhang et al., 2010). These experiments are crystal-free, which requires greater degrees of supersaturation to allow bubble nucleation, but some natural MORB samples also show supersaturation with respect to a $CO_2$-rich fluid therefore disequilibrium degassing maybe a common process (e.g., Aubaud et al., 2004; Fine and Stolper, 1986; Dixon et al., 1988; Stolper and Holloway, 1988; Dixon and Stolper, 1995). All solubility models assume equilibrium, hence this would mean calculated isobars, degassing trends, and fluid composition are not appropriate. Disequilibrium $CO_2$ degassing results in elevated $CO_2$ concentrations compared to the $H_2O$ concentrations, which looks similar to $H_2O$-loss. Therefore, another explanation for the deviation from closed- or open-system degassing paths in Figure 6.28 is variable degrees of $H_2O$-loss.

### 6.6.3. Volatile isotope ratios

The $\delta D$ data are quite scattered and probably result from a combination of degassing, $H_2O$-loss from the melt inclusion, and possibly crustal contamination (Figure 6.31). The range of $\delta D$ is similar to that of Allard

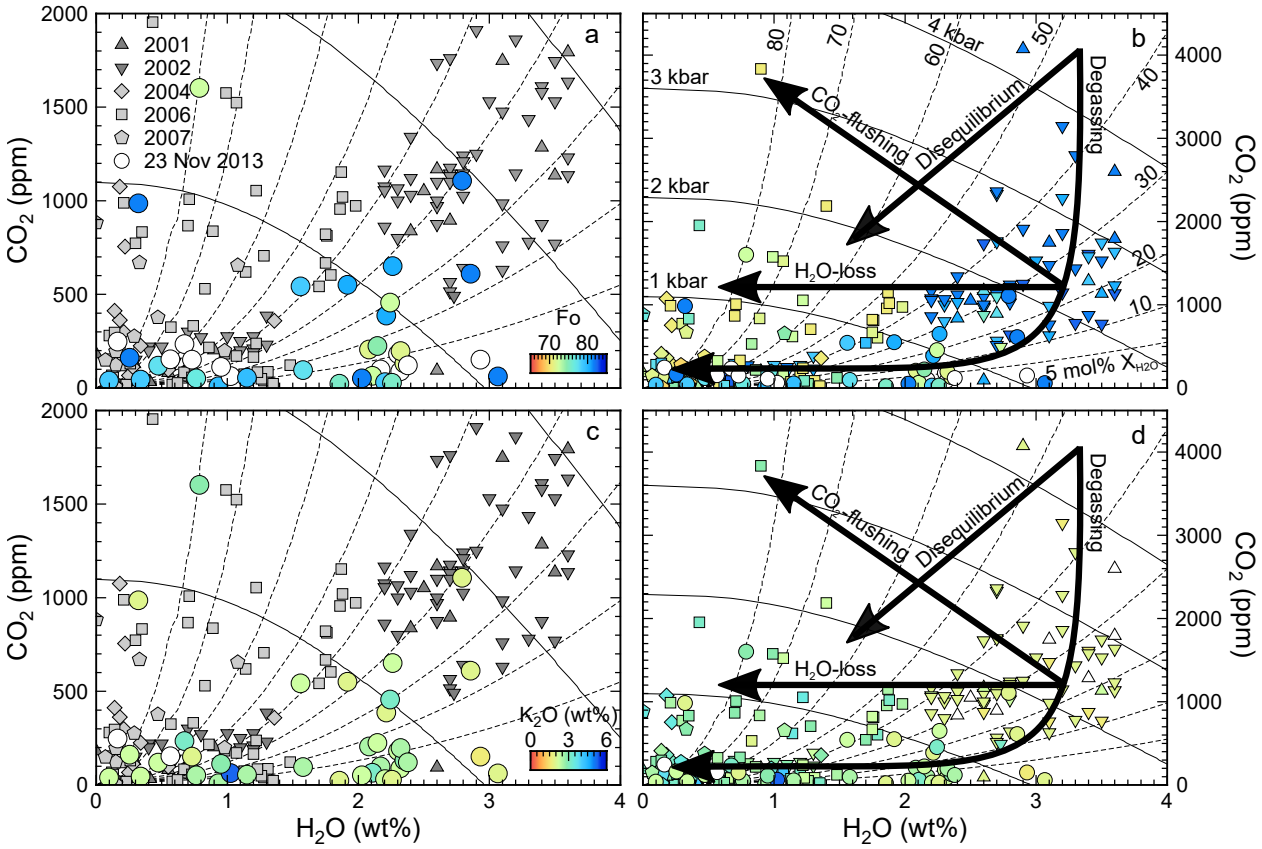


**Figure 6.28:** $H_2O$ and $CO_2$ concentrations for melt inclusions, embayments, and groundmass glass, where symbol shape indicates eruption year. For **(a)** and **(c)** colour indicates eruption type (dark grey is gas-rich and light grey is gas-poor) for literature data from Métrich et al. (2004) [2001], Spilliaert et al. (2006) [2002], and Collins et al. (2009) [2001, 2002, 2004, 2006, and 2007], except data from this study [23 November 2013] which are coloured by Fo and $K_2O$, respectively. In **(b)** and **(d)** all data are coloured by Fo and $K_2O$, respectively. Isobars (solid) and isopleths (dashed) shown are calculated using VolatileCalc at 46 wt% $SiO_2$ and 1140 °C and are labelled in **(b)**. Schematic trajectories for closed-system equilibrium and disequilibrium degassing, $H_2O$-loss, and $CO_2$-flushing from Caricchi et al. (2018) and Pichavant et al. (2018) are shown by thick, black arrows in **(b)** and **(d)**.

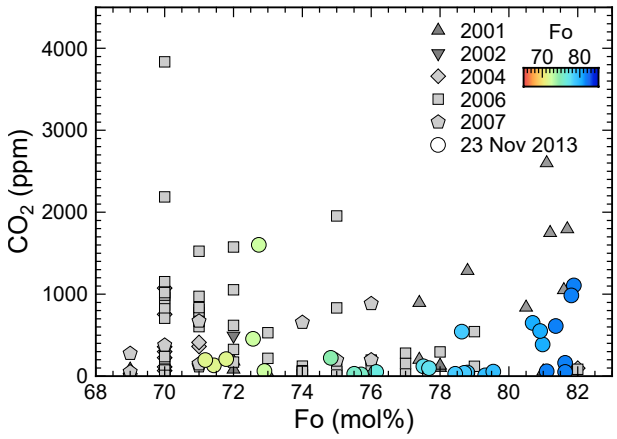


**Figure 6.29:** $CO_2$ concentration against host-olivine Fo for melt inclusions, where symbol shape indicates eruption year and colour indicates eruption type (dark grey is gas-rich and light grey is gas-poor), for literature data from Métrich et al. (2004) [2001], Spilliaert et al. (2006) [2002], and Collins et al. (2009) [2001, 2002, 2004, 2006, and 2007], except data from this study [23 November 2013] which are coloured by Fo.

et al. (2006b) for the 2001 eruption, shown schematically in Figure 6.31 as their data are only reported in a conference abstract. They report that melt inclusions with 2000–4000 ppm $CO_2$ and 3.2 $\pm$ 0.3 wt% $H_2O$ have $\delta$D = -20 ‰ (-90 to 0 ‰ range), whilst those with <1300 ppm $CO_2$ have $\delta$D = 0–40 ‰. They suggest that this isotopically heavier $H_2O$ represented $H_2O$-loss from ponding magma rather than post-entrapment

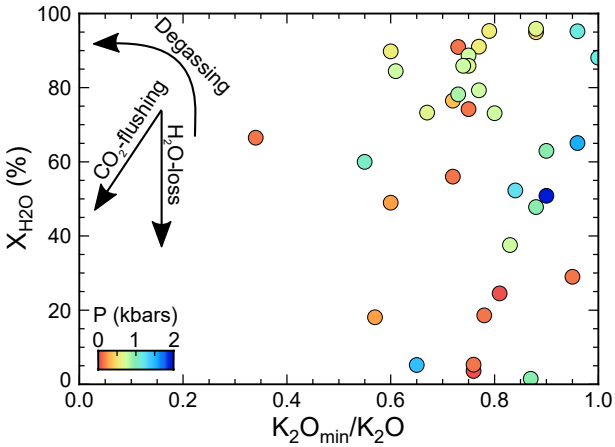


**Figure 6.30:** Fluid $X_{H_2O}$ against melt $K_2O_{min}/K_2O$ coloured by pressure (P), where $X_{H_2O}$ and P are calculated using VolatileCalc at 46 wt% $SiO_2$ and 1140 °C. Schematic trajectories for degassing, $H_2O$-loss, and $CO_2$-flushing from Caricchi et al. (2018) are shown.

loss of H, but could also be due to exchange with a D-enriched fluid. As the melt evolves, $H_2O$ and δD decrease due to closed- then open-system degassing down to -140 ‰. For comparison, high temperature gases (1000 °C) at Etna have -50 to -45 ‰ δD (Allard, 1978) but have likely interacted with surficial $H_2O$ (Allard, 1982).

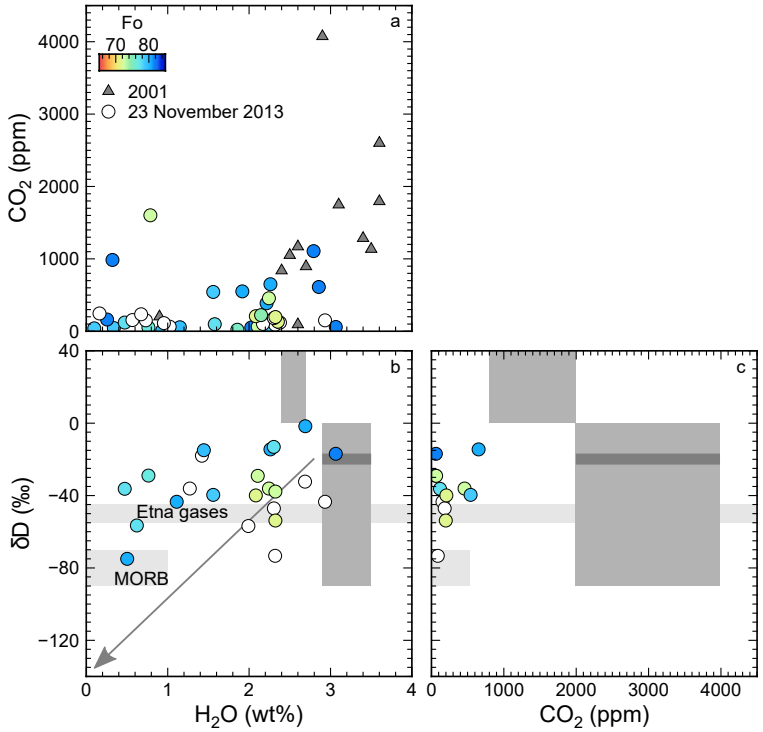


**Figure 6.31:** Glass $CO_2$, $H_2O$, and δD from melt inclusions which are triangles (Métrich et al., 2004) and shaded regions (Allard et al., 2006b) in dark grey for the 2001 eruption, or coloured by Fo if olivine-hosted or white if pyroxene-hosted for 23 November 2013 (this study): **(a)** $CO_2$-$H_2O$ with isobars calculated using VolatileCalc (46 wt% $SiO_2$ and 1140 °C), **(b)** δD-$H_2O$, and **(c)** δD-$CO_2$. δD ranges in light grey are for MORB and Etna gases (Allard, 1978).

There have been many studies of the carbon concentration and isotope ratio of the volcanic gases emitted at Etna since the 1970s, including sampling the groundwater, diffuse soil gases, fumaroles, and the plume (Aiuppa et al., 2004; Allard, 1983; Allard et al., 1991; Giammanco et al., 1998; Giammanco and Pecoraino, 2005; Martelli et al., 2008; Paonita et al., 2012; Rizzo et al., 2015, 2014; D'Alessandro et al., 1997). There appears to be a temporal trend in $\delta^{13}C$ values measured at Etna, starting in the 1970s at -4.5 ‰ $\delta^{13}C$ and

becoming progressively heavier, reaching -1 ‰ in 2010 (Chiodini et al., 2011). More recent measurements of the plume in 2013 and 2014 maintain these heavier values of -2.2 and -0.5 ‰ $\delta^{13}C$, respectively (Rizzo et al., 2015, 2014). This could reflect a change in the source, with either a greater crustal fluid contribution (Clocchiatti et al., 1988), changing magmatic source (Schiano et al., 2001; Tonarini et al., 2001), increasing contribution from the basement limestone (Chiodini et al., 2011), or increased mantle metasomatism from carbon-rich, slab-derived fluids (Frezzotti et al., 2009). Alternatively, the trend could be due to a constant bulk $\delta^{13}C$ (-4 ‰ $\delta^{13}C$) but decreasing amounts of degassing (Chiodini et al., 2011).

Paonita et al. (2012) calculated that the bulk $\delta^{13}C$ of the magma at Etna was -1.1 ‰ based on modelling He-Ar-$CO_2$ degassing trends of fumaroles at the Voragine summit crater. Their model required open-system degassing and mixing between two end-members: a deep magma from 2–4 kbar and a shallow magma at $\sim$1.3 kbar. This bulk $\delta^{13}C$ value is much heavier than mantle values of -6 to -4 ‰ (Cartigny et al., 2001), consistent with an additional component effecting the carbon isotope ratio. The bulk carbon concentration has been estimated as $\sim$2 wt% based on the C/S volcanic gas molar ratio (Aiuppa et al., 2007).

One melt inclusion has a measured carbon isotope ratio (-5.27 $\pm$ 2.4 ‰ $\delta^{13}C$, 460 ppm $CO_2$, and 2.24 wt% $H_2O$), which represents the only measurement of the carbon isotope ratio of the melt at Etna. This datum is consistent with degassing at Etna being an equilibrium process, as the melt is isotopically lighter than the gas measurements (e.g., Mattey, 1991; Mattey et al., 1990). Assuming the bulk $CO_2$ concentration is 2 wt% (Aiuppa et al., 2007) and a fractionation factor of +2 ‰ (Mattey, 1991) gives a bulk $\delta^{13}C$ of -3.3 $\pm$ 2.4 and +2.3 $\pm$ 2.4 ‰ assuming closed- and open-system degassing, respectively (Equations A.15 and A.24). The latter is far heavier than previous estimates and unrealistic, whilst the former is in the range of previous estimates. Conversely, assuming the bulk $\delta^{13}C$ is -1.1 ‰ (Paonita et al., 2012) and a fractionation factor of +2 ‰ (Mattey, 1991) gives bulk $CO_2$ concentrations of 4000 ppm (minimum) and 1000–12000 ppm for closed- and open-system degassing, respectively. The minimum for open-system degassing is too low as the maximum $CO_2$ concentration in melt inclusions was 1600 ppm $CO_2$ (Figure 6.19e), and as much as 4000 ppm $CO_2$ has been measured in melt inclusions from previous eruptions (Métrich et al., 2004). The value for closed-system degassing is a minimum because the maximum difference between the bulk and the melt is the fractionation factor (i.e., 2 ‰). Hence the lightest the melt can be -3.1 ‰, which is within error of the measured value for the melt inclusion.

These are very simply calculations, assuming a single step of either open- or closed-system equilibrium degassing, without magma mixing. Magma mixing, especially, is very important at Etna. Additionally, crustal contamination during ascent could also alter the carbon isotope signature. Clearly, more, higher precision carbon isotope data of melt inclusions are required to use stable isotope fractionation to infer the magmatic degassing history. Despite this, it is promising that the $\delta^{13}C$ of this single melt inclusion is at least consistent with previous degassing models at Etna.

## 6.7. Conclusions

Melt inclusion and mineral compositions from the 23 November 2013 eruption reveal that magma mixing occurred prior to eruption, and likely triggered the eruption (Figure 6.32). Olivine has two compositions, which relate to a hotter, deeper, more primitive magma and a cooler, shallower, more evolved magma, although the parental magma to both are the same. The more primitive magma was volatile-rich (minimum 1600 ppm $CO_2$ and 3 wt% $H_2O$) and degassed during ascent from $>$2 kbar. It mixed with the more evolved

magma (<1 kbar), which was more degassed. For this eruption, it appears that an injection of fresh magma was the trigger for eruption, rather than foam collapse (Jaupart and Vergniolle, 1989). This implies that intense paroxysms may be proceeded by precursory signals such as inflation and higher C/S gas emissions because they are related to new magma rather than just foam accumulation.

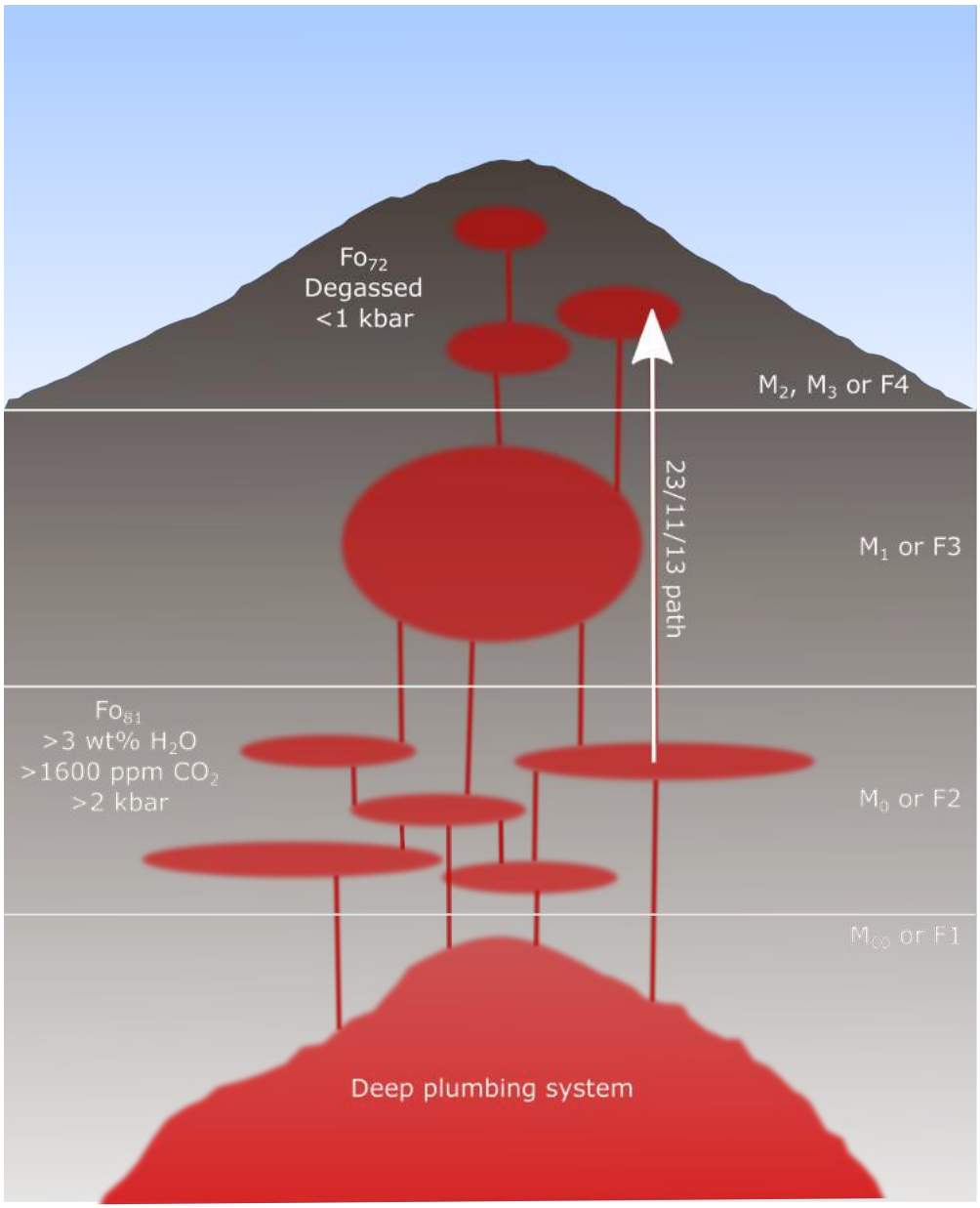


**Figure 6.32:** Schematic illustration of the plumbing system at Etna for the 23 November 2013, based on the olivine and melt inclusion composition. Magmatic environments from Giuffrida and Viccaro (2017), Giacomoni et al. (2018), and Kahl et al. (2015) (Table 6.1).

Simple closed-system degassing cannot explain the volatile compositions. Either there has been a component of $CO_2$-flushing or disequilibrium $CO_2$ exsolution, both of which result in apparently low $H_2O$ compared to equilibrium closed-system degassing. Alternatively, the low $H_2O$ could be due to post-entrapment $H_2O$-loss. These interpretations have very different meanings for the ascent of the magma, but it is not currently possible to discern between them. Hydrogen isotope data implies a combination of $H_2O$-loss and degassing. Unfortunately, there is insufficient carbon isotope data, but the single datum would imply

equilibrium, rather than disequilibrium, $CO_2$ degassing. Additionally, the volatile data represent a mixture of magmas, and hence would not be expected to lie on a single degassing path.

Compared to different eruption styles at Etna, the 23 November 2013 melt composition covers the range of those seen in highly explosive and effusive eruptions. The volatile concentrations are lower than the highly explosive eruptions but have higher $H_2O$ than the effusive eruptions. The highly explosive eruptions are linked to an injection of primitive magma, whilst the effusive eruptions are just the residual of this magma being erupted. Therefore, paroxysms are also triggered by injections of primitive magma but perhaps of smaller volume, and hence are subject to greater mixing with the more evolved end-member, reducing their explosivity.

# Chapter 7

# Concluding remarks

## 7.1. Overview

The aim of this thesis was to provide novel techniques for constraining the oxygen fugacity (using glass Fe oxidation state) and volatile composition of magmas prior to eruption using melt inclusions. In this thesis, I have presented three techniques for analysing melt inclusions using the electron probe to measure volatiles by difference accurately and Fe oxidation state, and the ion probe to measure carbon isotope ratios, in hydrous basaltic glass. I have applied these techniques, and other bulk and microanalytical techniques, to experimentally produced glasses to create carbon isotope SIMS glass standards and investigate volatile stable isotope fractionation during degassing; and natural melt inclusions from the 23 November 2013 eruption of Etna to assess post-entrapment modification and the influence of pre-eruptive melt composition on eruption dynamics.

## 7.2. Sub-surface charging is key for accurate EPMA of silicate glass

Anecdotally, it has been known for a long time that EPMA totals of hydrous silicate glass are low, but this had not been quantified and there was no explanation for these phenomena. The literature review in Chapter 2 compared volatiles by difference to measured volatile concentrations to quantify this problem, and showed how extensive is was for the first time. Sub-surface charging, where electrons are trapped within the silicate glass during EPMA (e.g., Cazaux, 1996), is known to impact the analysis of silicate glass through element migration and oxidation state changes (e.g., Fialin et al., 2011; Humphreys et al., 2006; Zhang et al., 2018). Additionally, modelling with Win X-ray (Demers and Gauvin, 2004; Gauvin et al., 2006) shows it can account for the reduction in the analytical total. Combining the literature review and the sub-surface charging modelling shows that hydrous silicate glass suffer greater internal electric fields than anhydrous silicate glass, hence $H_2O$ appears to effect the dielectric properties of silicate glass. Future work quantifying the effect of $H_2O$ and glass composition on the dielectric properties of silicate glass would help to understand this process further. A simple empirical correction, using hydrous glass standards, can greatly improve the accuracy of VBD. This provides an alternative technique for measuring the $H_2O$ concentration of melt inclusions, at higher spatial resolution than SIMS and FTIR, which also provides the full glass composition at the same time, including volatiles such as S, Cl, and F.

## 7.3. Towards higher precision Fe oxidation state using the electron probe

The method for measuring the Fe oxidation state in silicate glass developed in Chapter 3 allows the $Fe^{2+}/Fe_T$ to be analysed in a single melt inclusion using the electron probe. This was previously only possible using synchrotron-based techniques (Cottrell et al., 2009). The method can be applied to hydrous silicate glass, which currently cannot be analysed reliably using μXANES due to beam damage (Cottrell et al., 2018). It was shown that anhydrous silicate glass, which is typically thought of as stable under electron beams, does undergo beam damage. Anhydrous and hydrous silicate glass change Fe oxidation state via different mechanisms. Raman spectroscopy revealed that nanolites are formed during EPMA of hydrous silicate glass, which results in oxidation during analysis.

Use of this method on the experimental ETNA glasses produced in Chapter 5 showed that Fe reduction had occurred during glass synthesis due to $fH_2$ gradients across the capsule wall. The measured $Fe^{2+}/Fe_T$ was used to quantify the amount of $H_2O$ added to the capsule during the experimental run to constrain

the total volatile budget of the capsules. When applied to melt inclusions from Etna, it revealed that both post-entrapment crystallisation of the host-olivine, and changes in oxidation state, were responsible for the variable $K_{D(Fe-Mg)}^{ol-melt}$ measured.

This technique could be improved to give higher precision, as the current error of $\pm 0.1$ $Fe^{2+}/Fe_T$ cannot discern differences in Fe oxidation state between MORBs and arcs (0.68–0.87 $Fe^{2+}/Fe_T$; Kelley and Cottrell, 2009) or due to degassing (0.60–0.86 $Fe^{2+}/Fe_T$; Moussallam et al., 2014). Precision is dictated by the number of X-rays measured, hence measuring more X-rays per analysis spot would improve precision. Alternatively, fewer analyses would be required to achieve the same precision, therefore spatial resolution would be improved and analysis time reduced. One way to increase the number of X-rays is to increase the beam current, but this increasing the rate of redox change, which can become too rapid to correct for. Alternatively, the electron probe itself could be modified.

The JEOL JXA 8530F Hyperprobe at the School of Earth Sciences, University of Bristol, UK, has two TAP and one TAPH crystal, which limits the number of X-rays on Fe*L* that can be measured at the same time. H-type crystals lie on a smaller Rowland circle than normal WDS crystals. Hence, they are situated closer to the sample and therefore measure more X-rays at the same analytical conditions. The Cameca SX100 microprobe, also at the School of Earth Sciences, University of Bristol, UK, has two TAP and one LTAP crystal. L-type crystals have a larger Rowland circle, which improves wavelength resolution but typically measures fewer X-rays because it is further away from the sample. Figure 7.1 shows a comparison of all these TAP-type crystals. TAP-type crystals from the Cameca have higher count rates, and better wavelength resolution, than the JEOL and hence would produce more precise data. Unfortunately, these data were collected prior to the detector window in the Cameca LTAP being changed, after which absorption of soft X-rays increased, halving the count rates. Hence, the JEOL was used in Chapter 3.

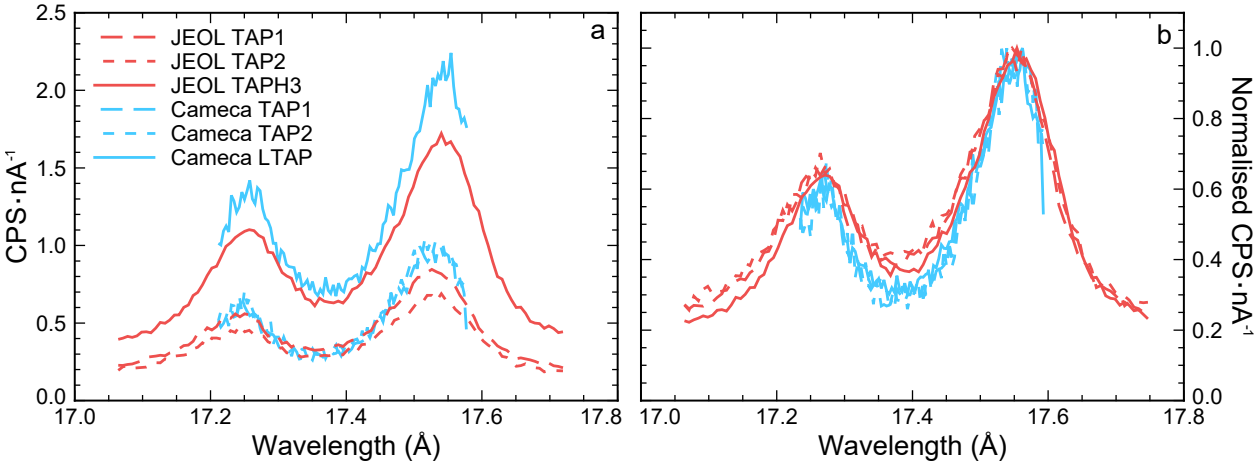


**Figure 7.1:** Fe*L* wavescans using different TAP-type crystals on VG-2 (Smithsonian microbeam basaltic glass standard, Table 2.4): **(a)** counts per second per nA beam current ($CPS{\cdot}nA^{-1}$) to compare count rates, and **(b)** wavescans normalised to the height of their Fe$L\alpha$ peak to compare wavelength resolution (lower saddle between the Fe$L\alpha$ and Fe$L\beta$ peaks indicates better wavelength resolution). Data are available in Table D.2.

An electron probe with five TAPH crystals (or LTAP depending on the exact crystals) would resolve smaller variations in Fe oxidation state or allow smaller melt inclusions to be analysed quicker. For instance, the set-up in Chapter 3 produced $\sim$1.4 $CPS{\cdot}nA^{-1}$ on Fe$L\alpha_f$ (two JEOL TAP crystals) and $\sim$1.0 $CPS{\cdot}nA^{-1}$ on

Fe$L\beta_f$ (one JEOL TAPH crystal). Conversely, if there were five Cameca LTAP crystals, the count rates would be doubled ($\sim$3 CPS·nA$^{-1}$ on Fe$L\alpha_f$ and $\sim$2 CPS·nA$^{-1}$ on Fe$L\beta_f$). For the same number of points (ten, 4 μm in diameter analyses per melt inclusion and therefore $\sim$20 μm in diameter region analysed) and total analysis time ($\sim$30 mins), the precision would be improved by 30 %. Alternatively, this would halve the number of points, and therefore analysis time, required for the same precision (i.e., five vs. ten points and 15 vs. 30 mins total per analysis, therefore $\sim$15 vs. $\sim$20 μm region in diameter analysed) improving the spatial resolution for single melt inclusions.

## 7.4. Accounting for the bubble in carbon isotope analysis of melt inclusions

Accurately measuring the carbon isotope ratio in melt inclusions is key in resolving many questions in petrology and volcanology. A step forward towards this is the synthesis and characterisation of three new hydrous, carbon-rich, basaltic glasses, with independently measured carbon isotope ratios, that can be used as standards for SIMS analysis (Chapter 4). Also, extensive work on a SIMS protocol for analysing carbon isotope ratios at high spatial resolution was conducted, which have showed the amendments required to achieve the goal of analysing single melt inclusions. The experimental protocol described in Chapter 5 highlighted where improvements can be made to obtain reliable carbon isotope fractionation factors between exsolved fluid and melt in the system basalt-$H_2O$-$CO_2$. Both these chapters provide invaluable groundwork to conduct future studies on carbon isotope fractionation during degassing. Applying these techniques to understanding the relative diffusivities of carbon isotopes in silicate melts would also be useful for investigating disequilibrium bubble growth (e.g., Pichavant et al., 2018; Watson, 2017).

A different, but related, problem is dealing with the bubbles found in melt inclusions. Volatiles in shrinkage, rather than co-entrapped, bubbles were originally in the melt at the time of entrapment (e.g., Maclennan, 2017; Moore et al., 2015; Wallace et al., 2015). Hence, only measuring the glass in the melt inclusions does not constrain the total volatile composition of the melt at the time of entrapment. As volatiles isotopically fractionate during bubble formation (e.g., Aubaud et al., 2004; Watson, 2017), the carbon isotope ratio of the melt will have been modified post-entrapment. This may have occurred under equilibrium or kinetically-controlled conditions, depending on the relative diffusion rates of $^{12}C$ and $^{13}C$ into the shrinkage bubble. There are two ways that this could be accounted for.

Firstly, the carbon isotope ratio of the fluid in the bubble could be measured using Raman spectroscopy (e.g., Li et al., 2016). Molecular $CO_2$ has four vibrational modes: a symmetric stretch, two bending modes, and an antisymmetric stretch. The symmetric stretch and the first excited state of the bending mode, have the same symmetry and almost the same energies, and hence can mix by Fermi resonance (Fermi, 1931). This produces a Fermi diad, which are two peaks where the peak positions have been changed due to Fermi resonance ($\sim$1285 and $\sim$1388 cm$^{-1}$, Gordon and McCubbin, 1966). The distance between the two peaks relates to the density of the $CO_2$ hence, if the volume of the bubble is known (e.g., using transmitted light microscopy or X-ray μ-tomography), the concentration of $CO_2$ in the bubble can be calculated (Kagi et al., 2003). Additionally, the isotope ratio of the $CO_2$ will affect the exact energy of the vibrational modes. This will also split the peaks, producing an additional peak at $\sim$1370 cm$^{-1}$ (Howard-Lock and Stoicheff, 1971). The relative areas of the different peaks has been used to infer carbon isotope ratios of synthetic and natural fluid inclusions (Li et al., 2016). This assumes that all the carbon remains in the fluid and does not precipitate as carbonates on the walls of the bubble (Mathez and Delaney, 1981; Moore et al., 2015). Also, comparing

the carbon isotope ratios of the bubble and melt will show whether bubble formation in melt inclusions is an equilibrium or kinetically-driven process.

Alternatively, the fluid in the bubble could be dissolved back into the melt prior to analysis, hence the melt will contain all the dissolved carbon (e.g., Mironov et al., 2015). This can be achieved by taking the melt inclusion to high pressure and temperature, which raises the $CO_2$ solubility, and then quenching it at a rate that prevents new bubble formation. The bulk carbon composition of the melt inclusion should not be altered because the carbon solubility is low, and diffusivity slow, in olivine (Tingle et al., 1988), but the hydrogen composition will be altered (e.g., Gaetani et al., 2012). Hence $H_2O$ concentrations, if required, will have to be analysed prior to heating using Raman spectroscopy as the melt inclusion cannot be exposed (e.g., Thomas et al., 2006). Dehydration of the melt inclusion decreases the melt density, and hence lowers the pressure in the melt inclusion, raising the homogenisation temperature of the bubble (Mironov et al., 2015). Instead, homogenising the melt inclusion under high $H_2O$ pressure (e.g., 500 MPa) hydrates the melt inclusion, increasing the internal pressure and hence the bubble dissolves into the melt (Mironov et al., 2015). In this case, there will be no bubble, hence only the glass in the melt inclusion needs to be analysed to recover the carbon isotope ratio of the melt at the time of entrapment.

## 7.5. Correlative microanalysis of melt inclusions to understand eruptions

Changes in the melt composition prior to the 23 November 2013 paroxysm were investigated by analysing melt inclusions using a variety of micro-analytical techniques (Raman, SIMS, and EPMA). By combining these techniques, changes in the major element composition and Fe oxidation state (EPMA) could be correlated with changes in the concentration ($H_2O$ – Raman; $H_2O$ and $CO_2$ – SIMS; and volatiles by difference, S, Cl, and F – EPMA) and isotope ratio ($\delta D$ and $\delta^{13}C$ – SIMS) of volatiles. Additionally, these changes were compared with variations in the olivine composition and the presence of nanolites in the melt inclusions. Such datasets are only available for a limited number of eruptions, but provide invaluable information on the magmatic processes occurring prior to eruption (degassing and magma mixing) but also the post-entrapment processes that modify the melt inclusion composition. This dataset is the first geochemical dataset on the 23 November 2013 eruption and the only melt inclusion study on the 2011–2013 eruptive sequence. As such, it provides the only direct measurement of the volatile concentration of the magma during this eruptive sequence, which is higher than previous estimates using thermodynamic modelling of the mineral assemblage (Giuffrida and Viccaro, 2017). This dataset adds to the growing volatile data available for Etna, which shows that volatile concentrations and magma mixing are important for governing the style of eruption (e.g., Carlo and Pompilio, 2004; Collins et al., 2009; Métrich et al., 2004; Moretti et al., 2018; Spilliaert et al., 2006).

A major improvement to the current dataset would be additional carbon isotope ratio measurements of the melt inclusions. Etna is a fantastic volcano to analyse the $\delta^{13}C$ of melt inclusions because there is already extensive knowledge about the carbon isotope systematics of the gases (Aiuppa et al., 2004; Allard, 1983; Allard et al., 1991; Giammanco et al., 1998; Giammanco and Pecoraino, 2005; Martelli et al., 2008; Paonita et al., 2012; Rizzo et al., 2015, 2014; D'Alessandro et al., 1997). The best target to investigate the carbon isotope systematics of the magma at Etna would be products from an eruption where the carbon isotope ratio of the plume had been measured prior to, and during, eruption. In this way the measurements of melt and gas could be directly compared.

# References


Abramoff, M., Magalhães, P. J., and Ram, S. J. (2004). Image processing with ImageJ. *Biophotonics international*, 11(7):36–42.

Abramson, E., Bollengier, O., and Brown, J. (2017). The water-carbon dioxide miscibility surface to 450 °C and 7 GPa. *American Journal of Science*, 317(9):967–989.

Aiuppa, A., Allard, P., D'Alessandro, W., Giammanco, S., Parello, F., and Valenza, M. (2004). Magmatic gas leakage at Mount Etna (Sicily, Italy): Relationships with the volcano-tectonic structures, the hydrological pattern and the eruptive activity. *Geophysical Monograph - American Geophysical Union*, 143:129–146.

Aiuppa, A., Cannata, A., Cannavò, F., Di Grazia, G., Ferrari, F., Giudice, G., Gurrieri, S., Liuzzo, M., Mattia, M., Montalto, P., Patanè, D., and Puglisi, G. (2010). Patterns in the recent 2007–2008 activity of Mount Etna volcano investigated by integrated geophysical and geochemical observations. *Geochemistry, Geophysics, Geosystems*, 11(9):Q09008.

Aiuppa, A., Federico, C., Giudice, G., Gurrieri, S., Liuzzo, M., Shinohara, H., Favara, R., and Valenza, M. (2006). Rates of carbon dioxide plume degassing from Mount Etna volcano. *Journal of Geophysical Research*, 111(B9):B09207.

Aiuppa, A., Moretti, R., Federico, C., Giudice, G., Gurrieri, S., Liuzzo, M., Papale, P., Shinohara, H., and Valenza, M. (2007). Forecasting Etna eruptions by real-time observation of volcanic gas composition. *Geology*, 35(12):1115–1118.

Akella, J. and Kennedy, G. C. (1971). Melting of gold, silver, and copper – Proposal for a new high-pressure calibration scale. *Journal of Geophysical Research*, 76(20):4969–4977.

Allard, P. (1978). *Composition isotopique et origine des constituants majeurs des gaz volcaniques*. PhD thesis, Université de Paris.

Allard, P. (1982). Stable isotope composition of hydrogen, carbon and sulphur in magmatic gases from rift and island arc volcanoes. *Bulletin Volcanologique*, 45(3):269–271.

Allard, P. (1983). The origin of hydrogen, carbon, sulphur, nitrogen and rare gases in volcanic exhalations: Evidence from isotope geochemistry. In *Forecasting Volcanic Events*, pages 337–386. Elsevier.

Allard, P., Behncke, B., D'Amico, S., Neri, M., and Gambino, S. (2006a). Mount Etna 1993–2005: Anatomy of an evolving eruptive cycle. *Earth-Science Reviews*, 78(1-2):85–114.

Allard, P., Carbonnelle, J., Dajlevic, D., Bronec, J. L., Morel, P., Robe, M. C., Maurenas, J. M., Faivre-Pierret, R., Martin, D., Sabroux, J. C., and Zettwoog, P. (1991). Eruptive and diffuse emissions of $CO_2$ from Mount Etna. *Nature*, 351(6325):387–391.

Allard, P., Métrich, N., Deloule, E., Belhadj, O., Mandeville, C., and Spilliaert, N. (2006b). First ion microprobe determination of water and sulfur isotopic ratios in melt inclusions of olivines at Mount Etna. In *American Geophysical Union, Fall Meeting 2006*.

Almeev, R., Holtz, F., Ariskin, A., and Kimura, J.-I. (2013). Storage conditions of Bezymianny Volcano parental magmas: Results of phase equilibria experiments at 100 and 700 MPa. *Contributions to Mineralogy and Petrology*, 166(5):1389–1414.

Alparone, S., Andronico, D., Lodato, L., and Sgroi, T. (2003). Relationship between tremor and volcanic activity during the South-East Crater eruption on Mount Etna in early 2000. *Journal of Geophysical Research: Solid Earth*, 108(B5):2241–2253.

Anderson, A. and Brown, G. (1993). $CO_2$ contents and formation pressures of some Kilauean melt inclusions. *American Mineralogist*, 78(7-8):794–803.

Andronico, D., Branca, S., Calvari, S., Burton, M., Caltabiano, T., Corsaro, R. A., Del Carlo, P., Garf, G., Lodato, L., Miraglia, L., Murè, F., Neri, M., Pecora, E., Pompilio, M., Salerno, G., and Spampinato, L. (2005). A multi-disciplinary study of the 2002–03 Etna eruption: Insights into a complex plumbing system. *Bulletin of Volcanology*, 67(4):314–330.

Andronico, D. and Corsaro, R. A. (2011). Lava fountains during the episodic eruption of South-East Crater (Mt. Etna), 2000: Insights into magma-gas dynamics within the shallow volcano plumbing system. *Bulletin of Volcanology*, 73(9):1165–1178.

Andronico, D., Cristaldi, A., and Scollo, S. (2008). The 4–5 September 2007 lava fountain at South-East Crater of Mt Etna, Italy. *Journal of Volcanology and Geothermal Research*, 173(3-4):325–328.

Andronico, D., Scollo, S., and Cristaldi, A. (2015). Unexpected hazards from tephra fallouts at Mt Etna: The 23 November 2013 lava fountain. *Journal of Volcanology and Geothermal Research*, 304:118–125.

Andronico, D., Scollo, S., Cristaldi, A., and Lo Castro, M. D. (2014). Representivity of incompletely sampled fall deposits in estimating eruption source parameters: A test using the 12–13 January 2011 lava fountain deposit from Mt. Etna volcano, Italy. *Bulletin of Volcanology*, 76(10):861.

Appora, I. (1998). *Étude expérimentale du fractionnement isotopique du carbone et de l'oxygène dans les systemès $CO_2$-carbonates liquides: Application aux contextes carbonatitiques*. PhD thesis, Université de Paris.

Arculus, R. J. (1985). Oxidation status of the mantle: Past and present. *Annual Review of Earth and Planetary Sciences*, 13:75–95.

Aubaud, C. (2002). *Processus de dégazage et sources mantelliques dans les magmas de type MORB et OIB*. PhD thesis, Université de Paris.

Aubaud, C., Pineau, F., Jambon, A., and Javoy, M. (2004). Kinetic disequilibrium of C, He, Ar and carbon isotopes during degassing of mid-ocean ridge basalts. *Earth and Planetary Science Letters*, 222(2):391–406.

Barberi, F., Civetta, L., Gasparini, P., Innocenti, F., Scandone, R., and Villari, L. (1974). Evolution of a section of the Africa-Europe plate boundary: Paleomagnetic and volcanological evidence from Sicily. *Earth and Planetary Science Letters*, 22(2):123–132.

Barker, S., Greaves, M., and Elderfield, H. (2003). A study of cleaning procedures used for foraminiferal Mg/Ca paleothermometry. *Geochemistry, Geophysics, Geosystems*, 4(9):8407.

Barr, J. A. and Grove, T. L. (2010). AuPdFe ternary solution model and applications to understanding the $fO_2$ of hydrous, high-pressure experiments. *Contributions to Mineralogy and Petrology*, 160(5):631–643.

Barry, P., Hilton, D., Füri, E., Halldórsson, S., and Grönvold, K. (2014). Carbon isotope and abundance systematics of Icelandic geothermal gases, fluids and subglacial basalts with implications for mantle plume-related $CO_2$ fluxes. *Geochimica et Cosmochimica Acta*, 134:74–99.

Barsanti, M., Papale, P., Barbato, D., Moretti, R., Boschi, E., Hauri, E., and Longo, A. (2009). Heterogeneous large total $CO_2$ abundance in the shallow magmatic system of Kilauea volcano, Hawaii. *Journal of Geophysical Research*, 114(B12):B12201.

Bastin, G. and Heijligers, H. (1988). Contamination phenomena in the electron probe microanalyzer. *Microbeam analysis: Proceedings of the annual conference of the Microbeam Analysis Society*, 23:325.

Bastin, G. and Heijligers, H. (1991). *Electron probe quantification*. Plenum Press, New York.

Baubron, J. C., Allard, P., and Toutain, J. P. (1990). Diffuse volcanic emissions of carbon dioxide from Vulcano Island, Italy. *Nature*, 344(6261):51–53.

Behncke, B., Branca, S., Corsaro, R. A., De Beni, E., Miraglia, L., and Proietti, C. (2014). The 2011–2012 summit activity of Mount Etna: Birth, growth and products of the new SE crater. *Journal of Volcanology and Geothermal Research*, 270:10–21.

Benhayoune, H. and Jbara, O. (1996). Some experimental evidence for the $\Phi(0)$ variation in EPMA of insulating materials. *X-Ray Spectrometry*, 25(5):229–232.

Berndt, J., Liebske, C., Holtz, F., Freise, M., Nowak, M., Zienbenbein, D., Hurkuck, W., and Koepke, J. (2002). A combined rapid-quench and $H_2$-membrane setup for internally heated pressure vessels: Description and application for water solubility in basaltic melts. *American Mineralogist*, 87:1717–1726.

Blank, J. (1993). *An experimental investigation of the behaviour of carbon dioxide in rhyolitic melt*. PhD thesis, California Institute of Technology.

Blank, J. and Brooker, R. (1994). Experimental studies of carbon dioxide in silicate melts: Solubility, speciation, and stable carbon isotope behaviour. *Reviews in Mineralogy and Geochemistry*, 30(1):157–186.

Blundy, J. and Cashman, K. (2008). Petrologic reconstruction of magmatic system variables and processes. *Reviews in Mineralogy and Geochemistry*, 69(1):179–239.

Blundy, J., Cashman, K., Rust, A., and Witham, F. (2010). A case for $CO_2$-rich arc magmas. *Earth and Planetary Science Letters*, 290(3-4):289–301.

Blundy, J., Melekhova, E., Ulmer, P., Pichavant, M., Humphreys, M., Ziberna, L., Cerantolo, V., and Brooker, R. (2018). Iron redox equilibria in hydrous basaltic melts and $Fe^{2+}$-Mg exchange between olivine and melt. In *EMPG-XVI*.

Bonaccorso, A., Bonforte, A., Calvari, S., Del Negro, C., Di Grazia, G., Ganci, G., Neri, M., Vicari, A., and Boschi, E. (2011a). The initial phases of the 2008–2009 Mount Etna eruption: A multidisciplinary approach for hazard assessment. *Journal of Geophysical Research: Solid Earth*, 116.

Bonaccorso, A., Caltabiano, T., Currenti, G., Del Negro, C., Gambino, S., Ganci, G., Giammanco, S., Greco, F., Pistorio, A., Salerno, G., Spampinato, S., and Boschi, E. (2011b). Dynamics of a lava fountain revealed by geophysical, geochemical and thermal satellite measurements: The case of the 10 April 2011 Mt Etna eruption. *Geophysical Research Letters*, 38(24):L24307.

Bonaccorso, A., Calvari, S., Linde, A., and Sacks, S. (2014). Eruptive processes leading to the most explosive lava fountain at Etna volcano: The 23 November 2013 episode. *Geophysical Research Letters*, 41(14):4912–4919.

Bonaccorso, A., Currenti, G., and Del Negro, C. (2013). Interaction of volcano-tectonic fault with magma storage, intrusion and flank instability: A thirty years study at Mt. Etna volcano. *Journal of Volcanology and Geothermal Research*, 251:127–136.

Bonnelle, C. (2004). Charge trapping in dielectrics. *Microscopy and Microanalysis*, 10(6):691–696.

Borisov, A. and Shapkin, A. (1990). A new empirical equation rating $Fe^{3+}/Fe^{2+}$ in magmas to their composition, oxygen fugacity, and temperature. *Geochemistry International*, 27:111–116.

Botcharnikov, R., Almeev, R., Koepke, J., and Holtz, F. (2008). Phase relations and liquid lines of descent in hydrous ferrobasalt: Implications for the Skaergaard intrusion and Columbia River flood basalts. *Journal of Petrology*, 49(9):1687–1727.

Botcharnikov, R., Koepke, J., Holtz, F., McCammon, C., and Wilke, M. (2005). The effect of water activity on the oxidation and structural state of Fe in a ferro-basaltic melt. *Geochimica et Cosmochimica Acta*, 69(21):5071–5085.

Bottinga, Y. (1969). Calculated fractionation factors for carbon and hydrogen isotope exchange in the system calcite-carbon dioxide-graphite-methane-hydrogen-water vapor. *Geochimica et Cosmochimica Acta*, 33(1):49–64.

Bottinga, Y. and Weill, D. F. (1970). Densities of liquid silicate systems calculated from partial molar volumes of oxide components. *American Journal of Science*, 269:169–182.

Bouhifd, M., Richet, P., Besson, P., Roskosz, M., and Ingrin, J. (2004). Redox state, microstructure and viscosity of a partially crystallized basalt melt. *Earth and Planetary Science Letters*, 218(1-2):31–44.

Brooker, R., Holloway, J., and Hervig, R. (1998). Reduction in piston-cylinder experiments: The detection of carbon infiltration into platinum capsules. *American Mineralogist*, 83:985–994.

Bucholz, C., Gaetani, G. A., Behn, M., and Shimizu, N. (2013). Post-entrapment modification of volatiles and oxygen fugacity in olivine-hosted melt inclusions. *Earth and Planetary Science Letters*, 374:145–155.

Buddington, A. and Lindsley, D. (1964). Iron-titanium oxide minerals and synthetic equivalents. *Journal of Petrology*, 5(2):310–357.

Burgess, K., Stroud, R. M., Dyar, M. D., and McCanta, M. C. (2016). Submicrometer-scale spatial heterogeneity in silicate glasses using aberration-corrected scanning transmission electron microscopy. *American Mineralogist*, 101(12):2677–2688.

Burnham, C. (1979). The importance of volatile constituents. In Yoder Jr, H., editor, *The evolution of the igneous rocks: Fiftieth*

*Anniversary Perspectives*, pages 439–482. University Press, Princeton, Princeton.

Burton, M., Neri, M., Andronico, D., Branca, S., Caltabiano, T., Calvari, S., Corsaro, R. A., Carlo, P. D., Lanzafame, G., Lodato, L., Miraglia, L., Salerno, G., and Spampinato, L. (2005). Etna 2004–2005: An archetype for geodynamically-controlled effusive eruptions. *Geophysical Research Letters*, 32(9):L09303.

Burton, M., Sawyer, G. M., and Granieri, D. (2013). Deep carbon emissions from volcanoes. *Reviews in Mineralogy and Geochemistry*, 75(1):323–354.

Buse, B. and Kearns, S. (2018). Quantification of olivine using Fe$L\alpha$ in electron probe microanalysis (EPMA). *Microscopy and Microanalysis*, 24(1):1–7.

Buse, B., Kearns, S., Clapham, C., and Hawley, D. (2016). Decontamination in the electron probe microanalysis with a Peltier-cooled cold finger. *Microscopy and Microanalysis*, 22(5):981–986.

Canil, D. (1997). Vanadium partitioning and the oxidation state of Archaean komatiite magmas. *Nature*, 389(6653):842–845.

Caricchi, L., Sheldrake, T. E., and Blundy, J. (2018). Modulation of magmatic processes by $CO_2$ flushing. *Earth and Planetary Science Letters*, 491:160–171.

Carlo, P. D. and Pompilio, M. (2004). The relationship between volatile content and the eruptive style of basaltic magma: The Etna case. *Annals of Geophysics*, 47(4).

Carmichael, I. (1991). The redox states of basic and silicic magmas: A reflection of their source regions? *Contributions to Mineralogy and Petrology*, 106(2):129–141.

Carmichael, I. and Ghiorso, M. (1990). The effect of oxygen fugacity on the redox state of natural liquids and their crystallizing phases. *Reviews in Mineralogy and Geochemistry*, 24(1):191–212.

Carmisciano, S., Rosa, I. M. D., Sarasini, F., Tamburrano, A., and Valente, M. (2011). Basalt woven fiber reinforced vinylester composites: Flexural and electrical properties. *Materials & Design*, 32(1):337–342.

Cartigny, P., Harris, J. W., and Javoy, M. (2001). Diamond genesis, mantle fractionations and mantle nitrogen content: A study of $\delta^{13}$C-N concentrations in diamonds. *Earth and Planetary Science Letters*, 185(1-2):85–98.

Cassidy, M., Manga, M., Cashman, K., and Bachmann, O. (2018). Controls on explosive-effusive volcanic eruption styles. *Nature Communications*, 9(1):2839.

Cazaux, J. (1996). Electron probe microanalysis of insulating materials: Quantification problems and some possible solutions. *X-Ray Spectrometry*, 25(6):265–280.

Chabiron, A., Alyoshin, A., Cuney, M., Deloule, E., Golubev, V. N., Velitchkin, V. I., and Poty, B. (2001). Geochemistry of the rhyolitic magmas from the Streltsovka caldera (Transbaikalia, Russia): A melt inclusion study. *Chemical Geology*, 175(3):273–290.

Chacko, T., Cole, D. R., and Horita, J. (2001). Equilibrium oxygen, hydrogen and carbon isotope fractionation factors applicable to geologic systems. *Reviews in Mineralogy and Geochemistry*, 43(1):1–81.

Chakraborty, S. (1997). Rates and mechanisms of Fe-Mg interdiffusion in olivine at 980–1300 °C. *Journal of Geophysical Research: Solid Earth*, 102(B6):12317–12331.

Cherifi, A., Dakka, M., and Toureille, A. (1992). The validation of the thermal step method. *IEEE Transactions on Electrical Insulation*, 27(6):1152–1158.

Cherniak, D. J. and Dimanov, A. (2010). Diffusion in pyroxene, mica and amphibole. *Reviews in Mineralogy and Geochemistry*, 72(1):641–690.

Chiodini, G., Caliro, S., Aiuppa, A., Avino, R., Granieri, D., Moretti, R., and Parello, F. (2011). First $^{13}C/^{12}C$ isotopic characterisation of volcanic plume $CO_2$. *Bulletin of Volcanology*, 73(5):531–542.

Clocchiatti, R. (1971). Composition chimique des inclusions vitreuses des phenocristaux de quartz de quelques laves acides par l'analyse a la sonde electronique. *Comptes rendus de l'Académie des Sciences*, 272:2045–2047.

Clocchiatti, R., Joron, J.-L., and Treuil, M. (1988). The role of selective alkali contamination in the evolution of recent historic lavas of Mt. Etna. *Journal of Volcanology and Geothermal Research*, 34(3-4):241–249.

Collins, S., Pyle, D., and Maclennan, J. (2009). Melt inclusions track pre-eruption storage and dehydration of magmas at Etna. *Geology*, 37(6):571–574.

Coltelli, M., Del Carlo, P., and Vezzoli, L. (1998). Discovery of a Plinian basaltic eruption of Roman age at Etna volcano, Italy. *Geology*, 26(12):1095.

Cooper, R. F., Fanselow, J. B., and Poker, D. B. (1996). The mechanism of oxidation of a basaltic glass: Chemical diffusion of network-modifying cations. *Geochimica et Cosmochimica Acta*, 60(17):3253–3265.

Cottrell, E. and Kelley, K. A. (2011). The oxidation state of Fe in MORB glasses and the oxygen fugacity of the upper mantle. *Earth and Planetary Science Letters*, 305(3-4):270–282.

Cottrell, E. and Kelley, K. A. (2013). Redox heterogeneity in mid-ocean ridge basalts as a function of mantle source. *Science*, 340(6138):1314–7.

Cottrell, E., Kelley, K. A., Lanzirotti, A., and Fischer, R. A. (2009). High-precision determination of iron oxidation state in silicate glasses using XANES. *Chemical Geology*, 268(3-4):167–179.

Cottrell, E., Lanzirotti, A., Mysen, B., Birner, S., Kelley, K., Botcharnikov, R., Davis, F., and Newville, M. (2018). A Mössbauer-based XANES calibration for hydrous basalt glasses reveals radiation-induced oxidation of Fe. *American Mineralogist*, 103:489–501.

Creighton, S., Stachel, T., Eichenberg, D., and Luth, R. (2010). Oxidation state of the lithospheric mantle beneath Diavik diamond mine, central Slave craton, NWT, Canada. *Contributions to Mineralogy and Petrology*, 159(5):645–657.

Creighton, S., Stachel, T., Matveev, S., Höfer, H., McCammon, C., and Luth, R. (2009). Oxidation of the Kaapvaal lithospheric mantle driven by metasomatism. *Contributions to Mineralogy and Petrology*, 157(4):491–504.

Cukierman, M. and Uhlmann, D. R. (1974). Effects of iron oxidation state on viscosity, lunar composition 15555. *Journal of Geophysical Research*, 79(11):1594–1598.

D'Alessandro, W., Giammanco, S., Parello, F., and Valenza, M. (1997). $CO_2$ output and $\delta^{13}C(CO_2)$ from Mount Etna as indicators of degassing of shallow asthenosphere. *Bulletin of Volcanology*, 58(6):455–458.

Dalou, C., Le Losq, C., and Mysen, B. (2015). *In situ* study of the fractionation of hydrogen isotopes between aluminosilicate melts and coexisting aqueous fluids at high pressure and high temperature: Implications for the $\delta$D in magmatic processes. *Earth and Planetary Science Letters*, 426:158–166.

Danyushevsky, L., Della-Pasqua, F. N., and Sokolov, S. (2000). Re-equilibration of melt inclusions trapped by magnesian olivine phenocrysts from subduction-related magmas: Petrological implications. *Contributions to Mineralogy and Petrology*, 138(1):68–83.

Danyushevsky, L., McNeill, A. W., and Sobolev, A. V. (2002). Experimental and petrological studies of melt inclusions in phenocrysts from mantle-derived magmas: An overview of techniques, advantages and complications. *Chemical Geology*, 183(1-4):5–24.

Danyushevsky, L. and Plechov, P. (2011). Petrolog3: Integrated software for modeling crystallization processes. *Geochemistry, Geophysics, Geosystems*, 12(7):Q07021.

Danyushevsky, L., Sobolev, A., and Dmitriev, L. (1988). Orthopyroxene-bearing low-Ti tholeiites: The new type of oceanic ridge tholeiite. *Transactions of USSR Academy of Sciences: Earth sciences section*, 292:102–105.

De Groot, F. (2001). High-resolution X-ray emission and X-ray absorption spectroscopy. *Chemical Reviews*, 101(6):1779–1808.

De Hoog, J. C., Taylor, B. E., and Van Bergen, M. J. (2009). Hydrogen-isotope systematics in degassing basaltic magma and application to Indonesian arc basalts. *Chemical Geology*, 266(3-4):256–266.

Deines, P. (1970). The carbon and oxygen isotopic composition of carbonates from the Oka carbonatite complex, Quebec, Canada. *Geochimica et Cosmochimica Acta*, 34(11):1199–1225.

Deines, P. (2004). Carbon isotope effects in carbonate systems. *Geochimica et Cosmochimica Acta*, 68(12):2659–2679.

Delaney, J. and Karsten, J. (1981). Ion microprobe studies of water in silicate melts: Concentration-dependent water diffusion in obsidian. *Earth and Planetary Science Letters*, 52(1):191–202.

Demers, H. and Gauvin, R. (2004). X-ray microanalysis of a coated nonconductive specimen: Monte Carlo simulation. *Microscopy and Microanalysis*, 10(6):776–782.

Des Marais, D. J. (1986). Carbon abundance measurements in oceanic basalts: The need for a consensus. *Earth and Planetary Science Letters*, 79(1-2):21–26.

Des Marais, D. J. and Moore, J. G. (1984). Carbon and its isotopes in mid-oceanic basaltic glasses. *Earth and Planetary Science Letters*, 69(1):43–57.

Devine, J. D., Gardner, J. E., Brack, H., Laynet, G. D., and Rutherford, M. J. (1995). Comparison of microanalytical methods for estimating $H_2O$ contents of silicic volcanic glasses. *American Mineralogist*, 80(3-4):319–328.

Di Carlo, I., Pichavant, M., Rotolo, S. G., and Scaillet, B. (2006). Experimental crystallization of a high-K arc basalt: The golden pumice, Stromboli volcano (Italy). *Journal of Petrology*, 47(7):1317–1343.

Di Genova, D., Caracciolo, A., and Kolzenburg, S. (2018). Measuring the degree of nanotilization of volcanic glasses: Understanding syn-eruptive processes recorded in melt inclusions. *Lithos*, 318-319:209–218.

Di Genova, D., Hess, K., Chevrel, M., and Dingwell, D. (2016). Models for the estimation of $Fe^{3+}/Fe_{tot}$ ratio in terrestrial and extraterrestrial alkali- and iron-rich silicate glasses using Raman spectroscopy. *American Mineralogist*, 101(4):943–952.

Di Genova, D., Kolzenburg, S., Wiesmaier, S., Dallanave, E., Neuville, D. R., Hess, K. U., and Dingwell, D. (2017a). A compositional tipping point governing the mobilization and eruption style of rhyolitic magma. *Nature*, 552(7684):235–238.

Di Genova, D., Romano, C., Giordano, D., and Alletti, M. (2014). Heat capacity, configurational heat capacity and fragility of hydrous magmas. *Geochimica et Cosmochimica Acta*, 1:314–333.

Di Genova, D., Romano, C., Hess, K. U., Vona, A., Poe, B. T., Giordano, D., Dingwell, D. B., and Behrens, H. (2013). The rheology of peralkaline rhyolites from Pantelleria Island. *Journal of Volcanology and Geothermal Research*, 249:201–216.

Di Genova, D., Sicola, S., Romano, C., Vona, A., Fanara, S., and Spina, L. (2017b). Effect of iron and nanolites on Raman spectra of volcanic glasses: A reassessment of existing strategies to estimate the water content. *Chemical Geology*, 475:76–86.

Di Muro, A., Métrich, N., Mercier, M., Giordano, D., Massare, D., and Montagnac, G. (2009). Micro-Raman determination of iron redox state in dry natural glasses: Application to peralkaline rhyolites and basalts. *Chemical Geology*, 259(1-2):78–88.

Di Muro, A., Villemant, B., Montagnac, G., Scaillet, B., and Reynard, B. (2006). Quantification of water content and speciation in natural silicic glasses (phonolite, dacite, rhyolite) by confocal micro-Raman spectrometry. *Geochimica et Cosmochimica Acta*, 70(11):2868–2884.

Dingwell, D. (1996). Volcanic Dilemma – Flow or Blow? *Science*, 273(5278):1054–1055.

Dingwell, D. and Virgo, D. (1987). The effect of oxidation state on the viscosity of melts in the system $Na_2O$-FeO-$Fe_2O_3$-$SiO_2$. *Geochimica et Cosmochimica Acta*, 51(2):195–205.

Dixon, J., Bindeman, I., Kingsley, R., Simons, K., Le Roux, P., Hajewski, T., Swart, P., Langmuir, C., Ryan, J., Walowski, K., Wada, I., and Wallace, P. (2017). Light stable isotopic compositions of enriched mantle sources: Resolving the dehydration paradox. *Geochemistry, Geophysics, Geosystems*, 18(11):3801–3839.

Dixon, J., Stolper, E., and Holloway, J. (1995). An experimental study of water and carbon dioxide solubilities in mid-ocean ridge basaltic liquids. Part I: Calibration and solubility models. *Journal of Petrology*, 36(6):1607–1631.

Dixon, J. E. and Stolper, E. M. (1995). An experimental study water and carbon dioxide solubilities in mid-ocean ridge basaltic liquids. Part II: Application to degassing. *Journal of Petrology*, 36(6):1633–1646.

Dixon, J. E., Stolper, E. M., and Delaney, J. (1988). Infrared spectroscopic measurements of $CO_2$ and $H_2O$ in the Juan de Fuca Ridge basaltic glasses. *Earth and Planetary Science Letters*, 90(1):87–104.

Dobson, P. F., Epstein, S., and Stolper, E. (1989). Hydrogen isotope fractionation between coexisting vapor and silicate glasses and melts at low pressure. *Geochimica et Cosmochimica Acta*, 53(10):2723–2730.

Donovan, J. and Tingle, T. (1996). An improved mean atomic number background correction for quantitative microanalysis. *Microscopy and Microanalysis*, 2(1):1–7.

Donovan, J. and Vicenzi, E. P. (2008). Water by EPMA – New developments. *Microscopy and Microanalysis*, 14(2):1274–1275.

Drew, D. L., Bindeman, I., Loewen, M. W., and Wallace, P. (2016). Initiation of large-volume silicic centers in the Yellowstone hotspot track: Insights from $H_2O$- and F-rich quartz-hosted rhyolitic melt inclusions in the Arbon Valley Tuff of the Snake River Plain. *Contributions to Mineralogy and Petrology*, 171(1):10.

Dungan, M. A. and Rhodes, J. M. (1978). Residual glasses and melt inclusions in basalts from DSDP Legs 45 and 46: Evidence for magma mixing. *Contributions to Mineralogy and Petrology*, 67(4):417–431.

Ebisuzaki, Y., Kass, W. J., and O'Keeffe, M. (1968). Solubility and diffusion of hydrogen and deuterium in platinum. *The Journal of Chemical Physics*, 49(8):3329–3332.

Enders, M., McCammon, C., Maresch, W., and Speer, D. (2000). Ferric/ferrous iron ratios in sodic amphiboles: Mössbauer analysis, stoichiometry-based model calculations and the high-resolution microanalytical flank method. *Contributions to Mineralogy and Petrology*, 140(2):135–147.

Erdmann, M. and Koepke, J. (2016). Silica-rich lavas in the oceanic crust: Experimental evidence for fractional crystallization under low water activity. *Contributions to Mineralogy and Petrology*, 171(10):83.

Exley, R., Mattey, D., Clague, D., and Pillinger, C. (1986). Carbon isotope systematics of a mantle 'hotspot': A comparison of Loihi Seamount and MORB glasses. *Earth and Planetary Science Letters*, 78(2-3):189–199.

Fakhfakh, S., Jbara, O., Belhaj, M., Fakhfakh, Z., Kallel, A., and Rau, E. I. (2003). An experimental approach for dynamic investigation of the trapping properties of glass-ceramic under electron beam irradiation from a scanning electron microscope. *The European Physical Journal Applied Physics*, 21(2):137–146.

Fakhfakh, S., Jbara, O., Rondot, S., Hadjadj, A., Patat, J. M., and Fakhfakh, Z. (2010). Analysis of electrical charging and discharging kinetics of different glasses under electron irradiation in a scanning electron microscope. *Journal of Applied Physics*, 108(9):093705.

Faure, F. and Schiano, P. (2005). Experimental investigation of equilibration conditions during forsterite growth and melt inclusion formation. *Earth and Planetary Science Letters*, 236(3-4):882–898.

Feig, S. T., Koepke, J., and Snow, J. E. (2006). Effect of water on tholeiitic basalt phase equilibria: An experimental study under oxidizing conditions. *Contributions to Mineralogy and Petrology*, 152(5):611–638.

Fermi, E. (1931). Über den Ramaneffekt des Kohlendioxyds. *Zeitschrift fr Physik*, 71(3-4):250–259.

Fialin, M., Bézos, A., Wagner, C., and Humler, E. (2004). Quantitative electron microprobe analysis of $Fe^{3+}/\Sigma Fe$: Basic concepts and experimental protocol for glasses. *American Mineralogist*, 89(4):654–662.

Fialin, M. and Wagner, C. (2012). Redox kinetics of iron in alkali silicate glasses exposed to ionizing beams: Examples with the electron microprobe. *Journal of Non-Crystalline Solids*, 358(12-13):1617–1623.

Fialin, M., Wagner, C., Métrich, N., Humler, E., Galoisy, L., and Bézos, A. (2001). $Fe^{3+}/\Sigma Fe$ vs. Fe$L\alpha$ peak energy for minerals and glasses: Recent advances with the electron microprobe. *American Mineralogist*, 86(4):456–465.

Fialin, M., Wagner, C., and Pascal, M.-L. (2011). Iron speciation using electron microprobe techniques: Application to glassy melt pockets within a spinel lherzolite xenolith. *Mineralogical Magazine*, 75(2):347–362.

Fiege, A., Holtz, F., Behrens, H., Mandeville, C. W., Shimizu, N., Crede, L. S., and Göttlicher, J. (2015). Experimental investigation of the S and S-isotope distribution between $H_2O$-S $\pm$ Cl fluids and basaltic melts during decompression. *Chemical Geology*, 393-394:36–54.

Field, L., Blundy, J., Brooker, R. A., Wright, T., and Yirgu, G. (2012). Magma storage conditions beneath Dabbahu volcano (Ethiopia) constrained by petrology, seismicity and satellite geodesy. *Bulletin of Volcanology*, 74(5):981–1004.

Fine, G. and Stolper, E. (1986). Dissolved carbon dioxide in basaltic glasses: Concentrations and speciation. *Earth and Planetary Science Letters*, 76(3-4):263–278.

Fischer, T. (2008). Fluxes of volatiles ($H_2O$, $CO_2$, $N_2$, Cl, F) from arc volcanoes. *Geochemical Journal*, 42(1):21–38.

Ford, C., Russel, D., Craven, J., and Fisk, M. (1983). Olivine-liquid equilibria: Temperature, pressure and composition dependence of the crystal/liquid cation partition coefficients for Mg, $Fe^{2+}$, Ca and Mn. *Journal of Petrology*, 24(3):256–266.

Fortin, M.-A., Watson, E., and Stern, R. (2017). The isotope mass effect on chlorine diffusion in dacite melt, with implications for fractionation during bubble growth. *Earth and Planetary Science Letters*, 480:15–24.

Freda, C., Gaeta, M., Giaccio, B., Marra, F., Palladino, D. M., Scarlato, P., and Sottili, G. (2011). $CO_2$-driven large mafic explosive eruptions: The Pozzolane Rosse case study from the Colli Albani Volcanic District (Italy). *Bulletin of Volcanology*, 73(3):241–256.

Frezzotti, M. L., Peccerillo, A., and Panza, G. (2009). Carbonate metasomatism and $CO_2$ lithosphere-asthenosphere degassing beneath the Western Mediterranean: An integrated model arising from petrological and geophysical data. *Chemical Geology*, 262(1-2):108–120.

Friedman, I., Long, W., and Smith, R. L. (1963). Viscosity and water content of rhyolite glass. *Journal of Geophysical Research*, 68(24):6523–6535.

Frost, D. and McCammon, C. (2008). The redox state of Earth's mantle. *Annual Review of Earth and Planetary Sciences*, 36(1):389–420.

Fuchs, P., Almeev, R., and Klugel, A. (2014). Experimental constraints on the formation of basanites-phonolite series (Cumbre Vieja, La Palma). *Goldschmidt Conference Abstracts*.

Gaetani, G. A., O'Leary, J. A., Shimizu, N., Bucholz, C., and Newville, M. (2012). Rapid reequilibration of $H_2O$ and oxygen fugacity in olivine-hosted melt inclusions. *Geology*, 40(10):915–918.

Gaetani, G. A. and Watson, E. (2000). Open system behavior of olivine-hosted melt inclusions. *Earth and Planetary Science Letters*, 183(1-2):27–41.

Gaetani, G. A. and Watson, E. (2002). Modeling the major-element evolution of olivine-hosted melt inclusions. *Chemical Geology*, 183(1-4):25–41.

Gaillard, F., Scaillet, B., Pichavant, M., and Bény, J. (2001). The effect of water and $fO_2$ on the ferric-ferrous ratio of silicic melts. *Chemical Geology*, 174(1-3):255–273.

Galle, B., Johansson, M., Rivera, C., Zhang, Y., Kihlman, M., Kern, C., Lehmann, T., Platt, U., Arellano, S., and Hidalgo, S. (2010). Network for Observation of Volcanic and Atmospheric Change (NOVAC) – A global network for volcanic gas monitoring: Network layout and instrument description. *Journal of Geophysical Research*, 115(D5):D05304.

Gauvin, R., Lifshin, E., Demers, H., Horny, P., and Campbell, H. (2006). Win X-ray: A new Monte Carlo program that computes X-ray spectra obtained with a scanning electron microscope. *Microscopy and Microanalysis*, 12:49–64.

Gedeon, O. and Jurek, K. (2002). Decay curve analysis of alkali-silicate glass exposed to electrons. *Microchimica Acta*, 139(1-4):67–70.

Gedeon, O., Jurek, K., and Hulnský, V. (1999). Fast migration of alkali ions in glass irradiated by electrons. *Journal of Non-Crystalline Solids*, 246(1-2):1–8.

Gennaro, M., Grassa, F., Martelli, M., Renzulli, A., and Rizzo, A. (2017). Carbon isotope composition of $CO_2$-rich inclusions in cumulate-forming mantle minerals from Stromboli volcano (Italy). *Journal of Volcanology and Geothermal Research*, 346:95–103.

Gerlach, T. M. and Taylor, B. E. (1990). Carbon isotope constraints on degassing of carbon dioxide from Kilauea Volcano. *Geochimica et Cosmochimica Acta*, 54(7):2051–2058.

Ghiorso, M. and Gualda, G. (2015). An $H_2O$-$CO_2$ mixed fluid saturation model compatible with rhyolite-MELTS. *Contributions to Mineralogy and Petrology*, 169(6):53.

Ghorbel, N., Fakhfakh, S., Jbara, O., Odof, S., Rondot, S., Fakhfakh, Z., and Kallel, A. (2005). EPMA analysis of insulating materials: Monte Carlo simulations and experiments. *Journal of Physics D: Applied Physics*, 38(8):1239–1247.

Giacomoni, P., Coltorti, M., Mollo, S., Ferlito, C., Braiato, M., and Scarlato, P. (2018). The 2011–2012 paroxysmal eruptions at Mt. Etna volcano: Insights on the vertically zoned plumbing system. *Journal of Volcanology and Geothermal Research*, 349:370–391.

Giammanco, S., Inguaggiato, S., and Valenza, M. (1998). Soil and fumarole gases of Mount Etna: Geochemistry and relations with volcanic activity. *Journal of Volcanology and Geothermal Research*, 81(3-4):297–310.

Giammanco, S. and Pecoraino, G. (2005). Geochemical characterization and temporal changes in parietal gas emissions at Mt. Etna (Italy) during the period July 2000–July 2003. *Terrestrial, Atmospheric and Oceanic Sciences*, 16(4):805–841.

Giordano, D. and Dingwell, D. (2003). Viscosity of hydrous Etna basalt: Implications for Plinian-style basaltic eruptions. *Bulletin of Volcanology*, 65(1):8–14.

Giordano, D., Russell, J. K., and Dingwell, D. (2008). Viscosity of magmatic liquids: A model. *Earth and Planetary Science Letters*, 271(1):123–134.

Giuffrida, M. and Viccaro, M. (2017). Three years (2011–2013) of eruptive activity at Mt. Etna: Working modes and timescales of the modern volcano plumbing system from micro-analytical studies of crystals. *Earth-Science Reviews*, 171:289–322.

Gladney, E. S. and Roelandts, I. (1988). 1987 compilation of elemental concentration data for USGS BIR-1, DNC-1 and W-2. *Geostandards and Geoanalytical Research*, 12(1):63–118.

Gonfiantini, R. (1984). Report to the Director General. Technical report, International Atomic Energy Agency, Vienna, Austria.

Gopon, P., Fournelle, J., Sobol, P. E., and Llovet, X. (2013). Low-voltage electron-probe microanalysis of Fe-Si compounds using soft X-rays. *Microscopy and Microanalysis*, 19(6):1698–1708.

Gordon, H. R. and McCubbin, T. (1966). The 2.8-micron bands of $CO_2$. *Journal of Molecular Spectroscopy*, 19(1-4):137–154.

Graham, C. M., Sheppard, S. M., and Heaton, T. H. (1980). Experimental hydrogen isotope studies – I. Systematics of hydrogen isotope fractionation in the systems epidote-$H_2O$, zoisite-$H_2O$ and AlO(OH)-$H_2O$. *Geochimica et Cosmochimica Acta*, 44(2):353–364.

Graham, T. (1846). Of the motion of gases. Part I. *Philosophical Transactions of the Royal Society (London)*, 4:573–632.

Grocke, S. B., Cottrell, E., De Silva, S., and Kelley, K. A. (2016). The role of crustal and eruptive processes versus source variations in controlling the oxidation state of iron in Central Andean magmas. *Earth and Planetary Science Letters*, 440:92–104.

Gurenko, A. A., Trumbull, R. B., Thomas, R., and Lindsay, J. M. (2005). A melt inclusion record of volatiles, trace elements and Li-B isotope variations in a single magma system from the Plat Pays Volcanic Complex, Dominica, Lesser Antilles. *Journal of Petrology*, 46(12):2495–2526.

Gvirtzman, Z. and Nur, A. (1999). The formation of Mount Etna as the consequence of slab rollback. *Nature*, 401(6755):782–785.

Halter, W. E., Pettke, T., Heinrich, C. A., and Rothen-Rutishauser, B. (2002). Major to trace element analysis of melt inclusions by laser-ablation ICP-MS: Methods of quantification. *Chemical Geology*, 183(1-4):63–86.

Hamilton, D., Burnham, C., and Osborn, E. (1964). The solubility of water and effects of oxygen fugacity and water content on crystallization in mafic magmas. *Journal of Petrology*, 5(1):21–39.

Hart, S. R. and Davis, K. E. (1978). Nickel partitioning between olivine and silicate melt. *Earth and Planetary Science Letters*, 40(2):203–219.

Hartley, M. E., Maclennan, J., Edmonds, M., and Thordarson, T. (2014). Reconstructing the deep $CO_2$ degassing behaviour of large basaltic fissure eruptions. *Earth and Planetary Science Letters*, 393:120–131.

Hartley, M. E., Neave, D., Maclennan, J., Edmonds, M., and Thordarson, T. (2015). Diffusive over-hydration of olivine-hosted melt inclusions. *Earth and Planetary Science Letters*, 425:168–178.

Hartley, M. E., Shorttle, O., Maclennan, J., Moussallam, Y., and Edmonds, M. (2017). Olivine-hosted melt inclusions as an archive

of redox heterogeneity in magmatic systems. *Earth and Planetary Science Letters*, 479:192–205.

Hauri, E. H. (2002). SIMS analysis of volatiles in silicate glasses, 2: Isotopes and abundances in Hawaiian melt inclusions. *Chemical Geology*, 183(1-4):115–141.

Hauri, E. H., Wang, J., Dixon, J., King, P. L., Mandeville, C., and Newman, S. (2002). SIMS analysis of volatiles in silicate glasses. *Chemical Geology*, 183(1-4):99–114.

Hayward, C. (2011). High spatial resolution electron probe microanalysis of tephras and melt inclusions without beam-induced chemical modification. *The Holocene*, 22(1):119–125.

Helo, C., Longpré, M.-A., Shimizu, N., Clague, D. A., and Stix, J. (2011). Explosive eruptions at mid-ocean ridges driven by $CO_2$-rich magmas. *Nature Geoscience*, 4(4):260–263.

Herd, C. (2008). Basalts as probes of planetary interior redox state. *Reviews in Mineralogy and Geochemistry*, 68(1):527–553.

Hinton, R. W. (1995). Ion microprobe analysis in geology. In *Microprobe Techniques in the Earth Sciences*, pages 235–289. Springer US, Boston, MA.

Höfer, H. E. (2002). Quantification of $Fe^{2+}/Fe^{3+}$ by electron microprobe analysis – New developments. *Mössbauer Spectroscopy*, 144-145:239–248.

Höfer, H. E. and Brey, G. (2007). The iron oxidation state of garnet by electron microprobe: Its determination with the flank method combined with major-element analysis. *American Mineralogist*, 92(5-6):873–885.

Höfer, H. E., Brey, G., Schulz-Dobrick, B., and Oberhansli, R. (1994). The determination of the oxidation state of iron by the electron microprobe. *European Journal of Mineralogy*, 6:407–418.

Holloway, J. and Blank, J. (1994). Application of experimental results to C-O-H species in natural melts. *Reviews in Mineralogy and Geochemistry*, 30:187–230.

Holloway, J. R. (1981). Volatile interactions in magmas. In R.C., N., A., N., and B.J., W., editors, *Thermodynamics of minerals and melts. Advances in physical geochemistry, vol 1.*, pages 273–293. Springer, New York, NY.

Holtz, F., Sato, H., Lewis, J., Behrens, H., and Nakada, S. (2004). Experimental petrology of the 1991–1995 Unzen dacite, Japan. Part I: Phase relations, phase composition and pre-eruptive conditions. *Journal of Petrology*, 46(2):319–337.

Howard-Lock, H. E. and Stoicheff, B. (1971). Raman intensity measurements of the Fermi diad $\nu_1$, $2\nu_2$ in $^{12}CO_2$ and $^{13}CO_2$. *Journal of Molecular Spectroscopy*, 37(2):321–326.

Humphreys, M., Kearns, S. L., and Blundy, J. (2006). SIMS investigation of electron-beam damage to hydrous, rhyolitic glasses: Implications for melt inclusion analysis. *American Mineralogist*, 91(4):667–679.

Huppert, H. E. and Woods, A. W. (2002). The role of volatiles in magma chamber dynamics. *Nature*, 420(6915):493–495.

Ihinger, P. (1991). *An experimental study of the interaction of water with granitic melt*. PhD thesis, California Institute of Technology.

Ihinger, P. D., Hervig, R. L., and McMillan, P. (1994). Analytical methods of volatiles in glasses. *Reviews in Mineralogy and Geochemistry*, 30:67–122.

Jambon, A. (1994). Earth degassing and large-scale geochemical cycling of volatile elements. *Reviews in Mineralogy and Geochemistry*, 30:479–518.

Jambon, A. and Zimmermann, J. L. (1990). Water in oceanic basalts: Evidence for dehydration of recycled crust. *Earth and Planetary Science Letters*, 101(2-4):323–331.

Jarosewich, E., Nelen, J., and Norberg, J. (1980). Reference samples for electron microprobe analysis. *Geostandards and Geoanalytical Research*, 4(1):43–47.

Jaupart, C. and Vergniolle, S. (1988). Laboratory models of Hawaiian and Strombolian eruptions. *Nature*, 331(6151):58–60.

Jaupart, C. and Vergniolle, S. (1989). The generation and collapse of a foam layer at the roof of a basaltic magma chamber. *Journal*

*of Fluid Mechanics*, 203:347–380.

Javoy, M. and Pineau, F. (1991). The volatiles record of a 'popping' rock from the Mid-Atlantic Ridge at 14 °N: Chemical and isotopic composition of gas trapped in the vesicles. *Earth and Planetary Science Letters*, 107(3-4):598–611.

Javoy, M., Pineau, F., and Iiyama, I. (1978). Experimental determination of the isotopic fractionation between gaseous $CO_2$ and carbon dissolved in tholeiitic magma. *Contributions to Mineralogy and Petrology*, 67(1):35–39.

Jbara, O., Cazaux, J., and Trebbia, P. (1995). Sodium diffusion in glasses during electron irradiation. *Journal of Applied Physics*, 78(2):868–875.

Jbara, O., Fakhfakh, S., Belhaj, M., Cazaux, J., Rau, E., Filippov, M., and Andrianov, M. (2002). A new experimental approach for characterizing the internal trapped charge and electric field build up in ground-coated insulators during their $e^-$ irradiation. *Nuclear Instruments and Methods in Physics Research Section B: Beam Interactions with Materials and Atoms*, 194(3):302–310.

Jbara, O., Fakhfakh, S., Belhaj, M., and Rondot, S. (2004). Charge implantation measurement on electron-irradiated insulating materials by means of a SEM technique. *Microscopy and Microanalysis*, 10:697–710.

Jbara, O., Portron, B., Mouze, D., and Cazaux, J. (1997). Electron probe microanalysis of insulating oxides: Monte Carlo simulations. *X-Ray Spectrometry*, 26(5):291–302.

Jenkyns, H. C., Gale, A. S., and Corfield, R. M. (1994). Carbon- and oxygen-isotope stratigraphy of the English Chalk and Italian Scaglia and its palaeoclimatic significance. *Geological Magazine*, 131(1):1–34.

Jurewicz, A. J. G. and Watson, E. (1988). Cations in olivine, Part 2: Diffusion in olivine xenocrysts, with applications to petrology and mineral physics. *Contributions to Mineralogy and Petrology*, 99(2):186–201.

Kagi, H., Yamamoto, J., and Kawakami, Y. (2003). Micro-Raman densimeter for $CO_2$ inclusions in mantle-derived minerals. *Applied Spectroscopy*, 57(11):1333–1339.

Kahl, M., Chakraborty, S., Pompilio, M., and Costa, F. (2015). Constraints on the nature and evolution of the magma plumbing system of Mt. Etna volcano (1991–2008) from a combined thermodynamic and kinetic modelling of the compositional record of minerals. *Journal of Petrology*, 56(10):2025–2068.

Kanaya, K., Okayama, S., Mouze, D., Cazaux, J., and Ferrier, R. P. (1972). Penetration and energy-loss theory of electrons in solid targets. *Journal of Physics D: Applied Physics*, 5(1):308.

Kawamoto, T. and Hirose, K. (1994). Au-Pd sample containers for melting experiments on iron and water bearing systems. *European Journal of Mineralogy*, 6:381–385.

Kelley, K. A. and Cottrell, E. (2009). Water and the oxidation state of subduction zone magmas. *Science*, 325(5940):605–7.

Kennedy, G. C. (1948). Equilibrium between volatiles and iron oxides in igneous rocks. *American Journal of Science*, 246(9):529–548.

Kent, A. J. (2008). Melt inclusions in basaltic and related volcanic rocks. *Reviews in Mineralogy and Geochemistry*, 69:273–331.

Keppler, H., Wiedenbeck, M., and Shcheka, S. S. (2003). Carbon solubility in olivine and the mode of carbon storage in the Earth's mantle. *Nature*, 424(6947):414–416.

King, P., Vennemann, T., Holloway, J., Hervig, R., Lowenstern, J., and Forneris, J. (2002). Analytical techniques for volatiles: A case study using intermediate (andesitic) glasses. *American Mineralogist*, 87(8-9):1077–1089.

Kingsley, R. H., Schilling, J.-G., Dixon, J., Swart, P., Poreda, R., and Simons, K. (2002). D/H ratios in basalt glasses from the Salas y Gomez mantle plume interacting with the East Pacific Rise: Water from old D-rich recycled crust or primordial water from the lower mantle? *Geochemistry, Geophysics, Geosystems*, 3(4):1–26.

Klimm, K., Kohn, S. C., O'Dell, L., Botcharnikov, R., and Smith, M. (2012). The dissolution mechanism of sulphur in hydrous silicate melts. I: Assessment of analytical techniques in determining the sulphur speciation in iron-free to iron-poor glasses. *Chemical Geology*, 322-323:237–249.

Kohlstedt, D. and Mackwell, S. (1998). Diffusion of hydrogen and intrinsic point defects in olivine. *Zeitschrift für Physikalische*

*Chemie*, 207(1-2):147–162.

Koornneef, J. M., Nikogosian, I., van Bergen, M. J., Smeets, R., Bouman, C., and Davies, G. R. (2015). TIMS analysis of Sr and Nd isotopes in melt inclusions from Italian potassium-rich lavas using prototype 1013 Ω amplifiers. *Chemical Geology*, 397:14–23.

Kress, V. and Carmichael, I. (1991). The compressibility of silicate liquids containing $Fe_2O_3$ and the effect of composition, temperature, oxygen fugacity and pressure on their redox states. *Contributions to Mineralogy and Petrology*, 108(1-2):82–92.

Lafuente, B., Downs, R., Yang, H., and Stone, N. (2015). The power of databases: The RRUFF project. In Armbruster, T. and Danisi, R., editors, *Highlights in Mineralogical Crystallography*, pages 1–30. De Gruyter.

Lamb, W., Guillemette, R., Popp, R., Fritz, S., and Chmiel, G. (2012). Determination of $Fe^{3+}/\Sigma Fe$ using the electron microprobe: A calibration for amphiboles. *American Mineralogist*, 97(5-6):951–961.

Lange, R. A. (1997). A revised model for the density and thermal expansivity of $K_2O$-$Na_2O$-CaO-MgO-$Al_2O_3$-$SiO_2$ liquids from 700 to 1900 K: Extension to crustal magmatic temperatures. *Contributions to Mineralogy and Petrology*, 130(1):1–11.

Lange, R. L. and Carmichael, I. (1990). Thermodynamic properties of silicate liquids with emphasis on density, thermal expansion and compressibility. *Reviews in Mineralogy and Geochemistry*, 24(1):25–64.

Le Voyer, M., Deloule, E., Kelley, K. A., Cartigny, P., Cottrell, E., and Hauri, E. H. (2014). Ion microprobe analyses of carbon isotope ratios in MORB. In *Goldschimdt Conference Abstracts*.

Lesne, P., Kohn, S. C., Blundy, J., Witham, F., Botcharnikov, R., and Behrens, H. (2011). Experimental simulation of closed-system degassing in the system basalt-$H_2O$-$CO_2$-S-Cl. *Journal of Petrology*, 52(9):1737–1762.

Li, J., Li, R., Zhao, B., Wang, N., and Cheng, J. (2016). Quantitative analysis and measurement of carbon isotopic compositions in individual fluid inclusions by micro-laser Raman spectrometry. *Analytical Methods*, 8(37):6730–6738.

Li, Z. and Lee, C. (2004). The constancy of upper mantle $fO_2$ through time inferred from V/Sc ratios in basalts. *Earth and Planetary Science Letters*, 228(3-4):483–493.

Lindsley, D. (1983). Pyroxene thermometry. *American Mineralogist*, 68(5-6):477–493.

Lineweaver, J. (1963). Oxygen outgassing caused by electron bombardment of glass. *Journal of Applied Physics*, 34:1786–1791.

Lloyd, A. S., Plank, T., Ruprecht, P., Hauri, E. H., and Rose, W. (2013). Volatile loss from melt inclusions in pyroclasts of differing sizes. *Contributions to Mineralogy and Petrology*, 165(1):129–153.

Long, D. (1977). *Raman Spectroscopy*. McGraw Hill Higher Education.

Lorenz, V. (1987). Phreatomagmatism and its relevance. *Chemical Geology*, 62(1-2):149–156.

Lowenstern, J. (1995). Applications of silicate-melt inclusions to the study of magmatic volatiles. In Thompson, J., editor, *Magmas, fluids and ore deposits. Mineralogical Assoication of Canada Short Course Volume no. 23*, pages 71–99.

Lowenstern, J. (2003). Melt inclusions come of age: Volatiles, volcanoes, and Sorby's legacy. *Developments in Volcanology*, 5:1–21.

Lu, F., Anderson, A. T., and Davis, A. M. (1995). Diffusional gradients at the crystal/melt interface and their effect on the compositions of melt inclusions. *The Journal of Geology*, 103(5):591–597.

Maclennan, J. (2017). Bubble formation and decrepitation control the $CO_2$ content of olivine-hosted melt inclusions. *Geochemistry, Geophysics, Geosystems*, 18(2):597–616.

Macpherson, C., Hilton, D. R., Newman, S., and Mattey, D. (1999). $CO_2$, $^{13}C/^{12}C$ and $H_2O$ variability in natural basaltic glasses: A study comparing stepped heating and FTIR spectroscopic techniques. *Geochimica et Cosmochimica Acta*, 63(11-12):1805–1813.

Macpherson, C. and Mattey, D. (1994). Carbon isotope variations of $CO_2$ in Central Lau Basin basalts and ferrobasalts. *Earth and Planetary Science Letters*, 121(3-4):263–276.

Mader, H. M., Llewellin, E. W., and Mueller, S. P. (2013). The rheology of two-phase magmas: A review and analysis. *Journal of*

*Volcanology and Geothermal Research*, 257:135–158.

Maeno, T., Hoshino, T., Futami, T., and Takada, T. (1989). Application of ultrasonic techniques to the measurement of spatial charge and electric field distributions in solid dielectric materials. *Electrical Engineering in Japan*, 109(5):58–64.

Malaspina, N., Scambelluri, M., Poli, S., Van Roermund, H., and Langenhorst, F. (2010). The oxidation state of mantle wedge majoritic garnet websterites metasomatised by C-bearing subduction fluids. *Earth and Planetary Science Letters*, 298(3-4):417–426.

Martelli, M., Caracausi, A., Paonita, A., and Rizzo, A. (2008). Geochemical variations of air-free crater fumaroles at Mt Etna: New inferences for forecasting shallow volcanic activity. *Geophysical Research Letters*, 35(21):L21302.

Martini, M. (1996). Chemical characters of the gaseous phase in different stages of volcanism: Precursors and volcanic activity. In *Monitoring and Mitigation of Volcano Hazards*, pages 199–219. Springer, Berlin, Heidelberg.

Mason, E., Edmonds, M., and Turchyn, A. V. (2017). Remobilization of crustal carbon may dominate volcanic arc emissions. *Science*, 357(6348):290–294.

Mathez, E. and Delaney, J. (1981). The nature and distribution of carbon in submarine basalts and peridotite nodules. *Earth and Planetary Science Letters*, 56:217–232.

Mathez, E. A. (1984). Influence of degassing on oxidation states of basaltic magmas. *Nature*, 310(5976):371–375.

Matjuschkin, V., Brey, G., Höfer, H. E., and Woodland, A. B. (2014). The influence of $Fe^{3+}$ on garnet-orthopyroxene and garnet-olivine geothermometers. *Contributions to Mineralogy and Petrology*, 167(2):972.

Mattey, D. (1991). Carbon dioxide solubility and carbon isotope fractionation in basaltic melt. *Geochimica et Cosmochimica Acta*, 55(11):3467–3473.

Mattey, D., Carr, R., Wright, I., and Pillinger, C. (1984). Carbon isotopes in submarine basalts. *Earth and Planetary Science Letters*, 70(2):196–206.

Mattey, D., Exley, R., and Pillinger, C. (1989). Isotopic composition of $CO_2$ and dissolved carbon species in basalt glass. *Geochimica et Cosmochimica Acta*, 53(9):2377–2386.

Mattey, D., Taylor, W. R., Green, D. H., and Pillinger, C. (1990). Carbon isotopic fractionation between $CO_2$ vapour, silicate and carbonate melts: An experimental study to 30 kbar. *Contributions to Mineralogy and Petrology*, 104(4):492–505.

McCammon, C. (1999). Methods for determination of $Fe^{3+}/\Sigma Fe$ in microscopic samples. In Gurney, J., Pascoe, M., and Richardson, S., editors, *Proceedings of the VII$^{th}$ International Kimberlite Conference, P. H. Nixon Volume*, pages 540–544. Red Roof Design, Cape Town, South Africa.

McIntosh, I. M., Nichols, A., Tani, K., and Llewellin, E. W. (2017). Accounting for the species-dependence of the 3500 $cm^{-1}$ $H_2O_t$ infrared molar absorptivity coefficient: Implications for hydrated volcanic glasses. *American Mineralogist*, 102(8):1677–1689.

Melekhova, E., Blundy, J., Robertson, R., and Humphreys, M. (2015). Experimental evidence for polybaric differentiation of primitive arc basalt beneath St. Vincent, Lesser Antilles. *Journal of Petrology*, 56(1):161–192.

Métrich, N., Allard, P., Spilliaert, N., Andronico, D., and Burton, M. (2004). 2001 flank eruption of the alkali- and volatile-rich primitive basalt responsible for Mount Etna's evolution in the last three decades. *Earth and Planetary Science Letters*, 228(1-2):1–17.

Métrich, N., Bertagnini, A., and Di Muro, A. (2009). Conditions of magma storage, degassing and ascent at Stromboli: New insights into the volcano plumbing system with inferences on the eruptive dynamics. *Journal of Petrology*, 51(3):603–626.

Métrich, N. and Clocchiatti, R. (1989). Melt inclusion investigation of the volatile behaviour in historic alkali basaltic magmas of Etna. *Bulletin of Volcanology*, 51(3):185–198.

Métrich, N. and Clocchiatti, R. (1996). Sulfur abundance and its speciation in oxidized alkaline melts. *Geochimica et Cosmochimica Acta*, 60(21):4151–4160.

Métrich, N. and Deloule, E. (2014). Water content, $\delta D$ and $\delta^{11}B$ tracking in the Vanuatu arc magmas (Aoba Island): Insights from

olivine-hosted melt inclusions. *Lithos*, 206-207:400–408.

Michael, P. J. and Cornell, W. C. (1998). Influence of spreading rate and magma supply on crystallization and assimilation beneath mid-ocean ridges: Evidence from chlorine and major element chemistry of mid-ocean ridge basalts. *Journal of Geophysical Research: Solid Earth*, 103(B8):18325–18356.

Mironov, N., Portnyagin, M., Botcharnikov, R., Gurenko, A., Hoernle, K., and Holtz, F. (2015). Quantification of the $CO_2$ budget and $H_2O$-$CO_2$ systematics in subduction-zone magmas through the experimental hydration of melt inclusions in olivine at high $H_2O$ pressure. *Earth and Planetary Science Letters*, 425:1–11.

Moore, L., Gazel, E., Tuohy, R., Lloyd, A., Esposito, R., Steele-MacInnis, M., Hauri, E. H., Wallace, P., Plank, T., and Bodnar, R. (2015). Bubbles matter: An assessment of the contribution of vapor bubbles to melt inclusion volatile budgets. *American Mineralogist*, 100(4):806–823.

Moretti, R., Métrich, N., Arienzo, I., Di Renzo, V., Aiuppa, A., and Allard, P. (2018). Degassing vs. eruptive styles at Mt. Etna volcano (Sicily, Italy). Part I: Volatile stocking, gas fluxing, and the shift from low-energy to highly explosive basaltic eruptions. *Chemical Geology*, 482:1–17.

Morgan, G. B. and London, D. (2005). Effect of current density on the electron microprobe analysis of alkali aluminosilicate glasses. *American Mineralogist*, 90(7):1131–1138.

Morizet, Y., Brooker, R., Iacono-Marziano, G., and Kjarsgaard, B. A. (2013). Quantification of dissolved $CO_2$ in silicate glasses using micro-Raman spectroscopy. *American Mineralogist*, 98(10):1788–1803.

Moussallam, Y., Edmonds, M., Scaillet, B., Peters, N., Gennaro, M., Sides, I., and Oppenheimer, C. (2016). The impact of degassing on the oxidation state of basaltic magmas: A case study of Kilauea volcano. *Earth and Planetary Science Letters*, 450:317–325.

Moussallam, Y., Oppenheimer, C., Scaillet, B., Gaillard, F., Kyle, P., Peters, N., Hartley, M. E., Berlo, K., and Donovan, A. (2014). Tracking the changing oxidation state of Erebus magmas, from mantle to surface, driven by magma ascent and degassing. *Earth and Planetary Science Letters*, 393:200–209.

Mujin, M. and Nakamura, M. (2014). A nanolite record of eruption style transition. *Geology*, 42(7):611–614.

Mujin, M., Nakamura, M., and Miyake, A. (2017). Eruption style and crystal size distributions: Crystallization of groundmass nanolites in the 2011 Shinmoedake eruption. *American Mineralogist*, 102(12):2367–2380.

Mysen, B. (2013a). Effects of fluid and melt density and structure on high-pressure and high-temperature experimental studies of hydrogen isotope partitioning between coexisting melt and aqueous fluid. *American Mineralogist*, 98(10):1754–1764.

Mysen, B. (2013b). Hydrogen isotope fractionation between coexisting hydrous melt and silicate-saturated aqueous fluid: An experimental study *insitu* at high pressure and temperature. *American Mineralogist*, 98(2-3):376–386.

Mysen, B. (2016). Experimentally-determined carbon isotope fractionation in and between methane-bearing melt and fluid to upper mantle temperatures and pressures. *Earth and Planetary Science Letters*, 445:28–35.

Mysen, B. (2017). Experimental, *insitu* carbon solution mechanisms and isotope fractionation in and between (C-O-H)-saturated silicate melt and silicate-saturated (C-O-H) fluid to upper mantle temperatures and pressures. *Earth and Planetary Science Letters*, 459:352–361.

Mysen, B., Virgo, D., and Seifert, F. A. (1982). The structure of silicate melts: Implications for chemical and physical properties of natural magma. *Reviews of Geophysics*, 20(3):353–383.

Mysen, B. O., Arculus, R. J., and Eggler, D. H. (1975). Solubility of carbon dioxide in melts of andesite, tholeiite, and olivine nephelinite composition to 30 kbar pressure. *Contributions to Mineralogy and Petrology*, 53(4):227–239.

Nakamura, A. and Schmalzried, H. (1983). On the nonstoichiometry and point defects of olivine. *Physics and Chemistry of Minerals*, 10(1):27–37.

Namiki, A. and Manga, M. (2008). Transition between fragmentation and permeable outgassing of low viscosity magmas. *Journal of Volcanology and Geothermal Research*, 169(1-2):48–60.

Nash, W. P. (1992). Analysis of oxygen with electron microprobe: Applications to hydrated glass and minerals. *American*

*Mineralogist*, 77:453–457.

Naumov, V. (2011). Rhyolitic melts in eastern Transbaikalia and the North Caucasus: Chemical composition, volatiles, and admixture elements (from data of study of melt inclusions in minerals). *Russian Geology and Geophysics*, 52(11):1368–1377.

Naumov, V. B., Tolstykh, M. L., Grib, E. N., Leonov, V. L., and Kononkova, N. N. (2008). Chemical composition, volatile components, and trace elements in melts of the Karymskii volcanic center, Kamchatka, and Golovnina volcano, Kunashir Island: Evidence from inclusions in minerals. *Petrology*, 16(1):1–18.

Newman, S., Epstein, S., and Stolper, E. (1988). Water, carbon dioxide, and hydrogen isotopes in glasses from the ca. 1340 A.D. eruption of the Mono Craters, California: Constraints on degassing phenomena and initial volatile content. *Journal of Volcanology and Geothermal Research*, 35(1-2):75–96.

Newman, S. and Lowenstern, J. (2002). VolatileCalc: A silicate melt-$H_2O$-$CO_2$ solution model written in Visual Basic for excel. *Computers & Geosciences*, 28(5):597–604.

Newman, S., Stolper, E., and Epstein, S. (1986). Measurement of water in rhyolitic glasses: Calibration of an infrared spectroscopic technique. *American Mineralogist*, 71:1527–1541.

Ni, H. and Keppler, H. (2013). Carbon in silicate melts. *Reviews in Mineralogy and Geochemistry*, 75:251–287.

Nichols, A., Carroll, M., and Höskuldsson, Á. (2002). Is the Iceland hot spot also wet? Evidence from the water contents of undegassed submarine and subglacial pillow basalts. *Earth and Planetary Science Letters*, 202(1):77–87.

Nicotra, E. and Viccaro, M. (2012). Transient uprise of gas and gas-rich magma batches fed the pulsating behavior of the 2006 eruptive episodes at Mt. Etna volcano. *Journal of Volcanology and Geothermal Research*, 227-228:102–118.

Nielsen, C. H. and Sigurdsson, H. (1981). Quantitative methods for electron microprobe analysis of sodium in natural and synthetic glasses. *American Mineralogist*, 66:547–552.

Nielsen, R. L., Michael, P. J., and Sours-Page, R. (1998). Chemical and physical indicators of compromised melt inclusions. *Geochimica et Cosmochimica Acta*, 62(5):831–839.

Nishida, T. (1995). Mössbauer effect in inorganic glasses. *Hyperfine Interactions*, 95(1):23–39.

Nolan, G. S. and Bindeman, I. (2013). Experimental investigation of rates and mechanisms of isotope exchange (O, H) between volcanic ash and isotopically-labeled water. *Geochimica et Cosmochimica Acta*, 111:5–27.

Ochs, F. A. and Lange, R. (1999). The density of hydrous magmatic liquids. *Science*, 283(5406):1314–1317.

Ohlhorst, S., Behrens, H., and Holtz, F. (2001). Compositional dependence of molar absorptivities of near-infrared $OH^-$ and $H_2O$ bands in rhyolitic to basaltic glasses. *Chemical Geology*, 174(1-3):5–20.

Okumura, S. and Nakashima, S. (2006). Water diffusion in basaltic to dacitic glasses. *Chemical Geology*, 227(1-2):70–82.

Osborn, E. F. (1959). Role of oxygen pressure in the crystallization and differentiation of basaltic magma. *American Journal of Science*, 257(9):609–647.

Pan, Y. and Batiza, R. (1998). Major element chemistry of volcanic glasses from the Easter Seamount Chain: Constraints on melting conditions in the plume channel. *Journal of Geophysical Research: Solid Earth*, 103(B3):5287–5304.

Paonita, A., Caracausi, A., Iacono-Marziano, G., Martelli, M., and Rizzo, A. (2012). Geochemical evidence for mixing between fluids exsolved at different depths in the magmatic system of Mt Etna (Italy). *Geochimica et Cosmochimica Acta*, 84:380–394.

Papale, P. (1999). Strain-induced magma fragmentation in explosive eruptions. *Nature*, 397(6718):425–428.

Papale, P. (2005). Determination of total $H_2O$ and $CO_2$ budgets in evolving magmas from melt inclusion data. *Journal of Geophysical Research*, 110(B3):B03208.

Papale, P., Neri, A., and Macedonio, G. (1998). The role of magma composition and water content in explosive eruptions: 1. Conduit ascent dynamics. *Journal of Volcanology and Geothermal Research*, 87(1-4):75–93.

Pichavant, M., Di Carlo, I., Le Gac, Y., Rotolo, S. G., and Scaillet, B. (2009). Experimental constraints on the deep magma feeding

system at Stromboli volcano, Italy. *Journal of Petrology*, 50(4):601–624.

Pichavant, M., Di Carlo, I., Rotolo, S. G., Scaillet, B., Burgisser, A., Le Gall, N., and Martel, C. (2013). Generation of $CO_2$-rich melts during basalt magma ascent and degassing. *Contributions to Mineralogy and Petrology*, 166(2):545–561.

Pichavant, M., Le Gall, N., and Scaillet, B. (2018). Gases as precursory signals: Experimental simulations, new concepts and models of magma degassing. In *Advances in Volcanology*, pages 1–16. Springer, Berlin, Heidelberg.

Pineau, F. and Javoy, M. (1983). Carbon isotopes and concentrations in mid-oceanic ridge basalts. *Earth and Planetary Science Letters*, 62(2):239–257.

Pineau, F. and Javoy, M. (1994). Strong degassing at ridge crests: The behaviour of dissolved carbon and water in basalt glasses at 14 °N, Mid-Atlantic Ridge. *Earth and Planetary Science Letters*, 123(1-3):179–198.

Pineau, F., Shilobreeva, S., Kadik, A., and Javoy, M. (1998). Water solubility and D/H fractionation in the system basaltic andesite-$H_2O$ at 1250 °C and between 0.5 and 3 kbars. *Chemical Geology*, 147(1-2):173–184.

Poret, M., Corradini, S., Merucci, L., Costa, A., Andronico, D., Montopoli, M., Vulpiani, G., and Freret-Lorgeril, V. (2018). Reconstructing volcanic plume evolution integrating satellite and ground-based data: Application to the 23 November 2013 Etna eruption. *Atmospheric Chemistry and Physics*, 18(7):4695–4714.

Potapkin, V., Chumakov, A., Smirnov, G., Celse, J.-P., Rüffer, R., McCammon, C., and Dubrovinsky, L. (2012). The $^{57}$Fe synchrotron mössbauer source at the ESRF. *Journal of Synchrotron Radiation*, 19(4):559–569.

Putirka, K. D. (2008). Thermometers and barometers for volcanic systems. *Reviews in Mineralogy and Geochemistry*, 69(1):61–120.

Pyle, D. M., Beattie, P. D., and Bluth, G. J. S. (1996). Sulphur emissions to the stratosphere from explosive volcanic eruptions. *Bulletin of Volcanology*, 57(8):663–671.

Qi, H., Coplen, T. B., Gehre, M., Vennemann, T. W., Brand, W. A., Geilmann, H., Olack, G., Bindeman, I. N., Palandri, J., Huang, L., and Longstaffe, F. J. (2017). New biotite and muscovite isotopic reference materials, USGS57 and USGS58, for $\delta^2$H measurements – A replacement for NBS 30. *Chemical Geology*, 467:89–99.

Reed, S. (1975). *Electron microprobe analysis*.

Richet, P., Bottinga, Y., and Javoy, M. (1977). A review of hydrogen, carbon, nitrogen, oxygen, sulphur, and chlorine stable isotope fractionation among gaseous molecules. *Annual Review of Earth and Planetary Sciences*, 5(1):65–110.

Richet, P., Roux, J., and Pineau, F. (1986). Hydrogen isotope fractionation in the system $H_2O$-liquid $NaAlSi_3O_8$: New data and comments on D/H fractionation in hydrothermal experiments. *Earth and Planetary Science Letters*, 78(1):115–120.

Richter, F. M., Davis, A. M., De Paolo, D. J., and Watson, E. (2003). Isotope fractionation by chemical diffusion between molten basalt and rhyolite. *Geochimica et Cosmochimica Acta*, 67(20):3905–3923.

Richter, F. M., Liang, Y., and Davis, A. M. (1999). Isotope fractionation by diffusion in molten oxides. *Geochimica et Cosmochimica Acta*, 63(18):2853–2861.

Richter, F. M., Watson, E., Mendybaev, R., Dauphas, N., Georg, B., Watkins, J., and Valley, J. (2009). Isotopic fractionation of the major elements of molten basalt by chemical and thermal diffusion. *Geochimica et Cosmochimica Acta*, 73(14):4250–4263.

Richter, F. M., Watson, E., Mendybaev, R., Teng, F.-Z., and Janney, P. E. (2008). Magnesium isotope fractionation in silicate melts by chemical and thermal diffusion. *Geochimica et Cosmochimica Acta*, 72(1):206–220.

Riker, J., Blundy, J., Rust, A. C., Botcharnikov, R., and Humphreys, M. (2015). Experimental phase equilibria of a Mount St. Helens rhyodacite: A framework for interpreting crystallization paths in degassing silicic magmas. *Contributions to Mineralogy and Petrology*, 170(1):6.

Rizzo, A., Liuzzo, M., Ancellin, M., and Jost, H. (2015). Real-time measurements of $\delta^{13}$C, $CO_2$ concentration, and $CO_2/SO_2$ in volcanic plume gases at Mount Etna, Italy, over 5 consecutive days. *Chemical Geology*, 411:182–191.

Rizzo, A. L., Jost, H.-J., Caracausi, A., Paonita, A., Liotta, M., and Martelli, M. (2014). Real-time measurements of the

concentration and isotope composition of atmospheric and volcanic $CO_2$ at Mount Etna (Italy). *Geophysical Research Letters*, 41(7):2382–2389.

Roberge, J., Delgado-Granados, H., and Wallace, P. J. (2009). Mafic magma recharge supplies high $CO_2$ and $SO_2$ gas fluxes from Popocatépetl volcano, Mexico. *Geology*, 37(2):107–110.

Robidoux, P., Frezzotti, M. L., Hauri, E. H., and Aiuppa, A. (2018). Shrinkage bubbles: The C-O-H-S magmatic fluid system at San Cristóbal volcano. *Journal of Petrology*, 59(11):2093–2122.

Roedder, E. (1979). Origin and significance of magmatic inclusions. *Bulletin de Mineralogie*, 102:487–510.

Roeder, P. L. and Emslie, R. F. (1970). Olivine-liquid equilibrium. *Contributions to Mineralogy and Petrology*, 29(4):275–289.

Roggensack, K. (1997). Explosive basaltic volcanism from Cerro Negro volcano: Influence of volatiles on eruptive style. *Science*, 277(5332):1639–1642.

Roman, D. C., Cashman, K., Gardner, C. A., Wallace, P., and Donovan, J. (2006). Storage and interaction of compositionally heterogeneous magmas from the 1986 eruption of Augustine volcano, Alaska. *Bulletin of Volcanology*, 68(3):240–254.

Rowe, M. C., Kent, A. J., and Nielsen, R. L. (2007). Determination of sulfur speciation and oxidation state of olivine hosted melt inclusions. *Chemical Geology*, 236(3-4):303–322.

Rutherford, M. and Devine, J. (1996). Preeruption pressure-temperature conditions and volatiles in the 1991 dacitic magma of Mount Pinatubo. *Fire and mud: Eruptions and lahars of Mount Pinatubo, Philippines*, pages 751–766.

Sato, M. (1978). Oxygen fugacity of basaltic magmas and the role of gas-forming elements. *Geophysical Research Letters*, 5(6):447–449.

Schellart, W. P. (2010). Mount Etna-Iblean volcanism caused by rollback-induced upper mantle upwelling around the Ionian slab edge: An alternative to the plume model. *Geology*, 38(8):691–694.

Schiano, P. (2003). Primitive mantle magmas recorded as silicate melt inclusions in igneous minerals. *Earth-Science Reviews*, 63(1-2):121–144.

Schiano, P., Clocchiatti, R., Ottolini, L., and Busa, T. (2001). Transition of Mount Etna lavas from a mantle-plume to an island-arc magmatic source. *Nature*, 412(6850):900–904.

Schiavi, F., Rosciglione, A., Kitagawa, H., Kobayashi, K., Nakamura, E., Nuccio, P. M., Ottolini, L., Paonita, A., and Vannucci, R. (2015). Geochemical heterogeneities in magma beneath Mount Etna recorded by 2001–2006 melt inclusions. *Geochemistry, Geophysics, Geosystems*, 16(7):2109–2126.

Schilling, J. G., Thompson, G., Kingsley, R., and Humphris, S. (1985). Hotspot-migrating ridge interaction in the South Atlantic. *Nature*, 313(5999):187–191.

Schuessler, J. A., Botcharnikov, R., Behrens, H., Misiti, V., and Freda, C. (2008). Amorphous materials: Properties, structure, and durability: Oxidation state of iron in hydrous phono-tephritic melts. *American Mineralogist*, 93(10):1493–1504.

Sessler, G. M. and Yang, G. M. (1998). Materials for advanced metallization. In *MAM '97 Abstracts Booklet, European Workshop*, volume 53, pages 38–47. Société française du vide.

Shaw, A., Hauri, E. H., Fischer, T., Hilton, D., and Kelley, K. (2008). Hydrogen isotopes in Mariana arc melt inclusions: Implications for subduction dehydration and the deep-Earth water cycle. *Earth and Planetary Science Letters*, 275(1-2):138–145.

Shaw, H. R. (1963). Obsidian-$H_2O$ viscosities at 1000 and 2000 bars in the temperature range 700 to 900 °C. *Journal of Geophysical Research*, 68(23):6337–6343.

Shilobreeva, S., Devirts, A., Kadik, A., and Lagutina, Y. (1991). Distribution of hyrodrogen isotopes at equilibrium in the system basalt-water at pressures of 3 kbars and temperature of 1250 °C. *Geokhimiya*, 7:1052–1056.

Shishkina, T., Botcharnikov, R., Holtz, F., Almeev, R., and Portnyagin, M. (2010). Solubility of $H_2O$- and $CO_2$-bearing fluids in tholeiitic basalts at pressures up to 500 MPa. *Chemical Geology*, 277(1-2):115–125.

Shishkina, T. A., Botcharnikov, R. E., Holtz, F., Almeev, R., Jazwa, A. M., and Jakubiak, A. A. (2014). Compositional and pressure effects on the solubility of $H_2O$ and $CO_2$ in mafic melts. *Chemical Geology*, 388:112–129.

Shorttle, O., Moussallam, Y., Hartley, M. E., Maclennan, J., Edmonds, M., and Murton, B. (2015). Fe-XANES analyses of Reykjanes Ridge basalts: Implications for oceanic crust's role in the solid Earth oxygen cycle. *Earth and Planetary Science Letters*, 427:272–285.

Silver, L. and Stolper, E. (1989). Water in albitic glasses. *Journal of Petrology*, 30(3):667–709.

Smith, D. G. W. and O'Nions, R. K. (1971). Investigations of the $L_{II,III}$ X-ray emission spectra of Fe by the electron microprobe Part I: Some aspects of the Fe $L_{II,III}$ spectra from metallic iron and haematite. *Journal of Physics D: Applied Physics*, 4(1):320.

Smith, V., Shane, P., and Nairn, I. A. (2010). Insights into silicic melt generation using plagioclase, quartz and melt inclusions from the caldera-forming Rotoiti eruption, Taupo Volcanic Zone, New Zealand. *Contributions to Mineralogy and Petrology*, 160(6):951–971.

Sobolev, A. V. and Shimizu, N. (1993). Ultra-depleted primary melt included in an olivine from the Mid-Atlantic Ridge. *Nature*, 363(6425):151–154.

Sommer, M. A. (1977). Volatiles $H_2O$, $CO_2$, and CO in silicate melt inclusions in quartz phenocrysts from the rhyolitic Bandelier air-fall and ash-flow tuff, New Mexico. *The Journal of Geology*, 85(4):423–432.

Sorby, H. (1858). On the microscopic structure of crystals, indicating the origin of minerals and rocks. *Geological Society of London Quarterly Journal*, 14(1):453–500.

Sparks, R. S. J. (1978). The dynamics of bubble formation and growth in magmas: A review and analysis. *Journal of Volcanology and Geothermal Research*, 3(1-2):1–37.

Spilliaert, N., Allard, P., Métrich, N., and Sobolev, A. V. (2006). Melt inclusion record of the conditions of ascent, degassing, and extrusion of volatile-rich alkali basalt during the powerful 2002 flank eruption of Mount Etna (Italy). *Journal of Geophysical Research*, 111(B4):B04203.

Stamper, C., Melekhova, E., Blundy, J., Arculus, R., Humphreys, M., and Brooker, R. (2014). Oxidised phase relations of a primitive basalt from Grenada, Lesser Antilles. *Contributions to Mineralogy and Petrology*, 167(1):954.

Steele-Macinnis, M., Esposito, R., and Bodnar, R. J. (2011). Thermodynamic model for the effect of post-entrapment crystallization on the $H_2O$-$CO_2$ systematics of vapor-saturated, silicate melt inclusions. *Journal of Petrology*, 52(12):2461–2482.

Stock, M. J., Humphreys, M. C. S., Smith, V. C., Johnson, R. D., and Pyle, D. M. (2015). New constraints on electron-beam induced halogen migration in apatite. *American Mineralogist*, 100(1):281–293.

Stolper, E. (1982). The speciation of water in silicate melts. *Geochimica et Cosmochimica Acta*, 46(12):2609–2620.

Stolper, E. (1989). Temperature dependence of the speciation of water in rhyolitic melts and glasses. *American Mineralogist*, 74(11-12):1247–1257.

Stolper, E. M. and Holloway, J. (1988). Experimental determination of the solubility of carbon dioxide in molten basalt at low pressure. *Earth and Planetary Science Letters*, 87(397-408).

Swart, P., Grady, M., and Pillinger, C. (1983). A method for the identification and elimination of contamination during carbon isotopic analyses of extraterrestrial samples. *Meteoritics*, 18(2):137–154.

Taylor, B. (1986). Magmatic volatiles: Isotopic variation of C, H, and S. *Reviews in Mineralogy and Geochemistry*, 16:185–226.

Taylor, B. and Westrich, H. (1985). Hydrogen isotope exchange and water solubility in experiments using natural rhyolite obsidian. In *EOS*, page 387.

Thomas, R. (2000). Determination of water contents of granite melt inclusions by confocal laser Raman microprobe spectroscopy. *American Mineralogist*, 85(5-6):868–872.

Thomas, R., Kamenetsky, V. S., and Davidson, P. (2006). Laser Raman spectroscopic measurements of water in unexposed glass inclusions. *American Mineralogist*, 91(2-3):467–470.

Tingle, T. N., Green, H. W., and Finnerty, A. A. (1988). Experiments and observations bearing on the solubility and diffusivity of carbon in olivine. *Journal of Geophysical Research: Solid Earth*, 93(B12):15289–15304.

Tonarini, S., Armienti, P., D'Orazio, M., and Innocenti, F. (2001). Subduction-like fluids in the genesis of Mt. Etna magmas: Evidence from boron isotopes and fluid mobile elements. *Earth and Planetary Science Letters*, 192(4):471–483.

Toplis, M. J., Dingwell, D., and Libourel, G. (1994). The effect of phosphorus on the iron redox ratio, viscosity, and density of an evolved ferro-basalt. *Contributions to Mineralogy and Petrology*, 117(3):293–304.

Trull, T., Pineau, F., Bottinga, Y., and Javoy, M. (1991). Experimental study of $CO_2$ bubble growth and $^{13}C/^{12}C$ isotopic fractionation in tholeiitic melt. In *4$^{th}$ silicate melt workshop: Program and abstracts*, page 7.

Turner, J. and Campbell, I. (1986). Convection and mixing in magma chambers. *Earth-Science Reviews*, 23(4):255–352.

Tuttle, O. (1952). Origin of the contrasting mineralogy of extrusive and plutonic salic rocks. *Journal of Geology, USA*, 60:107–124.

Ulmer, P. (1989). The dependence of the $Fe^{2+}$-Mg cation-partitioning between olivine and basaltic liquid on pressure, temperature and composition. *Contributions to Mineralogy and Petrology*, 101(3):261–273.

Urey, H. (1947). The thermodynamic properties of isotopic substances. *Journal of the Chemical Society*, 0:562–581.

Viccaro, M., Calcagno, R., Garozzo, I., Giuffrida, M., and Nicotra, E. (2015). Continuous magma recharge at Mt. Etna during the 2011–2013 period controls the style of volcanic activity and compositions of erupted lavas. *Mineralogy and Petrology*, 109(1):67–83.

Viccaro, M. and Cristofolini, R. (2008). Nature of mantle heterogeneity and its role in the short-term geochemical and volcanological evolution of Mt. Etna (Italy). *Lithos*, 105(3-4):272–288.

Vicenzi, E. P., Green, T., and Sie, S. (1994). Effect of oxygen fugacity on trace-element partitioning between immiscible silicate melts at atmospheric pressure: A proton and electron microprobe study. *Chemical Geology*, 117(1-4):355–360.

Virgo, D. and Mysen, B. (1985). The structural state of iron in oxidized vs. reduced glasses at 1 atm: A $^{57}$Fe Mössbauer study. *Physics and Chemistry of Minerals*, 12(2):65–76.

Wagner, C., Deloule, E., Fialin, M., and King, P. (2008). Dehydrogenation of kaersutitic amphibole under electron beam excitation recorded by changes in $Fe^{3+}/\Sigma Fe$: An EMP and SIMS study. *American Mineralogist*, 93(8-9):1273–1281.

Walker, J. C. G., Hays, P. B., and Kasting, J. F. (1981). A negative feedback mechanism for the long-term stabilization of Earth's surface temperature. *Journal of Geophysical Research*, 86(C10):9776–9782.

Wallace, P. (2005). Volatiles in subduction zone magmas: Concentrations and fluxes based on melt inclusion and volcanic gas data. *Journal of Volcanology and Geothermal Research*, 140(1-3):217–240.

Wallace, P. and Carmichael, I. (1992). Sulfur in basaltic magmas. *Geochimica et Cosmochimica Acta*, 56(5):1863–1874.

Wallace, P. and Carmichael, I. (1994). S speciation in submarine basaltic glasses as determined by measurements of S$K\alpha$ X-ray wavelength shifts. *American Mineralogist*, 79:161–167.

Wallace, P., Kamenetsky, V. S., and Cervantes, P. (2015). Melt inclusion $CO_2$ contents, pressures of olivine crystallization, and the problem of shrinkage bubbles. *American Mineralogist*, 100(4):787–794.

Watanabe, S., Mishima, K., and Matsuo, S. (1983). Isotopic ratios of carbonaceous materials incorporated in olivine crystals from the Hualālai volcano, Hawai'i. An approach to mantle carbon. *Geochemical Journal*, 17(2):95–104.

Watkins, J. M., De Paolo, D. J., Huber, C., and Ryerson, F. J. (2009). Liquid composition-dependence of calcium isotope fractionation during diffusion in molten silicates. *Geochimica et Cosmochimica Acta*, 73(24):7341–7359.

Watson, E. (1976). Glass inclusions as samples of early magmatic liquid: Determinative method and application to a South Atlantic basalt. *Journal of Volcanology and Geothermal Research*, 1:73–84.

Watson, E. (2017). Diffusive fractionation of volatiles and their isotopes during bubble growth in magmas. *Contributions to Mineralogy and Petrology*, 172(8):61.

Webster, J. D., Burt, D., and Aguillon, R. (1996). Volatile and lithophile trace-element geochemistry of Mexican tin rhyolite magmas deduced from melt inclusions. *Geochimica et Cosmochimica Acta*, 60(17):3267–3283.

Webster, J. D., Congdon, R. D., and Lyons, P. C. (1995). Determining pre-eruptive compositions of late Paleozoic magma from kaolinized volcanic ashes: Analysis of glass inclusions in quartz microphenocrysts from tonsteins. *Geochimica et Cosmochimica Acta*, 59(4):711–720.

Webster, J. D. and Duffield, W. A. (1991). Volatiles and lithophile elements in Taylor Creek Rhyolite: Constraints from glass inclusion analysis. *American Mineralogist*, 76(9-10):1628–1645.

Wengorsch, T., Fuchs, P., Almeev, R., and Klugel, A. (2012). Revealing true liquid compositions for natural phonolites from Cumbre Vieja volcano, La Palma Island. *EMPG-XIV. Kiel Germany*, 143.

Wilke, M. (2005). Fe in magma – An overview. *Annals of Geophysics*, 48(4-5):609–617.

Wilke, M., Behrens, H., Burkhard, D., and Rossano, S. (2002). The oxidation state of iron in silicic melt at 500 MPa water pressure. *Chemical Geology*, 189(1-2):55–67.

Wilke, M., Jugo, P. J., Klimm, K., Susini, J., Botcharnikov, R., Kohn, S. C., and Janousch, M. (2008). The origin of $S^{4+}$ detected in silicate glasses by XANES. *American Mineralogist*, 93(1):235–240.

Wilke, M., Klimm, K., and Kohn, S. C. (2011). Spectroscopic studies on sulfur speciation in synthetic and natural glasses. *Reviews in Mineralogy and Geochemistry*, 73(1):41–78.

Wilke, M., Partzsch, G. M., Bernhardt, R., and Lattard, D. (2005). Determination of the iron oxidation state in basaltic glasses using XANES at the *K*-edge. *Chemical Geology*, 220(1-2):143–161.

Williams, H. M., McCammon, C., Peslier, A. H., Halliday, A. N., Teutsch, N., Levasseur, S., and Burg, J.-P. (2004). Iron isotope fractionation and the oxygen fugacity of the mantle. *Science*, 304(5677):1656–1659.

Wilson, L., Sparks, R., and Walker, G. (1980). Explosive volcanic eruptions – IV. The control of magma properties and conduit geometry on eruption column behaviour. *Geophysical Journal International*, 63(1):117–148.

Witham, F., Blundy, J., Kohn, S. C., Lesne, P., Dixon, J., Churakov, S. V., and Botcharnikov, R. (2012). SolEx: A model for mixed COHSCl-volatile solubilities and exsolved gas compositions in basalt. *Computers & Geosciences*, 45:87–97.

Wittmaack, K. (1983). Secondary ion yield variations due to cesium implantation in silicon. *Surface Science*, 126(1-3):573–580.

Wood, B. J. (1990). An experimental test of the spinel peridotite oxygen barometer. *Journal of Geophysical Research*, 95(B10):15845–15851.

Wood, B. J., Bryndzia, L. T., and Johnson, K. E. (1990). Mantle oxidation state and its relationship to tectonic environment and fluid speciation. *Science*, 248(4953):337–45.

Yamashita, S., Kitamura, T., and Kusakabe, M. (1997). Infra-red spectroscopy of hydrous glasses of arc magma compositions. *Geochemical Journal*, 31(3):169–174.

Zhang, C., Almeev, R., Hughes, E., Borisov, A., Wolff, E., Höfer, H. E., Botcharnikov, R., and Koepke, J. (2018). Electron microprobe technique for the determination of iron oxidation state in silicate glasses. *American Mineralogist*, 103:1445–1454.

Zhang, Y. (1999). A criterion for the fragmentation of bubbly magma based on brittle failure theory. *Nature*, 402(6762):648–650.

Zhang, Y. and Behrens, H. (2000). $H_2O$ diffusion in rhyolitic melts and glasses. *Chemical Geology*, 169(1-2):243–262.

Zhang, Y., Jenkins, J., and Xu, Z. (1997). Kinetics of the reaction $H_2O + O \leftrightarrow 2OH$ in rhyolitic glasses upon cooling: Geospeedometry and comparison with glass transition. *Geochimica et Cosmochimica Acta*, 61(11):2167–2173.

Zhang, Y., Ni, H., and Chen, Y. (2010). Diffusion data in silicate melts. *Reviews in Mineralogy and Geochemistry*, 72:311–408.

# Appendices

# Appendix A – Stable isotope fractionation

## A.1. Notation for isotope ratios

As natural variations in isotope ratios are small, isotope ratios are reported using delta ($\delta$) notation in per mil (‰), which compares the isotopic ratio of a sample to a standard:

$$\delta = \left( \frac{R_{sample}}{R_{standard}} - 1 \right) \cdot 1000 \tag{A.1}$$

where $R_{sample}$ and $R_{standard}$ are the isotope ratio using concentrations of the heavier (numerator) to lighter (denominator) isotope for the sample and standard, respectively. If $R_{sample} > R_{standard}$, $\delta > 0$: whereas if $R_{sample} < R_{standard}$, $\delta < 0$. Isotope ratios used in this study are summarised in Table A.1.

**Table A.1:** Definition of isotope systems used in this study.

| Isotope system | R | Standard | $R_{standard}$ |
|---|---|---|---|
| $\delta D$ | $^{2}H/^{1}H$ | Vienna Standard Mean Ocean Water (VSMOW) | $1.5575 \times 10^{-4}$ |
| $\delta^{13}C$ | $^{13}C/^{12}C$ | Vienna Pee Dee Belemite (VPDB) | $1.1237 \times 10^{-2}$ |
| $\delta^{18}O$ | $^{18}O/^{16}O$ | Vienna Standard Mean Ocean Water (VSMOW) | $2.0052 \times 10^{-3}$ |

## A.2. Definitions of the fractionation factor

The fractionation factor of a stable isotope system describes the direction (which phase becomes enriched in the heavy isotope) and magnitude (the size of the enrichment) during isotopic fractionation. The $\alpha$ fractionation factor ($\alpha_{A-B}$) between phase A and B is given by:

$$\alpha_{A-B} = \frac{R_A}{R_B} \tag{A.2}$$

where $R_A$ and $R_B$ are the isotope ratios of phase A and B, respectively, expressed as the ratio of the concentration of the heavy to light isotope. The $\alpha$ fractionation factor can also be expressed using $\delta$-notation by rearranging Equation A.1:

$$R = \left( \frac{R_{standard}}{1000} \right) \cdot (\delta + 1000) \tag{A.3}$$

and substituting Equation A.3 into Equation A.2, such that:

$$\alpha_{A-B} = \left( \frac{1000 + \delta_A}{1000 + \delta_B} \right) \tag{A.4}$$

where $\delta_A$ and $\delta_B$ are the isotope ratios in $\delta$-notation of phase A and B, respectively. Alternatively, the $\Delta$ fractionation factor ($\Delta_{A-B}$) between phase A and B is given by:

$$\Delta_{A-B} = \delta_A - \delta_B \tag{A.5}$$

which can be related to $\alpha_{A–B}$ by subtracting $(1000 + \delta_B)/(1000 + \delta_B)$ (i.e., 1) from both sides of Equation A.4, and then approximating $1000 + \delta_B \approx 1000$ as $\delta_B \ll 1000$:

$$\alpha_{A–B} - 1 = \frac{\delta_A - \delta_B}{1000 - \delta_B} \approx \frac{\delta_A - \delta_B}{1000} \tag{A.6}$$

By substituting Equation A.5 into Equation A.6 and rearranging:

$$\Delta_{A–B} = 1000 \cdot (1 - \alpha_{A–B}) \tag{A.7}$$

If $\alpha_{A–B} \approx 1$, which is commonly appropriate, then $\ln \alpha_{A–B} \approx 1 - \alpha_{A–B}$, hence:

$$\Delta_{A–B} = 1000 \cdot \ln \alpha_{A–B} \tag{A.8}$$

## A.3. Stable isotope fractionation during degassing

For degassing of an exsolved fluid from a melt, Equation A.5 becomes:

$$\Delta_{f–m} = \delta_f - \delta_m \tag{A.9}$$

where $\Delta_{f–m}$ is the fractionation factor between exsolved fluid and melt, and $\delta_f$ and $\delta_m$ are the isotope ratios in $\delta$-notation of the exsolved fluid and melt, respectively.

### A.3.1. Closed-system degassing

Closed-system degassing occurs when the melt and exsolved fluid maintain equilibrium and no material is lost from the system, hence:

$$C_b = C_m - C_f \tag{A.10}$$

where $C_b$, $C_m$, and $C_f$ are the concentration of the volatile in the bulk, melt and fluid, respectively. From mass balance, the isotope ratios are related by:

$$C_b R_b = C_m R_m + C_f R_f \tag{A.11}$$

where $R_b$, $R_m$, and $R_f$ are the isotope ratios of the volatile expressed as ratio of the heavy to light isotope in the bulk, melt and fluid, respectively. This is approximately equal to:

$$C_b \delta_b = C_m \delta_m + C_f \delta_f \tag{A.12}$$

Rearranging Equation A.11 for $\delta_f$ and substituting Equation A.10 for $C_f$ gives:

$$\delta_f = \frac{C_b\delta_b - C_m\delta_m}{C_b - C_m} \tag{A.13}$$

which can be substituted into Equation A.9 to give:

$$\Delta_{f\text{–}m} = \left(\frac{C_b\delta_b - C_m\delta_m}{C_b - C_m}\right) - \delta_f \tag{A.14}$$

And then rearranged for $\delta_m$:

$$\delta_m = \delta_b - \Delta_{f\text{–}m}\left(1 - \frac{C_m}{C_b}\right) \tag{A.15}$$

Conversely, the relationship between the fluid concentration and isotope ratio is given by:

$$\delta_f = \delta_b + \Delta_{f\text{–}m}\left(1 - \frac{C_f}{C_b}\right) \tag{A.16}$$

The bulk values will equal the initial values if the melt was undersaturated at the onset of degassing.

### A.3.2. Open-system degassing

Alternatively, open-system degassing occurs when the melt and fluid are separated the instant any exsolved fluid forms. At the instant the exsolved fluid forms mass balance is conserved, hence:

$$\delta_f dC = d(\delta_m C) \tag{A.17}$$

where $dC$ is the amount of fluid formed with isotope ratio $\delta_f$, which is taken from the melt which now has isotope ratio $\delta_m$. Using the chain rule gives:

$$\delta_f dC = \delta_m dC + C d\delta_m \tag{A.18}$$

$$C d\delta_m = dC(\delta_f - \delta_m) \tag{A.19}$$

where $\delta_f - \delta_m$ can be substituted for $\Delta_{f\text{–}m}$ using Equation A.9, therefore:

$$C d\delta_m = \Delta_{f\text{–}m} dC \tag{A.20}$$

$$\frac{d\delta_m}{\Delta_{f\text{–}m}} = \frac{dC}{C} \tag{A.21}$$

If $dC$ is small and $\Delta_{f\text{–}m}$ is constant, this can be integrated to any point along the degassing path (i.e., when the melt contains $C_m$ of the volatile), therefore:

$$\frac{1}{\Delta_{f-m}} = \int_{\delta_b}^{\delta_m} d\delta_m = \int_{C_b}^{C_m} \frac{dC}{C} \tag{A.22}$$

$$\frac{\delta_m - \delta_m}{\Delta_{f-m}} = \ln \frac{C_m}{C_b} \tag{A.23}$$

which rearranged for $\delta_m$ gives:

$$\delta_m = \delta_f + \Delta_{f-m} \cdot \ln \frac{C_m}{C_b} \tag{A.24}$$

where $\Delta_{f-m}$ can be either the equilibrium or kinetic fractionation factor, depending on whether the instantaneous fluid formed is in equilibrium with melt or not, but must be constant throughout degassing.

# Appendix B
## Silicate glass compositions

**Table B.1:** Composition of silicate glasses used in Chapters 2 and 3.

**Table B.2:** Abbreviated sample names in Table B.1.

**Table B.1:** Composition of silicate glasses used in Chapters 2 and 3.

| Sample | $SiO_2$ | $TiO_2$ | $Al_2O_3$ | $FeO_T$ | MnO | MgO | CaO | $Na_2O$ | $K_2O$ | $P_2O_5$ | [a] | [a] | $H_2O$ | $CO_2$[b] | [c] | VBD[d] | MV[e] | [f] |
|---|---|---|---|---|---|---|---|---|---|---|---|---|---|---|---|---|---|---|
| Blundy et al. (2010) | | | | | | | | | | | Cl | $S_T$ | | | | | | |
| [001][g] | 67.94 | 0.34 | 14.50 | 1.75 | 0.01 | 0.47 | 2.54 | 3.92 | 1.97 | 0.09 | 0.14 | 0.01 | 5.14 | 114 | | 6.13 | 5.15 | 1 |
| [002][g] | 65.80 | 0.33 | 13.47 | 1.95 | 0.07 | 0.52 | 1.95 | 6.18 | 1.85 | 0.03 | 0.13 | 0.02 | 5.39 | 40 | | 7.50 | 5.39 | 1 |
| [003][g] | 67.36 | 0.52 | 13.46 | 1.99 | 0.05 | 0.61 | 2.03 | 4.12 | 2.08 | 0.18 | 0.11 | 0.00 | 6.07 | 397 | | 7.27 | 6.11 | 1 |
| may25-2-4 | 75.58 | 0.47 | 11.56 | 1.88 | 0.06 | 0.29 | 0.72 | 4.12 | 2.84 | 0.18 | 0.13 | 0.00 | 2.23 | 1215 | | 1.96 | 2.35 | 1 |
| may25-3-3 | 73.25 | 0.40 | 12.08 | 1.66 | 0.03 | 0.18 | 0.85 | 4.62 | 2.58 | 0.05 | 0.14 | 0.00 | 2.54 | 673 | | 3.98 | 2.61 | 1 |
| May25-8-1 | 76.63 | 0.39 | 11.69 | 1.56 | 0.03 | 0.35 | 0.77 | 3.90 | 2.72 | 0.07 | 0.10 | 0.00 | 1.16 | | | 1.62 | 1.16 | 1 |
| May25-9-1 | 76.31 | 0.55 | 11.98 | 1.58 | 0.00 | 0.25 | 0.63 | 4.00 | 2.83 | 0.10 | 0.10 | 0.02 | 1.59 | 154 | | 1.49 | 1.61 | 1 |
| [004][g] | 72.07 | 0.37 | 13.30 | 1.84 | 0.10 | 0.49 | 1.58 | 5.10 | 2.17 | 0.01 | 0.10 | 0.01 | 3.39 | 336 | | 2.66 | 3.42 | 1 |
| [005][g] | 74.20 | 0.27 | 12.34 | 1.79 | 0.00 | 0.28 | 1.06 | 5.18 | 2.60 | 0.07 | 0.13 | 0.01 | 2.67 | 245 | | 1.88 | 2.69 | 1 |
| [006][g] | 72.77 | 0.36 | 12.86 | 1.73 | 0.01 | 0.36 | 1.71 | 4.83 | 2.44 | 0.01 | 0.13 | 0.00 | 1.61 | 53 | | 2.60 | 1.62 | 1 |
| [007][g] | 69.05 | 0.35 | 14.62 | 1.98 | 0.08 | 0.44 | 2.46 | 4.70 | 2.01 | 0.17 | 0.13 | 0.05 | 4.01 | 160 | | 3.77 | 4.03 | 1 |
| [008][g] | 73.00 | 0.48 | 12.57 | 1.96 | 0.09 | 0.39 | 1.10 | 4.84 | 2.85 | 0.10 | 0.17 | 0.00 | 1.82 | 44 | | 2.23 | 1.82 | 1 |
| [009][g] | 73.42 | 0.41 | 11.74 | 1.94 | 0.08 | 0.36 | 1.06 | 5.39 | 2.54 | 0.09 | 0.12 | 0.01 | 1.92 | 89 | | 2.63 | 1.93 | 1 |
| [010][g] | 74.07 | 0.34 | 11.97 | 1.96 | 0.03 | 0.33 | 1.15 | 4.99 | 2.53 | 0.05 | 0.13 | 0.06 | 1.64 | 127 | | 2.21 | 1.65 | 1 |
| [011][g] | 70.92 | 0.30 | 11.84 | 1.82 | 0.05 | 0.26 | 1.15 | 5.08 | 2.49 | 0.05 | 0.13 | 0.01 | 2.75 | 173 | | 5.70 | 2.77 | 1 |
| [012][g] | 74.78 | 0.43 | 11.67 | 1.83 | 0.04 | 0.30 | 1.09 | 6.09 | 2.84 | 0.00 | 0.11 | 0.00 | 0.62 | | | 0.62 | 0.62 | 1 |
| [013][g] | 76.08 | 0.43 | 11.12 | 1.74 | 0.00 | 0.21 | 0.64 | 4.22 | 2.99 | 0.08 | 0.22 | 0.02 | 1.55 | 4154 | | 2.07 | 1.97 | 1 |
| [014][g] | 75.33 | 0.43 | 11.36 | 1.99 | 0.06 | 0.37 | 0.64 | 4.33 | 2.91 | 0.02 | 0.17 | 0.03 | 1.44 | | | 2.16 | 1.44 | 1 |
| [015][g] | 73.84 | 0.26 | 12.42 | 1.77 | 0.03 | 0.29 | 0.83 | 4.70 | 2.94 | 0.05 | 0.13 | 0.04 | 2.33 | 330 | | 2.53 | 2.36 | 1 |
| [016][g] | 77.39 | 0.36 | 11.47 | 1.64 | 0.00 | 0.21 | 0.63 | 4.45 | 3.00 | 0.08 | 0.17 | 0.00 | 0.27 | | | 0.42 | 0.27 | 1 |
| [017][g] | 76.41 | 0.48 | 11.49 | 1.60 | 0.06 | 0.15 | 0.51 | 4.83 | 2.87 | 0.07 | 0.15 | 0.03 | 0.80 | 57 | | 1.19 | 0.81 | 1 |
| [018][g] | 74.38 | 0.39 | 11.62 | 1.93 | 0.10 | 0.61 | 0.83 | 4.19 | 2.92 | 0.11 | 0.15 | 0.01 | 2.19 | 75 | | 2.55 | 2.20 | 1 |
| [019][g] | 77.62 | 0.43 | 11.19 | 1.49 | 0.02 | 0.21 | 0.55 | 4.30 | 3.01 | 0.02 | 0.16 | 0.00 | 0.22 | | | 0.83 | 0.22 | 1 |
| [020][g] | 77.62 | 0.43 | 11.19 | 1.49 | 0.02 | 0.21 | 0.55 | 4.30 | 3.01 | 0.02 | 0.16 | 0.00 | 0.34 | 71 | | 0.83 | 0.35 | 1 |
| [021][g] | 78.73 | 0.29 | 11.12 | 1.45 | 0.08 | 0.20 | 0.50 | 4.04 | 2.77 | 0.05 | 0.09 | 0.00 | 0.09 | | | 0.52 | 0.09 | 1 |
| [022][g] | 77.44 | 0.30 | 11.75 | 1.44 | 0.02 | 0.17 | 1.03 | 4.13 | 2.89 | 0.08 | 0.10 | 0.00 | 0.16 | | | 0.49 | 0.16 | 1 |
| [023][g] | 77.23 | 0.30 | 11.03 | 1.65 | 0.09 | 0.21 | 0.52 | 4.30 | 3.05 | 0.01 | 0.12 | 0.00 | 0.94 | | | 1.31 | 0.94 | 1 |
| [024][g] | 75.63 | 0.19 | 12.69 | 1.59 | 0.00 | 0.15 | 1.12 | 4.17 | 2.76 | 0.01 | 0.13 | 0.00 | 1.29 | | | 1.38 | 1.29 | 1 |

**Table B.1:** Composition of silicate glasses used in Chapters 2 and 3 *cont.*

| Sample | $SiO_2$ | $TiO_2$ | $Al_2O_3$ | $FeO_T$ | MnO | MgO | CaO | $Na_2O$ | $K_2O$ | $P_2O_5$ | [a] | [a] | $H_2O$ | $CO_2$[b] | [c] | VBD[d] | MV[e] | [f] |
|---|---|---|---|---|---|---|---|---|---|---|---|---|---|---|---|---|---|---|
| [025][g] | 76.42 | 0.47 | 11.04 | 1.66 | 0.05 | 0.23 | 0.69 | 4.44 | 3.22 | 0.03 | 0.13 | 0.05 | 1.46 | | | 1.42 | 1.46 | 1 |
| [026][g] | 70.30 | 0.55 | 14.72 | 1.76 | 0.06 | 0.40 | 1.85 | 5.12 | 2.30 | 0.13 | 0.13 | 0.00 | 2.70 | 112 | | 2.48 | 2.71 | 1 |
| [027][g] | 76.11 | 0.39 | 12.21 | 1.63 | 0.02 | 0.18 | 0.77 | 4.79 | 2.94 | 0.06 | 0.16 | 0.01 | 0.27 | 763 | | 0.56 | 0.35 | 1 |
| [028][g] | 78.00 | 0.38 | 10.72 | 1.71 | 0.06 | 0.09 | 0.40 | 4.04 | 4.25 | 0.05 | 0.15 | 0.00 | 0.16 | | | -0.04 | 0.16 | 1 |
| [029][g] | 78.27 | 0.27 | 10.68 | 1.69 | 0.05 | 0.13 | 0.28 | 4.05 | 3.94 | 0.14 | 0.15 | 0.00 | 0.31 | 395 | | 0.16 | 0.35 | 1 |
| [030][g] | 77.78 | 0.33 | 11.32 | 1.52 | 0.08 | 0.20 | 0.40 | 4.29 | 4.24 | 0.10 | 0.12 | 0.01 | 0.17 | 181 | | -0.55 | 0.19 | 1 |
| [031][g] | 69.84 | 0.43 | 16.53 | 1.57 | 0.05 | 0.21 | 1.55 | 6.28 | 2.32 | 0.27 | 0.10 | 0.03 | 0.15 | 208 | | 0.67 | 0.17 | 1 |
| [032][g] | 73.16 | 0.24 | 14.46 | 1.08 | 0.03 | 0.26 | 1.72 | 5.56 | 1.40 | 0.05 | 0.04 | 0.00 | 1.11 | 278 | | 1.88 | 1.14 | 1 |
| [033][g] | 73.16 | 0.42 | 13.45 | 1.33 | 0.01 | 0.07 | 0.30 | 3.91 | 6.31 | 0.06 | 0.07 | 0.00 | 0.21 | 101 | | 0.76 | 0.22 | 1 |
| [034][g] | 73.47 | 0.37 | 13.64 | 0.97 | 0.03 | 0.12 | 0.93 | 5.07 | 3.03 | 0.00 | 0.12 | 0.03 | 0.07 | 226 | | 2.13 | 0.09 | 1 |
| Blundy et al. (2018) | | | | | | | | | | | | | | | | | | |
| PU32 | 46.93 | 0.75 | 12.58 | 9.72 | 0.18 | 16.63 | 10.33 | 1.13 | 0.41 | 0.11 | | | 0.00 | | 0.83 | | | 2 |
| PU58 | 46.66 | 0.78 | 13.04 | 10.26 | 0.18 | 14.74 | 10.77 | 1.25 | 0.42 | 0.07 | | | 0.00 | | 0.21 | | | 2 |
| PU359 | 47.01 | 0.81 | 13.80 | 9.91 | 0.19 | 13.73 | 11.18 | 1.35 | 0.45 | 0.08 | | | 0.00 | | 0.75 | | | 2 |
| PU361 | 46.72 | 0.75 | 12.48 | 10.01 | 0.18 | 16.21 | 10.31 | 1.19 | 0.38 | 0.12 | | | 0.00 | | 0.23 | | | 2 |
| Botcharnikov et al. (2005) | | | | | | | | | | | | | | | | | | |
| B5 | 46.60 | 2.91 | 13.60 | 12.36 | | 6.05 | 10.24 | 2.51 | 0.27 | | | | 4.67 | | 0.46 | 4.72 | 4.67 | 1 |
| B6 | 48.17 | 2.98 | 14.08 | 12.94 | | 6.26 | 10.50 | 2.61 | 0.29 | | | | 2.00 | | 0.61 | 1.61 | 2.00 | 1 |
| B7 | 48.54 | 3.04 | 14.26 | 12.91 | | 6.28 | 10.67 | 2.67 | 0.28 | | | | 0.97 | | 0.77 | 1.02 | 0.97 | 1 |
| B8 | 48.68 | 3.08 | 14.45 | 12.67 | | 6.31 | 10.76 | 2.65 | 0.30 | | | | 0.82 | | 0.84 | 0.87 | 0.82 | 1 |
| B9 | 48.23 | 3.03 | 14.13 | 12.62 | | 6.20 | 10.54 | 2.59 | 0.32 | | | | 1.14 | | 0.71 | 1.93 | 1.14 | 1 |
| B10 | 47.80 | 2.96 | 14.00 | 12.61 | | 6.17 | 10.41 | 2.62 | 0.30 | | | | 2.43 | | 0.6 | 2.57 | 2.43 | 1 |
| B11 | 47.09 | 2.92 | 13.73 | 12.49 | | 6.00 | 10.13 | 2.55 | 0.30 | | | | 4.82 | | 0.81 | 4.53 | 4.82 | 1 |
| B12 | 48.85 | 3.08 | 14.35 | 12.02 | | 6.30 | 10.63 | 2.70 | 0.29 | | | | 1.90 | | 0.89 | 1.63 | 1.90 | 1 |
| B13 | 49.10 | 3.01 | 14.39 | 11.39 | | 6.25 | 10.74 | 2.71 | 0.30 | | | | 1.71 | | 0.9 | 1.98 | 1.71 | 1 |
| B14 | 49.72 | 3.11 | 14.48 | 11.33 | | 6.34 | 10.80 | 2.72 | 0.31 | | | | 1.06 | | 0.92 | 1.09 | 1.06 | 1 |
| B16 | 47.60 | 2.97 | 13.96 | 12.93 | | 6.17 | 10.27 | 2.50 | 0.30 | | | | 3.02 | | 0.82 | 3.04 | 3.02 | 1 |
| B17 | 47.06 | 2.89 | 13.80 | 12.65 | | 6.05 | 10.23 | 2.57 | 0.26 | | | | 4.67 | | 0.4 | 3.64 | 4.67 | 1 |
| B19 | 47.95 | 2.98 | 14.07 | 12.91 | | 6.21 | 10.39 | 2.62 | 0.29 | | | | 1.85 | | 0.48 | 1.83 | 1.85 | 1 |

**Table B.1:** Composition of silicate glasses used in Chapters 2 and 3 *cont.*

| Sample | $SiO_2$ | $TiO_2$ | $Al_2O_3$ | $FeO_T$ | MnO | MgO | CaO | $Na_2O$ | $K_2O$ | $P_2O_5$ | [a] | [a] | $H_2O$ | $CO_2$[b] | [c] | VBD[d] | MV[e] | [f] |
|---|---|---|---|---|---|---|---|---|---|---|---|---|---|---|---|---|---|---|
| B20 | 48.99 | 3.07 | 14.36 | 12.80 | | 6.33 | 10.69 | 2.78 | 0.29 | | | | 0.72 | | 0.75 | 0.33 | 0.72 | 1 |
| B21 | 47.50 | 2.93 | 13.79 | 12.34 | | 6.11 | 10.33 | 2.59 | 0.30 | | | | 2.90 | | 0.51 | 3.44 | 2.90 | 1 |
| B22 | 48.76 | 3.04 | 14.29 | 12.77 | | 6.26 | 10.60 | 2.71 | 0.30 | | | | 0.94 | | 0.72 | 0.87 | 0.94 | 1 |
| Chabiron et al. (2001) | | | | | | | | | | | Cl | F | | | | | | |
| F1 9 | 69.60 | 0.12 | 14.62 | 1.19 | 0.15 | | | 5.01 | 5.81 | | | 2.08 | 1.31 | | | 1.29 | 1.31 | 1 |
| F2 1 | 70.19 | 0.07 | 13.63 | 1.46 | 0.17 | 0.05 | | 5.05 | 5.62 | | | 2.16 | 1.07 | | | 1.44 | 1.07 | 1 |
| F2 2 | 72.59 | 0.03 | 11.93 | 1.18 | 0.15 | 0.05 | 0.05 | 4.92 | 4.88 | | 0.15 | 1.83 | 1.98 | | | 2.11 | 1.98 | 1 |
| F3 5 | 75.07 | 0.13 | 11.22 | 0.82 | 0.08 | | 0.03 | 4.36 | 4.52 | | 0.20 | 1.87 | 2.05 | | | 1.61 | 2.05 | 1 |
| F3 6 | 71.50 | 0.05 | 12.41 | 1.01 | 0.07 | 0.06 | 0.18 | 4.59 | 4.95 | | 0.20 | 2.68 | 2.17 | | | 2.19 | 2.17 | 1 |
| F4 4 | 73.03 | 0.07 | 11.75 | 1.14 | 0.13 | 0.03 | 0.11 | 4.74 | 4.53 | | 0.17 | 2.17 | 2.40 | | | 2.00 | 2.40 | 1 |
| F6 1 | 71.98 | 0.15 | 12.67 | 1.32 | 0.23 | | | 5.62 | 3.60 | | | 0.51 | 3.73 | | | 3.77 | 3.73 | 1 |
| F6 7 | 73.99 | 0.14 | 11.78 | 0.85 | 0.04 | 0.07 | 0.37 | 4.75 | 4.62 | | 0.18 | 0.93 | 2.03 | | | 2.19 | 2.03 | 1 |
| F6 10 | 75.71 | 0.11 | 11.51 | 0.64 | 0.14 | 0.04 | 0.24 | 4.83 | 4.47 | | 0.15 | 0.95 | 0.57 | | | 1.14 | 0.57 | 1 |
| Cottrell et al. (2009) | | | | | | | | | | | | | | | | | | |
| AII_-35 | 50.81 | 1.73 | 16.14 | 9.53 | | 7.40 | 11.20 | 2.75 | 0.15 | 0.14 | | | 0.00 | | | | | 2 |
| LW_0 | 49.42 | 1.94 | 17.21 | 10.17 | | 6.13 | 8.78 | 3.17 | 1.50 | 1.12 | | | 0.00 | | 0.84 | | | 2 |
| LW_10 | 49.42 | 1.94 | 17.21 | 10.17 | | 6.13 | 8.78 | 3.17 | 1.50 | 1.12 | | | 0.00 | | 0.77 | | | 2 |
| LW_-20 | 49.42 | 1.94 | 17.21 | 10.17 | | 6.13 | 8.78 | 3.17 | 1.50 | 1.12 | | | 0.00 | | 0.91 | | | 2 |
| Cottrell and Kelley (2011) | | | | | | | | | | | | | | | | | | |
| T558-R1 | 50.29 | 1.68 | 14.68 | 10.73 | 0.20 | 7.37 | 11.78 | 2.41 | 0.06 | 0.15 | | | 0.14 | | 0.84 | 0.47 | 0.14 | 1 |
| D12-5 | 49.70 | 1.28 | 15.50 | 9.40 | 0.15 | 8.53 | 12.30 | 2.42 | 0.03 | | | | 0.12 | | 0.837 | 0.52 | 0.12 | 1 |
| CH 17-4 | 50.20 | 1.32 | 16.32 | 8.76 | | 8.07 | 12.12 | 2.60 | 0.08 | 0.16 | | | 0.17 | | 0.85 | 0.22 | 0.17 | 1 |
| CH 19-3 | 50.28 | 1.29 | 15.88 | 9.14 | 0.13 | 8.93 | 12.25 | 2.58 | 0.10 | 0.12 | | | 0.15 | | 0.842 | -0.86 | 0.15 | 1 |
| CH 21-1 | 49.88 | 1.36 | 16.26 | 8.93 | 0.17 | 8.82 | 12.20 | 2.38 | 0.14 | 0.11 | | | 0.26 | | 0.85 | -0.40 | 0.26 | 1 |
| CH 30-1 | 50.42 | 1.88 | 13.87 | 11.51 | 0.24 | 7.24 | 11.37 | 2.67 | 0.10 | 0.17 | | | 0.24 | | 0.833 | 0.32 | 0.24 | 1 |
| CH 5-1 | 50.40 | 2.06 | 14.37 | 11.16 | 0.22 | 6.32 | 10.84 | 3.39 | 0.26 | 0.20 | | | 0.44 | | 0.834 | 0.57 | 0.44 | 1 |
| CH 6-1 | 50.48 | 1.95 | 14.74 | 10.42 | 0.22 | 6.99 | 11.04 | 3.02 | 0.32 | 0.21 | | | 0.34 | | 0.838 | 0.42 | 0.34 | 1 |
| CH 61-1 | 50.93 | 1.59 | 14.60 | 10.05 | 0.18 | 8.13 | 12.22 | 2.73 | 0.08 | 0.13 | | | 0.17 | | 0.837 | -0.82 | 0.17 | 1 |
| CH 84-2 | 51.17 | 1.72 | 14.51 | 10.72 | 0.21 | 7.64 | 12.05 | 2.76 | 0.15 | 0.10 | | | 0.20 | | 0.84 | -1.22 | 0.2 | 1 |

**Table B.1:** Composition of silicate glasses used in Chapters 2 and 3 *cont.*

| Sample | $SiO_2$ | $TiO_2$ | $Al_2O_3$ | $FeO_T$ | MnO | MgO | CaO | $Na_2O$ | $K_2O$ | $P_2O_5$ | [a] | [a] | $H_2O$ | $CO_2$[b] | [c] | VBD[d] | MV[e] | [f] |
|---|---|---|---|---|---|---|---|---|---|---|---|---|---|---|---|---|---|---|
| CH 15-2 | 50.42 | 1.46 | 15.08 | 9.51 | 0.13 | 8.06 | 12.12 | 2.56 | 0.11 | 0.18 | | | 0.19 | | 0.828 | 0.19 | 0.19 | 1 |
| CH 33-1 | 50.02 | 1.68 | 14.97 | 9.88 | 0.18 | 7.66 | 11.94 | 2.38 | 0.13 | 0.17 | | | 0.22 | | 0.847 | 0.82 | 0.22 | 1 |
| EN113 13D-1 | 48.91 | 1.50 | 17.11 | 8.70 | 0.04 | 8.15 | 11.75 | 3.54 | | 0.17 | | | 0.14 | | 0.845 | -0.02 | 0.14 | 1 |
| RAIT 02-D120 | 50.65 | 2.14 | 13.75 | 12.97 | | 6.18 | 10.45 | 2.75 | 0.15 | 0.21 | | | 0.32 | | 0.822 | 0.49 | 0.32 | 1 |
| RISE 3-D30 | 51.83 | 2.12 | 13.91 | 11.96 | | 6.28 | 10.86 | 2.85 | 0.22 | 0.17 | | | 0.33 | | 0.828 | -0.43 | 0.33 | 1 |
| RAIT 02 D 12-1 | 49.03 | 1.32 | 17.35 | 8.90 | | 8.70 | 11.40 | 2.78 | 0.14 | 0.17 | | | 0.20 | | 0.841 | 0.05 | 0.2 | 1 |
| SIQ D3-1 | 50.19 | 0.98 | 15.78 | 9.10 | | 8.78 | 12.84 | 1.97 | 0.05 | 0.14 | | | 0.06 | | 0.843 | 0.01 | 0.06 | 1 |
| TW74-D7-1 | 48.59 | 0.98 | 17.55 | 7.98 | | 9.51 | 12.22 | 2.30 | 0.04 | 0.06 | | | 0.08 | | 0.841 | 0.63 | 0.08 | 1 |
| SIQ D3-3 | 49.96 | 1.00 | 15.63 | 9.06 | | 8.75 | 12.87 | 1.96 | 0.05 | 0.13 | | | 0.06 | | 0.838 | 0.43 | 0.06 | 1 |
| K 10-34 | 48.06 | 0.99 | 17.33 | 8.54 | | 8.99 | 12.02 | 2.35 | 0.05 | 0.07 | | | 0.22 | | 0.851 | 1.46 | 0.22 | 1 |
| K 14-3 | 51.21 | 1.76 | 13.48 | 11.59 | | 6.19 | 10.86 | 2.50 | 0.17 | 0.17 | | | 0.48 | | 0.833 | 1.85 | 0.48 | 1 |
| K 18-21 | 50.72 | 1.76 | 13.93 | 11.18 | | 7.08 | 10.75 | 2.33 | 0.17 | 0.17 | | | 0.49 | | 0.832 | 1.70 | 0.49 | 1 |
| KK78-D17-14 | 49.59 | 0.86 | 16.12 | 9.19 | | 9.72 | 11.96 | 2.18 | 0.04 | 0.07 | | | 0.12 | | 0.849 | 0.12 | 0.12 | 1 |
| KK78-D17-4 | 49.46 | 0.84 | 16.06 | 9.19 | | 9.90 | 11.99 | 2.12 | 0.04 | 0.07 | | | 0.14 | | 0.854 | 0.18 | 0.14 | 1 |
| KK78-D17-32 | 49.63 | 0.85 | 16.19 | 9.24 | | 9.76 | 11.76 | 2.15 | 0.05 | 0.09 | | | 0.13 | | 0.856 | 0.13 | 0.13 | 1 |
| KK78-D17-3 | 49.77 | 0.85 | 15.86 | 9.28 | | 9.92 | 12.07 | 2.16 | 0.05 | 0.09 | | | 0.12 | | 0.859 | -0.20 | 0.12 | 1 |
| KK78-D21-2 | 48.41 | 0.93 | 16.98 | 9.58 | | 9.04 | 12.03 | 2.27 | 0.05 | 0.10 | | | 0.15 | | 0.846 | 0.45 | 0.15 | 1 |
| V33-7-3 | 51.70 | 1.71 | 15.95 | 8.70 | | 6.56 | 10.24 | 3.84 | 0.31 | 0.19 | | | 0.45 | | 0.845 | 0.65 | 0.45 | 1 |
| V33-8-8,7 | 52.23 | 1.28 | 16.63 | 7.72 | | 7.39 | 11.01 | 3.21 | 0.34 | 0.16 | | | 0.33 | | 0.853 | -0.10 | 0.33 | 1 |
| RSR1979-011-005 | 51.27 | 1.77 | 14.98 | 10.58 | | 6.83 | 10.61 | 3.10 | 0.10 | 0.17 | | | 0.33 | | 0.856 | 0.42 | 0.33 | 1 |
| SIIndianOcean | 52.91 | 1.27 | 15.45 | 9.13 | | 7.74 | 11.18 | 2.51 | 0.07 | 0.10 | | | 0.13 | | 0.842 | -0.52 | 0.13 | 1 |
| VG-2 | 50.82 | 1.85 | 14.06 | 11.84 | 0.22 | 6.71 | 11.12 | 2.62 | 0.19 | 0.20 | | | 0.02 | | 0.836 | 0.15 | 0.02 | 1 |
| T469-24 | 50.18 | 2.21 | 14.47 | 11.08 | 0.22 | 6.27 | 10.81 | 3.00 | 0.52 | 0.32 | | | 0.52 | | 0.834 | 0.72 | 0.52 | 1 |
| T464-03 | 51.14 | 1.66 | 15.31 | 9.92 | 0.19 | 7.05 | 11.27 | 2.69 | 0.50 | 0.27 | | | 0.44 | | 0.829 | -0.19 | 0.44 | 1 |
| T471-08 | 50.76 | 1.71 | 15.06 | 10.00 | 0.19 | 6.99 | 11.67 | 2.73 | 0.52 | 0.27 | | | 0.44 | | 0.829 | -0.09 | 0.44 | 1 |
| T469-22 | 50.85 | 1.68 | 14.99 | 9.90 | 0.22 | 7.13 | 11.77 | 2.71 | 0.48 | 0.26 | | | 0.43 | | 0.833 | -0.17 | 0.43 | 1 |
| T465-01 | 51.40 | 1.73 | 15.00 | 10.45 | 0.21 | 6.68 | 10.58 | 2.76 | 0.48 | 0.25 | | | 0.40 | | 0.838 | 0.27 | 0.4 | 1 |
| T471-14 | 50.68 | 1.76 | 14.81 | 10.07 | 0.22 | 7.12 | 11.52 | 2.76 | 0.43 | 0.24 | | | 0.40 | | 0.835 | 0.20 | 0.4 | 1 |
| T469-10 | 50.32 | 1.84 | 14.86 | 10.53 | 0.21 | 6.90 | 11.35 | 2.82 | 0.36 | 0.25 | | | 0.39 | | 0.833 | 0.36 | 0.39 | 1 |

**Table B.1:** Composition of silicate glasses used in Chapters 2 and 3 *cont.*

| Sample | $SiO_2$ | $TiO_2$ | $Al_2O_3$ | $FeO_T$ | MnO | MgO | CaO | $Na_2O$ | $K_2O$ | $P_2O_5$ | [a] | [a] | $H_2O$ | $CO_2$[b] | [c] | VBD[d] | MV[e] | [f] |
|---|---|---|---|---|---|---|---|---|---|---|---|---|---|---|---|---|---|---|
| T471-23 | 50.96 | 1.65 | 14.86 | 9.63 | 0.20 | 7.15 | 11.63 | 2.97 | 0.37 | 0.26 | | | 0.37 | | 0.827 | 0.13 | 0.37 | 1 |
| T463-04 | 51.04 | 1.46 | 15.77 | 9.09 | 0.19 | 7.58 | 12.08 | 2.46 | 0.42 | 0.22 | | | 0.37 | | 0.833 | -0.48 | 0.37 | 1 |
| JDF C2-1 | 52.00 | 2.56 | 13.20 | 14.31 | | 4.76 | 9.53 | 3.15 | 0.37 | 0.38 | | | 0.16 | | 0.87 | -0.47 | 0.16 | 1 |
| JDF C6-1 | 50.16 | 1.75 | 14.26 | 11.57 | | 7.22 | 11.46 | 2.33 | 0.16 | 0.18 | | | 0.22 | | 0.837 | 0.70 | 0.22 | 1 |
| JDF D11-2 | 48.65 | 1.44 | 15.37 | 10.26 | | 7.60 | 12.27 | 2.80 | 0.20 | 0.17 | | | 0.22 | | 0.833 | 1.05 | 0.22 | 1 |
| JDF D5-2 | 50.41 | 1.56 | 14.54 | 10.79 | | 7.34 | 11.95 | 2.23 | 0.22 | 0.20 | | | 0.20 | | 0.841 | 0.57 | 0.2 | 1 |
| JDFD2 | 50.95 | 1.88 | 13.99 | 12.22 | 0.22 | 6.50 | 10.96 | 2.62 | 0.20 | 0.22 | | | 0.45 | | 0.833 | 0.01 | 0.45 | 1 |
| 2D47-1 | 51.09 | 1.57 | 15.20 | 9.48 | 0.17 | 7.87 | 10.68 | 3.07 | 0.29 | 0.21 | | | 0.33 | | 0.841 | 0.20 | 0.33 | 1 |
| 523-2-1 | 50.33 | 1.44 | 14.86 | 9.84 | 0.16 | 8.50 | 10.95 | 2.64 | 0.34 | | | | 0.50 | | 0.857 | 0.78 | 0.5 | 1 |
| ALV 527 1-1 | 48.41 | 0.69 | 16.93 | 9.01 | | 9.48 | 12.56 | 2.00 | 0.07 | 0.06 | | | 0.14 | | 0.872 | 0.66 | 0.14 | 1 |
| TR138 11D-1 | 51.42 | 1.50 | 15.39 | 9.93 | | 7.37 | 11.39 | 2.82 | 0.09 | 0.14 | | | 0.23 | | 0.845 | -0.22 | 0.23 | 1 |
| TR138 2D-2 | 50.37 | 0.95 | 16.51 | 8.21 | 0.16 | 9.15 | 11.74 | 2.37 | 0.07 | 0.08 | | | 0.25 | | 0.857 | 0.26 | 0.25 | 1 |
| TR138 9D-4 | 51.55 | 1.58 | 14.99 | 10.06 | | 7.01 | 11.52 | 2.88 | 0.07 | 0.15 | | | 0.25 | | 0.855 | 0.03 | 0.25 | 1 |
| EN026 10D-3g | 51.37 | 1.41 | 15.43 | 9.68 | 0.18 | 7.59 | 11.46 | 2.44 | 0.30 | | | | 0.76 | | 0.844 | -0.03 | 0.76 | 1 |
| TR119 6D-1 | 51.20 | 1.09 | 14.80 | 9.76 | | 7.58 | 12.51 | 2.19 | 0.12 | 0.15 | | | 0.29 | | 0.85 | 0.44 | 0.29 | 1 |
| TR119 6D-4 | 51.38 | 1.25 | 14.54 | 10.48 | | 7.05 | 11.84 | 2.24 | 0.14 | 0.15 | | | 0.34 | | 0.841 | 0.74 | 0.34 | 1 |
| EN25 2D-4 | 50.84 | 1.30 | 14.71 | 11.25 | | 7.48 | 12.05 | 2.10 | 0.04 | 0.15 | | | 0.14 | | 0.835 | -0.13 | 0.14 | 1 |
| EN25 6D-3 | 51.50 | 1.29 | 14.16 | 12.20 | | 6.91 | 11.46 | 2.07 | 0.10 | 0.12 | | | 0.30 | | 0.845 | -0.02 | 0.3 | 1 |
| 2D43 | 50.33 | 1.84 | 14.82 | 9.96 | 0.19 | 7.71 | 10.80 | 2.89 | 0.73 | 0.31 | | | 0.54 | | 0.854 | 0.26 | 0.54 | 1 |
| CH98 DR11 | 50.14 | 1.46 | 14.81 | 10.30 | 0.19 | 8.67 | 11.23 | 2.53 | 0.07 | 0.15 | | | 0.23 | | 0.846 | 0.27 | 0.23 | 1 |
| Delaney and Karsten (1981) | | | | | | | | | | | | | | | | | | |
| DC-2 | 77.10 | 0.10 | 12.30 | 0.99 | | | 0.30 | 4.20 | 4.70 | | | | 0.20 | | | 0.20 | 0.20 | 1 |
| D119_edge | 74.40 | 0.10 | 11.80 | 0.90 | | | 0.20 | 4.20 | 4.30 | | | | 3.70 | | | 4.00 | 3.70 | 1 |
| D119_cenre | 76.10 | 0.10 | 12.00 | 0.99 | | | 0.30 | 4.20 | 4.90 | | | | 0.20 | | | 1.30 | 0.20 | 1 |
| C120_edge | 75.50 | 0.10 | 12.10 | 0.99 | | | 0.30 | 4.10 | 4.40 | | | | 3.70 | | | 2.40 | 3.70 | 1 |
| D120_centre | 76.60 | 0.10 | 12.20 | 1.08 | | | 0.30 | 4.20 | 4.80 | | | | 0.20 | | | 0.60 | 0.20 | 1 |
| D121_edge | 74.50 | 0.10 | 12.10 | 0.99 | | | 0.30 | 4.20 | 4.40 | | | | 3.70 | | | 3.30 | 3.70 | 1 |
| D121_centre | 77.30 | 0.10 | 12.60 | 0.99 | | | 0.30 | 4.20 | 4.80 | | | | 0.20 | | | -0.40 | 0.20 | 1 |
| D122_egde | 74.50 | 0.10 | 11.80 | 0.90 | | | 0.30 | 4.10 | 4.50 | | | | 1.60 | | | 3.70 | 1.60 | 1 |

**Table B.1:** Composition of silicate glasses used in Chapters 2 and 3 *cont.*

| Sample | $SiO_2$ | $TiO_2$ | $Al_2O_3$ | $FeO_T$ | MnO | MgO | CaO | $Na_2O$ | $K_2O$ | $P_2O_5$ | [a] | [a] | $H_2O$ | $CO_2$[b] | [c] | VBD[d] | MV[e] | [f] |
|---|---|---|---|---|---|---|---|---|---|---|---|---|---|---|---|---|---|---|
| D122_centre | 77.00 | 0.10 | 12.20 | 0.99 | | | 0.30 | 4.00 | 5.00 | | | | 0.20 | | | 0.30 | 0.20 | 1 |
| D123_edge | 73.90 | 0.10 | 11.80 | 0.90 | | | 0.30 | 4.00 | 4.60 | | | | 3.70 | | | 4.30 | 3.70 | 1 |
| D123_centre | 74.70 | 0.10 | 12.10 | 0.99 | | | 0.20 | 4.00 | 4.50 | | | | 3.70 | | | 3.30 | 3.70 | 1 |
| Devine et al. (1995) | | | | | | | | | | | Cl | F | | | | | | |
| VNM50-15 | 76.60 | 0.08 | 12.32 | 1.05 | 0.05 | 0.04 | 0.37 | 4.41 | 4.64 | | 0.1209 | 0.0859 | 0.16 | | | 0.12 | 0.16 | 1 |
| PCD | 76.40 | 0.07 | 12.44 | 1.02 | 0.03 | 0.02 | 0.53 | 4.21 | 4.68 | | 0.0671 | 0.0587 | 0.17 | | | 0.36 | 0.17 | 1 |
| IF35-1 | 74.39 | 0.03 | 13.65 | 0.56 | 0.13 | 0.04 | 0.47 | 4.25 | 4.21 | | 0.0117 | 0.0822 | 1.36 | | | 2.11 | 1.36 | 1 |
| M3N | 71.38 | 0.26 | 13.05 | 1.56 | 0.02 | 0.29 | 1.19 | 4.06 | 4.11 | | 0.0804 | 0.0561 | 3.95 | | | 3.77 | 3.95 | 1 |
| M6N | 69.47 | 0.30 | 12.84 | 1.48 | 0.05 | 0.25 | 1.19 | 4.05 | 4.02 | | 0.0946 | 0.0616 | 6.38 | | | 6.03 | 6.38 | 1 |
| 495 | 75.62 | 0.10 | 12.22 | 0.95 | 0.06 | 0.04 | 0.35 | 4.32 | 4.51 | | | | 1.42 | | | 1.72 | 1.42 | 1 |
| 508 | 75.01 | 0.09 | 11.96 | 0.93 | 0.06 | 0.04 | 0.34 | 4.19 | 4.41 | | | | 2.58 | | | 2.87 | 2.58 | 1 |
| 494 | 73.72 | 0.11 | 11.79 | 1.00 | 0.06 | 0.04 | 0.39 | 4.21 | 4.38 | | | | 4.09 | | | 4.19 | 4.09 | 1 |
| 498 | 73.75 | 0.09 | 11.78 | 0.65 | 0.03 | 0.04 | 0.33 | 4.31 | 4.46 | | | | 4.72 | | | 4.49 | 4.72 | 1 |
| 510 | 71.82 | 0.10 | 11.62 | 0.78 | 0.06 | 0.04 | 0.32 | 4.18 | 4.17 | | | | 6.23 | | | 6.82 | 6.23 | 1 |
| Di Genova et al. (2013, 2014, 2016) | | | | | | | | | | | $Cr_2O_3$ | | | | | | | |
| PS0.5 or PSG1 | 70.02 | 0.49 | 9.18 | 8.30 | 0.39 | 0.08 | 0.59 | 5.94 | 3.96 | 0.04 | 0.01 | | 0.72 | | 0.64 | 0.67 | 0.72 | 3 |
| PS2.2 or PSG2 | 69.97 | 0.48 | 9.01 | 8.34 | 0.36 | 0.06 | 0.59 | 5.80 | 3.99 | 0.04 | 0.00 | | 2.11 | | 0.52 | 0.91 | 2.11 | 3 |
| PS3.5 or PSG3 | 68.48 | 0.48 | 8.90 | 8.14 | 0.38 | 0.07 | 0.56 | 5.14 | 4.00 | 0.03 | 0.01 | | 3.57 | | 0.44 | 3.30 | 3.57 | 3 |
| PS1.1 or PSG6 | 69.78 | 0.49 | 9.09 | 8.44 | 0.37 | 0.08 | 0.58 | 5.74 | 3.99 | 0.02 | 0.01 | | 1.16 | | 0.54 | 0.98 | 1.16 | 3 |
| PSG dry | 70.05 | 0.49 | 9.15 | 8.58 | 0.38 | 0.08 | 0.57 | 5.82 | 4.08 | 0.03 | 0.01 | | 0.02 | | 0.30 | 0.09 | 0.02 | 1 |
| ETN dry | 48.95 | 1.67 | 17.00 | 10.08 | 0.24 | 5.54 | 10.18 | 3.72 | 1.85 | 0.01 | 0.47 | | 0.02 | | 0.24 | -0.56 | 0.02 | 1 |
| ETN 1.4 | 47.96 | 1.65 | 16.68 | 10.17 | 0.22 | 5.39 | 10.09 | 3.66 | 1.83 | 0.02 | 0.53 | | 1.48 | | 0.68 | 1.44 | 1.48 | 1 |
| ETN 2.9 | 47.90 | 1.61 | 16.62 | 10.15 | 0.20 | 5.29 | 9.92 | 3.59 | 1.78 | 0.01 | 0.47 | | 2.40 | | 0.68 | 2.10 | 2.40 | 1 |
| FR DRY | 56.55 | 0.81 | 17.92 | 6.59 | 0.17 | 2.36 | 5.52 | 4.55 | 4.53 | 0.01 | 0.45 | | 0.02 | | 0.21 | -0.04 | 0.02 | 1 |
| FR 1.6 | 56.30 | 0.80 | 17.89 | 6.11 | 0.16 | 2.23 | 5.25 | 4.50 | 4.49 | 0.01 | 0.35 | | 1.59 | | 0.68 | 1.69 | 1.59 | 1 |
| FR 2.7 | 55.14 | 0.78 | 17.44 | 6.74 | 0.16 | 2.17 | 5.25 | 4.37 | 4.32 | 0.02 | 0.42 | | 2.69 | | 0.72 | 2.98 | 2.69 | 1 |
| FR 3.8 | 54.69 | 0.77 | 17.41 | 6.35 | 0.17 | 2.14 | 5.20 | 4.30 | 4.32 | 0.02 | 0.43 | | 3.76 | | 0.59 | 3.91 | 3.76 | 1 |
| FR 6.3 | 53.49 | 0.76 | 16.73 | 6.19 | 0.14 | 2.09 | 4.99 | 4.06 | 4.22 | 0.01 | 0.44 | | 6.32 | | 0.66 | 6.65 | 6.32 | 1 |
| Di Genova et al. (2014, 2017a) | | | | | | | | | | | | | | | | | | |

**Table B.1:** Composition of silicate glasses used in Chapters 2 and 3 *cont.*

| Sample | $SiO_2$ | $TiO_2$ | $Al_2O_3$ | $FeO_T$ | MnO | MgO | CaO | $Na_2O$ | $K_2O$ | $P_2O_5$ | [a] | [a] | $H_2O$ | $CO_2$[b] | [c] | VBD[d] | MV[e] | [f] |
|---|---|---|---|---|---|---|---|---|---|---|---|---|---|---|---|---|---|---|
| AMS1 | 57.72 | 0.39 | 18.40 | 4.51 | 0.10 | 1.46 | 4.23 | 3.72 | 7.90 | 0.19 | | | 1.29 | | | | | 2 |
| AMS2 | 56.97 | 0.38 | 18.16 | 4.45 | 0.10 | 1.44 | 4.18 | 3.67 | 7.80 | 0.19 | | | 2.57 | | | | | 2 |
| AMS4 | 55.68 | 0.38 | 17.75 | 4.35 | 0.10 | 1.41 | 4.08 | 3.59 | 7.62 | 0.18 | | | 4.78 | | | | | 2 |
| Di Genova et al. (2016) | | | | | | | | | | | | | | | | | | |
| FSP1 | 72.53 | 0.44 | 8.70 | 9.02 | 0.34 | 0.17 | 0.45 | 4.59 | 4.09 | | | | 0.00 | | 0.17 | -1.16 | 0.00 | 3 |
| FSP2 | 71.89 | 0.43 | 8.78 | 8.78 | 0.35 | 0.16 | 0.43 | 4.37 | 4.01 | | | | 0.00 | | 0.26 | 0.07 | 0.00 | 3 |
| FSP3 | 72.94 | 0.42 | 8.92 | 8.55 | 0.37 | 0.17 | 0.44 | 4.46 | 4.10 | | | | 0.00 | | 0.42 | -0.93 | 0.00 | 3 |
| FSP4 | 71.93 | 0.43 | 8.97 | 8.93 | 0.37 | 0.17 | 0.46 | 4.72 | 4.18 | | | | 0.00 | | 0.38 | -0.77 | 0.00 | 3 |
| FSP5 | 73.75 | 0.41 | 9.06 | 7.73 | 0.30 | 0.15 | 0.37 | 4.08 | 3.94 | | | | 0.00 | | 0.31 | -0.38 | 0.00 | 3 |
| FSP6 | 73.11 | 0.43 | 8.97 | 8.34 | 0.37 | 0.17 | 0.47 | 4.55 | 4.18 | | | | 0.00 | | 0.60 | -0.96 | 0.00 | 3 |
| FSP7 | 73.44 | 0.43 | 9.05 | 7.71 | 0.35 | 0.17 | 0.40 | 4.08 | 3.99 | | | | 0.00 | | 0.65 | 0.08 | 0.00 | 3 |
| FSP8 | 74.62 | 0.45 | 9.05 | 7.17 | 0.38 | 0.18 | 0.45 | 4.06 | 4.05 | | | | 0.00 | | 0.74 | -0.62 | 0.00 | 3 |
| FSP9 | 74.24 | 0.44 | 9.01 | 7.04 | 0.36 | 0.17 | 0.47 | 4.19 | 4.14 | | | | 0.00 | | 0.76 | -0.24 | 0.00 | 3 |
| Di Genova et al. (2017a) | | | | | | | | | | | | | | | | | | |
| A or Y-A | 77.63 | 0.11 | 12.73 | 3.03 | 0.03 | 0.06 | 0.92 | 4.44 | 1.62 | 0.00 | | | 0.00 | | 0.45 | -0.76 | 0.00 | 3 |
| B or Y-B | 77.28 | 0.14 | 13.39 | 2.94 | 0.02 | 0.06 | 0.75 | 2.71 | 3.61 | 0.03 | | | 0.00 | | 0.56 | -1.07 | 0.00 | 3 |
| C | 77.56 | 0.11 | 12.42 | 1.52 | 0.04 | 0.08 | 0.85 | 3.07 | 4.08 | 0.04 | | | 0.00 | | 0.54 | 0.15 | 0.00 | 1 |
| D | 76.83 | 0.11 | 12.43 | 2.96 | 0.05 | 0.07 | 0.90 | 2.93 | 4.29 | 0.04 | | | 0.00 | | 0.43 | -0.80 | 0.00 | 1 |
| E of Y-E | 75.33 | 0.12 | 13.61 | 2.93 | 0.03 | 0.07 | 0.88 | 1.41 | 6.80 | 0.06 | | | 0.00 | | 0.43 | -1.43 | 0.00 | 3 |
| F | 78.87 | 0.10 | 12.52 | 1.55 | 0.04 | 0.06 | 0.84 | 1.01 | 5.28 | 0.02 | | | 0.00 | | 0.56 | -0.37 | 0.00 | 1 |
| G or Y-G | 77.86 | 0.12 | 11.69 | 2.99 | 0.04 | 0.07 | 0.85 | 1.05 | 5.34 | 0.00 | | | 0.00 | | 0.51 | -0.17 | 0.00 | 3 |
| H or Y-H | 77.25 | 0.10 | 11.95 | 2.62 | 0.06 | 0.22 | 1.08 | 3.23 | 4.35 | 0.05 | | | 0.00 | | 0.42 | -1.08 | 0.00 | 3 |
| I | 76.24 | 0.06 | 11.46 | 2.85 | 0.03 | 0.44 | 1.31 | 2.99 | 3.83 | 0.04 | | | 0.00 | | 0.42 | 0.57 | 0.00 | 1 |
| J or Y-J | 73.75 | 0.31 | 11.99 | 3.31 | 0.07 | 1.64 | 2.98 | 3.16 | 3.56 | 0.00 | | | 0.00 | | 0.40 | -0.99 | 0.00 | 3 |
| L or Y-L | 71.22 | 0.28 | 10.86 | 6.24 | 0.05 | 1.58 | 2.72 | 2.89 | 3.28 | 0.05 | | | 0.00 | | 0.39 | 0.40 | 0.00 | 3 |
| Drew et al. (2016) | | | | | | | | | | | | | | | | | | |
| PC-P1.2-2 | 72.09 | 0.03 | 11.76 | 0.63 | | 0.00 | 0.41 | 2.77 | 4.67 | | | | 4.94 | 196 | | 7.58 | 4.94 | 1 |
| PC-P1.4 | 71.84 | 0.03 | 12.36 | 0.68 | | 0.01 | 0.43 | 1.22 | 7.98 | | | | 4.69 | 179 | | 5.37 | 4.69 | 1 |
| PC-P2.6 | 71.31 | 0.06 | 11.54 | 0.66 | | 0.00 | 0.42 | 3.52 | 4.15 | | | | 3.45 | 270 | | 8.27 | 3.45 | 1 |

**Table B.1:** Composition of silicate glasses used in Chapters 2 and 3 *cont.*

| Sample | $SiO_2$ | $TiO_2$ | $Al_2O_3$ | $FeO_T$ | MnO | MgO | CaO | $Na_2O$ | $K_2O$ | $P_2O_5$ | [a] | [a] | $H_2O$ | $CO_2$[b] | [c] | VBD[d] | MV[e] | [f] |
|---|---|---|---|---|---|---|---|---|---|---|---|---|---|---|---|---|---|---|
| PC-P3.1-1 | 71.08 | 0.01 | 12.22 | 0.69 | | 0.00 | 0.43 | 1.24 | 8.61 | | | | 4.59 | 103 | | 5.63 | 4.59 | 1 |
| PC-P3.2 | 71.89 | 0.04 | 12.07 | 0.69 | | 0.00 | 0.43 | 2.51 | 4.50 | | | | 5.33 | 410 | | 7.78 | 5.33 | 1 |
| PC-P3.3 | 72.58 | 0.00 | 11.80 | 0.64 | | 0.00 | 0.42 | 3.56 | 4.11 | | | | 2.27 | 120 | | 6.82 | 2.27 | 1 |
| PC-P4.1 | 71.59 | 0.02 | 11.86 | 0.60 | | 0.00 | 0.34 | 4.01 | 4.15 | | | | 3.49 | 190 | | 7.36 | 3.49 | 1 |
| PC-P5.1-1 | 73.06 | 0.06 | 11.84 | 1.00 | | 0.03 | 0.44 | 3.11 | 5.15 | | | | 4.79 | 396 | | 5.21 | 4.79 | 1 |
| PC-P5.1-2 | 73.17 | 0.04 | 11.86 | 0.97 | | 0.03 | 0.43 | 3.15 | 5.22 | | | | 3.93 | 393 | | 5.03 | 3.93 | 1 |
| PC-P6.3-1 | 71.68 | 0.02 | 12.23 | 0.66 | | 0.00 | 0.42 | 1.24 | 8.04 | | | | 3.84 | 97 | | 5.63 | 3.84 | 1 |
| PC-P6.3-2 | 73.59 | 0.02 | 12.11 | 0.64 | | 0.00 | 0.41 | 3.15 | 4.90 | | | | 4.83 | 79 | | 5.11 | 4.83 | 1 |
| Gaillard et al. (2001) | | | | | | | | | | | | | | | | | | |
| NNO+6.6 1/1 | 73.62 | 0.00 | 11.04 | 0.50 | 0.00 | 0.00 | 0.00 | 3.56 | 4.34 | | | | 6.23 | | 0.03 | 6.89 | 6.23 | 1 |
| NNO+6.6 1/2 | 72.84 | 0.00 | 11.05 | 0.74 | 0.00 | 0.00 | 0.00 | 3.67 | 4.59 | | | | 6.16 | | 0.02 | 7.03 | 6.16 | 1 |
| NNO+6.6 1/7 | 67.85 | 0.27 | 11.76 | 2.73 | 0.00 | 0.01 | 0.33 | 5.29 | 4.41 | | | | 6.05 | | 0.01 | 7.04 | 6.05 | 1 |
| NNO+6.6 1/8 | 72.55 | 0.08 | 11.74 | 0.84 | 0.00 | 0.21 | 1.26 | 3.14 | 2.76 | | | | 5.95 | | 0.03 | 7.32 | 5.95 | 1 |
| NNO+6.6 1/9 | 68.09 | 0.09 | 14.81 | 0.57 | 0.00 | 0.03 | 0.21 | 4.07 | 3.52 | | | | 6.49 | | 0.03 | 8.56 | 6.49 | 1 |
| NNO+1.55 2/2 | 72.72 | 0.00 | 10.95 | 0.81 | 0.00 | 0.00 | 0.00 | 3.74 | 4.54 | | | | 6.10 | | 0.17 | 7.18 | 6.10 | 1 |
| NNO+1.55 2/3 | 72.30 | 0.00 | 11.23 | 1.59 | 0.00 | 0.00 | 0.00 | 3.71 | 4.38 | | | | 6.26 | | 0.13 | 6.63 | 6.26 | 1 |
| NNO+1.55 2/7 | 67.48 | 0.24 | 11.77 | 3.02 | 0.00 | 0.00 | 0.32 | 5.18 | 4.41 | | | | 6.15 | | 0.08 | 7.26 | 6.15 | 1 |
| NNO-0.72 3/2 | 72.21 | 0.00 | 10.94 | 0.78 | 0.00 | 0.00 | 0.00 | 3.75 | 4.44 | | | | 6.40 | | 0.23 | 7.82 | 6.40 | 1 |
| NNO-0.72 3/3 | 71.36 | 0.00 | 11.12 | 1.58 | 0.00 | 0.00 | 0.00 | 3.78 | 4.23 | | | | 6.25 | | 0.22 | 7.78 | 6.25 | 1 |
| NNO-0.72 3/4 | 71.21 | 0.00 | 10.80 | 2.37 | 0.00 | 0.00 | 0.00 | 3.62 | 4.24 | | | | 6.20 | | 0.19 | 7.55 | 6.20 | 1 |
| NNO-0.72 3/7 | 67.76 | 0.17 | 11.55 | 2.95 | 0.00 | 0.00 | 0.29 | 4.99 | 4.35 | | | | 6.38 | | 0.15 | 7.65 | 6.38 | 1 |
| NNO-0.72 3/8 | 72.27 | 0.10 | 11.38 | 0.89 | 0.00 | 0.09 | 1.15 | 3.10 | 2.64 | | | | 6.01 | | 0.54 | 8.33 | 6.01 | 1 |
| NNO-0.72 3/9 | 67.91 | 0.06 | 14.75 | 0.52 | 0.00 | 0.02 | 0.21 | 3.85 | 3.41 | | | | 6.47 | | 0.47 | 9.25 | 6.47 | 1 |
| NNO-1.35 4/1 | 72.94 | 0.00 | 11.03 | 0.33 | 0.00 | 0.00 | 0.00 | 3.62 | 4.36 | | | | 6.39 | | 0.26 | 7.69 | 6.39 | 1 |
| NNO-1.35 4/2 | 72.23 | 0.00 | 11.01 | 0.48 | 0.00 | 0.00 | 0.00 | 3.58 | 4.51 | | | | 6.25 | | 0.25 | 8.16 | 6.25 | 1 |
| NNO-1.35 4/3 | 71.87 | 0.00 | 11.20 | 0.82 | 0.00 | 0.00 | 0.00 | 3.71 | 4.36 | | | | 6.21 | | 0.25 | 7.98 | 6.21 | 1 |
| NNO-1.35 4/4 | 71.80 | 0.00 | 10.98 | 1.55 | 0.00 | 0.00 | 0.00 | 3.66 | 4.32 | | | | 6.25 | | 0.23 | 7.55 | 6.25 | 1 |
| NNO-1.35 4/5 | 71.75 | 0.00 | 10.92 | 1.86 | 0.00 | 0.00 | 0.00 | 3.71 | 4.04 | | | | 6.14 | | 0.26 | 7.57 | 6.14 | 1 |
| NNO-1.35 4/6 | 71.56 | 0.00 | 10.94 | 2.48 | 0.00 | 0.00 | 0.00 | 3.38 | 4.11 | | | | 6.10 | | 0.25 | 7.32 | 6.10 | 1 |

**Table B.1:** Composition of silicate glasses used in Chapters 2 and 3 *cont.*

| Sample | $SiO_2$ | $TiO_2$ | $Al_2O_3$ | $FeO_T$ | MnO | MgO | CaO | $Na_2O$ | $K_2O$ | $P_2O_5$ | [a] | [a] | $H_2O$ | $CO_2$[b] | [c] | VBD[d] | MV[e] | [f] |
|---|---|---|---|---|---|---|---|---|---|---|---|---|---|---|---|---|---|---|
| NNO-1.35 4/7 | 68.23 | 0.33 | 11.87 | 2.63 | 0.00 | 0.00 | 0.32 | 5.07 | 4.22 | | | | 6.10 | | 0.16 | 7.09 | 6.10 | 1 |
| NNO-1.35 4/8 | 72.55 | 0.14 | 11.82 | 0.50 | 0.00 | 0.20 | 1.18 | 3.12 | 2.58 | | | | 6.21 | | 0.64 | 7.89 | 6.21 | 1 |
| NNO-1.35 4/9 | 67.40 | 0.07 | 14.89 | 0.39 | 0.00 | 0.00 | 0.18 | 3.93 | 3.37 | | | | 6.63 | | 0.47 | 9.76 | 6.63 | 1 |
| Gurenko et al. (2005) | | | | | | | | | | | Cl | | | | | | | |
| 42384 | 73.50 | 0.21 | 12.18 | 1.91 | 0.05 | 0.22 | 1.61 | 3.52 | 2.69 | 0.02 | 0.24 | | 6.50 | | | 3.64 | 6.50 | 1 |
| 42392 | 74.97 | 0.14 | 12.09 | 1.93 | 0.06 | 0.16 | 1.44 | 3.35 | 3.07 | 0.01 | 0.25 | | 5.20 | | | 2.32 | 5.20 | 1 |
| 32-1 | 73.50 | 0.28 | 13.30 | 1.76 | 0.06 | 0.11 | 1.93 | 3.86 | 2.47 | 0.04 | 0.21 | | 5.80 | | | 2.28 | 5.80 | 1 |
| 38-1 | 75.37 | 0.20 | 12.56 | 1.93 | 0.06 | 0.21 | 1.84 | 3.97 | 2.54 | 0.01 | 0.24 | | 1.70 | | | 0.86 | 1.70 | 1 |
| 70-1 | 73.73 | 0.11 | 11.97 | 1.83 | 0.10 | 0.13 | 1.37 | 2.90 | 3.26 | 0.06 | 0.28 | | 5.80 | | | 4.06 | 5.80 | 1 |
| 71-1 | 74.01 | 0.16 | 12.55 | 1.82 | 0.06 | 0.15 | 1.91 | 2.97 | 2.56 | 0.02 | 0.23 | | 5.60 | | | 3.36 | 5.60 | 1 |
| 72-1 | 72.77 | 0.22 | 13.07 | 1.82 | 0.05 | 0.14 | 2.13 | 3.44 | 2.20 | 0.07 | 0.22 | | 5.10 | | | 3.67 | 5.10 | 1 |
| 74-1 | 73.70 | 0.22 | 12.38 | 1.93 | 0.06 | 0.16 | 1.79 | 3.04 | 3.04 | 0.04 | 0.26 | | 5.00 | | | 3.17 | 5.00 | 1 |
| 47-1 | 76.23 | 0.12 | 12.33 | 1.35 | 0.05 | 0.20 | 1.61 | 3.76 | 2.69 | 0.06 | 0.19 | | 3.40 | | | 1.26 | 3.40 | 1 |
| 55-1 | 75.63 | 0.19 | 12.65 | 1.71 | 0.05 | 0.27 | 1.74 | 3.55 | 2.66 | 0.01 | 0.24 | | 3.90 | | | 1.11 | 3.90 | 1 |
| 75-1 | 74.57 | 0.19 | 12.33 | 1.50 | 0.03 | 0.24 | 1.69 | 3.31 | 2.69 | 0.05 | 0.22 | | 4.80 | | | 3.01 | 4.80 | 1 |
| 77-1 | 75.53 | 0.17 | 12.41 | 1.61 | 0.05 | 0.25 | 1.54 | 3.29 | 2.75 | 0.02 | 0.24 | | 4.50 | | | 1.96 | 4.50 | 1 |
| Kelley and Cottrell (2009) | | | | | | | | | | | $S_T$ | | | | | | | |
| EN113_13D-1B | 48.16 | 1.48 | 17.17 | 8.88 | 0.20 | 7.91 | 11.70 | 3.22 | 0.02 | 0.10 | 0.0861 | | 0.14 | | 0.85 | 0.93 | 0.14 | 1 |
| ALV 527 1-1 | 48.41 | 0.69 | 16.93 | 9.01 | | 9.48 | 12.56 | 2.00 | 0.07 | 0.06 | 0.0867 | | 0.14 | | 0.87 | 0.57 | 0.14 | 1 |
| CH 6-1 | 50.48 | 1.95 | 14.74 | 10.42 | 0.22 | 6.99 | 11.04 | 3.02 | 0.32 | 0.21 | | | 0.34 | 170 | 0.84 | 0.42 | 0.36 | 1 |
| EN25 6D-3 | 51.50 | 1.29 | 14.16 | 12.20 | | 6.91 | 11.46 | 2.07 | 0.10 | 0.12 | | | 0.30 | | 0.85 | -0.01 | 0.30 | 1 |
| K 10-34 | 48.06 | 0.99 | 17.33 | 8.54 | | 8.99 | 12.02 | 2.35 | 0.05 | 0.07 | | | 0.22 | 177 | 0.85 | 1.46 | 0.24 | 1 |
| K 14-3 | 51.21 | 1.76 | 13.48 | 11.59 | | 6.19 | 10.86 | 2.50 | 0.17 | 0.17 | | | 0.48 | 120 | 0.83 | 1.85 | 0.49 | 1 |
| K 18-21 | 50.72 | 1.76 | 13.93 | 11.18 | | 7.08 | 10.75 | 2.33 | 0.17 | 0.17 | | | 0.49 | 161 | 0.83 | 1.70 | 0.51 | 1 |
| JDFD2 | 50.95 | 1.88 | 13.99 | 12.22 | 0.22 | 6.50 | 10.96 | 2.62 | 0.20 | 0.22 | | | 0.45 | 252 | 0.83 | 0.01 | 0.48 | 1 |
| 76-1-1 | 52.79 | 1.62 | 15.88 | 9.48 | | 7.23 | 10.37 | 3.48 | 0.23 | 0.18 | | | 0.73 | 180 | 0.84 | -1.43 | 0.75 | 1 |
| 71-1-14 | 51.70 | 1.11 | 16.50 | 7.72 | 0.15 | 6.34 | 11.70 | 2.99 | 0.42 | 0.20 | | | 1.82 | 128 | 0.81 | 1.01 | 1.83 | 1 |
| 74-1-1 | 51.09 | 1.13 | 17.83 | 7.22 | 0.15 | 7.72 | 11.83 | 2.75 | 0.30 | 0.17 | | | 1.00 | 112 | 0.83 | -0.33 | 1.01 | 1 |
| 46-1-6 | 51.46 | 1.12 | 16.95 | 7.81 | 0.15 | 7.07 | 11.56 | 2.70 | 0.22 | 0.15 | | | 1.41 | 111 | 0.83 | 0.66 | 1.42 | 1 |

**Table B.1:** Composition of silicate glasses used in Chapters 2 and 3 *cont.*

| Sample | $SiO_2$ | $TiO_2$ | $Al_2O_3$ | $FeO_T$ | MnO | MgO | CaO | $Na_2O$ | $K_2O$ | $P_2O_5$ | [a] | [a] | $H_2O$ | $CO_2$[b] | [c] | VBD[d] | MV[e] | [f] |
|---|---|---|---|---|---|---|---|---|---|---|---|---|---|---|---|---|---|---|
| 47-1-5 | 51.22 | 0.96 | 16.60 | 7.53 | 0.16 | 7.33 | 12.12 | 2.49 | 0.24 | 0.13 | | | 1.76 | 66 | 0.83 | 1.08 | 1.77 | 1 |
| 75-1-2 | 52.30 | 1.61 | 16.38 | 8.38 | | 7.33 | 10.60 | 3.27 | 0.35 | 0.18 | | | 0.72 | 227 | 0.84 | -0.55 | 0.74 | 1 |
| 73-2-1 | 51.90 | 1.41 | 17.15 | 7.82 | 0.15 | 6.69 | 10.53 | 3.56 | 0.33 | 0.18 | | | 1.15 | 160 | 0.83 | 0.13 | 1.17 | 1 |
| 80-1-3 | 49.56 | 0.84 | 17.93 | 8.61 | 0.16 | 8.60 | 11.55 | 2.40 | 0.35 | 0.14 | | | 0.57 | 295 | 0.85 | -0.28 | 0.60 | 1 |
| 82-1-1 | 51.40 | 1.27 | 16.60 | 7.94 | 0.16 | 6.43 | 11.22 | 3.07 | 0.24 | 0.17 | | | 1.69 | 109 | 0.82 | 1.34 | 1.70 | 1 |
| WOK 5-4 | 50.67 | 0.93 | 17.49 | 7.20 | 0.16 | 7.34 | 11.86 | 2.57 | 0.29 | 0.12 | | | 1.60 | 64 | 0.83 | 1.23 | 1.61 | 1 |
| WOK 10-1 | 51.85 | 1.24 | 16.15 | 8.21 | 0.14 | 6.60 | 11.16 | 2.91 | 0.26 | 0.13 | | | 1.14 | 120 | 0.83 | 1.19 | 1.15 | 1 |
| WOK 16-2 | 51.12 | 1.53 | 15.99 | 9.13 | 0.17 | 7.54 | 10.67 | 3.12 | 0.19 | 0.18 | | | 0.64 | 184 | 0.84 | 0.20 | 0.66 | 1 |
| WOK 28-3 | 49.95 | 1.22 | 17.56 | 9.22 | 0.22 | 7.61 | 11.14 | 3.21 | 0.10 | 0.13 | | | 0.50 | 183 | 0.85 | -0.51 | 0.52 | 1 |
| ALV 1833-11 | 51.13 | 1.04 | 17.16 | 7.55 | 0.15 | 7.55 | 11.92 | 2.86 | 0.25 | 0.18 | | | 1.20 | 102 | 0.84 | 0.08 | 1.21 | 1 |
| ALV 1839-21 | 51.45 | 1.17 | 17.84 | 7.63 | 0.14 | 7.47 | 11.41 | 2.58 | 0.27 | 0.13 | | | 1.21 | 94 | 0.83 | -0.23 | 1.22 | 1 |
| ALV 1840-3 | 51.83 | 1.18 | 16.86 | 7.99 | 0.15 | 6.78 | 10.66 | 3.09 | 0.30 | 0.13 | | | 1.26 | 113 | 0.83 | 0.88 | 1.27 | 1 |
| ALV 1846-9 | 49.67 | 0.57 | 17.45 | 7.03 | 0.16 | 6.95 | 13.46 | 2.07 | 0.71 | 0.13 | 0.0370 | | 1.89 | | 0.82 | 1.62 | 1.89 | 1 |
| ALV 1846-12 | 50.75 | 1.11 | 17.30 | 7.56 | 0.15 | 7.00 | 11.39 | 2.75 | 0.40 | 0.18 | | | 1.55 | 90 | 0.83 | 1.27 | 1.56 | 1 |
| 108153-A | 52.48 | 0.98 | 16.45 | 6.64 | 0.13 | 4.95 | 6.90 | 3.41 | 1.06 | 0.40 | 0.2500 | | 4.00 | 296 | 0.8 | 6.20 | 4.03 | 1 |
| 2A/22/5/92-A | 52.84 | 1.16 | 16.36 | 10.57 | 0.23 | 4.36 | 7.27 | 2.82 | 0.65 | 0.14 | 0.0790 | | 2.90 | 13 | 0.8 | 3.29 | 2.90 | 1 |
| 2A/22/5/92-B | 51.54 | 1.18 | 16.32 | 10.22 | 0.25 | 4.21 | 7.50 | 3.95 | 0.64 | 0.16 | 0.1026 | | 3.36 | 19 | 0.78 | 3.68 | 3.36 | 1 |
| G98-02 | 49.25 | 1.32 | 20.34 | 7.40 | 0.15 | 3.80 | 13.04 | 3.24 | 0.54 | 0.15 | | | 0.26 | 99 | 0.82 | 0.62 | 0.27 | 1 |
| 05AUNY17_1 | 48.73 | 0.66 | 17.19 | 7.82 | 0.14 | 4.45 | 10.50 | 2.16 | 0.54 | 0.17 | | | 5.39 | 145 | 0.68 | 7.36 | 5.40 | 1 |
| GUG BB | 44.61 | 1.10 | 17.81 | 11.53 | 0.21 | 5.87 | 12.10 | 1.95 | 0.33 | 0.10 | | | 2.80 | 176 | 0.76 | 4.08 | 2.82 | 1 |
| GUG D | 45.70 | 0.74 | 18.01 | 11.32 | 0.24 | 5.44 | 12.58 | 1.95 | 0.30 | 0.09 | 0.1894 | | 3.28 | | 0.73 | 3.10 | 3.28 | 1 |
| GUG DB | 51.99 | 1.05 | 14.79 | 12.56 | 0.26 | 4.74 | 7.79 | 2.78 | 0.56 | 0.13 | 0.0307 | | 2.23 | | 0.78 | 3.01 | 2.23 | 1 |
| GUG J-F | 46.01 | 0.80 | 18.14 | 11.80 | 0.26 | 4.85 | 12.50 | 1.98 | 0.33 | 0.04 | 0.2001 | | 3.25 | | 0.75 | 2.76 | 3.25 | 1 |
| SA 93-1 | 53.50 | 0.55 | 15.63 | 7.06 | 0.14 | 2.85 | 10.99 | 2.13 | 0.57 | 0.03 | 0.0537 | | 4.00 | | 0.69 | 6.25 | 4.00 | 1 |
| EN113_13D-1B | 48.28 | 1.20 | 18.36 | 7.84 | 0.14 | 7.82 | 12.15 | 3.25 | 0.01 | 0.09 | 0.0755 | | 0.14 | 93 | 0.85 | 0.65 | 0.15 | 1 |
| Lesne et al. (2011) | | | | | | | | | | | Cl | $S_T$ | | | | | | |
| MAS.1.A1 | 48.61 | 1.14 | 17.78 | 10.94 | | 3.29 | 9.21 | 2.62 | 1.18 | | 0.1150 | 0.0480 | 2.58 | 490 | 0.68 | 4.68 | 2.63 | 1 |
| MAS.1.A2 | 48.78 | 1.12 | 18.08 | 10.96 | | 3.52 | 9.04 | 2.66 | 1.18 | | 0.1425 | 0.0395 | 2.13 | 120 | 0.67 | 4.05 | 2.14 | 1 |
| MAS.1.A3 | 48.60 | 1.13 | 18.51 | 10.94 | | 3.26 | 8.99 | 2.68 | 1.19 | | 0.1480 | 0.0370 | 2.62 | 610 | 0.70 | 4.15 | 2.68 | 1 |

**Table B.1:** Composition of silicate glasses used in Chapters 2 and 3 *cont.*

| Sample | $SiO_2$ | $TiO_2$ | $Al_2O_3$ | $FeO_T$ | MnO | MgO | CaO | $Na_2O$ | $K_2O$ | $P_2O_5$ | [a] | [a] | $H_2O$ | $CO_2$[b] | [c] | VBD[d] | MV[e] | [f] |
|---|---|---|---|---|---|---|---|---|---|---|---|---|---|---|---|---|---|---|
| MAS.1.A4 | 48.93 | 1.14 | 18.44 | 10.92 | | 3.18 | 8.87 | 2.65 | 1.18 | | 0.1330 | 0.0310 | 2.54 | 750 | 0.72 | 4.19 | 2.62 | 3 |
| MAS.1.A5 | 49.53 | 1.15 | 18.12 | 10.65 | | 3.43 | 8.80 | 2.69 | 1.16 | | 0.1645 | 0.0410 | 2.22 | 225 | 0.66 | 3.86 | 2.24 | 3 |
| MAS.1.A6 | 49.48 | 1.13 | 17.91 | 10.72 | | 3.49 | 8.79 | 2.69 | 1.17 | | 0.1640 | 0.0374 | 2.39 | 345 | | | | 2 |
| MAS.1.A7 | 48.70 | 1.14 | 18.72 | 10.95 | | 3.36 | 8.82 | 2.70 | 1.19 | | 0.1260 | 0.0270 | 2.03 | 90 | 0.75 | 3.97 | 2.04 | 1 |
| MAS.1.A9 | 50.55 | 1.19 | 18.79 | 10.89 | | 3.40 | 9.02 | 2.81 | 1.21 | | 0.1320 | 0.0030 | 1.58 | 35 | | | | 2 |
| MAS.1.A10 | 49.71 | 1.17 | 18.68 | 10.84 | | 3.39 | 8.91 | 2.76 | 1.20 | | 0.1315 | 0.0165 | 2.86 | 1445 | | | | 2 |
| MAS.1.A10b | 50.30 | 1.16 | 18.59 | 10.75 | | 3.34 | 8.80 | 2.77 | 1.20 | | 0.1590 | 0.0040 | 2.75 | 1390 | | | | 2 |
| MAS.1.B2 | 48.57 | 1.16 | 17.83 | 11.00 | | 3.10 | 9.22 | 2.83 | 1.24 | | 0.1470 | 0.0870 | 2.20 | 65 | 0.69 | 4.41 | 2.21 | 1 |
| MAS.1.B3 | 48.30 | 1.15 | 17.96 | 10.98 | | 3.24 | 9.30 | 2.73 | 1.20 | | 0.1440 | 0.0835 | 2.44 | 450 | 0.68 | 4.53 | 2.49 | 1 |
| MAS.1.B4 | 48.70 | 1.14 | 18.27 | 10.71 | | 3.13 | 9.10 | 2.82 | 1.24 | | 0.1220 | 0.0605 | 2.55 | 705 | 0.82 | 4.49 | 2.62 | 3 |
| MAS.1.B5 | 49.09 | 1.14 | 18.26 | 10.73 | | 2.85 | 8.95 | 2.88 | 1.27 | | 0.1245 | 0.0935 | 2.24 | 195 | 0.68 | 4.23 | 2.26 | 3 |
| MAS.1.B6 | 49.19 | 1.14 | 18.51 | 10.36 | | 3.01 | 9.17 | 2.80 | 1.24 | | 0.1400 | 0.0950 | 2.41 | | | | | 2 |
| MAS.1.B7 | 49.43 | 1.17 | 18.06 | 10.96 | | 3.05 | 9.07 | 2.83 | 1.26 | | 0.1225 | 0.0505 | 1.83 | 75 | | | | 2 |
| MAS.1.B8 | 49.75 | 1.18 | 19.03 | 10.95 | | 3.23 | 9.15 | 2.91 | 1.23 | | 0.01510 | 0.0525 | 1.73 | 90 | | | | 2 |
| MAS.1.B9 | 50.86 | 1.19 | 18.54 | 10.90 | | 3.31 | 9.14 | 2.92 | 1.26 | | 0.1220 | 0.0060 | 1.64 | 35 | | | | 2 |
| St8.1.A1 | 48.06 | 0.75 | 17.47 | 6.90 | | 6.11 | 10.29 | 1.90 | 1.34 | | 0.1733 | 0.1733 | 2.70 | 515 | 0.64 | 6.55 | 2.75 | 1 |
| St8.1.A3 | 48.44 | 0.79 | 17.49 | 7.08 | | 5.95 | 10.12 | 1.93 | 1.38 | | 0.1595 | 0.1595 | 2.86 | 575 | 0.69 | 6.26 | 2.92 | 1 |
| St8.1.A4 | 48.19 | 0.76 | 17.48 | 6.97 | | 6.08 | 10.27 | 1.95 | 1.36 | | 0.1721 | 0.1721 | 3.05 | 960 | 0.67 | 6.34 | 3.15 | 1 |
| St8.1.A5 | 48.89 | 0.78 | 17.56 | 6.96 | | 6.28 | 10.33 | 1.97 | 1.34 | | 0.1979 | 0.1719 | 2.57 | 300 | 0.60 | 5.20 | 2.60 | 1 |
| St8.1.A10 | 49.85 | 0.79 | 17.60 | 6.98 | | 6.05 | 10.34 | 1.96 | 1.41 | | 0.2141 | 0.1564 | 3.17 | 1540 | 0.68 | 4.41 | 3.32 | 1 |
| St8.1.B2 | 49.36 | 0.80 | 17.73 | 6.94 | | 5.86 | 10.78 | 1.88 | 1.36 | | 0.1537 | 0.3043 | 2.40 | 60 | 0.66 | 4.58 | 2.41 | 3 |
| St8.1.B3 | 48.72 | 0.79 | 17.95 | 6.95 | | 5.88 | 10.68 | 1.93 | 1.34 | | 0.1985 | 0.3240 | 3.01 | 635 | 0.66 | 4.97 | 3.07 | 3 |
| St8.1.B4 | 49.33 | 0.82 | 17.69 | 6.96 | | 5.55 | 10.45 | 1.91 | 1.39 | | 0.1560 | 0.3140 | 3.11 | 920 | 0.68 | 5.19 | 3.20 | 3 |
| St8.1.B5 | 49.23 | 0.81 | 17.89 | 7.00 | | 5.67 | 10.57 | 1.89 | 1.36 | | 0.1570 | 0.3170 | 2.65 | 230 | 0.63 | 4.82 | 2.67 | 3 |
| St8.1.B6 | 49.35 | 0.78 | 17.71 | 6.98 | | 5.59 | 10.54 | 1.90 | 1.37 | | 0.1582 | 0.3230 | 2.76 | 415 | | | | 2 |
| St8.1.B7 | 50.02 | 0.82 | 17.99 | 7.05 | | 5.86 | 10.70 | 1.90 | 1.37 | | 0.1476 | 0.1607 | 1.87 | 60 | 0.68 | 3.73 | 1.88 | 3 |
| St8.1.B9 | 51.92 | 0.87 | 18.05 | 7.26 | | 6.34 | 10.95 | 1.98 | 1.44 | | 0.1485 | 0.0036 | 1.03 | 40 | | | | 2 |
| St8.1.B10 | 49.74 | 0.82 | 17.84 | 6.91 | | 5.92 | 10.41 | 1.98 | 1.38 | | 0.1635 | 0.3090 | 3.38 | 1490 | | | | 2 |

**Table B.1:** Composition of silicate glasses used in Chapters 2 and 3 *cont.*

| Sample | $SiO_2$ | $TiO_2$ | $Al_2O_3$ | $FeO_T$ | MnO | MgO | CaO | $Na_2O$ | $K_2O$ | $P_2O_5$ | [a] | [a] | $H_2O$ | $CO_2$[b] | [c] | VBD[d] | MV[e] | [f] |
|---|---|---|---|---|---|---|---|---|---|---|---|---|---|---|---|---|---|---|
| Melekhova et al. (2015) | | | | | | | | | | | $Cr_2O_3$ | NiO | | | | | | |
| BM3 | 47.53 | 0.81 | 16.02 | 7.72 | 0.16 | 9.16 | 11.64 | 2.11 | 0.16 | 0.10 | 0.07 | 0.10 | 2.94 | | 0.68 | 4.14 | 2.94 | 1 |
| BM6 | 46.88 | 0.86 | 16.13 | 6.63 | 0.16 | 9.41 | 10.96 | 2.15 | 0.15 | 0.12 | 0.06 | | 4.42 | | 0.55 | 6.16 | 4.42 | 1 |
| BM9 | 45.27 | 0.79 | 15.98 | 7.90 | 0.14 | 8.57 | 11.03 | 2.49 | 0.16 | 0.09 | 0.04 | | 5.34 | | 0.57 | 7.16 | 5.34 | 1 |
| BM17 | 45.58 | 0.75 | 14.61 | 8.58 | 0.20 | 10.91 | 10.99 | 2.28 | 0.17 | 0.13 | 0.03 | 0.03 | 6.70 | | 0.43 | 5.20 | 6.70 | 1 |
| BM33 | 45.37 | 0.70 | 13.88 | 7.30 | 0.34 | 13.63 | 10.30 | 2.23 | 0.14 | 0.08 | 0.13 | 0.02 | 4.46 | | 0.55 | 5.52 | 4.46 | 1 |
| BM34 | 51.23 | 0.42 | 17.64 | 4.65 | 0.17 | 4.83 | 7.81 | 2.92 | 0.26 | 0.17 | | | 7.20 | | 0.36 | 9.57 | 7.20 | 1 |
| BM37* | 45.93 | 0.82 | 15.85 | 7.58 | 0.15 | 8.35 | 11.73 | 2.67 | 0.16 | 0.09 | 0.01 | 0.02 | 5.20 | | 0.43 | 6.16 | 5.20 | 1 |
| BM38 | 46.44 | 0.79 | 14.99 | 8.49 | 0.17 | 11.34 | 11.29 | 2.15 | 0.15 | 0.08 | 0.05 | | 2.50 | | 0.45 | 3.54 | 2.50 | 1 |
| BM40 | 46.88 | 0.89 | 17.01 | 8.27 | 0.15 | 8.30 | 11.33 | 2.37 | 0.17 | 0.11 | 0.02 | | 3.05 | | 0.59 | 4.12 | 3.05 | 1 |
| BM46 | 45.26 | 0.68 | 13.69 | 7.36 | 0.15 | 13.69 | 10.27 | 2.23 | 0.14 | 0.08 | 0.13 | 0.01 | 4.52 | | 0.53 | 5.92 | 4.52 | 1 |
| RSV49_2 | 46.78 | 0.71 | 14.28 | 8.88 | 0.18 | 14.15 | 10.78 | 1.79 | 0.12 | 0.09 | 0.11 | 0.07 | 0.60 | | 0.79 | 1.85 | 0.60 | 1 |
| Naumov et al. (2008) | | | | | | | | | | | Cl | $S_T$ | | | | | | |
| K-35_58 | 71.76 | 0.21 | 13.16 | 0.94 | 0.03 | 0.27 | 0.83 | 4.97 | 3.32 | 0.00 | 0.20 | 0.01 | 4.75 | | | 4.20 | 4.75 | 1 |
| K-31_60 | 71.74 | 0.30 | 12.45 | 1.58 | 0.06 | 0.37 | 1.40 | 4.25 | 3.43 | 0.09 | 0.24 | 0.01 | 5.14 | | | 3.91 | 5.14 | 1 |
| K-31_61 | 71.85 | 0.29 | 12.36 | 1.38 | 0.06 | 0.26 | 1.25 | 4.21 | 3.15 | 0.03 | 0.17 | 0.00 | 5.87 | | | 4.84 | 5.87 | 1 |
| K-31_62 | 72.09 | 0.35 | 12.48 | 1.57 | 0.03 | 0.33 | 1.41 | 2.99 | 3.26 | 0.01 | 0.19 | 0.01 | 3.12 | | | 5.11 | 3.12 | 1 |
| K-31_65 | 72.35 | 0.27 | 12.09 | 1.39 | 0.10 | 0.25 | 1.27 | 3.86 | 3.26 | 0.04 | 0.16 | 0.00 | 4.96 | | | 4.81 | 4.96 | 1 |
| K-23_67 | 72.54 | 0.18 | 11.93 | 1.13 | 0.00 | 0.21 | 1.20 | 3.63 | 3.05 | 0.00 | 0.20 | 0.02 | 6.65 | | | 5.80 | 6.65 | 1 |
| 1 | 72.15 | 0.24 | 12.82 | 1.30 | 0.04 | 0.27 | 1.23 | 3.89 | 2.82 | 0.02 | 0.14 | | 4.89 | | | 4.94 | 4.89 | 1 |
| 2 | 72.83 | 0.11 | 12.51 | 0.51 | 0.06 | 0.12 | 0.66 | 3.32 | 3.82 | 0.04 | 0.11 | | 4.88 | | | 5.85 | 4.88 | 1 |
| 3 | 73.28 | 0.12 | 12.98 | 0.57 | 0.07 | 0.16 | 0.88 | 3.60 | 3.74 | 0.00 | 0.10 | | 4.20 | | | 4.44 | 4.20 | 1 |
| 4 | 74.02 | 0.09 | 12.44 | 0.54 | 0.13 | 0.06 | 0.62 | 3.72 | 3.92 | 0.06 | 0.11 | | 3.41 | | | 4.23 | 3.41 | 1 |
| 5 | 74.91 | 0.31 | 12.95 | 1.25 | 0.15 | 0.24 | 1.19 | 4.03 | 3.12 | 0.01 | 0.15 | | 0.90 | | | 1.55 | 0.90 | 1 |
| 6 | 75.67 | 0.11 | 12.83 | 0.67 | 0.11 | 0.10 | 0.68 | 3.64 | 4.12 | 0.04 | 0.10 | | 1.64 | | | 1.86 | 1.64 | 1 |
| 7 | 70.18 | 0.24 | 10.95 | 1.57 | 0.00 | 0.27 | 1.43 | 5.81 | 1.78 | 0.02 | 0.28 | | 6.68 | | | 7.30 | 6.68 | 1 |
| 8 | 72.12 | 0.19 | 11.78 | 1.25 | 0.15 | 0.21 | 1.35 | 4.79 | 1.83 | 0.02 | 0.26 | | 5.73 | | | 5.91 | 5.73 | 1 |
| 9 | 74.05 | 0.16 | 11.02 | 1.18 | 0.08 | 0.20 | 1.04 | 4.46 | 1.84 | 0.04 | 0.26 | | 4.98 | | | 5.54 | 4.98 | 1 |
| 10 | 77.02 | 0.16 | 9.29 | 0.90 | 0.04 | 0.19 | 0.98 | 4.10 | 1.69 | 0.10 | 0.19 | | 5.10 | | | 5.24 | 5.10 | 1 |

**Table B.1:** Composition of silicate glasses used in Chapters 2 and 3 *cont.*

| Sample | $SiO_2$ | $TiO_2$ | $Al_2O_3$ | $FeO_T$ | MnO | MgO | CaO | $Na_2O$ | $K_2O$ | $P_2O_5$ | [a] | [a] | $H_2O$ | $CO_2$[b] | [c] | VBD[d] | MV[e] | [f] |
|---|---|---|---|---|---|---|---|---|---|---|---|---|---|---|---|---|---|---|
| Naumov (2011) | | | | | | | | | | | Cl | F | | | | | | |
| 8-1/2 | 79.12 | 0.12 | 9.99 | 0.74 | 0.06 | 0.05 | 0.31 | 2.11 | 4.05 | 0.00 | 0.20 | 1.56 | 0.11 | | | 1.61 | 0.11 | 1 |
| 8-2/6 | 73.75 | 0.17 | 10.88 | 0.75 | 0.09 | 0.04 | 0.29 | 5.08 | 4.19 | 0.00 | 0.25 | 0.57 | 2.40 | | | 3.86 | 2.40 | 1 |
| 8-2/7 | 76.44 | 0.07 | 10.85 | 0.52 | 0.07 | 0.04 | 0.25 | 4.46 | 4.21 | 0.00 | 0.20 | 0.11 | 0.56 | | | 2.72 | 0.56 | 1 |
| 8-4/8 | 70.64 | 0.09 | 14.85 | 1.57 | 0.05 | 0.04 | 0.56 | 6.29 | 6.11 | 0.00 | 0.13 | 0.12 | 1.26 | | | -0.62 | 1.26 | 1 |
| 8-4/9 | 72.82 | 0.09 | 12.63 | 1.56 | 0.15 | 0.05 | 0.50 | 5.88 | 4.92 | 0.02 | 0.19 | 0.05 | 0.20 | | | 0.97 | 0.20 | 1 |
| 8-4/11 | 78.36 | 0.11 | 9.06 | 0.68 | 0.06 | 0.07 | 0.22 | 3.44 | 4.04 | 0.01 | 0.20 | 0.28 | 0.46 | | | 3.39 | 0.46 | 1 |
| 64-1/14 | 68.16 | 0.05 | 13.66 | 0.66 | 0.03 | 0.03 | 0.05 | 4.91 | 5.73 | 0.03 | 0.26 | 1.57 | 4.75 | | | 4.79 | 4.75 | 1 |
| 64-1/16 | 72.29 | 0.10 | 10.39 | 0.71 | 0.08 | 0.05 | 0.24 | 4.07 | 3.32 | 0.00 | 0.17 | 1.78 | 2.33 | | | 6.72 | 2.33 | 1 |
| 19-2/20 | 74.70 | 0.12 | 10.75 | 0.80 | 0.11 | 0.04 | 0.26 | 4.46 | 4.29 | 0.06 | 0.23 | 1.56 | 2.10 | | | 2.53 | 2.10 | 1 |
| K-1/21 | 81.26 | 0.08 | 8.73 | 0.51 | 0.06 | 0.06 | 0.49 | 3.06 | 3.04 | 0.05 | 0.08 | 0.02 | 0.25 | | | 2.50 | 0.25 | 1 |
| K-4/22 | 68.56 | 0.02 | 13.87 | 0.15 | 0.11 | 0.02 | 0.38 | 3.34 | 5.43 | 0.00 | 0.05 | 0.36 | 6.40 | | | 7.69 | 6.40 | 1 |
| K-4/24 | 72.55 | 0.04 | 12.65 | 0.50 | 0.12 | 0.08 | 0.64 | 5.27 | 4.62 | 0.04 | 0.10 | 0.03 | 0.65 | | | 3.30 | 0.65 | 1 |
| K-4/27 | 77.08 | 0.07 | 11.48 | 0.37 | 0.11 | 0.03 | 0.62 | 5.06 | 4.08 | 0.03 | 0.03 | 0.02 | 0.35 | | | 0.98 | 0.35 | 1 |
| K-5/30 | 73.92 | 0.04 | 10.94 | 0.50 | 0.04 | 0.07 | 0.72 | 2.68 | 4.24 | 0.02 | 0.08 | 0.08 | 5.94 | | | 6.61 | 5.94 | 1 |
| K-9/31 | 74.97 | 0.11 | 15.53 | 0.46 | 0.00 | 0.05 | 0.82 | 3.03 | 4.47 | 0.03 | 0.07 | 0.01 | 0.07 | | | 0.40 | 0.07 | 1 |
| Nichols et al. (2002) and Shorttle et al. (2015) | | | | | | | | | | | $S_T$ | | | | | | | |
| 12aD1 | 50.31 | 1.10 | 14.08 | 11.34 | 0.20 | 8.04 | 12.02 | 1.90 | 0.05 | 0.06 | 0.107 | | 0.21 | | 0.84 | 0.43 | 0.21 | 1 |
| 14D3 | 49.91 | 1.25 | 14.18 | 11.37 | 0.18 | 7.68 | 11.95 | 2.06 | 0.16 | 0.10 | 0.112 | | 0.32 | | 0.84 | 0.68 | 0.32 | 1 |
| 14D4 | 50.08 | 1.26 | 14.17 | 11.55 | 0.20 | 7.72 | 12.07 | 2.01 | 0.15 | 0.10 | 0.114 | | 0.30 | | 0.84 | 0.21 | 0.30 | 1 |
| 02D6 | 50.38 | 1.04 | 14.53 | 10.77 | 0.18 | 8.38 | 12.00 | 1.97 | 0.06 | 0.07 | 0.107 | | 0.20 | | 0.83 | 0.15 | 0.20 | 1 |
| 17D1 | 49.42 | 0.84 | 14.86 | 10.15 | 0.20 | 8.66 | 13.46 | 1.76 | 0.04 | 0.04 | 0.068 | | 0.15 | | 0.84 | 0.23 | 0.15 | 1 |
| 22D1 | 50.72 | 1.13 | 14.04 | 11.50 | 0.21 | 7.67 | 11.76 | 2.03 | 0.07 | 0.06 | 0.108 | | 0.20 | | 0.84 | 0.34 | 0.20 | 1 |
| 33aD1 | 50.35 | 1.00 | 14.36 | 10.66 | 0.18 | 7.97 | 11.96 | 2.06 | 0.07 | 0.07 | 0.107 | | 0.19 | | 0.84 | 0.87 | 0.19 | 1 |
| 49D5 | 50.08 | 1.13 | 14.17 | 11.31 | 0.17 | 8.17 | 11.79 | 1.99 | 0.07 | 0.10 | 0.115 | | 0.19 | | 0.84 | 0.53 | 0.19 | 1 |
| 59D1 | 50.06 | 1.15 | 13.96 | 11.11 | 0.17 | 8.03 | 11.63 | 2.03 | 0.07 | 0.10 | 0.120 | | 0.22 | | 0.84 | 1.19 | 0.22 | 1 |
| 62D5 | 49.84 | 1.04 | 14.51 | 11.38 | 0.20 | 8.29 | 11.82 | 2.04 | 0.05 | 0.07 | 0.112 | | 0.20 | | 0.84 | 0.27 | 0.20 | 1 |
| 67D6 | 50.44 | 1.19 | 14.16 | 11.61 | 0.20 | 7.59 | 11.98 | 2.13 | 0.07 | 0.10 | 0.122 | | 0.23 | | 0.84 | 0.03 | 0.23 | 1 |
| 75D10 | 50.53 | 1.10 | 14.77 | 11.52 | 0.20 | 7.95 | 12.18 | 2.14 | 0.06 | 0.09 | 0.124 | | 0.19 | | 0.84 | -1.05 | 0.19 | 1 |

**Table B.1:** Composition of silicate glasses used in Chapters 2 and 3 *cont.*

| Sample | $SiO_2$ | $TiO_2$ | $Al_2O_3$ | $FeO_T$ | MnO | MgO | CaO | $Na_2O$ | $K_2O$ | $P_2O_5$ | [a] | [a] | $H_2O$ | $CO_2$[b] | [c] | VBD[d] | MV[e] | [f] |
|---|---|---|---|---|---|---|---|---|---|---|---|---|---|---|---|---|---|---|
| 80D1 | 50.58 | 1.18 | 13.41 | 11.62 | 0.21 | 7.36 | 12.18 | 2.01 | 0.07 | 0.08 | 0.117 | | 0.20 | | 0.84 | 0.80 | 0.20 | 1 |
| 85D4 | 50.87 | 1.05 | 13.34 | 11.61 | 0.20 | 7.56 | 12.25 | 1.88 | 0.05 | 0.07 | 0.119 | | 0.16 | | 0.84 | 0.62 | 0.16 | 1 |
| 90D2 | 50.74 | 1.34 | 13.46 | 12.63 | 0.21 | 7.05 | 11.70 | 2.08 | 0.07 | 0.08 | 0.126 | | 0.23 | | 0.84 | 0.10 | 0.23 | 1 |
| 92D1 | 51.29 | 1.35 | 13.35 | 13.20 | 0.22 | 6.78 | 11.51 | 2.16 | 0.08 | 0.09 | 0.130 | | 0.22 | | 0.84 | -0.59 | 0.22 | 1 |
| 96D1 | 50.27 | 1.34 | 13.66 | 12.75 | 0.21 | 7.19 | 11.76 | 2.08 | 0.07 | 0.08 | 0.130 | | 0.22 | | 0.84 | 0.04 | 0.22 | 1 |
| 100D1 | 50.49 | 1.16 | 13.67 | 12.15 | 0.22 | 7.41 | 11.85 | 2.09 | 0.06 | 0.07 | 0.119 | | 0.18 | | 0.84 | 0.32 | 0.18 | 1 |
| 103D4 | 50.56 | 0.96 | 14.20 | 11.55 | 0.18 | 7.93 | 12.70 | 1.96 | 0.03 | 0.06 | 0.106 | | 0.13 | | 0.84 | -0.61 | 0.13 | 1 |
| 104D6 | 50.37 | 1.41 | 12.97 | 14.19 | 0.22 | 6.69 | 11.14 | 2.16 | 0.07 | 0.09 | 0.125 | | 0.24 | | 0.84 | 0.13 | 0.24 | 1 |
| 105D1 | 50.35 | 1.12 | 13.51 | 12.68 | 0.19 | 7.35 | 12.15 | 1.98 | 0.06 | 0.07 | 0.111 | | 0.18 | | 0.85 | 0.04 | 0.18 | 1 |
| 108D3 | 50.52 | 0.89 | 13.72 | 11.76 | 0.18 | 7.98 | 12.50 | 1.82 | 0.03 | 0.06 | 0.102 | | 0.12 | | 0.85 | 0.08 | 0.12 | 1 |
| 111D2 | 50.48 | 1.26 | 13.66 | 12.43 | 0.21 | 7.22 | 11.85 | 2.10 | 0.07 | 0.09 | 0.125 | | 0.20 | | 0.84 | 0.10 | 0.20 | 1 |
| 112D1 | 50.42 | 1.27 | 13.51 | 12.81 | 0.21 | 6.98 | 11.79 | 2.15 | 0.06 | 0.10 | 0.135 | | 0.20 | | 0.84 | 0.14 | 0.20 | 1 |
| 116D6 | 50.69 | 1.11 | 13.62 | 11.94 | 0.21 | 7.46 | 12.08 | 2.08 | 0.06 | 0.07 | 0.119 | | 0.15 | | 0.83 | 0.16 | 0.15 | 1 |
| 117D4 | 50.44 | 1.27 | 13.49 | 12.59 | 0.22 | 7.10 | 11.81 | 2.18 | 0.07 | 0.08 | 0.133 | | 0.18 | | 0.84 | 0.19 | 0.18 | 1 |
| 119D1 | 50.52 | 1.14 | 13.67 | 12.14 | 0.21 | 7.34 | 12.11 | 2.14 | 0.05 | 0.06 | 0.122 | | 0.21 | | 0.84 | 0.09 | 0.21 | 1 |
| 121D3 | 50.50 | 1.05 | 13.64 | 11.88 | 0.21 | 7.51 | 12.41 | 2.01 | 0.04 | 0.07 | 0.125 | | 0.13 | | 0.84 | 0.16 | 0.13 | 1 |
| 122D4 | 50.30 | 0.92 | 13.92 | 11.54 | 0.20 | 7.81 | 12.54 | 1.95 | 0.03 | 0.07 | 0.117 | | 0.12 | | 0.85 | 0.23 | 0.12 | 1 |
| 125D1 | 50.56 | 1.14 | 13.80 | 12.22 | 0.22 | 7.44 | 12.12 | 2.05 | 0.06 | 0.09 | 0.113 | | 0.16 | | 0.84 | -0.19 | 0.16 | 1 |
| 126D1 | 50.41 | 1.31 | 13.31 | 13.09 | 0.21 | 7.03 | 11.69 | 2.13 | 0.06 | 0.09 | 0.135 | | 0.20 | | 0.83 | 0.08 | 0.20 | 1 |
| 129D2 | 50.34 | 1.11 | 13.57 | 12.45 | 0.23 | 7.37 | 12.10 | 2.01 | 0.05 | 0.06 | 0.121 | | 0.19 | | 0.83 | 0.17 | 0.19 | 1 |
| 131D1 | 50.52 | 1.28 | 13.24 | 13.19 | 0.23 | 6.90 | 11.33 | 2.15 | 0.06 | 0.08 | 0.138 | | 0.15 | | 0.83 | 0.42 | 0.15 | 1 |
| 133D3 | 50.05 | 1.34 | 13.47 | 13.15 | 0.23 | 6.97 | 11.51 | 2.17 | 0.07 | 0.08 | 0.128 | | 0.16 | | 0.84 | 0.41 | 0.16 | 1 |
| 135D1 | 49.98 | 1.11 | 13.70 | 12.29 | 0.20 | 7.47 | 12.24 | 2.03 | 0.05 | 0.06 | 0.119 | | 0.16 | | 0.83 | 0.35 | 0.16 | 1 |
| 136D2 | 50.24 | 1.02 | 14.00 | 11.19 | 0.20 | 7.97 | 12.62 | 1.87 | 0.06 | 0.07 | 0.111 | | 0.15 | | 0.84 | 0.29 | 0.15 | 1 |
| 137D2 | 49.37 | 1.01 | 14.47 | 11.45 | 0.20 | 8.49 | 11.87 | 1.96 | 0.06 | 0.06 | 0.105 | | 0.20 | | 0.84 | 0.59 | 0.20 | 1 |
| 138D2 | 49.68 | 1.19 | 13.63 | 12.39 | 0.20 | 7.45 | 12.07 | 2.02 | 0.05 | 0.06 | 0.120 | | 0.18 | | 0.83 | 0.72 | 0.18 | 1 |
| 140D6 | 50.36 | 1.04 | 13.72 | 11.82 | 0.21 | 7.71 | 12.44 | 1.91 | 0.06 | 0.05 | 0.107 | | 0.17 | | 0.83 | 0.18 | 0.17 | 1 |
| 142D2 | 50.58 | 1.64 | 13.19 | 13.87 | 0.23 | 6.46 | 11.08 | 2.12 | 0.14 | 0.11 | 0.125 | | 0.35 | | 0.83 | 0.02 | 0.35 | 1 |
| 144D2 | 50.41 | 1.15 | 13.75 | 12.05 | 0.20 | 7.50 | 12.23 | 2.00 | 0.07 | 0.07 | 0.119 | | 0.17 | | 0.83 | 0.04 | 0.17 | 1 |

**Table B.1:** Composition of silicate glasses used in Chapters 2 and 3 *cont.*

| Sample | $SiO_2$ | $TiO_2$ | $Al_2O_3$ | $FeO_T$ | MnO | MgO | CaO | $Na_2O$ | $K_2O$ | $P_2O_5$ | [a] | [a] | $H_2O$ | $CO_2$[b] | [c] | VBD[d] | MV[e] | [f] |
|---|---|---|---|---|---|---|---|---|---|---|---|---|---|---|---|---|---|---|
| 145D1 | 50.44 | 1.30 | 13.42 | 12.84 | 0.22 | 7.11 | 11.67 | 1.98 | 0.09 | 0.09 | 0.117 | | 0.25 | | 0.83 | 0.31 | 0.25 | 1 |
| 146D1 | 50.54 | 1.10 | 13.59 | 12.03 | 0.22 | 7.54 | 12.26 | 1.87 | 0.07 | 0.07 | 0.109 | | 0.19 | | 0.83 | 0.22 | 0.19 | 1 |
| 147D5 | 49.43 | 1.01 | 14.24 | 11.77 | 0.20 | 8.72 | 11.81 | 1.88 | 0.07 | 0.07 | 0.096 | | 0.19 | | 0.83 | 0.34 | 0.19 | 1 |
| 147D6 | 49.91 | 1.03 | 14.29 | 11.50 | 0.19 | 8.73 | 11.94 | 1.87 | 0.07 | 0.07 | 0.107 | | 0.19 | | 0.83 | -0.08 | 0.19 | 1 |
| 150D3 | 50.15 | 1.52 | 13.38 | 13.15 | 0.22 | 6.94 | 11.60 | 2.04 | 0.15 | 0.11 | 0.120 | | 0.36 | | 0.84 | 0.20 | 0.36 | 1 |
| 153D3 | 48.89 | 0.98 | 15.26 | 10.45 | 0.17 | 9.01 | 12.42 | 1.89 | 0.07 | 0.06 | 0.086 | | 0.17 | | 0.83 | 0.40 | 0.17 | 1 |
| 154D1 | 50.21 | 1.32 | 13.91 | 12.55 | 0.21 | 7.26 | 11.89 | 2.00 | 0.14 | 0.09 | 0.108 | | 0.30 | | 0.83 | -0.08 | 0.30 | 1 |
| 155D6 | 49.83 | 1.08 | 14.52 | 11.36 | 0.18 | 8.09 | 12.21 | 1.92 | 0.09 | 0.07 | 0.089 | | 0.23 | | 0.83 | 0.22 | 0.23 | 1 |
| 157D3 | 49.63 | 1.11 | 14.66 | 11.20 | 0.18 | 8.50 | 12.15 | 1.92 | 0.10 | 0.07 | 0.090 | | 0.24 | | 0.83 | 0.05 | 0.24 | 1 |
| 158D2 | 50.36 | 1.44 | 13.54 | 12.75 | 0.21 | 6.89 | 11.46 | 2.06 | 0.15 | 0.13 | 0.129 | | 0.34 | | 0.83 | 0.46 | 0.34 | 1 |
| 160D4 | 50.33 | 1.44 | 13.62 | 12.79 | 0.20 | 6.86 | 11.45 | 2.04 | 0.13 | 0.13 | 0.121 | | 0.30 | | 0.84 | 0.48 | 0.30 | 1 |
| 162D2 | 50.41 | 1.41 | 13.55 | 12.77 | 0.20 | 6.90 | 11.45 | 2.00 | 0.13 | 0.13 | 0.125 | | 0.31 | | 0.84 | 0.52 | 0.31 | 1 |
| 164D5 | 50.50 | 1.46 | 13.35 | 13.02 | 0.23 | 6.75 | 11.42 | 2.05 | 0.15 | 0.13 | 0.130 | | 0.32 | | 0.84 | 0.39 | 0.32 | 1 |
| 169D6 | 50.51 | 1.42 | 13.52 | 13.10 | 0.23 | 6.68 | 11.41 | 2.11 | 0.15 | 0.12 | 0.118 | | 0.32 | | 0.84 | 0.23 | 0.32 | 1 |
| 173D1 | 50.81 | 1.52 | 13.31 | 13.25 | 0.22 | 6.51 | 11.29 | 2.15 | 0.19 | 0.11 | 0.125 | | 0.37 | | 0.84 | 0.09 | 0.37 | 1 |
| 175D8 | 49.34 | 1.44 | 13.90 | 12.36 | 0.18 | 7.20 | 11.46 | 2.07 | 0.20 | 0.15 | 0.101 | | 0.40 | | 0.84 | 1.23 | 0.40 | 1 |
| 177D3 | 48.79 | 1.29 | 14.40 | 11.31 | 0.17 | 7.94 | 12.20 | 1.96 | 0.18 | 0.12 | 0.079 | | 0.29 | | 0.84 | 1.25 | 0.29 | 1 |
| 179D3 | 49.46 | 1.28 | 14.41 | 11.38 | 0.19 | 7.80 | 12.27 | 1.96 | 0.18 | 0.11 | 0.086 | | 0.31 | | 0.84 | 0.54 | 0.31 | 1 |
| 182D3 | 49.82 | 1.55 | 13.90 | 12.72 | 0.21 | 7.06 | 11.31 | 2.10 | 0.18 | 0.15 | 0.113 | | 0.38 | | 0.84 | 0.49 | 0.38 | 1 |
| 185D4 | 49.21 | 1.70 | 13.77 | 12.77 | 0.23 | 7.28 | 11.90 | 2.11 | 0.18 | 0.15 | 0.097 | | 0.28 | | 0.83 | 0.22 | 0.28 | 1 |
| 98D3 | 50.69 | 1.32 | 13.57 | 12.74 | 0.22 | 7.16 | 11.75 | 2.06 | 0.07 | 0.07 | 0.126 | | 0.23 | | 0.84 | -0.20 | 0.23 | 1 |
| Riker et al. (2015) | | | | | | | | | | | | | | | | | | |
| PSB26 | 67.36 | 0.29 | 14.57 | 1.76 | 0.05 | 0.69 | 2.42 | 4.51 | 1.89 | 0.11 | | | 6.69 | 63 | 0.48 | 6.25 | 6.70 | 3 |
| PSB58 | 64.70 | 0.30 | 14.94 | 3.01 | 0.06 | 0.89 | 2.86 | 4.52 | 1.65 | 0.09 | | | 6.63 | 32 | 0.66 | 6.87 | 6.63 | 3 |
| PSB62 | 63.59 | 0.35 | 14.68 | 3.26 | 0.05 | 0.73 | 2.82 | 4.31 | 1.63 | 0.07 | | | 8.55 | 34 | 0.70 | 8.40 | 8.55 | 3 |
| PSB63 | 64.21 | 0.33 | 14.81 | 3.26 | 0.07 | 0.75 | 2.91 | 4.35 | 1.70 | 0.10 | | | 7.11 | 1001 | 0.76 | 7.41 | 7.21 | 3 |
| PSB64 | 64.39 | 0.33 | 14.90 | 3.20 | 0.06 | 0.64 | 2.88 | 4.48 | 1.73 | 0.11 | | | 6.00 | 1408 | 0.77 | 7.19 | 6.14 | 3 |
| PSB65 | 61.05 | 0.32 | 14.41 | 3.22 | 0.04 | 0.77 | 2.78 | 4.17 | 1.66 | 0.09 | | | 9.62 | 63 | 0.65 | 11.37 | 9.63 | 3 |
| PSB66 | 62.25 | 0.33 | 14.64 | 3.24 | 0.06 | 0.72 | 2.83 | 4.41 | 1.72 | 0.10 | | | 7.93 | 1700 | 0.74 | 9.61 | 8.10 | 3 |

**Table B.1:** Composition of silicate glasses used in Chapters 2 and 3 *cont.*

| Sample | $SiO_2$ | $TiO_2$ | $Al_2O_3$ | $FeO_T$ | MnO | MgO | CaO | $Na_2O$ | $K_2O$ | $P_2O_5$ | [a] | [a] | $H_2O$ | $CO_2$[b] | [c] | VBD[d] | MV[e] | [f] |
|---|---|---|---|---|---|---|---|---|---|---|---|---|---|---|---|---|---|---|
| PSB67 | 63.57 | 0.34 | 14.94 | 3.20 | 0.08 | 0.52 | 2.89 | 4.58 | 1.77 | 0.09 | | | 6.16 | 2329 | 0.77 | 7.95 | 6.39 | 3 |
| Smith et al. (2010) | | | | | | | | | | | | | | | | | | |
| Re1_910_1 | 72.11 | 0.14 | 11.62 | 0.95 | 0.10 | 0.20 | 1.09 | 3.94 | 2.94 | 0.00 | | | 4.12 | 799 | | 6.80 | 4.20 | 1 |
| Re1_910_2 | 73.39 | 0.13 | 11.34 | 0.77 | 0.03 | 0.12 | 0.60 | 3.92 | 3.26 | 0.08 | | | 3.55 | 442 | | 6.28 | 3.60 | 1 |
| Re1_910_3 | 71.77 | 0.12 | 12.14 | 0.80 | 0.08 | 0.14 | 0.95 | 3.83 | 3.23 | 0.01 | | | 3.41 | 366 | | 6.84 | 3.45 | 1 |
| Re1_911_p4-miC | 71.70 | 0.13 | 12.31 | 1.18 | 0.00 | 0.18 | 0.98 | 2.53 | 4.19 | 0.04 | | | 7.52 | | | 6.64 | 7.52 | 1 |
| Re1_911_p5-miB | 73.88 | 0.12 | 11.96 | 0.92 | 0.00 | 0.16 | 0.93 | 3.40 | 3.07 | 0.04 | | | 5.81 | | | 5.42 | 5.81 | 1 |
| Re2_915_1 | 73.48 | 0.13 | 11.71 | 0.96 | 0.01 | 0.13 | 0.77 | 3.62 | 3.01 | 0.00 | | | 4.01 | 303 | | 6.08 | 4.04 | 1 |
| Re2_915_2 | 73.18 | 0.13 | 11.86 | 0.80 | 0.03 | 0.11 | 0.83 | 4.07 | 3.02 | 0.00 | | | 4.75 | 289 | | 5.86 | 4.77 | 1 |
| Re2_915_3 | 73.15 | 0.13 | 11.40 | 0.82 | 0.04 | 0.11 | 0.74 | 3.80 | 3.11 | 0.03 | | | 4.50 | 295 | | 6.58 | 4.53 | 1 |
| Re2_915_4 | 72.59 | 0.14 | 11.72 | 0.80 | 0.01 | 0.14 | 0.76 | 3.78 | 3.06 | 0.03 | | | 4.32 | 260 | | 6.88 | 4.35 | 1 |
| Re2_915_miA | 74.26 | 0.15 | 11.99 | 0.95 | 0.03 | 0.17 | 1.09 | 3.36 | 2.91 | 0.00 | | | 5.66 | | | 5.00 | 5.66 | 1 |
| Re2_915_miB | 73.38 | 0.13 | 11.52 | 0.95 | 0.05 | 0.13 | 0.75 | 2.46 | 3.83 | 0.01 | | | 6.55 | | | 6.68 | 6.55 | 1 |
| Re2_915_miC | 73.14 | 0.14 | 12.03 | 0.96 | 0.05 | 0.12 | 0.89 | 3.19 | 3.01 | 0.04 | | | 5.07 | | | 6.32 | 5.07 | 1 |
| Re2_559-1_2 | 76.99 | 0.14 | 12.36 | 0.82 | 0.00 | 0.14 | 0.77 | 3.90 | 3.91 | 0.00 | | | 1.24 | 596 | | 0.87 | 1.30 | 1 |
| Re2_559-1_4 | 77.25 | 0.13 | 12.28 | 0.87 | 0.05 | 0.13 | 0.77 | 3.80 | 3.66 | 0.07 | | | 1.01 | 414 | | 0.89 | 1.05 | 1 |
| Re2_559-1_5 | 76.71 | 0.12 | 12.28 | 0.91 | 0.05 | 0.12 | 0.82 | 3.94 | 3.47 | 0.01 | | | 0.71 | 375 | | 1.46 | 0.74 | 1 |
| Re3_918_1 | 72.59 | 0.13 | 11.48 | 0.75 | 0.10 | 0.13 | 0.83 | 3.59 | 3.04 | 0.02 | | | 3.74 | 257 | | 7.26 | 3.76 | 1 |
| Re3_918_2 | 73.41 | 0.13 | 11.66 | 0.91 | 0.13 | 0.18 | 0.79 | 3.86 | 3.11 | 0.02 | | | 3.80 | 291 | | 5.70 | 3.83 | 1 |
| Re3_918_3 | 72.60 | 0.12 | 11.91 | 1.01 | 0.04 | 0.18 | 1.05 | 3.66 | 3.02 | 0.00 | | | 3.73 | 264 | | 6.30 | 3.76 | 1 |
| Re3_918_4 | 73.22 | 0.11 | 11.62 | 0.83 | 0.05 | 0.13 | 0.88 | 3.73 | 3.06 | 0.00 | | | 3.89 | 234 | | 6.28 | 3.92 | 1 |
| Re3_918_miA | 74.62 | 0.10 | 11.56 | 0.80 | 0.05 | 0.07 | 0.64 | 2.98 | 4.20 | 0.02 | | | 5.04 | | | 4.88 | 5.04 | 1 |
| Re3_918_miE | 75.13 | 0.10 | 11.70 | 0.92 | 0.02 | 0.11 | 0.73 | 3.62 | 3.49 | 0.03 | | | 4.88 | | | 4.04 | 4.88 | 1 |
| EQ1_P6-miA | 72.65 | 0.09 | 12.07 | 1.07 | 0.10 | | 0.82 | | 4.21 | 0.00 | | | 5.90 | | | 8.88 | 5.90 | 1 |
| EQ1_P5-miB | 72.71 | 0.12 | 11.89 | 0.89 | 0.05 | 0.09 | 0.76 | 3.29 | 4.28 | 0.00 | | | 4.70 | | | 5.83 | 4.70 | 1 |
| EQ4_P11-miC | 73.57 | 0.09 | 11.67 | 0.92 | 0.05 | 0.09 | 0.62 | 2.91 | 4.18 | 0.00 | | | 3.39 | | | 5.79 | 3.39 | 1 |
| EQ4_P11-miD | 74.91 | 0.09 | 12.01 | 0.88 | 0.03 | 0.09 | 0.73 | 3.31 | 4.25 | 0.00 | | | 6.20 | | | 3.60 | 6.20 | 1 |
| Stamper et al. (2014) | | | | | | | | | | | $Cr_2O_3$ | NiO | | | | | | |
| 10 | 43.30 | 1.02 | 14.00 | 8.71 | 0.18 | 10.53 | 11.99 | 2.05 | 0.56 | 0.27 | 0.07 | 0.02 | 3.59 | 5600 | 0.51 | 6.82 | 4.15 | 1 |

**Table B.1:** Composition of silicate glasses used in Chapters 2 and 3 *cont.*

| Sample | $SiO_2$ | $TiO_2$ | $Al_2O_3$ | $FeO_T$ | MnO | MgO | CaO | $Na_2O$ | $K_2O$ | $P_2O_5$ | [a] | [a] | $H_2O$ | $CO_2$[b] | [c] | VBD[d] | MV[e] | [f] |
|---|---|---|---|---|---|---|---|---|---|---|---|---|---|---|---|---|---|---|
| 12 | 44.01 | 1.15 | 15.19 | 8.85 | 0.20 | 9.60 | 10.53 | 2.71 | 0.79 | 0.28 | 0.01 | 0.04 | 3.77 | 3700 | 0.44 | 6.09 | 4.14 | 1 |
| 15 | 43.61 | 0.97 | 13.61 | 9.14 | 0.19 | 10.90 | 12.36 | 2.18 | 0.57 | 0.22 | 0.08 | 0.02 | 3.63 | 1500 | 0.49 | 5.63 | 3.78 | 1 |
| 22 or GRN22 | 44.05 | 1.00 | 13.78 | 9.02 | 0.21 | 10.39 | 12.07 | 2.25 | 0.61 | 0.25 | 0.03 | 0.04 | 2.90 | 1700 | 0.33 | 5.63 | 3.07 | 3 |
| 23 or GRN23 | 43.78 | 0.91 | 12.62 | 8.86 | 0.17 | 12.32 | 12.30 | 1.87 | 0.53 | 0.23 | 0.08 | 0.04 | 3.15 | 1500 | 0.43 | 5.73 | 3.30 | 3 |
| 25 or GRN25 | 44.33 | 0.93 | 12.66 | 9.00 | 0.18 | 12.66 | 12.36 | 1.84 | 0.52 | 0.20 | 0.07 | 0.03 | 3.42 | 1800 | 0.37 | 4.59 | 3.60 | 3 |
| 28 or GRN28 | 44.05 | 0.91 | 12.66 | 8.91 | 0.18 | 12.81 | 12.42 | 2.00 | 0.52 | 0.21 | 0.06 | 0.04 | 3.10 | 1400 | 0.30 | 4.54 | 3.24 | 3 |
| 30 | 43.53 | 0.92 | 12.89 | 9.01 | 0.17 | 12.55 | 12.33 | 2.07 | 0.55 | 0.25 | 0.07 | 0.04 | 3.73 | 1400 | 0.27 | 4.89 | 3.87 | 1 |
| 32 or GRN32 | 43.12 | 0.99 | 13.38 | 9.44 | 0.19 | 12.44 | 11.21 | 2.22 | 0.60 | 0.22 | 0.04 | 0.03 | 3.50 | 2000 | 0.31 | 5.39 | 3.70 | 3 |
| 33 | 43.28 | 0.89 | 12.22 | 8.69 | 0.17 | 13.81 | 12.15 | 1.93 | 0.53 | 0.21 | 0.12 | 0.02 | 3.77 | 13500 | 0.49 | 5.49 | 5.12 | 1 |
| 35 or GRN35 | 44.53 | 0.90 | 12.54 | 8.73 | 0.18 | 13.19 | 12.23 | 1.94 | 0.54 | 0.21 | 0.04 | 0.05 | 2.93 | 300 | 0.17 | 4.11 | 2.96 | 3 |
| 36 | 42.35 | 0.87 | 11.85 | 8.80 | 0.17 | 13.98 | 11.70 | 1.43 | 0.60 | 0.24 | 0.15 | 0.07 | 4.32 | 3800 | 0.14 | 6.95 | 4.70 | 1 |
| 38 | 43.60 | 0.87 | 12.14 | 8.97 | 0.18 | 14.41 | 11.98 | 2.00 | 0.52 | 0.22 | 0.14 | 0.06 | 2.89 | 1900 | 0.19 | 4.10 | 3.08 | 1 |
| 41 | 44.11 | 0.97 | 13.74 | 8.82 | 0.20 | 10.30 | 13.40 | 2.11 | 0.58 | 0.27 | 0.02 | 0.00 | 3.70 | 1400 | 0.29 | 4.78 | 3.84 | 1 |
| AN-1 or GRNAN1 | 45.31 | 0.94 | 12.94 | 9.57 | 0.19 | 13.08 | 13.22 | 2.24 | 0.57 | 0.24 | 0.06 | 0.05 | 0.28 | 400 | 0.32 | 0.87 | 0.32 | 3 |
| AN-2 | 45.38 | 0.92 | 12.55 | 8.93 | 0.20 | 15.07 | 12.72 | 2.13 | 0.57 | 0.24 | 0.14 | 0.03 | 0.32 | 500 | 0.39 | 0.51 | 0.37 | 1 |
| AN-3 | 45.26 | 0.96 | 12.41 | 9.51 | 0.18 | 13.82 | 12.85 | 2.18 | 0.58 | 0.24 | 0.10 | 0.04 | 0.38 | 600 | 0.31 | 1.14 | 0.44 | 1 |
| D-7 | 45.78 | 0.94 | 12.64 | 9.47 | 0.18 | 13.55 | 13.11 | 2.20 | 0.57 | 0.22 | 0.05 | 0.04 | 0.07 |  | 0.42 | 0.64 | 0.07 | 1 |
| R-1 or GRNR1 | 45.11 | 0.95 | 12.62 | 8.91 | 0.20 | 12.35 | 13.11 | 1.89 | 0.51 | 0.22 | 0.12 | 0.02 | 2.78 | 2100 | 0.56 | 3.55 | 2.99 | 3 |
| R-2 or GRNR2 | 44.30 | 1.08 | 13.72 | 9.58 | 0.20 | 10.00 | 12.51 | 2.30 | 0.60 | 0.27 | 0.04 | 0.04 | 3.26 | 3100 | 0.50 | 4.83 | 3.57 | 3 |
| R-5 | 44.72 | 0.95 | 12.35 | 9.34 | 0.19 | 12.15 | 13.19 | 2.14 | 0.51 | 0.24 | 0.08 | 0.06 | 2.56 | 2200 | 0.37 | 3.42 | 2.78 | 1 |
| R-6 or GRN6 | 44.43 | 0.92 | 11.65 | 9.17 | 0.20 | 13.83 | 12.55 | 1.95 | 0.49 | 0.24 | 0.14 | 0.05 | 2.90 | 2300 | 0.49 | 3.86 | 3.13 | 3 |
| RD-1 | 46.25 | 0.92 | 13.25 | 8.93 | 0.24 | 12.45 | 13.25 | 2.31 | 0.61 | 0.27 | 0.09 | 0.03 | 0.03 |  | 0.75 | 1.15 | 0.03 | 1 |
| W-1 | 43.74 | 1.02 | 14.20 | 8.82 | 0.17 | 9.06 | 13.13 | 2.35 | 0.65 | 0.28 | 0.03 | 0.02 | 4.99 | 2100 | 0.47 | 6.01 | 5.20 | 1 |
| W-3 | 43.43 | 0.90 | 12.28 | 9.10 | 0.20 | 13.00 | 12.70 | 2.08 | 0.55 | 0.22 | 0.05 | 0.08 | 3.07 |  | 0.31 | 4.71 | 3.07 | 1 |
| Webster and Duffield (1991) |  |  |  |  |  |  |  |  |  |  | Cl | F |  |  |  |  |  |  |
| IDC_1 | 73.20 | 0.01 | 14.79 | 0.62 | 0.04 |  | 0.16 | 3.54 | 5.67 |  | 0.26 | 0.61 | 1.10 |  |  | 1.03 | 1.10 | 1 |
| IDC_2 | 72.65 | 0.06 | 15.09 | 0.10 | 0.03 |  | 0.49 | 4.03 | 6.18 |  | 0.26 | 0.11 | 0.40 |  |  | 0.99 | 0.40 | 1 |
| IDC_3 | 76.54 | 0.11 | 13.02 | 0.16 | 0.02 |  | 0.40 | 3.43 | 5.39 |  | 0.31 |  | 0.55 |  |  | 0.60 | 0.55 | 1 |
| IDC_4 | 72.73 | 0.07 | 13.80 | 0.26 | 0.07 | 0.02 | 0.41 | 3.97 | 6.32 |  | 0.20 | 0.12 | 1.90 |  |  | 2.00 | 1.90 | 1 |

**Table B.1:** Composition of silicate glasses used in Chapters 2 and 3 *cont.*

| Sample | $SiO_2$ | $TiO_2$ | $Al_2O_3$ | $FeO_T$ | MnO | MgO | CaO | $Na_2O$ | $K_2O$ | $P_2O_5$ | [a] | [a] | $H_2O$ | $CO_2$[b] | [c] | VBD[d] | MV[e] | [f] |
|---|---|---|---|---|---|---|---|---|---|---|---|---|---|---|---|---|---|---|
| IDC_5 | 73.11 | 0.15 | 14.08 | 0.31 | 0.05 | 0.03 | 0.46 | 3.93 | 5.30 | | 0.29 | 0.15 | 1.00 | | | 2.11 | 1.00 | 1 |
| IDC_6 | 73.81 | 0.18 | 13.88 | 0.35 | 0.03 | 0.02 | 0.40 | 3.90 | 5.24 | | 0.26 | 0.03 | 0.90 | | | 1.86 | 0.90 | 1 |
| IDC_7 | 73.87 | 0.19 | 14.09 | 0.14 | 0.06 | | 0.30 | 4.21 | 6.29 | | 0.26 | 0.03 | 0.60 | | | 0.54 | 0.60 | 1 |
| IDC_8 | 72.96 | 0.12 | 14.02 | 0.13 | 0.03 | 0.01 | 0.46 | 3.97 | 6.33 | | 0.36 | 0.12 | 1.60 | | | 1.48 | 1.60 | 1 |
| IDC_9 | 74.73 | 0.09 | 13.31 | 0.07 | 0.08 | | 0.52 | 3.74 | 5.93 | | 0.33 | 0.34 | 0.85 | | | 0.85 | 0.85 | 1 |
| IDC_10 | 72.81 | 0.10 | 14.22 | 0.46 | 0.05 | 0.01 | 0.50 | 3.87 | 6.45 | | 0.34 | 0.18 | 1.00 | | | 0.96 | 1.00 | 1 |
| IDC_11 | 72.92 | 0.12 | 14.64 | 0.18 | 0.12 | 0.02 | 0.52 | 3.76 | 6.25 | | 0.36 | | 1.10 | | | 1.09 | 1.10 | 1 |
| IDC_12 | 73.57 | 0.13 | 14.05 | 0.28 | 0.08 | | 0.44 | 3.97 | 6.48 | | 0.34 | 0.04 | 0.60 | | | 0.59 | 0.60 | 1 |
| CBT_20 | 74.16 | 0.14 | 13.95 | 1.22 | 0.06 | | 0.22 | 3.84 | 5.34 | | 0.22 | 0.06 | 0.80 | | | 0.65 | 0.80 | 1 |
| CBT_21 | 72.77 | 0.11 | 13.97 | 0.96 | 0.06 | | 0.26 | 3.79 | 5.52 | | 0.28 | 0.03 | 2.30 | | | 2.14 | 2.30 | 1 |
| CBT_22 | 74.26 | 0.13 | 13.90 | 1.04 | 0.10 | | 0.25 | 3.79 | 5.48 | | 0.23 | 0.17 | 0.55 | | | 0.53 | 0.55 | 1 |
| CBT_23 | 72.79 | 0.11 | 13.72 | 0.91 | 0.09 | 0.04 | 0.23 | 4.15 | 5.80 | | 0.30 | 0.10 | 2.70 | | | 1.66 | 2.70 | 1 |
| CBT_24 | 73.62 | 0.11 | 13.72 | 0.80 | 0.14 | 0.03 | 0.25 | 4.31 | 5.83 | | 0.30 | 0.24 | 0.60 | | | 0.56 | 0.60 | 1 |
| CBT_25 | 73.54 | 0.10 | 13.34 | 0.96 | 0.09 | 0.04 | 0.34 | 4.56 | 5.55 | | 0.30 | 0.14 | 1.00 | | | 0.93 | 1.00 | 1 |
| CBT_26 | 73.49 | 0.15 | 14.45 | 0.76 | 0.15 | 0.01 | 0.32 | 5.96 | 5.96 | | 0.34 | 0.23 | 0.75 | | | -1.90 | 0.75 | 1 |
| Webster et al. (1995) | | | | | | | | | | | Cl | F | | | | | | |
| Y2 28Q4 P6 | 73.00 | 0.10 | 12.00 | 1.30 | 0.01 | 0.02 | 0.55 | 3.30 | 4.80 | | 0.09 | 0.30 | 3.50 | | | 4.39 | 3.50 | 1 |
| U 32IIQ14 Un | 72.90 | 0.05 | 12.20 | 0.99 | 0.03 | 0.05 | 0.48 | 3.60 | 4.60 | | 0.12 | 0.30 | 4.20 | | | 4.57 | 4.20 | 1 |
| Y 35Q5 P6 | 72.80 | 0.06 | 11.90 | 1.02 | 0.05 | 0.01 | 0.50 | 3.80 | 4.70 | 0.03 | 0.13 | 0.20 | 4.00 | | | 4.69 | 4.00 | 1 |
| Y 35Q8 P6 | 76.60 | 0.06 | 11.00 | 0.88 | 0.07 | 0.02 | 0.51 | 4.00 | 4.60 | 0.02 | 0.07 | 0.10 | 3.80 | | | 1.97 | 3.80 | 1 |
| O2 36IIQ6 LFC | 73.50 | 0.24 | 12.00 | 1.14 | 0.03 | 0.13 | 0.52 | 2.50 | 5.70 | | 0.02 | 0.04 | 2.80 | | | 4.05 | 2.80 | 1 |
| Y 47Q4 P6 | 73.20 | 0.05 | 11.50 | 1.02 | 0.07 | 0.00 | 0.46 | 3.30 | 4.80 | | 0.21 | 0.36 | 4.50 | | | 4.92 | 4.50 | 1 |
| Y 47Q6 P6 | 74.00 | 0.04 | 11.70 | 1.16 | 0.03 | 0.03 | 0.50 | 3.30 | 4.80 | | 0.12 | 0.18 | 3.10 | | | 4.01 | 3.10 | 1 |
| Y 88Q3 LA | 75.10 | 0.08 | 11.90 | 1.06 | 0.03 | 0.01 | 0.48 | 3.50 | 4.80 | | 0.13 | 0.10 | 3.80 | | | 2.69 | 3.80 | 1 |
| Y 88Q4 LA | 74.90 | 0.08 | 11.80 | 0.91 | 0.03 | 0.04 | 0.41 | 3.40 | 4.80 | | 0.14 | 0.05 | 4.50 | | | 3.34 | 4.50 | 1 |
| Y 89Q6 LB | 70.70 | 0.04 | 11.40 | 1.02 | 0.05 | 0.01 | 0.43 | 4.20 | 4.40 | 0.00 | 0.24 | 0.58 | 2.30 | | | 6.82 | 2.30 | 1 |
| Y 89Q9 LB | 70.50 | 0.05 | 11.60 | 1.03 | 0.04 | 0.02 | 0.44 | 5.10 | 4.30 | | 0.25 | 0.66 | 3.20 | | | 5.90 | 3.20 | 1 |
| Y 90IIQ9 LK | 71.40 | 0.11 | 11.60 | 1.15 | 0.00 | 0.06 | 0.45 | 3.40 | 4.50 | 0.04 | 0.13 | 0.52 | 2.40 | | | 6.51 | 2.40 | 1 |
| Y2 92Q5 LB | 72.30 | 0.04 | 12.00 | 0.98 | 0.05 | 0.01 | 0.45 | 3.90 | 4.30 | | 0.24 | 0.72 | 3.20 | | | 4.90 | 3.20 | 1 |

**Table B.1:** Composition of silicate glasses used in Chapters 2 and 3 *cont.*

| Sample | $SiO_2$ | $TiO_2$ | $Al_2O_3$ | $FeO_T$ | MnO | MgO | CaO | $Na_2O$ | $K_2O$ | $P_2O_5$ | [a] | [a] | $H_2O$ | $CO_2$[b] | [c] | VBD[d] | MV[e] | [f] |
|---|---|---|---|---|---|---|---|---|---|---|---|---|---|---|---|---|---|---|
| Y 92Q11 LB | 71.50 | 0.10 | 11.60 | 0.93 | 0.05 | 0.00 | 0.37 | 4.00 | 4.20 | | 0.24 | 0.61 | 3.70 | | | 6.30 | 3.70 | 1 |
| Y 92Q12 LB | 72.10 | 0.05 | 12.00 | 1.01 | 0.06 | 0.02 | 0.43 | 3.90 | 4.30 | | 0.23 | 0.58 | 3.80 | | | 5.21 | 3.80 | 1 |
| Y 93Q9 LK | 73.10 | 0.07 | 11.30 | 1.01 | 0.01 | 0.06 | 0.42 | 3.10 | 4.40 | 0.00 | 0.12 | 0.51 | 4.00 | | | 5.79 | 4.00 | 1 |
| O2 106Q17 UB | 72.50 | 0.12 | 11.90 | 0.49 | 0.05 | 0.04 | 0.57 | 3.10 | 4.50 | | 0.04 | 0.01 | 6.30 | | | 6.63 | 6.30 | 1 |
| O 125Q18 FC | 74.20 | 0.23 | 12.20 | 1.09 | 0.01 | 0.11 | 0.57 | 2.40 | 5.90 | | 0.02 | 0.27 | 2.50 | | | 2.88 | 2.50 | 1 |
| O 130Q2 K | 76.30 | 0.19 | 12.30 | 1.13 | 0.00 | 0.10 | 0.57 | 2.20 | 5.80 | | 0.03 | 0.20 | 3.10 | | | 1.05 | 3.10 | 1 |
| O 131Q2 K | 73.70 | 0.11 | 11.90 | 1.09 | 0.07 | 0.07 | 0.64 | 3.00 | 4.10 | | 0.07 | 0.02 | 5.30 | | | 5.11 | 5.30 | 1 |
| Y 190Q8 LB | 72.20 | 0.05 | 11.50 | 0.99 | 0.05 | | 0.43 | 3.90 | 4.50 | | 0.23 | 0.50 | 1.60 | | | 5.54 | 1.60 | 1 |
| Y 190Q9 LB | 72.20 | 0.05 | 11.50 | 0.99 | 0.05 | | 0.43 | 3.90 | 4.50 | | 0.23 | 0.50 | 4.10 | | | 5.54 | 4.10 | 1 |
| U 197Q4 Un | 74.30 | 0.05 | 12.30 | 1.21 | 0.04 | 0.05 | 0.54 | 3.40 | 4.90 | | 0.10 | 0.16 | 3.80 | | | 2.82 | 3.80 | 1 |
| U 197Q5 Un | 70.60 | 0.04 | 12.30 | 1.08 | 0.07 | 0.02 | 0.43 | 4.00 | 4.30 | | 0.21 | 0.55 | 5.20 | | | 6.28 | 5.20 | 1 |
| U 197Q7 Un | 71.30 | 0.05 | 12.30 | 1.05 | 0.02 | 0.05 | 0.45 | 3.90 | 4.30 | | 0.14 | 0.71 | 4.20 | | | 5.61 | 4.20 | 1 |
| Y 228Q3 UK | 72.70 | 0.13 | 11.80 | 1.38 | 0.02 | 0.04 | 0.49 | 3.20 | 5.20 | | 0.08 | 0.11 | 2.40 | | | 4.70 | 2.40 | 1 |
| Y 228Q5 UK | 70.80 | 0.08 | 12.00 | 1.10 | 0.00 | 0.00 | 0.48 | 4.00 | 4.30 | | 0.16 | 0.68 | 6.50 | | | 6.28 | 6.50 | 1 |
| Webster et al. (1996) | | | | | | | | | | | Cl | F | | | | | | |
| 1 | 72.60 | 0.04 | 13.10 | 0.86 | 0.02 | 0.00 | 0.63 | 4.59 | 4.72 | | 0.14 | 0.48 | 2.40 | | | 2.72 | 2.40 | 1 |
| 2 | 73.90 | 0.14 | 12.70 | 0.91 | 0.01 | 0.01 | 0.61 | 4.41 | 4.63 | | 0.12 | 0.45 | 1.70 | | | 2.01 | 1.70 | 1 |
| 3 | 73.20 | 0.05 | 12.70 | 0.84 | 0.02 | 0.05 | 0.69 | 4.22 | 4.37 | | 0.14 | 0.60 | 2.50 | | | 3.03 | 2.50 | 1 |
| 4 | 72.60 | 0.05 | 13.20 | 0.95 | 0.01 | 0.03 | 0.73 | 4.39 | 4.59 | | 0.09 | 0.44 | 2.40 | | | 2.81 | 2.40 | 1 |
| 5 | 72.10 | 0.05 | 13.60 | 0.98 | 0.02 | 0.03 | 0.73 | 4.79 | 4.48 | | 0.22 | 0.82 | 1.50 | | | 2.07 | 1.50 | 1 |
| 6 | 72.70 | 0.05 | 13.10 | 0.91 | 0.00 | 0.01 | 0.63 | 4.64 | 4.77 | | 0.14 | 0.47 | 1.70 | | | 2.48 | 1.70 | 1 |
| 7 | 72.60 | 0.05 | 13.00 | 0.96 | 0.03 | 0.01 | 0.70 | 3.82 | 4.96 | | 0.10 | 0.43 | 2.70 | | | 3.23 | 2.70 | 1 |
| 8 | 73.20 | 0.04 | 12.90 | 0.93 | 0.03 | 0.01 | 0.67 | 4.05 | 5.20 | | 0.13 | 0.32 | 1.90 | | | 2.42 | 1.90 | 1 |
| 9 | 73.40 | 0.04 | 12.50 | 0.87 | 0.02 | 0.00 | 0.60 | 4.78 | 4.50 | | 0.15 | 0.49 | 2.50 | | | 2.55 | 2.50 | 1 |
| 10 | 72.90 | 0.02 | 12.10 | 0.86 | 0.03 | 0.00 | 0.62 | 4.49 | 4.57 | | 0.13 | 0.44 | 3.60 | | | 3.74 | 3.60 | 1 |
| 11 | 72.80 | 0.03 | 12.60 | 0.92 | 0.02 | 0.03 | 0.60 | 3.51 | 4.77 | | 0.13 | 0.41 | 3.50 | | | 4.08 | 3.50 | 1 |
| 12 | 72.80 | 0.04 | 14.10 | 1.01 | 0.03 | 0.00 | 0.65 | 3.62 | 5.20 | | 0.14 | 0.51 | 0.90 | | | 1.79 | 0.90 | 1 |
| 13 | 73.60 | 0.04 | 13.90 | 0.94 | 0.04 | 0.03 | 0.76 | 4.28 | 4.82 | | 0.19 | 0.33 | 0.60 | | | 0.97 | 0.60 | 1 |
| 14 | 72.70 | 0.02 | 14.30 | 0.93 | 0.05 | 0.01 | 0.80 | 4.58 | 5.25 | | 0.22 | 0.62 | 0.20 | | | 0.42 | 0.20 | 1 |

**Table B.1:** Composition of silicate glasses used in Chapters 2 and 3 *cont.*

| Sample | $SiO_2$ | $TiO_2$ | $Al_2O_3$ | $FeO_T$ | MnO | MgO | CaO | $Na_2O$ | $K_2O$ | $P_2O_5$ | [a] | [a] | $H_2O$ | $CO_2$[b] | [c] | VBD[d] | MV[e] | [f] |
|---|---|---|---|---|---|---|---|---|---|---|---|---|---|---|---|---|---|---|
| 15 | 72.60 | 0.03 | 14.90 | 0.99 | 0.02 | 0.00 | 0.72 | 4.38 | 5.12 | | 0.24 | 0.57 | 0.40 | | | 0.32 | 0.40 | 1 |
| 16 | 72.50 | 0.01 | 14.90 | 0.76 | 0.02 | 0.00 | 0.45 | 4.82 | 5.30 | | 0.15 | 0.29 | 0.80 | | | 0.72 | 0.80 | 1 |
| 17 | 73.30 | 0.02 | 14.40 | 0.97 | 0.02 | 0.00 | 0.75 | 4.43 | 5.01 | | 0.18 | 0.62 | 0.30 | | | 0.19 | 0.30 | 1 |
| 18 | 74.30 | 0.04 | 13.80 | 0.83 | 0.03 | 0.00 | 0.69 | 4.18 | 4.94 | | 0.17 | 0.59 | 0.40 | | | 0.34 | 0.40 | 1 |
| 19 | 66.40 | 0.04 | 17.90 | 1.04 | 0.05 | 0.03 | 1.20 | 5.01 | 5.83 | | 0.27 | 1.07 | 0.80 | | | 1.04 | 0.80 | 1 |
| 21 | 66.60 | 0.03 | 17.80 | 1.08 | 0.04 | 0.04 | 1.06 | 4.88 | 5.81 | | 0.25 | 1.01 | 0.30 | | | 1.28 | 0.30 | 1 |
| 22 | 68.50 | 0.04 | 16.80 | 0.84 | 0.05 | 0.01 | 0.91 | 4.38 | 5.82 | | 0.22 | 0.91 | 0.30 | | | 1.43 | 0.30 | 1 |
| 29 | 72.10 | 0.03 | 14.40 | 1.18 | 0.03 | 0.02 | 0.74 | 4.29 | 5.42 | | 0.19 | 0.64 | 0.30 | | | 0.83 | 0.30 | 1 |
| 30 | 71.80 | 0.04 | 14.60 | 1.09 | 0.01 | 0.00 | 0.74 | 4.22 | 5.34 | | 0.21 | 1.00 | 0.20 | | | 0.83 | 0.20 | 1 |
| 31 | 71.60 | 0.02 | 14.70 | 1.03 | 0.04 | 0.04 | 0.80 | 4.09 | 5.26 | | 0.20 | 1.25 | 0.30 | | | 0.86 | 0.30 | 1 |
| Wilke et al. (2002) | | | | | | | | | | | | | | | | | | |
| H 850°C NNO | 68.42 | | 12.93 | 1.26 | | | 5.09 | 1.88 | | | | | 10.70 | | 0.95 | 10.41 | 10.70 | 1 |
| H 850°C C-O-H | 68.69 | | 12.66 | 1.29 | | | 5.04 | 1.88 | | | | | 10.80 | | 0.97 | 10.44 | 10.80 | 1 |
| H 850°C CCO | 66.93 | | 12.64 | 1.27 | | | 5.08 | 2.01 | | | | | 11.10 | | 0.97 | 12.07 | 11.10 | 1 |
| H 950°C HM | 68.64 | | 12.75 | 1.30 | | | 5.07 | 2.00 | | | | | 10.70 | | 0.63 | 10.19 | 10.70 | 1 |
| H 950°C C-O-H | 68.67 | | 12.66 | 1.30 | | | 5.04 | 1.87 | | | | | 11.10 | | 0.95 | 10.46 | 11.10 | 1 |
| Zhang et al. (1997) | | | | | | | | | | | | | | | | | | |
| Ka | 76.10 | 0.01 | 12.57 | 0.93 | | 0.01 | 0.51 | 3.92 | 4.79 | | | | 0.75 | | | 1.05 | 0.75 | 1 |
| Mn | 76.05 | 0.05 | 12.51 | 0.95 | | 0.03 | 0.54 | 4.09 | 4.74 | | | | 0.81 | | | 0.94 | 0.81 | 1 |
| 6b1 | 75.33 | 0.06 | 12.49 | 1.10 | | 0.02 | 0.52 | 3.94 | 5.24 | | | | 1.02 | | | 1.17 | 1.02 | 1 |
| POB10 | 75.81 | 0.13 | 12.54 | 0.89 | | 0.03 | 0.46 | 3.70 | 4.89 | | | | 1.17 | | | 1.45 | 1.17 | 1 |
| bb3b-11 | 75.64 | 0.12 | 12.42 | 0.95 | | 0.03 | 0.53 | 3.88 | 4.73 | | | | 1.75 | | | 1.59 | 1.75 | 1 |
| bb3b-12 | 74.39 | 0.12 | 12.49 | 1.12 | | 0.06 | 0.52 | 4.00 | 4.57 | | | | 2.66 | | | 2.61 | 2.66 | 1 |
| LV-81-18A-09 | 75.10 | 0.12 | 11.79 | 0.51 | | 0.01 | 0.35 | 3.06 | 5.12 | | | | 3.90 | | | 3.88 | 3.90 | 1 |
| 6b-964 | 73.56 | 0.08 | 11.67 | 0.59 | | 0.04 | 0.32 | 3.65 | 4.15 | | | | 5.40 | | | 5.87 | 5.40 | 1 |
| Zhang et al. (2018) and this study[h] | | | | | | | | | | | | | | | | | | |
| AR10 140ox | 49.91 | 0.97 | 15.67 | 9.16 | 0.17 | 9.49 | 11.89 | 2.20 | 0.06 | 0.08 | | | 0.00 | | 0.18 | | | 2 |
| AR11 BezBA | 54.98 | 0.99 | 17.47 | 8.31 | 0.17 | 5.71 | 8.52 | 3.01 | 0.97 | 0.16 | | | 0.00 | | 0.20 | | | 2 |
| AR12 KLA-1-6-22 | 45.01 | 3.78 | 13.02 | 10.14 | 0.18 | 8.67 | 11.92 | 3.39 | 1.63 | 0.97 | | | 0.00 | | 0.14 | | | 2 |

**Table B.1:** Composition of silicate glasses used in Chapters 2 and 3 *cont.*

| Sample | $SiO_2$ | $TiO_2$ | $Al_2O_3$ | $FeO_T$ | MnO | MgO | CaO | $Na_2O$ | $K_2O$ | $P_2O_5$ | [a] | [a] | $H_2O$ | $CO_2$[b] | [c] | VBD[d] | MV[e] | [f] |
|---|---|---|---|---|---|---|---|---|---|---|---|---|---|---|---|---|---|---|
| AR13 LS | 54.06 | 3.02 | 12.44 | 12.03 | 0.30 | 4.17 | 9.51 | 3.09 | 0.28 | 0.66 | | | 0.00 | | 0.18 | | | 2 |
| AR14 PF22 | 53.60 | 1.59 | 19.68 | 5.76 | 0.16 | 2.73 | 4.65 | 7.50 | 3.83 | 0.47 | | | 0.00 | | 0.13 | | | 2 |
| AR15 SC1 | 50.20 | 2.57 | 15.20 | 10.67 | 0.00 | 6.38 | 11.16 | 2.90 | 0.35 | 0.04 | | | 0.00 | | 0.18 | | | 2 |
| AR16 140ox | 50.46 | 1.00 | 16.08 | 7.85 | 0.18 | 10.38 | 12.53 | 1.94 | 0.06 | 0.09 | | | 0.00 | | 0.97 | | | 2 |
| AR17 BezBA | 53.94 | 0.98 | 17.37 | 8.56 | 0.20 | 6.22 | 8.99 | 2.83 | 0.88 | 0.17 | | | 0.00 | | 0.90 | | | 2 |
| AR18 KLA-1-6-22 | 44.19 | 4.18 | 13.63 | 8.97 | 0.23 | 9.80 | 13.25 | 3.06 | 1.30 | 0.94 | | | 0.00 | | 0.98 | | | 2 |
| AR19 LS | 51.19 | 3.77 | 11.99 | 14.80 | 0.34 | 4.44 | 9.56 | 2.70 | 0.23 | 0.61 | | | 0.00 | | 0.92 | | | 2 |
| AR20 PF22 | 53.82 | 1.63 | 19.79 | 4.67 | 0.19 | 3.11 | 5.52 | 7.38 | 3.65 | 0.49 | | | 0.00 | | 0.98 | | | 2 |
| AR21 SC1 | 50.38 | 3.22 | 16.06 | 7.50 | 0.00 | 7.64 | 12.60 | 2.53 | 0.25 | 0.03 | | | 0.00 | | 0.95 | | | 2 |
| AR35 BezBA | 53.87 | 0.99 | 17.39 | 8.76 | 0.19 | 5.84 | 8.66 | 2.95 | 0.95 | 0.17 | | | 0.00 | | 0.40 | | | 2 |
| AR36 KLA-1-6-22 | 43.21 | 3.76 | 12.84 | 12.18 | 0.19 | 9.07 | 11.51 | 3.58 | 1.62 | 0.87 | | | 0.00 | | 0.42 | | | 2 |
| AR37 LS | 50.89 | 3.67 | 11.75 | 15.59 | 0.34 | 4.16 | 9.11 | 2.84 | 0.27 | 0.27 | | | 0.00 | | 0.40 | | | 2 |
| AR38 PF22 | 52.99 | 1.57 | 19.43 | 5.90 | 0.17 | 2.78 | 4.71 | 7.57 | 3.83 | 0.48 | | | 0.00 | | 0.28 | | | 2 |
| AR39 SC1 | 47.93 | 2.93 | 14.92 | 12.86 | 0.00 | 6.34 | 10.77 | 2.67 | 0.30 | 0.03 | | | 0.00 | | 0.39 | | | 2 |
| AR40 140ox | 49.88 | 1.00 | 15.74 | 9.03 | 0.17 | 9.57 | 11.92 | 2.35 | 0.10 | 0.08 | | | 0.00 | | 0.91 | | | 2 |
| AR41 BezBA | 55.86 | 0.99 | 17.99 | 6.10 | 0.17 | 5.95 | 8.90 | 3.18 | 0.99 | 0.14 | | | 0.00 | | 0.91 | | | 2 |
| AR42 KLA-1-6-22 | 43.18 | 3.77 | 12.96 | 12.12 | 0.18 | 9.07 | 11.45 | 3.86 | 1.63 | 0.90 | | | 0.00 | | 0.90 | | | 2 |
| AR43 LS | 49.83 | 3.47 | 11.57 | 17.31 | 0.32 | 4.01 | 8.76 | 3.01 | 0.27 | 0.61 | | | 0.00 | | 0.88 | | | 2 |
| AR44 SC1 | 48.17 | 2.86 | 15.00 | 13.07 | -0.01 | 6.34 | 10.79 | 2.95 | 0.33 | 0.02 | | | 0.00 | | 0.91 | | | 2 |

*Notes*: Oxides/elements in wt% (except [b] which is in ppm) labelled along the top, except [a] which is either $Cr_2O_3$, NiO, Cl, $S_T$, or F depending on the study; [c] which is $Fe^{2+}/Fe_T$; [d] VBD = volatiles by difference; and [e] MV = measured volatiles. [f] indicates where the samples is used: 1 = individual glass compositions referred to in Table 2.1; 2 = individual glass compositions referred to in Table 3.1; and 3 = individual glass compositions referred to in Tables 2.1 and 3.1. [g] Sample names abbreviated – see Table B.2 for full sample names. [h] Major and minor element chemistry measured as described in Table 4.3.

**Table B.2:** Abbreviated samples names in Table B.1.

| No. | Sample name | No. | Sample name | No. | Sample name |
|---|---|---|---|---|---|
| [001] | 18/05/1980 KC519PFB 518b-4-1 | [013] | 16/10/1980 USNM115418-42 418-42-10-6 | [025] | 27/12/1980 USNM115427-1 427-1-2-2 |
| [002] | 18/05/1980 KC519PFB 518b-5-1 | [014] | 16/10/1980 USNM115418-42 418-42-2-2 | [026] | 27/12/1980 USNM115427-1 427-1-6-3 |
| [003] | 18/05/1980 KC519PFB plz-30-1 | [015] | 16/10/1980 USNM115418-42 418-42-2-3 | [027] | 27/12/1980 USNM115427-1 427-4-2-2 |
| [004] | 12/06/1980 KC612PF jun-9-1 | [016] | 16/10/1980 USNM115418-60-2 60-2-10-1 | [028] | 19/03/1982 USNM115773-18 773-18-1-3 |
| [005] | 22/07/1980 KC722U jul-1-1 | [017] | 16/10/1980 USNM115418-60-2 60-2-2-2 | [029] | 19/03/1982 USNM115773-18 773-18-3-1 |
| [006] | 07/08/1980 KC807B 807b-5-1 | [018] | 16/10/1980 USNM115418-60-2 60-2-2-4 | [030] | 19/03/1982 USNM115773-18 773-18-4-1 |
| [007] | 07/08/1980 KC807B 807b-6-1 | [019] | 16/10/1980 USNM115418-60-2 60-2-3-gm | [031] | 11/09/1984 SH184 sh184-3-1 |
| [008] | 07/08/1980 KC807B 807b-8-2 | [020] | 16/10/1980 USNM115418-60-2 60-2-3-gm2 | [032] | 11/09/1984 SH184 sh184-3-2 |
| [009] | 07/08/1980 KC807B 807b-8-3 | [021] | 16/10/1980 USNM115418-60-2 60-2-6-1 | [033] | 11/09/1984 SH184 sh184-5-1 |
| [010] | 07/08/1980 KC807B 807b-9-1 (tube) | [022] | 16/10/1980 USNM115418-60-2 60-2-6-2 | [034] | 11/09/1984 SH184 sh184-6-1 |
| [011] | 07/08/1980 KC807B 807b-9-3 | [023] | 16/10/1980 USNM115418-60-2 60-2-8-1 | | |
| [012] | 07/08/1980 KC807B 807b-9-4 | [024] | 27/12/1980 USNM115427-1 427-1-2-1 | | |

# Appendix C
## Chapter 2 data: Effects of sub-surface charging on VBD using EPMA

**Table C.1**: Intensity (*I*) of X-rays from St8.1.B composition from Win X-ray calculations.

**Table C.1:** Intensity ($I$) of X-rays from St8.1.B composition from Win X-ray calculations.

| | | $H_2O$ (wt%) | 0 | 5 | 10 | 0 | 5 | 10 | 0 | 5 | 10 | 0 | 5 | 10 | 0 | 5 | 10 |
|---|---|---|---|---|---|---|---|---|---|---|---|---|---|---|---|---|---|
| | | $F_{max}$ (V·nm$^{-1}$) | 0.00 | 0.00 | 0.00 | 0.10 | 0.10 | 0.10 | 0.05 | 0.05 | 0.05 | 0.15 | 0.15 | 0.15 | 0.20 | 0.20 | 0.20 |
| Line | Z | Energy (eV) | $I$ | $I$ | $I$ | $I'_{0.10}$ | $I'_{0.10}$ | $I'_{0.10}$ | $I'_{0.05}$ | $I'_{0.05}$ | $I'_{0.05}$ | $I'_{0.15}$ | $I'_{0.15}$ | $I'_{0.15}$ | $I'_{0.20}$ | $I'_{0.20}$ | $I'_{0.20}$ |
| O$K\alpha_1$ | 8 | 523 | 41.93 | 42.73 | 43.96 | 42.01 | 42.79 | 44.04 | 41.98 | 42.76 | 44.00 | 42.05 | 42.85 | 44.09 | 42.03 | 42.81 | 44.10 |
| Na$K\alpha_1$ | 11 | 1041.0 | 742.4 | 662.7 | 589.0 | 741.6 | 661.7 | 588.4 | 741.9 | 662.3 | 588.6 | 741.1 | 661.5 | 588.0 | 740.4 | 660.4 | 587.6 |
| Na$K\alpha_2$ | 11 | 1041.0 | 372.8 | 332.7 | 295.7 | 372.3 | 332.2 | 295.4 | 372.5 | 332.5 | 295.5 | 372.1 | 332.1 | 295.2 | 371.7 | 331.6 | 295.0 |
| Mg$K\alpha_1$ | 12 | 1254 | 4671 | 4272 | 3907 | 4647 | 4246 | 3886 | 4659 | 4260 | 3896 | 4633 | 4236 | 3872 | 4623 | 4221 | 3863 |
| Mg$K\alpha_2$ | 12 | 1254 | 2348 | 2147 | 1964 | 2336 | 2134 | 1953 | 2342 | 2141 | 1958 | 2328 | 2129 | 1946 | 2323 | 2121 | 1941 |
| Al$K\alpha_1$ | 13 | 1487 | 19910 | 18640 | 17380 | 19740 | 18450 | 17220 | 19830 | 18540 | 17300 | 19640 | 18370 | 17120 | 19570 | 18270 | 17050 |
| Al$K\alpha_2$ | 13 | 1486 | 9994 | 9355 | 8724 | 9909 | 9259 | 8643 | 9954 | 9308 | 8681 | 9858 | 9220 | 8591 | 9826 | 9171 | 8556 |
| Al$K\beta_1$ | 13 | 1553 | 332.7 | 313.3 | 293.6 | 329.5 | 309.7 | 290.5 | 331.2 | 311.6 | 292.0 | 327.6 | 308.2 | 288.6 | 326.5 | 306.4 | 287.3 |
| Si$K\alpha_1$ | 14 | 1740 | 59640 | 56670 | 53680 | 59050 | 55970 | 53070 | 59370 | 56320 | 53360 | 58690 | 55680 | 52680 | 58460 | 55330 | 52420 |
| Si$K\alpha_2$ | 14 | 1739 | 29990 | 28490 | 26990 | 29690 | 28140 | 26680 | 29850 | 28320 | 26830 | 29510 | 28000 | 26490 | 29400 | 27820 | 26360 |
| Si$K\beta_1$ | 14 | 1832 | 2452 | 2343 | 2229 | 2424 | 2310 | 2201 | 2439 | 2327 | 2214 | 2408 | 2297 | 2183 | 2398 | 2281 | 2171 |
| K$K\alpha_1$ | 19 | 3313 | 2863 | 2806 | 2728 | 2809 | 2740 | 2667 | 2837 | 2772 | 2695 | 2779 | 2712 | 2631 | 2758 | 2681 | 2604 |
| K$K\alpha_2$ | 19 | 3310 | 1449 | 1419 | 1380 | 1421 | 1387 | 1349 | 1436 | 1402 | 1364 | 1406 | 1372 | 1331 | 1395 | 1357 | 1318 |
| K$K\beta_1$ | 19 | 3589 | 527.3 | 518.0 | 504.5 | 516.9 | 505.5 | 492.9 | 522.3 | 511.5 | 498.3 | 511.1 | 500.1 | 486.0 | 507.0 | 494.2 | 480.8 |
| Ca$K\alpha_1$ | 20 | 3691 | 17880 | 17520 | 17070 | 17530 | 17090 | 16660 | 17710 | 17300 | 16850 | 17330 | 16900 | 16420 | 17190 | 16700 | 16240 |
| Ca$K\alpha_2$ | 20 | 3688 | 9068 | 8886 | 8656 | 8887 | 8667 | 8447 | 8980 | 8773 | 8545 | 8788 | 8571 | 8328 | 8714 | 8468 | 8233 |
| Ca$K\beta_1$ | 20 | 4012 | 3505 | 3442 | 3358 | 3433 | 3355 | 3275 | 3470 | 3397 | 3314 | 3394 | 3317 | 3227 | 3364 | 3275 | 3189 |
| Ti$K\alpha_1$ | 22 | 4510 | 797 | 786 | 756 | 781 | 766 | 736 | 789 | 776 | 745 | 772 | 757 | 725 | 765 | 747 | 716 |
| Ti$K\alpha_2$ | 22 | 4504 | 405 | 399 | 384 | 397 | 389 | 374 | 401 | 394 | 379 | 393 | 385 | 368 | 389 | 380 | 364 |
| Ti$K\beta_1$ | 22 | 4931 | 169 | 167 | 161 | 166 | 163 | 156 | 167 | 165 | 158 | 164 | 161 | 154 | 162 | 159 | 152 |
| Fe$K\alpha_1$ | 26 | 6403 | 4519 | 4297 | 4095 | 4436 | 4195 | 3979 | 4477 | 4244 | 4036 | 4396 | 4147 | 3924 | 4357 | 4103 | 3871 |
| Fe$K\alpha_2$ | 26 | 6390 | 2308 | 2194 | 2091 | 2265 | 2142 | 2032 | 2286 | 2167 | 2061 | 2245 | 2118 | 2004 | 2225 | 2095 | 1977 |
| Fe$K\beta_1$ | 26 | 7057 | 951.3 | 904.8 | 862.5 | 933.7 | 883.1 | 837.9 | 942.3 | 893.6 | 849.9 | 925.2 | 873.0 | 826.2 | 917.0 | 863.5 | 814.9 |
| Fe$L\alpha$ | 26 | 705 | 37.44 | 32.39 | 28.12 | 37.52 | 32.43 | 28.18 | 37.50 | 32.41 | 28.15 | 37.57 | 32.49 | 28.21 | 37.54 | 32.44 | 28.22 |
| Fe$L\beta_1$ | 26 | 717 | 2.050 | 1.787 | 1.563 | 2.054 | 1.789 | 1.567 | 2.053 | 1.788 | 1.565 | 2.057 | 1.792 | 1.569 | 2.056 | 1.790 | 1.569 |

# Appendix D – Chapter 3 data: High-resolution EPMA of $Fe^{2+}/Fe_T$ in silicate glass

## D.1. Time-dependent ratio flank method protocol

1. Set analytical conditions: 15 kV accelerating voltage, 10 nA beam current and focussed beam. Focus z.
2. Assign spectrometers: TAPs (e.g., TAP, LTAP, and TAPH) on F$K\alpha$, PETs on K$K\alpha$, and LIFs on Fe$K\alpha$.
3. Change conditions: 10 μm beam diameter (may need 50 nA beam current for peaking up on $MgF_2$).
4. Peak-up spectrometers and set PHA windows: F$K\alpha$ on $MgF_2$, K$K\alpha$ on sanidine, and Fe$K\alpha$ on basaltic glass.
5. Calculate current Fe$L\alpha_f$ and Fe$L\beta_f$ positions using spectrometer positions from F$K\alpha$ peak positions.
6. New spectrometer set-up: change TAPs to Fe$L\alpha_f$ and Fe$L\beta_f$.
7. If using Probe for EPMA software: select MAN backgrounds, collect standards (e.g., on sanidine, basaltic glass, NaCl, and MgO) otherwise software will not let you export the data.
   (a) If using Probe for EPMA software use time-dependent intensity option: each measurement is 120 s with 24 intervals.
   (b) Otherwise, each measurement 5 s. Either add 24 measurements on the same point or add a line scan of 24 points where the start and end position are the same.
8. Collect unknowns and standards (e.g., ten analyses per sample).
9. Average data for each sample.
10. Process data
11. Produce calibration curve and calculate $Fe^{2+}/Fe_T$ for unknowns.

**Table D.1:** Wavescan data of Fe*L* for glasses in Figure 3.3.

| Accelerating voltage | 15 kV | | | | | 30 kV | |
|---|---|---|---|---|---|---|---|
| L (mm) | AR10 | AR14 | AR16 | AR19 | AR20 | AR14 | AR19 |
| 186.35 | 0.70 | 0.58 | 0.64 | 0.89 | 0.51 | 0.71 | 0.91 |
| 186.42 | 0.71 | 0.56 | 0.65 | 0.94 | 0.54 | 0.69 | 0.96 |
| 186.50 | 0.73 | 0.58 | 0.70 | 0.97 | 0.55 | 0.70 | 0.96 |
| 186.57 | 0.71 | 0.60 | 0.72 | 1.04 | 0.65 | 0.75 | 0.98 |
| 186.64 | 0.81 | 0.59 | 0.72 | 1.05 | 0.62 | 0.73 | 0.99 |
| 186.71 | 0.90 | 0.67 | 0.83 | 1.10 | 0.62 | 0.75 | 1.04 |
| 186.78 | 0.87 | 0.66 | 0.81 | 1.11 | 0.63 | 0.75 | 1.09 |
| 186.85 | 0.92 | 0.74 | 0.80 | 1.20 | 0.68 | 0.78 | 1.12 |
| 186.92 | 0.88 | 0.75 | 0.87 | 1.29 | 0.66 | 0.79 | 1.14 |
| 186.99 | 0.98 | 0.77 | 0.90 | 1.35 | 0.68 | 0.83 | 1.18 |
| 187.06 | 1.07 | 0.83 | 0.94 | 1.43 | 0.79 | 0.83 | 1.23 |
| 187.13 | 1.16 | 0.89 | 1.05 | 1.52 | 0.78 | 0.85 | 1.27 |
| 187.20 | 1.22 | 0.90 | 0.99 | 1.59 | 0.82 | 0.92 | 1.35 |
| 187.27 | 1.28 | 0.95 | 1.04 | 1.66 | 0.80 | 0.92 | 1.42 |
| 187.34 | 1.30 | 0.97 | 1.13 | 1.86 | 0.84 | 0.95 | 1.47 |
| 187.41 | 1.38 | 0.94 | 1.29 | 1.93 | 0.89 | 0.94 | 1.54 |
| 187.49 | 1.43 | 1.02 | 1.26 | 1.97 | 0.93 | 0.96 | 1.60 |
| 187.56 | 1.42 | 1.07 | 1.23 | 2.07 | 0.96 | 0.96 | 1.66 |
| 187.63 | 1.45 | 1.06 | 1.36 | 2.15 | 0.99 | 0.97 | 1.72 |
| 187.70 | 1.50 | 1.12 | 1.36 | 2.29 | 0.93 | 0.97 | 1.72 |
| 187.77 | 1.41 | 1.07 | 1.31 | 2.24 | 0.94 | 0.97 | 1.75 |
| 187.84 | 1.49 | 1.05 | 1.34 | 2.40 | 0.97 | 0.98 | 1.80 |
| 187.91 | 1.45 | 1.05 | 1.39 | 2.33 | 0.95 | 0.98 | 1.79 |
| 187.98 | 1.40 | 1.08 | 1.30 | 2.37 | 1.00 | 0.94 | 1.77 |
| 188.05 | 1.37 | 0.99 | 1.31 | 2.34 | 0.87 | 0.95 | 1.76 |
| 188.12 | 1.33 | 0.96 | 1.30 | 2.25 | 0.87 | 0.96 | 1.69 |
| 188.19 | 1.33 | 0.97 | 1.29 | 2.21 | 0.83 | 0.92 | 1.66 |
| 188.26 | 1.28 | 0.90 | 1.21 | 1.99 | 0.89 | 0.90 | 1.56 |
| 188.33 | 1.17 | 0.91 | 1.03 | 1.89 | 0.85 | 0.89 | 1.53 |
| 188.40 | 1.14 | 0.84 | 1.06 | 1.68 | 0.77 | 0.88 | 1.42 |
| 188.48 | 1.10 | 0.87 | 1.06 | 1.69 | 0.74 | 0.84 | 1.39 |
| 188.55 | 1.02 | 0.78 | 0.94 | 1.56 | 0.69 | 0.81 | 1.28 |
| 188.62 | 0.98 | 0.79 | 0.90 | 1.46 | 0.74 | 0.84 | 1.32 |
| 188.69 | 0.96 | 0.76 | 0.93 | 1.46 | 0.67 | 0.81 | 1.24 |
| 188.76 | 0.98 | 0.77 | 0.82 | 1.46 | 0.66 | 0.81 | 1.26 |
| 188.83 | 0.93 | 0.71 | 0.79 | 1.32 | 0.60 | 0.79 | 1.21 |
| 188.90 | 0.91 | 0.74 | 0.85 | 1.35 | 0.67 | 0.77 | 1.16 |
| 188.97 | 0.86 | 0.70 | 0.86 | 1.27 | 0.63 | 0.79 | 1.17 |
| 189.04 | 0.91 | 0.73 | 0.83 | 1.28 | 0.65 | 0.79 | 1.16 |
| 189.11 | 0.87 | 0.67 | 0.84 | 1.30 | 0.62 | 0.80 | 1.16 |
| 189.18 | 0.88 | 0.70 | 0.80 | 1.32 | 0.66 | 0.83 | 1.19 |
| 189.25 | 0.88 | 0.71 | 0.82 | 1.28 | 0.66 | 0.78 | 1.18 |
| 189.32 | 0.91 | 0.67 | 0.80 | 1.36 | 0.64 | 0.83 | 1.19 |
| 189.39 | 0.93 | 0.76 | 0.85 | 1.36 | 0.66 | 0.82 | 1.24 |

**Table D.1:** Wavescan data of Fe*L* for glasses in Figure 3.3 *cont.*

| L (mm) | AR10 | AR14 | AR16 | AR19 | AR20 | AR14 | AR19 |
|---|---|---|---|---|---|---|---|
| 189.47 | 0.98 | 0.74 | 0.91 | 1.36 | 0.67 | 0.81 | 1.24 |
| 189.54 | 0.96 | 0.81 | 0.96 | 1.41 | 0.68 | 0.86 | 1.26 |
| 189.61 | 1.00 | 0.88 | 0.94 | 1.51 | 0.74 | 0.88 | 1.25 |
| 189.68 | 1.05 | 0.87 | 1.02 | 1.52 | 0.76 | 0.93 | 1.32 |
| 189.75 | 1.05 | 0.87 | 1.07 | 1.59 | 0.82 | 0.93 | 1.38 |
| 189.82 | 1.14 | 0.93 | 1.07 | 1.68 | 0.84 | 0.94 | 1.39 |
| 189.89 | 1.27 | 1.02 | 1.14 | 1.72 | 0.88 | 0.96 | 1.44 |
| 189.96 | 1.35 | 1.07 | 1.30 | 1.85 | 0.94 | 0.99 | 1.51 |
| 190.03 | 1.53 | 1.17 | 1.31 | 2.00 | 1.06 | 1.03 | 1.58 |
| 190.10 | 1.63 | 1.22 | 1.36 | 2.08 | 1.07 | 1.12 | 1.64 |
| 190.17 | 1.65 | 1.36 | 1.43 | 2.09 | 1.15 | 1.19 | 1.68 |
| 190.24 | 1.85 | 1.49 | 1.55 | 2.22 | 1.21 | 1.23 | 1.78 |
| 190.31 | 2.10 | 1.57 | 1.59 | 2.35 | 1.27 | 1.32 | 1.85 |
| 190.38 | 2.18 | 1.73 | 1.71 | 2.55 | 1.36 | 1.41 | 1.90 |
| 190.46 | 2.31 | 1.80 | 1.86 | 2.53 | 1.46 | 1.46 | 1.98 |
| 190.53 | 2.51 | 1.86 | 1.81 | 2.70 | 1.44 | 1.51 | 2.02 |
| 190.60 | 2.66 | 1.92 | 1.90 | 2.93 | 1.60 | 1.50 | 2.12 |
| 190.67 | 2.72 | 2.00 | 2.02 | 3.06 | 1.62 | 1.53 | 2.22 |
| 190.74 | 2.73 | 2.03 | 2.10 | 3.21 | 1.67 | 1.51 | 2.31 |
| 190.81 | 2.77 | 2.03 | 2.01 | 3.42 | 1.66 | 1.56 | 2.39 |
| 190.88 | 2.76 | 1.89 | 2.13 | 3.43 | 1.68 | 1.54 | 2.46 |
| 190.95 | 2.67 | 1.91 | 2.15 | 3.50 | 1.63 | 1.54 | 2.49 |
| 191.02 | 2.67 | 1.87 | 2.22 | 3.63 | 1.54 | 1.48 | 2.55 |
| 191.09 | 2.58 | 1.85 | 2.13 | 3.50 | 1.50 | 1.43 | 2.50 |
| 191.16 | 2.41 | 1.72 | 2.09 | 3.38 | 1.52 | 1.39 | 2.54 |
| 191.23 | 2.32 | 1.61 | 1.94 | 3.29 | 1.50 | 1.33 | 2.47 |
| 191.30 | 2.20 | 1.54 | 1.81 | 3.24 | 1.30 | 1.26 | 2.34 |
| 191.37 | 1.94 | 1.41 | 1.76 | 3.02 | 1.22 | 1.23 | 2.25 |
| 191.44 | 1.88 | 1.33 | 1.63 | 2.84 | 1.20 | 1.18 | 2.13 |
| 191.52 | 1.78 | 1.25 | 1.50 | 2.67 | 1.15 | 1.14 | 1.99 |
| 191.59 | 1.67 | 1.16 | 1.39 | 2.49 | 1.02 | 1.05 | 1.87 |
| 191.66 | 1.56 | 1.16 | 1.29 | 2.28 | 0.95 | 1.05 | 1.80 |
| 191.73 | 1.48 | 1.09 | 1.15 | 2.03 | 0.93 | 1.01 | 1.63 |
| 191.80 | 1.38 | 0.94 | 1.06 | 1.81 | 0.80 | 0.98 | 1.49 |
| 191.87 | 1.28 | 0.99 | 0.97 | 1.65 | 0.80 | 0.96 | 1.45 |
| 191.94 | 1.12 | 0.89 | 0.92 | 1.45 | 0.74 | 0.92 | 1.39 |
| 192.01 | 1.19 | 0.86 | 0.83 | 1.45 | 0.73 | 0.88 | 1.26 |
| 192.08 | 1.10 | 0.77 | 0.75 | 1.31 | 0.68 | 0.90 | 1.23 |
| 192.15 | 0.99 | 0.74 | 0.81 | 1.18 | 0.63 | 0.84 | 1.17 |
| 192.22 | 0.94 | 0.73 | 0.69 | 1.11 | 0.70 | 0.86 | 1.13 |
| 192.29 | 0.94 | 0.68 | 0.69 | 1.14 | 0.62 | 0.84 | 1.10 |
| 192.36 | 0.87 | 0.66 | 0.66 | 0.99 | 0.54 | 0.79 | 1.06 |
| 192.43 | 0.80 | 0.67 | 0.66 | 0.95 | 0.54 | 0.78 | 1.04 |
| 192.51 | 0.77 | 0.64 | 0.62 | 0.92 | 0.50 | 0.79 | 1.04 |
| 192.58 | 0.78 | 0.57 | 0.57 | 0.87 | 0.52 | 0.81 | 1.00 |

**Table D.1:** Wavescan data of Fe*L* for glasses in Figure 3.3 *cont.*

| L (mm) | AR10 | AR14 | AR16 | AR19 | AR20 | AR14 | AR19 |
|---|---|---|---|---|---|---|---|
| 192.65 | 0.70 | 0.60 | 0.57 | 0.80 | 0.49 | 0.77 | 0.99 |
| 192.72 | 0.69 | 0.56 | 0.51 | 0.85 | 0.44 | 0.76 | 0.97 |
| 192.79 | 0.68 | 0.54 | 0.57 | 0.79 | 0.48 | 0.73 | 0.99 |
| 192.86 | 0.65 | 0.52 | 0.56 | 0.84 | 0.44 | 0.72 | 0.96 |
| 192.93 | 0.61 | 0.48 | 0.52 | 0.76 | 0.47 | 0.73 | 0.93 |
| 193.00 | 0.59 | 0.47 | 0.50 | 0.76 | 0.45 | 0.72 | 0.94 |

*Notes:* Intensity in CPS·nA$^{-1}$.

**Table D.2:** Wavescan data of Fe*L* for VG-2 in Figure 7.1.

| | Cameca | | | | JEOL | | |
|---|---|---|---|---|---|---|---|
| λ (Å) | LTAP | TAP | TAP | λ (Å) | TAP | TAP | TAPH |
| 17.212 | 0.90 | 0.37 | 0.51 | 17.064 | 0.23 | 0.19 | 0.39 |
| 17.215 | 0.99 | 0.44 | 0.58 | 17.071 | 0.22 | 0.18 | 0.38 |
| 17.219 | 1.01 | 0.47 | 0.56 | 17.078 | 0.23 | 0.20 | 0.39 |
| 17.223 | 1.00 | 0.46 | 0.54 | 17.085 | 0.23 | 0.20 | 0.40 |
| 17.227 | 1.09 | 0.52 | 0.48 | 17.092 | 0.23 | 0.22 | 0.41 |
| 17.231 | 1.12 | 0.47 | 0.62 | 17.099 | 0.23 | 0.22 | 0.41 |
| 17.235 | 1.09 | 0.50 | 0.61 | 17.105 | 0.24 | 0.21 | 0.42 |
| 17.239 | 1.32 | 0.54 | 0.55 | 17.112 | 0.25 | 0.21 | 0.44 |
| 17.242 | 1.29 | 0.60 | 0.68 | 17.119 | 0.26 | 0.21 | 0.44 |
| 17.246 | 1.21 | 0.59 | 0.57 | 17.126 | 0.28 | 0.22 | 0.44 |
| 17.250 | 1.25 | 0.54 | 0.71 | 17.133 | 0.28 | 0.23 | 0.47 |
| 17.254 | 1.34 | 0.55 | 0.62 | 17.140 | 0.29 | 0.24 | 0.50 |
| 17.258 | 1.30 | 0.61 | 0.66 | 17.147 | 0.29 | 0.24 | 0.50 |
| 17.262 | 1.35 | 0.66 | 0.59 | 17.154 | 0.29 | 0.27 | 0.52 |
| 17.265 | 1.42 | 0.61 | 0.55 | 17.161 | 0.31 | 0.26 | 0.55 |
| 17.269 | 1.30 | 0.57 | 0.58 | 17.168 | 0.31 | 0.29 | 0.55 |
| 17.273 | 1.27 | 0.55 | 0.53 | 17.174 | 0.33 | 0.29 | 0.60 |
| 17.277 | 1.37 | 0.56 | 0.47 | 17.181 | 0.35 | 0.29 | 0.62 |
| 17.281 | 1.35 | 0.50 | 0.50 | 17.188 | 0.36 | 0.30 | 0.68 |
| 17.285 | 1.24 | 0.55 | 0.42 | 17.195 | 0.38 | 0.33 | 0.70 |
| 17.289 | 1.17 | 0.47 | 0.51 | 17.202 | 0.43 | 0.34 | 0.75 |
| 17.292 | 1.16 | 0.41 | 0.37 | 17.209 | 0.43 | 0.37 | 0.81 |
| 17.296 | 1.11 | 0.42 | 0.41 | 17.216 | 0.47 | 0.35 | 0.85 |
| 17.300 | 1.01 | 0.40 | 0.41 | 17.223 | 0.45 | 0.40 | 0.87 |
| 17.304 | 1.01 | 0.43 | 0.36 | 17.230 | 0.48 | 0.40 | 0.93 |
| 17.308 | 0.87 | 0.42 | 0.41 | 17.236 | 0.52 | 0.40 | 0.99 |
| 17.312 | 0.97 | 0.39 | 0.36 | 17.243 | 0.54 | 0.41 | 1.02 |
| 17.316 | 0.95 | 0.35 | 0.34 | 17.250 | 0.53 | 0.45 | 1.05 |
| 17.319 | 0.88 | 0.32 | 0.29 | 17.257 | 0.56 | 0.44 | 1.07 |
| 17.323 | 0.86 | 0.33 | 0.35 | 17.264 | 0.54 | 0.48 | 1.09 |
| 17.327 | 0.86 | 0.33 | 0.36 | 17.271 | 0.56 | 0.44 | 1.10 |
| 17.331 | 0.86 | 0.31 | 0.36 | 17.278 | 0.55 | 0.45 | 1.10 |
| 17.335 | 0.79 | 0.33 | 0.33 | 17.285 | 0.51 | 0.42 | 1.06 |

**Table D.2:** Wavescan data of Fe*L* for VG-2 in Figure 7.1 *cont.*

| λ (Å) | LTAP | TAP | TAP | λ (Å) | TAP | TAP | TAPH |
|---|---|---|---|---|---|---|---|
| 17.339 | 0.83 | 0.34 | 0.33 | 17.292 | 0.51 | 0.41 | 1.05 |
| 17.343 | 0.74 | 0.31 | 0.27 | 17.299 | 0.45 | 0.42 | 0.96 |
| 17.346 | 0.75 | 0.27 | 0.31 | 17.305 | 0.42 | 0.38 | 0.95 |
| 17.350 | 0.78 | 0.27 | 0.33 | 17.312 | 0.43 | 0.37 | 0.89 |
| 17.354 | 0.71 | 0.27 | 0.30 | 17.319 | 0.42 | 0.33 | 0.83 |
| 17.358 | 0.77 | 0.27 | 0.30 | 17.326 | 0.37 | 0.34 | 0.80 |
| 17.362 | 0.70 | 0.28 | 0.34 | 17.333 | 0.38 | 0.31 | 0.79 |
| 17.366 | 0.68 | 0.26 | 0.34 | 17.340 | 0.34 | 0.30 | 0.71 |
| 17.370 | 0.72 | 0.32 | 0.27 | 17.347 | 0.36 | 0.31 | 0.72 |
| 17.373 | 0.69 | 0.30 | 0.31 | 17.354 | 0.34 | 0.28 | 0.66 |
| 17.377 | 0.79 | 0.29 | 0.31 | 17.361 | 0.34 | 0.29 | 0.65 |
| 17.381 | 0.71 | 0.28 | 0.33 | 17.368 | 0.33 | 0.29 | 0.61 |
| 17.385 | 0.69 | 0.30 | 0.36 | 17.374 | 0.33 | 0.29 | 0.66 |
| 17.389 | 0.75 | 0.30 | 0.29 | 17.381 | 0.33 | 0.29 | 0.64 |
| 17.393 | 0.67 | 0.32 | 0.36 | 17.388 | 0.33 | 0.29 | 0.63 |
| 17.397 | 0.76 | 0.30 | 0.32 | 17.395 | 0.35 | 0.29 | 0.63 |
| 17.400 | 0.71 | 0.31 | 0.32 | 17.402 | 0.35 | 0.30 | 0.64 |
| 17.404 | 0.70 | 0.32 | 0.35 | 17.409 | 0.36 | 0.29 | 0.63 |
| 17.408 | 0.77 | 0.29 | 0.36 | 17.416 | 0.35 | 0.30 | 0.66 |
| 17.412 | 0.79 | 0.33 | 0.39 | 17.423 | 0.38 | 0.33 | 0.72 |
| 17.416 | 0.78 | 0.37 | 0.40 | 17.430 | 0.39 | 0.35 | 0.73 |
| 17.420 | 0.80 | 0.32 | 0.36 | 17.437 | 0.39 | 0.32 | 0.76 |
| 17.423 | 0.81 | 0.33 | 0.45 | 17.443 | 0.42 | 0.36 | 0.82 |
| 17.427 | 0.76 | 0.37 | 0.40 | 17.450 | 0.44 | 0.36 | 0.82 |
| 17.431 | 0.86 | 0.37 | 0.47 | 17.457 | 0.45 | 0.38 | 0.86 |
| 17.435 | 0.84 | 0.37 | 0.40 | 17.464 | 0.50 | 0.41 | 0.93 |
| 17.439 | 0.90 | 0.38 | 0.43 | 17.471 | 0.53 | 0.44 | 0.99 |
| 17.443 | 0.99 | 0.39 | 0.50 | 17.478 | 0.53 | 0.46 | 1.04 |
| 17.447 | 0.97 | 0.44 | 0.55 | 17.485 | 0.60 | 0.47 | 1.11 |
| 17.450 | 0.97 | 0.41 | 0.56 | 17.492 | 0.60 | 0.52 | 1.14 |
| 17.454 | 1.01 | 0.46 | 0.57 | 17.499 | 0.63 | 0.53 | 1.20 |
| 17.458 | 1.01 | 0.52 | 0.56 | 17.506 | 0.67 | 0.55 | 1.31 |
| 17.462 | 1.13 | 0.50 | 0.66 | 17.512 | 0.68 | 0.56 | 1.37 |
| 17.466 | 1.16 | 0.55 | 0.57 | 17.519 | 0.76 | 0.60 | 1.48 |
| 17.470 | 1.26 | 0.51 | 0.63 | 17.526 | 0.79 | 0.64 | 1.53 |
| 17.474 | 1.24 | 0.59 | 0.68 | 17.533 | 0.80 | 0.63 | 1.58 |
| 17.477 | 1.19 | 0.58 | 0.72 | 17.540 | 0.83 | 0.68 | 1.64 |
| 17.481 | 1.34 | 0.70 | 0.78 | 17.547 | 0.85 | 0.68 | 1.65 |
| 17.485 | 1.38 | 0.64 | 0.74 | 17.554 | 0.83 | 0.64 | 1.72 |
| 17.489 | 1.49 | 0.67 | 0.80 | 17.561 | 0.82 | 0.69 | 1.65 |
| 17.493 | 1.48 | 0.72 | 0.86 | 17.568 | 0.79 | 0.65 | 1.67 |
| 17.497 | 1.49 | 0.69 | 0.92 | 17.575 | 0.78 | 0.63 | 1.62 |
| 17.501 | 1.49 | 0.73 | 0.97 | 17.581 | 0.74 | 0.59 | 1.57 |
| 17.504 | 1.55 | 0.70 | 0.85 | 17.588 | 0.68 | 0.56 | 1.46 |
| 17.508 | 1.69 | 0.78 | 0.94 | 17.595 | 0.64 | 0.54 | 1.38 |

**Table D.2:** Wavescan data of Fe*L* for VG-2 in Figure 7.1 *cont.*

| λ (Å) | LTAP | TAP | TAP | λ (Å) | TAP | TAP | TAPH |
|---|---|---|---|---|---|---|---|
| 17.512 | 1.72 | 0.83 | 0.95 | 17.602 | 0.59 | 0.51 | 1.26 |
| 17.516 | 1.74 | 0.87 | 1.05 | 17.609 | 0.54 | 0.47 | 1.22 |
| 17.520 | 1.83 | 0.87 | 0.97 | 17.616 | 0.47 | 0.42 | 1.10 |
| 17.524 | 1.91 | 0.99 | 1.02 | 17.623 | 0.43 | 0.38 | 1.00 |
| 17.528 | 2.03 | 0.96 | 0.95 | 17.630 | 0.40 | 0.36 | 0.90 |
| 17.531 | 1.89 | 0.92 | 1.03 | 17.637 | 0.39 | 0.34 | 0.80 |
| 17.535 | 2.08 | 0.89 | 1.02 | 17.644 | 0.35 | 0.33 | 0.78 |
| 17.539 | 2.03 | 0.92 | 1.00 | 17.650 | 0.34 | 0.28 | 0.71 |
| 17.543 | 2.10 | 0.98 | 1.00 | 17.657 | 0.32 | 0.28 | 0.65 |
| 17.547 | 2.07 | 0.89 | 0.92 | 17.664 | 0.30 | 0.26 | 0.60 |
| 17.551 | 2.19 | 0.98 | 0.93 | 17.671 | 0.27 | 0.22 | 0.60 |
| 17.554 | 2.06 | 1.00 | 0.94 | 17.678 | 0.28 | 0.23 | 0.56 |
| 17.558 | 2.10 | 0.94 | 0.89 | 17.685 | 0.27 | 0.24 | 0.51 |
| 17.562 | 2.24 | 0.95 | 0.88 | 17.692 | 0.26 | 0.23 | 0.50 |
| 17.566 | 2.03 | 0.93 | 0.81 | 17.699 | 0.25 | 0.21 | 0.50 |
| 17.570 | 1.89 | 0.84 | 0.74 | 17.706 | 0.24 | 0.21 | 0.47 |
| 17.574 | 1.88 | 0.90 | 0.77 | 17.713 | 0.25 | 0.19 | 0.48 |
| 17.578 | 1.80 | 0.73 | 0.71 | 17.719 | 0.24 | 0.19 | 0.46 |
| 17.581 | 1.82 | 0.76 | 0.66 | 17.726 | 0.22 | 0.19 | 0.44 |
| 17.585 | 1.76 | 0.76 | 0.63 | 17.733 | 0.22 | 0.19 | 0.44 |
| 17.589 | 1.70 | 0.69 | 0.51 | 17.740 | 0.21 | 0.19 | 0.42 |
| 17.593 | 1.18 | 0.41 | 0.23 | 17.747 | 0.21 | 0.19 | 0.40 |

*Notes:* Intensity in CPS·nA$^{-1}$.

**Table D.3:** Fits to Equation 3.2.

| Sample | $I_0$ | *s.d.* | $I_\infty$ | *s.d.* | $I_0'$ ($s^{-1}$) | *s.d.* | $I_0$ | *s.d.* | $I_\infty$ | *s.d.* | $I_0'$ ($s^{-1}$) | *s.d.* | $I_0$ | *s.d.* | $I_\infty$ | *s.d.* | $I_0'$ ($s^{-1}$) | *s.d.* |
|---|---|---|---|---|---|---|---|---|---|---|---|---|---|---|---|---|---|---|
| | #1: 15 kV, 50 nA, 10 μm | | | | | | #2: 15 kV, 50 nA, 4 μm | | | | | | #3: 15 kV, 50 nA, 4 μm | | | | | |
| AR10 | 0.61 | *0.02* | 0.68 | *0.01* | 0.0019 | *0.0014* | 0.69 | *0.02* | 0.82 | *0.03* | 0.0018 | *0.0009* | 0.61 | *0.02* | 0.72 | *0.01* | 0.0038 | *0.0022* |
| AR11 | 0.65 | *0.02* | 0.69 | *0.01* | 0.0012 | *0.0017* | 0.67 | *0.02* | 0.77 | *0.01* | 0.0049 | *0.0028* | 0.69 | *0.01* | 0.65 | *0.00* | 0.0000 | *0.0001* |
| AR12 | 0.66 | *0.02* | 0.71 | *0.02* | 0.0011 | *0.0011* | 0.71 | *0.03* | 0.84 | *0.01* | 0.0060 | *0.0032* | 0.58 | *0.04* | 0.75 | *0.00* | 0.0212 | *0.0115* |
| AR13 | 0.72 | *0.02* | 0.80 | *0.04* | 0.0010 | *0.0009* | 0.80 | *0.01* | 0.78 | *0.00* | 0.0001 | *0.0001* | | | | | | |
| AR14 | 0.61 | *0.01* | 0.58 | *0.00* | 0.0000 | *0.0001* | 0.67 | *0.01* | 0.70 | *0.00* | 0.0000 | *0.0001* | 0.60 | *0.01* | 0.65 | *0.00* | 0.0001 | *0.0002* |
| AR15 | 0.67 | *0.01* | 0.75 | *0.00* | 0.0007 | *0.0003* | 0.74 | *0.18* | 0.78 | *0.00* | 0.0101 | *0.0955* | | | | | | |
| AR16 | 0.82 | *0.02* | 0.78 | *0.00* | -0.0003 | *0.0004* | 0.86 | *0.00* | 0.86 | *0.00* | 0.0000 | *0.0000* | 0.78 | *0.01* | 0.74 | *0.00* | -0.0002 | *0.0002* |
| AR17 | 0.85 | *0.02* | 0.00 | *0.00* | 0.0000 | *0.0000* | 0.92 | *0.01* | 0.83 | *0.00* | -0.0009 | *0.0003* | 0.85 | *0.02* | 0.79 | *0.01* | -0.0017 | *0.0019* |
| AR18 | 0.82 | *0.01* | 0.84 | *0.00* | 0.0000 | *0.0001* | 0.88 | *0.02* | 0.89 | *0.00* | 0.0002 | *0.0007* | 0.83 | *0.01* | 0.77 | *0.00* | 0.0000 | *0.0001* |
| AR19 | 0.90 | *0.02* | 0.92 | *0.00* | 0.0006 | *0.0014* | 0.95 | *0.03* | 0.98 | *0.00* | 0.0010 | *0.0019* | 0.95 | *0.01* | 0.89 | *0.00* | -0.0003 | *0.0002* |
| AR20 | 0.79 | *0.03* | 0.61 | *0.01* | -0.0112 | *0.0044* | 1.35 | *3.20* | 0.67 | *0.00* | -0.4243 | *3.0461* | 0.67 | *0.04* | 0.61 | *0.01* | -0.0045 | *0.0073* |
| AR21 | 0.81 | *0.01* | 0.77 | *0.00* | -0.0002 | *0.0002* | 0.85 | *0.01* | 0.81 | *0.00* | 0.0000 | *0.0002* | 0.81 | *0.01* | 0.77 | *0.00* | -0.0003 | *0.0003* |
| AR35 | 0.69 | *0.03* | 0.75 | *0.01* | 0.0028 | *0.0032* | 0.76 | *0.03* | 0.82 | *0.01* | 0.0032 | *0.0038* | 0.74 | *0.01* | 0.76 | *0.00* | -0.0001 | *0.0001* |
| AR36 | 0.79 | *0.02* | 0.82 | *0.01* | 0.0019 | *0.0033* | 0.81 | *0.03* | 0.91 | *0.01* | 0.0039 | *0.0030* | 0.79 | *0.01* | 0.00 | *0.00* | 0.0004 | *0.0001* |
| AR37 | 0.84 | *0.01* | 0.87 | *0.00* | 0.0000 | *0.0001* | 0.90 | *0.01* | 0.86 | *0.00* | -0.0002 | *0.0002* | 0.80 | *0.01* | 0.82 | *0.00* | 0.0000 | *0.0001* |
| AR38 | 0.70 | *0.05* | 0.62 | *0.01* | -0.0102 | *0.0142* | 0.75 | *0.05* | 0.66 | *0.01* | -0.0099 | *0.0113* | 0.62 | *0.01* | 0.62 | *0.00* | 0.0000 | *0.0000* |
| AR39 | 0.74 | *0.02* | 0.82 | *0.03* | 0.0014 | *0.0012* | | | | | | | 0.77 | *0.01* | 0.88 | *0.00* | 0.0018 | *0.0006* |
| AR40 | 0.86 | *0.01* | 0.85 | *0.00* | 0.0001 | *0.0000* | 0.92 | *0.02* | 0.89 | *0.00* | -0.0002 | *0.0004* | 0.86 | *0.07* | 0.75 | *0.01* | -0.0209 | *0.0282* |
| AR41 | 0.81 | *0.01* | 0.78 | *0.00* | -0.0002 | *0.0003* | 0.81 | *0.01* | 0.74 | *0.00* | 0.0000 | *0.0002* | 0.80 | *0.02* | 0.71 | *0.04* | -0.0013 | *0.0010* |
| AR42 | 0.92 | *0.01* | 0.94 | *0.00* | 0.0000 | *0.0001* | 0.96 | *0.03* | 0.00 | *0.00* | 0.0000 | *0.0000* | 0.88 | *0.01* | 0.91 | *0.00* | 0.0000 | *0.0001* |
| AR43 | 1.08 | *0.03* | 1.05 | *0.01* | -0.0021 | *0.0063* | 1.09 | *0.03* | 1.07 | *0.01* | -0.0009 | *0.0042* | 1.00 | *0.01* | 0.99 | *0.00* | -0.0001 | *0.0004* |
| AR44 | 0.88 | *0.03* | 0.94 | *0.00* | 0.0061 | *0.0087* | 0.95 | *0.01* | 0.99 | *0.00* | 0.0002 | *0.0002* | 0.89 | *0.01* | 0.89 | *0.00* | 0.0000 | *0.0000* |
| 22 | 0.68 | *0.02* | 0.72 | *0.01* | 0.0012 | *0.0015* | | | | | | | 0.77 | *0.02* | 0.62 | *0.02* | -0.0030 | *0.0012* |
| 23 | 0.74 | *0.01* | 0.70 | *0.00* | -0.0002 | *0.0002* | | | | | | | 0.75 | *0.02* | 0.63 | *0.02* | -0.0026 | *0.0011* |
| 25 | 0.73 | *0.01* | 0.71 | *0.00* | -0.0003 | *0.0005* | | | | | | | 0.72 | *0.01* | 0.67 | *0.02* | -0.0010 | *0.0009* |
| 28 | 0.73 | *0.01* | 0.70 | *0.00* | 0.0000 | *0.0001* | | | | | | | 0.74 | *0.01* | 0.60 | *0.03* | -0.0019 | *0.0007* |
| 32 | 0.74 | *0.01* | 0.67 | *0.00* | -0.0002 | *0.0002* | | | | | | | 0.75 | *0.02* | 0.52 | *0.14* | -0.0015 | *0.0007* |
| 35 | 0.63 | *0.03* | 0.69 | *0.01* | 0.0031 | *0.0037* | | | | | | | 0.69 | *0.01* | 0.37 | *1.28* | -0.0007 | *0.0005* |

**Table D.3:** Fits to Equation 3.2 *cont.*

| Sample | $I_0$ | *s.d.* | $I_\infty$ | *s.d.* | $I'_0$ ($s^{-1}$) | *s.d.* | $I_0$ | *s.d.* | $I_\infty$ | *s.d.* | $I'_0$ ($s^{-1}$) | *s.d.* | $I_0$ | *s.d.* | $I_\infty$ | *s.d.* | $I'_0$ ($s^{-1}$) | *s.d.* |
|---|---|---|---|---|---|---|---|---|---|---|---|---|---|---|---|---|---|---|
| AN1 | 0.67 | *0.01* | 0.73 | *0.00* | 0.0008 | *0.0004* | | | | | | | 0.69 | *0.02* | 0.77 | *0.01* | 0.0018 | *0.0011* |
| R1 | 0.77 | *0.01* | 0.75 | *0.00* | -0.0002 | *0.0003* | | | | | | | 0.78 | *0.01* | 0.58 | *0.11* | -0.0015 | *0.0006* |
| R2 | 0.71 | *0.01* | 0.75 | *0.00* | 0.0000 | *0.0001* | | | | | | | 0.69 | *0.01* | 0.57 | *0.15* | -0.0007 | *0.0005* |
| R6 | 0.82 | *0.02* | 0.80 | *0.01* | -0.0008 | *0.0021* | | | | | | | 0.79 | *0.01* | 0.59 | *0.03* | -0.0023 | *0.0005* |
| ETNA01 | 0.78 | *0.03* | 0.74 | *0.00* | -0.0020 | *0.0036* | | | | | | | | | | | | |
| ETNA02 | 0.81 | *0.02* | 0.71 | *0.09* | -0.0009 | *0.0007* | 0.84 | *0.01* | 0.69 | *0.01* | -0.0040 | *0.0011* | | | | | | |
| ETNA03 | 0.66 | *0.19* | 0.74 | *0.01* | 0.0244 | *0.1087* | 0.83 | *0.02* | 0.73 | *0.03* | -0.0015 | *0.0009* | | | | | | |
| ETNA04 | 0.81 | *0.01* | 0.48 | *1.09* | -0.0008 | *0.0005* | 0.87 | *0.02* | 0.69 | *0.02* | -0.0042 | *0.0014* | | | | | | |
| ETNA05 | 0.78 | *0.02* | 0.55 | *0.27* | -0.0011 | *0.0006* | 0.91 | *0.02* | 0.69 | *0.00* | -0.0132 | *0.0030* | | | | | | |
| ETNA06 | 0.80 | *0.03* | 0.73 | *0.01* | -0.0044 | *0.0045* | 0.83 | *0.01* | 0.72 | *0.04* | -0.0014 | *0.0007* | | | | | | |
| ETNA07 | 0.75 | *0.01* | 0.76 | *0.00* | -0.0001 | *0.0000* | 0.92 | *0.20* | 0.77 | *0.01* | -0.0516 | *0.1315* | | | | | | |
| ETNA08 | 0.76 | *0.01* | 0.74 | *0.00* | -0.0004 | *0.0007* | 0.79 | *0.01* | 0.74 | *0.00* | -0.0005 | *0.0004* | | | | | | |
| ETNA09 | 0.80 | *0.01* | 0.61 | *0.06* | -0.0019 | *0.0007* | 0.82 | *0.02* | 0.67 | *0.01* | -0.0041 | *0.0014* | | | | | | |
| ETNA10 | 0.80 | *0.02* | 0.56 | *0.14* | -0.0016 | *0.0006* | 0.84 | *0.02* | 0.69 | *0.01* | -0.0090 | *0.0031* | | | | | | |
| ETNA11 | 0.81 | *0.01* | 0.62 | *0.08* | -0.0015 | *0.0005* | 0.86 | *0.04* | 0.72 | *0.00* | -0.0095 | *0.0057* | | | | | | |
| ETNA12 | 0.81 | *0.01* | 0.72 | *0.00* | -0.0010 | *0.0004* | | | | | | | | | | | | |
| ETNA13 | 0.82 | *0.01* | 0.62 | *0.08* | -0.0017 | *0.0006* | 0.86 | *0.02* | 0.70 | *0.01* | -0.0067 | *0.0024* | | | | | | |
| ETNA14 | 0.80 | *0.01* | 0.67 | *0.02* | -0.0022 | *0.0008* | 0.81 | *0.02* | 0.70 | *0.01* | -0.0043 | *0.0018* | | | | | | |
| ETNA15 | 0.82 | *0.02* | 0.75 | *0.03* | -0.0011 | *0.0010* | 0.84 | *0.01* | 0.39 | *0.84* | -0.0012 | *0.0005* | | | | | | |
| ETNA16 | 0.80 | *0.02* | 0.66 | *0.05* | -0.0015 | *0.0008* | 0.80 | *0.02* | 0.68 | *0.02* | -0.0022 | *0.0014* | | | | | | |
| ETNA17 | 0.82 | *0.01* | 0.51 | *0.28* | -0.0012 | *0.0004* | 0.86 | *0.03* | 0.71 | *0.01* | -0.0078 | *0.0032* | | | | | | |
| ETNA24 | 0.83 | *0.02* | 0.55 | *0.20* | -0.0015 | *0.0006* | 0.88 | *0.02* | 0.70 | *0.01* | -0.0073 | *0.0018* | | | | | | |
| ETNA25 | 0.83 | *0.02* | 0.74 | *0.03* | -0.0016 | *0.0010* | | | | | | | | | | | | |
| ETNA26 | 0.83 | *0.02* | 0.73 | *0.00* | -0.0009 | *0.0004* | 0.84 | *0.01* | 0.68 | *0.02* | -0.0030 | *0.0009* | | | | | | |
| ETNA27 | 0.83 | *0.01* | 0.67 | *0.11* | -0.0012 | *0.0006* | 0.86 | *0.02* | 0.70 | *0.01* | -0.0058 | *0.0022* | | | | | | |
| ETNA28 | 0.82 | *0.01* | 0.56 | *0.16* | -0.0016 | *0.0006* | 0.84 | *0.02* | 0.70 | *0.01* | -0.0088 | *0.0032* | | | | | | |
| ETNA29 | 0.83 | *0.02* | 0.67 | *0.04* | -0.0022 | *0.0010* | 0.92 | *0.03* | 0.70 | *0.01* | -0.0120 | *0.0036* | | | | | | |
| ETNA30 | 0.75 | *0.01* | 0.70 | *0.05* | -0.0005 | *0.0005* | 0.80 | *0.02* | 0.74 | *0.05* | -0.0007 | *0.0008* | | | | | | |
| MAS.1.A4 | 0.82 | *0.02* | 0.80 | *0.00* | -0.0003 | *0.0009* | | | | | | | 0.85 | *0.02* | 0.63 | *0.03* | -0.0035 | *0.0010* |

**Table D.3:** Fits to Equation 3.2 *cont.*

| Sample | $I_0$ | *s.d.* | $I_\infty$ | *s.d.* | $I'_0$ ($s^{-1}$) | *s.d.* | $I_0$ | *s.d.* | $I_\infty$ | *s.d.* | $I'_0$ ($s^{-1}$) | *s.d.* | $I_0$ | *s.d.* | $I_\infty$ | *s.d.* | $I'_0$ ($s^{-1}$) | *s.d.* |
|---|---|---|---|---|---|---|---|---|---|---|---|---|---|---|---|---|---|---|
| MAS.1.A5 | 0.85 | *0.02* | 0.81 | *0.00* | -0.0011 | *0.0011* | | | | | | | 0.83 | *0.01* | 0.63 | *0.02* | -0.0029 | *0.0007* |
| MAS.1.A6 | 0.83 | *0.01* | 0.80 | *0.00* | -0.0006 | *0.0005* | | | | | | | 0.80 | *0.02* | 0.64 | *0.03* | -0.0027 | *0.0011* |
| MAS.1.A9 | 0.84 | *0.01* | 0.78 | *0.00* | -0.0004 | *0.0002* | | | | | | | 0.85 | *0.01* | 0.14 | *1.33* | -0.0015 | *0.0005* |
| MAS.1.A10 | 0.82 | *0.02* | 0.78 | *0.00* | -0.0007 | *0.0006* | | | | | | | 0.86 | *0.02* | 0.65 | *0.01* | -0.0058 | *0.0014* |
| MAS.1.A10b | 0.84 | *0.01* | 0.76 | *0.00* | -0.0009 | *0.0004* | | | | | | | 0.84 | *0.02* | 0.66 | *0.01* | -0.0057 | *0.0017* |
| MAS.1.B4 | 0.82 | *0.01* | 0.76 | *0.00* | -0.0005 | *0.0003* | 0.91 | *0.02* | 0.70 | *0.02* | -0.0044 | *0.0013* | | | | | | |
| MAS.1.B5 | 0.85 | *0.02* | 0.79 | *0.01* | -0.0028 | *0.0023* | 0.87 | *0.02* | 0.67 | *0.05* | -0.0023 | *0.0009* | | | | | | |
| MAS.1.B6 | 0.78 | *0.03* | 0.00 | *0.00* | 0.0000 | *0.0000* | 0.85 | *0.02* | 0.66 | *0.05* | -0.0024 | *0.0010* | | | | | | |
| MAS.1.B7 | 0.81 | *0.01* | 0.78 | *0.00* | -0.0001 | *0.0002* | 0.92 | *0.02* | 0.63 | *0.17* | -0.0021 | *0.0009* | | | | | | |
| MAS.1.B8 | 0.84 | *0.02* | 0.83 | *0.01* | -0.0005 | *0.0020* | 0.90 | *0.02* | 0.78 | *0.00* | -0.0020 | *0.0007* | | | | | | |
| MAS.1.B9 | 0.80 | *0.06* | 0.83 | *0.01* | 0.0053 | *0.0213* | 0.91 | *0.02* | 0.76 | *0.00* | -0.0017 | *0.0005* | | | | | | |
| St8.1.B2 | 0.69 | *0.01* | 0.68 | *0.00* | -0.0001 | *0.0004* | 0.75 | *0.02* | 0.63 | *0.10* | -0.0010 | *0.0007* | | | | | | |
| St8.1.B3 | 0.70 | *0.01* | 0.65 | *0.00* | -0.0004 | *0.0003* | 0.74 | *0.02* | 0.67 | *0.03* | -0.0012 | *0.0012* | | | | | | |
| St8.1.B4 | 0.73 | *0.02* | 0.66 | *0.06* | -0.0007 | *0.0008* | 0.76 | *0.03* | 0.68 | *0.01* | -0.0032 | *0.0025* | | | | | | |
| St8.1.B5 | 0.70 | *0.02* | 0.63 | *0.25* | -0.0004 | *0.0006* | 0.80 | *0.03* | 0.69 | *0.01* | -0.0047 | *0.0030* | | | | | | |
| St8.1.B6 | 0.70 | *0.01* | 0.65 | *0.00* | -0.0003 | *0.0002* | 0.77 | *0.02* | 0.67 | *0.02* | -0.0022 | *0.0014* | | | | | | |
| St8.1.B7 | 0.71 | *0.01* | 0.72 | *0.00* | 0.0001 | *0.0003* | 0.78 | *0.02* | 0.68 | *0.04* | -0.0015 | *0.0009* | | | | | | |
| St8.1.B9 | 0.72 | *0.02* | 0.78 | *0.01* | 0.0023 | *0.0022* | 0.83 | *0.01* | 0.71 | *0.00* | -0.0007 | *0.0003* | | | | | | |
| St8.1.B10 | 0.71 | *0.01* | 0.67 | *0.01* | -0.0011 | *0.0010* | 0.77 | *0.02* | 0.67 | *0.01* | -0.0030 | *0.0014* | | | | | | |
| AMS1 | | | | | | | | | | | | | 0.66 | *0.01* | 0.67 | *0.00* | 0.0000 | *0.0001* |
| AMS2 | | | | | | | | | | | | | 0.70 | *0.01* | 0.00 | *0.00* | -0.0003 | *0.0002* |
| AMS4 | | | | | | | | | | | | | 0.71 | *0.04* | 0.69 | *0.00* | -0.0015 | *0.0045* |
| FSP1 | | | | | | | | | | | | | 0.62 | *0.01* | 0.67 | *0.00* | 0.0003 | *0.0003* |
| FSP2 | | | | | | | | | | | | | 0.64 | *0.01* | 0.71 | *0.00* | 0.0001 | *0.0001* |
| FSP3 | | | | | | | | | | | | | 0.66 | *0.01* | 0.63 | *0.00* | 0.0000 | *0.0001* |
| FSP4 | | | | | | | | | | | | | 0.63 | *0.01* | 0.68 | *0.00* | 0.0002 | *0.0001* |
| FSP5 | | | | | | | | | | | | | 0.63 | *0.01* | 0.67 | *0.00* | 0.0003 | *0.0003* |
| FSP6 | | | | | | | | | | | | | 0.60 | *0.04* | 0.65 | *0.01* | 0.0039 | *0.0084* |
| FSP7 | | | | | | | | | | | | | 0.65 | *0.01* | 0.60 | *0.00* | 0.0000 | *0.0001* |

**Table D.3:** Fits to Equation 3.2 *cont.*

| Sample | $I_0$ | *s.d.* | $I_\infty$ | *s.d.* | $I_0'$ ($s^{-1}$) | *s.d.* | $I_0$ | *s.d.* | $I_\infty$ | *s.d.* | $I_0'$ ($s^{-1}$) | *s.d.* | $I_0$ | *s.d.* | $I_\infty$ | *s.d.* | $I_0'$ ($s^{-1}$) | *s.d.* |
|---|---|---|---|---|---|---|---|---|---|---|---|---|---|---|---|---|---|---|
| FSP8 | | | | | | | | | | | | | 0.63 | *0.01* | 0.68 | *0.00* | 0.0001 | *0.0001* |
| FSP9 | | | | | | | | | | | | | 0.74 | *0.08* | 0.64 | *0.00* | -0.0251 | *0.0407* |
| PSG1 | | | | | | | | | | | | | 0.73 | *0.06* | 0.66 | *0.00* | -0.0142 | *0.0273* |
| PSG2 | | | | | | | | | | | | | 0.66 | *0.01* | 0.64 | *0.00* | 0.0000 | *0.0001* |
| PSG3 | | | | | | | | | | | | | 0.69 | *0.06* | 0.65 | *0.00* | -0.0069 | *0.0216* |
| PSG6 | | | | | | | | | | | | | 0.63 | *0.05* | 0.66 | *0.00* | 0.0056 | *0.0214* |
| PSB26 | 0.77 | *0.02* | 0.72 | *0.00* | -0.0001 | *0.0002* | 0.74 | *0.02* | 0.68 | *0.27* | -0.0004 | *0.0009* | | | | | | |
| PSB27 | 0.68 | *1.34* | 0.75 | *0.00* | 0.0335 | *1.1644* | 0.72 | *0.01* | 0.73 | *0.00* | -0.0001 | *0.0001* | | | | | | |
| PSB58 | 0.69 | *0.02* | 0.63 | *0.37* | -0.0002 | *0.0006* | | | | | | | | | | | | |
| PSB62 | 0.66 | *0.01* | 0.68 | *0.00* | 0.0000 | *0.0001* | 0.74 | *0.03* | 0.68 | *0.01* | -0.0027 | *0.0028* | | | | | | |
| PSB63 | 0.68 | *0.02* | 0.61 | *0.00* | -0.0004 | *0.0003* | 0.73 | *0.02* | 0.66 | *0.00* | -0.0009 | *0.0006* | | | | | | |
| PSB64 | 0.65 | *0.01* | 0.63 | *0.00* | 0.0000 | *0.0002* | 0.70 | *0.01* | 0.71 | *0.00* | 0.0000 | *0.0001* | | | | | | |
| PSB65 | 0.68 | *0.02* | 0.38 | *6.95* | -0.0003 | *0.0007* | 0.76 | *0.03* | 0.68 | *0.01* | -0.0046 | *0.0039* | | | | | | |
| PSB66 | 0.68 | *0.01* | 0.63 | *0.00* | -0.0003 | *0.0003* | 0.73 | *0.10* | 0.70 | *0.00* | -0.0045 | *0.0374* | | | | | | |
| PSB67 | 0.69 | *0.01* | 0.64 | *0.00* | -0.0003 | *0.0003* | 0.71 | *0.02* | 0.65 | *0.00* | -0.0002 | *0.0003* | | | | | | |
| AII_-35 | 0.86 | *0.03* | 0.83 | *0.00* | -0.0015 | *0.0030* | 0.89 | *0.02* | 0.85 | *0.13* | -0.0003 | *0.0008* | 0.86 | *0.01* | 0.78 | *0.40* | -0.0003 | *0.0004* |
| LW_0 | 0.83 | *0.03* | 0.86 | *0.01* | 0.0021 | *0.0052* | 0.91 | *0.03* | 0.00 | *0.00* | 0.0000 | *0.0000* | 0.87 | *0.03* | 0.84 | *0.01* | -0.0014 | *0.0036* |
| LW_10 | | | | | | | 0.83 | *0.03* | 0.91 | *0.01* | 0.0055 | *0.0060* | 0.84 | *0.03* | 0.86 | *0.01* | 0.0006 | *0.0038* |
| LW_-20 | 0.85 | *0.01* | 0.84 | *0.00* | 0.0000 | *0.0001* | 0.90 | *0.01* | 0.94 | *0.00* | 0.0000 | *0.0001* | 0.82 | *0.01* | 0.87 | *0.00* | 0.0001 | *0.0001* |
| VG2 | 0.89 | *0.02* | 0.92 | *0.01* | 0.0009 | *0.0016* | 0.94 | *0.01* | 0.95 | *0.00* | 0.0000 | *0.0002* | 0.81 | *0.05* | 0.88 | *0.00* | 0.0135 | *0.0191* |
| VGA99 | 1.11 | *0.65* | 0.91 | *0.01* | -0.0824 | *0.4837* | 0.94 | *0.01* | 0.97 | *0.00* | 0.0000 | *0.0001* | 0.86 | *0.02* | 0.89 | *0.01* | 0.0012 | *0.0025* |
| PU32 | 0.86 | *0.01* | 0.80 | *0.00* | -0.0002 | *0.0002* | | | | | | | | | | | | |
| PU359 | 0.82 | *0.02* | 0.84 | *0.00* | 0.0004 | *0.0008* | 0.86 | *1.09* | 0.87 | *0.00* | 0.0035 | *0.9550* | | | | | | |
| PU361 | 0.69 | *0.02* | 0.74 | *0.17* | 0.0003 | *0.0007* | | | | | | | | | | | | |
| PU58 | 0.66 | *0.01* | 0.70 | *0.00* | 0.0003 | *0.0002* | 0.73 | *0.03* | 0.77 | *0.00* | 0.0022 | *0.0038* | | | | | | |
| | #4: 15 kV, 50 nA, 4 μm | | | | | | #5: 15 kV, 50 nA, 15 μm | | | | | | | | | | | |
| MAS.1.A4 | | | | | | | 0.77 | *0.01* | 0.74 | *0.00* | 0.0000 | *0.0001* | | | | | | |
| MAS.1.A5 | | | | | | | 0.75 | *0.01* | 0.74 | *0.00* | -0.0001 | *0.0002* | | | | | | |
| St8.1.B2 | 0.70 | *0.01* | 0.39 | *0.74* | -0.0009 | *0.0005* | | | | | | | | | | | | |

**Table D.3:** Fits to Equation 3.2 *cont.*

| Sample | $I_0$ | *s.d.* | $I_\infty$ | *s.d.* | $I'_0$ ($s^{-1}$) | *s.d.* | $I_0$ | *s.d.* | $I_\infty$ | *s.d.* | $I'_0$ ($s^{-1}$) | *s.d.* | $I_0$ | *s.d.* | $I_\infty$ | *s.d.* | $I'_0$ ($s^{-1}$) | *s.d.* |
|---|---|---|---|---|---|---|---|---|---|---|---|---|---|---|---|---|---|---|
| St8.1.B3 | 0.73 | *0.02* | 0.61 | *0.01* | -0.0036 | *0.0016* | | | | | | | | | | | | |
| St8.1.B4 | 0.70 | *0.02* | 0.59 | *0.02* | -0.0022 | *0.0010* | | | | | | | | | | | | |
| St8.1.B5 | 0.68 | *0.02* | 0.61 | *0.02* | -0.0013 | *0.0010* | | | | | | | | | | | | |
| St8.1.B7 | 0.74 | *0.02* | 0.61 | *0.05* | -0.0019 | *0.0013* | | | | | | | | | | | | |
| AMS1 | 0.69 | *0.02* | 0.57 | *0.06* | -0.0014 | *0.0010* | 0.61 | *0.01* | 0.55 | *0.00* | -0.0004 | *0.0003* | | | | | | |
| AMS2 | 0.65 | *0.01* | 0.62 | *0.00* | -0.0003 | *0.0003* | 0.62 | *0.01* | 0.60 | *0.00* | -0.0002 | *0.0004* | | | | | | |
| AMS4 | 0.70 | *0.03* | 0.64 | *0.01* | -0.0026 | *0.0026* | 0.62 | *0.01* | 0.64 | *0.00* | -0.0001 | *0.0001* | | | | | | |
| FSP1 | 0.62 | *0.01* | 0.65 | *0.00* | 0.0000 | *0.0001* | 0.55 | *0.01* | 0.61 | *0.09* | 0.0004 | *0.0006* | | | | | | |
| FSP2 | 0.60 | *0.01* | 0.75 | *3.43* | 0.0002 | *0.0004* | 0.57 | *0.01* | 0.55 | *0.00* | 0.0001 | *0.0000* | | | | | | |
| FSP3 | 0.62 | *0.01* | 0.61 | *0.00* | 0.0000 | *0.0001* | 0.58 | *0.01* | 0.61 | *0.00* | 0.0001 | *0.0001* | | | | | | |
| FSP4 | 0.55 | *0.06* | 0.62 | *0.00* | 0.0139 | *0.0258* | 0.58 | *0.01* | 0.60 | *0.00* | 0.0000 | *0.0001* | | | | | | |
| FSP5 | 0.61 | *0.01* | 0.65 | *0.00* | 0.0001 | *0.0001* | 0.56 | *0.01* | 0.61 | *0.00* | 0.0005 | *0.0003* | | | | | | |
| FSP6 | 0.60 | *0.02* | 0.63 | *0.00* | 0.0005 | *0.0008* | 0.58 | *0.01* | 0.62 | *0.00* | 0.0000 | *0.0001* | | | | | | |
| FSP7 | 0.61 | *0.01* | 0.66 | *0.00* | 0.0002 | *0.0002* | 0.59 | *0.01* | 0.59 | *0.00* | 0.0000 | *0.0003* | | | | | | |
| FSP8 | 0.62 | *0.01* | 0.62 | *0.00* | 0.0000 | *0.0002* | 0.58 | *0.02* | 0.00 | *0.00* | 0.0000 | *0.0000* | | | | | | |
| FSP9 | 0.62 | *0.01* | 0.63 | *0.00* | -0.0001 | *0.0000* | 0.69 | *0.15* | 0.60 | *0.00* | -0.0235 | | | | | | | |
| PSG1 | 0.63 | *0.01* | 0.62 | *0.00* | 0.0000 | *0.0001* | 0.64 | *0.02* | 0.57 | *0.01* | -0.0033 | *0.0025* | | | | | | |
| PSG2 | 0.64 | *0.01* | 0.60 | *0.00* | -0.0001 | *0.0001* | 0.63 | *0.02* | 0.58 | *0.00* | -0.0024 | *0.0023* | | | | | | |
| PSG3 | 0.80 | *0.23* | 0.62 | *0.00* | -0.0728 | *0.1804* | 0.60 | *0.01* | 0.59 | *0.00* | 0.0000 | *0.0000* | | | | | | |
| PSG6 | 0.67 | *0.03* | 0.62 | *0.00* | -0.0054 | *0.0088* | 0.62 | *0.02* | 0.57 | *0.00* | -0.0024 | *0.0024* | | | | | | |
| Y-A | 0.63 | *0.03* | 0.00 | *0.00* | 0.0000 | *0.0000* | 0.60 | *0.03* | 0.56 | *0.01* | -0.0015 | *0.0024* | | | | | | |
| Y-B | 0.63 | *0.00* | 0.63 | *0.00* | 0.0000 | *0.0000* | 0.57 | *0.01* | 0.59 | *0.00* | 0.0000 | *0.0001* | | | | | | |
| Y-E | 0.63 | *0.01* | 0.66 | *0.00* | 0.0000 | *0.0001* | 0.58 | *0.02* | 0.55 | *0.16* | -0.0002 | *0.0007* | | | | | | |
| Y-G | 0.63 | *0.02* | 0.61 | *0.00* | 0.0000 | *0.0002* | 0.61 | *0.01* | 0.58 | *0.00* | -0.0002 | *0.0003* | | | | | | |
| Y-H | 0.62 | *0.01* | 0.64 | *0.00* | 0.0001 | *0.0002* | 0.58 | *0.01* | 0.51 | *0.00* | -0.0004 | *0.0003* | | | | | | |
| Y-J | 0.63 | *0.01* | 0.67 | *0.00* | -0.0001 | *0.0001* | 0.58 | *0.01* | 0.62 | *0.00* | -0.0001 | *0.0001* | | | | | | |
| Y-L | 0.60 | *0.02* | 0.00 | *0.00* | 0.0000 | *0.0000* | 0.60 | *0.02* | 0.56 | *0.01* | -0.0017 | *0.0020* | | | | | | |
| PSB58 | 0.69 | *0.02* | 0.61 | *0.03* | -0.0013 | *0.0012* | | | | | | | | | | | | |
| PSB62 | 0.66 | *0.01* | 0.52 | *0.44* | -0.0005 | *0.0004* | 0.61 | *0.03* | 0.59 | *0.01* | -0.0011 | *0.0032* | | | | | | |

**Table D.3:** Fits to Equation 3.2 *cont.*

| Sample | $I_0$ | *s.d.* | $I_\infty$ | *s.d.* | $I_0'$ ($s^{-1}$) | *s.d.* | $I_0$ | *s.d.* | $I_\infty$ | *s.d.* | $I_0'$ ($s^{-1}$) | *s.d.* | $I_0$ | *s.d.* | $I_\infty$ | *s.d.* | $I_0'$ ($s^{-1}$) | *s.d.* |
|---|---|---|---|---|---|---|---|---|---|---|---|---|---|---|---|---|---|---|
| PSB63 | 0.64 | *0.01* | 0.61 | *0.00* | -0.0002 | *0.0002* | 0.79 | *0.08* | 0.58 | *0.01* | -0.0364 | | | | | | | |
| PSB64 | 0.64 | *0.00* | 0.64 | *0.00* | 0.0000 | *0.0000* | 0.60 | *0.02* | 0.00 | *0.00* | 0.0000 | *0.0000* | | | | | | |
| PSB65 | 0.80 | *0.01* | 0.70 | *0.00* | -0.0009 | *0.0004* | 0.64 | *0.02* | 0.57 | *0.05* | -0.0007 | *0.0007* | | | | | | |
| PSB66 | 0.67 | *0.02* | 0.63 | *0.01* | -0.0022 | *0.0026* | 0.59 | *0.01* | 0.60 | *0.00* | 0.0000 | *0.0002* | | | | | | |
| PSB67 | 0.78 | *0.02* | 0.74 | *0.00* | 0.0002 | *0.0002* | 0.59 | *0.03* | 0.00 | *0.00* | 0.0000 | *0.0000* | | | | | | |
| AII_-35 | 0.82 | *0.01* | 0.82 | *0.00* | 0.0000 | *0.0001* | | | | | | | | | | | | |
| LW_0 | 0.91 | *0.04* | 0.83 | *0.01* | -0.0077 | *0.0080* | 0.78 | *0.01* | 0.75 | *0.00* | 0.0000 | *0.0001* | | | | | | |
| LW_10 | 0.80 | *0.01* | 0.83 | *0.00* | 0.0001 | *0.0001* | 0.77 | *0.01* | 0.80 | *0.00* | 0.0002 | *0.0002* | | | | | | |
| LW_-20 | 0.83 | *0.02* | 0.00 | *0.00* | 0.0000 | *0.0000* | 0.82 | *0.01* | 0.78 | *0.04* | -0.0004 | *0.0007* | | | | | | |
| VG2 | 0.86 | *0.02* | 0.85 | *0.00* | -0.0001 | *0.0003* | 0.80 | *0.02* | 0.79 | *0.02* | -0.0002 | *0.0015* | | | | | | |
| VGA99 | 0.92 | *0.01* | 0.91 | *0.00* | 0.0001 | *0.0000* | 0.88 | *0.01* | 0.91 | *0.00* | -0.0001 | *0.0001* | | | | | | |
| PU32 | 0.82 | *0.01* | 0.84 | *0.00* | 0.0000 | *0.0001* | 0.74 | *0.01* | 0.70 | *0.00* | 0.0001 | *0.0001* | | | | | | |
| PU359 | 0.81 | *0.01* | 0.82 | *0.00* | 0.0000 | *0.0002* | 0.66 | *0.59* | 0.76 | *0.00* | 0.0443 | | | | | | | |
| PU361 | 0.66 | *0.02* | 0.76 | *0.05* | 0.0011 | *0.0009* | 0.57 | *0.07* | 0.64 | *0.00* | 0.0173 | | | | | | | |
| PU58 | 0.64 | *0.02* | 0.77 | *0.09* | 0.0011 | *0.0007* | 0.62 | *0.01* | 0.66 | *0.00* | 0.0003 | *0.0003* | | | | | | |

*Notes:* Title refers to session no.: accelerating voltage, beam current, beam diameter. Errors of one standard deviation (*s.d.*) shown in *italics*.

# Appendix E – Technique comparison

A variety of bulk and microanalytical techniques were used to measure the $H_2O$ and $CO_2$ concentrations of the ETNA glasses described in Chapters 4 and 5, which are compared in Figure E.1. $H_2O$ concentrations were measured using the bulk technique of TCEA (Section 5.2.6) and four different microanalytical techniques: SIMS-4f (Section 4.2.2), EPMA (Section 2.5.3), FTIR (Section 4.2.2), and Raman (Section 6.3.2) (Figure E.1a). All techniques produce very similar results, but TCEA, SIMS-4f, and FTIR agree very well, whilst EPMA-VBD slightly overestimates and Raman slightly underestimates. No sub-surface charging correction was applied to the EPMA-VBD measurements as no VBD standards were collected during analysis to produce the calibration, consistent with the findings of Chapter 2. Raman $H_2O$ concentrations are vastly underestimated when nanolites are present, as discussed previously by Di Genova et al. (2017b). Nanolites do not appear to affect the other methods, although no measurements of nanolite-bearing glasses were made using FTIR. EPMA-VBD, as a by difference technique, has the largest errors ($\sim$0.75 wt%) although these could be improved by using a higher precision technique to estimate $Fe^{2+}/Fe_T$. TCEA, SIMS-4f, and FTIR have the smallest errors ($<$0.1 wt%), and SIMS-4f has the highest spatial resolution ($\sim$15 μm diameter region).

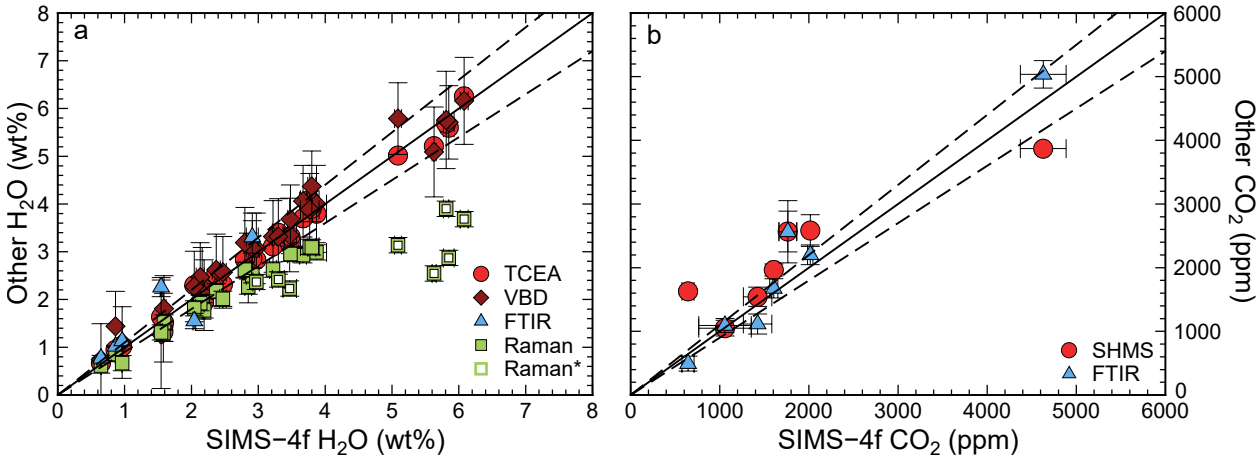


**Figure E.1:** Comparison of different analytical techniques for measuring glass **(a)** $H_2O$ concentration (ETNA glasses from Chapters 4 and 5) and **(b)** $CO_2$ concentration (ETNA glasses from Chapter 4), which are plotted against SIMS-4f measurements and the symbol indicates the technique. Raman* indicates nanolites present in the glass (open-symbols). The black, solid line indicates the 1-to-1 relationship, whereas the black, dashed lines are 10 % deviations from this.

$CO_2$ concentrations were measured using the bulk technique of SHMS (Section 4.2.2) and two microanalytical techniques: SIMS-4f (Section 4.2.2) and FTIR (Section 4.2.2) (Figure E.1b). SIMS-4f and FTIR agree well, whilst SHMS tends to overestimate the $CO_2$ concentration in comparison to SIMS-4f. In some cases the difference between the SIMS-4f measurements and the SHMS or FTIR measurements are $>$20 %. This may reflect inhomogeniety in the samples, which would cause discrencies between the techniques as SHMS is a bulk technique and different areas were analysed for SIMS-4f and FTIR. Alternatively, this may be due to incomplete removal of carbon contamination (e.g., absorbed and surficial) during SHMS. All techniques have similar errors ($\sim$9 % relative for SHMS, $\sim$7 % rel. for SIMS-4f, and $\sim$12 % rel. for FTIR), but (as for $H_2O$) SIMS-4f has the highest spatial resolution.

Figure E.2 shows a comparison of $H_2O$ concentration measured using different microanalytical techniques

(SIMS-4f, SIMS-1270($^1H_2^+/^1H^+$), SIMS-1270($^1H^+$/PB), EPMA-VBD, and Raman) on the same melt inclusion. Data are compared to SIMS-4f measuements, except Raman measurements which are compared to VBD as melt inclusions were not analysed using both Raman and SIMS-4f. Generally, all techniques agree well, although some EPMA-VBD measurement and SIMS-1270($^1H^+$/PB) measurements are much higher than the SIMS-4f measurements.

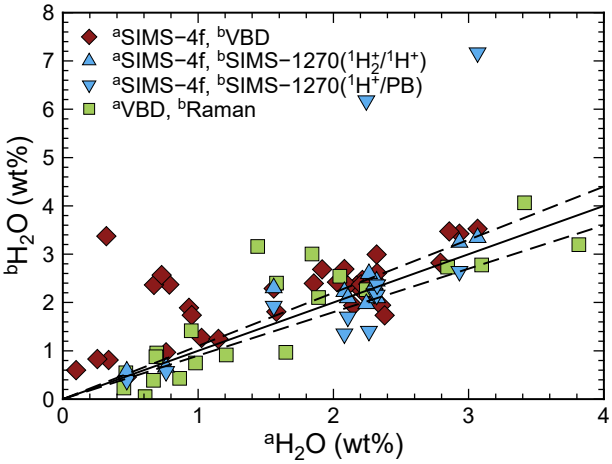


**Figure E.2:** Comparison of different analytical techniques for measuring melt inclusion $H_2O$ concentration and the symbols shows the two techniques being compared, where the value for technique 'a' is shown on the x-axis and 'b' is shown on the y-axis. VBD and both the SIMS-1270 techniques are compared to SIMS-4f, whereas Raman is compared to VBD as no melt inclusions were measured using both SIMS-4f and Raman. The black, solid line indicates the 1-to-1 relationship, whereas the black, dashed lines are 10 % deviations from this.

# Appendix F – Nanolite formation in silicate glass

## F.1. Raman spectroscopy

Raman spectra were collected as described Section 6.3.2 on all ETNA glasses in Chapters 4 and 5. Degree of nanolitisation (N#) (Equation 6.7, Di Genova et al. 2018) ranged from 0.66 to 3.70 (Table F.1), where N# $< 1.5$ have no clearly observable magnetite peak in the Raman spectra (Figure F.1).

**Table F.1:** Degree of nanolitisation (N#) for ETNA glasses measured using Equation 6.7.

| Sample | N# | *s.d.* | Sample | N# | *s.d.* | Sample | N# | *s.d.* | Sample | N# | *s.d.* |
|---|---|---|---|---|---|---|---|---|---|---|---|
| ETNA01 | 0.82 | *0.06* | ETNA09 | 0.92 | *0.04* | ETNA17 | 1.05 | *0.06* | ETNA31 | 0.80 | *0.04* |
| ETNA02 | 0.80 | *0.03* | ETNA10 | 0.94 | *0.05* | ETNA24 | 0.82 | *0.06* | ETNA32 | 0.77 | *0.10* |
| ETNA03 | 3.70 | *0.29* | ETNA11 | 1.07 | *0.10* | ETNA25 | 0.66 | *0.02* | ETNA33 | 0.72 | *0.02* |
| ETNA04 | 0.82 | *0.04* | ETNA12 | 0.82 | *0.03* | ETNA26 | 0.70 | *0.06* | ETNA34 | 0.86 | *0.07* |
| ETNA05 | 1.47 | *0.06* | ETNA13 | 1.35 | *0.05* | ETNA27 | 0.77 | *0.05* | ETNA35 | 1.07 | *0.03* |
| ETNA06 | 3.59 | *0.45* | ETNA14 | 2.07 | *0.08* | ETNA28 | 0.82 | *0.02* | ETNA36 | 0.85 | *0.05* |
| ETNA07 | 3.53 | *0.34* | ETNA15 | 0.78 | *0.05* | ETNA29 | 0.78 | *0.05* | | | |
| ETNA08 | 3.22 | *0.20* | ETNA16 | 2.00 | *0.09* | ETNA30 | 3.12 | *0.28* | | | |

*Notes*: Errors of one standard deviation ($s.d.$) shown in $italics$.

## F.2. Nanolite formation

Magnetite nanolites were detected in some glasses using Raman spectroscopy, indicated by N# $> 1.5$ (Figure F.1). All glasses with $H_2O > 5$ wt% contain magnetite nanolites, indicated by a prominent peak at ~670 $cm^{-1}$ (N# $\approx 3$), and those run at 1 kbar with $H_2O \geqslant 3$ wt% have a smaller peak at ~670 $cm^{-1}$ (N# $\approx 2$), indicating fewer magnetite nanolites (Di Genova et al., 2018) (Figure F.1). EPMA can cause the precipitation of Fe-bearing nanolites during analysis (Section 3.5), but areas selected for Raman spectroscopy had not been analysed previously using EPMA.

Magnetite nanolites can form as the glass quenches, if there is sufficient Fe in the glass (Di Genova et al., 2017a). The temperature decrease on the quench oxidises the melt as $fO_2$ depends on temperature (e.g., Kress and Carmichael, 1991) (Figure 1.3), which can cause precipitation of magnetite nanolites if they form before the melt passes through the glass transition temperature (Di Genova et al., 2017a). All glasses had the same quench rate (~150 $°C \cdot s^{-1}$; Berndt et al. 2002), therefore this cannot be the cause of the differences in the formation of nanolites. Low melt viscosity facilitates nanolite formation on the quench, as Fe can diffuse faster to form the nanolites, which is consistent with high $H_2O$ glasses containing nanolites as $H_2O$ is a strong control on melt viscosity (e.g., Giordano et al., 2008) (Figure F.2a). These glasses also have the lowest $Fe^{2+}/Fe_T$ (~0.5–0.7), and oxidised Fe promotes nanolite formation (Figure F.2b) (Di Genova et al., 2017a). The most hydrous 1 kbar experiments also contain magnetite nanolites, but contain <5 wt% $H_2O$ and are fairly oxidised ($Fe^{2+}/Fe_T \approx 0.7$), although fewer nanolites than are present in the high $H_2O$ glasses (Figure F.2). On the other hand, there are more oxidised glassed with higher $H_2O$ concentrations that do not contain nanolites (Figure F.2). Further work is needed to understand the controls on the formation of quench nanolites, but it maybe that pressure or fluid composition is also important for nanolite formation.

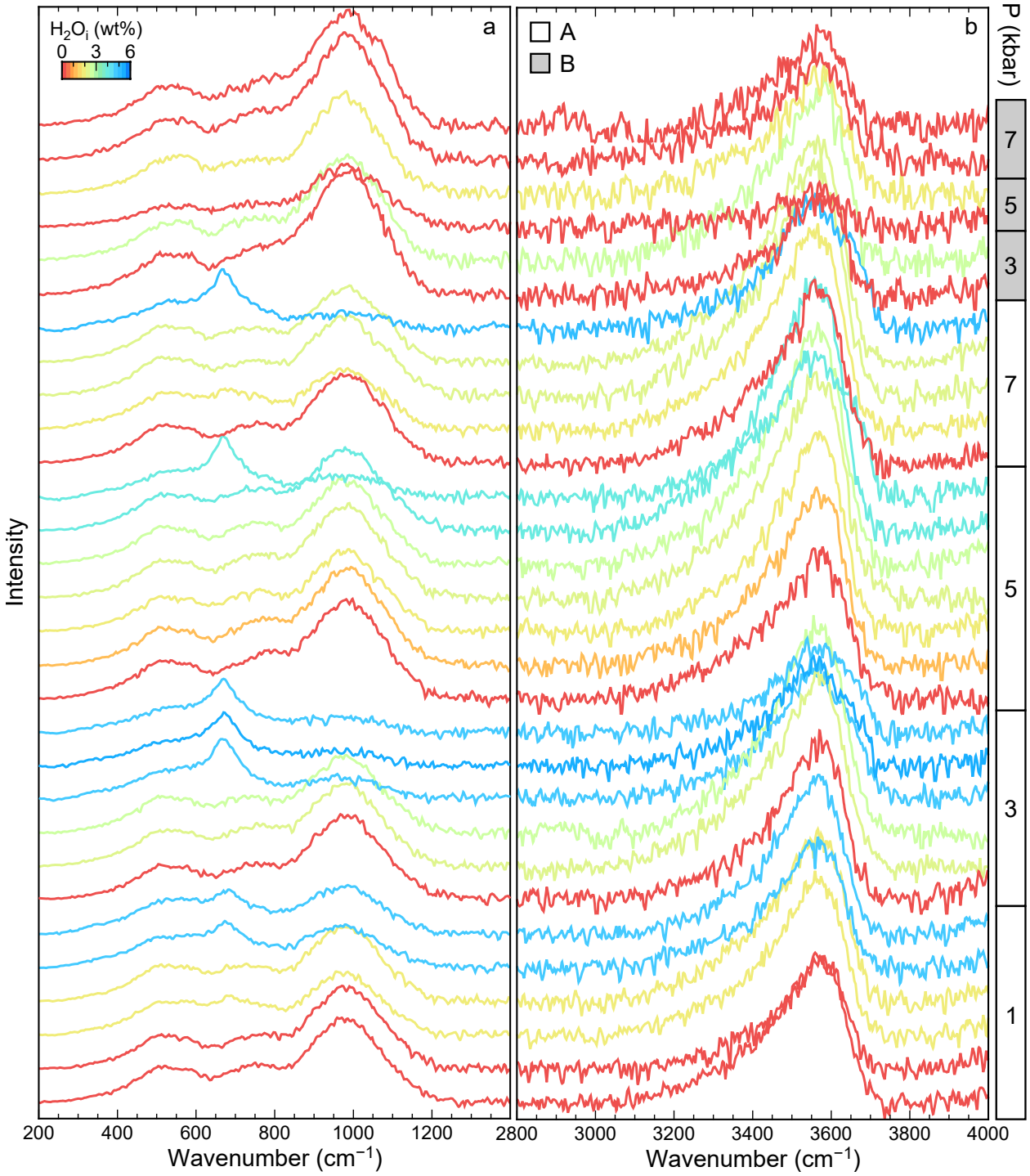


**Figure F.1:** Raman spectra for ETNA glasses in Chapters 4 and 5, which have been corrected for temperature, excitation line effects and backgrounds (Di Genova et al., 2017b). **(a)** low wavenumber and **(b)** high wavenumber regions, which are grouped by pressure and coloured by initial $H_2O$ concentration. White and grey boxes on the right-hand side indicate A and B glasses respectively. One spectrum is shown per glass, which are offset for clarity, and intensity units are arbitrary.

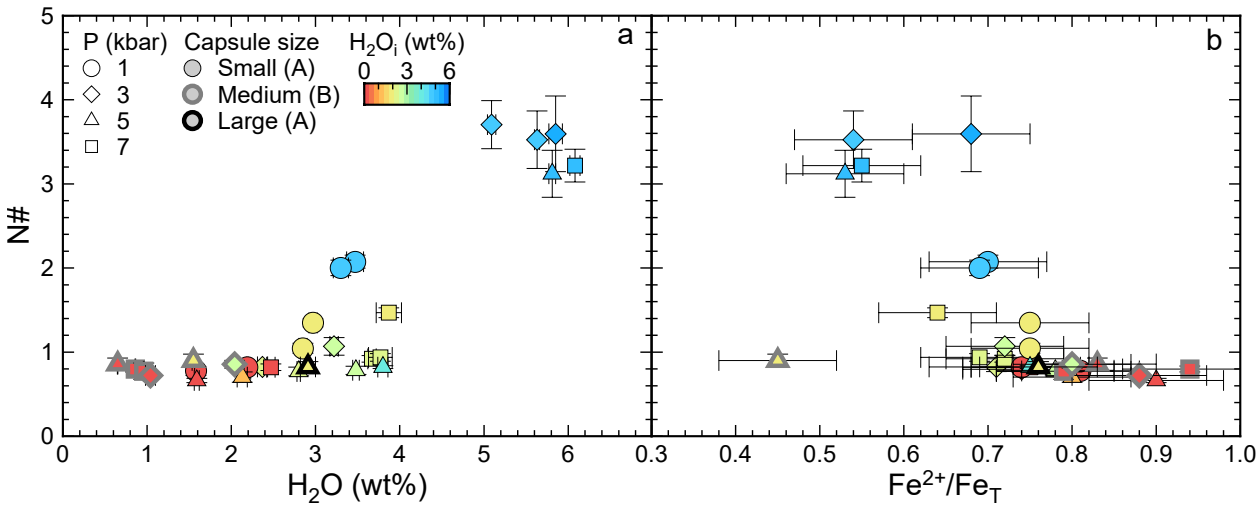


**Figure F.2:** Degree of nanolitisation (N#, Equation 6.7, Di Genova et al. 2018) against **(a)** $H_2O$ and **(b)** Fe oxidation state, where symbol shape indicates pressure, outline capsule size, and colour initial $H_2O$ concentration.

# Appendix G – Calculating fugacities and activities

## G.1. Theory

During glass synthesis, the melt in the capsule equilibrates to the $fH_2$ imposed by the IHPV by concurrent $H_2$ infiltration and oxidation and Fe loss and reduction (Section 5.2.1):

$$H_2 + \frac{1}{2}O_2 \rightleftharpoons H_2O \tag{G.1}$$

$$FeO^{melt} \rightleftharpoons Fe^{alloy} + \frac{1}{2}O_2 \tag{G.2}$$

$$Fe_2O_3 \rightleftharpoons 2FeO + \frac{1}{2}O_2 \tag{G.3}$$

The equilibrium constant for Equation G.1 is:

$$K_W = \frac{fH_2O}{fH_2\sqrt{fO_2}} \tag{G.4}$$

where $fH_2O$ can be substituted for activity using:

$$fH_2O = aH_2O \cdot fH_2O^* \tag{G.5}$$

where $^*$ indicates a specified reference state, hence:

$$fH_2O^* = fH_2{}^* \cdot \sqrt{fO_2^*} \cdot K_W^* \tag{G.6}$$

which gives:

$$fO_2 = \frac{aH_2O^2 \cdot fO_2^* \cdot (fH_2^*)^2 \cdot (K_W^*)^2}{fH_2^2 \cdot K_W^2} \tag{G.7}$$

Taking the logarithm of both sides gives:

$$\log fO_2 = 2\log aH_2O + c \tag{G.8}$$

where:

$$c = \log \frac{fO_2^* \cdot (fH_2^*)^2 \cdot (K_W^*)^2}{fH_2^2 \cdot K_W^2} \tag{G.9}$$

which is constant at fixed pressure and temperature.

## G.2. Application to the experimental data

All experiments were conducted at the same temperature (1250 °C) therefore, from Equation G.8, each set of experiments run at the same pressure should have a linear relationship for $\log fO_2$ against $\log aH_2O$ with a slope of two. The glass $Fe^{2+}/Fe_T$ can be used to calculate $fO_2$ using Kress and Carmichael (1991) (Figure G.1a). The melt $H_2O$ concentration can be used to estimate the $aH_2O$ at a given pressure, temperature, and melt composition using Burnham (1979) (Figure G.1b). Figure G.1c shows $fO_2$ using Kress and Carmichael (1991) against $aH_2O$ using Burnham (1979) for all glasses, whilst Figure G.1d is a subset of the data which all have the same capsule size and anhydrous glass composition. For the subset of the data shown in Figure G.1d, the best fit through each pressure has been calculated using Equation G.8. Data for 1 and 3 kbar agree well with the model (i.e., slope $\sim$2), whilst 5 and 7 kbar have a slope $>$2.

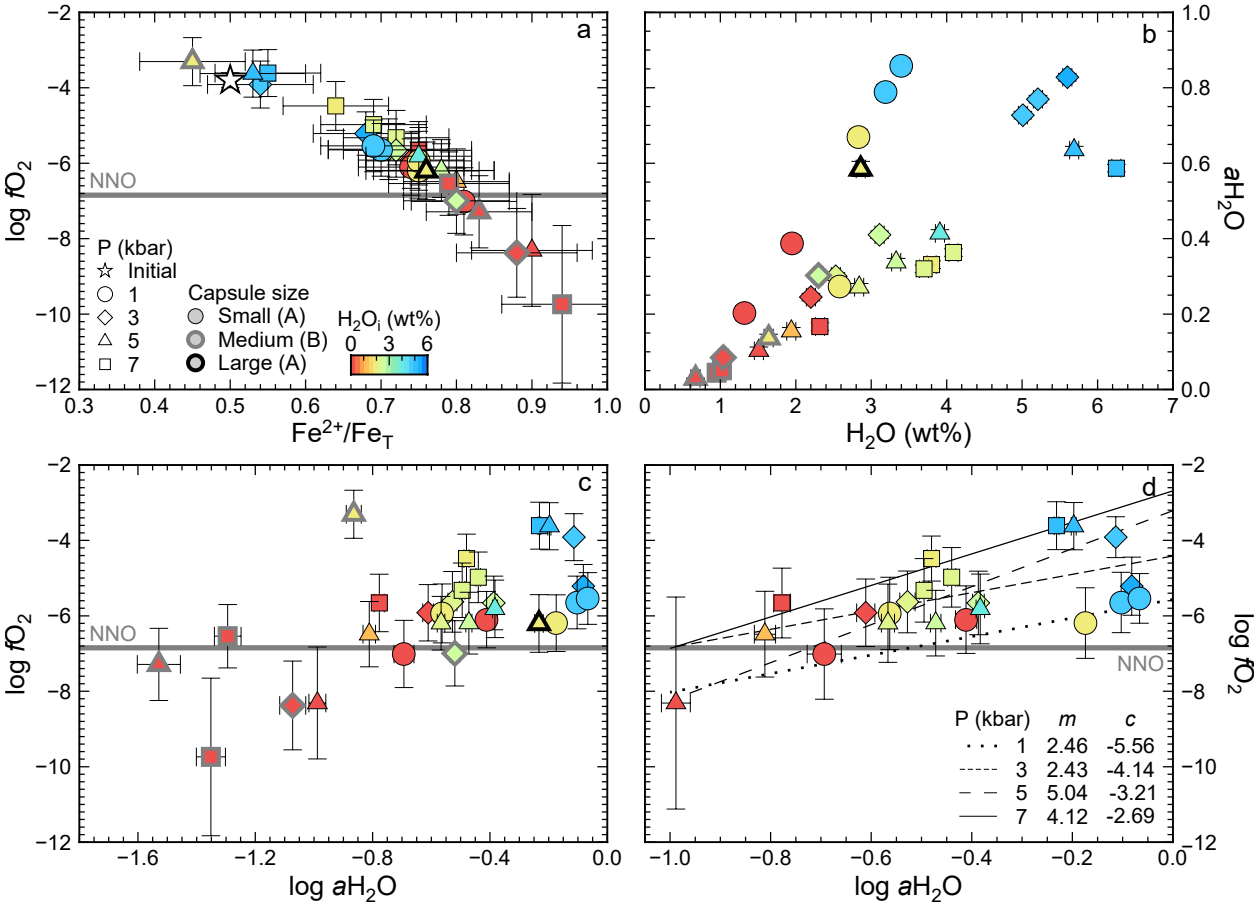


**Figure G.1:** Oxygen fugacity ($fO_2$) and $H_2O$ activity ($aH_2O$) for experimental glasses, where symbol shape indicates pressure, outline capsule size, and colour initial $H_2O$ concentration: **(a)** $\log fO_2$ calculated using Kress and Carmichael (1991) against $Fe^{2+}/Fe_T$ for all glasses; **(b)** $aH_2O$ calculated using Burnham (1979) against $H_2O$ concentration; $\log fO_2$ against $\log aH_2O$ (Burnham, 1979) for **(c)** all experiments and **(d)** small capsules only, with best fits for each pressure using Equation G.8. The NNO buffer is shown for reference.

## G.3. Calculating the $fH_2$ gradient

We can calculate the $fH_2$ gradient at the start of the experiment by comparing the initial and final $fH_2$ in the capsules ($fH_2^i$ and $fH_2^f$, respectively). Assuming $H_2O$ equilibrium was been reached (Section 5.7.2), $fH_2^f$ is the same as the IHPV $fH_2$, which is providing the driving force. $fH_2^i$ can be calculated using the initial

$Fe^{2+}/Fe_T$ and $H_2O$ from the weighed-in measurements to calculate $fO_2^i$ and $aH_2O^i$, which are shown in Figures G.1a and G.2a. $H_2O$ has been set at 0.01 wt% for initially anhydrous glasses. Two values of $aH_2O_i > 1$, which correspond to the most hydrous 1 kbar experiments as they would have been saturated at the start of the experiment and therefore would not have had all their $H_2O$ dissolved in the melt. Using Equation G.9, $c$ can be calculated for the initial ($c^i$) and final ($c^f$) $fO_2$ and $aH_2O$. As $\log(fO_2^* \cdot (fH_2^*)^2 \cdot (K_W^*)^2)$ is constant, and $K_W$ is constant at a given temperature and pressure:

$$\Delta fH_2 = \frac{fH_2^i}{fH_2^f} = \sqrt{\exp(c^f - c^i)} \tag{G.10}$$

which is a measure of the gradient driving $H_2$ diffusion into the capsule. $\Delta fH_2$ increases with decreasing initial $H_2O$ as the difference between the capsule and the IHPV is greatest (Figure G.2b). Fe loss ($\Delta Fe_T$) and final $Fe^{2+}/Fe_T$ also correlate with initial $H_2O$ showing they are changing in response to $\Delta fH_2$ (Figures G.2c and d).

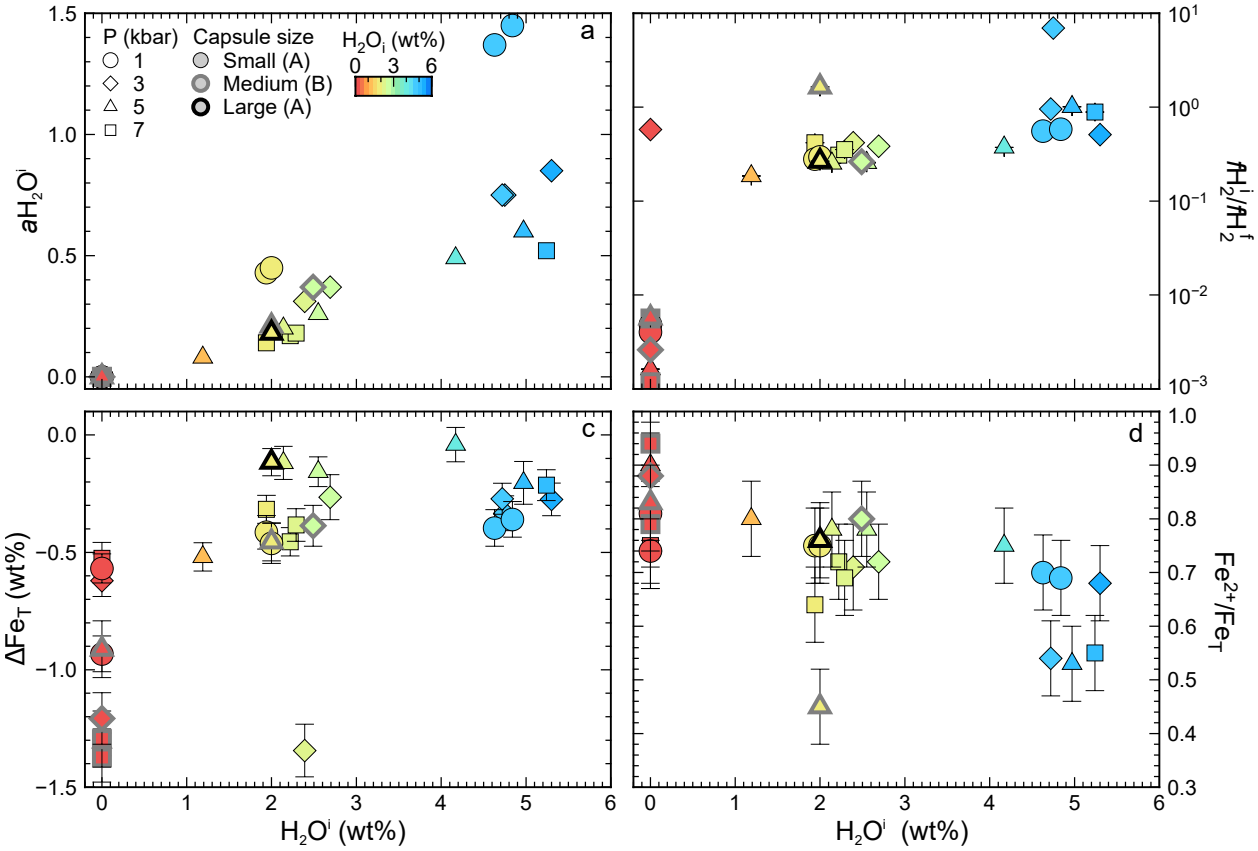


**Figure G.2:** **(a)** initial $H_2O$, **(b)** $fH_2$ gradient, **(c)** change in Fe concentration ($\Delta Fe_T$), and **(d)** final $Fe^{2+}/Fe_T$ against initial $H_2O$, where symbol shape indicates pressure, outline capsule size, and colour initial $H_2O$ concentration.

## G.4. Calculating $aH_2O$

Alternatively, $aH_2O$ can be calculated using Equation G.7 by setting the reference state as the intrinsic redox conditions of the IHPV at $aH_2O = 1$. Assuming $K_W$ and $fH_2$ are constant at fixed pressure and temperature (i.e., $K_W$ only depends on P and T, and $H_2$ diffuses fast enough to maintain $fH_2$ inside and outside the

capsule), Equation G.7 becomes:

$$fO_2^{cap} = fO_2^{IHPV} \cdot (aH_2O)^2 \tag{G.11}$$

$$\log(fO_2^{cap}) = \log(fO_2^{IHPV}) + 2\log(aH_2O) \tag{G.12}$$

where subscript IHPV indicates the intrinsic redox conditions in the IHPV being the reference state and subscript cap being the conditions within the capsule. Therefore, $aH_2O$ can be calculated using:

$$\log aH_2O = \frac{1}{2}\log\frac{fO_2^{cap}}{fO_2^{IHPV}} \tag{G.13}$$

The intrinsic redox state of the IHPV has been measured twice and gives values of NNO+3.5 (Berndt et al., 2002) and NNO+2.6 (Schuessler et al., 2008). Results using both $fO_2^{IHPV}$ are shown in Figure G.3 and show that calculated $aH_2O$ is very sensitive to the choice of $fO_2^{IHPV}$. Some values of $aH_2O > 1$ for $fO_2^{IHPV}$ = NNO+2.6, therefore the actual $fO_2^{IHPV}$ must be more positive than this. Activity calculated in this way is far less than that calculated using Burnham (1979), except at $H_2O > 5$ wt%. Burnham (1979) has a linear relationship between $aH_2O$ and dissolved $H_2O$, whereas using $fO_2^{IHPV}$ to calculate $aH_2O$ increases rapidly at high dissolved $H_2O$ concentrations regardless of $fO_2^{IHPV}$ chosen (Figures G.1b and G3). As $aH_2O$ calculated in this way depends so critically on $fO_2^{IHPV}$, which was not measured during these experiments, these $aH_2O$ are treated with caution.

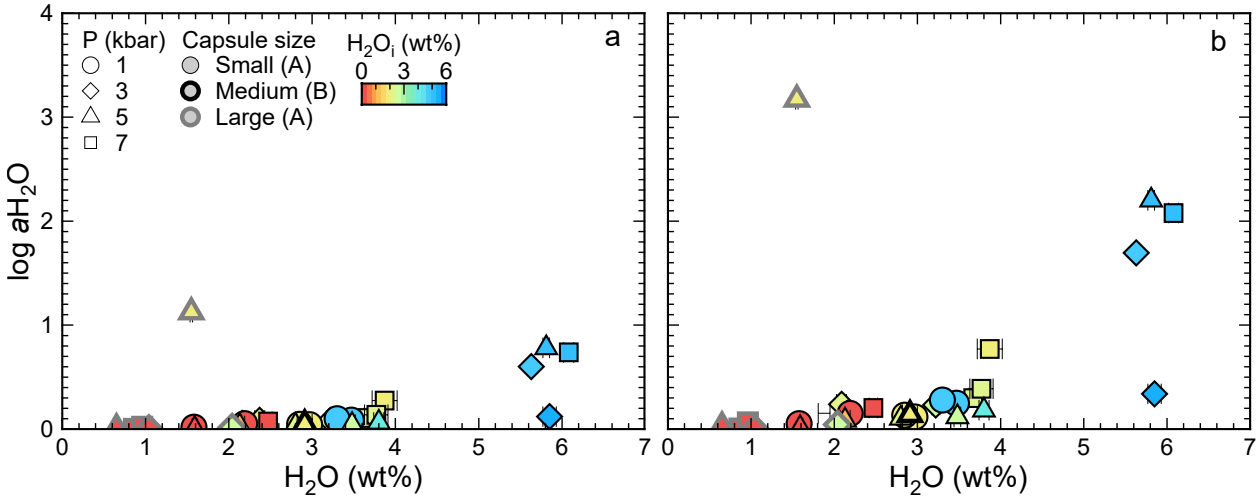


**Figure G.3**: $H_2O$ activity ($aH_2O$) calculated assuming an intrinsic IHPV $fO_2$ **(a)** NNO+3.5 (Berndt et al., 2002) and **(b)** NNO+2.6 (Schuessler et al., 2008), where symbol shape indicates pressure, outline capsule size, and colour initial $H_2O$ concentration.

# Appendix H

## Chapter 6 data: Melt inclusion study of the 23/11/13 Etna eruption

**Table H.1:** Olivine compositions.

**Table H.2:** Pyroxene compositions.

**Table H.3:** Plagioclase inclusion compositions.

**Table H.4:** Description of glass analyses.

**Table H.5:** Raman data on melt inclusions, embayments, and matrix glass.

**Table H.6:** SIMS data on melt inclusions, embayments, and matrix glass.

**Table H.7:** EPMA data on melt inclusions, embayments, and matrix glass.

**Table H.1:** Olivine compositions ($n$ = 282).

| Sample | $SiO_2$ | $Al_2O_3$ | FeO | MnO | MgO | CaO | $Na_2O$ | $P_2O_5$ | NiO | Fo |
|---|---|---|---|---|---|---|---|---|---|---|
| ETNAB_a1 | 39.25 | 0.04 | 16.71 | 0.26 | 43.22 | 0.23 | 0.02 | 0.03 | 0.09 | 82.2 |
| ETNAB_a2 | 38.79 | 0.05 | 19.28 | 0.31 | 41.28 | 0.28 | 0.01 | 0.07 | 0.07 | 79.2 |
| ETNAB_a3 | 38.47 | 0.03 | 21.07 | 0.37 | 39.51 | 0.31 | 0.02 | 0.05 | 0.04 | 77.0 |
| ETNAB_a4 | 37.99 | 0.04 | 24.27 | 0.52 | 37.01 | 0.33 | 0.02 | 0.03 | -0.01 | 73.1 |
| ETNAB_a5 | 37.71 | 0.03 | 25.60 | 0.55 | 35.85 | 0.33 | 0.02 | 0.02 | 0.01 | 71.4 |
| ETNAB_a6 | 38.09 | 0.04 | 22.30 | 0.48 | 38.26 | 0.36 | 0.02 | 0.10 | 0.02 | 75.4 |
| ETNAB_a7 | 38.40 | 0.03 | 21.33 | 0.39 | 39.28 | 0.23 | 0.02 | 0.03 | 0.06 | 76.6 |
| ETNAB_aa1 | 37.78 | 0.05 | 24.90 | 0.57 | 36.04 | 0.39 | 0.03 | 0.07 | 0.01 | 72.1 |
| ETNAB_aa2 | 38.73 | 0.04 | 18.66 | 0.32 | 41.41 | 0.29 | 0.01 | 0.03 | 0.06 | 79.8 |
| ETNAB_aa3 | 38.86 | 0.04 | 19.68 | 0.32 | 40.84 | 0.26 | 0.01 | 0.03 | 0.07 | 78.7 |
| ETNAB_aa4 | 38.40 | 0.04 | 20.21 | 0.36 | 39.93 | 0.25 | 0.02 | 0.05 | 0.06 | 77.9 |
| ETNAB_b1 | 37.77 | 0.04 | 25.48 | 0.57 | 35.89 | 0.38 | 0.03 | 0.04 | 0.01 | 71.5 |
| ETNAB_b2 | 37.50 | 0.04 | 25.76 | 0.57 | 35.51 | 0.40 | 0.02 | 0.03 | 0.00 | 71.1 |
| ETNAB_b3 | 38.95 | 0.03 | 18.51 | 0.30 | 41.72 | 0.23 | 0.01 | 0.02 | 0.08 | 80.1 |
| ETNAB_b4 | 38.92 | 0.03 | 18.29 | 0.31 | 41.92 | 0.23 | 0.01 | 0.01 | 0.08 | 80.3 |
| ETNAB_b5 | 39.30 | 0.04 | 17.46 | 0.29 | 42.52 | 0.24 | 0.02 | 0.04 | 0.09 | 81.3 |
| ETNAB_b7 | 37.66 | 0.04 | 25.20 | 0.55 | 36.10 | 0.38 | 0.02 | 0.02 | 0.02 | 71.9 |
| ETNAB_b8 | 39.04 | 0.03 | 18.34 | 0.29 | 41.74 | 0.25 | 0.02 | 0.03 | 0.05 | 80.2 |
| ETNAB_e1 | 37.83 | 0.04 | 25.07 | 0.51 | 36.62 | 0.24 | 0.02 | 0.04 | 0.03 | 72.2 |
| ETNAB_e3 | 39.09 | 0.04 | 17.01 | 0.27 | 42.61 | 0.24 | 0.02 | 0.03 | 0.09 | 81.7 |
| ETNAB_e4 | 38.33 | 0.04 | 21.60 | 0.42 | 38.74 | 0.30 | 0.02 | 0.05 | 0.02 | 76.2 |
| ETNAB_e5 | 38.17 | 0.04 | 22.75 | 0.44 | 37.89 | 0.24 | 0.02 | 0.03 | 0.05 | 74.8 |
| ETNAB_e6 | 37.65 | 0.05 | 25.52 | 0.55 | 35.90 | 0.33 | 0.03 | 0.03 | 0.03 | 71.5 |
| ETNAB_e7 | 39.14 | 0.04 | 17.81 | 0.28 | 41.99 | 0.24 | 0.02 | 0.02 | 0.08 | 80.8 |
| ETNAB_e8 | 37.70 | 0.03 | 25.37 | 0.55 | 35.81 | 0.39 | 0.03 | 0.02 | 0.01 | 71.6 |
| ETNAB_e9 | 38.66 | 0.05 | 20.21 | 0.36 | 40.20 | 0.23 | 0.02 | 0.02 | 0.03 | 78.0 |
| ETNAB_f1 | 38.73 | 0.03 | 19.89 | 0.37 | 40.36 | 0.29 | 0.02 | 0.02 | 0.04 | 78.3 |
| ETNAB_f2 | 37.91 | 0.04 | 24.53 | 0.51 | 36.66 | 0.25 | 0.02 | 0.02 | 0.05 | 72.7 |
| ETNAB_f4 | 39.09 | 0.03 | 17.90 | 0.28 | 42.23 | 0.24 | 0.01 | 0.05 | 0.08 | 80.8 |
| ETNAB_f5 | 37.43 | 0.03 | 26.89 | 0.66 | 34.71 | 0.32 | 0.03 | 0.05 | 0.01 | 69.7 |
| ETNAB_f6 | 37.49 | 0.04 | 26.48 | 0.59 | 35.16 | 0.30 | 0.02 | 0.03 | 0.02 | 70.3 |
| ETNAB_f7 | 39.13 | 0.03 | 17.22 | 0.27 | 42.97 | 0.24 | 0.01 | 0.03 | 0.11 | 81.6 |
| ETNAB_f9 | 38.83 | 0.03 | 19.43 | 0.35 | 40.69 | 0.30 | 0.02 | 0.02 | 0.06 | 78.9 |
| ETNAB_f10 | 39.28 | 0.05 | 17.72 | 0.28 | 42.18 | 0.25 | 0.01 | 0.02 | 0.08 | 80.9 |
| ETNAB_f11 | 38.54 | 0.05 | 20.73 | 0.38 | 39.58 | 0.29 | 0.01 | 0.03 | 0.03 | 77.3 |
| ETNAB_f13 | 37.95 | 0.04 | 23.36 | 0.57 | 37.50 | 0.24 | 0.03 | 0.06 | 0.02 | 74.1 |
| ETNAB_g1 | 37.62 | 0.04 | 25.93 | 0.58 | 35.50 | 0.39 | 0.03 | 0.04 | 0.03 | 70.9 |
| ETNAB_g2 | 38.80 | 0.04 | 19.05 | 0.32 | 41.06 | 0.22 | 0.02 | 0.03 | 0.07 | 79.3 |
| ETNAB_g3 | 36.78 | 0.03 | 30.49 | 0.75 | 31.72 | 0.36 | 0.03 | 0.04 | 0.00 | 65.0 |
| ETNAB_g4 | 38.60 | 0.04 | 21.05 | 0.38 | 39.58 | 0.31 | 0.01 | 0.02 | 0.05 | 77.0 |
| ETNAB_g5 | 38.97 | 0.04 | 19.38 | 0.31 | 41.08 | 0.26 | 0.02 | 0.03 | 0.06 | 79.1 |
| ETNAB_c3 | 37.74 | 0.04 | 25.75 | 0.55 | 35.72 | 0.36 | 0.03 | 0.04 | 0.01 | 71.2 |
| ETNAB_c4 | 38.75 | 0.04 | 19.94 | 0.34 | 40.67 | 0.25 | 0.01 | 0.02 | 0.06 | 78.4 |
| ETNAB_c6 | 39.21 | 0.03 | 17.44 | 0.27 | 42.63 | 0.21 | 0.02 | 0.02 | 0.09 | 81.3 |
| ETNAB_c7 | 37.49 | 0.04 | 26.58 | 0.63 | 34.54 | 0.42 | 0.02 | 0.04 | 0.02 | 69.8 |

**Table H.1:** Olivine compositions ($n$ = 282) *cont.*

| Sample | $SiO_2$ | $Al_2O_3$ | FeO | MnO | MgO | CaO | $Na_2O$ | $P_2O_5$ | NiO | Fo |
|---|---|---|---|---|---|---|---|---|---|---|
| ETNAB_c8 | 39.15 | 0.03 | 17.85 | 0.27 | 41.97 | 0.25 | 0.01 | 0.02 | 0.09 | 80.7 |
| ETNAB_d2 | 37.36 | 0.04 | 27.28 | 0.62 | 34.13 | 0.42 | 0.03 | 0.07 | 0.02 | 69.0 |
| ETNAB_d3 | 39.17 | 0.03 | 17.45 | 0.27 | 42.28 | 0.24 | 0.02 | 0.02 | 0.08 | 81.2 |
| ETNAB_d5 | 37.37 | 0.04 | 27.51 | 0.60 | 34.18 | 0.41 | 0.03 | 0.05 | 0.00 | 68.9 |
| ETNAB_d6 | 38.57 | 0.04 | 21.52 | 0.40 | 39.12 | 0.23 | 0.02 | 0.04 | 0.03 | 76.4 |
| REDh_nrMIbig | 39.30 | 0.03 | 16.95 | 0.27 | 43.00 | 0.22 | 0.00 | 0.01 | 0.10 | 81.9 |
| REDh_nrMIsmall | 39.17 | 0.03 | 17.30 | 0.28 | 42.38 | 0.22 | 0.01 | 0.01 | 0.07 | 81.4 |
| REDh_core | 39.20 | 0.03 | 16.89 | 0.27 | 43.02 | 0.20 | 0.01 | 0.02 | 0.08 | 81.9 |
| REDr1_nrMI-out | 39.29 | 0.08 | 18.03 | 0.29 | 41.97 | 0.36 | 0.01 | 0.01 | 0.07 | 80.6 |
| REDr1_nrMI-out | 39.39 | 0.04 | 17.96 | 0.28 | 42.20 | 0.31 | 0.01 | 0.01 | 0.06 | 80.7 |
| REDr1_nrMI-out | 39.36 | 0.04 | 17.96 | 0.29 | 42.10 | 0.29 | 0.01 | 0.01 | 0.07 | 80.7 |
| REDr1_nrMI-out | 39.26 | 0.03 | 17.98 | 0.28 | 42.24 | 0.27 | 0.01 | 0.01 | 0.08 | 80.7 |
| REDr1_nrMI-out | 39.13 | 0.03 | 17.79 | 0.28 | 42.05 | 0.25 | 0.01 | 0.00 | 0.08 | 80.8 |
| REDr1_nrMI-out | 39.23 | 0.04 | 17.79 | 0.29 | 42.21 | 0.24 | 0.00 | 0.01 | 0.08 | 80.9 |
| REDr1_nrMI-out | 39.22 | 0.03 | 17.91 | 0.28 | 42.11 | 0.24 | 0.00 | 0.01 | 0.08 | 80.7 |
| REDr1_nrMI-out | 39.35 | 0.02 | 17.93 | 0.28 | 42.21 | 0.24 | 0.00 | 0.01 | 0.08 | 80.8 |
| REDr1_nrMI-out | 39.20 | 0.03 | 17.87 | 0.28 | 42.35 | 0.22 | 0.00 | 0.01 | 0.06 | 80.9 |
| REDr1_nrMI-out | 39.18 | 0.03 | 17.69 | 0.27 | 42.24 | 0.23 | 0.00 | 0.01 | 0.09 | 81.0 |
| REDr1_core | 39.16 | 0.03 | 17.73 | 0.29 | 42.17 | 0.23 | 0.00 | 0.02 | 0.08 | 80.9 |
| REDn_nrMInobubble | 39.35 | 0.03 | 17.10 | 0.25 | 43.17 | 0.26 | 0.01 | 0.01 | 0.10 | 81.8 |
| REDn_core | 39.29 | 0.03 | 17.19 | 0.24 | 42.87 | 0.19 | 0.01 | 0.01 | 0.09 | 81.6 |
| REDg_nrMI | 38.70 | 0.04 | 19.96 | 0.33 | 40.74 | 0.25 | 0.01 | 0.04 | 0.04 | 78.4 |
| REDg_core | 38.75 | 0.04 | 19.91 | 0.31 | 40.81 | 0.16 | 0.02 | 0.05 | 0.06 | 78.5 |
| REDg_core | 38.90 | 0.04 | 19.56 | 0.31 | 41.30 | 0.19 | 0.01 | 0.04 | 0.04 | 79.0 |
| REDg_core | 38.87 | 0.04 | 19.12 | 0.31 | 41.48 | 0.18 | 0.01 | 0.04 | 0.05 | 79.5 |
| REDe1_nrMI | 38.27 | 0.02 | 22.89 | 0.48 | 38.17 | 0.28 | 0.00 | 0.02 | 0.02 | 74.8 |
| REDe1_core | 38.09 | 0.03 | 23.28 | 0.48 | 37.70 | 0.29 | 0.01 | 0.02 | 0.02 | 74.3 |
| REDe1_core | 38.22 | 0.03 | 23.33 | 0.47 | 37.89 | 0.31 | 0.01 | 0.01 | 0.02 | 74.3 |
| REDe1_core | 38.29 | 0.02 | 22.87 | 0.47 | 38.49 | 0.29 | 0.01 | 0.02 | 0.01 | 75.0 |
| REDe3_nrMI | 38.98 | 0.03 | 18.98 | 0.33 | 41.42 | 0.26 | 0.02 | 0.02 | 0.07 | 79.6 |
| REDe3_core | 39.02 | 0.04 | 18.61 | 0.30 | 41.61 | 0.21 | 0.01 | 0.02 | 0.08 | 79.9 |
| REDe3_core | 39.17 | 0.03 | 18.16 | 0.29 | 42.07 | 0.21 | 0.01 | 0.02 | 0.07 | 80.5 |
| REDe3_core | 39.30 | 0.03 | 17.84 | 0.27 | 42.31 | 0.23 | 0.01 | 0.02 | 0.08 | 80.9 |
| RED17_nrMIbubble | 38.28 | 0.04 | 22.16 | 0.44 | 38.74 | 0.29 | 0.01 | 0.03 | 0.03 | 75.7 |
| RED17_nrMInobubble | 38.49 | 0.04 | 22.39 | 0.45 | 38.71 | 0.28 | 0.01 | 0.02 | 0.03 | 75.5 |
| RED17_core | 38.45 | 0.03 | 22.46 | 0.46 | 38.56 | 0.26 | 0.02 | 0.02 | 0.03 | 75.4 |
| REDd_nrMIbubble | 38.81 | 0.03 | 19.63 | 0.32 | 40.70 | 0.23 | 0.01 | 0.01 | 0.07 | 78.7 |
| REDd_nrMInobubble | 39.05 | 0.03 | 19.70 | 0.34 | 41.08 | 0.22 | 0.01 | 0.00 | 0.07 | 78.8 |
| REDd_core | 39.40 | 0.03 | 17.68 | 0.26 | 42.39 | 0.22 | 0.01 | 0.01 | 0.09 | 81.0 |
| REDd_core | 39.31 | 0.03 | 17.99 | 0.30 | 42.22 | 0.21 | 0.01 | 0.07 | 0.07 | 80.7 |
| REDd_core | 39.35 | 0.03 | 18.42 | 0.29 | 41.80 | 0.22 | 0.01 | 0.01 | 0.08 | 80.2 |
| CYAN_h1_Ol_nr33.64 | 38.29 | 0.05 | 20.84 | 0.38 | 40.31 | 0.29 | 0.02 | 0.02 | 0.04 | 77.5 |
| CYAN_h2_core_Ol | 37.17 | 0.04 | 26.52 | 0.59 | 34.88 | 0.41 | 0.02 | 0.03 | 0.00 | 70.1 |
| CYAN_h3_core_Ol | 38.33 | 0.04 | 19.79 | 0.32 | 40.86 | 0.22 | 0.02 | 0.01 | 0.06 | 78.6 |
| CYAN_h4_core_Ol | 37.95 | 0.03 | 24.56 | 0.49 | 37.09 | 0.27 | 0.02 | 0.02 | 0.03 | 72.9 |

**Table H.1:** Olivine compositions ($n$ = 282) *cont.*

| Sample | $SiO_2$ | $Al_2O_3$ | FeO | MnO | MgO | CaO | $Na_2O$ | $P_2O_5$ | NiO | Fo |
|---|---|---|---|---|---|---|---|---|---|---|
| CYAN_g6_nr48.41_Ol | 38.75 | 0.04 | 17.99 | 0.29 | 42.18 | 0.31 | 0.02 | 0.00 | 0.08 | 80.7 |
| CYAN_g6_core_Ol | 39.06 | 0.04 | 17.91 | 0.29 | 42.71 | 0.22 | 0.02 | 0.02 | 0.10 | 81.0 |
| CYAN_g2_nrMI_Ol | 37.30 | 0.05 | 25.42 | 0.57 | 35.66 | 0.39 | 0.02 | 0.04 | 0.01 | 71.4 |
| CYAN_g2_core_Ol | 36.97 | 0.04 | 26.09 | 0.56 | 35.31 | 0.39 | 0.03 | 0.08 | 0.01 | 70.7 |
| CYAN_f2_nrMI_Ol | 37.95 | 0.04 | 20.96 | 0.40 | 39.54 | 0.27 | 0.01 | 0.02 | 0.04 | 77.1 |
| CYAN_f2_core_Ol | 37.82 | 0.04 | 21.19 | 0.40 | 39.22 | 0.35 | 0.02 | 0.01 | 0.03 | 76.7 |
| CYAN_e5_nrMI_Ol | 38.31 | 0.03 | 18.95 | 0.33 | 41.02 | 0.25 | 0.02 | 0.02 | 0.08 | 79.4 |
| CYAN_e3_nrMI_Ol | 37.44 | 0.07 | 25.68 | 0.56 | 36.66 | 0.39 | 0.03 | 0.03 | 0.01 | 71.8 |
| CYAN_e2_nrMI_Ol | 37.24 | 0.05 | 24.29 | 0.51 | 36.66 | 0.32 | 0.01 | 0.02 | 0.01 | 72.9 |
| CYAN_e2_core_Ol | 36.90 | 0.05 | 25.62 | 0.54 | 35.70 | 0.32 | 0.02 | 0.04 | 0.01 | 71.3 |
| CYAN_e1_nrT_Ol | 37.31 | 0.04 | 24.85 | 0.56 | 36.87 | 0.40 | 0.02 | 0.01 | 0.02 | 72.6 |
| CYAN_e1_nr36.00_Ol | 37.04 | 0.04 | 24.56 | 0.56 | 36.75 | 0.41 | 0.03 | 0.01 | 0.03 | 72.7 |
| CYAN_e1_core_Ol | 37.02 | 0.03 | 25.10 | 0.55 | 36.18 | 0.41 | 0.02 | 0.02 | 0.00 | 72.0 |
| CYAN_d4_nrMI_Ol | 38.32 | 0.04 | 21.93 | 0.52 | 39.26 | 0.21 | 0.02 | 0.02 | 0.00 | 76.1 |
| CYAN_d4_nrfakeMI_Ol | 38.10 | 0.03 | 22.59 | 0.66 | 38.07 | 0.17 | 0.02 | 0.03 | 0.00 | 75.0 |
| CYAN_d4_nrMG_Ol | 37.98 | 0.03 | 22.14 | 0.59 | 38.18 | 0.21 | 0.01 | 0.02 | 0.02 | 75.5 |
| CYAN_d4_core_Ol | 37.57 | 0.03 | 23.38 | 0.79 | 37.67 | 0.13 | 0.02 | 0.04 | 0.00 | 74.2 |
| CYAN_c2_nrMIbubble_Ol | 38.56 | 0.03 | 17.78 | 0.29 | 42.48 | 0.23 | 0.01 | 0.00 | 0.08 | 81.0 |
| CYAN_c2_core_Ol | 38.49 | 0.03 | 17.92 | 0.29 | 42.61 | 0.22 | 0.01 | 0.01 | 0.08 | 80.9 |
| Etna231113Pyroxenes_l5 | 38.13 | 0.05 | 22.09 | 0.43 | 38.75 | 0.22 | 0.01 | | | 75.8 |
| Etna231113Pyroxenes_k13 | 37.96 | 0.05 | 24.10 | 0.52 | 36.78 | 0.38 | 0.02 | | | 73.1 |
| Etna231113Pyroxenes_j7 | 37.58 | 0.04 | 25.14 | 0.54 | 35.80 | 0.30 | 0.02 | | | 71.7 |
| Etna231113Pyroxenes_i6 | 37.63 | 0.05 | 22.36 | 0.44 | 38.27 | 0.32 | 0.01 | | | 75.3 |
| Etna231113Pyroxenes_i5 | 37.54 | 0.04 | 25.53 | 0.56 | 35.73 | 0.33 | 0.02 | | | 71.4 |
| CYAN_e5_core_Ol | 38.81 | 0.03 | 17.47 | 0.28 | 43.05 | 0.20 | 0.01 | 0.01 | | 81.5 |
| CYAN_h1_Ol_nrbubble | 37.65 | 0.04 | 20.42 | 0.38 | 39.49 | 0.26 | 0.01 | 0.01 | 0.05 | 77.5 |
| CYAN_h1_Ol_nrbig | 37.86 | 0.04 | 19.88 | 0.36 | 40.30 | 0.30 | 0.01 | 0.01 | 0.05 | 78.3 |
| CYAN_h2_nr5292_Ol | 36.74 | 0.04 | 25.50 | 0.59 | 35.34 | 0.33 | 0.01 | 0.03 | 0.00 | 71.2 |
| CYAN_h3_nrMI_Ol | 37.83 | 0.04 | 19.59 | 0.31 | 39.99 | 0.38 | 0.02 | 0.02 | 0.08 | 78.4 |
| CYAN_e7_nrMI_Ol | 38.26 | 0.04 | 17.45 | 0.27 | 42.02 | 0.26 | 0.01 | 0.00 | 0.07 | 81.1 |
| CYAN_e7_core_Ol | 38.31 | 0.04 | 17.92 | 0.31 | 41.83 | 0.27 | 0.00 | 0.02 | 0.07 | 80.6 |
| CYAN_c2_nrMIlong_Ol | 37.82 | 0.04 | 19.02 | 0.33 | 40.90 | 0.25 | 0.01 | 0.03 | 0.06 | 79.3 |
| CYAN_a3_core_Ol | 38.34 | 0.03 | 19.59 | 0.33 | 41.18 | 0.22 | 0.01 | 0.02 | 0.08 | 78.9 |
| CYAN_a3_nrMI_Ol | 38.33 | 0.05 | 20.27 | 0.35 | 39.59 | 0.25 | 0.01 | 0.01 | 0.05 | 77.7 |
| Etna 231113 Ol a2_nr32.09 | 37.51 | 0.06 | 29.26 | 0.74 | 33.34 | 0.34 | 0.04 | 0.03 | 0.01 | 67.0 |
| Etna 231113 Ol a2_nr30.98 | 37.40 | 0.05 | 29.21 | 0.72 | 33.38 | 0.31 | 0.04 | 0.04 | 0.02 | 67.1 |
| Etna 231113 Ol a2_core | 37.26 | 0.04 | 30.08 | 0.72 | 32.49 | 0.34 | 0.02 | 0.01 | 0.02 | 65.8 |
| Etna 231113 Ol a6_nr36.26 | 38.55 | 0.04 | 23.09 | 0.47 | 38.17 | 0.30 | 0.01 | 0.01 | 0.03 | 74.7 |
| Etna 231113 Ol a6_core | 38.38 | 0.05 | 24.43 | 0.52 | 37.40 | 0.31 | 0.02 | 0.02 | 0.03 | 73.2 |
| Etna 231113 Ol a9_11.79 | 37.98 | 0.05 | 26.41 | 0.58 | 35.18 | 0.40 | 0.02 | 0.02 | 0.02 | 70.4 |
| Etna 231113 Ol a9_core | 37.82 | 0.04 | 27.18 | 0.60 | 34.99 | 0.35 | 0.03 | 0.03 | 0.02 | 69.6 |
| Etna 231113 Ol a11_nr25.48 | 39.37 | 0.05 | 18.39 | 0.29 | 42.25 | 0.25 | 0.02 | 0.01 | 0.08 | 80.4 |
| Etna 231113 Ol a11_nr12.05 | 39.40 | 0.04 | 18.27 | 0.28 | 42.28 | 0.27 | 0.02 | 0.02 | 0.09 | 80.5 |
| Etna 231113 Ol a11_core | 39.24 | 0.05 | 18.83 | 0.29 | 41.61 | 0.23 | 0.02 | 0.02 | 0.08 | 79.8 |
| Etna 231113 Ol a12_nrn.d. | 39.40 | 0.04 | 17.27 | 0.27 | 42.75 | 0.25 | 0.01 | 0.02 | 0.08 | 81.5 |

**Table H.1:** Olivine compositions ($n$ = 282) *cont.*

| Sample | $SiO_2$ | $Al_2O_3$ | FeO | MnO | MgO | CaO | $Na_2O$ | $P_2O_5$ | NiO | Fo |
|---|---|---|---|---|---|---|---|---|---|---|
| Etna 231113 Ol a12_nr41.76 | 39.39 | 0.04 | 17.81 | 0.28 | 42.41 | 0.26 | 0.01 | 0.01 | 0.10 | 80.9 |
| Etna 231113 Ol a12_core | 39.24 | 0.05 | 18.98 | 0.30 | 41.58 | 0.23 | 0.02 | 0.02 | 0.08 | 79.6 |
| Etna 231113 Ol a13_nr20.69 | 38.37 | 0.05 | 23.36 | 0.46 | 37.98 | 0.31 | 0.02 | 0.02 | 0.05 | 74.3 |
| Etna 231113 Ol a13_core | 38.33 | 0.05 | 24.25 | 0.50 | 37.28 | 0.27 | 0.02 | 0.02 | 0.04 | 73.3 |
| Etna 231113 Ol a17_nr61.31 | 38.39 | 0.06 | 23.75 | 0.47 | 37.72 | 0.39 | 0.03 | 0.03 | 0.03 | 73.9 |
| Etna 231113 Ol a17_core | 38.06 | 0.05 | 25.25 | 0.50 | 36.42 | 0.29 | 0.01 | 0.02 | 0.04 | 72.0 |
| Etna 231113 Ol a178_nrn.d. | 38.07 | 0.05 | 24.48 | 0.51 | 36.54 | 0.38 | 0.03 | 0.01 | 0.03 | 72.7 |
| Etna 231113 Ol a178_nr33.42 | 37.96 | 0.05 | 25.27 | 0.53 | 36.08 | 0.34 | 0.02 | 0.01 | 0.02 | 71.8 |
| Etna 231113 Ol a178_core | 38.07 | 0.04 | 25.16 | 0.50 | 36.37 | 0.30 | 0.02 | 0.01 | 0.03 | 72.0 |
| Etna231113Ol b4_nr7.55 | 38.86 | 0.05 | 21.68 | 0.39 | 39.33 | 0.32 | 0.02 | 0.02 | 0.04 | 76.4 |
| Etna231113Ol b4_nr9.42 | 38.85 | 0.04 | 21.84 | 0.40 | 39.40 | 0.32 | 0.03 | 0.02 | 0.03 | 76.3 |
| Etna231113Ol b4_core | 38.65 | 0.04 | 22.98 | 0.46 | 38.38 | 0.37 | 0.03 | 0.02 | 0.03 | 74.9 |
| Etna231113Ol b5_nrMG | 38.53 | 0.04 | 23.84 | 0.60 | 37.62 | 0.22 | 0.03 | 0.03 | 0.01 | 73.8 |
| Etna231113Ol b5_core | 38.25 | 0.04 | 25.25 | 0.90 | 36.32 | 0.12 | 0.02 | 0.01 | 0.01 | 71.9 |
| Etna231113Ol b7_nr88.25 | 39.65 | 0.04 | 16.91 | 0.25 | 43.10 | 0.27 | 0.01 | 0.01 | 0.10 | 82.0 |
| Etna231113Ol b7_nr41.65 | 39.67 | 0.05 | 16.95 | 0.27 | 42.92 | 0.28 | 0.02 | 0.02 | 0.10 | 81.9 |
| Etna231113Ol b7_nr26.27 | 39.62 | 0.04 | 17.10 | 0.26 | 42.98 | 0.24 | 0.01 | 0.01 | 0.11 | 81.8 |
| Etna231113Ol b7_core | 39.69 | 0.03 | 16.90 | 0.27 | 43.42 | 0.22 | 0.02 | 0.01 | 0.10 | 82.1 |
| Etna231113Ol b10_nr37.90 | 39.05 | 0.04 | 19.67 | 0.33 | 40.79 | 0.30 | 0.01 | 0.01 | 0.06 | 78.7 |
| Etna231113Ol b10_core | 39.36 | 0.04 | 18.32 | 0.28 | 42.14 | 0.22 | 0.02 | 0.02 | 0.10 | 80.4 |
| Etna231113Ol b14_nr37.53 | 38.97 | 0.06 | 20.81 | 0.37 | 39.91 | 0.27 | 0.02 | 0.01 | 0.04 | 77.4 |
| Etna231113Ol b14_core | 39.15 | 0.05 | 19.82 | 0.33 | 40.58 | 0.25 | 0.01 | 0.03 | 0.06 | 78.5 |
| Etna231113Ol c2_nr10.64 | 39.34 | 0.05 | 19.40 | 0.32 | 41.31 | 0.26 | 0.01 | 0.01 | 0.06 | 79.1 |
| Etna231113Ol c2_core | 39.08 | 0.03 | 21.16 | 0.36 | 40.01 | 0.27 | 0.02 | 0.01 | 0.05 | 77.1 |
| Etna231113Ol c3_nr20.07 | 39.02 | 0.05 | 21.58 | 0.41 | 39.38 | 0.23 | 0.01 | 0.01 | 0.03 | 76.5 |
| Etna231113Ol c3_core | 39.16 | 0.05 | 21.20 | 0.39 | 39.79 | 0.22 | 0.03 | 0.02 | 0.05 | 77.0 |
| Etna231113Ol c10_nr45.28 | 39.54 | 0.04 | 17.57 | 0.28 | 42.69 | 0.27 | 0.02 | 0.01 | 0.09 | 81.2 |
| Etna231113Ol c10_nr45.06 | 39.44 | 0.05 | 17.62 | 0.28 | 42.17 | 0.29 | 0.02 | 0.02 | 0.08 | 81.0 |
| Etna231113Ol c10_core | 39.61 | 0.03 | 17.45 | 0.27 | 42.79 | 0.26 | 0.01 | 0.01 | 0.09 | 81.4 |
| Etna231113Ol c12_nr1 | 38.34 | 0.04 | 24.27 | 0.50 | 36.95 | 0.30 | 0.03 | 0.01 | 0.02 | 73.1 |
| Etna231113Ol c12_nr2 | 39.21 | 0.03 | 18.96 | 0.32 | 41.43 | 0.29 | 0.02 | 0.01 | 0.07 | 79.6 |
| Etna231113Ol c12_nr3 | 38.24 | 0.04 | 24.71 | 0.53 | 36.46 | 0.36 | 0.03 | 0.01 | 0.02 | 72.5 |
| Etna231113Ol c12_core | 37.50 | 0.05 | 29.42 | 0.69 | 32.78 | 0.31 | 0.03 | 0.03 | 0.01 | 66.5 |
| Etna231113Ol c14_nr20.12 | 38.82 | 0.04 | 20.80 | 0.38 | 39.88 | 0.22 | 0.02 | 0.02 | 0.05 | 77.4 |
| Etna231113Ol c14_nr13.62 | 38.78 | 0.04 | 21.40 | 0.40 | 39.42 | 0.22 | 0.01 | 0.01 | 0.06 | 76.7 |
| Etna231113Ol c14_core | 38.18 | 0.04 | 25.06 | 0.54 | 36.31 | 0.18 | 0.03 | 0.03 | 0.02 | 72.1 |
| Etna231113Ol d6_nr50.99 | 39.58 | 0.04 | 17.91 | 0.29 | 42.56 | 0.26 | 0.02 | 0.01 | 0.07 | 80.9 |
| Etna231113Ol d6_core | 39.48 | 0.04 | 17.83 | 0.28 | 42.42 | 0.24 | 0.02 | 0.01 | 0.09 | 80.9 |
| Etna231113Ol d7_nr19.13 | 39.53 | 0.05 | 17.96 | 0.29 | 42.29 | 0.28 | 0.03 | 0.01 | 0.07 | 80.8 |
| Etna231113Ol d7_c | 39.68 | 0.03 | 17.07 | 0.25 | 43.02 | 0.22 | 0.02 | 0.02 | 0.09 | 81.8 |
| Etna231113Ol d8_c | 39.21 | 0.04 | 20.36 | 0.40 | 40.26 | 0.23 | 0.02 | 0.02 | 0.06 | 77.9 |
| Etna231113Ol d9_nr29.05 | 38.33 | 0.06 | 25.22 | 0.50 | 36.60 | 0.32 | 0.04 | 0.04 | 0.02 | 72.1 |
| Etna231113Ol d9c | 38.28 | 0.05 | 25.21 | 0.52 | 36.42 | 0.30 | 0.04 | 0.05 | 0.03 | 72.0 |
| Etna231113Ol d11_nr1 | 39.31 | 0.05 | 17.89 | 0.30 | 41.79 | 0.29 | 0.02 | 0.03 | 0.08 | 80.6 |
| Etna231113Ol d11_nr2 | 39.19 | 0.06 | 18.62 | 0.32 | 41.58 | 0.29 | 0.02 | 0.03 | 0.07 | 79.9 |

**Table H.1:** Olivine compositions ($n$ = 282) *cont.*

| Sample | $SiO_2$ | $Al_2O_3$ | FeO | MnO | MgO | CaO | $Na_2O$ | $P_2O_5$ | NiO | Fo |
|---|---|---|---|---|---|---|---|---|---|---|
| Etna231113Ol d11_c | 39.44 | 0.05 | 18.18 | 0.29 | 42.04 | 0.27 | 0.02 | 0.03 | 0.06 | 80.5 |
| Etna231113Ol d13_nr26.62 | 39.09 | 0.05 | 20.47 | 0.34 | 40.18 | 0.26 | 0.03 | 0.01 | 0.05 | 77.8 |
| Etna231113Ol d13_nr31.23 | 38.77 | 0.04 | 21.39 | 0.38 | 39.49 | 0.28 | 0.02 | 0.01 | 0.05 | 76.7 |
| Etna231113Ol d13_c | 39.15 | 0.04 | 19.80 | 0.33 | 40.90 | 0.26 | 0.02 | 0.01 | 0.06 | 78.6 |
| Etna231113Ol d15_c | 38.30 | 0.05 | 24.13 | 0.50 | 37.09 | 0.31 | 0.02 | 0.03 | 0.04 | 73.3 |
| Etna231113Ol e5_c | 39.79 | 0.05 | 16.66 | 0.25 | 43.49 | 0.22 | 0.01 | 0.02 | 0.11 | 82.3 |
| Etna231113Ol e7_nr1 | 39.02 | 0.05 | 20.34 | 0.34 | 40.61 | 0.32 | 0.01 | 0.02 | 0.06 | 78.1 |
| Etna231113Ol e7_nr2 | 38.90 | 0.05 | 20.88 | 0.37 | 39.82 | 0.30 | 0.02 | 0.01 | 0.05 | 77.3 |
| Etna231113Ol e7_nr3 | 38.93 | 0.06 | 20.80 | 0.37 | 39.83 | 0.31 | 0.02 | 0.01 | 0.05 | 77.3 |
| Etna231113Ol e7_nr4 | 38.80 | 0.05 | 21.76 | 0.39 | 39.31 | 0.29 | 0.02 | 0.00 | 0.05 | 76.3 |
| Etna231113Ol e7_nr5 | 39.00 | 0.06 | 21.11 | 0.37 | 39.86 | 0.27 | 0.02 | 0.01 | 0.05 | 77.1 |
| Etna231113Ol e7_nr6 | 38.69 | 0.06 | 22.11 | 0.40 | 39.11 | 0.39 | 0.03 | 0.02 | 0.05 | 75.9 |
| Etna231113Ol e7_nr59.12 | 38.95 | 0.04 | 20.76 | 0.36 | 39.98 | 0.27 | 0.02 | 0.01 | 0.05 | 77.4 |
| Etna231113Ol e7_nr24.99 | 38.93 | 0.04 | 20.93 | 0.35 | 39.99 | 0.30 | 0.03 | 0.02 | 0.06 | 77.3 |
| Etna231113Ol e7_nr30.77 | 38.79 | 0.05 | 21.69 | 0.40 | 39.64 | 0.32 | 0.02 | 0.01 | 0.06 | 76.5 |
| Etna231113Ol e7_c | 37.91 | 0.05 | 26.43 | 0.58 | 35.51 | 0.33 | 0.03 | 0.02 | 0.03 | 70.5 |
| Etna231113Ol e9_nr45.28 | 37.72 | 0.06 | 26.52 | 0.59 | 35.35 | 0.38 | 0.03 | 0.03 | 0.02 | 70.4 |
| Etna231113Ol e9_c | 37.69 | 0.04 | 26.81 | 0.58 | 34.45 | 0.37 | 0.03 | 0.02 | 0.02 | 69.6 |
| Etna231113Ol e11_nr22.41 | 39.07 | 0.05 | 18.77 | 0.30 | 41.27 | 0.28 | 0.01 | 0.01 | 0.07 | 79.7 |
| Etna231113Ol e11_c | 38.99 | 0.04 | 18.74 | 0.30 | 41.52 | 0.27 | 0.01 | 0.01 | 0.07 | 79.8 |
| Etna231113Ol e11_nr12.48 | 38.82 | 0.04 | 19.60 | 0.34 | 40.67 | 0.28 | 0.02 | 0.01 | 0.06 | 78.7 |
| Etna231113Ol e11_nr14.42 | 39.13 | 0.07 | 18.92 | 0.30 | 41.09 | 0.33 | 0.02 | 0.02 | 0.06 | 79.5 |
| Etna231113Ol e11_nr15.16 | 38.97 | 0.04 | 19.52 | 0.31 | 40.82 | 0.28 | 0.02 | 0.01 | 0.06 | 78.8 |
| Etna231113Ol e14_nr64.18 | 38.55 | 0.05 | 21.68 | 0.37 | 39.20 | 0.28 | 0.02 | 0.01 | 0.05 | 76.3 |
| Etna231113Ol e14_nr35.96 | 38.52 | 0.05 | 22.12 | 0.40 | 38.56 | 0.30 | 0.02 | 0.01 | 0.05 | 75.7 |
| Etna231113Ol e14_nr39.45 | 37.99 | 0.74 | 23.64 | 0.45 | 35.82 | 0.44 | 0.23 | 0.04 | 0.04 | 73.0 |
| Etna231113Ol e14_nr30.42 | 38.75 | 0.04 | 19.71 | 0.31 | 40.64 | 0.28 | 0.02 | 0.01 | 0.06 | 78.6 |
| Etna231113Ol e14_c | 38.95 | 0.05 | 20.04 | 0.32 | 40.45 | 0.24 | 0.02 | 0.02 | 0.07 | 78.3 |
| Etna231113Ol f4_nr31.84 | 38.82 | 0.04 | 22.34 | 0.43 | 38.86 | 0.21 | 0.02 | 0.03 | 0.01 | 75.6 |
| Etna231113Ol f4_c | 38.80 | 0.05 | 22.29 | 0.45 | 38.88 | 0.20 | 0.02 | 0.04 | 0.00 | 75.7 |
| Etna231113Ol f3_nr19.95 | 38.39 | 0.06 | 25.03 | 0.54 | 36.34 | 0.40 | 0.03 | 0.01 | 0.04 | 72.1 |
| Etna231113Ol f3_c | 38.30 | 0.06 | 25.56 | 0.54 | 36.32 | 0.35 | 0.03 | 0.03 | 0.03 | 71.7 |
| Etna231113Ol f4_nr11.15 | 38.04 | 0.06 | 26.21 | 0.57 | 35.45 | 0.38 | 0.03 | 0.03 | 0.02 | 70.7 |
| Etna231113Ol f4_c | 38.05 | 0.05 | 26.32 | 0.56 | 35.65 | 0.38 | 0.03 | 0.04 | 0.02 | 70.7 |
| Etna231113Ol f10_nr12.99 | 39.00 | 0.04 | 18.62 | 0.31 | 41.38 | 0.29 | 0.03 | 0.02 | 0.07 | 79.8 |
| Etna231113Ol f10_c | 38.87 | 0.05 | 19.29 | 0.32 | 40.89 | 0.30 | 0.02 | 0.02 | 0.05 | 79.1 |
| Etna231113Ol f12_nr21.26 | 38.78 | 0.05 | 20.59 | 0.36 | 40.00 | 0.26 | 0.02 | 0.02 | 0.05 | 77.6 |
| Etna231113Ol f12_c | 38.66 | 0.05 | 20.55 | 0.37 | 40.07 | 0.23 | 0.02 | 0.01 | 0.05 | 77.7 |
| Etna231113Ol g3_nr43.05 | 39.23 | 0.06 | 18.87 | 0.32 | 41.24 | 0.27 | 0.02 | 0.01 | 0.06 | 79.6 |
| Etna231113Ol g3_nr35.69 | 39.42 | 0.05 | 18.55 | 0.31 | 41.82 | 0.26 | 0.02 | 0.01 | 0.07 | 80.1 |
| Etna231113Ol g3_nr30.15 | 39.66 | 0.04 | 17.82 | 0.29 | 42.37 | 0.25 | 0.02 | 0.02 | 0.08 | 80.9 |
| Etna231113Ol g3_nr21.25 | 39.30 | 0.05 | 19.16 | 0.31 | 41.25 | 0.27 | 0.02 | 0.01 | 0.07 | 79.3 |
| Etna231113Ol g3_c | 39.49 | 0.04 | 18.41 | 0.29 | 42.21 | 0.24 | 0.02 | 0.00 | 0.08 | 80.3 |
| Etna231113Ol g4_nr16.76 | 39.11 | 0.05 | 19.26 | 0.31 | 41.00 | 0.27 | 0.02 | 0.02 | 0.07 | 79.1 |
| Etna231113Ol g4_nr19.99 | 39.14 | 0.05 | 20.22 | 0.35 | 40.21 | 0.27 | 0.02 | 0.02 | 0.06 | 78.0 |

**Table H.1:** Olivine compositions ($n$ = 282) *cont.*

| Sample | $SiO_2$ | $Al_2O_3$ | FeO | MnO | MgO | CaO | $Na_2O$ | $P_2O_5$ | NiO | Fo |
|---|---|---|---|---|---|---|---|---|---|---|
| Etna231113Ol g4_c | 39.24 | 0.04 | 19.54 | 0.34 | 40.75 | 0.24 | 0.02 | 0.02 | 0.07 | 78.8 |
| Etna231113Ol g5_nr44.09 | 39.53 | 0.05 | 17.73 | 0.28 | 42.37 | 0.26 | 0.03 | 0.01 | 0.09 | 81.0 |
| Etna231113Ol g5_c | 39.35 | 0.05 | 17.88 | 0.26 | 41.92 | 0.23 | 0.02 | 0.02 | 0.09 | 80.7 |
| Etna231113Ol g8_c | 37.78 | 0.07 | 24.94 | 0.52 | 36.13 | 0.31 | 0.03 | 0.08 | 0.02 | 72.1 |
| Etna231113Ol g13_nr1 | 38.51 | 0.06 | 21.02 | 0.37 | 39.42 | 0.25 | 0.02 | 0.03 | 0.05 | 77.0 |
| Etna231113Ol g13_nr2 | 38.25 | 0.04 | 21.30 | 0.40 | 38.82 | 0.26 | 0.01 | 0.02 | 0.03 | 76.5 |
| Etna231113Ol g13_nr32.95 | 38.55 | 0.05 | 20.75 | 0.36 | 39.50 | 0.26 | 0.02 | 0.01 | 0.06 | 77.2 |
| Etna231113Ol g13_nr67.67 | 38.40 | 0.04 | 20.71 | 0.36 | 39.72 | 0.27 | 0.03 | 0.01 | 0.04 | 77.4 |
| Etna231113Ol g13_n77.33 | 38.67 | 0.06 | 19.82 | 0.33 | 40.35 | 0.26 | 0.02 | 0.05 | 0.07 | 78.4 |
| Etna231113Ol h4_n20.57 | 38.40 | 0.05 | 22.52 | 0.42 | 38.36 | 0.35 | 0.03 | 0.01 | 0.03 | 75.2 |
| Etna231113Ol h4_n20.47 | 38.50 | 0.04 | 21.86 | 0.40 | 38.94 | 0.35 | 0.02 | 0.01 | 0.04 | 76.0 |
| Etna231113Ol h4_n19.42 | 38.55 | 0.05 | 21.31 | 0.38 | 39.42 | 0.31 | 0.02 | 0.01 | 0.05 | 76.7 |
| Etna231113Ol h4_c | 38.59 | 0.05 | 20.96 | 0.36 | 39.76 | 0.34 | 0.02 | 0.01 | 0.05 | 77.2 |
| Etna231113Ol h8_nr39.82 | 38.01 | 0.05 | 23.22 | 0.47 | 37.43 | 0.40 | 0.04 | 0.01 | 0.02 | 74.2 |
| Etna231113Ol h8_c | 37.57 | 0.04 | 26.00 | 0.57 | 35.32 | 0.37 | 0.04 | 0.01 | 0.02 | 70.8 |
| Etna231113Ol h9_nr8.73 | 38.93 | 0.05 | 18.49 | 0.28 | 41.46 | 0.26 | 0.02 | 0.03 | 0.07 | 80.0 |
| Etna231113Ol h9_nr12.64 | 38.60 | 0.05 | 19.28 | 0.31 | 40.80 | 0.26 | 0.02 | 0.00 | 0.06 | 79.0 |
| Etna231113Ol h9_nr16.38 | 38.84 | 0.04 | 18.54 | 0.30 | 41.59 | 0.28 | 0.02 | 0.01 | 0.07 | 80.0 |
| Etna231113Ol h9_c | 39.04 | 0.04 | 18.51 | 0.30 | 41.49 | 0.26 | 0.02 | 0.03 | 0.08 | 80.0 |
| Etna231113Ol h12_nr25.66 | 38.58 | 0.04 | 19.24 | 0.30 | 40.79 | 0.26 | 0.01 | 0.02 | 0.06 | 79.1 |
| Etna231113Ol h12_nr38.80 | 38.58 | 0.04 | 19.53 | 0.30 | 40.50 | 0.25 | 0.02 | 0.01 | 0.07 | 78.7 |
| Etna231113Ol h12_nr54.73 | 38.48 | 0.05 | 19.66 | 0.30 | 40.56 | 0.25 | 0.01 | 0.01 | 0.07 | 78.6 |
| Etna231113Ol h12_c | 38.46 | 0.05 | 19.72 | 0.31 | 40.56 | 0.24 | 0.02 | 0.02 | 0.07 | 78.6 |
| Etna231113Ol h13_nr10.06 | 37.51 | 0.06 | 25.93 | 0.55 | 35.45 | 0.40 | 0.02 | 0.03 | 0.02 | 70.9 |
| Etna231113Ol h13_nr15.23 | 37.63 | 0.05 | 24.83 | 0.51 | 36.29 | 0.38 | 0.02 | 0.01 | 0.04 | 72.3 |
| Etna231113Ol h13_nr18.80 | 37.65 | 0.04 | 25.49 | 0.53 | 35.71 | 0.40 | 0.02 | 0.01 | 0.02 | 71.4 |
| Etna231113Ol h13_nr10.23 | 37.49 | 0.06 | 25.79 | 0.54 | 35.35 | 0.38 | 0.04 | 0.00 | 0.03 | 71.0 |
| Etna231113Ol h13_nr91.38 | 37.52 | 0.06 | 25.27 | 0.55 | 35.81 | 0.40 | 0.03 | 0.04 | 0.02 | 71.6 |
| Etna231113Ol h13_nr23.71 | 37.42 | 0.05 | 25.78 | 0.52 | 35.36 | 0.44 | 0.03 | 0.02 | 0.02 | 71.0 |
| Etna231113Ol h13_c | 37.62 | 0.05 | 25.50 | 0.52 | 35.94 | 0.36 | 0.02 | 0.02 | 0.03 | 71.5 |
| Etna231113Ol i2_nr34,42 | 38.02 | 0.06 | 24.77 | 0.51 | 36.63 | 0.40 | 0.03 | 0.02 | 0.02 | 72.5 |
| Etna231113Ol i2_nr31.09 | 38.14 | 0.06 | 23.50 | 0.48 | 37.46 | 0.39 | 0.03 | 0.05 | 0.03 | 74.0 |
| Etna231113Ol i2_nr25.01 | 38.32 | 0.05 | 23.14 | 0.46 | 37.63 | 0.36 | 0.03 | 0.03 | 0.02 | 74.3 |
| Etna231113Ol i2_c | 37.88 | 0.06 | 26.16 | 0.55 | 35.34 | 0.38 | 0.04 | 0.03 | 0.01 | 70.7 |
| Etna231113Ol i3_nr12.77 | 38.90 | 0.06 | 19.98 | 0.35 | 40.70 | 0.27 | 0.01 | 0.01 | 0.06 | 78.4 |
| Etna231113Ol i3_nr20.32 | 39.00 | 0.09 | 18.66 | 0.30 | 41.59 | 0.28 | 0.02 | 0.03 | 0.07 | 79.9 |
| Etna231113Ol i3_c | 38.93 | 0.05 | 19.67 | 0.30 | 40.71 | 0.24 | 0.02 | 0.02 | 0.07 | 78.7 |
| Etna231113Ol i6_nr17.66 | 38.83 | 0.05 | 19.73 | 0.33 | 40.74 | 0.25 | 0.02 | 0.01 | 0.06 | 78.6 |
| Etna231113Ol i6_c | 38.92 | 0.04 | 18.16 | 0.29 | 42.00 | 0.23 | 0.01 | 0.01 | 0.08 | 80.5 |
| Etna231113Ol i8_nr14.35 | 37.63 | 0.04 | 24.36 | 0.51 | 36.77 | 0.32 | 0.03 | 0.02 | 0.03 | 72.9 |
| Etna231113Ol i8_nr12.47 | 38.17 | 0.05 | 21.50 | 0.37 | 38.97 | 0.28 | 0.02 | 0.01 | 0.05 | 76.4 |
| Etna231113Ol i8_c | 37.24 | 0.05 | 26.32 | 0.58 | 35.06 | 0.30 | 0.02 | 0.04 | 0.03 | 70.4 |
| Etna231113Ol i10_nr52.88 | 38.24 | 0.04 | 20.30 | 0.33 | 39.83 | 0.26 | 0.02 | 0.02 | 0.06 | 77.8 |
| Etna231113Ol i10_nr22.33 | 38.41 | 0.05 | 20.40 | 0.33 | 40.10 | 0.25 | 0.02 | 0.02 | 0.06 | 77.8 |
| Etna231113Ol i10_nr31.66 | 38.25 | 0.05 | 20.58 | 0.36 | 39.60 | 0.29 | 0.02 | 0.01 | 0.06 | 77.4 |

**Table H.1:** Olivine compositions ($n$ = 282) *cont.*

| Sample | $SiO_2$ | $Al_2O_3$ | FeO | MnO | MgO | CaO | $Na_2O$ | $P_2O_5$ | NiO | Fo |
|---|---|---|---|---|---|---|---|---|---|---|
| Etna231113Ol i10_c | 38.35 | 0.05 | 20.29 | 0.34 | 39.97 | 0.25 | 0.02 | 0.03 | 0.06 | 77.8 |
| Etna231113Ol i11_nr33.92 | 36.97 | 0.05 | 27.66 | 0.60 | 33.91 | 0.39 | 0.03 | 0.03 | 0.02 | 68.6 |
| Etna231113Ol i11_c | 37.03 | 0.04 | 27.87 | 0.60 | 33.95 | 0.38 | 0.03 | 0.06 | 0.02 | 68.5 |
| Etna231113Ol i12_nr14.31 | 38.82 | 0.05 | 18.13 | 0.29 | 41.83 | 0.25 | 0.01 | 0.02 | 0.09 | 80.4 |
| Etna231113Ol i12_nr9.42 | 38.61 | 0.05 | 18.84 | 0.28 | 41.20 | 0.24 | 0.02 | 0.01 | 0.08 | 79.6 |
| Etna231113Ol i12_nr26.65 | 38.83 | 0.06 | 17.84 | 0.28 | 41.96 | 0.29 | 0.01 | 0.03 | 0.07 | 80.7 |
| Etna231113Ol j4_nr43.22 | 38.21 | 0.05 | 21.78 | 0.42 | 38.48 | 0.27 | 0.02 | 0.02 | 0.05 | 75.9 |
| Etna231113Ol j4_c | 38.93 | 0.05 | 17.97 | 0.28 | 41.89 | 0.24 | 0.02 | 0.02 | 0.09 | 80.6 |
| Etna231113Ol j8_nr11.08 | 38.10 | 0.05 | 21.21 | 0.39 | 39.38 | 0.31 | 0.02 | 0.03 | 0.02 | 76.8 |
| Etna 231113Ol b1_c | 37.74 | -0.02 | 25.30 | 0.51 | 36.74 | 0.28 | 0.03 | 0.02 | 0.03 | 72.1 |
| Etna 231113Ol b1_c | 37.63 | -0.02 | 25.77 | 0.54 | 35.90 | 0.34 | 0.04 | 0.02 | 0.03 | 71.3 |
| Etna 231113Ol c6_c | 38.59 | 0.07 | 21.78 | 0.42 | 39.22 | 0.38 | 0.03 | 0.03 | 0.03 | 76.2 |

*Notes:* All oxides are in wt% measured using EPMA as described in Section 6.3.4. Fo calculated using Equation 6.9. Sample names denote the mount (e.g., Etna2311Ol), followed by the crystal (e.g., i10), then 'c' or 'core' indicates a measurement was taken in the middle of the intersected crystal or 'nr' indicates a measurement was taken next to the specified melt inclusion (e.g., nr11.08) which are specified in Table H.4.

**Table H.2:** Pyroxene compositions ($n$ = 68).

| Sample | $SiO_2$ | $TiO_2$ | $Al_2O_3$ | $FeO_T$ | MnO | MgO | CaO | $Na_2O$ | $K_2O$ | $Cr_2O_3$ | Wo | Fs | En |
|---|---|---|---|---|---|---|---|---|---|---|---|---|---|
| Etna231113Pyroxenes_m11 | 51.75 | 0.60 | 2.07 | 7.55 | 0.44 | 14.83 | 21.72 | 0.53 | 0.02 | 0.04 | 46.8 | 8.7 | 44.5 |
| Etna231113Pyroxenes_m10 | 48.53 | 1.72 | 4.80 | 8.70 | 0.21 | 12.90 | 22.61 | 0.53 | 0.00 | -0.01 | 50.9 | 8.7 | 40.4 |
| Etna231113Pyroxenes_m9 | 50.30 | 0.95 | 3.41 | 7.07 | 0.21 | 14.54 | 22.73 | 0.28 | 0.01 | 0.03 | 49.0 | 7.5 | 43.6 |
| Etna231113Pyroxenes_m8 | 48.30 | 1.49 | 5.25 | 7.21 | 0.16 | 13.60 | 23.30 | 0.39 | 0.00 | 0.02 | 52.3 | 5.3 | 42.4 |
| Etna231113Pyroxenes_m7 | 49.54 | 1.00 | 4.26 | 7.14 | 0.14 | 14.35 | 22.90 | 0.28 | 0.00 | 0.01 | 50.0 | 6.4 | 43.6 |
| Etna231113Pyroxenes_m6 | 47.39 | 1.56 | 5.91 | 7.55 | 0.11 | 13.13 | 23.35 | 0.37 | 0.00 | 0.01 | 53.2 | 5.2 | 41.6 |
| Etna231113Pyroxenes_m5 | 50.07 | 0.94 | 3.73 | 6.58 | 0.10 | 14.76 | 23.25 | 0.25 | 0.00 | 0.24 | 50.1 | 5.6 | 44.3 |
| Etna231113Pyroxenes_m4 | 46.84 | 1.52 | 6.61 | 7.45 | 0.13 | 12.92 | 23.21 | 0.35 | 0.00 | 0.06 | 53.5 | 5.1 | 41.4 |
| Etna231113Pyroxenes_m3 | 48.24 | 1.32 | 5.53 | 6.62 | 0.09 | 13.67 | 23.72 | 0.28 | 0.00 | 0.35 | 52.9 | 4.8 | 42.4 |
| Etna231113Pyroxenes_m2 | 48.39 | 1.54 | 4.89 | 8.34 | 0.19 | 13.26 | 22.79 | 0.49 | 0.00 | 0.03 | 51.4 | 6.9 | 41.6 |
| Etna231113Pyroxenes_l1 | 49.29 | 1.31 | 3.67 | 8.58 | 0.21 | 13.23 | 22.32 | 0.51 | 0.01 | -0.05 | 49.7 | 9.3 | 41.0 |
| Etna231113Pyroxenes_l2 | 47.98 | 1.52 | 5.32 | 7.46 | 0.16 | 13.39 | 22.94 | 0.35 | 0.01 | 0.03 | 51.6 | 6.5 | 41.9 |
| Etna231113Pyroxenes_l3 | 45.35 | 2.08 | 7.59 | 7.92 | 0.11 | 12.24 | 23.02 | 0.34 | 0.01 | 0.27 | 54.2 | 5.7 | 40.1 |
| Etna231113Pyroxenes_l4 | 49.56 | 1.15 | 4.50 | 6.85 | 0.13 | 14.09 | 23.36 | 0.26 | 0.01 | 0.04 | 50.8 | 6.6 | 42.6 |
| Etna231113Pyroxenes_l6 | 48.10 | 1.78 | 5.05 | 8.82 | 0.20 | 12.52 | 22.49 | 0.55 | 0.00 | 0.00 | 51.1 | 9.3 | 39.6 |
| Etna231113Pyroxenes_l7 | 48.80 | 1.42 | 4.67 | 8.00 | 0.19 | 13.20 | 22.35 | 0.49 | 0.00 | 0.00 | 50.1 | 8.8 | 41.2 |
| Etna231113Pyroxenes_l8 | 47.79 | 1.58 | 5.50 | 8.16 | 0.15 | 12.93 | 22.70 | 0.44 | 0.00 | 0.01 | 51.6 | 7.5 | 40.9 |
| Etna231113Pyroxenes_l9 | 49.47 | 1.12 | 4.56 | 6.80 | 0.12 | 13.98 | 22.95 | 0.27 | 0.01 | 0.04 | 50.1 | 7.5 | 42.4 |
| Etna231113Pyroxenes_l11 | 49.73 | 1.05 | 4.04 | 6.84 | 0.13 | 14.28 | 23.22 | 0.24 | 0.01 | 0.16 | 50.3 | 6.7 | 43.0 |
| Etna231113Pyroxenes_l12 | 48.52 | 1.49 | 4.82 | 8.46 | 0.19 | 13.06 | 22.45 | 0.55 | 0.00 | 0.00 | 50.8 | 8.1 | 41.1 |
| Etna231113Pyroxenes_k12 | 50.40 | 1.22 | 3.43 | 7.36 | 0.28 | 14.38 | 22.25 | 0.56 | 0.00 | 0.02 | 48.7 | 7.5 | 43.8 |
| Etna231113Pyroxenes_k11 | 49.72 | 1.25 | 3.46 | 8.01 | 0.21 | 13.94 | 22.10 | 0.44 | 0.00 | 0.01 | 48.6 | 8.8 | 42.6 |
| Etna231113Pyroxenes_k10 | 50.00 | 1.04 | 3.79 | 7.13 | 0.15 | 14.57 | 22.92 | 0.34 | 0.01 | 0.03 | 49.8 | 6.1 | 44.1 |
| Etna231113Pyroxenes_k9 | 48.54 | 1.24 | 5.06 | 7.75 | 0.18 | 13.65 | 22.67 | 0.40 | 0.01 | -0.01 | 50.9 | 6.5 | 42.6 |
| Etna231113Pyroxenes_k8 | 49.80 | 1.24 | 3.96 | 7.31 | 0.24 | 14.09 | 22.47 | 0.55 | 0.01 | 0.04 | 49.8 | 6.8 | 43.4 |
| Etna231113Pyroxenes_k7 | 49.01 | 1.40 | 4.19 | 8.74 | 0.20 | 13.15 | 22.14 | 0.56 | 0.00 | 0.01 | 49.7 | 9.2 | 41.1 |
| Etna231113Pyroxenes_k5 | 45.41 | 2.08 | 7.87 | 8.30 | 0.11 | 12.19 | 23.15 | 0.35 | 0.01 | 0.06 | 54.5 | 5.6 | 39.9 |
| Etna231113Pyroxenes_k4 | 47.17 | 1.46 | 6.27 | 7.23 | 0.12 | 13.00 | 23.24 | 0.30 | 0.01 | 0.04 | 53.0 | 5.8 | 41.2 |
| Etna231113Pyroxenes_k3 | 47.14 | 1.80 | 6.18 | 8.50 | 0.16 | 12.66 | 22.62 | 0.43 | 0.00 | 0.03 | 51.9 | 7.6 | 40.4 |

**Table H.2:** Pyroxene compositions ($n$ = 68) *cont.*

| Sample | $SiO_2$ | $TiO_2$ | $Al_2O_3$ | $FeO_T$ | MnO | MgO | CaO | $Na_2O$ | $K_2O$ | $Cr_2O_3$ | Wo | Fs | En |
|---|---|---|---|---|---|---|---|---|---|---|---|---|---|
| Etna231113Pyroxenes_k2 | 51.90 | 0.59 | 1.85 | 7.64 | 0.46 | 15.15 | 21.70 | 0.51 | 0.00 | 0.03 | 46.5 | 8.3 | 45.2 |
| Etna231113Pyroxenes_k1 | 48.14 | 1.30 | 5.63 | 6.93 | 0.11 | 13.66 | 23.37 | 0.27 | 0.01 | 0.10 | 52.2 | 5.3 | 42.5 |
| Etna231113Pyroxenes_j2 | 47.26 | 1.68 | 6.30 | 7.46 | 0.12 | 13.20 | 23.11 | 0.31 | 0.01 | 0.07 | 52.4 | 5.9 | 41.7 |
| Etna231113Pyroxenes_j3 | 46.26 | 1.67 | 7.25 | 8.07 | 0.10 | 12.38 | 23.30 | 0.30 | 0.00 | 0.08 | 54.0 | 6.1 | 39.9 |
| Etna231113Pyroxenes_j4 | 48.19 | 1.60 | 5.57 | 7.70 | 0.19 | 13.23 | 22.48 | 0.38 | 0.00 | 0.01 | 50.4 | 8.3 | 41.3 |
| Etna231113Pyroxenes_j5 | 47.81 | 1.37 | 6.00 | 6.96 | 0.10 | 13.37 | 23.43 | 0.32 | 0.00 | 0.11 | 52.8 | 5.2 | 41.9 |
| Etna231113Pyroxenes_j6 | 48.21 | 1.29 | 5.57 | 6.56 | 0.09 | 13.76 | 23.38 | 0.29 | 0.01 | 0.20 | 52.2 | 5.0 | 42.8 |
| Etna231113Pyroxenes_j8 | 48.29 | 1.39 | 5.25 | 7.61 | 0.15 | 13.50 | 22.71 | 0.34 | 0.00 | -0.03 | 50.8 | 7.1 | 42.0 |
| Etna231113Pyroxenes_j9 | 48.48 | 1.49 | 4.79 | 8.58 | 0.22 | 12.96 | 22.26 | 0.50 | 0.00 | 0.00 | 50.2 | 9.1 | 40.7 |
| Etna231113Pyroxenes_j10 | 47.21 | 1.96 | 5.86 | 8.81 | 0.20 | 12.43 | 22.19 | 0.50 | 0.00 | 0.00 | 51.1 | 9.2 | 39.8 |
| Etna231113Pyroxenes_j13 | 49.55 | 1.28 | 3.95 | 8.50 | 0.25 | 13.66 | 21.60 | 0.65 | 0.00 | 0.01 | 48.5 | 8.9 | 42.6 |
| Etna231113Pyroxenes_j14 | 50.98 | 0.76 | 2.84 | 8.01 | 0.23 | 15.09 | 21.61 | 0.29 | 0.00 | 0.09 | 48.5 | 8.9 | 42.6 |
| Etna231113Pyroxenes_i13 | 49.09 | 1.10 | 4.81 | 6.05 | 0.07 | 14.17 | 23.49 | 0.25 | 0.00 | 0.32 | 51.5 | 5.3 | 43.2 |
| Etna231113Pyroxenes_i12 | 45.82 | 1.85 | 7.75 | 8.16 | 0.12 | 12.26 | 23.09 | 0.37 | 0.00 | 0.01 | 54.1 | 5.9 | 40.0 |
| Etna231113Pyroxenes_i11 | 48.81 | 1.20 | 5.08 | 7.01 | 0.12 | 13.82 | 23.09 | 0.28 | 0.00 | 0.01 | 51.0 | 6.5 | 42.5 |
| Etna231113Pyroxenes_i10 | 50.27 | 0.98 | 3.78 | 7.14 | 0.19 | 14.42 | 22.61 | 0.31 | 0.00 | -0.01 | 48.8 | 7.9 | 43.3 |
| Etna231113Pyroxenes_i9 | 47.30 | 1.95 | 5.84 | 8.68 | 0.17 | 12.40 | 22.47 | 0.50 | 0.00 | 0.02 | 51.5 | 8.9 | 39.6 |
| Etna231113Pyroxenes_i7 | 49.24 | 1.34 | 4.16 | 8.41 | 0.17 | 13.34 | 22.17 | 0.52 | 0.01 | 0.00 | 49.4 | 9.2 | 41.4 |
| Etna231113Pyroxenes_i4 | 49.35 | 1.30 | 3.97 | 8.23 | 0.22 | 13.55 | 22.23 | 0.46 | 0.00 | 0.00 | 49.2 | 9.0 | 41.7 |
| Etna231113Pyroxenes_i3 | 48.14 | 1.42 | 5.53 | 7.34 | 0.12 | 13.40 | 22.91 | 0.35 | 0.00 | 0.06 | 51.4 | 6.8 | 41.8 |
| Etna231113Pyroxenes_i2 | 49.77 | 1.29 | 3.83 | 9.07 | 0.24 | 13.42 | 21.48 | 0.60 | 0.01 | 0.03 | 47.8 | 10.7 | 41.5 |
| Etna231113Pyroxenes_i1 | 47.64 | 1.84 | 5.46 | 8.79 | 0.20 | 12.59 | 22.12 | 0.50 | 0.01 | 0.06 | 50.6 | 9.4 | 40.0 |
| CYAN_d2_nr52.74_Px | 45.40 | 1.76 | 7.37 | 8.92 | 0.14 | 12.20 | 23.51 | 0.46 | 0.01 | -0.04 | 56.2 | 3.2 | 40.6 |
| CYAN_d2_nr36.66_Px | 47.09 | 1.44 | 5.87 | 7.04 | 0.11 | 13.51 | 23.15 | 0.30 | 0.00 | 0.24 | 52.9 | 4.2 | 42.9 |
| CYAN_d2_nr36.66_Px | 47.46 | 1.34 | 5.84 | 6.91 | 0.13 | 13.56 | 22.94 | 0.32 | 0.00 | 0.29 | 52.2 | 4.9 | 42.9 |
| CYAN_d2_core_Px | 46.82 | 1.51 | 6.62 | 7.56 | 0.11 | 13.13 | 22.62 | 0.34 | 0.00 | 0.00 | 52.1 | 5.9 | 42.1 |
| CYAN_c3_core_Px | 48.53 | 1.19 | 4.45 | 7.75 | 0.15 | 13.64 | 22.65 | 0.42 | 0.00 | 0.04 | 50.9 | 6.4 | 42.7 |
| CYAN_c1_nrMI_Px | 48.42 | 1.44 | 4.68 | 8.13 | 0.17 | 13.41 | 22.52 | 0.40 | 0.00 | -0.02 | 50.5 | 7.7 | 41.8 |
| CYAN_c1_core_Px | 46.73 | 1.92 | 5.55 | 9.10 | 0.19 | 12.35 | 21.94 | 0.45 | 0.00 | -0.02 | 50.8 | 9.4 | 39.8 |

**Table H.2:** Pyroxene compositions ($n$ = 68) *cont.*

| Sample | $SiO_2$ | $TiO_2$ | $Al_2O_3$ | $FeO_T$ | MnO | MgO | CaO | $Na_2O$ | $K_2O$ | $Cr_2O_3$ | Wo | Fs | En |
|---|---|---|---|---|---|---|---|---|---|---|---|---|---|
| CYAN_b2_core_Px | 50.45 | 0.79 | 2.79 | 8.03 | 0.29 | 13.97 | 22.15 | 0.56 | 0.00 | 0.02 | 48.8 | 8.4 | 42.8 |
| CYAN_b3_nrMI_Px | 46.80 | 1.60 | 6.18 | 7.32 | 0.10 | 12.98 | 22.84 | 0.33 | 0.01 | 0.01 | 52.5 | 6.0 | 41.5 |
| CYAN_b3_core_Px | 46.50 | 1.51 | 6.67 | 7.28 | 0.10 | 13.03 | 23.14 | 0.28 | 0.00 | 0.08 | 53.4 | 4.9 | 41.8 |
| CYAN_b4_core_Px | 47.04 | 1.65 | 5.79 | 8.59 | 0.18 | 12.68 | 22.30 | 0.48 | 0.00 | 0.00 | 51.6 | 7.5 | 40.8 |
| CYAN_a4_core_Px | 48.38 | 1.50 | 4.45 | 8.80 | 0.23 | 12.77 | 21.93 | 0.57 | 0.00 | 0.00 | 49.9 | 9.7 | 40.4 |
| CYAN_a4_nrMI_Px | 47.51 | 1.59 | 5.55 | 8.24 | 0.20 | 13.18 | 22.29 | 0.48 | 0.00 | 0.00 | 51.2 | 6.7 | 42.1 |
| CYAN_a4_core_Px | 48.39 | 1.53 | 4.43 | 8.64 | 0.20 | 13.27 | 21.89 | 0.57 | 0.00 | 0.03 | 49.8 | 8.3 | 42.0 |
| CYAN_a2_core_Px | 46.89 | 1.44 | 5.79 | 7.73 | 0.12 | 13.21 | 22.71 | 0.37 | 0.00 | 0.03 | 52.4 | 5.2 | 42.4 |
| CYAN_a2_nr32.46_Px | 47.24 | 1.33 | 5.65 | 8.03 | 0.12 | 13.19 | 22.78 | 0.38 | 0.02 | 0.02 | 52.4 | 5.4 | 42.2 |
| CYAN_a2_nr26.28_Px | 46.52 | 1.55 | 6.31 | 8.24 | 0.15 | 12.70 | 22.37 | 0.41 | 0.01 | 0.10 | 52.1 | 6.6 | 41.2 |

*Notes:* All oxides are in wt% measured using EPMA as described in Section 6.3.4. Wo, En, and Fs calculated using Equation 6.10. Sample names denote the mount (e.g., CYAN), followed by the crystal (e.g., a4), then 'c' or 'core' indicates a measurement was taken in the middle of the intersected crystal or 'nr' indicates a measurement was taken next to the specified melt inclusion (e.g., nr26.28) which are specified in Table H.4.

**Table H.3:** Plagioclase inclusion compositions.

| Sample | $SiO_2$ | $TiO_2$ | $Al_2O_3$ | FeO | MnO | MgO | CaO | $Na_2O$ | $K_2O$ | $P_2O_5$ | $H_2O$ | An | Or | Ab |
|---|---|---|---|---|---|---|---|---|---|---|---|---|---|---|
| Etna231113Pyroxenes_j12 | 46.43 | 0.04 | 33.50 | 0.72 | 0.02 | 0.04 | 17.02 | 1.60 | 0.12 | | 0.00 | 91.8 | 0.4 | 7.8 |
| CYAN_c1_10um | 48.30 | 0.21 | 30.08 | 1.47 | 0.02 | 0.24 | 15.00 | 2.87 | 0.52 | 0.08 | 1.15 | 83.8 | 1.7 | 14.5 |
| CYAN_c3-53.80_10um | 48.18 | 0.06 | 30.66 | 0.80 | 0.01 | 0.07 | 15.00 | 3.05 | 0.20 | 0.02 | 1.95 | 83.9 | 0.7 | 15.4 |
| CYAN_c3-33.79_10um | 47.73 | 0.03 | 31.64 | 0.72 | 0.00 | 0.06 | 16.02 | 2.62 | 0.18 | 0.03 | 0.97 | 86.6 | 0.6 | 12.8 |
| CYAN_a4_10um | 50.21 | 0.07 | 29.78 | 0.74 | 0.00 | 0.06 | 13.61 | 3.81 | 0.31 | 0.02 | 1.38 | 78.9 | 1.1 | 20.0 |

*Notes:* All oxides are in wt% measured using EPMA as described in Section 6.3.4. An, Or, and Ab calculated using Equation 6.11. Sample names denote the mount (e.g., CYAN), followed by the crystal (e.g., c1), then the beam size used for analysis. As plagioclase inclusions were analysed using the same set-up as glasses, the $H_2O$ concentration is calculated.

**Table H.4:** Description of glass analyses ($n$ = 224).

| No. | Type | Host | Mount 1 | Crystal 1 | Inclusion 1 | Mount 2 | Crystal 2 | Inclusion 2 | Mount 3 | Crystal 3 | Fo | Wo | Fs | En |
|---|---|---|---|---|---|---|---|---|---|---|---|---|---|---|
| G001 | | Pyroxene | Etna Pyroxene | j11 | | BLUE | a2 | 28.37/36.66 | CYAN | d2 | | 52.2 | 4.9 | 42.9 |
| G002 | MI | Pyroxene | Etna Pyroxene | j11 | | BLUE | a2 | 73.76/52.74 | CYAN | d2 | | 56.2 | 3.2 | 40.6 |
| G003 | MI | Pyroxene | Etna Pyroxene | c7 | | BLUE | b1 | | CYAN | c3 | | 50.9 | 6.4 | 42.7 |
| G004 | | Olivine | Etna Pyroxene | c2 | | BLUE | b2 | | CYAN | c2 | 81.0 | | | |
| G005 | MI | Olivine | Etna Pyroxene | c2 | | BLUE | b2 | | CYAN | c2 | 79.3 | | | |
| G006 | MI | Olivine | Etna Pyroxene | c2 | | BLUE | b2 | 28.06 | CYAN | c2 | 80.9 | | | |
| G007 | MI | Olivine | Etna Pyroxene | c2 | | BLUE | b2 | 43.74 | CYAN | c2 | 80.9 | | | |
| G008 | MI | Olivine | Etna Pyroxene | c2 | | BLUE | b2 | 58.8 | CYAN | c2 | 80.9 | | | |
| G009 | MI | Pyroxene | Etna Pyroxene | c10 | | BLUE | b3 | | | | | | | |
| G010 | | Olivine | Etna Crystal | 82 | | BLUE | b4 | | CYAN | g3 | | | | |
| G011 | MI | Pyroxene | Etna Crystal | 25 | | BLUE | b5 | | CYAN | c1 | | 50.5 | 7.7 | 41.8 |
| G012 | | Pyroxene | Etna Crystal | 11 | | BLUE | c1 | 55.64 | CYAN | b3 | | 52.5 | 6.0 | 41.5 |
| G013 | MI | Olivine | Etna Ol | 91 | | BLUE | h4 | T | CYAN | e1 | 72.6 | | | |
| G014 | MI | Olivine | Etna Ol | 91 | | BLUE | h4 | | CYAN | e1 | 72.7 | | | |
| G015 | MI | Olivine | Etna Ol | 88 | | BLUE | h5 | 50.73 | CYAN | g2 | 71.4 | | | |
| G016 | MI | Olivine | Etna Ol | 46 | | BLUE | h6 | 30.75 | CYAN | e5 | 79.4 | | | |
| G017 | MI | Olivine | Etna mm | 3 | | BLUE | h7 | 48.41 | CYAN | g6 | 80.7 | | | |
| G018 | MI | Olivine | Etna mm | 3 | | BLUE | h7 | 43.25 | CYAN | g6 | 81.0 | | | |
| G019 | | Olivine | Etna Ol | 25 | | BLUE | i2 | | CYAN | d4 | 76.1 | | | |
| G020 | MG | Olivine | Etna Ol | 25 | | BLUE | i2 | | CYAN | d4 | 75.0 | | | |
| G021 | MG | Olivine | Etna Ol | 25 | | BLUE | i2 | | CYAN | d4 | 75.5 | | | |
| G022 | MI | Olivine | Etna mm | 21 | | BLUE | i3 | | CYAN | e7 | 81.1 | | | |
| G023 | MI | Pyroxene | Etna mm | 18 | | BLUE | i4 | 24.42 | CYAN | g1 | | | | |
| G024 | MI | Olivine | Etna mm | 17 | | BLUE | i5 | | CYAN | e3 | 71.8 | | | |
| G025 | MI | Olivine | Etna mm | 16 | | BLUE | j1 | | CYAN | e2 | 72.9 | | | |
| G026 | | Olivine | Etna mm | 4 | | BLUE | j3 | | CYAN | f2 | 77.1 | | | |
| G027 | MI | Pyroxene | Etna mm | 5 | | GREEN | c4 | | CYAN | h6 | | | | |

**Table H.4:** Description of glass analyses ($n$ = 224) *cont.*

| No. | Type | Host | Mount 1 | Crystal 1 | Inclusion 1 | Mount 2 | Crystal 2 | Inclusion 2 | Mount 3 | Crystal 3 | Fo | Wo | Fs | En |
|---|---|---|---|---|---|---|---|---|---|---|---|---|---|---|
| G028 | MI | Pyroxene | Etna mm | 5 | | GREEN | c4 | 36.7 | CYAN | h6 | | | | |
| G029 | | Pyroxene | Etna Pyroxene | d7 | | PINK | a2 | 48.25 | | | | | | |
| G030 | | Olivine | Etna Crystal | 74 | | PINK | b2 | | CYAN | b2 | | | | |
| G031 | | Pyroxene | Etna Pyroxene | a5 | | PINK | b5 | 33.43 | | | | | | |
| G032 | | Pyroxene | Etna Pyroxene | a5 | | PINK | b5 | 35.14 | | | | | | |
| G033 | MI | Pyroxene | Etna Pyroxene | e16 | | PINK | b6 | 32.46 | CYAN | a2 | | 52.4 | 5.4 | 42.2 |
| G034 | MI | Pyroxene | Etna Pyroxene | e16 | | PINK | b6 | 26.48 | CYAN | a2 | | 52.1 | 6.6 | 41.2 |
| G035 | | Pyroxene | Etna Pyroxene | g8 | | PINK | b7 | 36.08 | CYAN | b2 | | 48.8 | 8.4 | 42.8 |
| G036 | | Olivine | Etna mm | 25 | | PINK | c3 | 50.83 | | | | | | |
| G037 | MI | Olivine | Etna mm | 22 | | PINK | c4 | 33.64 | CYAN | h1 | 77.5 | | | |
| G038 | MI | Olivine | Etna mm | 22 | | PINK | c4 | 29.24 | CYAN | h1 | 77.5 | | | |
| G039 | MI | Olivine | Etna mm | 22 | | PINK | c4 | | CYAN | h1 | 77.5 | | | |
| G040 | MI | Olivine | Etna mm | 22 | | PINK | c4 | | CYAN | h1 | 78.3 | | | |
| G041 | MI | Olivine | Etna mm | 22 | | PINK | c4 | | CYAN | h1 | 77.5 | | | |
| G042 | MI | Olivine | Etna mm | 22 | | PINK | c4 | 23.4 | CYAN | h1 | 77.5 | | | |
| G043 | MI | | Etna mm | 22 | | PINK | c4 | 25.99 | CYAN | h1 | | | | |
| G044 | MI | Olivine | Etna mm | 19 | | PINK | c5 | 52.92 | CYAN | h2 | 71.2 | | | |
| G045 | MI | Olivine | Etna mm | 19 | | PINK | c5 | 41.54 | CYAN | h2 | 70.1 | | | |
| G046 | | Olivine | Etna mm | 14 | | PINK | c6 | 46.06 | CYAN | h3 | 78.6 | | | |
| G047 | MI | Olivine | Etna mm | 2 | | PINK | c7 | 46.04 | CYAN | h4 | 72.9 | | | |
| G048 | MI | Pyroxene | Etna Pyroxene | b8 | | PINK | d3 | 30.72 | CYAN | i1 | | | | |
| G049 | MI | Olivine | | | | | | | CYAN | a3 | 77.7 | | | |
| G050 | MI | Olivine | Etna A | g2 | | Red | d | | | | 78.8 | | | |
| G051 | MI | Olivine | Etna A | g2 | | Red | d | | | | 78.7 | | | |
| G052 | MI | Olivine | | | | Red | e1 | | | | 74.8 | | | |
| G053 | MI | Olivine | | | | Red | e1 | | | | 74.8 | | | |
| G054 | MI | Olivine | | | | Red | e1 | | | | 74.8 | | | |
| G055 | MI | Olivine | | | | Red | e3 | | | | 79.6 | | | |
| G056 | MI | Olivine | Etna A | h7 | | Red | g | | | | 78.4 | | | |

**Table H.4:** Description of glass analyses ($n$ = 224) *cont.*

| No. | Type | Host | Mount 1 | Crystal 1 | Inclusion 1 | Mount 2 | Crystal 2 | Inclusion 2 | Mount 3 | Crystal 3 | Fo | Wo | Fs | En |
|---|---|---|---|---|---|---|---|---|---|---|---|---|---|---|
| G057 | MI | Olivine | Etna A | i12 | | Red | h | | | | 81.9 | | | |
| G058 | MI | Olivine | Etna A | i12 | | Red | h | | | | 81.4 | | | |
| G059 | MI | Olivine | | | | Red | 17 | | | | 75.7 | | | |
| G060 | MI | Olivine | | | | Red | 17 | | | | 75.5 | | | |
| G061 | MI | Olivine | | | | Red | n | | | | 81.8 | | | |
| G062 | MG | Olivine | | | | Red | n | | | | 81.6 | | | |
| G063 | MI | Olivine | | | | Red | n | | | | 81.6 | | | |
| G064 | MI | Olivine | | | | Red | n | | | | 81.6 | | | |
| G065 | MI | Olivine | | | | Red | r1 | | | | 80.9 | | | |
| G066 | MI | | Etna 231113 Olivine | a1 | 14.71 | | | | | | | | | |
| G067 | | | Etna 231113 Olivine | a1 | 14.77 | | | | | | | | | |
| G068 | MI | Olivine | Etna 231113 Olivine | a2 | 32.09 | | | | | | 67.0 | | | |
| G069 | MG | Olivine | Etna 231113 Olivine | a2 | 30.98 | | | | | | 67.1 | | | |
| G070 | MI | Olivine | Etna 231113 Olivine | a6 | 36.26 | | | | | | 74.7 | | | |
| G071 | MI | Olivine | Etna 231113 Olivine | a9 | 11.79 | | | | | | 70.4 | | | |
| G072 | MG | Olivine | Etna 231113 Olivine | a11 | 12.05 | | | | | | 80.5 | | | |
| G073 | MI | Olivine | Etna 231113 Olivine | a11 | 25.48 | | | | | | 80.4 | | | |
| G074 | MI | Olivine | Etna 231113 Olivine | a12 | | | | | | | 81.5 | | | |
| G075 | MG | Olivine | Etna 231113 Olivine | a12 | 41.76 | | | | | | 80.9 | | | |
| G076 | MI | Olivine | Etna 231113 Olivine | a13 | 20.69 | | | | | | 74.3 | | | |
| G077 | MG | Olivine | Etna 231113 Olivine | a17 | 61.31 | | | | | | 73.9 | | | |
| G078 | MI | Olivine | Etna 231113 Olivine | a18 | | | | | | | 72.7 | | | |
| G079 | MI | Olivine | Etna 231113 Olivine | a18 | 33.42 | | | | | | 71.8 | | | |
| G080 | MI | Olivine | Etna 231113 Olivine | a18 | 19.8 | | | | | | 72.0 | | | |
| G081 | MI | Olivine | Etna 231113 Olivine | b1 | 25.38 | | | | | | 72.1 | | | |
| G082 | MI | Olivine | Etna 231113 Olivine | b4 | 9.42 | | | | | | 76.3 | | | |
| G083 | MI | Olivine | Etna 231113 Olivine | b4 | 7.55 | | | | | | 76.4 | | | |
| G084 | MG | Olivine | Etna 231113 Olivine | b5 | | | | | | | 73.8 | | | |
| G085 | MG | Olivine | Etna 231113 Olivine | b7 | 88.25 | | | | | | 82.0 | | | |

**Table H.4:** Description of glass analyses ($n$ = 224) *cont.*

| No. | Type | Host | Mount 1 | Crystal 1 | Inclusion 1 | Mount 2 | Crystal 2 | Inclusion 2 | Mount 3 | Crystal 3 | Fo | Wo | Fs | En |
|---|---|---|---|---|---|---|---|---|---|---|---|---|---|---|
| G086 | MI | Olivine | Etna 231113 Olivine | b7 | 26.27 | | | | | | 81.8 | | | |
| G087 | MI | Olivine | Etna 231113 Olivine | b7 | 41.65 | | | | | | 81.9 | | | |
| G088 | MI | Olivine | Etna 231113 Olivine | b10 | 37.9 | | | | | | 78.7 | | | |
| G089 | MG | Olivine | Etna 231113 Olivine | b14 | 37.53 | | | | | | 77.4 | | | |
| G090 | MI | Olivine | Etna 231113 Olivine | c1 | 27.78 | | | | | | | | | |
| G091 | MG | | Etna 231113 Olivine | c1 | 38.01 | | | | | | | | | |
| G092 | MI | Olivine | Etna 231113 Olivine | c2 | 10.64 | | | | | | 79.1 | | | |
| G093 | MI | Olivine | Etna 231113 Olivine | c2 | 18.04 | | | | | | | | | |
| G094 | MI | Olivine | Etna 231113 Olivine | c3 | 20.07 | | | | | | 76.5 | | | |
| G095 | MI | Olivine | Etna 231113 Olivine | c6 | 38.15 | | | | | | 76.2 | | | |
| G096 | MI | Olivine | Etna 231113 Olivine | c6 | 31.95 | | | | | | 76.2 | | | |
| G097 | MI | Olivine | Etna 231113 Olivine | c6 | | | | | | | 76.2 | | | |
| G098 | MI | Olivine | Etna 231113 Olivine | c10 | 45.28 | | | | | | 81.2 | | | |
| G099 | MI | Olivine | Etna 231113 Olivine | c10 | 45.06 | | | | | | 81.0 | | | |
| G100 | MI | Olivine | Etna 231113 Olivine | c10 | | | | | | | 81.4 | | | |
| G101 | MI | Olivine | Etna 231113 Olivine | c12 | 1 | | | | | | 73.1 | | | |
| G102 | MI | Olivine | Etna 231113 Olivine | c12 | 2 | | | | | | 79.6 | | | |
| G103 | MI | Olivine | Etna 231113 Olivine | c12 | 3 | | | | | | 72.5 | | | |
| G104 | MI | Olivine | Etna 231113 Olivine | c12 | 4 | | | | | | 66.5 | | | |
| G105 | MI | Olivine | Etna 231113 Olivine | c14 | 20.12 | | | | | | 77.4 | | | |
| G106 | MI | Olivine | Etna 231113 Olivine | c14 | 13.62 | | | | | | 76.7 | | | |
| G107 | MI | Olivine | Etna 231113 Olivine | d6 | 50.99 | | | | | | 80.9 | | | |
| G108 | MI | Olivine | Etna 231113 Olivine | d7 | 19.13 | | | | | | 80.8 | | | |
| G109 | MI | Olivine | Etna 231113 Olivine | d8 | 9.4 | | | | | | 77.9 | | | |
| G110 | MI | Olivine | Etna 231113 Olivine | d9 | 29.05 | | | | | | 72.1 | | | |
| G111 | MI | Olivine | Etna 231113 Olivine | d11 | 1 | | | | | | 80.6 | | | |
| G112 | MG | Olivine | Etna 231113 Olivine | d11 | 2 | | | | | | 79.9 | | | |
| G113 | MG | Olivine | Etna 231113 Olivine | d13 | 26.61 | | | | | | 77.8 | | | |
| G114 | MG | Olivine | Etna 231113 Olivine | d13 | 31.23 | | | | | | 76.7 | | | |

**Table H.4:** Description of glass analyses ($n$ = 224) *cont.*

| No. | Type | Host | Mount 1 | Crystal 1 | Inclusion 1 | Mount 2 | Crystal 2 | Inclusion 2 | Mount 3 | Crystal 3 | Fo | Wo | Fs | En |
|---|---|---|---|---|---|---|---|---|---|---|---|---|---|---|
| G115 | MG | Olivine | Etna 231113 Olivine | d13 | | | | | | | 78.6 | | | |
| G116 | MI | Olivine | Etna 231113 Olivine | d15 | 1 | | | | | | 73.3 | | | |
| G117 | MI | Olivine | Etna 231113 Olivine | e5 | 1 | | | | | | 82.3 | | | |
| G118 | MI | Oxide | Etna 231113 Olivine | e6 | 22.76 | | | | | | | | | |
| G119 | | Olivine | Etna 231113 Olivine | e7 | 1 | | | | | | | | | |
| G120 | MI | Olivine | Etna 231113 Olivine | e7 | 2 | | | | | | 77.3 | | | |
| G121 | MI | Olivine | Etna 231113 Olivine | e7 | 3 | | | | | | 77.3 | | | |
| G122 | MI | Olivine | Etna 231113 Olivine | e7 | 4 | | | | | | 76.3 | | | |
| G123 | MG | Olivine | Etna 231113 Olivine | e7 | 5 | | | | | | 77.1 | | | |
| G124 | MI | Olivine | Etna 231113 Olivine | e7 | 6 | | | | | | 75.9 | | | |
| G125 | MI | Olivine | Etna 231113 Olivine | e7 | 59.12 | | | | | | 77.4 | | | |
| G126 | MI | Olivine | Etna 231113 Olivine | e7 | 24.99 | | | | | | 77.3 | | | |
| G127 | MI | Olivine | Etna 231113 Olivine | e7 | 30.7 | | | | | | 76.5 | | | |
| G128 | MI | Olivine | Etna 231113 Olivine | e9 | 45.28 | | | | | | 70.4 | | | |
| G129 | MI | Olivine | Etna 231113 Olivine | e11 | 22.41 | | | | | | 79.7 | | | |
| G130 | MI | Olivine | Etna 231113 Olivine | e11 | 14.42 | | | | | | 79.5 | | | |
| G131 | MI | Olivine | Etna 231113 Olivine | e11 | 15.16 | | | | | | 78.8 | | | |
| G132 | MI | Olivine | Etna 231113 Olivine | e11 | 12.48 | | | | | | 78.7 | | | |
| G133 | MG | Olivine | Etna 231113 Olivine | e14 | 64.18 | | | | | | 76.3 | | | |
| G134 | MG | Olivine | Etna 231113 Olivine | e14 | 35.96 | | | | | | 75.7 | | | |
| G135 | MI | Olivine | Etna 231113 Olivine | e14 | 39.45 | | | | | | 73.0 | | | |
| G136 | MI | Olivine | Etna 231113 Olivine | e14 | 30.42 | | | | | | 78.6 | | | |
| G137 | | | Etna 231113 Olivine | e16 | 18.31 | | | | | | | | | |
| G138 | MI | Olivine | Etna 231113 Olivine | f3 | 19.95 | | | | | | 72.1 | | | |
| G139 | MI | Olivine | Etna 231113 Olivine | f4 | 31.84 | | | | | | 75.6 | | | |
| G140 | MI | Olivine | Etna 231113 Olivine | f5 | 11.15 | | | | | | 70.7 | | | |
| G141 | MI | Olivine | Etna 231113 Olivine | f10 | 27.72 | | | | | | 79.1 | | | |
| G142 | MI | Olivine | Etna 231113 Olivine | f10 | 12.99 | | | | | | 79.8 | | | |
| G143 | MI | Olivine | Etna 231113 Olivine | f10 | 19.51 | | | | | | 79.1 | | | |

**Table H.4:** Description of glass analyses ($n$ = 224) *cont.*

| No. | Type | Host | Mount 1 | Crystal 1 | Inclusion 1 | Mount 2 | Crystal 2 | Inclusion 2 | Mount 3 | Crystal 3 | Fo | Wo | Fs | En |
|---|---|---|---|---|---|---|---|---|---|---|---|---|---|---|
| G144 | MI | Olivine | Etna 231113 Olivine | f12 | 21.26 | | | | | | 77.6 | | | |
| G145 | MG | Olivine | Etna 231113 Olivine | g3 | 21.25 | | | | | | 79.3 | | | |
| G146 | MI | Olivine | Etna 231113 Olivine | g3 | 43.05 | | | | | | 79.6 | | | |
| G147 | MG | Olivine | Etna 231113 Olivine | g3 | 35.69 | | | | | | 80.1 | | | |
| G148 | MG | Olivine | Etna 231113 Olivine | g3 | 30.15 | | | | | | 80.9 | | | |
| G149 | MI | Olivine | Etna 231113 Olivine | g4 | 16.76 | | | | | | 79.1 | | | |
| G150 | MI | Olivine | Etna 231113 Olivine | g4 | 19.99 | | | | | | 78.0 | | | |
| G151 | MG | Olivine | Etna 231113 Olivine | g5 | 44.09 | | | | | | 81.0 | | | |
| G152 | MI | Olivine | Etna 231113 Olivine | g7 | 16.01 | | | | | | | | | |
| G153 | MG | Olivine | Etna 231113 Olivine | g8 | 21.49 | | | | | | 72.1 | | | |
| G154 | MI | Olivine | Etna 231113 Olivine | g8 | 16.21 | | | | | | 72.1 | | | |
| G155 | MG | Olivine | Etna 231113 Olivine | g13 | 2 | | | | | | 76.5 | | | |
| G156 | MG | Olivine | Etna 231113 Olivine | g13 | 1 | | | | | | 77.0 | | | |
| G157 | MI | Olivine | Etna 231113 Olivine | g13 | 32.95 | | | | | | 77.2 | | | |
| G158 | MG | Olivine | Etna 231113 Olivine | g13 | 67.67 | | | | | | 77.4 | | | |
| G159 | MG | Olivine | Etna 231113 Olivine | g13 | 77.33 | | | | | | 78.4 | | | |
| G160 | MI | Olivine | Etna 231113 Olivine | h4 | 20.57 | | | | | | 75.2 | | | |
| G161 | MI | Olivine | Etna 231113 Olivine | h4 | 20.47 | | | | | | 76.0 | | | |
| G162 | MI | Olivine | Etna 231113 Olivine | h4 | 19.42 | | | | | | 76.7 | | | |
| G163 | MG | Olivine | Etna 231113 Olivine | h8 | 39.82 | | | | | | 74.2 | | | |
| G164 | MI | Olivine | Etna 231113 Olivine | h9 | 8.73 | | | | | | 80.0 | | | |
| G165 | MI | Olivine | Etna 231113 Olivine | h9 | 12.64 | | | | | | 79.0 | | | |
| G166 | MI | Olivine | Etna 231113 Olivine | h9 | 16.38 | | | | | | 80.0 | | | |
| G167 | | Olivine | Etna 231113 Olivine | h9 | n.d. | | | | | | | | | |
| G168 | MI | Olivine | Etna 231113 Olivine | h12 | 25.66 | | | | | | 79.1 | | | |
| G169 | MI | Olivine | Etna 231113 Olivine | h12 | 38.8 | | | | | | 78.7 | | | |
| G170 | MI | Olivine | Etna 231113 Olivine | h12 | 54.73 | | | | | | 78.6 | | | |
| G171 | MI | Olivine | Etna 231113 Olivine | h13 | 10.06 | | | | | | 70.9 | | | |
| G172 | MI | Olivine | Etna 231113 Olivine | h13 | 15.23 | | | | | | 72.3 | | | |

**Table H.4:** Description of glass analyses ($n$ = 224) *cont.*

| No. | Type | Host | Mount 1 | Crystal 1 | Inclusion 1 | Mount 2 | Crystal 2 | Inclusion 2 | Mount 3 | Crystal 3 | Fo | Wo | Fs | En |
|---|---|---|---|---|---|---|---|---|---|---|---|---|---|---|
| G173 | MI | Olivine | Etna 231113 Olivine | h13 | 18.8 | | | | | | 71.4 | | | |
| G174 | MI | Olivine | Etna 231113 Olivine | h13 | 10.32 | | | | | | 71.0 | | | |
| G175 | MG | Olivine | Etna 231113 Olivine | h13 | 91.38 | | | | | | 71.6 | | | |
| G176 | MI | Olivine | Etna 231113 Olivine | h13 | 23.71 | | | | | | 71.0 | | | |
| G177 | | | Etna 231113 Olivine | h15 | 27.3 | | | | | | | | | |
| G178 | MG | Olivine | Etna 231113 Olivine | i2 | 34.42 | | | | | | 72.5 | | | |
| G179 | MG | Olivine | Etna 231113 Olivine | i2 | 31.09 | | | | | | 74.0 | | | |
| G180 | MG | Olivine | Etna 231113 Olivine | i2 | 25.01 | | | | | | 74.3 | | | |
| G181 | MG | Olivine | Etna 231113 Olivine | i2 | | | | | | | 70.7 | | | |
| G182 | MI | Olivine | Etna 231113 Olivine | i3 | 20.32 | | | | | | 79.9 | | | |
| G183 | MI | Olivine | Etna 231113 Olivine | i3 | 12.77 | | | | | | 78.4 | | | |
| G184 | MI | Olivine | Etna 231113 Olivine | i6 | 17.66 | | | | | | 78.6 | | | |
| G185 | MI | Olivine | Etna 231113 Olivine | i8 | 14.35 | | | | | | 72.9 | | | |
| G186 | MI | Olivine | Etna 231113 Olivine | i8 | 12.47 | | | | | | 76.4 | | | |
| G187 | MI | Olivine | Etna 231113 Olivine | i10 | 52.88 | | | | | | 77.8 | | | |
| G188 | MI | Olivine | Etna 231113 Olivine | i10 | 22.33 | | | | | | 77.8 | | | |
| G189 | | | Etna 231113 Olivine | i10 | 31.66 | | | | | | | | | |
| G190 | MI | Olivine | Etna 231113 Olivine | i11 | 33.92 | | | | | | 68.6 | | | |
| G191 | MI | Olivine | Etna 231113 Olivine | i12 | 26.65 | | | | | | 80.7 | | | |
| G192 | MI | Olivine | Etna 231113 Olivine | i12 | 14.31 | | | | | | 80.4 | | | |
| G193 | MI | Olivine | Etna 231113 Olivine | i12 | 9.42 | | | | | | 79.6 | | | |
| G194 | MI | Olivine | Etna 231113 Olivine | j4 | 43.22 | | | | | | 75.9 | | | |
| G195 | MI | Olivine | Etna 231113 Olivine | j8 | 11.08 | | | | | | 76.8 | | | |
| G196 | | Olivine | EtnaOlA | f1 | 33.61 | | | | | | | | | |
| G197 | | Olivine | EtnaOlA | f2 | 63.09 | | | | | | | | | |
| G198 | | Olivine | EtnaOlA | f3 | 44.41 | | | | | | | | | |
| G199 | | Olivine | EtnaOlA | g2 | 40.28 | | | | | | | | | |
| G200 | | Olivine | EtnaOlA | h10 | 57.28 | | | | | | | | | |
| G201 | | Olivine | EtnaOlA | h11 | 109.67 | | | | | | | | | |

**Table H.4:** Description of glass analyses ($n$ = 224) *cont.*

| No. | Type | Host | Mount 1 | Crystal 1 | Inclusion 1 | Mount 2 | Crystal 2 | Inclusion 2 | Mount 3 | Crystal 3 | Fo | Wo | Fs | En |
|---|---|---|---|---|---|---|---|---|---|---|---|---|---|---|
| G202 | | Olivine | EtnaOlA | h11 | 54.84 | | | | | | | | | |
| G203 | | Olivine | EtnaOlA | h11 | 57.49 | | | | | | | | | |
| G204 | | Olivine | EtnaOlA | h11 | 63.09 | | | | | | | | | |
| G205 | | Olivine | EtnaOlA | h11 | 66.17 | | | | | | | | | |
| G206 | | Olivine | EtnaOlA | h11 | 71.76 | | | | | | | | | |
| G207 | | Olivine | EtnaOlA | h2 | 43.46 | | | | | | | | | |
| G208 | | Olivine | EtnaOlA | h3 | 54.7 | | | | | | | | | |
| G209 | | Olivine | EtnaOlA | h7 | 39.95 | | | | | | | | | |
| G210 | | Olivine | EtnaOlA | h9 | 40.47 | | | | | | | | | |
| G211 | | Olivine | EtnaOlA | i12 | 52.31 | | | | | | | | | |
| G212 | | Olivine | EtnaOlA | i12 | 80.32 | | | | | | | | | |
| G213 | | Olivine | EtnaOlB | a1 | 28.76 | | | | | | 82.2 | | | |
| G214 | | Olivine | EtnaOlB | b2 | 31.2 | | | | | | 71.1 | | | |
| G215 | | Olivine | EtnaOlB | b2 | 48.37 | | | | | | 71.1 | | | |
| G216 | | Olivine | EtnaOlB | f9 | 39.66 | | | | | | 78.9 | | | |
| G217 | | Olivine | EtnaOlB | g4 | 38.12 | | | | | | 77.0 | | | |
| G218 | | Olivine | EtnaOlB | h11 | 30.98 | | | | | | | | | |
| G219 | | Olivine | EtnaOlB | h2 | 28.86 | | | | | | | | | |
| G220 | | Olivine | EtnaOlB | h8 | 40.63 | | | | | | | | | |
| G221 | | Olivine | EtnaOlB | h8 | 82.89 | | | | | | | | | |
| G222 | | Olivine | EtnaOlB | i14 | 33.72 | | | | | | | | | |
| G223 | | Olivine | EtnaOlB | j13 | 55.89 | | | | | | | | | |
| G224 | | Olivine | EtnaOlB | j14 | 43.46 | | | | | | | | | |

*Notes:* No. is the unique identifier for each glass (G) analysis. Type refers to melt inlcusion (MI), matrix glass (MG), or blank if not noted. As crystals were remounted multiple times, the sample name (mount, crystal, inclusion number) for each mount is given for comparing with Tables H.1 and H.2. Fo (if olivine) and Wo/En/Fs (if pyroxene) are given where measured (Tables H.1 and H.2).

**Table H.5:** Raman data on melt inclusions, embayments, and matrix glass ($n$ = 129).

| No. | $H_2O$ (wt%) | *s.d.* | Nanolites | N# | *s.d.* | No. | $H_2O$ (wt%) | *s.d.* | Nanolites | N# | *s.d.* |
|---|---|---|---|---|---|---|---|---|---|---|---|
| G066 | | | N | | | G150 | | | Y | | |
| G067 | | | Y | 1.37 | *0.07* | G151 | 1.42 | | N | 0.81 | *0.06* |
| G068 | 2.54 | | N | 0.92 | *0.06* | G152 | | | N | | |
| G069 | 3.00 | | N | 1.23 | *0.28* | G153 | | | N | | |
| G070 | | | Y | 1.81 | *0.17* | G155 | | | Y | 1.14 | *0.05* |
| G071 | | | N | | | G156 | | | Y | | |
| G072 | | | N | | | G158 | | | Y | 1.09 | *0.07* |
| G073 | 2.73 | | N | 0.93 | *0.08* | G160 | | | N | | |
| G074 | | | Y | | | G161 | | | N | | |
| G075 | | | Y | 2.38 | *0.09* | G163 | | | Y | 1.52 | *0.07* |
| G076 | | | Y | 2.09 | *0.14* | G166 | | | N | | |
| G077 | 0.05 | | N | 0.75 | *0.05* | G167 | 3.96 | | N | 1.08 | *0.14* |
| G078 | 2.10 | | N | 0.75 | *0.03* | G168 | | | Y | 2.08 | *0.16* |
| G079 | | | Y | | | G169 | | | Y | 2.61 | *0.26* |
| G080 | | | Y | 5.78 | *0.43* | G170 | | | Y | 2.48 | *0.08* |
| G081 | | | Y | | | G175 | 0.43 | | N | 0.86 | *0.08* |
| G085 | | | Y | 2.12 | *0.11* | G176 | | | N | | |
| G086 | 3.20 | | N | 0.71 | *0.08* | G177 | | | Y | | |
| G087 | | | N | | | G178 | 0.92 | | N | 0.81 | *0.08* |
| G088 | 0.97 | | N | 0.86 | *0.03* | G182 | | | Y | 1.21 | *0.06* |
| G089 | | | Y | 3.07 | *0.23* | G183 | | | Y | 2.13 | *0.06* |
| G090 | 2.91 | | N | 1.18 | *0.08* | G184 | | | N | | |
| G091 | | | Y | 1.19 | *0.09* | G186 | | | N | | |
| G093 | | | N | | | G187 | | | Y | 2.84 | *0.18* |
| G094 | | | Y | 3.09 | *0.19* | G188 | | | Y | | |
| G095 | | | Y | 1.63 | *0.08* | G189 | | | Y | 1.84 | *0.11* |
| G096 | | | Y | 1.50 | *0.08* | G191 | 2.78 | | N | 0.75 | *0.05* |
| G097 | | | N | | | G192 | | | N | | |
| G098 | | | N | | | G193 | | | N | | |
| G099 | | | Y | 2.03 | *0.10* | G194 | 0.55 | | N | 0.93 | *0.06* |
| G100 | 4.06 | | N | 0.71 | *0.04* | G196 | | | Y | 1.31 | *0.08* |
| G101 | | | N | | | G197 | 4.63 | *0.23* | N | 0.80 | *0.02* |
| G102 | | | Y | 3.23 | *0.17* | G198 | | | Y | 1.50 | *0.11* |
| G103 | | | N | | | G199 | | | Y | 2.67 | *0.16* |
| G104 | | | N | | | G200 | | | Y | 2.96 | *0.23* |
| G105 | | | N | | | G201 | | | Y | 1.52 | *0.07* |
| G106 | 3.16 | | N | 1.04 | *0.04* | G202 | | | Y | 1.34 | *0.06* |
| G107 | | | Y | | | G203 | 3.25 | *0.16* | N | 0.82 | *0.01* |
| G110 | | | N | | | G204 | | | Y | 1.09 | *0.04* |
| G111 | | | N | | | G205 | | | Y | 1.08 | *0.05* |
| G112 | | | N | | | G206 | 2.91 | *0.14* | N | 0.78 | *0.03* |
| G113 | 0.39 | | N | 0.77 | *0.03* | G207 | 1.33 | *0.07* | N | 0.74 | *0.03* |
| G114 | 0.23 | | N | 0.85 | *0.02* | G208 | | | Y | 2.27 | *0.15* |
| G116 | | | Y | 1.07 | *0.04* | G209 | 4.93 | *0.24* | N | 0.75 | *0.03* |
| G117 | | | N | | | G210 | | | Y | 1.08 | *0.07* |

**Table H.5:** Raman data on melt inclusions, embayments, and matrix glass ($n$ = 129) *cont.*

| No. | $H_2O$ (wt%) | *s.d.* | Nanolites | N# | *s.d.* | No. | $H_2O$ (wt%) | *s.d.* | Nanolites | N# | *s.d.* |
|---|---|---|---|---|---|---|---|---|---|---|---|
| G118 | 2.40 | | N | 0.87 | *0.05* | G211 | | | Y | 2.81 | *0.24* |
| G119 | 0.77 | | N | 0.88 | *0.08* | G212 | | | Y | 3.38 | *0.29* |
| G120 | | | N | | | G213 | | | Y | 1.80 | *0.08* |
| G121 | 0.96 | | N | 1.21 | *0.06* | G214 | | | Y | 1.26 | *0.03* |
| G122 | 0.88 | | N | 1.02 | *0.13* | G215 | | | Y | 2.31 | *0.15* |
| G123 | | | Y | 1.37 | *0.08* | G216 | | | Y | 2.43 | *0.13* |
| G124 | 0.75 | | N | 1.14 | *0.03* | G217 | | | Y | 1.56 | *0.08* |
| G130 | 2.26 | | N | 0.72 | *0.08* | G218 | | | Y | 1.49 | *0.08* |
| G135 | | | N | | | G219 | | | Y | 6.70 | *0.79* |
| G137 | | | N | | | G220 | | | Y | 1.68 | *0.12* |
| G138 | | | Y | 1.63 | *0.14* | G221 | | | Y | 3.70 | *0.31* |
| G141 | | | Y | 1.16 | *0.08* | G222 | | | Y | 1.48 | *0.06* |
| G143 | | | Y | 1.52 | *0.09* | G223 | | | Y | 1.40 | *0.13* |
| G146 | | | Y | 1.14 | *0.07* | G224 | | | Y | 1.21 | *0.06* |
| G147 | | | Y | 1.61 | *0.08* | | | | | | |

*Notes:* No. is the unique identifier for each glass (G) analysis (Table H.4). Raman data collected as described in Section 6.3.2. $H_2O$ concentration calculated using Equation 6.8 and the empirical calibrations in Figure 6.8. Nanolites refers to a manual inspection of the Raman spectrum to ascertain if nanolites were present using the presence (Y) or absence (N) of a peak at $\sim$670 $cm^{-1}$ (Section 6.3.2). N# is the degree of nanolitisation defined by Di Genova et al. (2018) using Equation 6.7. Errors of one standard deviation ($s.d.$) shown in *italics*.

**Table H.6:** SIMS data on melt inclusions, embayments, and matrix glass ($n$ = 49).

| | SIMS-4f $CO_2$ | | | SIMS-4f $H_2O$ | | | | | | | | SIMS-1270 | | |
|---|---|---|---|---|---|---|---|---|---|---|---|---|---|---|
| No. | MgO | $CO_2$[a] | CaO | $H_2O$ | Li[a] | F[a] | Mg | Cl[a] | $K_2O$ | CaO | $TiO_2$ | $\delta D$[b] | $H_2O$[c] | $H_2O$[d] |
| G001 | 4.81 | 153 | 6.53 | 2.93 | 31 | 1153 | 2.91 | 1856 | 2.68 | 6.84 | 1.54 | -43.4 | 3.24 | 2.64 |
| G002 | 4.03 | 182 | 6.15 | 2.30 | 22 | 1200 | 2.52 | 1627 | 3.38 | 6.40 | 1.52 | -47.1 | 2.37 | 2.18 |
| G004 | 3.30 | 387 | 7.85 | 2.21 | 9 | 1342 | 2.69 | 2065 | 2.89 | 9.28 | 1.90 | | | |
| G005 | 3.24 | 10 | 6.94 | 0.93 | 15 | 1232 | 2.30 | 1679 | 3.45 | 6.95 | 1.84 | | | |
| G006 | | | | | | | | | | | | -74.9 | 0.50 | 0.37 |
| G008 | | | | | | | | | | | | -43.4 | 1.11 | 0.90 |
| G010 | 4.64 | 100 | 6.93 | 2.17 | 14 | 1182 | 2.88 | 1670 | 3.18 | 7.36 | 1.32 | | | |
| G011 | 5.53 | 248 | 7.25 | 0.16 | 7 | 646 | 5.26 | 435 | 1.89 | 12.24 | 1.52 | | | |
| G012 | 2.45 | 89 | 4.63 | 2.32 | 15 | 1097 | 2.20 | 1354 | 3.54 | 5.76 | 1.42 | -73.3 | 2.44 | 2.16 |
| G013* | 3.60 | 457 | 5.44 | 2.24 | 19 | 1450 | 2.07 | 1405 | 4.59 | 5.56 | 1.32 | -36.1 | 1.98 | 6.18 |
| G014 | 6.93 | 1602 | 7.77 | 0.79 | 8 | 703 | 6.16 | 664 | 1.60 | 13.37 | 0.88 | | | |
| G015 | 3.32 | 132 | 5.31 | 2.35 | 20 | 1544 | 1.99 | 1397 | 4.23 | 5.42 | 1.38 | | | |
| G016 | | | | | | | | | | | | -15.0 | 1.44 | 1.02 |
| G017 | 4.48 | 652 | 7.55 | 2.26 | 9 | 1300 | 2.97 | 2045 | 3.10 | 8.94 | 1.90 | -14.5 | 2.60 | 1.40 |
| G018 | | | | | | | | | | | | -1.6 | 2.69 | 1.68 |
| G019 | 5.58 | 52 | 7.07 | 0.76 | 15 | 1199 | 5.46 | 1685 | 3.22 | 6.76 | 1.68 | -28.9 | 0.66 | 0.57 |
| G022 | 3.90 | 62 | 7.75 | 3.07 | 10 | 1167 | 2.40 | 1877 | 2.74 | 8.37 | 1.85 | -16.9 | 3.34 | 7.17 |
| G023 | 2.36 | 64 | 3.86 | 1.03 | 24 | 929 | 1.52 | 2860 | 7.93 | 4.04 | 1.92 | | | |

**Table H.6:** SIMS data on melt inclusions, embayments, and matrix glass ($n$ = 49) *cont.*

| | SIMS-4f $CO_2$ | | | SIMS-4f $H_2O$ | | | | | | | | SIMS-1270 | | |
|---|---|---|---|---|---|---|---|---|---|---|---|---|---|---|
| No. | MgO | $CO_2$[a] | CaO | $H_2O$ | Li[a] | F[a] | Mg | Cl[a] | $K_2O$ | CaO | $TiO_2$ | $\delta D$[b] | $H_2O$[c] | $H_2O$[d] |
| G024 | 3.52 | 207 | 5.37 | 2.08 | 17 | 1483 | 2.22 | 1746 | 3.81 | 5.26 | 1.36 | -39.9 | 2.23 | 1.35 |
| G025 | 3.44 | 65 | 5.73 | 2.11 | 18 | 1274 | 2.03 | 1153 | 4.12 | 5.47 | 1.62 | -29.1 | 2.09 | 1.70 |
| G026 | | | | | | | | | | | | -13.0 | 2.30 | 1.72 |
| G027 | 5.04 | 112 | 7.17 | 0.95 | 8 | 574 | 5.84 | 779 | 1.64 | 13.23 | 1.56 | | | |
| G029 | | | | | | | | | | | | -56.9 | 1.99 | 0.93 |
| G030 | | | | | | | | | | | | -18.0 | 1.42 | 0.98 |
| G031 | | | | | | | | | | | | -36.0 | 1.27 | 0.25 |
| G033 | 2.73 | 235 | 5.03 | 0.67 | 5 | 1289 | 2.76 | 2067 | 3.87 | 6.20 | 1.62 | | | |
| G034 | 2.83 | 151 | 5.42 | 0.73 | 17 | 941 | 3.71 | 1677 | 2.06 | 8.28 | 1.27 | | | |
| G036 | | | | | | | | | | | | -32.2 | 2.69 | 2.35 |
| G037 | 3.86 | 121 | 7.69 | 0.47 | 9 | 899 | 10.01 | 1522 | 2.54 | 6.94 | 1.07 | -36.3 | 0.58 | 0.39 |
| G038 | | | | | | | | | | | | -56.6 | 0.62 | 0.25 |
| G043 | 3.87 | 154 | 6.10 | 0.57 | 13 | 1180 | 8.10 | 1670 | 3.13 | 5.43 | 1.01 | | | |
| G044 | 2.86 | 198 | 5.15 | 2.32 | 21 | 1367 | 2.08 | 1800 | 3.36 | 4.70 | 1.68 | -53.8 | 2.10 | 2.37 |
| G046 | 3.13 | 543 | 7.10 | 1.56 | 9 | 841 | 12.38 | 1103 | 2.11 | 5.38 | 1.21 | -39.6 | 2.30 | 1.92 |
| G047 | | | | | | | | | | | | -37.8 | 2.32 | 1.88 |
| G048 | 3.28 | 121 | 6.57 | 2.38 | 22 | 1311 | 2.64 | 1614 | 3.26 | 6.55 | 1.76 | | | |
| G049 | 3.40 | 97 | 7.08 | 1.58 | 14 | 1183 | 2.70 | 1601 | 3.30 | 7.11 | 1.80 | | | |
| G050 | 4.11 | 46 | 7.30 | 0.34 | 12 | 1301 | 2.34 | 1789 | 3.16 | 7.29 | 1.95 | | | |
| G051 | 3.90 | 41 | 7.52 | 0.10 | 13 | 931 | 2.39 | 1413 | 3.18 | 7.41 | 1.95 | | | |
| G052 | 4.22 | 225 | 6.27 | 2.15 | 13 | 1022 | 2.32 | 1576 | 3.24 | 6.09 | 1.66 | | | |
| G055 | 3.52 | 56 | 7.23 | 1.15 | 18 | 1275 | 2.48 | 1651 | 3.58 | 7.98 | 1.96 | | | |
| G056 | 4.10 | 31 | 6.60 | 2.21 | 12 | 1152 | 2.66 | 1476 | 3.19 | 6.76 | 1.83 | | | |
| G057 | 4.88 | 1108 | 7.22 | 2.79 | 9 | 1249 | 3.15 | 1933 | 3.05 | 9.05 | 1.95 | | | |
| G058 | 4.68 | 611 | 7.13 | 2.86 | 9 | 1381 | 2.96 | 1906 | 2.90 | 8.63 | 1.90 | | | |
| G059 | 7.62 | 23 | 6.18 | 1.86 | 12 | 1003 | 6.10 | 1131 | 2.64 | 6.05 | 1.29 | | | |
| G060 | 3.82 | 28 | 6.87 | 2.26 | 14 | 1290 | 2.30 | 1576 | 2.90 | 6.99 | 1.44 | | | |
| G061 | 3.93 | 986 | 7.79 | 0.32 | 7 | 437 | 3.45 | 165 | 0.82 | 8.29 | 2.37 | | | |
| G062 | 4.20 | 163 | 7.57 | 0.26 | 11 | 995 | 2.71 | 1311 | 3.26 | 7.61 | 1.90 | | | |
| G063 | 5.99 | 52 | 6.68 | 2.03 | 12 | 1084 | 3.37 | 1338 | 3.18 | 6.70 | 1.76 | | | |
| G065 | 3.57 | 551 | 7.98 | 1.92 | 9 | 1184 | 2.69 | 1755 | 2.99 | 9.70 | 1.93 | | | |

*Notes:* No. is the unique identifier for each glass (G) analysis (Table H.4). SIMS data collected as described in Section 6.3.3. Elements/oxides are given in wt%, except [a] which are in ppm and [b] which are in ‰. [c] is $H_2O$ concentration using $^1H_2^+/^1H^+$ and [d] is $H_2O$ concentration using $^1H^+$/PB. G013* has $\delta^{13}C$ of -5.27 $\pm$ 2.4 ‰.

**Table H.7:** EPMA data on melt inclusions, embayments, and matrix glass ($n$ = 169).

| No. | $SiO_2$ | $TiO_2$ | $Al_2O_3$ | $FeO_T$ | MnO | MgO | CaO | $Na_2O$ | $K_2O$ | $P_2O_5$ | Cl | S | F | $Fe^{2+}/Fe_T$ | *s.d.* | VBD | *s.d.* |
|---|---|---|---|---|---|---|---|---|---|---|---|---|---|---|---|---|---|
| G001 | 46.53 | 1.50 | 15.94 | 9.04 | 0.16 | 4.82 | 9.60 | 3.66 | 1.80 | 0.62 | 0.1754 | 0.2871 | 0.1139 | | | 3.42 | *0.35* |
| G002 | 46.02 | 1.47 | 16.85 | 8.98 | 0.19 | 4.25 | 9.33 | 5.02 | 2.34 | 0.66 | 0.1723 | 0.2810 | 0.1307 | | | 2.47 | *0.35* |
| G004 | 43.45 | 1.83 | 16.97 | 9.66 | 0.16 | 4.17 | 12.73 | 3.56 | 1.99 | 0.53 | 0.1651 | 0.3440 | 0.0945 | | | 2.47 | *0.37* |
| G005 | 46.49 | 1.78 | 16.82 | 9.98 | 0.21 | 3.49 | 9.91 | 4.28 | 2.47 | 0.69 | 0.1505 | 0.1278 | 0.0937 | | | 1.89 | *0.38* |
| G010 | 46.37 | 1.15 | 15.86 | 10.99 | 0.21 | 4.21 | 9.90 | 3.94 | 2.41 | 0.66 | 0.1682 | 0.1748 | 0.1308 | 0.84 | *0.09* | 2.35 | *0.15* |
| G012 | 46.87 | 1.66 | 16.53 | 10.36 | 0.23 | 3.42 | 8.45 | 3.84 | 2.40 | 0.76 | 0.2013 | 0.1790 | 0.1342 | 0.67 | *0.08* | 3.00 | *0.14* |
| G013 | 49.12 | 1.28 | 15.32 | 9.93 | 0.23 | 3.42 | 7.75 | 4.56 | 3.28 | 0.97 | 0.1608 | 0.0901 | 0.1286 | 0.60 | *0.07* | 2.15 | *0.13* |
| G014 | 49.05 | 0.99 | 15.85 | 10.20 | 0.22 | 2.98 | 8.35 | 4.08 | 2.75 | 0.79 | 0.2004 | 0.1256 | 0.1445 | 0.47 | *0.06* | 2.37 | *0.13* |
| G015 | 50.55 | 1.39 | 15.52 | 9.53 | 0.21 | 3.10 | 7.56 | 4.69 | 2.95 | 0.88 | 0.1604 | 0.0482 | 0.1496 | 0.76 | *0.09* | 1.94 | *0.14* |
| G016 | 46.52 | 1.69 | 16.56 | 10.14 | 0.19 | 3.89 | 9.88 | 4.28 | 2.42 | 0.67 | 0.1495 | 0.1682 | 0.1072 | | | 1.79 | *0.38* |
| G017 | 43.58 | 1.78 | 16.98 | 9.76 | 0.15 | 4.69 | 12.23 | 3.59 | 2.13 | 0.60 | 0.1735 | 0.3294 | 0.1108 | 0.67 | *0.08* | 2.29 | *0.14* |
| G019 | 46.51 | 1.72 | 16.99 | 10.67 | 0.19 | 3.49 | 10.35 | 4.58 | 2.49 | 0.67 | 0.1612 | 0.1682 | 0.0965 | 0.69 | *0.08* | 0.97 | *0.14* |
| G020 | 46.69 | 1.74 | 17.04 | 10.57 | 0.20 | 3.35 | 10.33 | 4.20 | 2.40 | 0.64 | 0.1574 | 0.1704 | 0.0892 | | | 1.17 | *0.39* |
| G021 | 46.71 | 1.79 | 17.07 | 10.06 | 0.20 | 3.51 | 10.08 | 4.42 | 2.49 | 0.67 | 0.1669 | 0.1607 | 0.1115 | | | 1.27 | *0.38* |
| G022 | 44.47 | 1.81 | 16.56 | 9.78 | 0.17 | 3.58 | 11.77 | 3.11 | 1.87 | 0.54 | 0.1834 | 0.2612 | 0.1011 | 0.63 | *0.07* | 3.53 | *0.14* |
| G023 | 50.23 | 1.95 | 15.87 | 9.70 | 0.20 | 2.34 | 5.55 | 5.01 | 5.29 | 1.05 | 0.3485 | 0.0777 | 0.0997 | 0.73 | *0.08* | 1.27 | *0.13* |
| G024 | 49.41 | 1.37 | 14.48 | 10.42 | 0.23 | 3.40 | 7.54 | 4.66 | 2.68 | 0.92 | 0.1947 | 0.0248 | 0.1173 | 0.64 | *0.07* | 2.69 | *0.14* |
| G025 | 49.88 | 1.62 | 15.66 | 9.31 | 0.21 | 2.84 | 7.81 | 4.67 | 3.02 | 0.84 | 0.1265 | 0.0467 | 0.1368 | 0.80 | *0.09* | 2.35 | *0.14* |
| G027 | 49.45 | 1.54 | 17.96 | 9.53 | 0.22 | 2.45 | 7.20 | 4.35 | 2.98 | 0.79 | 0.2343 | 0.1917 | 0.1279 | 0.75 | *0.08* | 1.74 | *0.14* |
| G028 | 48.77 | 1.66 | 18.35 | 8.47 | 0.21 | 2.17 | 7.96 | 4.38 | 2.46 | 0.69 | 0.2191 | 0.2380 | 0.1103 | | | 2.49 | *0.33* |
| G033 | 45.99 | 1.61 | 17.14 | 11.21 | 0.22 | 3.10 | 6.41 | 5.37 | 3.14 | 1.06 | 0.3035 | 0.0732 | 0.1477 | 0.60 | *0.05* | 2.37 | *0.14* |
| G034 | 45.46 | 1.32 | 16.68 | 13.84 | 0.25 | 3.18 | 6.70 | 5.03 | 1.88 | 0.66 | 0.2868 | 0.0645 | 0.0884 | 0.53 | *0.06* | 2.57 | *0.13* |
| G037 | 45.75 | 1.36 | 17.88 | 10.20 | 0.18 | 3.28 | 12.53 | 4.07 | 2.31 | 0.61 | 0.1842 | 0.1850 | 0.1278 | | | 0.46 | *0.36* |
| G038 | 47.14 | 1.12 | 18.80 | 9.90 | 0.19 | 3.45 | 9.05 | 4.96 | 2.76 | 0.80 | 0.2208 | 0.1462 | 0.1732 | | | 0.44 | *0.34* |
| G039 | 43.78 | 1.61 | 17.08 | 11.23 | 0.21 | 4.16 | 12.91 | 3.70 | 2.03 | 0.59 | 0.1738 | 0.2044 | 0.0907 | | | 1.01 | *0.41* |
| G040 | 44.53 | 1.36 | 16.74 | 11.39 | 0.19 | 3.70 | 12.40 | 4.16 | 2.39 | 0.71 | 0.1933 | 0.2323 | 0.1429 | | | 0.75 | *0.41* |
| G041 | 45.32 | 1.33 | 17.38 | 10.47 | 0.19 | 4.16 | 12.48 | 3.96 | 2.18 | 0.67 | 0.1792 | 0.1734 | 0.1397 | | | 0.47 | *0.37* |
| G042 | 44.89 | 1.38 | 17.41 | 10.77 | 0.19 | 3.55 | 12.52 | 4.01 | 2.26 | 0.65 | 0.1918 | 0.1955 | 0.1056 | | | 0.80 | *0.39* |
| G044 | 50.79 | 1.67 | 15.24 | 9.75 | 0.24 | 3.03 | 6.49 | 4.75 | 2.46 | 0.88 | 0.2304 | 0.1043 | 0.1274 | 0.81 | *0.09* | 2.61 | *0.14* |

**Table H.7:** EPMA data on melt inclusions, embayments, and matrix glass ($n$ = 169) *cont.*

| No. | $SiO_2$ | $TiO_2$ | $Al_2O_3$ | $FeO_T$ | MnO | MgO | CaO | $Na_2O$ | $K_2O$ | $P_2O_5$ | Cl | S | F | $Fe^{2+}/Fe_T$ | *s.d.* | VBD | *s.d.* |
|---|---|---|---|---|---|---|---|---|---|---|---|---|---|---|---|---|---|
| G046 | 44.51 | 1.84 | 17.79 | 9.41 | 0.16 | 3.46 | 11.95 | 3.64 | 2.15 | 0.59 | 0.1852 | 0.2994 | 0.1325 | 0.66 | *0.08* | 2.29 | *0.14* |
| G048 | 48.41 | 1.81 | 16.97 | 9.16 | 0.20 | 3.85 | 8.77 | 3.96 | 2.43 | 0.75 | 0.1886 | 0.1667 | 0.1307 | | | 1.74 | *0.35* |
| G049 | 46.93 | 1.82 | 16.98 | 9.67 | 0.18 | 3.26 | 9.93 | 4.43 | 2.48 | 0.68 | 0.1635 | 0.1689 | 0.1526 | 0.70 | *0.08* | 1.81 | *0.14* |
| G050 | 47.87 | 1.89 | 17.42 | 10.01 | 0.19 | 3.57 | 9.89 | 3.99 | 2.23 | 0.70 | 0.1429 | 0.1540 | 0.0867 | | | 0.81 | *0.37* |
| G051 | 47.94 | 1.92 | 17.52 | 9.82 | 0.18 | 3.57 | 9.92 | 4.12 | 2.38 | 0.74 | 0.1381 | 0.1541 | 0.1315 | 0.55 | *0.07* | 0.60 | *0.13* |
| G052 | 48.73 | 1.65 | 16.23 | 10.00 | 0.22 | 3.82 | 8.40 | 4.20 | 2.25 | 0.64 | 0.1621 | 0.0687 | 0.0726 | | | 1.94 | *0.38* |
| G053 | 48.41 | 1.61 | 16.13 | 10.07 | 0.20 | 3.87 | 8.55 | 4.25 | 2.27 | 0.70 | 0.1536 | 0.0646 | 0.0842 | | | 1.98 | *0.38* |
| G054 | 48.62 | 1.61 | 16.35 | 10.23 | 0.21 | 3.69 | 8.44 | 3.86 | 2.26 | 0.65 | 0.1521 | 0.0676 | 0.0616 | | | 2.07 | *0.39* |
| G055 | 46.50 | 1.79 | 16.80 | 10.21 | 0.19 | 3.55 | 10.16 | 4.75 | 2.41 | 0.69 | 0.1727 | 0.1542 | 0.0872 | | | 1.25 | *0.38* |
| G056 | 46.21 | 1.80 | 16.65 | 10.03 | 0.19 | 4.12 | 9.49 | 3.95 | 2.27 | 0.62 | 0.1531 | 0.1922 | 0.0962 | | | 2.38 | *0.38* |
| G057 | 43.30 | 1.91 | 16.17 | 9.61 | 0.15 | 5.02 | 12.47 | 3.37 | 2.00 | 0.54 | 0.1503 | 0.3421 | 0.1132 | 0.52 | *0.07* | 2.82 | *0.14* |
| G058 | 43.44 | 1.82 | 16.57 | 9.53 | 0.17 | 4.27 | 12.19 | 3.19 | 1.87 | 0.57 | 0.1675 | 0.3169 | 0.0604 | 0.51 | *0.07* | 3.47 | *0.13* |
| G059 | 46.77 | 1.43 | 16.57 | 10.57 | 0.24 | 3.78 | 9.43 | 3.76 | 2.03 | 0.70 | 0.1599 | 0.1889 | 0.0910 | | | 2.39 | *0.40* |
| G060 | 46.76 | 1.39 | 16.26 | 10.82 | 0.23 | 3.66 | 9.73 | 3.71 | 2.04 | 0.70 | 0.1536 | 0.1951 | 0.0911 | | | 2.38 | *0.41* |
| G061 | 43.61 | 1.94 | 16.55 | 9.38 | 0.15 | 3.93 | 12.42 | 3.09 | 2.05 | 0.56 | 0.1780 | 0.3422 | 0.1124 | | | 3.37 | *0.36* |
| G062 | 47.07 | 1.81 | 16.86 | 10.16 | 0.20 | 4.25 | 10.11 | 4.21 | 2.36 | 0.70 | 0.1325 | 0.1472 | 0.1171 | 0.53 | *0.07* | 0.83 | *0.13* |
| G063 | 46.66 | 1.74 | 16.43 | 9.79 | 0.17 | 3.72 | 9.66 | 4.32 | 2.32 | 0.67 | 0.1532 | 0.1439 | 0.1468 | 0.68 | *0.08* | 2.42 | *0.14* |
| G064 | 46.89 | 1.74 | 16.53 | 9.70 | 0.19 | 4.08 | 9.39 | 4.44 | 2.35 | 0.67 | 0.1516 | 0.1443 | 0.0518 | | | 2.02 | *0.37* |
| G065 | 42.88 | 1.86 | 16.84 | 9.79 | 0.15 | 4.10 | 12.98 | 3.51 | 2.05 | 0.53 | 0.1629 | 0.3393 | 0.1368 | | | 2.68 | *0.38* |
| G066 | 48.17 | 1.65 | 17.37 | 9.04 | 0.17 | 1.82 | 10.59 | 4.55 | 2.07 | 0.72 | 0.1655 | 0.1704 | | | | 2.37 | *0.41* |
| G068 | 53.74 | 0.90 | 14.83 | 9.69 | 0.26 | 2.46 | 5.25 | 5.97 | 2.95 | 1.17 | 0.2861 | 0.0417 | | 1.08 | *0.07* | 2.05 | *0.13* |
| G069 | 53.39 | 0.81 | 15.11 | 9.81 | 0.25 | 2.71 | 5.52 | 6.37 | 2.75 | 0.78 | 0.2291 | 0.0171 | | 0.98 | *0.07* | 1.84 | *0.14* |
| G070 | 46.78 | 1.36 | 16.43 | 11.10 | 0.24 | 3.91 | 9.83 | 3.97 | 1.92 | 0.56 | 0.1611 | 0.2196 | | | | 2.30 | *0.50* |
| G071 | 51.70 | 1.24 | 16.17 | 9.01 | 0.19 | 2.23 | 7.49 | 5.09 | 3.11 | 0.82 | 0.2414 | 0.0848 | | | | 1.77 | *0.44* |
| G072 | 43.57 | 2.05 | 17.64 | 9.44 | 0.16 | 2.37 | 13.02 | 3.82 | 1.99 | 0.56 | 0.1955 | 0.3340 | | | | 3.29 | *0.41* |
| G073 | 44.04 | 2.00 | 17.13 | 9.73 | 0.17 | 3.79 | 12.48 | 3.49 | 1.90 | 0.56 | 0.1730 | 0.3085 | | | | 2.85 | *0.43* |
| G074 | 43.92 | 2.01 | 17.68 | 9.12 | 0.14 | 3.49 | 12.54 | 3.52 | 2.09 | 0.57 | 0.1945 | 0.3592 | | | | 2.95 | *0.41* |
| G075 | 47.24 | 1.91 | 17.21 | 9.95 | 0.18 | 3.62 | 9.98 | 4.34 | 2.53 | 0.69 | 0.1578 | 0.1577 | | 0.67 | *0.07* | 1.45 | *0.15* |
| G076 | 50.38 | 1.49 | 16.71 | 9.21 | 0.19 | 3.05 | 7.43 | 4.51 | 2.92 | 0.79 | 0.2496 | 0.0970 | | | | 2.00 | *0.43* |

**Table H.7:** EPMA data on melt inclusions, embayments, and matrix glass ($n$ = 169) *cont.*

| No. | $SiO_2$ | $TiO_2$ | $Al_2O_3$ | $FeO_T$ | MnO | MgO | CaO | $Na_2O$ | $K_2O$ | $P_2O_5$ | Cl | S | F | $Fe^{2+}/Fe_T$ | *s.d.* | VBD | *s.d.* |
|---|---|---|---|---|---|---|---|---|---|---|---|---|---|---|---|---|---|
| G077 | 48.91 | 1.86 | 17.10 | 9.99 | 0.19 | 3.55 | 8.08 | 5.15 | 3.12 | 0.85 | 0.1822 | 0.0384 | | | | 0.61 | *0.80* |
| G078 | 47.82 | 1.82 | 16.94 | 9.78 | 0.17 | 4.05 | 9.04 | 4.24 | 2.33 | 0.69 | 0.1535 | 0.0986 | | | | 1.89 | *0.46* |
| G079 | 46.76 | 1.79 | 16.72 | 10.25 | 0.20 | 4.09 | 9.78 | 4.18 | 2.23 | 0.68 | 0.1482 | 0.1496 | | | | 2.00 | *0.48* |
| G080 | 50.34 | 1.49 | 16.17 | 9.99 | 0.20 | 3.30 | 7.01 | 4.75 | 2.77 | 0.79 | 0.1572 | 0.0957 | | 0.80 | *0.07* | 2.18 | *0.13* |
| G081 | 46.35 | 1.41 | 17.55 | 9.94 | 0.19 | 4.35 | 10.59 | 3.50 | 2.21 | 0.60 | 0.1872 | 0.2310 | | 0.83 | *0.07* | 2.17 | *0.13* |
| G082 | 48.89 | 1.35 | 17.45 | 8.70 | 0.15 | 1.97 | 10.35 | 4.52 | 2.13 | 0.63 | 0.1507 | 0.1712 | | | | 2.42 | *0.40* |
| G083 | 48.80 | 1.35 | 17.76 | 8.39 | 0.16 | 2.00 | 10.78 | 4.50 | 2.05 | 0.55 | 0.1391 | 0.1762 | | | | 2.28 | *0.39* |
| G084 | 48.12 | 1.93 | 17.38 | 9.43 | 0.19 | 3.59 | 9.20 | 4.70 | 2.91 | 0.68 | 0.1505 | 0.0849 | | | | 1.07 | *0.53* |
| G085 | 44.41 | 1.85 | 15.74 | 9.60 | 0.16 | 4.71 | 11.76 | 3.31 | 1.78 | 0.51 | 0.1708 | 0.3266 | | 0.87 | *0.07* | 4.12 | *0.12* |
| G086 | 44.38 | 2.01 | 16.73 | 8.03 | 0.14 | 2.24 | 15.13 | 3.53 | 1.12 | 0.59 | 0.1834 | 0.3660 | | | | 3.81 | *0.35* |
| G087 | 44.13 | 1.96 | 16.79 | 8.68 | 0.15 | 3.05 | 13.30 | 3.40 | 1.80 | 0.58 | 0.1779 | 0.3514 | | | | 3.84 | *0.38* |
| G088 | 46.98 | 1.79 | 16.85 | 9.94 | 0.18 | 4.03 | 9.45 | 4.85 | 2.45 | 0.67 | 0.1494 | 0.1637 | | | | 1.65 | *0.48* |
| G089 | 47.04 | 1.73 | 17.20 | 9.20 | 0.19 | 4.08 | 9.70 | 4.21 | 0.92 | 0.19 | 0.1625 | 0.0417 | | | | 3.62 | *0.40* |
| G092 | 44.66 | 2.04 | 17.79 | 9.11 | 0.13 | 2.37 | 12.65 | 3.52 | 1.83 | 0.53 | 0.1690 | 0.2562 | | | | 3.35 | *0.40* |
| G094 | 48.81 | 1.56 | 17.57 | 9.41 | 0.16 | 3.61 | 8.22 | 4.26 | 2.45 | 0.69 | 0.2138 | 0.1672 | | | | 1.92 | *0.45* |
| G095 | 49.29 | 1.01 | 15.89 | 10.76 | 0.26 | 3.71 | 8.22 | 4.08 | 2.43 | 0.68 | 0.1867 | 0.1273 | | | | 2.21 | *0.49* |
| G096 | 48.97 | 1.12 | 15.31 | 11.22 | 0.25 | 3.95 | 9.14 | 3.94 | 2.18 | 0.64 | 0.1762 | 0.1303 | | | | 1.93 | *0.53* |
| G097 | 49.84 | 1.25 | 15.15 | 10.83 | 0.26 | 3.33 | 8.12 | 4.42 | 2.38 | 0.67 | 0.2008 | 0.1194 | | | | 2.24 | *0.49* |
| G098 | 44.52 | 1.89 | 16.11 | 9.44 | 0.17 | 4.13 | 12.06 | 3.22 | 1.92 | 0.55 | 0.1804 | 0.3225 | | 0.92 | *0.07* | 4.03 | *0.12* |
| G099 | 44.25 | 1.85 | 15.88 | 10.04 | 0.16 | 4.68 | 12.06 | 3.11 | 1.81 | 0.52 | 0.1448 | 0.3027 | | 0.76 | *0.07* | 3.69 | *0.13* |
| G100 | 44.21 | 2.03 | 16.76 | 9.16 | 0.14 | 3.04 | 13.11 | 3.53 | 1.90 | 0.54 | 0.1874 | 0.3508 | | | | 3.41 | *0.40* |
| G101 | 48.32 | 1.29 | 13.69 | 11.73 | 0.25 | 2.25 | 11.99 | 3.39 | 1.80 | 0.54 | 0.2115 | 0.2638 | | | | 2.81 | *0.52* |
| G102 | 46.65 | 1.85 | 17.41 | 10.10 | 0.18 | 3.56 | 9.96 | 4.25 | 2.27 | 0.59 | 0.1639 | 0.1704 | | | | 1.88 | *0.48* |
| G103 | 47.81 | 1.40 | 13.39 | 12.29 | 0.26 | 2.28 | 12.47 | 3.41 | 1.77 | 0.53 | 0.2267 | 0.2694 | | | | 2.52 | *0.55* |
| G104 | 47.10 | 1.78 | 17.28 | 9.59 | 0.19 | 2.71 | 10.91 | 3.88 | 1.99 | 0.57 | 0.1868 | 0.1928 | | | | 2.44 | *0.44* |
| G105 | 47.75 | 1.80 | 17.10 | 9.66 | 0.20 | 3.44 | 9.26 | 4.75 | 2.39 | 0.65 | 0.1874 | 0.1500 | | | | 1.76 | *0.47* |
| G106 | 43.99 | 1.84 | 16.91 | 11.25 | 0.21 | 6.27 | 10.91 | 3.51 | 1.85 | 0.55 | 0.1522 | 0.2868 | | | | 1.44 | *0.56* |
| G107 | 44.56 | 1.84 | 17.58 | 9.45 | 0.14 | 4.50 | 12.00 | 3.63 | 1.97 | 0.59 | 0.1677 | 0.2824 | | 0.84 | *0.07* | 2.45 | *0.13* |
| G108 | 46.17 | 1.97 | 18.64 | 8.14 | 0.13 | 2.36 | 11.92 | 4.09 | 2.20 | 0.58 | 0.1696 | 0.2468 | | | | 2.33 | *0.38* |

**Table H.7:** EPMA data on melt inclusions, embayments, and matrix glass ($n$ = 169) *cont.*

| No. | $SiO_2$ | $TiO_2$ | $Al_2O_3$ | $FeO_T$ | MnO | MgO | CaO | $Na_2O$ | $K_2O$ | $P_2O_5$ | Cl | S | F | $Fe^{2+}/Fe_T$ | *s.d.* | VBD | *s.d.* |
|---|---|---|---|---|---|---|---|---|---|---|---|---|---|---|---|---|---|
| G109 | 48.12 | 2.16 | 18.53 | 8.39 | 0.18 | 2.39 | 8.76 | 4.76 | 2.98 | 0.90 | 0.2184 | 0.1916 | | | | 1.63 | *0.42* |
| G110 | 50.17 | 1.26 | 16.67 | 10.11 | 0.23 | 2.80 | 8.27 | 4.88 | 2.27 | 0.70 | 0.1681 | 0.1183 | | | | 1.54 | *0.50* |
| G111 | 45.26 | 2.01 | 18.49 | 8.80 | 0.14 | 2.41 | 12.92 | 3.89 | 2.06 | 0.59 | 0.1996 | 0.2981 | | | | 1.99 | *0.42* |
| G112 | 47.42 | 1.78 | 17.17 | 10.25 | 0.20 | 4.04 | 9.80 | 4.47 | 2.47 | 0.65 | 0.1573 | 0.1669 | | | | 0.89 | *0.62* |
| G113 | 50.61 | 1.90 | 17.17 | 9.53 | 0.20 | 2.98 | 6.75 | 5.57 | 3.71 | 0.97 | 0.2308 | 0.0342 | | 1.17 | *0.07* | 0.67 | *0.21* |
| G114 | 49.06 | 1.94 | 17.90 | 9.33 | 0.20 | 3.24 | 7.82 | 5.31 | 3.37 | 0.82 | 0.1962 | 0.0778 | | | | 0.45 | *1.17* |
| G115 | 51.16 | 1.77 | 17.04 | 9.15 | 0.21 | 2.99 | 6.90 | 4.93 | 3.69 | 1.10 | 0.2037 | 0.0165 | | | | 0.53 | *0.86* |
| G116 | 47.98 | 2.00 | 16.79 | 10.90 | 0.20 | 3.67 | 9.16 | 4.49 | 2.94 | 0.72 | 0.1694 | 0.1409 | | | | 0.47 | *1.26* |
| G117 | 44.92 | 1.97 | 17.92 | 9.19 | 0.17 | 3.32 | 12.16 | 3.76 | 1.99 | 0.57 | 0.1751 | 0.2844 | | | | 2.41 | *0.42* |
| G118 | 50.52 | 2.25 | 16.38 | 9.92 | 0.30 | 3.91 | 8.24 | 5.26 | 0.56 | 0.18 | 0.0560 | 0.0285 | | | | 1.58 | *0.49* |
| G120 | 44.77 | 1.70 | 18.03 | 10.69 | 0.17 | 4.21 | 12.30 | 3.80 | 2.10 | 0.58 | 0.1716 | 0.2006 | | | | 0.76 | *0.71* |
| G121 | 46.05 | 1.23 | 17.68 | 10.65 | 0.19 | 4.14 | 11.57 | 4.06 | 2.27 | 0.62 | 0.2022 | 0.1849 | | | | 0.69 | *0.75* |
| G122 | 47.30 | 1.21 | 19.13 | 9.54 | 0.17 | 3.65 | 8.83 | 5.18 | 2.75 | 0.80 | 0.2275 | 0.1385 | | | | 0.69 | *0.69* |
| G123 | 47.79 | 1.16 | 19.43 | 9.40 | 0.17 | 3.50 | 8.19 | 5.35 | 2.93 | 0.84 | 0.2405 | 0.1279 | | 0.93 | *0.07* | 0.86 | *0.18* |
| G124 | 45.48 | 1.37 | 17.59 | 11.08 | 0.20 | 4.20 | 12.27 | 3.74 | 2.10 | 0.61 | 0.1797 | 0.1914 | | 0.99 | *0.06* | 0.98 | *0.17* |
| G125 | 50.05 | 1.89 | 17.15 | 9.13 | 0.17 | 3.41 | 6.90 | 5.41 | 3.63 | 1.09 | 0.2536 | 0.0268 | | 0.84 | *0.07* | 0.80 | *0.19* |
| G126 | 44.44 | 1.75 | 17.72 | 11.16 | 0.19 | 4.19 | 12.22 | 3.69 | 2.02 | 0.59 | 0.1764 | 0.2000 | | | | 1.02 | *0.63* |
| G127 | 44.78 | 1.54 | 17.46 | 11.54 | 0.19 | 4.17 | 12.43 | 3.83 | 2.04 | 0.57 | 0.1784 | 0.1997 | | 0.65 | *0.06* | 0.72 | *0.20* |
| G128 | 51.05 | 1.40 | 15.62 | 9.82 | 0.19 | 3.12 | 7.29 | 5.42 | 2.63 | 0.99 | 0.2062 | 0.0162 | | | | 1.49 | *0.49* |
| G129 | 44.63 | 1.98 | 18.01 | 9.62 | 0.16 | 3.02 | 11.99 | 3.55 | 2.02 | 1.01 | 0.1682 | 0.2633 | | | | 2.39 | *0.44* |
| G130 | 45.32 | 2.03 | 18.59 | 8.94 | 0.12 | 2.49 | 12.25 | 3.82 | 2.10 | 0.57 | 0.1823 | 0.2757 | | | | 2.24 | *0.41* |
| G131 | 47.54 | 1.77 | 17.40 | 10.50 | 0.19 | 3.51 | 9.74 | 4.49 | 2.72 | 0.69 | 0.1763 | 0.1366 | | | | 0.69 | *0.75* |
| G132 | 47.66 | 1.83 | 17.40 | 10.23 | 0.20 | 3.17 | 10.05 | 4.59 | 2.60 | 0.70 | 0.1698 | 0.1429 | | | | 0.78 | *0.67* |
| G133 | 49.58 | 2.22 | 16.98 | 8.74 | 0.16 | 3.49 | 7.05 | 5.44 | 3.66 | 1.15 | 0.2389 | 0.0426 | | | | 0.83 | *0.55* |
| G134 | 50.42 | 2.04 | 17.30 | 8.43 | 0.17 | 3.37 | 6.96 | 5.57 | 3.75 | 1.07 | 0.2283 | 0.0350 | | | | 0.44 | *1.11* |
| G135 | 50.40 | 1.79 | 16.67 | 9.54 | 0.20 | 3.31 | 6.89 | 5.36 | 3.55 | 1.11 | 0.2031 | 0.0232 | | | | 0.60 | *0.78* |
| G136 | 46.00 | 1.28 | 18.14 | 9.55 | 0.15 | 4.07 | 11.86 | 4.02 | 2.32 | 0.66 | 0.2001 | 0.1734 | | | | 1.03 | *0.54* |
| G138 | 49.14 | 1.09 | 15.95 | 11.09 | 0.25 | 3.52 | 9.22 | 3.90 | 2.02 | 0.61 | 0.1751 | 0.1569 | | | | 1.87 | *0.52* |
| G139 | 49.12 | 1.50 | 17.64 | 9.51 | 0.21 | 3.06 | 7.98 | 4.21 | 2.57 | 0.73 | 0.2039 | 0.1864 | | | | 2.06 | *0.44* |

**Table H.7:** EPMA data on melt inclusions, embayments, and matrix glass ($n$ = 169) *cont.*

| No. | $SiO_2$ | $TiO_2$ | $Al_2O_3$ | $FeO_T$ | MnO | MgO | CaO | $Na_2O$ | $K_2O$ | $P_2O_5$ | Cl | S | F | $Fe^{2+}/Fe_T$ | *s.d.* | VBD | *s.d.* |
|---|---|---|---|---|---|---|---|---|---|---|---|---|---|---|---|---|---|
| G140 | 51.50 | 1.51 | 15.78 | 8.98 | 0.22 | 2.18 | 9.16 | 4.64 | 2.79 | 0.83 | 0.2552 | 0.1249 | | | | 1.36 | *0.46* |
| G141 | 45.26 | 2.01 | 17.51 | 9.47 | 0.18 | 2.92 | 11.55 | 3.64 | 1.93 | 0.57 | 0.1604 | 0.2511 | | | | 3.06 | *0.42* |
| G142 | 47.18 | 1.88 | 17.84 | 9.92 | 0.16 | 2.94 | 10.12 | 4.32 | 2.32 | 0.64 | 0.1662 | 0.1823 | | | | 1.53 | *0.49* |
| G143 | 46.58 | 1.89 | 17.68 | 9.85 | 0.17 | 2.91 | 10.65 | 4.15 | 2.13 | 0.63 | 0.1557 | 0.2055 | | | | 1.99 | *0.46* |
| G144 | 47.50 | 1.87 | 17.67 | 9.40 | 0.20 | 2.56 | 9.99 | 4.23 | 2.21 | 0.69 | 0.1531 | 0.1659 | | | | 2.26 | *0.43* |
| G145 | 47.67 | 1.82 | 17.42 | 9.59 | 0.20 | 2.91 | 9.79 | 4.90 | 2.42 | 0.68 | 0.1624 | 0.1514 | | | | 1.51 | *0.48* |
| G146 | 44.07 | 2.03 | 17.45 | 10.09 | 0.18 | 3.20 | 12.45 | 3.56 | 2.05 | 0.56 | 0.1872 | 0.3275 | | | | 2.56 | *0.45* |
| G147 | 47.06 | 1.80 | 17.09 | 9.75 | 0.16 | 3.81 | 9.41 | 4.88 | 2.37 | 0.70 | 0.1386 | 0.1606 | | | | 1.77 | *0.47* |
| G148 | 47.36 | 1.87 | 17.18 | 10.31 | 0.19 | 3.82 | 9.33 | 4.82 | 2.95 | 0.71 | 0.1574 | 0.1076 | | | | 0.73 | *0.71* |
| G149 | 46.24 | 1.54 | 19.17 | 8.28 | 0.15 | 2.55 | 10.37 | 4.31 | 2.58 | 0.75 | 0.2581 | 0.3771 | | | | 2.36 | *0.38* |
| G150 | 45.65 | 1.98 | 18.77 | 9.40 | 0.16 | 2.27 | 12.17 | 3.84 | 1.86 | 0.56 | 0.1503 | 0.2663 | | | | 1.96 | *0.44* |
| G151 | 47.01 | 1.88 | 17.43 | 10.52 | 0.20 | 4.25 | 9.96 | 4.16 | 2.12 | 0.61 | 0.1581 | 0.1769 | | | | 0.95 | *0.61* |
| G152 | 46.27 | 1.86 | 18.39 | 9.03 | 0.14 | 3.07 | 11.08 | 4.16 | 2.02 | 0.63 | 0.1804 | 0.3281 | | | | 1.91 | *0.43* |
| G153 | 47.50 | 1.79 | 17.25 | 10.18 | 0.21 | 3.59 | 9.78 | 4.68 | 2.36 | 0.68 | 0.1618 | 0.1476 | | | | 1.07 | *0.56* |
| G154 | 52.44 | 1.62 | 16.15 | 8.82 | 0.18 | 2.78 | 6.78 | 5.10 | 3.28 | 0.98 | 0.1552 | 0.0100 | | | | 1.15 | *0.48* |
| G155 | 47.40 | 1.79 | 17.20 | 10.08 | 0.16 | 3.90 | 9.72 | 4.40 | 2.38 | 0.67 | 0.1681 | 0.1618 | | | | 1.27 | *0.53* |
| G156 | 47.90 | 1.72 | 17.38 | 9.86 | 0.16 | 3.98 | 9.27 | 4.49 | 2.45 | 0.67 | 0.1692 | 0.1614 | | | | 1.15 | *0.53* |
| G157 | 47.85 | 1.72 | 16.78 | 10.16 | 0.20 | 4.15 | 9.66 | 4.18 | 2.20 | 0.69 | 0.1578 | 0.1476 | | | | 1.37 | *0.52* |
| G158 | 47.28 | 1.80 | 17.24 | 10.02 | 0.19 | 4.07 | 9.50 | 4.34 | 2.45 | 0.67 | 0.1814 | 0.1681 | | | | 1.36 | *0.51* |
| G159 | 47.39 | 1.78 | 17.14 | 9.57 | 0.19 | 4.33 | 8.75 | 4.51 | 2.39 | 0.67 | 0.1532 | 0.1518 | | | | 1.99 | *0.45* |
| G160 | 46.66 | 1.49 | 15.74 | 11.89 | 0.19 | 2.85 | 11.59 | 3.73 | 1.72 | 0.47 | 0.1801 | 0.2061 | | | | 2.10 | *0.55* |
| G161 | 46.57 | 1.72 | 16.41 | 10.69 | 0.19 | 2.83 | 11.84 | 3.67 | 1.84 | 0.59 | 0.1511 | 0.2090 | | | | 2.15 | *0.49* |
| G162 | 46.80 | 1.84 | 16.82 | 10.43 | 0.20 | 2.79 | 11.11 | 4.04 | 1.96 | 0.60 | 0.1529 | 0.2212 | | | | 2.00 | *0.49* |
| G163 | 47.28 | 1.82 | 17.05 | 10.85 | 0.22 | 3.92 | 9.25 | 5.05 | 2.81 | 0.69 | 0.1585 | 0.1308 | | | | 0.43 | *1.49* |
| G164 | 44.46 | 2.19 | 18.35 | 8.25 | 0.14 | 2.17 | 13.92 | 3.72 | 1.93 | 0.60 | 0.1905 | 0.3747 | | | | 2.55 | *0.38* |
| G165 | 48.05 | 1.78 | 18.10 | 9.95 | 0.19 | 3.85 | 8.88 | 4.23 | 2.87 | 0.59 | 0.1649 | 0.0914 | | | | 0.78 | *0.65* |
| G166 | 44.42 | 1.96 | 16.84 | 9.05 | 0.15 | 3.01 | 13.02 | 3.48 | 1.99 | 0.59 | 0.1789 | 0.3282 | | | | 3.38 | *0.40* |
| G168 | 44.61 | 1.83 | 17.73 | 10.33 | 0.17 | 3.37 | 11.32 | 3.61 | 1.86 | 0.55 | 0.1751 | 0.2692 | | | | 2.79 | *0.46* |
| G169 | 44.74 | 1.83 | 17.58 | 10.26 | 0.15 | 3.44 | 11.28 | 3.46 | 1.83 | 0.55 | 0.1828 | 0.2696 | | | | 2.95 | *0.45* |

**Table H.7:** EPMA data on melt inclusions, embayments, and matrix glass ($n$ = 169) *cont.*

| No. | $SiO_2$ | $TiO_2$ | $Al_2O_3$ | $FeO_T$ | MnO | MgO | CaO | $Na_2O$ | $K_2O$ | $P_2O_5$ | Cl | S | F | $Fe^{2+}/Fe_T$ | *s.d.* | VBD | *s.d.* |
|---|---|---|---|---|---|---|---|---|---|---|---|---|---|---|---|---|---|
| G170 | 44.89 | 1.74 | 17.02 | 10.62 | 0.19 | 4.32 | 10.87 | 3.38 | 1.76 | 0.52 | 0.1548 | 0.2643 | | | | 2.82 | *0.47* |
| G171 | 47.89 | 1.65 | 17.22 | 10.38 | 0.21 | 3.25 | 8.94 | 5.08 | 2.49 | 1.09 | 0.2196 | 0.0787 | | | | 0.94 | *0.61* |
| G172 | 47.69 | 1.53 | 17.79 | 10.86 | 0.22 | 3.56 | 9.86 | 4.59 | 2.36 | 0.83 | 0.1765 | 0.0864 | | | | 0.21 | *-0.97* |
| G173 | 47.46 | 1.86 | 17.08 | 10.79 | 0.23 | 3.35 | 10.27 | 4.53 | 2.29 | 0.68 | 0.2227 | 0.1016 | | | | 0.68 | *0.78* |
| G174 | 47.85 | 1.37 | 17.62 | 10.94 | 0.23 | 3.27 | 9.85 | 4.88 | 2.38 | 0.80 | 0.2052 | 0.0914 | | | | 0.23 | *-1.36* |
| G175 | 49.93 | 2.01 | 16.75 | 9.19 | 0.18 | 3.07 | 6.47 | 5.75 | 3.93 | 1.15 | 0.2202 | 0.0269 | | | | 0.86 | *0.57* |
| G176 | 47.49 | 1.41 | 17.46 | 11.15 | 0.23 | 3.50 | 10.30 | 4.53 | 2.23 | 0.72 | 0.1890 | 0.0866 | | | | 0.36 | *2.86* |
| G178 | 47.69 | 1.87 | 16.92 | 10.49 | 0.20 | 3.92 | 9.95 | 3.88 | 2.28 | 0.65 | 0.1556 | 0.1106 | | | | 1.21 | *0.56* |
| G179 | 47.43 | 1.96 | 17.22 | 10.57 | 0.20 | 3.32 | 10.49 | 3.99 | 2.15 | 0.72 | 0.1368 | 0.1256 | | | | 1.07 | *0.59* |
| G180 | 48.65 | 1.84 | 17.15 | 10.53 | 0.21 | 3.81 | 9.64 | 3.81 | 2.28 | 0.76 | 0.1263 | 0.0524 | | | | 0.69 | *0.75* |
| G181 | 49.10 | 1.78 | 17.46 | 9.57 | 0.17 | 3.54 | 8.69 | 4.79 | 2.58 | 0.77 | 0.1267 | 0.0248 | | | | 0.91 | *0.58* |
| G182 | 47.10 | 1.80 | 17.14 | 10.09 | 0.16 | 3.58 | 10.04 | 4.56 | 2.33 | 0.62 | 0.1670 | 0.1738 | | | | 1.46 | *0.51* |
| G183 | 47.74 | 1.78 | 17.43 | 9.99 | 0.17 | 3.61 | 9.84 | 4.35 | 2.54 | 0.70 | 0.1915 | 0.1689 | | | | 0.96 | *0.58* |
| G184 | 47.43 | 1.88 | 17.29 | 10.16 | 0.19 | 3.27 | 9.90 | 4.42 | 2.55 | 0.67 | 0.1580 | 0.1525 | | | | 1.24 | *0.54* |
| G185 | 49.09 | 1.41 | 16.13 | 9.22 | 0.24 | 1.89 | 12.13 | 4.17 | 1.78 | 0.62 | 0.1944 | 0.2820 | | | | 1.91 | *0.44* |
| G186 | 46.46 | 1.76 | 17.50 | 9.49 | 0.17 | 1.92 | 12.40 | 3.80 | 1.97 | 0.55 | 0.1810 | 0.2756 | | | | 2.36 | *0.43* |
| G187 | 44.90 | 1.78 | 17.53 | 10.22 | 0.17 | 4.31 | 10.66 | 3.72 | 1.85 | 0.56 | 0.1596 | 0.2150 | | | | 2.61 | *0.46* |
| G188 | 45.50 | 1.83 | 17.96 | 10.09 | 0.16 | 3.31 | 10.93 | 3.70 | 1.89 | 0.58 | 0.1732 | 0.2038 | | | | 2.44 | *0.46* |
| G190 | 52.02 | 1.24 | 15.18 | 9.67 | 0.22 | 2.92 | 6.62 | 5.30 | 3.42 | 1.07 | 0.1230 | 0.0064 | | | | 1.45 | *0.49* |
| G191 | 44.39 | 1.87 | 17.36 | 9.35 | 0.15 | 3.77 | 12.08 | 3.48 | 1.96 | 0.54 | 0.1821 | 0.2903 | | | | 3.10 | *0.41* |
| G192 | 46.90 | 1.70 | 17.02 | 10.38 | 0.17 | 3.62 | 10.23 | 4.77 | 2.37 | 0.63 | 0.1689 | 0.1664 | | | | 1.19 | *0.55* |
| G193 | 44.75 | 2.02 | 18.08 | 9.19 | 0.18 | 2.22 | 12.74 | 3.60 | 1.91 | 0.60 | 0.1709 | 0.3210 | | | | 2.86 | *0.41* |
| G194 | 50.96 | 1.78 | 16.91 | 9.31 | 0.21 | 3.00 | 6.54 | 5.33 | 3.84 | 1.13 | 0.2197 | 0.0267 | | | | 0.47 | *1.09* |
| G195 | 47.55 | 1.70 | 17.83 | 9.76 | 0.17 | 3.41 | 8.74 | 4.67 | 2.60 | 0.73 | 0.1907 | 0.1768 | | | | 1.63 | *0.48* |

*Notes*: No. is the unique identifier for each glass (G) analysis (Table H.4). EPMA data collected as described in Section 6.3.4. Elements/oxides are given in wt%. Errors of one standard deviation (*s.d.*) given in *italics*.